Sensing of Human Micro-vibration Transmitted Along Solid Using Pico-Tesla Magneto-impedance Sensor (pT-MI Sensor)

K. Mohri[1, 2], Y. Nakamura[3], T. Uchiyama[4], Y. Mohri[5], Yu. Mohri[6], and Y. Inden[7]

[1]Nagoya Industrial Science Research Institute (NISRI), Nagoya 464-0819, Japan
[2]Aichi Micro Intelligent Co., Tokai 476-8666, Japan
[3]Yamazaki Mazak Optonics Co., Minokamo 505-0037, Japan
[4]Graduate School of Eng., Nagoya University, Nagoya 464-8603, Japan
[5]Graduate School of Eng., Meijo University, Nagoya 468-8502, Japan
[6]Graduate School of Arts, Meijo University, Nagoya 468-8502, Japan
[7]Graduate School of Med., Nagoya University, Nagoya 466-8550, Japan

Abstract— A new sensitive measurement method for the human micro-vibration (MV) is presented using a pico-Tesla resolution magneto-impedance sensor (pT-MI sensor). Various MV such as for the spinal-cord, the heart beat and following blood flow pulsation, and muscle tremors are stably detected by touching the skin position directly or indirectly via any solid transmission media to the sensor head which is dynamically rotated with more than 1.8 micro angular degree in the geomagnetic field. A blood flow promotion effect is detected using the MV sensing at the shoulder and the back of subjects after application of 6 Hz, 1 μT pulse magnetic field in 10 min.

1. INTRODUCTION

Since a finding by H. Rohracher in 1946 [1], the micro-vibration (MV) of the human skin have been widely investigated up to now comparing with the electroencephalogram (EEG) and electrocardiogram (ECG) with aspects of the physiology [2], the clinical application to the central nervous system (CNS) diseases [3], and the psychological application [4]. In the psychiatric clinical application, the frequency spectrum of MV is considered corresponding to that of the EEG such that normal subjects show the highest 8–13 Hz components as the α wave comparing with neurosis patients showing the highest 3–7 Hz components (θ wave) and schizophrenia patients showing the highest 14–40 Hz (β wave), respectively [3]. Recently, the MV attracts attention for measurements of bio signals at the spinal-cord and other various position of the human body such as the thenar and the parietal for the CNS diagnosis and personal monitoring of physiological and psychiatric conditions at the peripheral nervous system (PNS) such as median, ulnar, ischiatic and tibial nerves for dairy health in which application of the ECG and EEG is difficult in the sensitivity and instrument usability.

For measurement of the MV, the piezo-electric element acceleration sensor (PZA sensor) has conventionally been used which is adhered on the skin and detects the MV stress (force). Therefore, a signal to noise ratio (S/N) of the PZA sensor decreases when the MV displacement is measured by double time integration of the PZA output using analog integrator circuits with a low accuracy for ultra-low frequency range. On the contrary, we constructed a highly sensitive magnetic field sensor having 1 pico-Tesla (0.01 μG) resolution using the amorphous wire & CMOS IC Magneto-Impedance sensor ("pT-MI sensor") [5] for detection of the MV displacement. The MV displacement is measured when the skin displacement rotates the pT-MI sensor head with more than 1.8 micro angular degree in the geomagnetic field.

2. SPINE MICRO-VIBRATION MEASUREMENT

A spinal cord bio signal reflects the consciousness activity for control of four limbs motion with the voluntary muscle and the motion state of four limbs. The autonomous motion of inner organs with the smooth muscle also generates a bio signal at the spinal cord. However, measurement of the spinal cord bio signal is rather difficult using an electric method such as the ECG and EEG due to unmeasurable level of the electric signal. Figure 1 represents measured results of the spinal cord MV signal for a 68 aged healthy man quietly sitting on a stool using the pT-MI sensor in which a center position of the spinal column of the subject touches perpendicularly to the pT-MI sensor amorphous wire head via his cloths. The upper part is at the eyes open state and the lower part is at the eyes closed state, respectively. Sensor output represents as a magnitude of the magnetic field **Hz** due to a change of the sensor head rotation in the geomagnetic field of around ±50 μT, where 1 nT corresponds to a dynamic change of 1.8×10^{-3} angular degree.

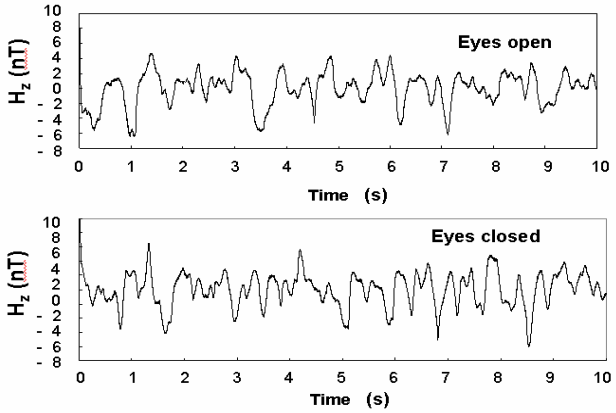

Figure 1: Measured MV time series of a 68 aged man at the center position of his spinal column by attaching perpendicularly to the pT-MI sensor head: the upper part is at eyes open state, and the lower part is at eyes closed state, respectively.

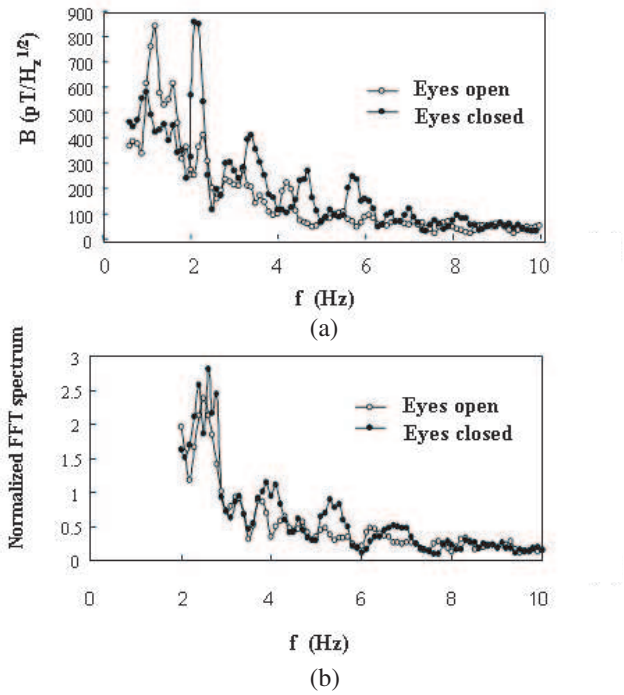

Figure 2: FFT frequency spectrum for the spinal cord MV time series at eyes open and eyes closed states: for 68 aged man in (a), and for 48 aged man in (b).

Figure 2 illustrates FFT frequency spectrum of the spinal cord MV time series for the 68 aged man shown in Figure 1 in (a), and for 48 aged man quietly sitting on a stool in (b). Both cases showed a remarkable change in the frequency spectrum while almost no change was observed in the amplitude of the MV time series. The magnitude of 3–7 Hz components increased with more than 2 times when eyes closed, which corresponds to the increase of the θ wave (4–6 Hz components) in the EEG when eyes closed due to decrease of the consciousness. Measured results suggest a possibility of detection of the consciousness degree at the spinal column position even on the cloths.

3. BLOOD-FLOW MICRO-VIBRATION MEASUREMENT

The MV originated by the blood flow pulsation is also detected using the pT-MI sensor as illustrated in Figure 3. A MV time series of a 68 aged man quietly sitting on a chair at his right-side shoulder on the cloths after a hard writing work showed a highest frequency spectrum component of around $6 \sim 7$ Hz in (a) in which his blood pressure was around 140 mmHg in the maximum and around 90 mmHg in the minimum. The MV time series changed as shown in (b) after sitting quietly in a

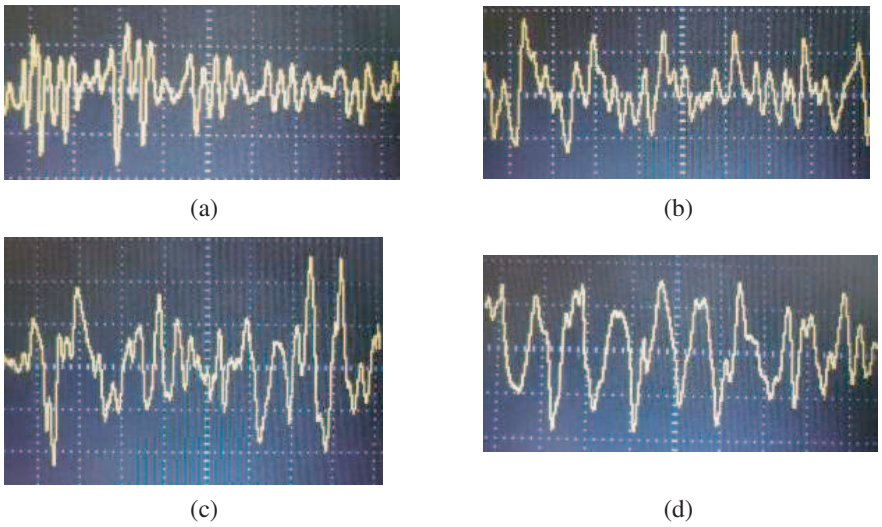

Figure 3: MV waveforms on the cloths of 68 aged man and 69 aged woman before and after exposure of 6 Hz, 1 μT magnetic field for 10 min showing the blood flow promotion. (a) MV at the right-side shoulder of 68 aged man: 10 nT/div, 0.5 s/div. (b) MV after exposure of 6 Hz, 1 μT magnetic field for 10 min: 10 nT/div, 0.5 s/div. (c) MV at the right-side back of 69 aged woman: 10 nT/div, 0.5 s/div. (d) MV after exposure of 6 Hz, 1 μT magnetic field for 10 min: 10 nT/div, 0.5 s/div.

1 m diameter coil generating 6 Hz, 1 μT magnetic field in 10 min which reveals a highest frequency spectrum component of around 1.2 Hz due to promotion of the blood flow possibly due to increase of the vascular softness. The blood pressure decreased to around 116 mmHg in the maximum and 74 mmHg in the minimum, respectively. Similar change of the MV was obtained for a 69 aged woman quietly sitting on a stool at her right-side back on the cloths showing the highest frequency spectrum component of around 4 Hz in (c). The MV time series changed as illustrated in (d) after sitting quietly in the same coil magnetic field in 10 min with the highest frequency spectrum component of around 1.1 Hz due to promotion of the blood flow. These measured results are estimated as a possible evidence of the Magneto-Protonics in which a ultra low frequency magnetic field promotes the bio-cell energy ATP production with activated proton in the cell water [5].

The effect of the magneto-protonics using 6 Hz, 1 μT in 10 min continued around 20 min, after that the MV time series returned from (b) and (d) to (a) and (c), respectively.

4. DISCUSSIONS

The origin of the MV has been widely discussed up to now with the cardio ballistic vibration and some automatic oscillation of muscles. Both cases seems to be appeared in Figure 3, where a cardiac ballistic accompanied tremor in (a), and an autonomic vibration in (b). Recently, mechanisms of automatic oscillation of the smooth muscle is clarified with a series of cell operations such that (1) a pacemaker neuron in the local neural network triggers to open Ca^{2+} channels with the active electric potential in the cell membrane, (2) Ca^{2+} connects with the protein Troponin-C, and then (3) smooth muscle tension starts [6]. The pacemaker neuron operation is modulated with the autonomous nervous system with the sympathetic and parasympathetic nervous system which is controlled with the brain function. The whole body surface is covered with the smooth muscle including the blood vessel muscle resulting the MV at arbitrary position of the whole body skin. We measured the MV at various positions of the skin of a 68 aged man confirming the highest frequency spectrum component changed from around $3 \sim 4$ Hz to $6 \sim 8$ Hz with tension at the voluntary muscle surface, while no change at the little muscle surfaces such as the glabellar with 2 Hz due to the eyeball oscillation, the elbow, the knee, the nose, and the malleolus with around 3 Hz. The MV is transmitted via any solid such as thin wood bars up to 4 m long, alloy rods and pipes, ceramics, cloths, plastics, and ice while no transmission in water and gases.

5. CONCLUSIONS

(1) The MV is stably detected using the pT-MI sensor in the geomagnetic field by touching a human skin position directly or indirectly via any solid to the sensor head.

(2) The spinal cord perpendicular MV time series changed its FFT frequency spectrum increasing the θ-wave component with eyes closed.
(3) The MV is transmitted along any solid but not in water and gases.
(4) Origin of the MV of smooth muscle is discussed considering Ca^{2+} oscillation.

Further MV measurements are needed for larger number normal and patient subjects for MV application to medical diagnosis.

REFERENCES

1. Rohracher, H., "Schwingungen des menschlichen organismus," *Anz. d. Wissench.*, Vol. 3, 230, 1946.
2. Gottlieb, S. and C. J. Lippold, "The 4–6 Hz tremor during sustained contraction in normal human subjects," *J. Physiol.*, Vol. 336, 499–509, 1982.
3. Rohracher, H. and K. Inanaga, *Die Mikrovibration*, Verlag Huber, Bern, 1969.
4. Reiffenstein, L., F. Zeits, and E. U. Angew, "Experimente uber die konditionierbarkeit der mikrovibration," *Psychol.*, Vol. 14, 483, 1967.
5. Mohri, K., M. Fukushima, Y. Mohri, and Yu. Mohri, "Detection of magnetization of 6 Hz, 10 μT magnetic field applied water using pT-MI sensor," *Progress in Electromagnetics Research Symposium*, Xi'an, China, March 22–26, 2010.
6. Torihashi, S., T. Fujimoto, and S. Nakayama, "Calcium oscillation linked to pacemaking of interstitia cells of Cajal," *J. Biol. Chem.*, Vol. 277, 19191–19197, 2002.

Numerical Modelling for Evaluation of Biological Effects Due to High Frequency Radiations in Indoor Environment

M. Cacciola, G. Megali, D. Pellicanò, M. Versaci, and F. C. Morabito
Department Via Graziella Feo di Vito, DIMET, University "Mediterranea" of Reggio Calabria
I-89100 Reggio Calabria, Italy

Abstract— Wireless personal communication is a rapidly expanding sector, particularly in the field of wireless local area networks. In an indoor wireless network system, an user can be close to the radiating antenna. Therefore, it is important to consider possible health hazards due to this type of exposure. This paper presents an approach to estimate and evaluate the main characteristics, i.e., Specific Absorption Rate and temperature rise, related to human exposure to electromagnetic field radiated by common wireless devices such as Wireless Access Points or Hot-Spot. The assessment is done numerically using two different approaches, respectively Ray-Tracing model and Finite Element Method. The general goal is to provide an efficient and sufficiently accurate method to assess human head exposure to electromagnetic fields at a frequency of 2.45 [GHz] and for different types of exposure conditions.

1. INTRODUCTION

In the recent years, wireless personal communications have registered a rapidly expansion in particularly in the field of wireless local area networks (WLANs). The existing applications of WLANs are spread spectrum systems operating at the Industrial Scientific Medical (ISM) frequency (2.45 [GHz]) and the Unlicensed National Information Infrastructure (U-NII) (5.5 [GHz]) [1]. Although this framework has given numerously advantages to people, the steadily increasing use of these new technologies may result in greater radio-frequency (RF) exposure in homes and work places. Health agencies have expressed their concern about cumulative exposure [2]. In this paper we focus our attention on the risks of human head exposure to such devices evaluating some important parameters, i.e., Specific Absorption Rate (SAR) and superficial temperature increasing. In this analysis, it is important to underline that WLAN systems use almost omni-directional antennas. The user can be close to the radiating antenna, where the ElectroMagnetic (EM) field assumes its highest values. As a consequence, it is important to consider the possible health hazard due to such systems and, in particular, to define criteria and thresholds for human safety [3]. Our goal is to verify if actual standards in wireless devices respect the Institute of Electrical and Electronic Engineers (IEEE), International Commission on Non-Ionozing Radiation Protection (ICNRIP) and European Committee for Electrotechnical Standardization (CENELEC) standards. Thus, our goal is to quantify the absorbed power by a biological organism exposed to a EM field and determine its distribution. For our purposes, we approached the problem in two steps. Firstly, we realized the indoor environment and set antenna specifications to evaluate EM field that propagates inside several scenarios. Afterward, retaining previously results, we exploited a FEM approach for simulating the EM absorption of a human head.

2. APPROACH TO THE IN-STUDY PROBLEM

Human tissues exposed to EM field absorb its energy and are subjected to different effects depending principally on its frequency. We focus our attention on effects produced by high frequency radiations, particularly at 2.45 [GHz] because of our interest in WLAN applications. The analysis can be consequentially reduced to the determination of $\mathrm{SAR} = \sigma\|\mathbf{E}\|^2/\rho$, expressing the power absorbed per unit of mass, where σ is the conductivity of human brain tissue, ρ the density, and $\|\mathbf{E}\|$ is the norm of the electric field. Studies about the interaction of EM field with human bodies were investigated since '80s when WLAN technology did not exist yet. Advances started in '90s with more performing computers and softwares [1]. Studies were focused on single parts of human body (e.g., the head) and not to the whole body since high frequency radiations. The main advantages of actual tools is the precise modeling of human head by importing MRI images and setting the parameters of different tissues. In addition, it has to model not only the direct radiation, but also the effects of scattering. FEM approach retrieve accurate results and can be exploited for multiphysics analysis, i.e., for studying the effects of EM field on the SAR and temperature of human heads. But, in presence of large scenarios, FEM is affected by high computational complexity. In order

Table 1: Parameters imposed for WLAN antenna.

Parameter		
	Omnidirectional	Unidirectional
Gain	5.0 (dBi)	6.0 (dBi)
Polarization	Vertical	Vertical
E-Plane half-power beamwidth	100.00	105.00
E-Plane first null beamwidth	170.00	165.00
H-Plane half-power beamwidth	90.00	90.00
H-Plane first null beamwidth	180.00	180.00

to decrease the computational load of FEM, we reduced the in-study environment, reproducing indoor scenarios in a Ray Tracing [4, 5] based environment, evaluating the EM field propagation and retaining the results for the subsequent FEM based step. Within Ray Tracing based software, we realized wireless antennas by referring to common commercial antennas. Moreover, we evaluated the EM field by placing different fictitious receivers, delimitating a volumetric area in which is supposed to stay the human head. In this way, we consider as much common situations as possible and provided a variety of results (see Table 1). Subsequently, we introduced our results in a FEM based software, where the human head has been imported by SAM Phantom provided by IEEE and IEC in their studies about SAR measurements [6–10]. Here, a cube has been modeled, containing the human head. Suitable boundary conditions have been applied to cube's surfaces, satisfying the theorem of equivalence [11] and exploiting the Ray Tracing numerical results. In this way, we have the same EM effects on the head without modeling the whole large scenarios within the FEM software. Thus, Maxwell equations have been exploited to calculate energy filed that invests the head model. Particularly, our model solves the vector Helmholtz equation everywhere in the domain for an imposed frequency:

$$\nabla \times \frac{1}{\mu_r} \nabla \times \mathbf{E} - k_0^2 \epsilon_r \mathbf{E} = 0 \tag{1}$$

where μ_r is the relative permeability (1.35 [S/m]), k_0 is the free-space wave vector, and ϵ_r is the permittivity for a vacuum (56). Constant values of brain tissues have been taken from Schmid studies [12, 13]. With this approach, we are able not only to evaluate EM field that invests the head model, but also the EM field inside the head. In this way we can determine also how radiation energy is absorbed by head tissues, thus calculating the SAR values for the head subdomain. The SAR value is an average over a region of either 10 [g] or 1 [g] of brain tissue, depending on national rules. This model does not calculate the average value and so it refers to the local SAR value. The maximum local SAR value is always higher than the maximum SAR value. In our case, we calculate SAR distribution in the head both on the surface and in depth. To evaluate temperature increases, instead, Bio-heat equation has been exploited [14]:

$$\nabla \cdot (-k \nabla T) = \rho_b c_b \omega_b (T_b - T) + Q_{met} + Q_{ext} \tag{2}$$

where ρ_b is the blood density, c_b the specific heat of blood, ω_b the perfusion rate of blood, T_b the blood temperature, Q_{met} the metabolic thermic source and Q_{ext} the spatial thermic source. Constant values were previously set referring to Schmid's works [12, 13]. Since our multiphysic approach, it has been possible to calculated directly the Q_{ext} within the FEM software package by referring to the Joule effect inside the head, exposed to EM radiation. The Bio-heat equation models the heating of the head with a heating loss due to the blood flow. This heat loss depends on the heat capacity and density of the blood, and on the blood perfusion rate. The perfusion rate varies significantly in different parts of the human body, and the Table 2 presents the values used in the present work. In order to numerically solve the approached problem, different meshes have been generated with different degrees of accuracy, depending on head sections we were interested in. But, for wave-propagation problem such ours, it is necessary to limit the mesh size according to the problem's minimum wavelength (typically five elements per wavelength to properly resolve the wave). Our main goal is to verify that the SAR values respect the international ICNRIP standards of 2 [W/kg] for head and body. Then, we want to establish the temperature increase respect to the measured SAR values. Post processing of data consists in plotting the different variables of

Table 2: Parts of human body and relatively perfusion rates.

Part	**Perfusion Rate**
Brain	$2 \cdot 10^{-3}$ [(ml/s)/ml]
Bone	$3 \cdot 10^{-4}$ [(ml/s)/ml]
Skin	$3 \cdot 10^{-4}$ [(ml/s)/ml]

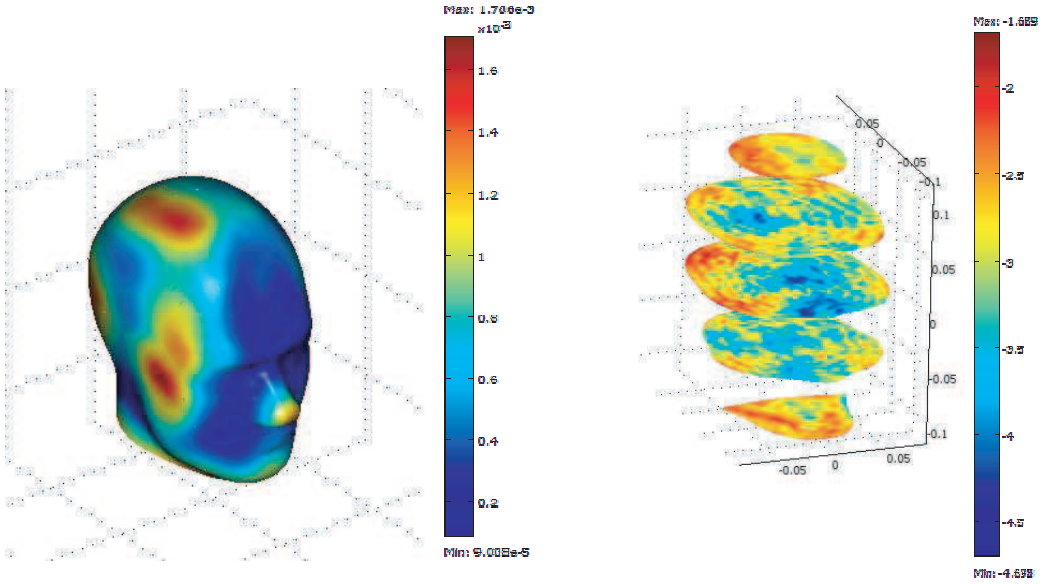

(a) Surface plot (b) Slice view

Figure 1: SAR distribution calculated within the FEM based software.

interest using slice plot or surface plot. Fig. 1(a) depicts a surface plot of temperature increase for a wireless antenna positioned at 50 [cm] at the right of the head, whist Fig. 1(b) shows the slice plot of the correspondent logarithmic value of SAR distribution in head model. Temperature plots draw the areas where the increase of temperature is concentrated and where the peak value is reached. SAR distribution, instead, allow to verify that limits are respected and study how the radiation penetrate in the model. For example, it is possible to see that the radiation penetrate mostly from the right (where the antenna is positioned), but other areas are interested in temperature increasing due to the presence of reflected radiations. Different simulations were carried out for analyzing the EM effects with the distance between the antenna and the head model. As we expected, both temperature and SAR decrease with the distance, and calculated values are influenced by reflected radiation. Particularly, there is a decrement of $5 * 10^{-4}$ [°C] for temperature and $17.5 * 10^{-4}$ [W/kg] for SAR. Now, we present results by varying the height of the antenna from the floor, with a fixed position of the head phantom, in order to study the variation of our parameters of interest according the height of the antenna. Figure 3 shows how values increase with the height of the antenna from the floor. This can be explained since the antenna is moving closer to the head model. But, when the antenna is moved over 175 [cm], the curve of temperature increases in spite of the increasing distance between the head and the antenna itself. In this case, please consider scattering phenomena due to the presence of roof. After, we focused our attention on the effect of 7 [cm]-thick brick wall, positioned between the antenna and the head model, in order to simulate the case of two rooms close each other. The presence of the wall causes a decrement of values of $4.5 * 10^{-4}$ [°C] for temperature and $1.5 * 10^{-3}$ [W/kg] for SAR, according to the fact that quite part of radiation is absorbed by the wall. Other cases with antenna positioned in different placed were examined, but never registering values higher than the standard limit. For instance, we examined the case of antenna positioning on a desk close to a user: in this case, simulations showed a temperature increment at the bottom part of the head near the chin, but values do not exceed standard limits. All these cases are referred to an omni-directional antenna. Considering directive antennas, peaks values of temperature and SAR are positioned in correspondence of axis of maximal directivity.

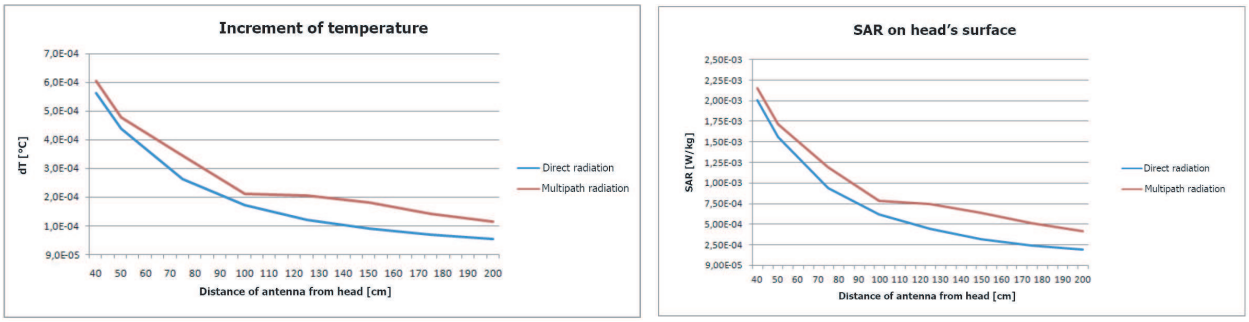

(a) Temperature (b) SAR

Figure 2: Trends of in-study quantities respect to the distance of analysis.

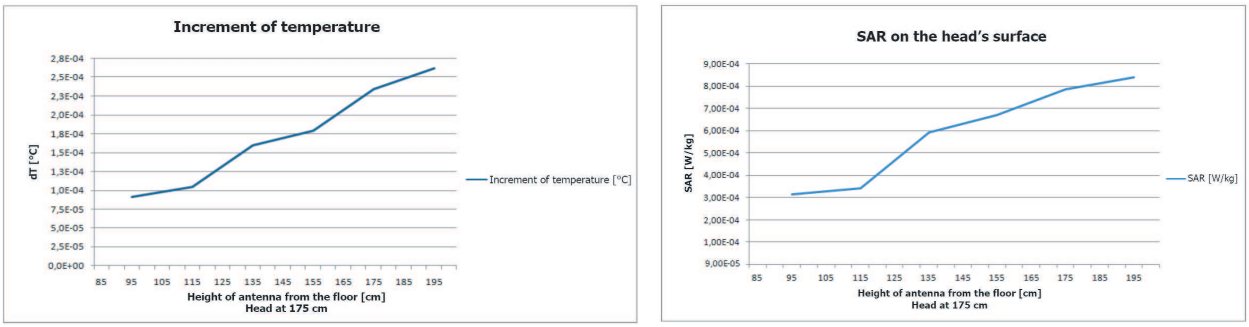

(a) Temperature (b) SAR

Figure 3: Trend of in-study quantities respect to the height of the antenna.

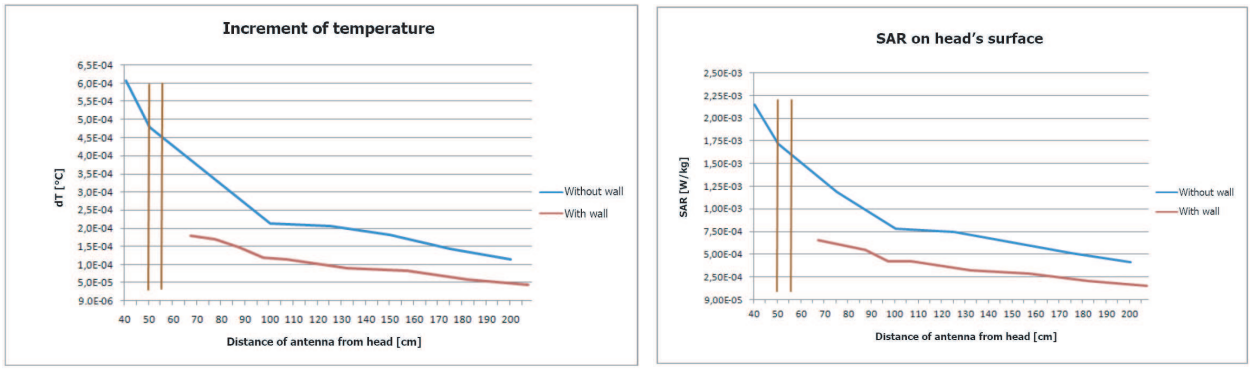

(a) Temperature (b) SAR

Figure 4: Trend of in-study quantities in presence of obstacles.

We considered also these cases, showing that calculated values were a little bit higher than the case of omni-directional antenna, and temperature increments are more concentrated in the areas of direct exposure. On the contrary, when user is not positioned in correspondence of the maximum directivity axis, omni-directional antennas have registered values higher than directive ones. For instance, in this last case, at a distance of 2.0 [m], the increment of temperature is $4 * 10^{-6}$ [°C] with a directive antenna and 10^{-5} [°C] with an omni-directional antenna.

3. CONCLUSIONS

In this study, we analyzed the effects of EM field exposure to human head from WLAN instrumentations like Access-Point or Hot-Spot. Our interest was focused on SAR evaluation and temperature increase due to EM-wave propagation. Based on numerical simulations carried out with a joint Ray-Tracing and FEM based approach, interaction between EM field and head model has been investigated. For this reason, different scenarios have been implemented. The proposed method provides a good overall accuracy in determining these effects, as our simulations demonstrate.

Numerical models remarked that the distance between antenna and user is the most important parameter for determining the intensity of SAR and temperature increments as well as the exposed area of the human head. Within this framework, we have analyzed field penetration: the radiation penetrates till 1 [cm] of deepness, specially when the antenna is positioned in front of the user (in this case, the eyes, for their composition, are the organs that absorb most part of radiation). Anyway, results of our simulations never overcame the thresholds imposed by international laws. The proposed study shows preliminary results, since we consider general cases. Further improvements could analyze particular situations and investigate other wireless technologies using different frequency ranges, in order to establish the impact on human safety.

REFERENCES

1. Bernardi, P., M. Cavagnaro, and S. Pisa, "Assessment of the potential risk for humans exposed to millimeter-wave wireless LANs: The power absorbed in the eye," *Wireless Networks*, Vol. 3, No. 6, 511–517, 1997.
2. Kuhn, S., L. Urs, A. Kramer, and N. Kuster, "Assessment methods for demonstrating compliance with safety limits of wireless devices used in home and office environments," *IEEE Trans. on Electromagnetic Compatibility*, Vol. 49, No. 3, 519–525, 2007.
3. Bernardi, P., M. Cavagnaro, S. Pisa, and E. Piuzzi, "SAR distribution and temperature increase in an anatomical model of the human eye exposed to the field radiated by the user antenna in a wireless LAN," *IEEE Trans. on Microwave Theory and Techniques*, Vol. 46, No. 12, 2074–2082, 1998.
4. Glassner, A., *An Introduction to Ray Tracing*, Academic Press, New York, NY, USA, 1989.
5. Shirley, P. and K. R. Morley, *Realistic Ray Tracing*, 2nd Edition, A. K. Peters, New Jersey, USA, 2001.
6. International Commission on Radiation Units and Measurements, "Radiation quantities and units," ICRU Report 33 (Bethesda, MD: ICRU), 1980.
7. Electronics Communications Committee (ECC) within the European Conference Postal and Telecommunications Administrations. "Measuring Non-Ionizing Electromagnetic Radiation (9 kHz–300 GHz)," 2003.
8. Human Exposure to Radio Frequency Fields From Handheld and Body-Mounted Wireless Communication Devices-Human Models, Instrumentation and Procedures, Part 1: Procedure to Determine the Specific Absorption Rate (SAR) for Handheld Devices Used in Close Proximity to the Ear (Frequency Range of 300 MHz to 3 GHz), IEC 62209 Part 1, 2005.
9. IEEE Recommended Practice for Determining the Peak Spatial-Average Specific Absorption Rate (SAR) in the Human Head From Wireless Communications Devices: Measurement Techniques, IEEE Standard 1528-2003, 2003.
10. Basic Standard for the Measurement of Specific Absorption Rate Related to Human Exposure to Electromagnetic Fields From Mobile Phones (300 MHz–3 GHz), CENELEC EN 50361: 2001. 2001.
11. Franceschetti, G., *Campi Elettromagnetici*, Boringhieri, Turin, Italy, 1983 (in Italian language).
12. Schmid, G., G. Neubauer, and P. R. Mazal, "Dielectric properties of human brain tissue measured less than 10 hours post-mortem at frequencies from 800–2,450 MHz," *Bioelectromagnetics*, Vol. 24, No. 6, 423–430, 2003.
13. Schmid, G., G. Neubauer, F. Alesch, and U. M. Illievich, "Dielectric properties of porcine brain tissue in the transition from life to death at frequencies from 800–1,900 MHz," *Bioelectromagnetics*, Vol. 24, No. 6, 413–423, 2003.
14. Penees, H. H., "Analysis of tissue and arterial blood temperatures in the resting human forearm," *J. Appl. Physiol.*, Vol. 1, 93–122, 1948.

Waveguide-based Applicators for Local Microwave Thermotherapy: Feasibility Study of Matrix Array Treatment

Barbora Vrbova and Jan Vrba
Department of Electromagnetic Field, Faculty of Electrical Engineering
Czech Technical University in Prague, Technicka 2, 166 27 Prague 6, Czech Republic

Abstract— In this article we deal with feasibility study of microwave cancer treatment by array of waveguide based applicators. Paper brings description of design, realization and evaluation of two, three or four microwave waveguide-based applicators set-up intended to treat malignant tumors, which are located on the surface of biological tissue. This tissue is in our work simulated by homogeneous agar phantom, which has similar dielectric and thermal characteristics as the biological tissue. In this article we use a composition of several applicators to enlarge the irradiated surface and to observe shapes of SAR distribution on a planar and cylindrical agar phantom.

1. INTRODUCTION

Hyperthermia is a thermotherapeutical method used for fulguration of cancerous cells by artificially increased temperatures due to electromagnetic field exposure [1]. Cancerous cells are less resistant to temperature load than healthy cells. When increasing temperature of treated area up to 45°C then the self protective mechanism of a cell increases the blood flow to create refrigeration of given tissue area and to prevent further warm up and damage of the tissue. The destruction of tumor cell with more than 2 cm in diameter occurs at 41°C, when the blood flow decreases by further temperature elevation. Thereafter the temperature in the tumor cells increases faster which leads to its destruction. Also the lack of nutrients in capillaries inside the tumors and its insufficient oxidation contributes to cell destruction. The size of hyperthermic dosage is given by conjunction temperature and time. The duration of a single treatment should not exceed 50 minutes [1]. One of the disadvantages is the generation of blisters and particularly the limitation of the area of effective treatment.

The hyperthermic system consists of high-performance generator controlled by a computer [2]. There is a high-frequency electromagnetic wave leading from the generator to the applicator by microwave coaxial feeder. A water bolus is placed between the applicator aperture and the tissue to prevent the formation of hot spots. The temperature of the tissue is measured by a thermo camera and by a system of thermal sensors. Biological tissue represents a lossy media for electromagnetic waves, that means that electromagnetic energy can create the temperature increase in the cancer tissue. The spatial configuration of the tissue temperature depends on the type of microwave applicator, on frequency of the electromagnetic wave and then on both dielectric and thermal parameters of the tissue in treated area. In our work we use frequency of 434 MHz, dedicated for medical purposes.

Technical purpose of this article is to describe the design, realization and evaluation of microwave applicators. There are different types of applicators generally known, however, this article focuses on two types for local thermotherapy — the microwave strip-line applicator with TEM mode and the microwave horn antenna applicator with TE_{10} mode. Both applicators are made from highly conductible material — copper.

2. DESCRIPTION OF HYPERTHERMIA TREATMENT APPLICATOR

Applicator is generally used for transition of high-frequency electromagnetic energy from generator through its aperture into the biological tissue (in our case using the frequency of 434 MHz) and ensures by medical doctors required distribution of temperature in given treated area. The electromagnetic energy enters into the applicator through co-axial feeding structure via N type connector. The applicator is filled with suitable dielectric material to prevent the reflection of energy back to generator.

Applicator this paper deals with consists of two parts/sections — firstly either waveguide section or stripline transmission line section and then follows stripline horn section. Coaxial feeder brings electromagnetic power firstly to either waveguide section or stripline transmission line section, from it then the power goes to stripline horn, which then provides very good impedance matching to biological tissue. It enables to adjust dimension of effective treatment area as well.

2.1. Microwave Stripline Applicator with TEM Wave

Dimensions of the discussed applicator have to be suitably chosen for radiation of TEM wave from stripline horn aperture at given working frequency 434 MHz. The upper and bottom plates of the horn aperture are made from highly conductible material (copper in our case) which is also used for the short-circuited part of stripline section. This ensures the excitation of TEM wave in our applicator. Whole stripline structure is made from one piece of material (copper, 1.5 mm thick).

The lateral sides of the applicator have to be made from dielectric materials, which are parallel with the electric field strength lines (E-field plane). Lateral sides of applicators are made of acrylic glass, which is 2 mm thick. The important parameter in waveguide design is the wave length of the applicator, which is dependent on dielectric permittivity:

$$\lambda_v = \frac{c_0}{f\sqrt{\varepsilon_r}} = \frac{3\times 10^8}{434\times 10^6\sqrt{78}} = 0.078\,\mathrm{m} \tag{1}$$

where $\varepsilon_r(\mathrm{H_2O}) = 78$.

The dimensions (width and heights) of stripline transmission structure are 50×30 mm and the length of both stripline and horn part of the applicator equals to wave length. The final dimensions [3] of horn aperture are 120×80 mm.

2.2. Microwave Waveguide Applicator with $\mathrm{TE_{10}}$ Mode

The dimensions of rectangular waveguide applicator are chosen suitably to create only the dominant $\mathrm{TE_{10}}$ mode. Cut-off frequency of $\mathrm{TE_{10}}$ mode has to be lower than the working frequency of the hyperthermia system and working frequency has to be lower than the cut-off frequency of the following $\mathrm{TE_{20}}$ mode.

In our case the width of waveguide is $a = 5$ cm and the height of waveguide is $b = 2.2$ cm. The elementary length of the applicator [4] has been chosen as $d = 6$ cm. For verification of creation of $\mathrm{TE_{10}}$ wave in the applicator with the above mentioned chosen parameters on a working frequency of 434 MHz we can use the following calculations:

$$f_{c,\mathrm{TE_{10}}} = \frac{c_0}{2a\sqrt{\varepsilon_r\mu_r}} = \frac{3\times 10^8}{2.0.05\sqrt{1.81}} = 333.3\,\mathrm{MHz}. \tag{2}$$

From $b < \frac{a}{2}$ following $\mathrm{TE_{20}}$ will be created:

$$f_{c,\mathrm{TE_{20}}} = \frac{k_c c_0}{2\pi\sqrt{\varepsilon_r\mu_r}} = \frac{c_0}{2\pi\sqrt{\varepsilon_r\mu_r}}\frac{2\pi}{a} = \frac{3\times 10^8}{0.05\sqrt{1.81}} = 666.6\,\mathrm{MHz}. \tag{3}$$

The previous calculations prove that at a working frequency of 434 MHz there will be only the dominant $\mathrm{TE_{10}}$ mode travelling along the waveguide. For this type of applicator we can calculate another important parameter — the wavelength:

$$\lambda_v = \frac{\lambda_0}{\sqrt{\varepsilon_r\mu_r}\sqrt{1-\left(\frac{f_c}{f}\right)^2}} = \frac{\frac{3\times 10^3}{434\times 10^6}}{\sqrt{1.81}\sqrt{1-\left(\frac{333.3\times 10^6}{434\times 10^6}\right)^2}} = 0.12\,\mathrm{m}. \tag{4}$$

3. SIMULATIONS

The stripline applicator has been simulated by the SEMCAD X EM Field simulator and the microwave waveguide applicator with $\mathrm{TE_{10}}$ mode in CST MICROWAVE STUDIO program.

3.1. The Impendant Adjustment of Applicators

For the ideal transition of electromagnetic energy from the generator to the applied load this transition has to be reflection-free. The length of stripline excitation probe has been by simulations chosen to be 27 mm and the distance from the short circuit plane 15 mm. The microwave waveguide applicator with $\mathrm{TE_{10}}$ mode has the same distance from the short circuit plane as the waveguide, however its length of excitation probe is 11 mm. The excitation probe of both applicators is made of copper wire with 2 mm in diameter. The stripline applicator has been tuned [3] to reflection parameter $S_{11} = -32.3$ dB in the SEMCAD program. Microwave waveguide applicator has been tuned [4] to $S_{11} = -26.92$ dB in CST program. The effective treatment depth 2 cm under the surface of agar phantom has been determined by these simulations.

4. MATRIX OF SEVERAL APPLICATORS

When the tumors cover large area of the human body, e.g., on the arm, leg, back or stomach area, we can use applicators with bigger dimensions or to create a matrix of several smaller applicators.

In our case we have concentrated on the second possibility — the matrix. In the following chapters we have concentrated on exposure of the planar and cylindrical agar phantom with a matrix of several applicators of the same type.

4.1. Composition of Several Applicators on Planar Phantom

In this article we focus on the matrix layout with 4 applicators of the same kind side by side on a planar agar phantom (Figure 1). For greater exposure area we used case of 4 microwave stripline applicators spaced into a 2×2 matrix placed on a planar agar phantom.

On the next picture is the layout of SAR distribution for microwave stripline applicator with TEM wave (Figure 2 left) and on next figure (Figure 2 right) we can observe the shape of the SAR distribution in the effective depth of about 2 cm below the surface of agar phantom.

In both cases, the spatial distribution of SAR distribution creates 2 maxima at the central vertical using 4 applicators. The applicator effective area is 40%, which was computed using the automatical script based on histogram fuzzification and k-means clustering [5].

4.2. Composition of Several Applicators on a Cylindrical Phantom

Cylindrical agar phantom was used to simulate the hand of the human body. Four microwave strip applicators were used to positioned within the cylindrical phantom with angular distance each from other 90° (Figure 3). Diameter of cylindrical agar phantom is 8 cm. Applicators are placed to cylindrical agar phantom, so that the electric field intensity vector is parallel to the longitudinal axis of the phantom.

In the middle of such a cylindrical phantom then there is a rounded shape SAR distribution, which is about half the diameter smaller than the phantom, and that is 4 cm as seen in the following figure (Figure 4).

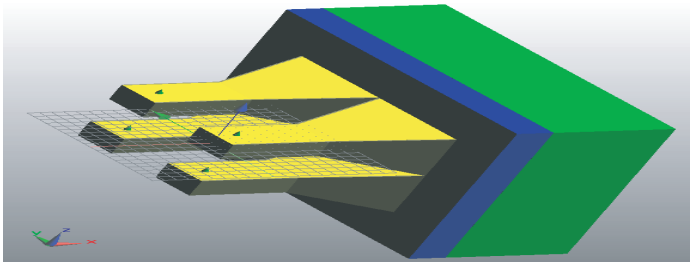

Figure 1: Matrix of four applicators.

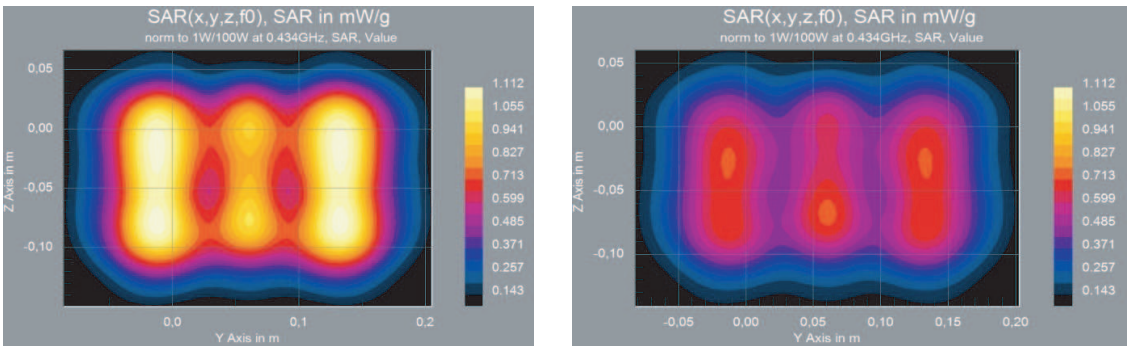

Figure 2: SAR distribution at a depth of 1 cm (left); SAR distribution at effective depth (right).

Composition of four applicators on a cylindrical phantom could be used in medical practice to treat tumors located in the hand. The change in amplitude or phase of individual applicators determines the shape of the SAR distribution in the place to be treated.

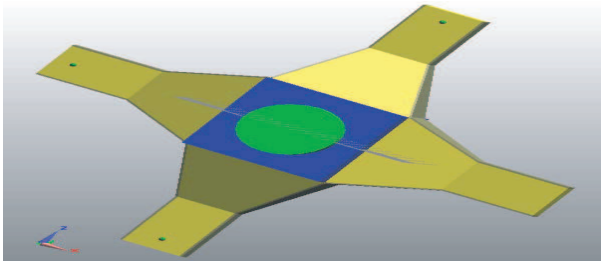

Figure 3: Composition of four applicators on cylindrical agar phantom.

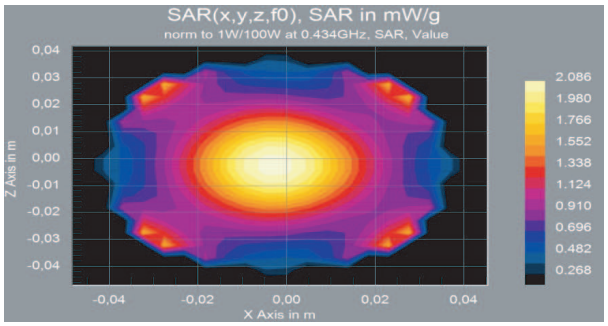

Figure 4: SAR distribution of four applicators.

5. CONCLUSION

The applicators used have been tuned to the suitable level of parameter S_{11}. Microwave stripline applicator reached the value of $S_{11} = -33.4\,\mathrm{dB}$ and waveguide applicator has been tuned to the value of $S_{11} = -23.23\,\mathrm{dB}$.

The applicators have been tested by thermo vision and their effective depth of effective heating remained at 2 cm under the tissue surface. Therefore the applicators are suitable for treatment of tumors located immediately under the surface of biological tissue.

ACKNOWLEDGMENT

This research is supported by Grant Agency of the Czech Republic, project: "Non-standard application of physical fields — analogy, modelling, verification and simulation" (102/08/H081) and the SEMCAD software was provided for SEMCAD X Student Research Award 2009 competition by Schmid & Partner Engineering AG (SPEAG).

REFERENCES

1. Falk, H. M. and R. D. Issels, "Hyperthermia in oncology," *International Journal of Hyperthermia*, Vol. 17, No. 1, 1–18, 2001.
2. Vrba, J., "Medical applications of microwaves," Praha, 2007, ISBN 978-80-01-02705-9.
3. Vrbová, B., "Microstrip applicator for local thermotherapy," Diploma Thesis, Praha, 2009.
4. Louda, V., "Matrix composition of waveguide applicators for local thermotherapy," Diploma Thesis, Praha, 2009.
5. Vorlicek, J. and J. Rusz, "Useful Matlab tool for radio frequency designer," *Technical Computing Prague 2009, Full paper CD-ROM Proceedings*, (P. Byron Ed.), Humusoft s.r.o. & Institute of Chemical Technology, Prague, 2009.

The Absorption Capability Measurements of the Free Space Absorbers

L. Nowosielski, M. Wnuk, R. Kubacki, and R. Przesmycki
Faculty of Electronics, Military University of Technology, 2 Gen. S. Kaliski str., 00-908 Warsaw, Poland

Abstract— The article refers to problems related to the absorption measurements of materials absorbing electromagnetic waves (Radar Absorbing Materials — RAM). The methodology of measurements, description of the original laboratory stand for measuring the absorption characteristics of the examined materials as a function of the testing signal angle of incidence and for measuring radar cross section (RCS) were introduced. Results of the above mentioned measurements for a metal plate covered with a sample absorbing material were also published.

1. INTRODUCTION

The article introduces the original methods of measurement and results of the measurement of the electromagnetic waves absorption level of the sample absorbing material. A metal plate (50×54) cm covered with absorbing material formed by a sponge saturated with graphite compounds was an object of research. As a reference material for evaluating absorption of the respective materials a metal plate not covered with absorbing material was used. Fig. 1 shows the appearance of the respective samples.

2. DESCRIPTION OF THE MEASURING METHOD

The article introduces two methods for measuring absorption level of the tested materials. One of them is based on a parameter, in the radar technique defined as a Radar Cross Section (RCS), which is a measure of the signal level refracted by an object at a given testing signal level. The second method is based on measuring absorption characteristics of the tested materials as a function of the testing signal angle of incidence.

2.1. The Measurement of the Characteristics of Tested Materials as a Function of the Testing Signal Angle of Incidence

The measurement of the characteristics of tested materials as a function of the testing signal angle of incidence is divided into two stages. The first stage is a reference measurement where a signal reflected from a reference plate, which wasn't covered by the absorbing material, is measured. In the second stage, the measurement of the signal level reflected from a plate covered with an absorbing material is performed. In the processed methods of measurement a relative difference between signals measured in these two stages is the measure of the material electromagnetic waves absorption.

The absorption level of different absorbing materials placed on the metal plate is evaluated comparing to the level of the signal reflected from a metal plate not covered with the absorbing material. The absorption level is heavily dependent on the angle of the plate surface covered with the absorbing material in relation to the transmitting (receiving) antenna aperture and the obtained results allow to estimate at which angle the maximum absorption value of the tested material can be achieved. Block scheme of the laboratory stand is shown in Fig. 2.

The measurement methodology is based on measuring the signal reflected from the surface covered with the tested absorbing material. The testing signal is generated by a microwave generator

Figure 1: An appearance of the respective testing samples. Sample No 1 — a metal plate not covered with absorbing material (reference material). Sample No 2 — a metal plate covered with absorbing material (RAM).

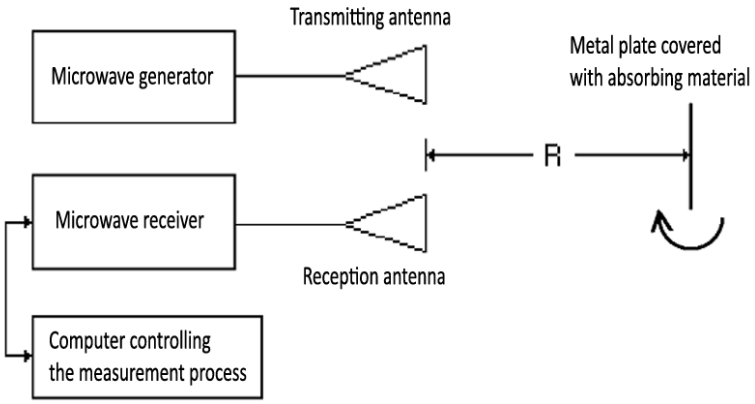

Figure 2: The block scheme of the laboratory stand.

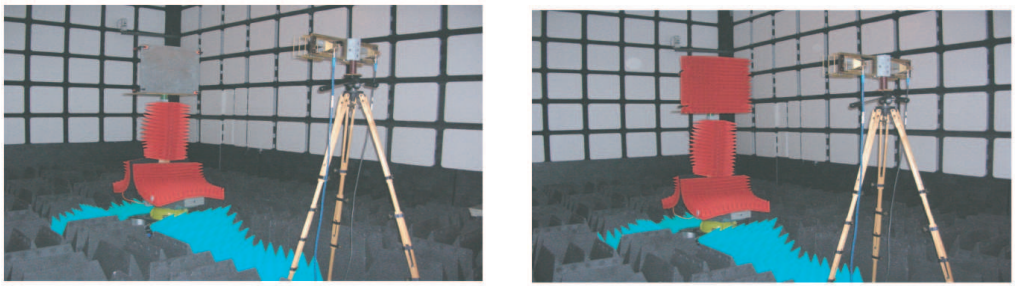

Figure 3: The view of the laboratory stand with a metal plate not covered (reference material) and covered with absorbing material.

with a horn transmitting antenna. The signal reflected from the surface covered with the absorbing material is measured with a horn reception antenna and a microwave receiver. Measurements are performed in an anechoic chamber covered with absorbers to avoid reflecting from the floor and walls (Fig. 3). Measurements involved the following equipment:

- high frequency signal source — HP 8362 series generator,
- high frequency amplifier, operating at the testing frequency (the frequency at which the absorbing material is tested),
- two horn antennas,
- Agilent 8511A frequency converter,
- HP 8530 microwave receiver,
- rotary head for measuring absorbing characteristics.

2.2. Radar Cross Section Measurement

The measurement of radar cross section of absorbing materials placed on the metal plate (50×54) cm was executed in a measuring arrangement shown in Fig. 2. In contrast to measuring the absorption characteristics of examined materials as a function of the testing signal angle of incidence, in case of the RCS measurement no change of the plate angle is performed.

A precise arrangement of the plate with absorbing material in relation to the testing signal source was performed by means of a laser beam placed on the transmitting (receiving) antenna aperture and a mirror placed on the plate with tested material. The arrangement of the transmitting (receiving) antenna in such a way that the generated laser beam reflects from the mirror and covers the point where it was originally generated, proves that the aperture of the transmitting (receiving) antenna is parallel to the surface of the metal plate covered with absorbing material.

The radar cross section defines a measure of the electromagnetic wave reflection from a given object. A theoretical value of RCS for a flat, rectangular and perfectly reflecting surface can be

evaluated with the following equation [2]:

$$\sigma = \frac{4\pi\, a^2\, b^2}{\lambda^2}, \tag{1}$$

where:

σ — radar cross section in [m^2],
λ — wavelength in [m],
a, b — height and width of the rectangular reflecting surface in [m].

σ value for a metal plate reflecting the incident electromagnetic wave can be calculated with the following equation [2]:

$$\frac{P_{RX}}{P_{TX}} = \sigma \frac{G^2\lambda^2}{(4\pi)^2\, R^4}, \tag{2}$$

where:

P_{RX} — power of the signal reflected from a metal plate in [W],
P_{TX} — power of the transmitted signal in [W],
G — antenna gain (transmitting and receiving antenna have the same value of gain),
R — antennas distance from the metal plate in [m].

In order to evaluate σ value, P_{RX} value of the signal refracted from the metal plate should be measured as well as P_{TX} power of the transmitted signal value. For evaluating σ value also K coefficient is necessary:

$$K = \frac{G^2\lambda^2}{(4\pi)^2\, R^4}, \tag{3}$$

The above dependency is a component part of Eq. (2). K value defines parameters of the measuring system and depends on the testing signal wavelength. Having a reference object with a known σ value, K coefficient value can be evaluated with the following dependency:

$$\frac{P_{RX}}{P_{TX}} = \sigma \cdot K, \tag{4}$$

In the above dependency P_{RX} and P_{TX} values are obtained as a result of measuring the reference object. In this case a metal plate (50×54) cm not covered with RAM (radar absorbing materials) was used as a reference object. σ parameter value for the tested metal plate should be evaluated with Eq. (1).

K coefficient value describing the laboratory stand with the metal reference plate with σ value as well as P_{RX} and P_{TX} values obtained from measurements, should be evaluated from Eq. (4) after executing the following transformations:

$$\begin{aligned} &\frac{P_{RX}}{P_{TX}} = \sigma \cdot K / 10\log \\ &10\log\frac{P_{RX}}{P_{TX}} = 10\log\sigma + 10\log K \\ &10\log K = 10\log\frac{P_{RX}}{P_{TX}} - 10\log\sigma \\ &K = 10^{\frac{10\log\frac{P_{RX}}{P_{TX}} - 10\log\sigma}{10}} \end{aligned} \tag{5}$$

K values, characteristic for the measuring system, were used to count σ_{RAM} parameter value for the metal plate (50×54) cm covered with RAM. Eq. (4) should be used to count σ_{RAM} parameter

after executing the following transformations:

$$\begin{aligned} \frac{P_{RX}}{P_{TX}} &= \sigma_{RAM} \cdot K / 10\log \\ 10\log\frac{P_{RX}}{P_{TX}} &= 10\log\sigma_{RAM} + 10\log K \\ 10\log\sigma_{RAM} &= 10\log\frac{P_{RX}}{P_{TX}} - 10\log K \\ \sigma_{RAM} &= 10^{\frac{10\log\frac{P_{RX}}{P_{TX}} - 10\log K}{10}} \end{aligned} \tag{6}$$

In the above equation the value calculated with Eq. (5) should be taken for K. σ_{RAM} parameter values obtained for the metal plate (50×54) cm, covered with RAM are given in the table with measurement results in the next point.

3. MEASURING RESULTS

3.1. The Absorption Characteristics of the Examined Materials as a Function of the Testing Signal Angle of Incidence

The results of the absorption characteristics measurements of the tested material as a function of the testing signal angle of incidence and its frequency are presented below. The following characteristics are presented in polar coordinates (Fig. 4).

Because of the laboratory stand construction, the tested material was illuminated by the transmitting antenna only in range of the rotary head turning angle $(-90° \div 90°)$. On the basis of the obtained measuring results it should be found that the bigger the testing signal angle of incidence on the plate covered with a tested material is, the bigger refraction it proves. The phenomenon of absorption is dominating for parallel angles of the transmitting (receiving) antennas aperture and the surface covered with the tested material. For this value of the angle the absorption phenomenon is dominating. In relation to the above, the absorption readings taken are representative results, which can be used for comparative analyzing using other materials. The value of absorption describes the difference between two signals: reflected from the tested material and the metal plate. For the signal's frequency of 3 GHz it is 12 dB, while it's 11 dB for 4 GHz.

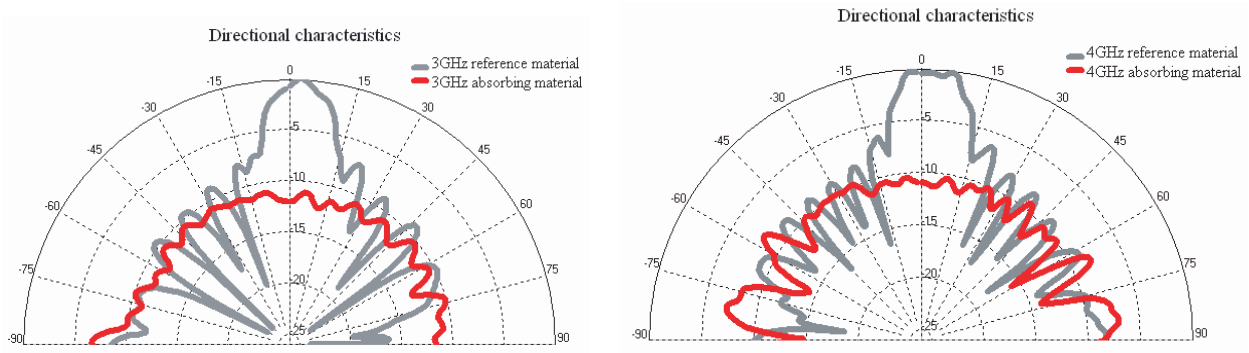

Figure 4: The absorption characteristics of the examined materials as a function of the testing signal angle of incidence in polar coordinates.

Table 1: 1: The value σ_{RAM} and indirect parameters for sample No. 2 and the measurement distance $R = 2$ m.

Testing signal frequency f	[MHz]	2000	2500	3000	3500	4000	4200
Radar cross section σ of a rectangular, perfectly reflecting surface	[m^2]	40.69	63.59	91.56	124.62	162.78	179.46
Radar cross section σ_{RAM} for a metal plate covered with RAM	[m^2]	5.62	2.11	1.53	1.50	1.45	1.24

3.2. Radar Cross Section Measurement

The results of the radar cross section measurements are presented in Table 1. The measures were taken for the rotary head angle where the phenomenon of absorption dominates. The presented results allow to conclude that RCS decreases along with the tested signals frequency increase.

4. CONCLUSIONS

The standpoint for measuring material absorption described in this article can be efficiently used for comparative testing of different materials. The presented measures of absorption fairly define electromagnetic waves absorption of varying materials.

REFERENCES

1. Eugene, F. K., F. S. John, and T. T. Michael, *Radar Cross Section*, Scitech Publisching, INC, 2004.
2. Mirabel, C. R., M. M. Inacio, and F. Roselena, "Radar cross section measurement (8–12 GHz) of magnetic and dielectric microwave absorbing thin sheets," *Revista de Fisica Aplicada e Instrumentacao*, Vol. 15, No. 1, 2002.

The Expanded Uncertainty for Radio Frequency Immunity Testing

Rafał Przesmycki, **Leszek Nowosielski**, **Marian Wnuk**, **and Roman Kubacki**
Faculty of Electronics, Military University of Technology, 2 Gen. S. Kaliski str., Warsaw 00-908, Poland

Abstract— This paper is concerned with the problems of electromagnetic compatibility for RF (Radio Frequency) immunity testing according to the EN 61000-4-3 standard. The measurement uncertainty budget calculation techniques recommended in standardizing documents are barely described and very often they are not adapted to the specific needs of tests performed within the scope of EMC (Electromagnetic Compatibility). The authors focused attention on presentation of the measurement uncertainty budget calculation algorithm. The information related to measurement uncertainty of RF signal test level setting during the RF immunity test in an anechoic chamber are presented. The example of uncertainty budget for laboratory stand used by accredited EMC laboratory for RF immunity testing of information technology equipment is precisely described too.

1. INTRODUCTION

EMC (Electromagnetic Compatibility) testing is a process of taking measurement. Whenever you measure a quantity, the result is never an exactly correct value: The value you report will inevitably differ from the true value by some amount, hopefully small. This applies whether you are measuring length, voltage, time or any other parameter, complex or simple. EMC measurement are no different in this respect. But the subject of measurement uncertainty in EMC tests is more complex than most.

EMC test standards include a specification of what has to be measured and define a method for measuring it. For any given electromagnetic field strength measurement method, there are usually several sources of measurement uncertainty, although only one or two may dominate. Each individual source has to be analysed. A values to each of these sources have to be assigned and then summed using an appropriate manner to give the total measurement uncertainty.

2. IMMUNITY TEST ACCORDING THE EN 61000-4-3 STANDARD

The EN 61000-4-3 standard is applicable to the immunity requirements of electrical and electronic equipment to radiated electromagnetic energy. It establishes test levels and the required test procedures.

Above standard requires a radiated RF field generated by an antenna in a shielded anechoic chamber enclosure using a pre-calibrated field, swept from 80 MHz to 1000 MHz with the step size not exceeding 1% previous frequency and dwell time sufficient to allow the EUT (Equipment Under Test) to respond. The antenna faces each of the four sides of the EUT in each polarization, hence there are minimum 8 tests in all. In order to assure of the generated field uniformity the anechoic chamber is required or another alternative test sites. Severity levels are unmodulated and has to be level 1, 3 or 10 V/m. The actual applied signals is modulated to 80% with a 1 kHz sine wave.

3. MEASUREMENT UNCERTAINTY COMPONENTS OF THE MEASURAND

The measurand is the hypothetical test field strength (without an EUT) at the point of the UFA (Uniform Field Area) selected according to the field calibration process. The diagram shown in Figure 1 describes the measurement uncertainty components on the resultant uncertainty in level setting.

The diagram applies to calibration and test processes and it is not exhaustive. The most important measurement uncertainty components have to be selected for the uncertainty budget. As a minimum, the components listed in the example uncertainty budget (see Chapter 5) shall be used for the calculation of the uncertainty budgets in order to get comparable budgets for different test sites or laboratories. It is noted that a laboratory may include additional components in the calculation of the measurement uncertainty, on the basic of its particular circumstances.

4. UNCERTAINTY BUDGET

An uncertainty budget lists the most likely error sources and individually estimates their limits of uncertainty and probability distribution. To establish this list you need a reasonable degree of

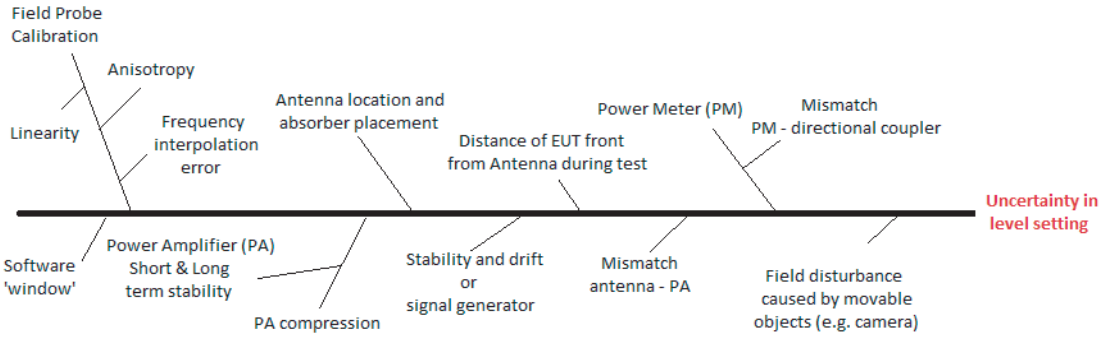

Figure 1: Measurement uncertainty components for immunity test.

familiarity with the test method and the test instrumentation. When creating the list, it is better to be inclusive rather than exclusive of the components — if a particular component turns out to be negligible, it is still better to acknowledge its presence and include it at a low value than to ignore a component that may increase of the resultant uncertainty significantly. Once you have analyzed each component, the individual components are summed to produce the final result for the measurement. Un during the analysis, sources of uncertainty can be grouped into one of two categories A or B based on their method of evaluation.

4.1. Type a Method

Type A method evaluation is done by calculation from a series of repeated observations, using statistical methods, and resulting in a probability distribution that is assumed to be normal. For any measurement method, you should make a type A evaluation on that procedure and configuration that is typically involved in the test. This will give a measure of the likely contribution due to random fluctuations, for instance uncontrolled variations in antenna position, the test environment, or losses through cable re-connection.

In general case, you will be testing many different types EUT and it is rarely practical to perform many repeat measurements on each type. Therefore the Type A method that is analyzed in this way does not include a contribution for random variation due to EUT, but such variations from all other sources in the measurement set-up can be determined. On the other hand, if you will always be testing one type of EUT — for instance in the production control environment — then the repeated measurements can be done on this EUT and the evaluation then does include this source. A determination of the uncertainty due to random contributions is given by the standard deviation $s(q_k)$ of a series of n measurements q_k:

$$(q_k) = \sqrt{\frac{1}{n-1}\sum_{k=1}^{n}(q_k - Q)^2} \tag{1}$$

where Q is the mean value of the n measurements. The $s(q_k)$ value is used directly for the uncertainty budget calculations due to random contributions, excluding the effects of the EUT, when only one measurement is made on the EUT. But if the result of the measurement is close to the limit, it is advisable to perform several measurements on the EUT itself, at least for frequencies that are critical. In this case, the uncertainty is reduced in the way described by the following formula:

$$s(Q) = \frac{s(q_k)}{\sqrt{n}} \tag{2}$$

So that four repeat measurement on the EUT, will halve the uncertainty due to random effects. Note that this has no effect on other contributions, which are analyzed as Type B factors. If these dominate the uncertainty budget, then it is questionable whether making repeat measurements on the EUT, to reduce the random contribution, is worthwhile.

4.2. Type B Method

Type B evaluation is done by means other that used for Type A, for example, data from calibration certificates, previous measurements, manufacturers specifications or an understanding of

instrument behavior, or other relevant information. It applies to systematic effects which remain constant during the measurement but which may change if the measurement conditions, method or equipment are altered. Equipment calibration, mismatch errors, and due to constant deviations in the physical set-up are examples of these effects. If possible and practical, corrections for systematic effects should be applied.

A typical example of such a case would be where the measuring equipment calibration certificate gives a value for the correct reading for a given indication. You could then add this correction to the result so that only the uncertainty of the calibration itself would be left to account for. In practice, it is usually simpler to leave such errors uncorrected and use an overall value either from the manufacturer's specification — or take a maximum error from the calibration certificate, extended by the calibration uncertainty, and apply that.

Other Type B contributions, not derived from calibration data or similar, have to be calculated from a knowledge of the nature of the test, often stated in simplified form. For instance, deviations in field strength due to errors in antenna separation are normally assumed to follow a $1/r$ law, and so you can calculate a contribution based on the degree of control exercised over the separation distance. Strictly, the $1/r$ assumption is not properly justified, but many such simplifications are necessary to keep uncertainty calculations in the realm of practicability.

4.3. Summation of Two Methods

Type A contributions are already in the form of a standard uncertainty and need no further treatment. Type B contributions need a further step before they can be summed. This involves determining the appropriate probability distribution for each contribution.

For EMC tests, the relevant probability distributions are: **Normal:** Uncertainties derived from multiple contributions, for example calibration uncertainties with a statement of confidence; **rectangular:** Equal probability of the true value lying anywhere between two limits, for example manufacturer's specifications; **U-shaped:** Applicable to mismatch uncertainty, where the probability of the true value being close to the measured value is low; **triangular:** The probability of the true value lying at the point between two limits increases uniformly from zero at the extremities to the maximum at the center; should be assigned where the majority of the values between the limits lie around the central point.

The distributions describes the variation in probability of the true value lying at any particular difference from the measured result. It's actual form will often be unknown, and an assumption has to be made, based on prior knowledge or theory, that it approximates to one of the common forms. You can then calculate the standard uncertainty $u(x_i)$, for the assigned form from simple expressions (see Figure 2). If a particular uncertainty contribution is not in the same units as the required total uncertainty then strictly speaking the contribution should be converted using a

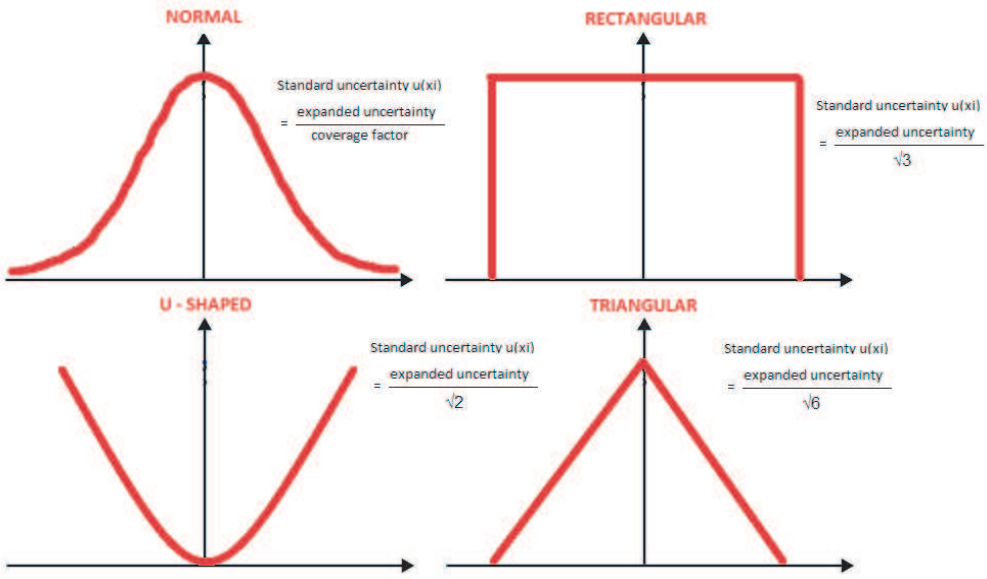

Figure 2: Probability distribution.

"sensitive coefficient" c_i. This then gives a series of output contributions $u_i(y)$. Practically, it is easier to leave the sensitive coefficients at unity and quote all uncertainty contributions in the same units, so that summation becomes straightforward. A rigorous approach would in many cases need a non-linear sensitivity coefficient, for which the computational effort is rarely justified. Once each contribution has been converted as above to a standard uncertainty, the combined uncertainty $u_i(y)$, is obtained for m contributions by taking the square root of the sum of squares of the individual standard uncertainties:

$$u_c(y) = \sqrt{\sum_{i=1}^{m} u_i^2(y)} \tag{3}$$

Finally, you have to calculate the expanded uncertainty U. This defines an interval about the measured result that will include the true value with a specified level of confidence. The interval is greater than the standard uncertainty so there is a higher probability that it encompasses the value of the measurand. The expanded uncertainty is obtained by multiplying the combined standard uncertainty by a coverage factor k, which is set to 2 for a level of confidence of 95%. Other confidence levels can be obtained with different values of k, but the value 95% is usual for industrial and commercial measurement.

5. CALCULATION EXAMPLES FOR EXPANDED UNCERTAINTY

In this chapter is described example of how to set up an uncertainty budget for EMC immunity tests. It must be recognized that the contributions that apply for UFA calibration and for immunity test process may not be the same. This leads to different uncertainty budget for each process. Tables 1 and 2 give examples of an uncertainty budget for level setting. The uncertainty budget consist of two parts, the uncertainty for calibration and the uncertainty for test.

In above tables are used fallows symbols: **FP** is a combination of calibration uncertainty, field probe unbalance (anisotropy), field probe frequency response and temperature sensitivity. Normally this data can be obtained from the probe data sheet or calibration certificate. $\mathbf{PM}_{cal}$ and $\mathbf{PM}_{test}$ are the uncertainty of the power meter, including its sensor, taken from either the manufacturer's specification (and treated as a rectangular contribution) or a calibration certificate (and treated

Table 1: Example of uncertainty budget for calibration process.

Symbol	Uncertainty Source X_i	$U(x_i)$	Unit	Distribution	Divisor		$u(x_i)$	Unit	c_i	$u_i(y)$	Unit	$u_i(y)^2$
FP	Field Probe Calibration	1,90	dB	normal	2	2	0,95	dB	1	0,95	dB	0,90
PM_{cal}	Power Meter	0,30	dB	rectangular	√3	1,73	0,17	dB	1	0,17	dB	0,03
PA_{cal}	PA rapid gain variation	0,20	dB	rectangular	√3	1,73	0,12	dB	1	0,12	dB	0,01
SW_{cal}	SW leveling precision	0,60	dB	rectangular	√3	1,73	0,35	dB	1	0,35	dB	0,12
					$\sum u_i(y)^2$							1,07
					$u_c = \sqrt{\sum u_i(y)^2}$							1,03
					Expanded Uncertainty for k = 2 (level of confidence of 95%)							2,07

Table 2: Example of uncertainty budget for level setting.

Symbol	Uncertainty Source X_i	$U(x_i)$	Unit	Distribution	Divisor		$u(x_i)$	Unit	c_i	$u_i(y)$	Unit	$u_i(y)^2$
CAL	Calibration	2,07	dB	normal	2	2	1,04	dB	1	1,04	dB	1,07
AL.	Antenna location variation and absorber placement	0,38	dB	k = 1	1	1	0,38	dB	1	0,38	dB	0,14
PM_{test}	Power Meter	0,30	dB	rectangular	√3	1,73	0,17	dB	1	0,17	dB	0,03
PA_{test}	PA rapid gain variation	0,20	dB	rectangular	√3	1,73	0,12	dB	1	0,12	dB	0,01
SW_{test}	SW leveling precision	0,50	dB	rectangular	√3	1,73	0,29	dB	1	0,29	dB	0,08
SG	Signal generator stability	0,13	dB	rectangular	√3	1,73	0,08	dB	1	0,08	dB	0,01
					$\sum u_i(y)^2$							1,35
					$u_c = \sqrt{\sum u_i(y)^2}$							1,16
					Expanded Uncertainty for k = 2 (level of confidence of 95%)							2,32

Table 3: Example of the test level multiplier for 95% confidence and revised test level.

Test level multiplier for 95% confidence		Antilog (2,32dB / 20)		1,306	
Revised test level	For:	3	V	3,92	V
		10	V	13,06	V

as a normal contribution). If the same power meter is used for both calibration and test, this contribution can be reduced to the repeatability and linearity of the power meter. $\mathbf{PA}_{cal}$ and $\mathbf{PA}_{test}$ are including the uncertainty derived from rapid gain variation of the power amplifier after the steady status has been reached. $\mathbf{SW}_{cal}$ and $\mathbf{SW}_{test}$ are the uncertainty derived from the discrete step size of the frequency generator and software windows for level setting during the calibration process. The software window can usually be adjusted by the test laboratory. **CAL** is the expanded uncertainty of the forward power needed to establish the test field strength for calibration. **AL** is the uncertainty derived from removal and replacement of the antenna and absorbers. The antenna location variation and absorber placement are type A contributions, i.e., their uncertainty can be evaluated by statistical analysis of series of observation. Type A contributions are normally not part of the uncertainty of measurement equipment, however these contributions were taken into account because of their high importance and their close relation to the measurement equipment. **SG** is a drift of the signal generator during the dwell time.

6. CONCLUSION

The calculated expanded uncertainty may be applied to tests done in accordance with EN 61000-4-3 in an anechoic chamber. The field strength is calibrated over a uniform area and then the same forward power is re-played in the presence of the EUT, one face at a time aligned with the uniform area. The budget assumes that the $(0 \div 6)$ dB field uniformity requirement has been achieved. There is disagreement as how the resulting uncertainty value should be used. In the Table 3 is shown the test level multiplier for 95% confidence and revised test level for described example uncertainty budget.

If it is not added in, so that, say, the stress level is set to 3 V, then the implication is that there is no more than 50% confidence that the specification stress level has been applied. If it is added (stress set to 3.92 V/m in the above example) then is 95% confidence that the EUT has been tested to at least the specification level. Assuming the distribution within the interval is normal, this sets the uncertainty interval to a 95% confidence level, which will then result in a 95% confidence of application of at least the correct stress.

REFERENCES

1. "Testing and measurement techniques — Radiated, radio-frequency, electromagnetic field immunity test," *Electromagnetic Compatibility (EMC)*, Part 4-3, IEC 61000-4-3, 2007.
2. "The EMC measurement uncertainty a handy guide," www.schaffner.com.
3. "RF immunity testing a handy guide," www.schaffner.com.

Multi-spectral Optoelectronic Sensor Employing Cavity Enhanced Absorption Spectroscopy

Jacek Wojtas, **Zbigniew Bielecki**, **Janusz Mikołajczyk**,
Mirosław Nowakowski, **and Beata Rutecka**
Institute of Optoelectronics, Military University of Technology
2 Kaliskiego Str., Warsaw 00-908, Poland

Abstract— In the paper, a multi-spectral optoelectronic sensor basing on cavity enhanced absorption spectroscopy (CEAS) is presented. In the sensor a special photoreceiver was used. The photoreceiver is characterized by wide range of the detected wavelengths. The optical signal from many laser sources can be measured using the photoreceiver. Thanks to this, in one cavity, a value of absorption coefficient at a few different wavelengths can be determined parallel. In the CEAS technique a beam of the laser radiation is injected under a very small angle related to the optical axis of the cavity. The radiation is reflected inside the optical cavity, similarly as inside a multipass cell. Through to this, dense structure modes are received. All systems operating on the basis of CEAS method can work with weak modes structure, and they are of low sensitivity to instabilities. The CEAS sensors can obtain sensitivity of about $10^{-9}\,\mathrm{cm}^{-1}$.

1. INTRODUCTION

Cavity enhanced absorption spectroscopy is one of the most sensitive methods of gases detection. The CEAS technique was proposed in 1998 by Engel. It is based on injection a beam of radiation under the very small angle (φ) in relation to the optical axis of cavity (i.e., off axis). The radiation is reflected inside the optical cavity similarly as inside multipass cell (Fig. 1). Therefore, dense structure modes are received. The weakly modes structure of the resonance cavity causes that the all system has the small sensibility on the changes of the cavity and the laser frequency [1, 2]. Sensors using CEAS method attain sensitivity amounting about $10^{-9}\,\mathrm{cm}^{-1}$ [3].

Typical CEAS system, designed for the measurement of a trace gases concentration, consists of a pulse radiation source, optical cavity, photoreceiver, and a signal processing system [4–6]. In the experimental setup two lasers and two optical lanes are used (Fig. 2). The setup makes it possible to detect a trace concentration of two gases with different absorption spectra at the same time. Using the special constructed photoreceiver the optical signals from the lasers are registered. The photoreceiver works with telecommunication techniques, well-known as time division multiplexing. Each of the laser is assigned to the suitable measurement channel — the strictly determined temporary window. In this window, the signal from the exits of the optical cavity is registered. Such sensor is able to detect trace concentration of two gases at the same time. For the detection of one gas, developed method provides increase in sensor sensitivity, because one gas can be investigated at the two different wavelength of its absorption spectra. The presented setup is of the greatest interest with respect to the possible applications. For example, it can be used in environment monitoring, luggage monitoring in ports, on airports, entry points, as well as in strategic objects and rooms also in undertakings connected with the counteraction to terrorist attacks.

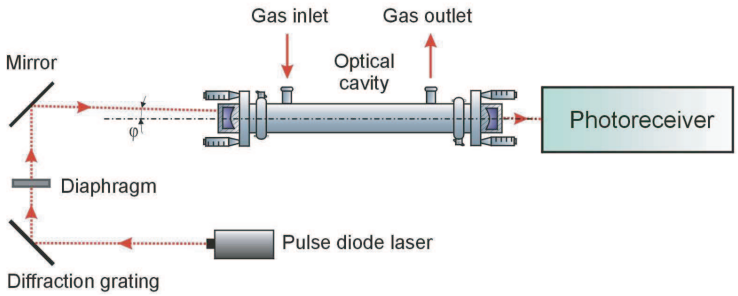

Figure 1: Idea of CEAS setup.

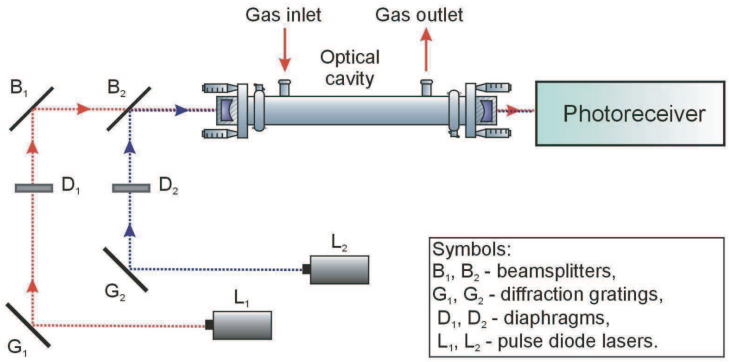

Figure 2: Scheme of multi-spectral CEAS sensor.

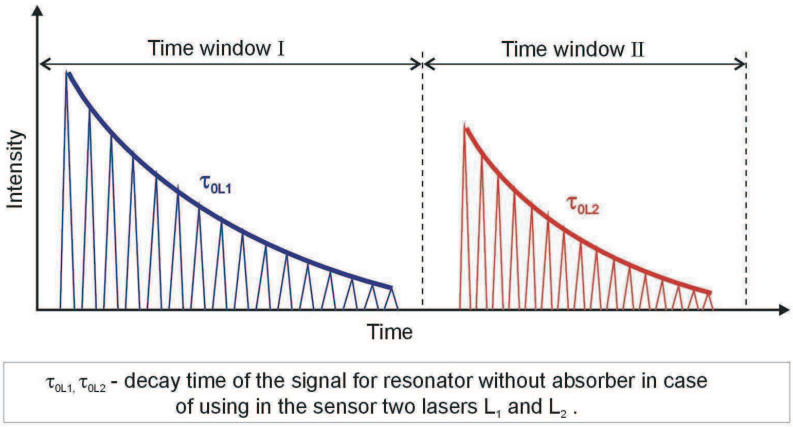

Figure 3: Example of the cavity output signal.

The concentration of investigated gas N is determined on the base of time constant of the signal decay and can be described by the formula

$$N = \frac{1}{c\sigma}\left(\frac{1}{\tau} - \frac{1}{\tau_0}\right), \tag{1}$$

where τ_0 and τ are the time constants of the exponential decay of the output signal for empty resonator and for the resonator filled with the absorber (investigate gas) respectively, σ is the absorption cross section of investigate gas, c is the light speed [7, 8].

In the cavity without absorber the decay time τ_0 is relative to the light speed, the optical cavity length and the mirrors reflectivity. For cavity filled with the absorber the decay time τ is additionally dependent on absorption index of the detected gas. In practice the following dependence $\tau_0 > \tau$ is observed. Thereby, the main parameter determined duration of the measuring-window is the decay time τ_0 (Fig. 3).

2. EXPERIMENT

The view of the experimental setup is presented in Fig. 4. An essential element of the system is photoreceiver which registers optical signals from two lasers (red one and blue one). The elaboration of the special lasers driver was also necessary. Therefore, a digital signal processing system provides possibility to set the time-windows and to register signals from the cavity. In the spectroscopy of losses in optical cavity this is unique technique.

The setup consists of two measurement lanes. In the first one, AlGaInP laser emitted at the wavelength of 630 nm can be used (type HL6312G/13G, Hitachi) [9]. It is a low-cost laser, usually applied as a light source in bar code readers, laser scribers and various other types of optical instruments. For example, 414 nm pulsed laser diode (TopGaN) can be mounted in the second lane. The laser generates radiation pulses with duration of about 50 ns and repetition rate of 1 kHz [10].

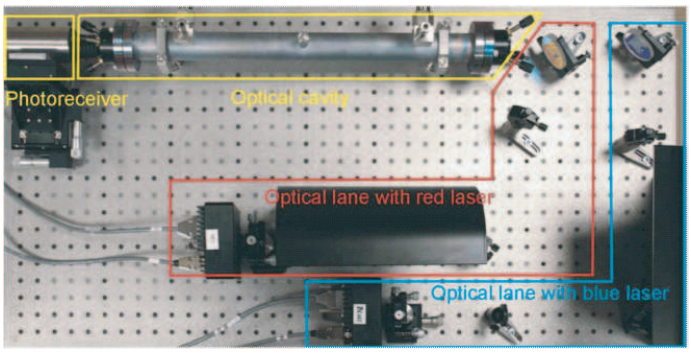

Figure 4: Experimental setup — top view.

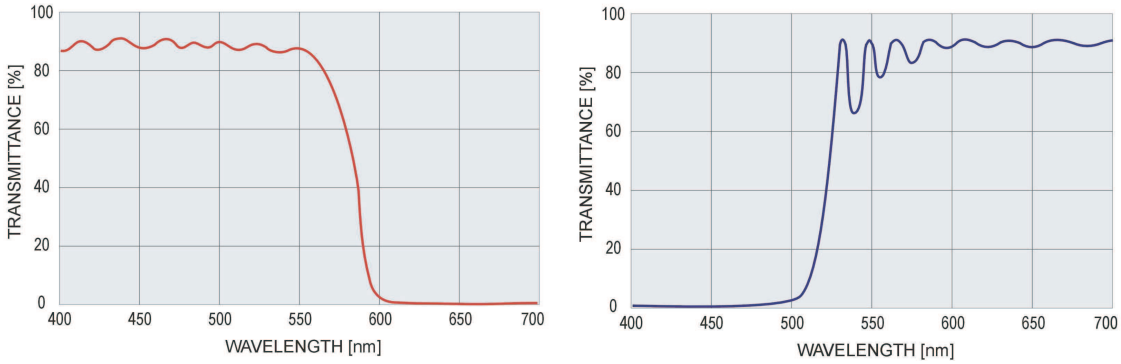

Figure 5: Transmittance of beam splitters: (a) SWP-45-R660-T420 and (b) LWP-45-R420-T660.

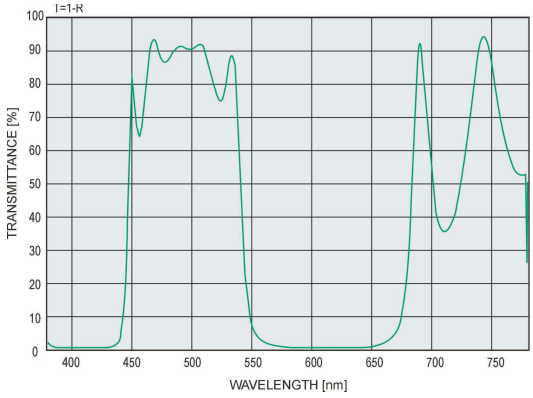

Figure 6: Transmittance of the cavity mirrors.

Next, the laser beams are formed with lens, diaphragms and diffraction gratings. The broadband fluorescence of the diode lasers affected the output signal are eliminated by diffraction grating. Furthermore, the off-axis arrangement allows to avoid influence of the laser radiation reflected from the cavity front mirror on laser emission. The beams are directed with beam splitters into the optical cavity. There are used beam splitters (CVI Melles Griot), the transmission characteristics of which are presented in Fig. 5.

The optical cavity is built up by two spherical mirrors. The mirrors reflectivities reach value of 0.999 at the wavelength of interest (Fig. 6). The distance between the mirrors is 50 cm. The optical signal from the cavity is detected with a photomultiplier (PMT) Hammamatsu firm type R7518.

PMT can be treated as a current source characterized by high resistance. Therefore, to amplify signal from PMT in wide dynamic range, transimpedance preamplifier is used. The output signal form the preamp was recorded with a hi-speed digital oscilloscope.

Moreover, during experiments the signal-to-noise ratio is improved by the use of coherent aver-

aging procedure according the formula

$$\frac{S_C}{N_C} = S_{AC}\left(\frac{N_{AC}}{\sqrt{N_p}}\right)^{-1}, \tag{2}$$

where S_{AC}/N_{AC} — signal to noise power ratio, N_p — number of the averaging samples [11].

3. CONCLUSION

The described setup is characterized by high sensitivity. In case of nitrogen dioxide detection we obtain sensitivity of about $10^{-9}\,\mathrm{cm}^{-1}$. That is why the sensor can be applied to ambience monitoring. Furthermore, it could be a significant instrument for national security. This sensor has real chances to use e.g., for the monitoring of luggage in ports, on airports, at entry points, in strategic for the state objects and rooms, in undertakings with the counteraction to terrorist attacks as well. Besides the mentioned applications, the applied CEAS method makes possible the elaboration of the portable sensor.

ACKNOWLEDGMENT

The project is financed by the Polish Ministry of Science and Higher Education (O N515 115836).

REFERENCES

1. Engel, G. S., E. J. Moyer, F. N. Ketusch, and J. G. Anderson, "Innovations in cavity enhanced laser absorption spectroscopy: Using in situ measurements to probe the mechanisms driving climate change," *Earth Science Technology Conference, Laser Sensor Technologies*, Jun. 2003.
2. Wojtas, J., A. Czyzewski, T. Stacewicz, Z. Bielecki, and J.Mikolajczyk, "Cavity enhanced spectroscopy for NO_2 detection," *Proceedings of the SPIE*, Vol. 5954, 174–178, 2005.
3. Wojtas, J., A. Czyzewski, T. Stacewicz, and Z. Bielecki, "Sensitive detection of NO_2 with cavity enhanced spectroscopy," *Optica Applicata*, Vol. 36, 2006.
4. Bielecki, Z., W. Kolosowski, G. Rozanski, and J. Wojtas, "Nitrogen dioxide detection using optoelectronic sensor," *Computational Methods and Experimental Measurements XIII*, 809–818, WIT Press, 2007.
5. Berden, G., R. Peeters, and G. Meijer, "Cavity ring-down spectroscopy: Experimental schemes and applications," *International Reviews in Physical Chemistry*, Vol. 19, No. 4., 565–607, 2000.
6. Kasyutich, V. L., C. S. E. Bale, C. E. Canosa-Mas, C. Pfrang, S. Vaughan, and R. P. Wayne, "Cavity-enhanced absorption: detection of nitrogen dioxide and iodine monoxide using a violet laser diode," *Applied Physics B*, Vol. 76, No. 6, 691–698, 2003.
7. Bielecki, Z., M. Leszczyński, K. Holc, L. Marona, J. Mikołajczyk, M. Nowakowski, P. Perlin, B. Rutecka, T. Stacewicz, and J. Wojtas, "Sub-ppb NO_X detection by CEAS system with blue and IR diode laser," *Computational Methods and Experimental Measurements XIV*, 809–818, WIT Press, 2009.
8. Courtillot, I., J. Morville, V. Motto-Ros, and D. Romanini, "Sub-ppb NO_2 detection by optical feedback cavity-enhanced absorption spectroscopy with a blue diode laser," *Applied Physics B*, Vol. 85, 407–412, 2006.
9. "Datasheet of the HL6312G/13G," ODE-208-190H (Z), Rev. 8, Hitachi, Jan. 2003.
10. TopGaN, http://www.topgan.eu/?what=text&id=15.
11. Wojtas, J. and Z. Bielecki, "Signal processing system in the cavity enhanced spectroscopy," *Opto-Electron. Rev.*, Vol. 16, No. 4, 44–51, 2008.

Free Space Optics Second Generation versus Shorter Wavelengths

M. Nowakowski, Z. Bielecki, J. Mikołajczyk, J. Wojtas, and M. Gutowska
Institute of Optoelectronics, Military University of Technology
2 Kaliskiego Str., 00-908 Warsaw, Poland

Abstract— The paper presents construction of broadband optical system devoted to free space optical communication using long wavelength quantum cascade laser and a heterostructural thermally cooled HgCdTe photodetector. This system should characterize with lower sensitivity to adverse meteorological conditions when compared with the systems operating in the near IR.

1. INTRODUCTION

The development of broadband optical telecommunications in free space — (Free Space Optics — FSO) is utilizing a long-wave infrared radiation (8–13 μm). A significant advantage of the technology in comparison with currently available optical communications systems is lesser scattering of radiation by aerosols, clouds and dust. This is particularly important in urban areas and in conditions of high smoke ex. on the battlefield.

When selecting optical radiation sources and detection systems it should be taken into account: the radiation power, the range of wavelengths, and the possibility of cooperation with peripheral circuits, in particular allowing for co-operation of the link with the existing cable networks.

The choice of the wavelength range is mainly conditioned by the transmission properties of the atmosphere and approaching to provide security for both users and outsiders.

2. FSO SYSTEMS AND ATMOSPHERE INFLUENCE

The atmosphere affects the amplitude of detected optical signals mainly through: selective absorption, scattering and turbulence. In order to obtain high SNR the radiation of the background should be also minimized.

In practice, the most important weather factor affecting the performance of optical links is fog. The analysis of the impact of other atmospheric conditions, which include: dust, rain and snow, shows that the effectiveness of transmission within the range of wavelengths (8–13 μm) is better or comparable to the already used systems operating in the range of near infrared [1–4].

In Figure 1, the atmosphere transmission received during computer simulation in foggy conditions for visibilities of 700 m (a) and 50 m (b) is presented.

It could be noticed, radiation of the wavelength of 0.8 μm and 1.5 μm is much more attenuated (several size levels) compared to the wavelength of 10 μm. This represents an important argument of the choice of the wavelength of 10 μm in the suggested link.

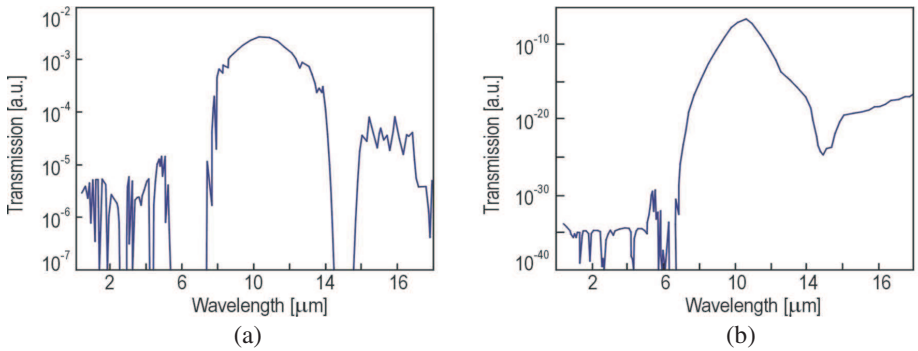

Figure 1: Atmosphere transmission for visibilities of 700 m (a) and 50 m (b).

3. QUANTUM CASCADE LASERS

The development of quantum cascade lasers technology makes it possible to construct a new wireless optical link [5–9]. In the normal temperature (from −40°C + 70°C) obtained by using the Peltier cooler, the QCL lasers operate only in a pulse mode with low duty level. It is related to the

generation of a large amount of heat in the semiconductor structure. Therefore, the current pulses driving the laser should be characterized by low rise time (around 10 ns) with the pulse duration of 100 ns. The investigations of QCL lasers were made for two different laser systems. The first one was purchased in Alpes Lasers with a laser S2008a12. The system consists of a laser structure emitting radiation at a wavelength of 10.5 µm, a bias unit, current driver and control system of laser temperature (TEC controller). The results showed that for low values of pulse duration, the laser can operate with a maximum frequency of 1.3 MHz. Along with the increase in the duration of the pulse it could be observed a frequency threshold. The peak power of the laser decreases rapidly at the threshold. This phenomenon is caused by the current limit of the laser driver. The acceptable average value of the laser current is about 0.08 A. The slight increase in temperature of the laser structure was also observed with increase in pulse frequency. The investigation results also show that the radiation power is a function of repetition rate, which decreases as the rate increases. Similar studies were carried out for different values of pulse duration. With the minimum pulse width of 20 ns, the amplitude rise of 20% was observed. Above this value the amplitude of the emitted pulses increased sharply to a maximum and remained practically constant (Figure 2).

The second investigated laser was designed by Cascade Technologies. The research results showed the energy parameters of the laser were changed with the working conditions of the laser (pulse frequency and duration, laser temperature, bias voltage). Figure 3(a) presents the signals registered at the output of photoreceiver for a constant value of pulse duration and changing repetition rate.

It is noticed that the radiation energy is not affected substantially by pulse frequencies. The observed differences are insubstantial and do not demonstrate any regularities. The studies were conducted in the frequency range of 5 kHz to 100 kHz.

The investigations of the impact of the pulse duration on the shape of the radiation pulse were made for a fixed frequency of 100 kHz. The pulse duration was changed between 20 ns to 500 ns. The results show that the pulse duration affects both the shape of the laser pulse and radiation energy (Figure 3(b)).

Apart from the threshold value of pulse duration (20 ns), changes were observed in the shape of the signal. The changes can be described by the Gaussian curve for duration of 30–80 ns, a rectangular shape (100–180 ns) and by the sawtooth function (above 200 ns). The increase in the pulse duration above value of 120 ns decreases the amplitude of the pulses.

4. DETECTION MODULE

An important place in the optical link is taken by the detectors. The construction of photodetectors applied in the presented link is made of $Hg_{1-x}Cd_xTe$ multilayer structure (consisting of 6–20 layers).

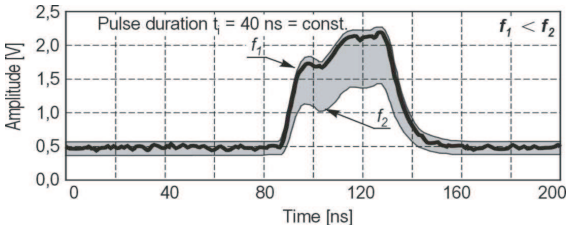

Figure 2: Laser energy for different pulse repetition.

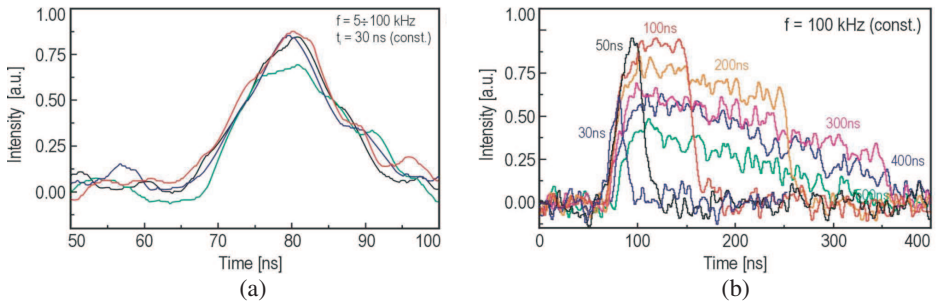

Figure 3: Laser radiation for different values of pulse repetition (a) and pulse duration (b).

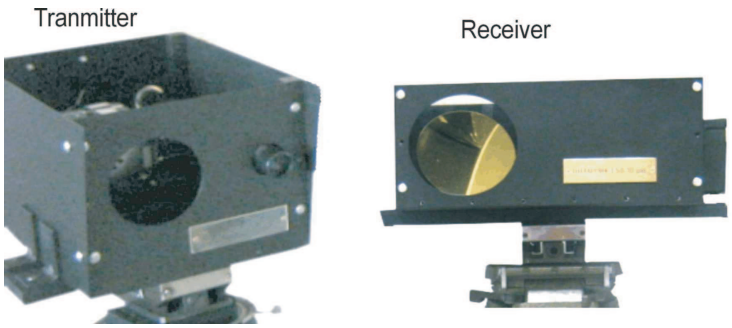

Figure 4: View of the designed FSO system.

The heterostructures was obtained by a low-temperature epitaxy using the method of pyrolysis of metal-organic compounds (MOCVD).

Detectivities of photodiodes were determined by the manufacturer, Vigo SA, based on the measurement of both the current sensitivity and dark current. The dark current measurement makes it possible to calculate the value of current of the shot noise — a dominant type of noise.

At room temperature the photodiodes are characterized by a long-wavelength range of sensitivity of $\lambda_{1/2} = 10$ µm. The decrease in the temperature of the detector to 230 K causes a shift $\lambda_{1/2}$ to about 13.5 µm. The photodiode was an important element of the detection module [10].

In the housing of the module there is a radiation detector, a two-stage thermo-electrical cooler with a temperature sensor, a wideband transimpedance preamp, a miniature fan diffusing heat emitted by a the cooler, heat pipes taking off the heat from the cooler to a fan and a cooler controller.

5. DESIGNED FSO SYSTEM

The view of the constructed FSO link is shown in Figure 4. It consists of a transmitter and photoreceiver. The functional properties of the link is determined by the construction of the transmitter. The transmitter consists of three main components: a head with the laser and optical unit, a module control of the laser work and a communication interface (RS232).

The main task of the head is to produce radiation beam of relevant power-spatial parameters. The control module provides the proper work of the laser. The communication interface with a computer and software is responsible for processing information into appropriate signals controlling the laser pulses [11–13].

In the receiver system the above-mentioned detection module and a parabolic mirror were used. The mirror is characterized by a high brightness (F/# 1.5) and a big active diameter (101.6 mm). In addition, this element does not introduce spherical aberration and provides small pole aberrations compared with the size of the detector.

The main aim of the preliminary investigations was to determine the energy of the transmitter beam in the laboratory conditions. For the maximum distance between the transmitter and receiver (55 m), the preamp of the detection module was still in a saturation point. Therefore, it was decided to carry out measurements out of the laboratory. The outdoor researches makes it also possible to determine the impact of weather conditions on the amplitude of the received signal. The maximum distance between the transmitter and the receiver was 470 m. For the good weather conditions, the results of the studies have shown that the FSO link works properly. The distance studies on greater distances were limited by terrain obstacles.

6. CONCLUSIONS

The developed optical link works properly both in laboratory and field conditions. In the event of bad weather conditions (moderate fog or haze) it can effectively ensure the continuity of a transmission link. When comparing the data obtained during the computer simulations and experimental studies for foggy conditions, similar values of decrease in the amplitude of the received signal were received. The carried out analyses show that in foggy conditions it could provide a transmission range of about 1 700 meters with a bit error rate 10^{-12}. The disadvantage of the presented link is too low acceptable transmission speed. This is due to the limitations resulting from the employed laser (maximum pulse frequency). However, a continuous development of the described technology

will contribute to improve features and reduce the price. Therefore it could be assumed that in the near future the QCL lasers generated radiation in the wavelength range of 10 μm will be commonly used in FSO applications.

REFERENCES

1. Juarez, J. C., "Free-space optical communications for next-generation military networks," *IEEE Communications Magazine*, 46–51, November 2006.
2. Kinkade, K., "Free-space optics builds invisible bridges," *Laser Focus World*, No. 12, 2003.
3. Manor, H. and A. Argon, "Performance of an optical wireless communication system as a function of wavelength," *Applied Optics*, Vol. 42, No. 21, July 1, 2003.
4. Capasso, F., et al., "Quantum cascade lasers: Ultrahigh-speed. Operation, optical wireless communication, narrow linewidth, and far-infrared emission," *IEEE Journal of Quantum Electronics*, Vol. 38, No. 6, June 2002.
5. Achour, M., "Free-space optics wavelength selection: 10 μm versus shorter wavelengths," http://www.ulmtech.com.
6. Faist, J., "Continuous-wave, room temperature quantum cascade lasers," OPN 32–36, May 2006.
7. Maulini, R., A. Mohan, M. Giovannini, J. Faist, and E. Gini, "External cavity quantum-cascade laser tunable from 8.2 to 10.4 μm using a gain element with a heterogeneous cascade," *Appl. Phys. Lett.*, Vol. 88, 2006.
8. Hofstetter, D., M. Beck, T. Aellen, and S. Blust, "High frequency modulation of a quantum cascade lasers using a monolithically integrated intracavity modulator," *IEEE Photonics Techn. Letters*, Vol. 15, No. 8, 1044–1046, 2003. www.alpeslasers.ch/.
9. Piotrowski, A., W. Gawron, K. Klos, J. Pawluczyk, J. Piotrowski, P. Madejczyk, and A. Rogalski, "Improvements in MOCVD growth of $Hg_{1-x}Cd_xTe$ heterostructures for uncooled infrared photodetectors," *Proc. SPIE*, Vol. 5957, 116, 2005.
10. Bielecki, Z., W. Kolosowski, J. Mikolajczyk, M. Nowakowski, E. Sedek, and J. Wojtas, *Free-Space Optical Communications Using Quantum Cascade Laser, MIKON 2008, Conf. Proc.*, Vol. 2, 295–298, 2008.
11. Bielecki, Z., W. Kolosowski, and J. Mikolajczyk, "Free-space optical data link using quantum cascade laser," *PIERS Proceedings*, 108–111, Cambridge, USA, July 2–6, 2008.
12. Mikolajczyk, J., Z. Bielecki, M. Nowakowski, and J. Wojtas, "Second generation FSO for communications systems," *IRS2 Conference Proc.*, 313–316, 2008.

Infrared Detection Module for Free Space Optics

Marcin Ratajczyk[1], **Ryszard Paliwoda**[1], **Maciej Rzeczkowski**[1], **Waldemar Gawron**[2], **Jarosław Pawluczyk**[1], **and Józef Piotrowski**[1]

[1]VIGO System S.A., 05-850 Ozarow Mazowiecki, 129/133 Poznanska str., Poland
[2]Institute of Applied Physics, Military University of Technology, 2 Kaliskiego Str., Warsaw 00-908, Poland

Abstract— Free space optics (FSO) communication in LWIR range is less sensitive to atmosphere features. VIGO System S.A. — company from Poland — develops high performance detector module optimized for LWIR range. We present new detection module dedicated to open space optical communication optimized for 10 µm.

Module specification:

- Detector: PVI-2TE-10 photodiode with immersion lens, thermoelectrically cooled.
- Operating temperature range: $-30 \ldots +60°C$.
- Detector temperature stabilization precision: 0.01°C.
- Detector time constant: < 1 ns.
- Preamplifier bandwidth: 100 MHz.
- Input current noise: $5\,pA/\sqrt{Hz}$.
- Detector capacity < 5 pF.

Detection module is based on PVI-2TE-10 HgCdTe photodiode, thermoelectrically cooled by two stage Peltier cooler. It is optimized for long wavelength — 10 µm. TEC controller stabilizes detector temperature with high precision in wide ambient temperature range. Immersion lens enables optimization of the detector physical dimensions, decreasing detector capacity and time constant.

Module parameters enables maximum transmission speed 100 Mb/s. Low bit error rate requires correct transmission with low and high signal level. Detector and preamplifier have wide linear working range, noise optimization provides module high detectivity. DC reverse bias increases dynamic resistance and improves frequency response.

1. INTRODUCTION

A new trend in the development of broadband free-space optical communication is the application of long-wave infrared radiation (8–14 µm) [1–4]. The main advantage of this solution is decreased radiation scattering in aerosols and dusts.

Until recently, the lack of suitable radiation sources and detectors constituted the main problem area. The existing devices were expensive and not user-friendly. It appears that the problem of radiation sources may soon be solved by the development of quantum cascade lasers [5].

Uncooled photodetectors of long-wave infrared radiation are also currently under development. The main requirements for long-wave detectors for free-space optical communication are as follows:

High sensitivity. High sensitivity is necessary to achieve low error ratio using low laser beam power and in small-aperture optics. In practice, performance close to fundamental limits are required [6].

High operation speed. Subnanosecond response time is typically required for the present optical links.

Other requirements. Detectors should be convenient in use, reliable, and inexpensive. The size of the active element should be comparable to the beam spot size in the focal plane of the optical system. Large variation in the radiation power results in a requirement of adequately wide range of linear responsivity.

The requirements of high sensitivity and speed were met by HgCdTe photodiodes available as early as the 1970's. However, such devices required liquid nitrogen cooling and were expensive, which in practice prevented their broad application. We report here recent progress in the development of broadband detection modules with HgCdTe long-wave (≈ 10 µm) photodetectors operating without cryogenic cooling.

2. PRACTICAL REALIZATION OF HIGH-SENSITIVITY AND HIGH-SPEED PHOTODETECTORS OF LONG-WAVE RADIATION OPERATING WITHOUT CRYOGENIC COOLING

The long-wave infrared radiation detection at near-ambient temperatures have been discussed in many original papers and reviewed in the recently published monograph [7].

2.1. Device Architecture

Photodetectors are composed of multi-layer (6–20 layers) $Hg_{1-x}Cd_xTe$ heterostructures obtained from low-temperature metal organic chemical vapor deposition epitaxy. This technology has been discussed in detail in study [8].

Figure 1 presents a construction diagram of the device, which has been simplified for reference purposes. However, the actual architecture is more complex, as the diagram does not show lesser functional layers, additional layers added to obtain a required composition and doping profile, as well as transient layers with gradations of composition and doping.

The device architecture has been optimized with the use of computer-aided simulation [9]. The thicknesses of subsequent layers, bandgap profiles, types and levels of donor and acceptor doping have been obtained from calculations. The results are as follows:

- optimal relation between absorption of exact wavelength radiation and the thermal generation rate of carriers in the absorber area,
- minimized thermal generation and recombination of carriers in contact and transient areas, and on the surface of the heterostructure,
- elimination of short-wave radiation noise by adequate choice of N^+ layer composition,
- good and fast collection of optically generated carriers,
- minimized parasitic impedances at the mesa structure base, wide bandgap contact areas and at the contact between the heterostructure and the metallization,
- minimized RC time constant.

The contact metallization additionally functions as a mirror reflecting low-absorption long-wave radiation back to the absorber. Buffer, absorber and contact layer thicknesses are chosen to create, along with the contact metallization, a resonant cavity, which is not particularly perfect but offers an increase in device quantum efficiency in the long-wave range [7].

Photodiode heterostructure is monolithically integrated with immersion lens which functions as an effective optical concentrator. In the hemispherical immersion lens, the optical area is increased n^2 times the physical area, where n is the refraction index of lens material. This solution allows for a radical decrease in the thermal generation and recombination of carriers, also the noise power, which is decreased proportionally to a decline in absorber volume. A greater (n^4) increase is obtained for a hyperhemispherical lens. For gallium arsenide lens ($n = 3.4$), the optical area is increased by approx. 1 and 2 orders of magnitude, for hemispherical and hyperhemispherical lenses respectively.

Another advantage of immersion lenses is a decrease in electric capacity, which declines proportionately to a decrease in the absorber area. This results in a radical drop in the RC time constant. However, the use of immersion lens also has its disadvantages, such as increased manufacturing costs and, in the case of hyperhemispheric lenses, limited field of view and lowered radiation saturation threshold. Such solutions allow for a radical increase of detectivity and operating speed as compared to conventional, non-immersed detectors.

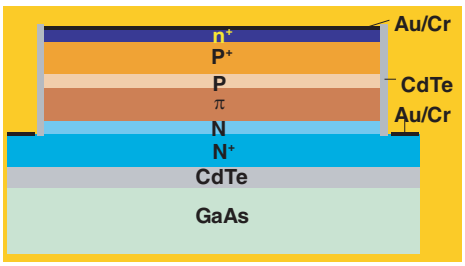

Figure 1: Diagram section of photodiode heterostructure for approx. 10 µm wavelength radiation detection in temperature 200–300 K.

3. CHARACTERISTICS OF PHOTODETECTORS

Photodiode detectivity is specified on the basis of current sensitivity and dark current measurements, and the latter is used in the calculations of shot noise current, i.e., the dominating noise type in the device frequency operating band.

The RMS shot noise current can be calculated with the application of the following formula:

$$I_n = (2 \cdot g \cdot q \cdot I \cdot B)^{1/2} \tag{1}$$

where q — elementary charge, I — photodiode dark current, g — photodiode electrical gain, B — noise bandwidth.

Table 1 presents parameters of $Hg_{1-x}Cd_xTe$ photodiode.

Table 1: Parameters of $Hg_{1-x}Cd_xTe$ photodiode.

Parameter	Units	Value
Ambient Temperature	K	293
Detector Temperature	K	228
Cooler Current	A	0.7
Thermistor Resistance	kΩ	38
Detector Resistance	Ω	40
Optical area	mm^2	1
Reverse Bias Voltage	mV	−150
Current Responsivity ±20% (10 µm)	A/W	1.7
Current Noise Density	$pA/Hz^{1/2}$	42
Detectivity ±20% (10 µm)	$cmHz^{1/2}/W$	4E + 09

3.1. Operating Speeds

Figure 2 presents the measured relation between the time constant of the photodiode response and the bias voltage. The experiment employed pulse quantum cascade lasers and detectors connected to DC transimpedance preamplifiers of high operating speed. The preamplifiers maintained a constant voltage level at the photodiode during the measurement of time constant for a given voltage setting.

Photodiodes without bias voltage are characterized by relatively long time constants. In the case of uncooled photodiodes without bias, the time constants were practically equal to the carrier lifetime of absorber material. The time constants of photodiodes without bias cooled to 230 K and 210 K were somewhat greater than for uncooled ones, but significantly lower than the carrier lifetimes of absorber material. Such relations suggest that in uncooled photodiodes without bias, signal fadeout is specified mainly by recombination of carriers in the absorber volume. In cooled photodiodes without reverse bias, the time constant is determined by both the recombination of carriers in the absorber and diffusion transport to contact areas.

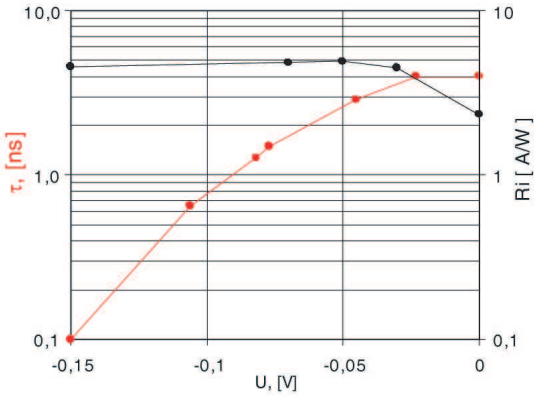

Figure 2: Relations between current responsivity and time constant of photodiode and bias voltage at 210 K.

4. DETECTION MODULE

MIPAC detection module (Figure 3, Table 2) constitutes a modification of the OEM series detection modules developed and manufactured by Vigo System S.A. The housing features a radiation detector, one-, up to four-stage thermoelectric cooler with temperature sensor, broadband transimpedance pre-amplifier, and (in certain models) cooler controller. At the moment, the development process concentrates on the miniaturization of the detection module for its future placement inside ceramic flat pack package. The current signal from the detector is received by a broadband (up to 300 MHz) transimpedance amplifier with resultant transimpedance up to 100 kV/A. The amplifier provides an option of DC supply of reverse bias voltage to the detector ($100 \div 600$ mV), which constitutes the prerequisite for obtaining maximum signal/noise ratio in a broad frequency band. Reverse voltage causes low-frequency noise, which have, however, little impact on the total noise level of the broadband amplifier, as the bandwidth with dominating $1/f$ noise, i.e., 10 kHz–2 MHz, is significantly smaller than the bandwidth of the detection module.

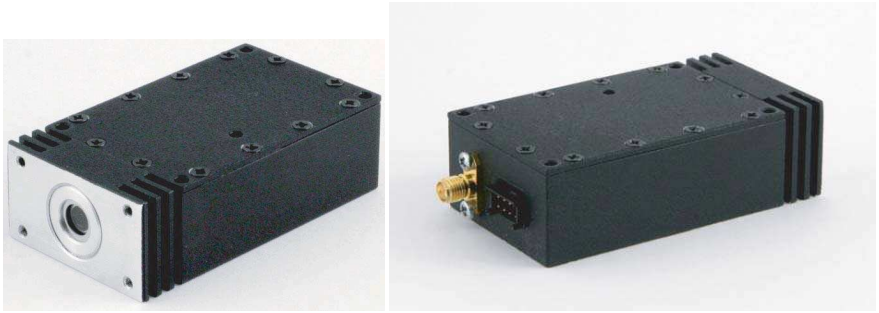

Figure 3: Integrated broadband detection module $\approx 10\,\mu$m.

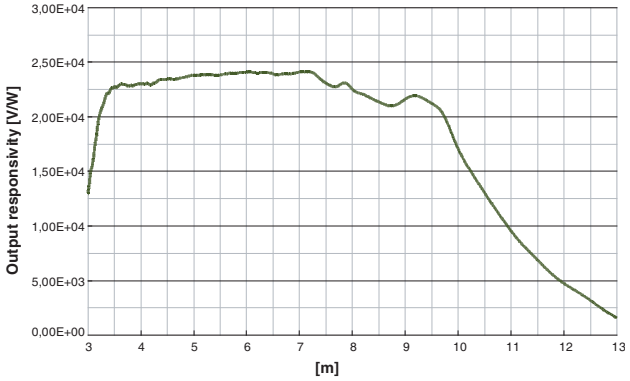

Figure 4: Normalized responsivity spectral characteristics of $Hg_{1-x}Cd_xTe$ photodiode (reverse bias 150 mV).

Table 2: Parameters of broadband detection module $\approx 10\,\mu$m.

Parameter	**Units**	**Value**
Transimpedance @ $R_{LOAD} = 50\,\Omega$	V/A	10E + 3
Bandwidth (3 dB)	MHz	$0.001 - 150$
Output Voltage Swing @ $R_{LOAD} = 50\,\Omega$	V	± 1
Output Noise Density @ $f_0 = 100$ kHz	nV/$\sqrt{\text{Hz}}$	140
Average Total Output Noise Density *(averaged over PA bandwidth)*	nV/$\sqrt{\text{Hz}}$	816
Voltage Responsivity $\pm 20\%$ (10 µm)	V/W	16900
Detectivity $\pm 20\%$ (10 µm) *(averaged over PA bandwidth)*	cm$\sqrt{\text{Hz}}$/W	2E + 9
Thermistor Resistance	kΩ	38
TEC Voltage	V	0.7
TEC optimal Current	A	0.7
Stability of Temperature	K	0.01

Figure 4 presents the spectral characteristic of responsivity of photodiode cooled with two-stage thermoelectric cooler, measured in the manner specified above, at reverse voltage.

Table 2 presents parameters of detection module.

5. CONCLUSION

Broadband detection modules for long-wave infrared radiation (8–14 µm) have been developed for their application in second generation optoelectronic free-space communication links.

The analysis covered the sources of optical radiation with wavelength near 10 µm and detectors sensitive to that wavelength. The wavelength was chosen due to lesser attenuation caused by small-particle fogs and increased eye safety in comparison to the other two bands utilized in optoelectronic links, i.e., 780–850 nm and 520–1600 nm.

A carried out analysis of the available literature on the subject suggests that the best parameters of a mobile link can be obtained by the application of cascade lasers as the radiation source. Either continuous-wave or pulse kind lasers may be used.

Optical radiation receiver should be characterized by very high sensitivity. For that purpose, a Polish detector manufactured by Vigo System has been used. High sensitivity was obtained by combining a multi-layer $Hg_{1-x}Cd_xTe$ heterostructure with an immersion lens that has been optimized for 10 µm wavelength radiation detection. To decrease the noise level the detector was equipped with a two-stage thermoelectric cooler.

The constructors believe that the use of a quantum cascade laser generating approx. 10 µm wavelength radiation and highly sensitive detector that has been optimized for that wavelength will allow for the creation of a second generation optoelectronic link, which ensures better range in adverse weather conditions as compared to the currently available options.

ACKNOWLEDGMENT

The authors would like to thank the Ministry of Science and Higher Education for their support in the field. The article was developed under research grant No. OR00008606.

REFERENCES

1. Holejko, K., "Łacza optyczne w otwartej przestrzeni," *Przeglad Telekomunikacyjny*, Vol. 4, 118–124, 2005.
2. Juarez, J. C., "Free-space optical communications for next-generation military networks," *IEEE Communications Magazine*, 46–51, November 2006.
3. Kinkade, K., "Free-space optics builds invisible bridges," *Laser Focus World*, Vol. 12, 2003.
4. Achour, M., "Free-space optics wavelength selection: 10 µm versus shorter wavelengths," http://www.ulmtech.com.
5. www.alpeslasers.ch.
6. Frendinandow, E. and T. Mitsev, "Link range of free space laser communication system," *Microwave Review*, 41–42, December 2003.
7. Piotrowski, J. and A. Rogalski, "High-operating-temperature infrared photodetectors," *Ed. SPIE*, Bellingham, ISBN: 9780819465351, 2007.
8. Piotrowski, A., W. Gawron, K. Klos, J. Pawluczyk, J. Piotrowski, P. Madejczyk, and A. Rogalski, "Improvements in MOCVD growth of $Hg_{1-x}Cd_xTe$ heterostructures for uncooled infrared photodetectors," *Proc. SPIE*, Vol. 5957, 108–116, 2005.
9. Józwikowski, K., W. Gawron, J. Piotrowski, and A. Jóźikowska, "Enhanced numerical modelling of non-cooled long wavelength multi-junction (Cd, Hg)Te photodiodes," *IEE Proc. — Circuits Devices Syst.*, Vol. 150, 65–71, 2003.

Simulation of Beam Filling Effect on Spaceborne Precipitation Radar Rainfall Retrieval

Honggang Yin[1], **Ailan Lan**[2], **and Hu Yang**[1]

[1]National Satellite Meteorological Center, China
[2]Center for Space Science and Applied Research CAS, China

Abstract— In order to estimate rain rate quantitatively, the parameters measured by a spaceborne precipitation radar are usually assumed to be uniform within the antenna beam. It means that the rainfall spreads uniformly within a range of a few kilometers. However, in most cases of convective rain, the footprint size of spaceborne radar may be larger than the rain cell size, then the reflectivity and the path integrated attenuation are not accurate due to nonuniform beam filling. As a result, the retrieved rain rate is also biased. In this paper, beam filling effects on spaceborne precipitation radar are investigated theoretically according to whether rain attenuation can be neglected. Furthermore data from the Airborne Rain Mapping Radar are used to simulate observations from spaceborne precipitation radar with different beam width.

1. INTRODUCTION

Global precipitation measurement is essential not only for the climate modeling and weather forecasting but also for the research of the global change. Since the earth surface is mostly covered by sea water, it is necessary to observe this important atmospheric variable from space. There is more attractive to use spaceborne radar to measure precipitation than to use passive techniques, because it is able to provide the most overall detection of rainfall field that can be thought currently. The Precipitation Radar (PR) aboard the Tropical Rainfall Measuring Mission (TRMM) satellite is the first-ever spaceborne instrument [1]. A spaceborne radar like the Dual-frequency Precipitation Radar (DPR) on the Global Precipitation Measurement (GPM) core satellite [2], which will be installed on the FengYun-3 Precipitation Measurement Satellite (FY3 PMS), is also being developed in China.

The horizontal resolution of spaceborne precipitation radar impacts on the precipitation measurement. Firstly, the natural Doppler spectrum of rain is broadened by the antenna beam. Secondly, the altitude that surface clutter can contaminate the rain echo is proportional to the resolution. The most important is that the measurement accuracy of precipitation also relates to the horizontal resolution, because the reflectivity measured by spaceborne precipitation radar is the weighted average of the actual of rain field. The instantaneous fields of view of all the spaceborne precipitation radar as mentioned above are about 5 km. Therefore only when the rain field is uniform within a range of a few kilometers, the measured reflectivity is equal to the actual value. Such an assumption may be valid for widespread stratiform rain. While in most cases of convective rain, the rain field is inhomogeneous within the resolution volume, the effects of nonuniform beam filling (NUBF) occur.

In this paper, beam filling effects on spaceborne precipitation radar are investigated theoretically according to whether rain attenuation can be neglected. Because the frequency and observing geometry of the Airborne Rain Mapping Radar (ARMAR) are close to those of the FY3 DPR, the data with high resolution from ARMAR are used to simulate observations from spaceborne precipitation radar with different beam width [3].

2. THEORY OF NUBF EFFECTS

The total backscattering power from the precipitation particles in volume cell dV that the spaceborne precipitation radar can receive is expressed as

$$dP_r(R_0) = C_1 Z_e(R) A_r(R) G_r dR G_a^2(\theta, \varphi)\, d\Omega / R_0^2 \tag{1}$$

where C_1 is a constant determined by system specifications, Z_e the radar effective reflectivity factor, A_r the path attenuation, G_r the range weighting function, G_a the antenna gain pattern, and R_0 the range from the radar to the resolution volume.

Firstly, the case of rain with uniform beam filling (UBF) is considered. For a uniform rain field, $Z(R) = Z(R_0)$ and $A_r(R) = A_r(R_0)$, then the received rain power is

$$P_r(R_0) = C_1 Z_e(R_0) A_r(R_0) \int_L G_r dR \int_\Omega G_a^2 d\Omega / R_0^2 \tag{2}$$

So the reflectivity measured by a spaceborne precipitation radar can be written as

$$Z^m(R_0) = P_r(R_0) R^2 / C_1 = Z_e(R_0) A_r(R_0) \int_L G_r dR \int_\Omega G_a^2 d\Omega \tag{3}$$

This formulation means that when the attenuation caused by rainfall is weak, the accurate rain rate I can be estimated from the measured reflectivity by using an appropriate $Z_e - I$ relation.

When the rain attenuation is too large to be neglected, the path integrated attenuation (PIA) measured by spaceborne radar is needed to estimate the rain rate. The received sea surface echo power in a rain area is given as

$$P_{s1}(\theta_0) = C_2 \iint_s A_s(\theta, \varphi) \sigma^0 G_a^2(\theta, \varphi) G_r \sin\theta \cos\theta d\theta d\varphi \tag{4}$$

where θ_0 is the incidence angle at the midpoint of the resolution volume, C_2 another constant determined by system specifications, and A_s the path attenuation of sea clutter. In general the sea surface normalized radar backscattering sections σ^0 is invariable within the effective radar resolution volume. Using$G_{r1} = G_r \sin\theta \cos\theta$, then (4) can be rewritten as

$$P_{s1}(\theta_0) = C_2 \sigma^0(\theta_0) \iint_s A_s(\theta, \varphi) G_a^2 G_{r1} d\theta d\varphi \tag{5}$$

The sea surface echo in the clear area received by the spaceborne radar with the same observing geometry is

$$P_{s2}(\theta_0) = C_2 \sigma^0(\theta_0) \iint_s G_a^2 G_{r1} d\theta d\varphi \tag{6}$$

Therefore the PIA measured by a spaceborne precipitation radar is expressed as

$$A^m(\theta_0) = P_{s1}(\theta_0) / P_{s2}(\theta_0) = \iint_s A_s(\theta, \varphi) G_a^2 G_{r1} d\theta d\varphi / \iint_s G_a^2 G_{r1} d\theta d\varphi \tag{7}$$

In the case of UBF, $A_s(\theta, \varphi) = A_s(\theta_0)$, so it can obtained from (7) that $A^m(\theta_0) = A_s(\theta_0)$. It is obvious that the rain rate can be accurately estimated from the measured PIA by using the surface reference technique (SRT) [4].

However, for convective rain, the horizontal resolution of the spaceborne precipitation radar as mentioned above may be larger than the size of rain cell, so the effect of NUBF will occur. Here we also firstly analyze the case that the rain attenuation can be neglected. In this case the rain echo received by spaceborne radar is

$$P_r(R_0) = C_1 \int_L \int_\Omega Z_e(R) G_r G_a^2 dR d\Omega / R_0^2 \tag{8}$$

Then the measured reflectivity can be expressed as

$$Z_a^m(R_0) = \int_L \int_\Omega Z_e(R) G_r G_a^2 dR d\Omega = a \int_L \int_\Omega I(R)^b G_r G_a^2 dR d\Omega \tag{9}$$

where the subscript a denotes "apparent". Equation (9) illustrate that the measured reflectivity is a weighting average of the actual. As a result, the estimated rain rate is erroneous due to NUBF effects.

Next is the case in which the attenuation is innegligible and the SRT method will be used. The PIA measured by spaceborne radar is

$$A_a^m(\theta_0) = \iint_s A_s(\theta, \varphi) G_n d\theta d\varphi = \iint_s 10^{-0.2 \int_0^D \alpha I(s)^\beta ds} G_n d\theta d\varphi \tag{10}$$

where $G_n = G_a^2 G_{r1} / \iint_s G_a^2 G_{r1} d\theta d\varphi$. It can be seen from (10) that the relation between PIA and I is far away from linearity. There NUBF effects also bring error to the PIA and to the estimated rain rate in the end.

3. NUMERICAL SIMULATION

Here we investigate the statistical nature of NUBF effects on spaceborne precipitation radar with different horizontal resolution using numerical simulation. In the simulation, the high resolution data measured by ARMAR in two different field experiments are used as the actual value, system parameters of simulated spaceborne precipitation radar are listed in Table 1. The range resolution is set to 50 m in order to avoid the effect of weighting average along range direction on the statistical nature of NUBF. The following precipitation-backscattering relation is used [5]

$$\begin{aligned} Z &= 189I^{1.43} \\ k &= 0.0222I^{1.14} \end{aligned} \tag{11}$$

Table 1: System parameters of the spaceborne precipitation radar used in simulation.

Parameter		Value
Satellite altitude		400 km
Frequency		13.6 GHz
Antenna	Gain pattern	Gaussian distribution, PSL (peak sidelobe level) = −35 dB
	Resolution	PSL beamwidth is equal to 2.5 times the 3 dB beamwidth
Range resolution		50 m
System noise		10 dBZ

Table 2: Statistics of rain retrieval error caused by NUBF for rain cases study.

Event / Horizontal Resolution	TOGA COARE				CAMEX-3			
	Reflectivity		Rain rate		Reflectivity		Rain rate	
	Relative error (%)	RMS error (dBZ)	Relative error (%)	RMS error (mm/h)	Relative error (%)	RMS error (dBZ)	Relative error (%)	RMS error (mm/h)
2 km	1.95	0.8285	9.61	0.7128	4.91	1.9915	26.08	1.8603
5 km	2.8	1.1395	14.28	1.0042	8.19	3.1129	51.02	2.5651
7 km	3.02	1.2467	15.5	1.1161	10.16	3.7284	66.21	2.8349

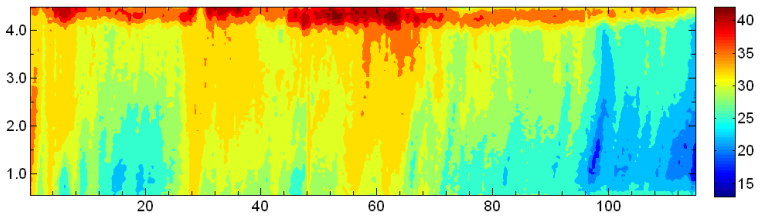

(a) True reflectivity (dBZ)

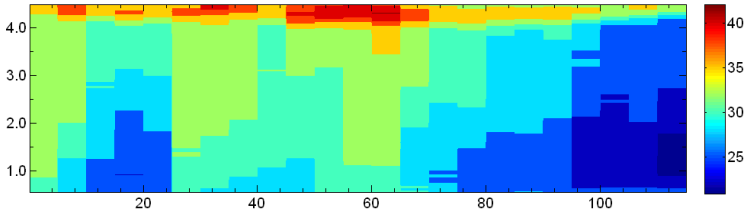

(b) Measured reflectivity (dBZ, horizontal resolution is 5 km)

Figure 1: Vertical sections of stratiform event (TOGA COARE).

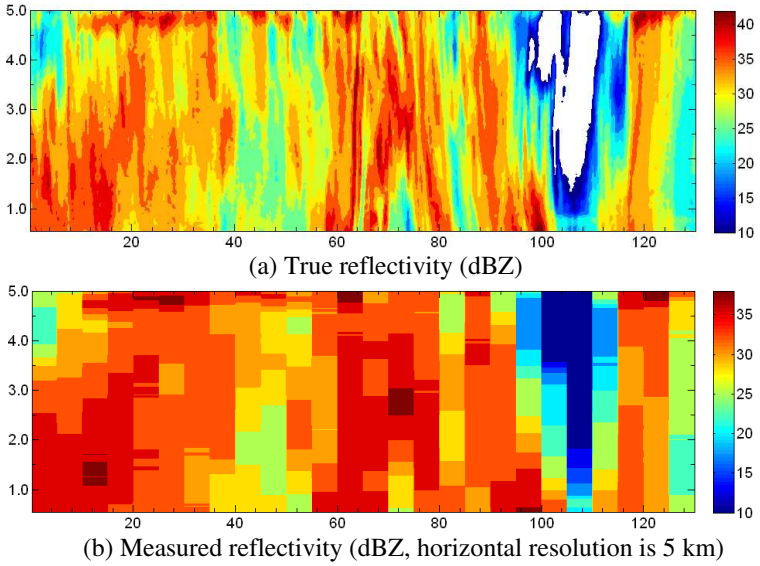

Figure 2: Vertical sections of convective event (CAMEX-3).

The first rain case is the Tropical Ocean Global Atmosphere Coupled Ocean-Atmosphere Response Experiment (TOGA COARE) field campaign on 10 February 1993, shown in Fig. 1(a). The abscissa represents horizontal distance from subsatellite point and the ordinate represents the height of rain cell. This case was a typical stratiform event. The reflectivity distribution measured by spaceborne precipitation radar is given in Fig. 1(b). The second rain case study (Figs. 2(a) and 2(b)) comes from observing of the Hurricane Bonnie during the Third Convection and Moisture Experiment (CAMEX-3), which was a typical convective rainfall. The statistic characterizations of errors caused by NUBF under different radar resolution for the two rain cases are summarized in Table 2. This conclusion can be drawn from the statistics that the deviation of the measured reflectivity from the actual is much more than the measurement accuracy of radar (which is about 1 dB usually) while the antenna beam of spaceborne precipitation radar is nonuniformly filled by convective rain.

4. CONCLUSION

The effects of nonuinform beam filling under different radar horizontal resolutions on rainfall retrieval with the spaceborne precipitation radar have been examined in this paper. We first deduced the formulations of the measured radar effective reflectivity factor and path integrated attenuation under the effect of NUBF. Then we presented the simulated results using the high resolution data from ARMAR. All these analyses indicate that NUBF is a major error source in quantitative rainfall estimate with a spaceborne precipitation radar when the resolution size of the radar is comparable or larger than the rain cell size. Therefore some super-resolution methods need to be introduced to reduce the bias induced by NUBF during the design of the FY3 DPR.

REFERENCES

1. Kozu, T., T. Kawanishi, H. Kuroiwa, et al., "Development of precipitation radar onboard the TRMM satellite," *IEEE Trans. Geoscience and Remote Sensing*, Vol. 39, No. 1, 102–116, 2001.
2. Iugchi, T., R. Oki, E. A. Smith, and Y. Furuhama, "Global Precipitation Measurement program and the development of dual-frequency precipitation radar," *Journal of the Communications Research Laboratory*, Vol. 49, No. 2, 37–45, 2002.
3. Durden, S. L., E. Im, F. K. Li, W. Ricketts, A. Tamer, and W. Wilson, "ARMAR: An airborne rain mapping radar," *Journal of Atmosphere and Oceanic Technology*, Vol. 11, 727–737, 1994.
4. Meneghini, R., J. Eckerman, and D. Atlas, "Determination of rain rate from a spaceborne radar using measurements of total attenuation," *IEEE Trans. Geoscience and Remote Sensing*, Vol. 21, 34–43, 1983.
5. Mega, T., H. Hanado, K. Okamoto, and R. Ushio, "Rain parameters calculated from raindrop size distribution for the design of future spaceborne precipitation radar," *URSI XXVII General Assembly*, [s. n.], 2002.

Comparison of ASAR IM Data and ASAR WS Data in Investigating Co-seismic Deformation of Yutian Earthquake

Xi'ai Cui[1], **Qiming Zeng**[1, 2], **Cunren Liang**[1], **and Jian Jiao**[1]

[1]Institute of Remote Sensing and GIS, Peking University, Beijing 100871, China
[2]Key Lab of Spatial Information Integration and Applications of Beijing Municipal Peking University, Beijing 100871, China

Abstract— An Ms 7.3 earthquake occurred in Yutian (Mar. 21, 2008 local time in China), which is located in Xinjiang Province, several hundred kilometers north of the convergent India-Eurasia plate boundary. Up to 2,200 houses were damaged or flattened and four houses collapsed. The earthquake cost great direct economic losses. In our research, we use Differential Interferometric Synthetic Aperture Radar (D-InSAR) technology to study the co-seismic deformation of the Yutian earthquake and get IM/IM interferogram and WS/WS interferogram. The IM/IM interferogram has fair fringes, showing the deformation clearly in two dimensions. And in the IM/IM interferogram we can find that 105 km width of the IM mode data is not enough to cover the northwestern region of the fault. Due to the limited coverage of IM mode data we can not get the complete co-seismic deformation field. The 405 km width of the WS mode data can overcome this shortcoming. And in the displacement result using the WS data, we can clearly observe that the northwestern region falls and the southeastern region rises. The maximum falling amount is 54 cm and the maximum rising amount is 65 cm. Both the IM/IM interferogram and the WS/WS interferogram can provide useful information about this specific earthquake for the seismological researchers. By comparing the two modes (IM and WS) in investigating co-seismic deformation of the earthquake, we can get more reliable conclusion about Yutian Earthquake.

1. INTRODUCTION

An Ms 7.3 earthquake occurred on March 21, 2008 at 06:33:00 Beijing time in Yutian in the Xinjiang-Xizang border region in China. The epicenter of the earthquake is located at 35.6°N, 81.6°E. The March 21, 2008 event is the first earthquake larger than Ms 7, since the Ms 8.1 earthquake occurred in November, 2001 in the west of Kunlun Mt. in the Qinghai-Xinjiang border. And the Yutian earthquake is one of the largest known historical earthquakes to have occurred in the northern Tibetan Plateau west of the Kunlun Fault System. The earthquake cost great direct economic losses. Up to 2,200 houses were damaged or flattened and four houses collapsed.

Because there are few ground stations, we can hardly use regular investigating methods to survey the Yutian earthquake. Differential Interferometric Synthetic Aperture Radar (D-InSAR) is becoming more and more popular in investigating crustal deformation [3]. In our study, we use the D-InSAR technology to observe the displacement of the Yutian earthquake, with ENVISAT ASAR data and the SRTM 3"-DEM data. Two modes of the ASAR data have been applied, including the Image Mode (IM) and the Wide Swath Mode (WS).

2. STUDY AREA AND DATA USED

2.1. Tectonic Background

The Yutian earthquake took place as a result of normal faulting in the tectonically complex region of the northern Tibetan Plateau. It occurred several hundred kilometers north of the convergent India-Eurasia plate boundary, where the Indian Plate is moving northwards with respect to Eurasia at a rate of approximately 46 mm/yr [1] The uplifted Tibetan Plateau is spreading to the east and, as a result, is an area of east-west extension and eastward crustal motion within a larger region of generally north-south convergence. The Yutian earthquake may reflect the interplay amongst these major tectonic forces. Yutian locates at the intersection of the AltynTagh fault and Kunlun fault Its situation is so special that we should not miss any chance to study this area.

2.2. Data Description and Data Selection

As Fig. 2 shows, the IM image covers only approximately 100 km, but the WS image covers a 400 km wide stripe. We can notice that the WS data will be sufficient for large scale deformation study. Considering the location of Yutian, we found three tracks (track 248, track 477 and track 155) pass our study area (as in Fig. 3). Track 248 and track 477 are descending pass; track 155 is an ascending pass. They are all IM data.

The Yutian earthquake results from the fault dislocation. Taking the spatial distribution of aftershocks into account, we proposed that the slip direction of the specific fault is NE-SW. So only a track can cover both the northwestern part and the southeastern part of the fault. According to Fig. 3, we can know that track 155 is more appropriate than track 248 or track 477. In addition, in our experiment results we can also find track 155 images can obtain a better interferogram. So the IM data we choose track 155 to devote a full discussion.

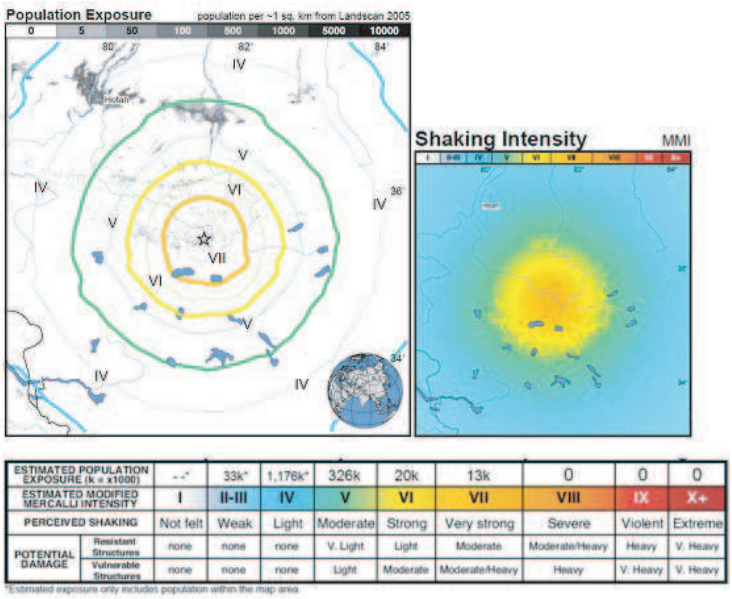

Figure 1: Map of estimated population exposure and shaking intensity (USGS).

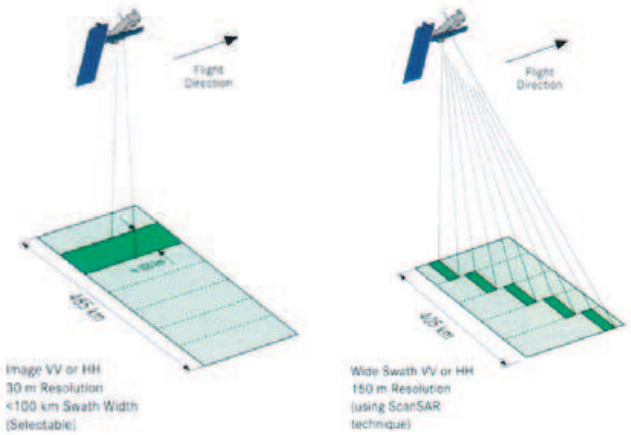

Figure 2: Envisat ASAR IM & WS modes.

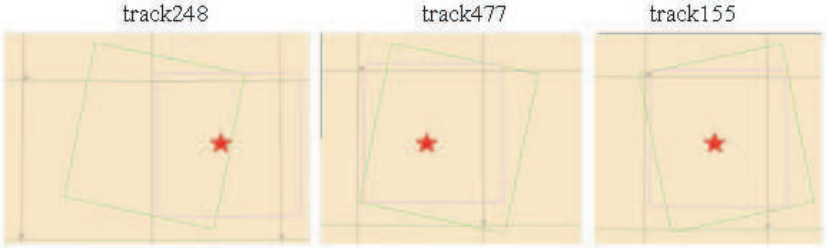

Figure 3: Coverage of track 248, track 477 and track 155. (Red star represents the epicenter; the red rectangular is 100 km × 100 km; the green rectangular stands for the coverage of each track).

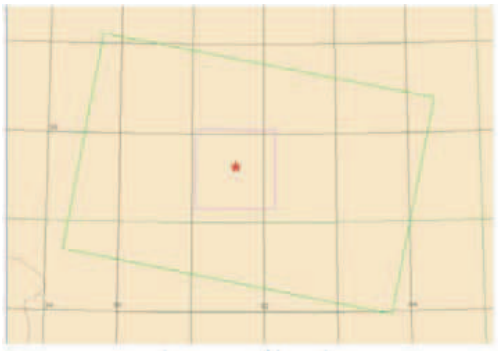

Figure 4: Coverage of the WS data. (Red star represents the epicenter; the red rectangular is 100 km × 100 km; the green rectangular stands for the coverage of WS data).

Table 1: Baselines of InSAR pairs of track 155 (Eolisa).

Temporal / B_{perp}	2007-4-13	2007-6-22	2007-7-27	2007-8-31	2008-2-22	2008-5-2
2007-4-13		70	105	140	315	385
2007-6-22	502		35	70	245	315
2007-7-27	394	108		35	210	280
2007-8-31	808	306	414		175	245
2008-2-22	239	263	155	569		70
2008-5-2	284	218	110	524	45	

Table 2: List of the used IM-IM and WS-WS InSAR pairs.

Master	Slave	track	mode	B_{perp}/m
20080222	20080502	155	IM-IM	45
20071129	20080417	434	WS-WS	N/A

The WS data covers a larger area, as is shown in Fig. 4.

2.3. Selected Data

In Table 1, we can notice that the 20080222-20080502 will be the best choice for the D-InSAR processing [2]. This InSAR pair has a smaller normal baseline and a shorter temporal baseline. In the same way we choose a proper WS InSAR pairs 20071129-20080417. The Table 2 is our selected result.

3. RESULTS

3.1. Result of IM-IM InSAR Pairs

The IM-IM interferogram has clear fringes. And from the fringe pattern we can distinctly discover that track 155 does not cover the whole area the Yutian earthquake affected. But in the mean time it shows a lot of details of the fringe pattern.

3.2. Result of WS-WS InSAR Pairs

The WS-WS interferogram covers 400 km × 400 km. It shows the complete fringe pattern of the co-seismic deformation filed of the Yutian earthquake, as is shown in Fig. 6. The black rectangular in Fig. 6 is the coverage of the IM data. And Fig. 7 gives the LOS displacement distribution. This displacement map will help the earthquake researchers a lot.

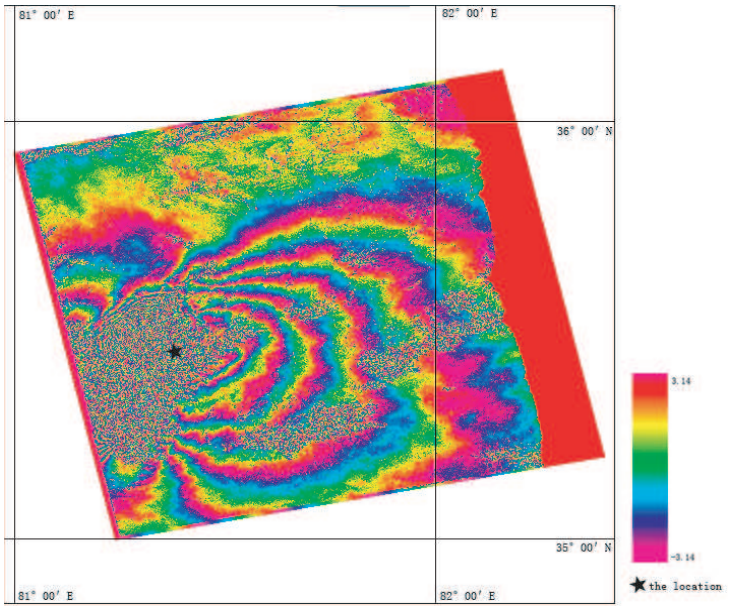

Figure 5: IM-IM Interferogram (actual perpendicular baseline: −28.2 m).

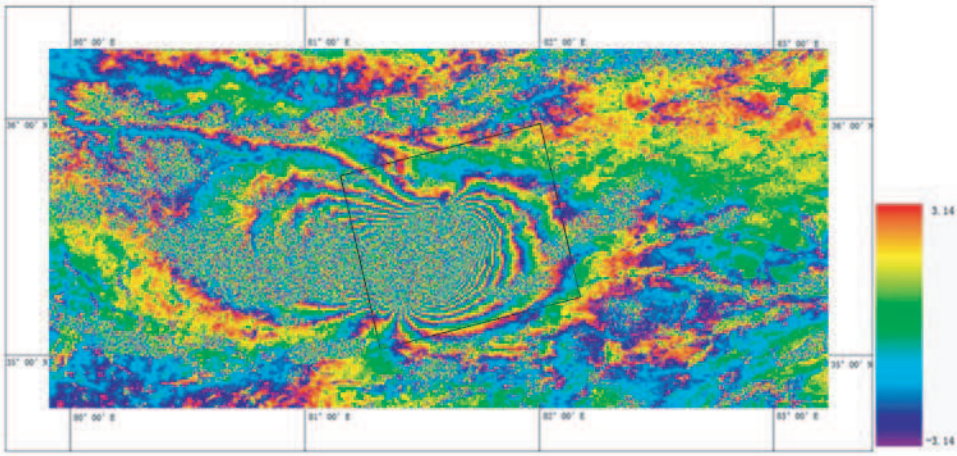

Figure 6: Part of WS-WS Interferogram (actual perpendicular baseline: 182.5 m).

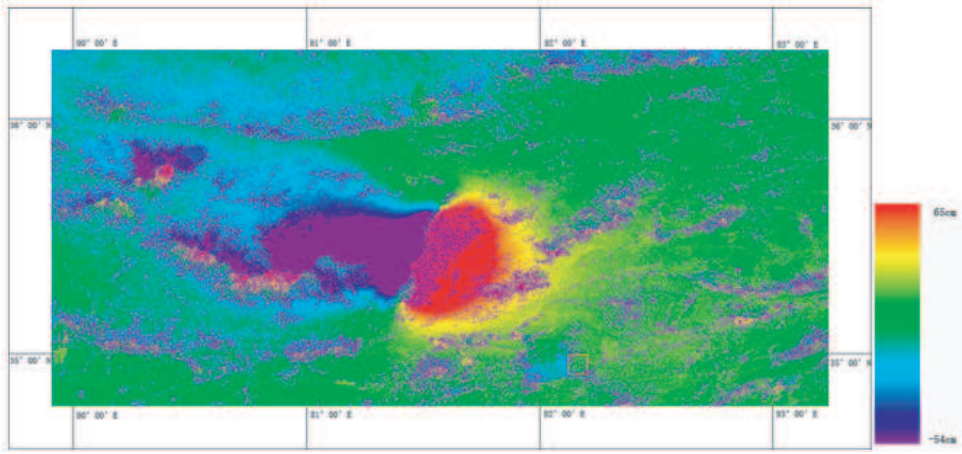

Figure 7: Part of WS-WS LOS displacement map. (Negative value stands for falling; Positive value stands for rising).

4. CONCLUSION AND DISCUSSION

The IM/IM interferogram has fair fringes, showing the deformation clearly in two dimensions. And in the IM/IM interferogram we can find that 105 km width of the IM mode data is not enough to cover the northwestern region of the fault. Due to the limited coverage of IM mode data we can not get the complete co-seismic deformation field. The 405 km width of the WS mode data can overcome this shortcoming. And in the displacement result using the WS data, we can clearly observe that the northwestern region falls and the southeastern region rises. The maximum falling amount is 54 cm and the maximum rising amount is 65 cm. Both the IM/IM interferogram and the WS/WS interferogram can provide useful information about this specific earthquake for the seismological researchers. By comparing the two modes (IM and WS) in investigating co-seismic deformation of the earthquake, we can get more reliable conclusion about Yutian Earthquake.

ACKNOWLEDGMENT

We are grateful to ESA for supplying the ASAR IM and WS data via Dragon Program.

REFERENCES

1. http://earthquake.usgs.gov/.
2. Zhang, H., Q. Zeng, Y. Liu, X. Li, and L. Gao. "The optimum selection of common master image for series of differential SAR processing to estimate long and slow ground deformation," *IGARSS'05 Proceedings*, 4586–4589, Seoul, Korea, July 2005.
3. Massonnet, D., M. Rossi, and C. Carmona, "The displacement field of the Landers earthquake mapped by radar interferometry," *Nature*, 138–142, 1993.

Design of Electrometric Amplifier for Aspiration Condenser Measurement

Z. Roubal and M. Steinbauer
Faculty of Electrical Engineering and Communication, Brno University of Technology
Kolejní 2906/4, Brno 612 00, Czech Republic

Abstract— It was confirmed that concentration of light air ions has positive influence on human health. When measuring the concentration of light air ions using aspiration condenser, we meet problems related to measurement of very low current of order 10^{-12} A. In this paper we will analyze possible sources of error, caused by noise, real properties of used operational amplifier and leakage current. Based on these analysis, a new electrometric amplifier with minimalised systematic error will be designed.

1. INTRODUCTION

Measurement of concentration of air ions and air ions mobility spectrum is very actual problem [1]. At the DTEEE we have designed a gerdien tube of new construction [2, 3] and we needed to design high quality electrometric amplifier, which is able to measure current I_{ion} generated by air ions with sufficient accuracy. Crucial property of this amplifier is low input current, because it must be capable to measure current of order 10^{-14} A. Other critical parameters of amplifier are equivalent input noise current and input noise voltage. If a high value resistor is used as a current-to-voltage converter, this acts as an additive source of noise. In this paper we will describe several will be individual potentiality realisation measuring very small current generate gerdien tube.

2. ELECTROMETRIC AMPLIFIER WITH INSTRUMENTAL OPERATIONAL AMPLIFIER

The circuit diagram of measuring current amplifier is shown in Figure 1. The current flowing thru the gerdien tube is sensing on resistor R_1 and amplified by the instrument electrometric amplifier INA116. This operational amplifier has very low input current 100 fA, thereby the systematic error is suppressed. By the relays R_{E3} and R_{E4} the gain coefficient can be switched so it is possible to measure in the wide band of air ions concentration values. INA116 has pins 2/4 and 5/7 connected to the input buffers which we use to active shielding of aspiration condenser and to eliminate earth-leakage currents on the PCB. Operational amplifier OPA121 is used as the source with low output impedance to offset compensation of INA116. During the measurement process the INA116 offset is firstly set with relays R_{E1} switched off. Thanks to this compensation we can suppress the residual influence of the operational amplifier INA116 input currents. After this the capacitor C_1 is charged

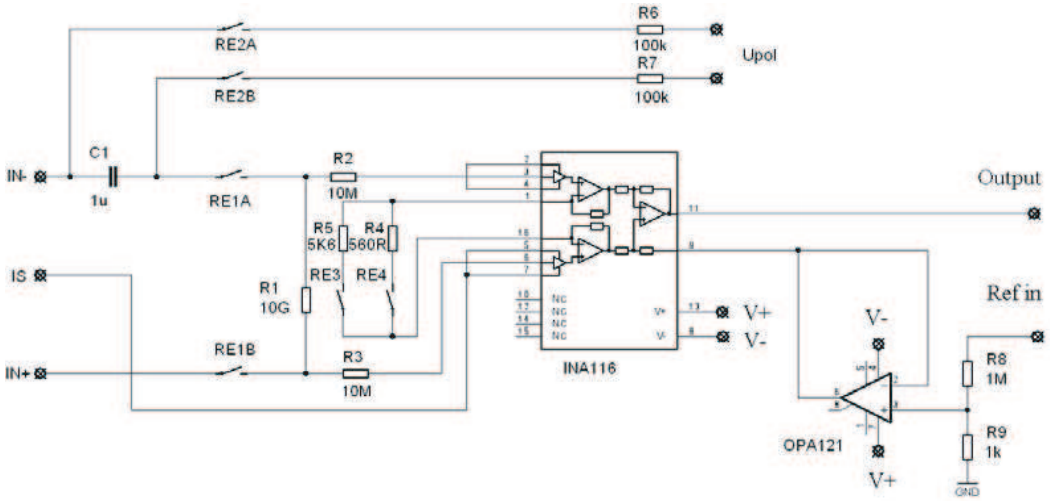

Figure 1: The circuit diagram of measuring.

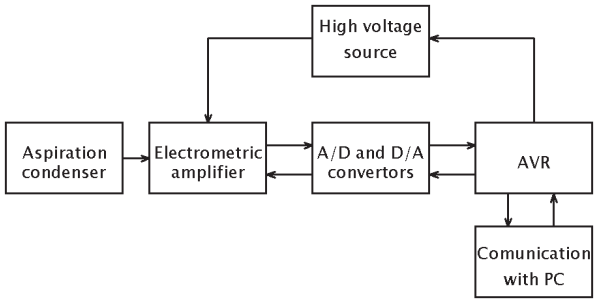

Figure 2: Block circuit diagram measuring system electrometric amplifier.

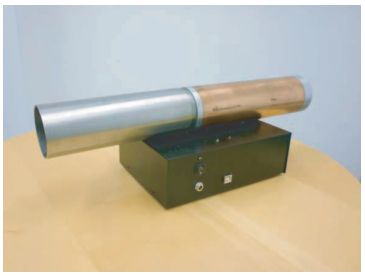

Figure 3: The new construction of measurement system.

by the voltage U_{POL} switching the R_{E2} relay on. In the next step relay R_{E2} switch off and relay R_{E1} switch on and the current from tube is measured. When changing the gain coefficient of OA INA116 it is necessary to set the offset again.

Electrometric amplifier is equipped by digital unit with microcontroller AVR, which controls calibrating and measuring process, sets up polarization voltage and communicates with PC. Block diagram of whole system is in the Figure 2. EEPROM is used as storage for correction constants. These constants serves for elimination of input bias current and condenser leak current influence and are set during calibration. The Figure 3 shows final construction of new measurement system.

3. ELECTROMETRIC AMPLIFIER WITH FEEDBACK AMMETER

Feedback ammeter has practically zero input resistance, in contrast to shunt ammeter. Our design uses the precise operational amplifier LMP7721, with guaranteed bias current smaller than 20 fA and typical value 3 fA. The LMP7721 is the standard type operational amplifier. Because there isn't input for compensation offset voltage, it is necessary to use external compensation, see Figure 4 and Figure 5.

For feedback ammeter based on near ideal amplifier with gain A, input current I_{bias} and input offset voltage U_{OS} we can write [4, 5]

$$U_{out} = \frac{U_{out}}{A} - (I_{ion} - I_{bias}) \cdot R_f + U_{OS}. \tag{1}$$

We may be neglect first part of the Equation (1), because the gain of used operation amplifier 10^6. Further from Equation (1) is considerable that we must compensate the offset voltage for minimal value U_{out}. Last significant component of (1) is input offset current I_{bias}. This current increases two times every 10°C and causes fluctuation of output voltage with temperature change.

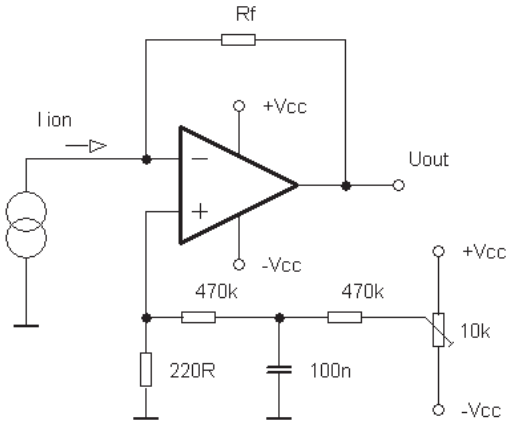

Figure 4: Analog compensation of offset voltage.

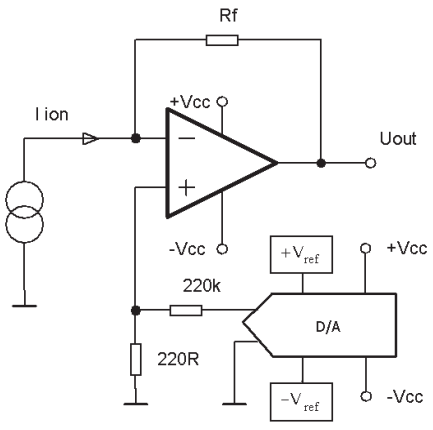

Figure 5: Application of D/A convertor for compensation of offset voltage.

If we measure air ions in the wide temperature range, we have to use thermoelectric cooling to stabilize circuit temperature. When all this requirements are fulfilled, we can write simple equation

$$U_{out} = -I_{ion} \cdot R_f. \tag{2}$$

The next source of error is noise generated by operational amplifier and feedback resistor. Output noise voltage is derived in [5]. The U_N is noise input voltage operation amplifier, the I_N^- is inverting input current noise OA, k is Boltzmann's constant, T is absolute temperature and Δf is noise bandwidth.

$$U_{NO} = \sqrt{U_N^2 + \left(I_N{}^- \cdot R_f\right)^2 + 4kTR_f\Delta f}. \tag{3}$$

After recalculation to input noise current, we have

$$I_{NI} = \sqrt{\left(\frac{U_N}{R_f}\right)^2 + \left(I_N^-\right)^2 + \frac{4kT\Delta f}{R_f}}. \tag{4}$$

We have optimized the resistance R_f for minimum input noise current I_{NI} using the simulator PSpice. For this simulation we had to prepare noise model of OA LMP7721.

Practically we are limited by produced high-impedance resistors. The stabile resistors with low additional noise manufactured in Tesla Blatna have maximum value 10 GΩ. For this resistance the input noise current is about 16 fA.

4. ELECTROMETRIC AMPLIFIER WITH FEEDBACK COULOMBMETER

For very small current is advantageous to measure the charge over time instead of current. Output voltage of feedback coulombmeter for zero initial condition is

$$U_{out} = -\frac{1}{C_{int}} \int_0^{T_{int}} i_{ions}(t) \cdot dt. \tag{5}$$

The C_{int} is feedback integration capacity. If we measure U_{out} at the end of integration interval T_{int}, we can determine average current for this interval

$$I_{AVG} = \frac{U_{out} \cdot C_{int}}{T_{int}} \tag{6}$$

The coulombmeter theoretically hasn't Johnson's noise [6], so the charge method of current measurement results in lower noise than direct current measurement with feedback ammeter. The coulombmeter has current noise less than 1 fA peak to peak [6].

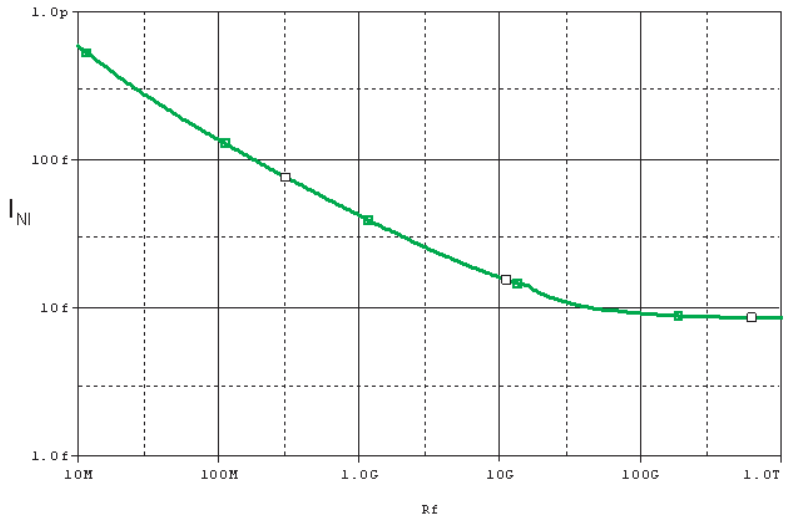

Figure 6: The dependence of input noise current on feedback resistance R_f for $\Delta f = 1$ Hz.

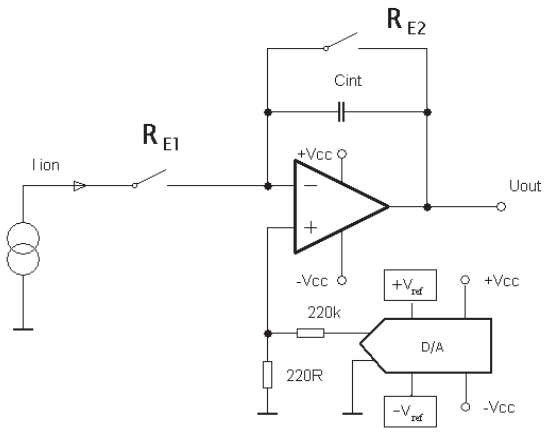

Figure 7: Coulombmeter with automatic zero adjusting.

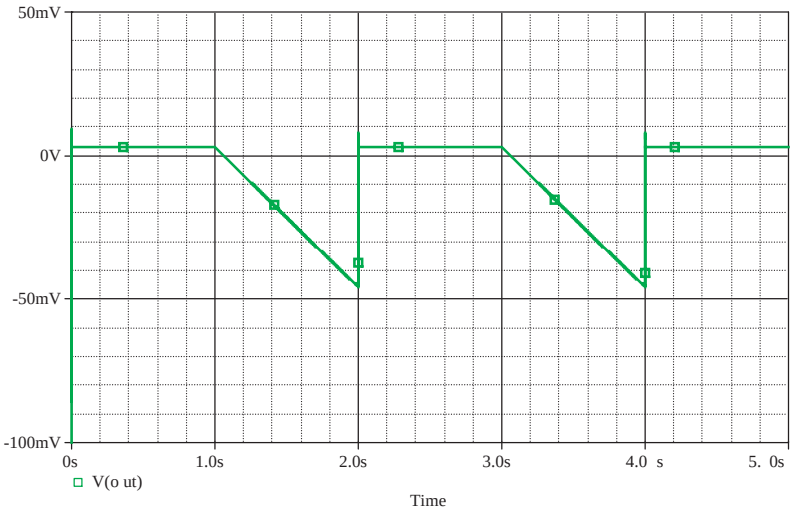

Figure 8: The output voltage of coulombmeter for $I_{ion} = 1\,\text{pA}$, $C_{int} = 20\,\text{pF}$ and $T_{int} = 1\,\text{s}$.

In the Figure 7 is measuring current amplifier with automatic zero adjusting at the beginning of measuring interval. Firstly, the relay R_{E1} is switched off and R_{E2} is switched on. Consequently input offset voltage U_{OS} is compensated using D/A convertor. This step is important, because input offset voltage create additive error. In the next step, the input bias current is measured with both relays switched off and obtained value is used for correction of current (6).

Output of the coulombmeter is connected to fast 16-bit A/D convertor ADS8519 and data are processed in AVR microprocessor. The integration condenser C_{int} must be of high quality. The best type is polystyrene condenser with insulation resistance of order $10^{12}\,\Omega$ and with low dielectric absorption, which causes non-zero initial conditions. In the Figure 8 is example of output signal of realized coulombmeter. The most advantage of coulombmeter is in large measuring range without need of changing integration condenser, we can simply change integration interval. It is possible to measure thru six decade without capacity switching [7].

5. CONCLUSION

We have designed the new measurement system with automatic calibration and correction of condenser leakage current and with digital compensation of offset voltage. For feedback ammeter type of electrometric amplifier we derived optimal feedback resistance using simulation program. For this purpose the noise model of LMP7721 was prepared, which respect noise $1/f$ in the low frequency. The input noise current of suggested amplifier has value 16 fA for 10 GΩ feedback resistor. It is necessary to use quality measuring resistor with low additional noise. The best result for measurement of low current gives the coulombmeter, which has theoretically zero Johnson's noise, but

is very sensitive to offset voltage. This problem was solved with automatic zero adjusting and measuring algorithm which compensate real properties of operational amplifier. The most advantage of coulombmeter is in large measuring range.

ACKNOWLEDGMENT

The researches described in the paper were financially supported by research plans MSM 0021630513 and MSM 0021630516 of the Ministry of Education, Youth and Sports of the Czech Republic.

REFERENCES

1. Charry, J. M. and R. Kavet, *Air Ions: Physical and Biological Aspects*, CRC Press, Inc. Boca Raton, Florida, 1987.
2. Vojtek, T., T. Skoupil, P. Fiala, and K. Bartusek, "Accuracy of air ion field measurement," *PIERS Proceedings*, 412–415, Cambridge, USA, March 26–29, 2006.
3. Steinbauer, M., P. Fiala, K. Bartusek, and Z. Szabó, "Experiments with accuracy of air ion field measurement," *PIERS Proceedings*, 1062–1066, Hangzhou, China, March 24–28, 2008.
4. Tardif, A., "Remarks on the construction and design of a solid-state photometer for astronomy," *International Amateur-Professional Photoelectric Photometry Communication*, No. 12, 41–59, 1983.
5. Dostál, J., "Operacní Zesilovace," *BEN*, Praha, 2005.
6. Dostál, J., "Low level measurement," *Keithley*, USA, 2004.
7. Burkhardt, W., M. Iacopini, and P. Maranesi, "Picoammeter for ion chamber spans six decades without range switching," *The Institute of Electrical and Electronics Engineers*, Vol. 30, No. 1, 311–313, 1983.

Calculation of Angstrom Coefficient of Nano-size Particles in Liquid Environment

Gholamreza Shayeganrad[1], **Leila Mashhadi**[2], **and Tahereh Ghanbarirad**[1]

[1]Islamic Azad University, Karaj Branch, Karaj, Iran
[2]Physics Department, Amirkabir University of Technology, Tehran, Iran

Abstract— One of the optical properties of nano-size particles in the liquid environment is the optical thickness. Optical thickness is measure of amount direct light reaching a detector that respond to a single wavelength of light. It is affected by absorption and scattering. The portion of optical thickness due to nanoparticles is called nanoparticles optical thickness or nanoparticles optical depth, τ. In this work, we have shown that τ can be related to percent transmission of direct light. Moreover, the Angstrom coefficient is defined which express the wavelength dependence of extinction coefficient, α_e. The obtained values of α_e can be used in principle to evaluate particle size and determine the size distribution of the particles.

1. INTRODUCTION

Interest in study and production of nanoscale structures is increased and developed during the last two decades. The term nanoparticle represents particles that are composed of up to lo^6 atoms or less but confined to size less than 100 nm. Because of small size and high percentage of surface atoms, their properties differ from those of the same atoms bonded together to form bulk materials and introduces many size-dependent phenomena. For instance, many of the beautiful colors of stained-glass windows are a result of the presence of small metal oxide clusters in the glass, having a size comparable to the wavelength of light. Particles of different sizes scatter different wavelengths and imparting different colors to the glass. The finite size of the particle confines the spatial distribution of the electrons, leading to the quantized energy levels due to size effect.

In general, nanoparticles due to their smaller size, interparticle interactions, and a large surface to volume ratio, exhibit interesting unique properties which include nonlinear optical behavior, increased mechanical strength, enhanced diffusivity, high specific heat, magnetic behavior and electric resistivity, etc [1]. They are attracting a great deal of attention because of their applications in the field of biotechnology [2], sensors [3], medical diagnostics [4], electronics [5], ceramics [6], catalysis [7], high performance engineering materials, magnetic data storage, optics and conducting adhesives and nanocomposites [8–10].

During the last decade, while formation of nano-particles under laser ablation of solids in gas and vacuum has been drastically explored, formation in liquid environment has been much less investigated. Commonly, nanoparticles of various species of materials such as metals [11–14], metal oxides [15–17], semiconductors [18–20], and organic materials [21, 22] are obtainable by irradiating intense laser light onto those materials located in solvents.

The aim of this paper is to describe optical properties of nano-size particles in the liquid environment based on the optical depth which is altered by absorption and scattering. Moreover, the wavelength dependence of optical thickness is studied by introducing the Angstrom coefficient which is suitable for evaluating particle size and determining the size distribution of the particles.

In this work the following assumptions have been considered:

1. The scattering of the monochoromatic or quasi-monohoromatic light that the its amplitude is either constant or fluctuates with time much more slowly than $\exp(-\omega t)$, where ω is the angular frequency and t is time.
2. The elastic scattering in which scattered light has the same frequency as the incident light.
3. The medium surrounding the scatter is homogeneous, linear, isotopic, and nonabsorbing.

2. THE ANGSTROM COEFFICIENT

Optical thickness (or optical depth) is a measure of the amount of direct light reaching a detector that responds to a single wavelength of light. Optical thickness of nano-particles is affected by both

scattering and absorption. The portion of optical thickness due to absorption and scattering nanoparticles are called absorption optical thickness (AOT) and scattering optical thickness (SOT), respectively, which are defined as:

$$\tau = -\ln(T) \qquad \text{or} \qquad T = \exp(-\tau) \tag{1}$$

The whole optical depth of nanoparticles, τ is defined as follows:

$$\tau(\lambda) = \tau_a(\lambda) + \tau_s(\lambda) \tag{2}$$

where τ_a and τ_s are absorption and scattering optical depth, respectively, $T = I/I_0$ denotes the transmittance, I_0 is the incident intensity and I is the transmitted intensity received by detector.

The dependence of optical thickness to wavelength can be defined through Angstrom power law:

$$\tau = \beta\lambda^{-\alpha} \tag{3}$$

In this formula, β denotes Angstrom's coefficient, α denotes the Angstrom's exponent, and λ represents the wavelength. α and β are independent of wavelength, and can be used to describe the size distribution of nano-particles.

3. SINGLE NANOSPHERE SCATTERING

In a group of nanoparticles which are randomly positioned and widely separated, each particle is excited by the external field and the secondary fields scattered by all other particles. However, if the number of particles is sufficiently small and their separation is sufficiently large, the contribution of the secondary waves to the field exciting each particle is much smaller than the external field. Therefore, the total scattered field can be well approximated by the sum of the fields generated by the individual particles in response to the external field in isolation from the other particles so called the single scattering approximation. Under this condition, the optical absorption and scattering properties of a homogeneous metal nanosphere of volume V embedded in an optically homogeneous nonabsorbing medium can be calculated using e.g., Mie's theory [23, 24]. The AOT and SOT of small spherical metal particles embedded in a nonabsorbing medium can be written as follows:

$$\tau_a = \frac{18\pi N_s V \varepsilon_m^{3/2}}{\lambda} \frac{\varepsilon_2}{(\varepsilon_1 + 2\varepsilon_m)^2 + \varepsilon_2^2} \tag{4a}$$

$$\tau_s = \frac{24\pi^3 N_s V^2 \varepsilon_m^2}{\lambda^4} \frac{(\varepsilon_1 - \varepsilon_m)^2 + \varepsilon_2^2}{(\varepsilon_1 + 2\varepsilon_m)^2 + \varepsilon_2^2} \tag{4b}$$

where $\varepsilon = \varepsilon_1 + i\varepsilon_2$ and ε_m, are the dielectric constant of the spheres and the medium, respectively, N_s is the number of spheres per aria perpendicular to the beam direction, and λ is the wavelength of the incident light.

Comparing these equations with Eq. (3), the Angstrom's coefficient and Angstrom's exponent of absorption and scattering are given by:

$$\beta_a = 18\pi N_s V \varepsilon_m^{3/2} \frac{\varepsilon_2}{(\varepsilon_1 + 2\varepsilon_m)^2 + \varepsilon_2^2}, \quad \alpha_a = 1 \tag{5a}$$

$$\beta_s = 24\pi^3 N_s V^2 \varepsilon_m^2 \frac{(\varepsilon_1 - \varepsilon_m)^2 + \varepsilon_2^2}{(\varepsilon_1 + 2\varepsilon_m)^2 + \varepsilon_2^2}, \quad \alpha_s = 4 \tag{5b}$$

The absorption coefficient is related to the imaginary part of the complex dielectric constant of the spheres, ε_2. The principle of the color changes by small particles lies in minimizing the denominator of Eq. (8a), that predicts the existence of an absorption peak at wavelength λ_R when

$$\varepsilon_1(\lambda_R) = -2\varepsilon_m \tag{6}$$

This condition is known as resonance or surface plasmon resonance (SPR). The SPR wavelength λ_R can be determined by Angstrom's coefficient based on the particle properties, ε, and its local

environment, ε_m. At the condition of SPR or resonance, Eqs. (5a) and (5b) are simplified to

$$\beta_a = \frac{18\pi N_s V \varepsilon_m^{3/2}}{\varepsilon_2} \tag{7a}$$

$$\beta_s = 24\pi^3 N_s V^2 \varepsilon_m^2 \left[\frac{9\varepsilon_m^2}{\varepsilon_2^2} + 1\right] \tag{7b}$$

in which in the small size approximation the absorption Angstrom's coefficient, β_a, is much larger than scattering Angstrom's coefficient, β_s.

On the other hand, according to quantum mechanics theory, we would introduce nanoparticles by quantized energy as:

$$E = \frac{n_x^2\pi^2\hbar^2}{2mL_x^2} + \frac{n_y^2\pi^2\hbar^2}{2mL_y^2} + \frac{n_z^2\pi^2\hbar^2}{2mL_z^2} \tag{8}$$

where L_i and n_i $(i = x, y, z)$ are particle dimension and integer number, respectively. It is interesting to note that nanoparticle or cluster potential, in comparison to the atom, is not necessarily spherical symmetric and separation of the discrete energy levels are in order of meV. From Eq. (8), we see that energy depends inversely to the nanoparticles size. Therefore, clusters of different sizes will have different electronic structures, and different energy-level separations. With increasing size of the particles number of discrete energy levels will be increased and shift of the levels decreased which leads to absorb larger wavelength by larger clusters. This means that clusters with different sizes have different colors, and hence the size of the clusters can be used to engineer the color of the materials. Because the clusters have discrete energy levels, they will own a series of peaks corresponding to the separations of the energy levels of the cluster. SPR wavelength determines the separation between the lower occupied level and higher unoccupied energy level.

The SOT can be related to the nano-particle size distribution (NPSD) (i.e., the $n(x, R)$) by following integral:

$$\beta_s = \int_0^\infty Q_e(R)\pi R^2 n(x, R)dR \tag{9}$$

where R is the particle radius and $Q_e(R, \lambda)$ denotes efficiency of scattering can be written as:

$$Q_e(R) = \frac{128\pi^5 R^6 \varepsilon_m^2}{3} \frac{(\varepsilon_1 - \varepsilon_m)^2 + \varepsilon_2^2}{(\varepsilon_1 + 2\varepsilon_m)^2 + \varepsilon_2^2} \tag{10}$$

Since $n(x, R)$ cannot be written analytically, a numerical approach is followed to separate $n(x, R)$ into two parts as $N(x, R) = h(x, R) \cdot f(x, R)$, where $h(x, R)$ is rapidly varying function with R and $f(x, R)$ is slowly varying. Hence the above equation changes to

$$\beta_s = \int_0^\infty Q_e(R)\pi R^2 f(x, R)h(x, R)dR \tag{11}$$

If $f(x, R)$ is assumed to be constant, a system of linear equations results, which may be written as:

$$\beta_s = Af(x, R) + \eta \tag{12}$$

where

$$A = \int_0^\infty Q_e(R)\pi R^2 h(x, R)dR \tag{13}$$

and η is an error which arises due to deviation between the measured τ_s and theoretical.

4. DEPENDENT PARTICLE GROUP SCATTERING

When the scattering medium contains very many metal nanoparticles, the single-scattering approximation and therefore equations above are no longer valid. Now one must explicitly take into account that each particle is illuminated by light scattered by other particles as well as by the attenuated incident light. This means that each particle scatters light that has already been scattered by other particles, so that the light inside the scattering medium and the light leaving the medium have a diffuse component. On the other hand, the oscillating dipoles of neighboring particles influence the

frequency of a central particle and this effect must be considered. This effect is called dipole-dipole interactions between neighboring nanoparticles. In this case, a traditional and simplest approach to describe the optical response of the system is effective medium theories [25, 26]. These techniques assume an effective dielectric constant corresponds to the particles and surrounding medium in which provides us to calculate the absorption and reflection coefficients.

Through the various available effective medium theories, Maxwell-Garnett's theory is much suitable to describe these dipole-dipole interactions. The effective dielectric constant comprises the metal nanoparticles, ε, and surrounding medium, ε_m, is calculated as:

$$\varepsilon_{av} = (n_{av} + ik_{av})^2 = \varepsilon_m \frac{\varepsilon\,(1+2\phi) + 2\varepsilon_m\,(1-\phi)}{\varepsilon\,(1-\phi) + \varepsilon_m\,(2+\phi)} \tag{14}$$

where $0 \leq \phi \leq 1$ is the metal nanopartcles volume fraction. The transmittance, T, of radiation with a wavelength λ through the nanoparticles and surrounding medium can be calculated as:

$$T = \exp(-\tau)\,\frac{(1-R)^2 + 4R\sin^2\varphi}{1 + R^2\exp(-2\tau) - 2R\cos(\theta+2\varphi)\exp(-\tau)} \tag{15}$$

where $\theta = 4\pi n_{av} l/\lambda$, $\varphi = \tan^{-1}[2k_{av}/(n_{av}^2 + k_{av}^2 - 1)]$ and R is the reflectance at normal incidence

$$R = \frac{(n_{av}-1)^2 + (\xi\lambda/4\pi)^2}{(n_{av}+1)^2 + (\xi\lambda/4\pi)^2} \tag{16}$$

in which $\xi = 4\pi k_{av}/\lambda$ is the absorption coefficient. If the absorption is very small ($n_{av} \gg k_{av}$), Eq. (16) reduces to

$$R = \frac{(n_{av}-1)^2}{(n_{av}+1)^2} \tag{17}$$

When the absorption coefficient is much larger than $4\pi/\lambda$, which means a penetration depth of less than wavelength, the second term in Eq. (16) becomes dominant and the reflectivity becomes $R(\alpha > 4\pi/\lambda) = 100\%$.

5. CONCLUSION

The peak wavelength of the optical absorption, which largely determines the color, depends on the size, and on the type of metal particle. Single scattering approximation, is credible when the number of particles is sufficiently small and their separation is sufficiently large, predict the surface plasmon resonance (SPR) wavelength λ_R can be determined by Angstrom's coefficient depend on the particle properties, ε, and its local environment, ε_m. The absorption occurs because electrons are induced by the photons of the incident light to make transitions between the lower occupied levels and higher unoccupied energy levels of the materials. When the scattering medium contains very many metal nanoparticles, the single-scattering approximation and therefore single scattering approximation is no longer valid. In addition dipole-dipole interactions between neighboring nanoparticles must be considered. Under these conditions, Maxwell-Garnett's theory is much suitable by definition an effective dielectric constant comprises the metal nanoparticles, ε, and surrounding medium, ε_m.

REFERENCES

1. Gleiter, H., "Nanostructured materials: Basic concepts and microstructure," *Acta Materialia*, Vol. 48, 1–29, 2000.
2. Mirkin, C. A., R. L. Letsinger, R. C. Muic, and J. J. Storhoff, "A DNA-based method for rationally assembling nanoparticles into macroscopic materials," *Nature*, Vol. 382, 607–609, 1996.
3. Taton, T. A., C. A. Mirkin, and R. L. Letsinger, "Scanometric DNA array detection with nanoparticle probes," *Science*, Vol. 289, 1757–1760, 2000.
4. Storhoff, J. J., R. Elghanian, R. C. Mucic, C. A. Mirkin, and R. L. Letsinger, "One-pot colorimetric differentiation of polynucleotides with single base imperfections using gold nanoparticle probes," *J. Am. Chem. Soc.*, Vol. 120, 1959–1964, 1998.
5. Kastner, M. A., "Artificial atoms," *Phys. Today*, Vol. 46, 24, 1993.
6. Freer, R., "Nanoceramics," Institute of Materials, London, 1993.

7. Eichhorn, B. W. and S. Alayoglu, "PtRu core-shell nanoparticles for heterogeneous catalysis," IPC8 Class: AB01J2340FI, USPC Class: 429 17.
8. Dagani, R., "Fullerenes in nature: C_{60}," *Chem. Eng. News*, Vol. 77, 54–63, 1992.
9. Hamillton, J. F. and R. C. Baetzold, "Catalysis by small metal clusters," *Science*, Vol. 205, 1213–1220, 1979.
10. Schmid, G., "Large clusters and colloids. metals in the embryonic state," *Chem. Rev.*, Vol. 92, 1709–1727, 1992.
11. Yang, G. W., "Laser ablation in liquids: Application in the synthesis of nanocrystals," *J. Phys. Chem. B*, Vol. 52, 647–698, 2007.
12. Pyatenko, A., K. Shimokawa, M. Yamaguchi, O. Nishimura, and M. Suzuki, "Synthesis of silver nanoparticles by laser ablation in pure water," *Appl. Phys. A: Mater. Sci. Process.*, Vol. 79, 803–806, 2004.
13. Kawasaki, M. and K. Masuda, "Laser fragmentation of suspended gold flakes via spherical submicroparticles to fine nanoparticles," *J. Phys. Chem. B*, Vol. 109, 9379–9388, 2005.
14. Nichols, W. T., T. Sasaki, and N. Koshizaki, "Laser ablation of a platinum target in water. I. Ablation mechanisms," *J. Appl. Phys.*, Vol. 100, 114–912, 2006.
15. Tsuji, T., T. Hamagami, T. Kawamura, J. Yamaki, and M. Tsuji, "Laser ablation of cobalt and cobalt oxides in liquids: Influence of solvent on composition of prepared nanoparticles," *Appl. Surf. Sci.*, Vol. 243, 214–219, 2005.
16. Phuoc, T. X., B. H. Howard, D. V. Martello, Y. Soong, and M. K. Chyu, "Synthesis of $Mg(OH)_2$, MgO, and Mg nanoparticles using laser ablation of magnesium in water and solvents," *Optics and Lasers in Engineering*, Vol. 46, 829–834, 2008.
17. Singh, S. C. and R. Gopal, "Synthesis of colloidal zinc oxide nanoparticles by pulsed laser ablation in aqueous media," *Physica E: Low-dimensional Systems and Nanostructures*, Vol. 40, 724–730, 2008.
18. Anikin, K. V., N. N. Melnik, A. V. Simakin, G. A. Shafeev, V. V. Voronov, and A. G. Vitukhnovsky, "Formation of ZnSe and CdS quantum dots via laser ablation in liquids," *Chem. Phys. Lett.*, Vol. 366, 357–360, 2002.
19. Asahi, T., T. Sugiyama, and H. Masuhara, "Laser fabrication and spectroscopy of organic nanoparticles," *Acc. Chem. Res.*, Vol. 41, 1790–1798, 2008.
20. Chen, Q. H. and W. G. Zhang, "Successive preparation of decorated zinc oxide organic sol by pulsed laser ablation and their luminescence characteristics," *Appl. Surf. Sci.*, Vol. 253, 3751–3756, 2007.
21. Sugiyama, T., T. Asahi, and H. Masuhara, "Formation of 10 nm-sized Oxo (phtalocyaninato) vanadium (IV) particles by femtosecond laser ablation in water," *Chem. Lett.*, Vol. 33, 724–725, 2004.
22. Semaltianos, N. G., S. Logothetidis, W. Perrie, S. Romani, R. J. Potter, M. Sharp, P. French, G. Dearden, and K. G. Watkins, "II–VI semiconductor nanoparticles synthesized by laser ablation," *Applied Physics A: Materials Science & Processing*, Vol. 94, 641–647, 2008.
23. Kreibig, U. and M. Vollmer, *Optical Properties of Metal Clusters*, Springer, Berlin, 1995.
24. Bohren, C. F. and D. R. Huffman, *Absorption and Scattering of Light by Small Particles*, Wiley, New-York, 1998.
25. Ung, T., L. M. L. Liz-Marzan, and P. Mulvaney, "Optical properties of thin films of $Au@SiO_2$ particles," *J. Phys. Chem. B*, Vol. 105, 3441–3452, 2001.
26. Liz-Marzán, L. M., "Nanometals formation and color," *Materialstoday*, 26–31, Fabrary 2004.

Application of Genetic Algorithm for of a Partially Immersed Non-uniform Conductivity Cylinder

Wei Chien[1], **Hua-Pin Chen**[2], **Chi-Hsien Sun**[3], **Chien-Ching Chiu**[3], **and Yi Sun**[4]

[1]Electronic Engineering Department, De Lin Institute of Technology
Tu-Cheng, Taiwan, R.O.C.
[2]Department of Electronic Engineering and Institute of Electronic Engineering
Ming Chi University of Technology, Taiwan, R.O.C.
[3]Electrical Engineering Department, Tamkang University
Tamsui, Taiwan, R.O.C.
[4]School of Electrical Engineering, Beijing Jiaotong University, Beijing, China

Abstract— We consider the inverse problem of determining both the shape and the conductivity of a partially immersed non-uniform conductivity cylinder from knowledge of the far-field pattern of TM waves by solving the ill posed nonlinear equation. Based on the boundary condition and the measured scattered field, a set of nonlinear integral equations is derived and the imaging problem is reformulated into an optimization problem. The genetic algorithm is then employed to find out the global extreme solution of the object function. As a result, the shape and the conductivity of the conductor can be obtained.

1. INTRODUCTION

Microwave imaging of the electromagnetic properties of unknown scatterers by inverting scattered field measurements is of great interest because it is associated with numerous applications in biomedical imaging, nondestructive testing, geophysical exploration, etc. In general, inverse scattering is a nonlinear and ill-posed problem [1]. Recently, many methods have been proposed to reconstruct the shape of a 2-D perfect conductor cylinder. General speaking, two main kinds of approaches have been developed. The first is based on gradient searching schemes such as the Newton-Kantorovitch method [2] and the Levenberg-Marguart algorithm [3]. These methods are highly dependent on the initial guess and tend to get trapped in a local extreme. In contrast, the second approach is population-based evolutionary algorithms, such as genetic algorithm [4], particle swarm optimization [5]. Most of the conducing objects are placed in a homogeneous space, while a buried imperfect conductor is reconstructed using GA by Chiu [6]. In this paper, the scattering object is not immersed in a single medium, but instead is located right at the interface of two mediums, the theoretical and numerical analysis of the scattering problem become much more difficult. To the best of our knowledge, there are no investigations on the electromagnetic imaging of partially immersed non-uniform conductivity cylinder. In this paper, the electromagnetic imaging of a partially immersed non-uniform conductivity cylinder is first reported using GA. In Section 2, the relevant theory and formulation are presented. In Section 3, the details of the improved SSGA are given. Numerical results for reconstructing objects of different shapes and conductivies are shown in Section 4. Finally, some conclusions are drawn in Section 4.

2. THEORETICAL FORMULATION

An imperfectly conducting cylinder with conductivity $s(q)$ is partially immersed in a lossy homogeneous half-space, as shown in Fig. 1. Media in regions 1 and 2 are characterized by permittivities and conductivities (e_1, s_1) and (ε_2, σ_2) respectively. A non-uniform conductivity cylinder is illuminated by a transverse magnetic (TM) plane wave. The cylinder is of an infinite extent in the z direction, and its cross-section is described in polar coordinates in the x, y plane by the equation $r = F(q)$, i.e., the object is a star-like shape. We assume that time dependence of the field is harmonic with the factor $\exp(jwt)$. Let E^{inc} denote the incident field from region 1 with incident angle f_1. Owing to the interface between regions 1 and 2, the incident plane wave generates two waves that would exist in the absence of the conducting object. Thus, the unperturbed field is given by

$$E^i(x,y) = \begin{cases} E_1^i(x,y) = e^{-jk_1(x\sin f_1+(y+a)\cos f_1)} + \mathrm{R}e^{-jk_1(x\sin f_1-(y+a)\cos f_1)}, & y \le -a \\ E_2^i(x,y) = Te^{-jk_2(x\sin f_2+(y+a)\cos f_2)}, & y > -a \end{cases} \quad (1)$$

$$R = \frac{1-n}{1+n}, \quad T = \frac{2}{1+n}, \quad n = \frac{\cos f_2}{\cos f_1}\sqrt{\frac{e_2 - js_2(q)/w}{e_1 - js_1(q)/w}}$$
$$k_i^2 = w^2 e_i m_0 - jwm_0 s_i(q), \quad \mathrm{Im}(k_i) \le 0, \quad k_1 \sin f_1 = k_2 \sin f_2, \quad i = 1, 2$$

Since the cylinder is partially immersed, the equivalent current exists both in the upper half space and the lower half space. As a result, the details of Green's function are given first as follows:

(1) When the equivalent current exists in the upper half space, the Green's function for the line source in the region 1, can be expressed as

$$G_1(x, y; x', y') = \begin{cases} G_{21}(x, y; x', y'), & y > -a \\ G_{11}(x, y; x', y') = G_{f11}(x, y; x', y') + G_{s11}(x, y; x', y'), & y \le -a \end{cases} \tag{2}$$

where

$$G_{21}(x, y; x', y') = \frac{1}{2p}\int_{-\infty}^{\infty} \frac{j}{g_1 + g_2} e^{-jg_2(y+a)} e^{jg_1(y'+a)} e^{-ja(x-x')} da \tag{2a}$$
$$G_{f11}(x, y; x', y') = \frac{j}{4} H_0^{(2)}\left[k_1\sqrt{(x-x')^2 + (y-y')^2}\right] \tag{2b}$$
$$G_{s11}(x, y; x', y') = \frac{1}{2p}\int_{-\infty}^{\infty} \frac{j}{2g_1}\left(\frac{g_1 - g_2}{g_1 + g_2}\right) e^{jg_1(y+2a+y')} e^{-ja(x-x')} da \tag{2c}$$
$$g_i^2 = k_i^2 - a^2, \quad i = 1, 2, \quad \mathrm{Im}(g_i) \le 0, \quad y' < -a$$

(2) When the equivalent current exists in the lower half space, the Green's function for the line source in the region 2, is

$$G_2(x, y; x', y') = \begin{cases} G_{12}(x, y; x', y'), & y \le -a \\ G_{22}(x, y; x', y') = G_{f22}(x, y; x', y') + G_{s22}(x, y; x', y'), & y > -a \end{cases} \tag{3}$$

where

$$G_{12}(x, y; x', y') = \frac{1}{2p}\int_{-\infty}^{\infty} \frac{j}{g_1 + g_2} e^{jg_1(y+a)} e^{-jg_2(y'+a)} e^{-ja(x-x')} da \tag{3a}$$
$$G_{f22}(x, y; x', y') = \frac{j}{4} H_0^{(2)}\left[k_2\sqrt{(x-x')^2 + (y-y')^2}\right] \tag{3b}$$
$$G_{s22}(x, y; x', y') = \frac{1}{2p}\int_{-\infty}^{\infty} \frac{j}{2g_2}\left(\frac{g_2 - g_1}{g_2 + g_1}\right) e^{-jg_2(y+y'+2a)} e^{-ja(x-x')} da \tag{3c}$$
$$g_i^2 = k_i^2 - a^2, \quad i = 1, 2, \quad \mathrm{Im}(g_i) \le 0, \quad y' > -a$$

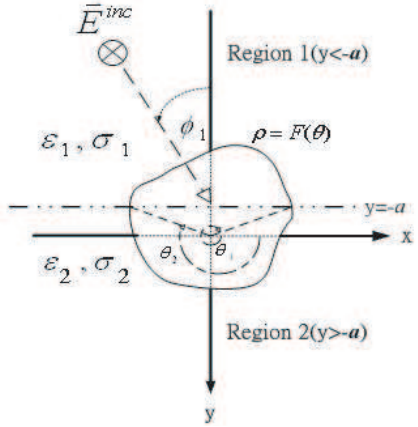

Figure 1: Geometry of the problem in (x, y).

For the direct scattering problem, the scattered field E^S is calculated by assuming that the shape is known. For the inverse problem, we assume the approximate center of the scatterer, which in fact can be any point inside the scatterer, is known. Then, the shape function $F(q)$ and conductivity function $s(q)$ can be expanded as:

$$F(q) = \sum_{n=0}^{N/2} B_n \cos(nq) + \sum_{n=1}^{N/2} C_n \sin(nq) \tag{4}$$

$$s(q) = \sum_{n=0}^{N/2} D_n \cos(nq) + \sum_{n=1}^{N/2} E_n \sin(nq) \tag{5}$$

where B_n, C_n, D_n and E_n are real numbers to be determined, and $2(N+1)$ is the number of unknowns for the shape function and conductivity function.

3. NUMERICAL RESULTS

Let us consider a non-uniform conductivity cylinder which is partially immersed in a lossless half-space ($S_1 = S_2 = 0$) and the parameter a is set to zero. The permittivity in region 1 and region 2 is characterized by $e_1 = e_0$ and $e_2 = 2.56e_0$, respectively. The frequency of the incident wave are chosen to be 1 GHz, with incident angles f_1 equal to 45° and 315°, respectively. For each incident wave 8 measurements are made at the points equally separated on a semi-circle with the radius of 3 m in region 1. Therefore, there are totally 16 measurements in each simulation. The number of unknowns is set to be 18 (i.e., $2(N+1) = 18$), to save the computation time. The population size of 100 is chosen and rank selection scheme is used with the top 30 individuals being reproduced accords to the rank. The search range for the unknown coefficient of the shape function is chosen

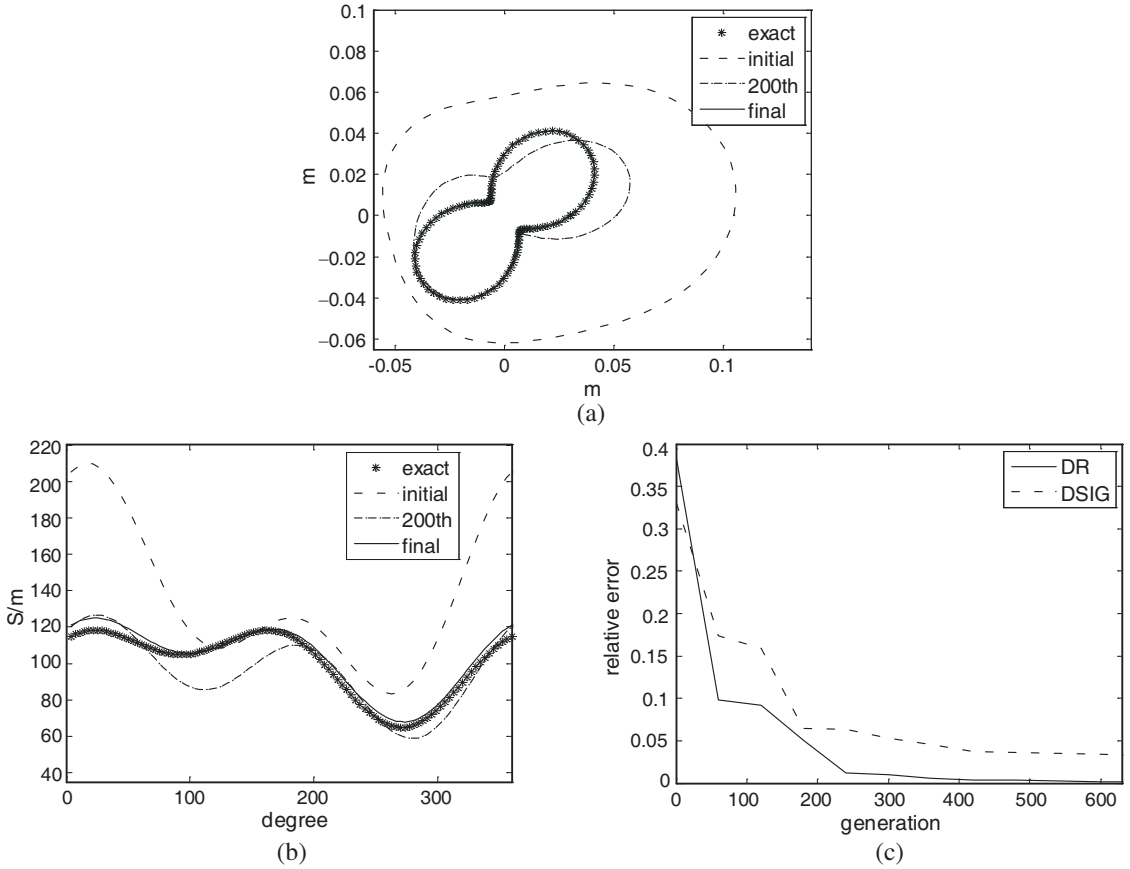

Figure 2: (a) Shape function for example 1. The star curve represents the exact shape, while the solid curves are calculated shape in iteration process. (b) Conductivity function for example 1. The star curve represents the exact conductivies, while the solid curves are calculated conductivies in iteration process. (c) The shape and conductivity function errors versus generation.

to be from 0 to 0.1 and the unknown coefficient of the conductivity is chosen to be from 1 to 200 S/m. The extreme values of the coefficient of the shape function can be determined by the prior knowledge of the objects. The crossover rate is set to 0.1 such that only 10 iterations are performed per generation. The mutation probability is set to 0.05 and the value of a in (11) is chosen to be 0.001. In the examples the size of scatter is about the wavelength, so the frequency is in the resonance range.

In the first example, the shape and conductivity function are chosen to be $F(q) = (0.03 + 0.2\sin 2q)$ m and $s(q) = (100 + 15\cos 2q + 20\sin q)$ S/m. The reconstructed shape function and conductivity function for the best population member are plotted in Fig. 2(a) and Fig. 2(b). The errors for the reconstructed shape DR and the reconstructed conductivity DSIG are shown in Fig. 2(c), of which DR and DSIG are defined as

$$\mathrm{DR} = \left\{ \frac{1}{N'} \sum_{i=1}^{N'} \left[F^{cal}(q_i) - F(q_i) \right]^2 / F^2(q_i) \right\}^{1/2} \tag{6}$$

$$\mathrm{DSIG} = \left\{ \frac{1}{N'} \sum_{i=1}^{N'} \left[s^{cal}(q_i) - s(q_i) \right]^2 / s^2(q_i) \right\}^{1/2} \tag{7}$$

where N' is set to 100. Quantities DR and DSIG provide measures of how well $F^{cal}(q)$ approximates $F(q)$ and $s^{cal}(q)$ approximates $s(q)$, respectively. From Fig. 2(a), Fig. 2(b) and Fig. 2(c), it is clear that the reconstruction of the shape and the conductivity function are quite good.

4. CONCLUSION

We have presented a study of applying the genetic algorithm to reconstruct the shape and conductivity of a partially immersed metallic object through the measured of scattered E fields. Based on the boundary condition and the measured scattered fields, we have derived a set of nonlinear integral equations and reformulated the imaging problem into an optimization one. By using the genetic algorithm, the shape and conductivity of the object can be reconstructed, even when the initial guess is far from exact one Numerical results also illustrate that the conductivity reconstruction is more sensitive to noise than the shape reconstruction is.

ACKNOWLEDGMENT

This work was supported by National Science Council, Republic of China, under Grant NSC-98-2221-E-237-001.

REFERENCES

1. Sabatier, P. C., "Theoretical considerations for inverse scattering," *Radio Science*, Vol. 18, 1–18, Jan. 1983.
2. Roger, A., "Newton-Kantorovitch algorithm applied to an electromagnetic inverse problem," *IEEE Transactions on Antennas and Propagation*, Vol. 29, 232–238, Mar. 1981.
3. Colton, D. and P. Monk, "A novel method for solving the inverse scattering problem for time-harmonic acousticwaves in the resonance region II," *SIAM J. Appl. Math.*, Vol. 46, 506–523, Jun. 1986.
4. Chien, W. and C.-C. Chiu, "Using NU-SSGA to reduce the searching time in inverse problem of a buried metallic object," *IEEE Transactions on Antennas and Propagation*, Vol. 53, No. 10, 3128–3134, Oct. 2005.
5. Huang, C.-H., C.-C. Chiu, C.-L. Li, and K.-C. Chen, "Time domain inverse scattering of a two-dimensional homogenous dielectric object with arbitrary shape by particle swarm optimization," *Progress In Electromagnetics Research*, PIER 82, 381–400, 2008.
6. Chiu, C. C. and W. T. Chen, "Electromagnetic imaging for an imperfectly conducting cylinder by the genetic algorithm," *IEEE Trans. Microwave Theory and Tec.*, Vol. 48, 1901–1905, Nov. 2000.

An Iteration Method for Solving the Asymptotic Equation of Optically Thick Layers

Guangyuan Zhao[1] and Xianming Sun[2]

[1]School of Computer Science and Technology
Shandong University of Technology, ZiBo, Shandong 255049, China
[2]School of Electrical and Electronic Engineering
Shandong University of Technology, ZiBo, Shandong 255049, China

Abstract— For optically thick plane-parallel homogeneous layers, the reflection may be approximated by using so-called asymptotic expressions, which involve the reflection properties of the corresponding semi-infinite layer and the leading eigensolution of the equation of radiative transfer. In this paper, equations are derived for computing the escape function, diffusion pattern, diffusion exponent, and the reflection of semi-infinite clouds by using an iteration method. This method is suitable for numerical computations and is valid throughout the full range of single scattering albedos. The present formulations are validated by comparing them with established methods of radiative transfer.

1. INTRODUCTION

The radiation inside and emerging from a plane-parallel homogeneous atmosphere with a general law of single scattering and with arbitrary optical thickness can be calculated using various computational schemes. However, the solution of these methods becomes increasingly difficult as optical thickness increases. Consequently, it is very important that simple asymptotic expressions for the quantities characterizing the radiation field may be found for particles layers of large optical thickness. The asymptotic relations have been derived by various authors using different methods. The relations show that the reflected intensity can be expressed in especially simple functional forms [1–3].

In spite of the advantages of the asymptotic theory, it is difficult to apply them directly for the calculation of the reflection functions of particle layers. This is because they include two unknown function, i.e., escape function and reflection function of semi-infinite layer, and three unknown constants. van de Hulst [4] suggested using an asymptotic fitting method whereby computational results from the doubling method are fit to known general forms of the asymptotic equations. Nakajima and King [5] derived matrix equation for computing the functions and constants that appeared in the asymptotic expressions by using discrete ordinates method of radiative transfer.

In this paper, we use an iterative method to solve the Ambartsumian's nonlinear integral equation, suggested by Mishchenko et al. [6], by expanding the phase function in a Legendre polynomial series. The diffusion pattern and the diffusion exponent are obtained by solving a characteristic equation with a combination of the normalization condition of diffusion pattern and the so-called Sobolev-van de Hulst relation. After these have been determined, escape function is obtained by iteration of an integral equation for it. This is a simple and accurate technique for computing the functions and constants included in the asymptotic expression. The formulation for computation of the asymptotic expression is summarized in Section 2. Comparisons of the accuracy of this method with asymptotic fitting and discrete ordinates methods are presented in Section 3, followed by a conclusion presented in Section 4.

2. FORMULATION OF THE ASYMPTOTIC EXPRESSION

The asymptotic expression for the reflection function of a non-conservative plane-parallel homogeneous layer with sufficiently large optical thickness τ_0 is given by [2–5]

$$R(0;-\mu,\mu_0,\phi) = R_\infty(-\mu,\mu_0,\phi) - \frac{ml\exp(-2k\tau_0)}{1-l^2\exp(-2k\tau_0)} \times K(\mu)K(\mu_0) \tag{1}$$

In this expression μ_0 is the cosine of the solar zenith angle, μ is the cosine of the emerging zenith angle, ϕ is the azimuth angle measured from the solar plane, $R_\infty(-\mu,\mu_0\phi)$ is the reflection function of a semi-infinite layer having the same optical properties as the finite layer, $K(\mu)$ is the

escape function, m and l are constants determined by the optical properties of the medium. This expression pertains to the case of the surface albedo $A_g = 0.0$, and it is a simplification of the more general expression first derived by King [2, 3, 5], which assume the atmosphere is vertically homogeneous with a surface that reflects radiation according to Lambert's law with albedo A_g.

The function $R_\infty(-\mu, \mu_0\phi)$ can be obtained by solving the Ambartsumian's nonlinear integral equation [6–9]

$$\begin{aligned} R_\infty(\mu, \mu_0, \phi, \phi_0) \;=\; & \frac{\omega_0}{4(\mu+\mu_0)} F(-\mu, \mu_0, \phi, \phi_0) \\ & + \frac{\mu_0\omega_0}{4\pi(\mu+\mu_0)} \int_0^1 \int_0^{2\pi} F(\mu, \phi, \mu', \phi') \times R_\infty(\mu', \phi', \mu_0, \phi_0) d\mu' d\phi' \\ & + \frac{\mu\omega_0}{4\pi(\mu_0+\mu)} \int_0^1 \int_0^{2\pi} F(\mu_0, \phi_0\mu', \phi') \times R_\infty(\mu', \phi', \mu, \phi) d\mu' d\phi' \\ & + \frac{\omega_0\mu\mu_0}{4\pi^2(\mu_0+\mu)} \int_0^1 d\phi' \int_0^{2\pi} R_\infty(\mu', \phi', \mu, \phi) d\mu' \\ & \times \int_0^{2\pi} d\phi'' \int_0^1 F(-\mu', \phi', \mu'', \phi'') R_\infty(\mu'', \phi'', \mu_0, \phi_0) d\mu'' \end{aligned} \tag{2}$$

where ω_0 is the single scattering albedo, $F(\mu, \mu_0, \phi, \phi_0)$ is the single scattering phase function referred to the meridian, which is the plane containing the direction of emergence and the local normal. The phase function can usually be known with reference to the scattering plane as a function of the scattering angle θ for single scattering,

Following the method of Mishchenko et al. [6], the Ambartsumian's nonlinear integral equation is converted to a system of $n \times n$ nonlinear algebraic equations by using a Gauss quadrature formula on the interval $\mu \in [0, 1]$ with n division points μ_p and weights w_p

$$\begin{aligned} (\mu_p + \mu_q) R^m(\mu_p, \mu_q) \;=\; & \frac{\omega_0}{4} F^m(-\mu_p, \mu_q) + \frac{\omega_0}{2} \mu_q \sum_{s=1}^{S_{\max}} w_s F^m(\mu_p, \mu_s) R^m(\mu_s, \mu_q) \\ & + \frac{\omega_0}{2} \mu_p \sum_{s=1}^{S_{\max}} w_s R^m(\mu_p, \mu_s) F^m(\mu_s, \mu_q) \\ & + \omega_0 \mu_p \mu_q \sum_{s=1}^{S_{\max}} \sum_{s'=1}^{S_{\max}} w_s w_s R^m(\mu_p, \mu_s) F^m(-\mu_s, \mu_{s'}) R^m(\mu_{s'}, \mu_q) \end{aligned} \tag{3}$$

This system is solved by simple iterations using the initial approximation is

$$R_0^m(\mu_p, \mu_q) = \frac{\omega_0}{4(\mu_p + \mu_q)} F^m(-\mu_p, \mu_q) \tag{4}$$

Diffusion pattern $i(\mu)$ can be found by the so-called Sobolev-van de Hulst relation [7]

$$i(-\mu) = 2 \int_0^1 R^0(\mu, \mu_0) i(\mu_0) \mu_0 d\mu_0 \tag{5}$$

and it, as well as the diffusion exponent, can also be obtained by the following equation systems [6]

$$i(\mu)(1 - k\mu) = \frac{\omega_0}{2} \int_{-1}^1 i(\mu') F^0(\mu, \mu') d\mu' \tag{6}$$

$$\frac{\omega_0}{2} \int_{-1}^{+1} i(\mu) d\mu = 1 \tag{7}$$

$$\frac{1}{2} \int_{-1}^1 F^0(\mu, \mu') d\mu' = 1 \tag{8}$$

Eqs. (7) and (8) are the normalization conditions of diffusion pattern and phase function, respective. From Eqs. (6), (7), and (8), we find the following expression for the diffusion exponent

$$k = \frac{2(1-\omega_0)}{\omega_0 \int_{-1}^{1} \mu i(\mu) d\mu} \tag{9}$$

Replacing the integrals by respective quadrature sums, we obtain

$$i(\pm\mu_p) = \frac{\omega_0}{2(1 \mp k\mu_p)} \sum_{q=1}^{n} w_q [i(\mu_q) F^0(\pm\mu_p, \mu_q) + i(-\mu_q) F^0(\pm\mu_p, -\mu_q)] \tag{10}$$

$$\frac{\omega_0}{2} \sum_{p=1}^{n} w_p [i(\mu_p) + i(-\mu_p)] = 1 \tag{11}$$

$$k = \frac{2(1-\omega_0)}{\omega_0 \sum\limits_{p=1}^{n} w_p \mu_p [i(\mu_p) - i(-\mu_p)]} \tag{12}$$

substituting $k = \sqrt{1-\omega_0}$, $i(\mu_p) = 2$ and $i(-\mu_p) = \frac{1}{2}$ as the initial approximation, the iteration process is continued until the $i(\mu_p)$ and $i(-\mu_p)$ converge within a limit. Parameter m, i.e.,

$$m = 2 \int_{-1}^{1} i^2(\mu) \mu d\mu \tag{13}$$

can be found when $i(\mu_p)$ and $i(-\mu_p)$ are obtained.

Once m, k, $i(\pm\mu_p)$, and the reflection $R_\infty(-\mu, \mu_0\phi)$ have been determined, $K(\mu)$ can be obtained by an integral equation, i.e.,

$$K(\mu) = \frac{i(\mu)}{m} - \frac{2}{m} \int_0^1 R_\infty(\mu, \mu') i(-\mu') \mu' d\mu' \tag{14}$$

where

$$R_\infty(\mu, \mu_0) = \frac{1}{2\pi} \int_0^{2\pi} R_\infty(\mu, \mu_0, \phi) d\phi = R^0(\mu, \mu_0) \tag{15}$$

Constant l and n can be determined by $K(\mu)$ and $i(\mu)$

$$l = 2 \int_0^1 K(\mu) i(-\mu) d\mu \tag{16}$$

$$n = 2 \int_0^1 K(\mu) \mu d\mu \tag{17}$$

3. RESULTS

In order to test the validity of the method presented in Section 2, we have computed the asymptotic functions and constants for a Henyey-Greenstein phase function having an asymmetry factor $g = 0.85$ and single scattering albedos $\omega_0 = 0.999$, 0.9, 0.6. In Table 1, we summarize values of the diffusion exponent k obtained by using Asymptotic fitting and discrete ordinates method (DOM).

In Table 1, we can see that the method presented in this paper is sufficiently accurate for most application of radiative transfer in optically thick atmospheres.

Table 1: Diffusion exponent k derived by several different method.

$\omega_0 = 0.6$	$\omega_0 = 0.9$	$\omega_0 = 0.999$	N	Method
0.56979	0.23713	0.02124	59	Asymptotic fitting
0.56950	0.23713	0.02124	10	DOM
0.56950	0.237129	0.0212427		Method of this paper

In Table 2, we summarize values of asymptotic constants l, m and n derived by using three different methods for a Henyey-Greenstein phase function ($g = 0.85$). In addition to the asymptotic fitting method and discrete ordinate method , these constants have been determined by using the method of this paper, for which l and n can be obtained from Eqs. (16) and (17) and m from the Eq. (13). King [1] parameterized both l, m and a the full range of single scattering albedos using a different method of solutionand these results are very close to the results presented in Table 1.

Values of escape function, diffusion pattern, and plane albedo of a semi-infinite layer are summarized in Tables 3–4.

Table 2: Asymptotic constants l, m, n derived by several different methods.

ω_0	l	m	n	N	Method
0.999	0.81708	0.37769	0.90635	59	Asymptotic fitting
	0.81708	0.37769	0.90635	10	DOM
	0.81708	0.377686	0.906355		Method of this paper
0.9	0.12494	4.32592	0.44738	59	Asymptotic fitting
	0.1294	4.33017	0.44716	10	DOM
	0.124940	4.33017	0.447157		Method of this paper
0.6	0.01150	12.0149	0.23125	59	Asymptotic fitting
	0.01134	13.0016	0.22125	10	DOM
	0.0113435	13.0016	0.221246		Method of this paper

Table 3: Escape function $K(\mu)$ derived by several methods.

ω_0	$\mu = 1$	$\mu = 0.5$	$\mu = 0.1$	N	Method
0.999	1.15505	0.78568	0.42189	59	Asymptotic fitting
	1.1558	0.78568	0.42182	40	DOM
	1.1558	0.78567595	0.421817474		Method of this paper
0.9	0.72565	0.31740	0.1414	59	Asymptotic fitting
	0.72877	0.31663	0.14113	40	DOM
	0.7287691	0.316625940	0.14113033		Method of this paper
0.6	0.54111	0.09442	0.02543	59	Asymptotic fitting
	0.63289	0.007999	0.02259	40	DOM
	0.6329201	0.007999197	0.0225915692		Method of this paper

Table 4: Diffusion pattern $i(\mu)$ derived by several different methods.

ω_0	$\mu = 1$	$\mu = 0.5$	$\mu = 0$	N	Method
0.999	1.14862	1.06962	0.99639	59	Asymptotic fitting
	1.14866	1.06961	0.99640	40	DOM
	1.148665	1.0696074	0.99640428		Method of this paper
0.9	3.18110	1.44537	0.70379	59	Asymptotic fitting
	3.180906	1.4447	0.70363	40	DOM
	3.18907885	1.444475	0.7036261		Method of this paper
0.6	6.96337	1.12056	0.25374	59	Asymptotic fitting
	8.22991	1.04426	0.24591	40	DOM
	8.230261	1.04426	0.24590676		Method of this paper

4. CONCLUSIONS

We have derived the asymptotic equations of the radiative transfer equation in optically thick and vertically homogeneous plane-parallel layers by using an iteration method. Our method differs substantially from the method through experiment derivation of van de Hulst and the discrete ordinates method derived by Nakajima and King. We have shown how to calculate the various functions and constants arising in asymptotic theory by suing the iteration method.

REFERENCES

1. King, M. D., "A method for determining the single scattering albedo of clouds through observation of the internal scattered radiation field," *J. Atmos. Sci.*, Vol. 38, 2031–2044, 1981.
2. King, M. D., "Determination of the scaled optical thickness of clouds from reflected solar radiation measurements," *J. Atmos. Sci.*, Vol. 44, 1734–1751, 1987.
3. Nakajima, T. and M. D. King, "Determination of the optical thickness and effective particle radius of clouds from reflected solar radiation measurements. Part I: Theory," *J. Atmos. Sci.*, Vol. 47, 1878–1893, 1990.
4. Van de Hulst, H. C., "Asymptotic fitting, a method for solving anisotropic transfer problems in thick layers," *J. Comput. Phys.*, Vol. 3, 291–306, 1968.
5. Nakajima, T. and M. D. King, "Asymptotic theory for optical thick layers: Application to the discrete ordinates method," *Applied Optics*, Vol. 31, 7669–7683, 1992.
6. Mishchenko, M. I., J. M. Dlugach, E. G. Yanovitskji, and N. T. Zakharova, "Bidirectional reflectance of flat, optically thick particulate layers: An efficient radiative transfer solution and applications to snow and soil surfaces," *Journal of Quantitative Spectroscopy & Radiative Transfer*, Vol. 63, 409–432, 1999.
7. Sobolev, V. V., *Light Scattering in Planetary Atmospheres*, Chaps. 2 and 3, 24–65, Pergamon Oxford, 1975.

Error Analysis of Using Henyey-Greensterin in Monte Carlo Radiative Transfer Simulations

Guangyuan Zhao[1] and Xianming Sun[2]

[1]School of Computer Science and Technology
Shandong University of Technology, ZiBo, Shandong 255049, China
[2]School of Electrical and Electronic Engineering
Shandong University of Technology, ZiBo, Shandong 255049, China

Abstract— Mie and Henyey-Greenstein phase functions of discrete random media with a special size distribution are compared; sampling technique of Mie phase function are given, sampled results are compared with Henyey-Greenstein phase function. Based on these two phase functions, the scattering characteristics of clear sky cumulus are computed by using of the Monte Carlo method. From the results, we can conclude that it will cause large errors in the Monte Carlo radiative transfer simulations with the H-G phase function instead of the Mie phase function.

1. INTRODUCTION

When studying multiple scattering in planetary atmospheres using Monte Carlo methods, the real phase functions should be simulated using the statistical method to define the new photon direction after each scattering event. However, the angular characteristics of the atmosphere particles, even if the particles are assumed to be spherical, can not be approximated with sufficient accuracy by asymptotic expressions based on geometrical optics or Green's function approximations.

Usually we model the phase function using the Henyey-Greenstein or modified Henyey-Greenstein with as precise a value of asymmetry factor g as possible. But even in this case, these functions are sometimes a poor approximation of real phase function. Instead of using these phase function, we propose to simulate real phase function directly. Though this means an increase in calculation time, this will improve the computation accuracy.

This paper is organized as following, in Section 2, we introduce the computation Mie phase function for spherical atmosphere particles. In Section 3, we give the Monte Carlo simulations of Henyey-Greenstein and other real functions, and compare each of them. Section 4 provides the simulated results in Monte Carlo multiple scattering, and we will analyze the errors and the reasons.

2. COMPARISON OF MIE AND HENYEY-GREENSTEIN PHASE FUNCTION

Due to the variability of physical properties of clouds both in space and time domains, the size of clouds particles is polydisperse. Thus one can consider a radius of a droplet, r, as a random value, which is characterized by the distribution function $f(r)$. In most cases, the function $f(r)$ can be represented by gamma distribution, modified gamma distribution, log normal distribution, power law distribution, etc. [1]. Hansen and Travis [2] (1974) found that the effective radius and variance

$$r_{ef} = \frac{\int_0^\infty r\pi r^2 f(r)dr}{\int_0^\infty \pi r^2 f(r)dr} \tag{1}$$

$$v_{ef} = \frac{\int_0^\infty (r - r_{ef})^2 \pi r^2 f(r)dr}{r_{ef}^2 \int_0^\infty \pi r^2 f(r)dr} \tag{2}$$

are important parameters for any particle-size distribution. Hansen [2] found that the size distribution for different cloud with the same values of r_{ef} and v_{ef} will have similar scattering properties. Therefore, we can simply choose the gamma distribution defined as Equation (3),

$$f(r) = \text{const} \times r^{(1-3b)/b} \exp\left(\frac{-r}{ab}\right) \tag{3}$$

where $a = r_{ef}$, $b = v_{ef}$. In particular, we use $b = 1/9$ in this paper.

Phase function $P(\theta)$ is an important parameter to evaluate the scattering characteristics of discrete random media, and it does not depend on the concentration of particles, but on the

refractive index, shape and size. It can be calculated by Mie theory for spherical particles [3], but it does not have a simple analytical expression. In many cases, the Mie phase functions are replaced by Henyey-Greenstein (H-G) function.

$$P_{HG}(\theta, g) = \frac{1 - g^2}{[1 + g^2 - 2g\cos(\theta)]^{3/2}} \tag{4}$$

where

$$g = \langle \cos(\theta) \rangle = \frac{1}{2} \int_0^{\pi} P(\theta) \sin(\theta) \cos(\theta) d\theta$$

is the asymmetry factor, and θ is the scattering angle.

In Fig. 1, we compared the H-G phase function with a real Mie phase function. In this paper, the parameters of random media we used are: the particle shape is spherical, the size distribution is Gamma distribution, and the effective radius and effective variance are 6 μm and 1/9, respectively. The incident wavelength are 0.7 μm (a) and 3.3 μm (b).

From the graphes, we can see that H-G phase function reproduces the forward peak of Mie scattering phase function quite well, but it fails to reproduce the backscattering behavior. The Mie phase function shows a ripple, but the H-G phase function acts quite smoothly. So, this reproduction will cause big errors.

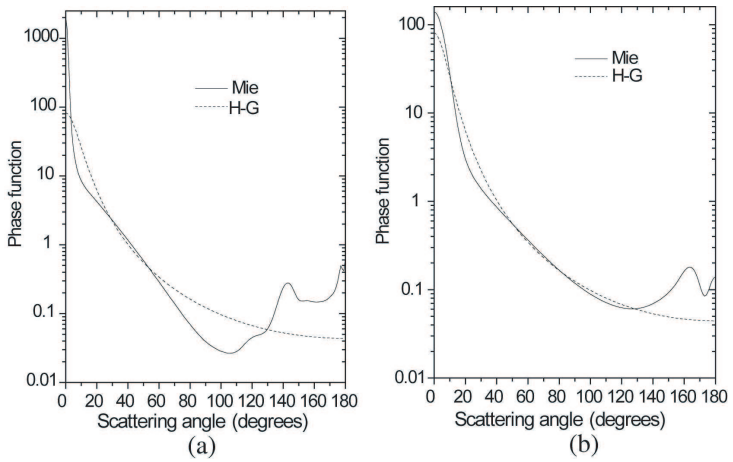

Figure 1: Comparison of Mie and H-G phase function. (a) Incident wavelength is 0.7 μm. (b) Incident wavelength is 3.3 μm, and the particles that in random medium is characterized by gamma distribution and the effective radius is 6 μm, effective variance is 1/9.

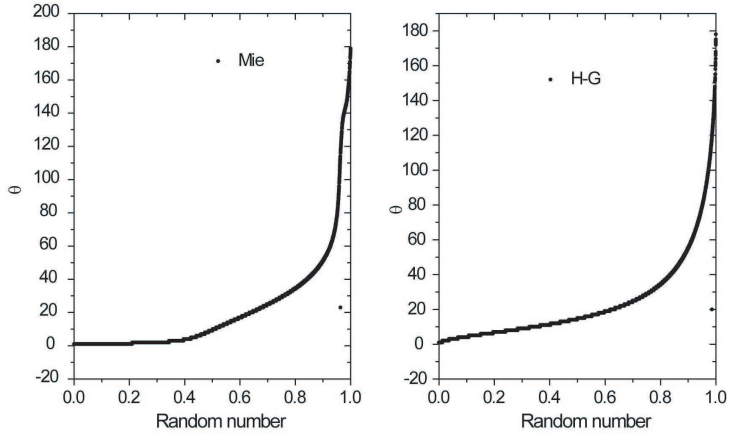

Figure 2: Samplings of scattering θ from Mie and H-G phase function.

3. SAMPLING OF SCATTERING ANGLES

When a photon launched to a discrete random media, it will interact with the particles. One important question is which direction it will be scattered. In Monte Carlo radiative transfer simulation, the scattering direction is sampled with the help of statistical theory. If the scattering in discrete random media is characterized by the Henyey-Greenstein phase function, the generating function for the Henyey-Greenstein phase function is

$$\cos\theta = \begin{cases} \frac{1}{2g}\cdot\left[(1+g^2)-\left(\frac{1-g^2}{1-g+2g\xi}\right)^2\right], & g\neq 0 \\ 2\xi-1, & g=0 \end{cases} \tag{5}$$

where ξ is a uniform random number between 0 and 1.

The sampling of scattering direction for Mie phase function is very difficult, because it do not have an analytical expression. In this paper, we use the method of Dominique [4]. We create a table of phase function versus the scattering angle, and then normalize this table such that the sum of all the phase function is equal to one. We generate a random number and then compare it with the normalized table to find which scattering angle θ corresponds to that number. The most obvious way to determine θ is find a n such that

$$\sum_{i=1}^{n-1} p_i < \xi \leq \sum_{i=1}^{n} p_i \tag{6}$$

In Fig. 2, we give the sampling of the scattering angle. From the graph, we can see that the trend of the sampling is same, but the sampling of the H-G phase function is more smoothly.

4. EVALUATION OF THE SCATTERING CHARACTERISTICS OF TOTAL LAYER USING MONTE CARLO METHOD

In order to test the errors which caused by the using of H-G phase function reproduce the real Mie phase function, we evaluate the scattering characteristics of a particle layer. The incident wavelength is 1.2 µm, the optical thickness is 2 and 4 (thinner), 16 and 32 (thicker), the phase function is the one which we evaluated in Fig. 1. In Fig. 3 and Fig. 4, we give the reflection function and transmission function, which is defined as follow [5–7]:

$$R(\mu_0,\mu,\phi) = \frac{I_r(\mu_0,\mu,\phi)}{I^*(\mu_0)} \tag{7}$$

$$T(\mu_0,\mu,\phi) = \frac{I_t(\mu_0,\mu,\phi)}{I^*(\mu_0)} \tag{8}$$

where, $I_r(\mu_0,\mu,\phi)$ and $I_t(\mu_0,\mu,\phi)$ is the reflected intensity and transmitted intenshety. $I^*(\mu_0)$ is the light intensity that reflected by ideal Lambertian reflector.

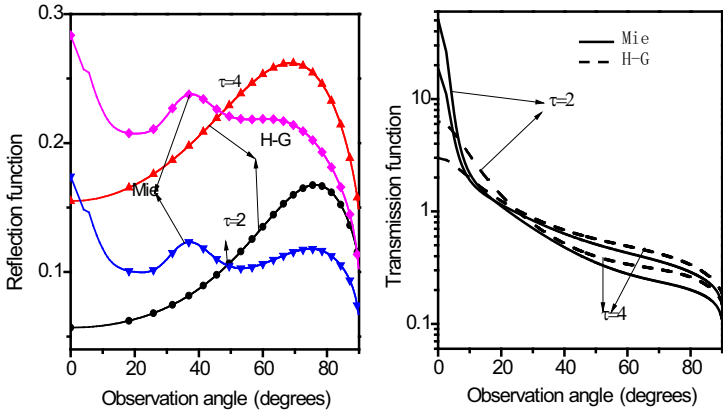

Figure 3: Reflection function and transmission function obtained by two different phase function. The optical thickness are $\tau = 4$ and $\tau = 2$, respectively.

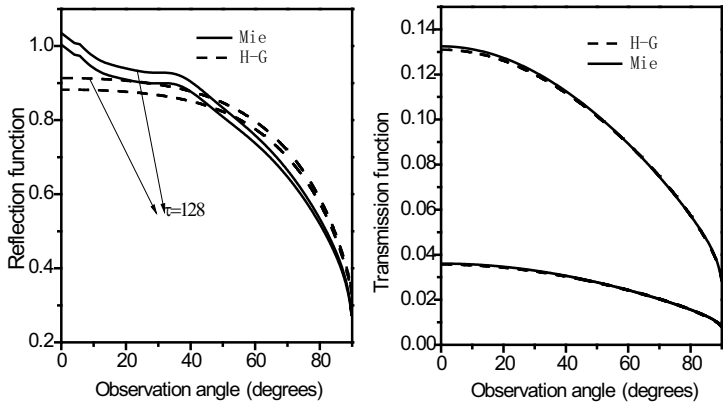

Figure 4: Reflection function and transmission function obtained by two different phase function. The optical thickness are $\tau = 64$ and $\tau = 128$, respectively.

From the graphs, we can see that the errors become smaller with the increasing of the optical thickness. The reason is that the single scattering is in the majority, so the single scattering phase function will affect the result greatly, but as the increasing of the optical thickness, the single scattering characteristics will be smoothed greatly.

Two obvious features of the reflection function are the backscattering enhancement caused by the glory in the Mie phase function and the strong forward scattering caused by the phase function at small scattering angles. The scattering characteristics of the H-G phase function exhibit only the second feature, which is explained by the absence of the backscattering phase function peak.

From the graph of the transmission function, we can see that the errors are still very big, especially when the optical thickness is smaller. However, the errors of the transmission functions are smaller than the reflection functions. This can be explained by the multiple scattering smoothed the characteristics of the single scattering phase function.

Thus, even we use a H-G phase function with as precise a value of asymmetry factor g as possible to model real phase function still will cause big errors, and Fig. 3 and Fig. 4 make a strong case against using H-G phase function in multiple scattering computations for discrete random media.

5. CONCLUSIONS

In this paper, the errors generated by the reproduction of Mie phase function by H-G phase function in Monte Carlo radiative transfer simulations are discussed. The results show that errors caused by the use of the H-G phase function can be very large. The errors can be unequivocally attributed to the phase function differences, and the results also make a strong case against using approximate phase function in multiple scattering computations for particulate media.

REFERENCES

1. Hansen, J. E., "Multiple scattering of polarized light in planetary atmosphere. Part I: The doubling method," *J. Atmos. Sci.*, Vol. 28, 120–125, 1971.
2. Hansen, J. E. and L. D. Travis, "Light scattering in planetary atmosphere," *Space. Sci. Rev.*, Vol. 16, No. 1, 527–610, 1974.
3. Wiscombe, W, J., "Improved Mie scattering algorithms," *Appl. Opt.*, Vol. 19, 1505–1509, 1980.
4. Dominique, T., "Henyey-Greenstein and Mie phase functions in Monte Carlo radiative transfer computations," *Appl. Opt.*, Vol. 35, No. 18, 3270–3274, 1996.
5. Sun, X. M., Y. P. Han, and X. W. Shi, "Applicaion of asymptotic theory for computing the reflection of optically thick clouds," *J. Opt. A: Pure Appl. Opt.*, Vol. 8, 1074–1079, 2006.
6. Mishchenko, M. I. and J. M. Dlugach, "Bidirectional reflectance of flat, optically thick particulate layer: An efficient radiative transfer solution and application to snow and soil surfaces," *J. Quant. Spectrosc. Radiat. Transfer.*, Vol. 63, No. 2, 409–432, 1999.
7. Van de Hulst, H. C., *Multiple Lights Scattering: Tables, Formulas and Application*, Academic Press, New York, 1980.

2-D Image Reconstruction from Microwave Scattering Data

Jie Li and Jiadong Xu
School of Electronics and Information, Northwestern Polytechnical University, Xi'an, China

Abstract— The microwave imaging based on the diffraction tomography and the interpolation methods has been studied. Three interpolation methods, the nearest-neighbor, bilinear, and bi-sinc, are chosen to increase imaging accuracy and efficiency. Different transformations between rectangular and polar-like coordinates are presented. The reconstruct results show that the introduced bi-sinc interpolation method consumes less time and gets more accurate image.

1. INTRODUCTION

Electromagnetic imaging has found many applications in the nondestructive testing, geophysical exploration, and biomedical imaging. The non-ionizing low power microwaves have lower health hazard compared with other methods such as X-rays.

However, it is well known in the inverse scattering community that most inverse scattering problems are nonlinear and ill-posed (ill-conditioned). Many methods have been proposed for solving Electromagnetic inverse problems. These methods can be classified into two groups. The first group is based on the diffraction tomography under the Born approximation [1–3]. This approach is relatively straightforward to implement and usually efficient in computation due to the linearization of the problem. The disadvantage, however, is that the type of imaged objects is usually weak, and this approach is not applicable to high-contrast objects. The second group solves the nonlinear equations of inverse problems using the numerical methods [4, 5]. The advantage of this approach is the modeling versatility for any type of imaged objects. The disadvantage, however, is its vast time consumption and computation cost.

In this paper, we present and compare three interpolation methods used in the tomography-based microwave imaging. Corresponding transformations between rectangular and polar-like coordinates are introduced. These three interpolation methods are implemented to reconstruct the cross section of a 2-D object.

2. THEORY AND FORMULATION

2.1. Configuration of a 2-D Inverse Problem

The geometry of a cylindrical object with arbitrary-shaped cross section is shown in Fig. 1(a). Its orientation is along the z axis and the cross section is on the x-y plane. Let's assume the relative dielectric permittivity is $\varepsilon_r(x, y)$ and permeability is that of vacuum μ_0.

Assume this 2-D object is illuminated by a plane wave. ψ^i is the incident field which parallel with z axel. The scattered field ψ^s is still parallel with z axel and satisfied with the following equation:

$$\left(\nabla^2 + k_0^2\right)\psi^s(x, y) = -\psi(x, y)o(x, y) \tag{1}$$

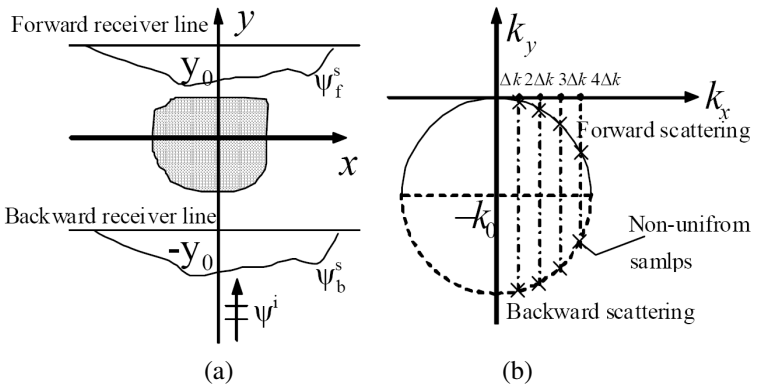

Figure 1: (a) Geometry of a 2-D cylindrical object illuminated by plane wave. (b) Fourier transform of scattering field of the object (solid semicircular arc: forward scattering, broken semicircular arc: backward scattering).

where k_0 is the wave number of background medium. ψ is the total field. $o(x, y)$ is the objective function where $o(x, y) = k_0^2(\varepsilon_r - 1)$. The solution of the linearized (1) of the inverse scattering problem is

$$\psi^s = \int G(x - x', y - y')o(x', y')\psi(x', y')ds' \tag{2}$$

where G is the 2-D Green's function as: $G(x - x', y - y') = -\frac{j}{4}H_0^{(2)}(k_0\sqrt{(x - x')^2 + (y - y')^2})$.

Under the Born approximation and omitted evanescent wave, the Fourier transform of the scattered field ψ^s, which is measured at linear arrays located at $y = \pm y_0$, satisfies (3):

$$\psi^s(k_x, \pm y_0) = -\frac{j\pi}{k_y + k_0}O(k_x, k_y)e^{j(k_y + k_0)y_0} \tag{3}$$

where

$$k_y = \pm\sqrt{k_0^2 - k_x^2} - k_0^2 \quad |k_x| \le k_0 \tag{4}$$

Equation (3) is the relation between the 2-D Fourier transform of the object function and the 1-D Fourier transform of the scatter field at the receiving line. The transform data in Fourier domain disperse at a semicircular arc. This conclusion is based on the Born approximation. Equation (4) defines the two semicircular arcs with radius k_0 and center by the wave vector $\vec{k}_0$ of incident wave in the Fourier domain shown in Fig. 1(b). One arc represents the forward scattering; the other represents the backward scattering.

2.2. Fourier-domain Interpolation

The angular diversity has been used to achieve the object function in Fourier frequency domain. A single frequency plan wave illuminating from 16 views provides the information of object shown as Fig. 2. Because one point of the Frequency domain is passed by two quad circular arcs, one of which has been chosen as better.

The samples in frequency domain are available over circular arcs, whereas, it is convenient for the FFT method to deal with samples over a rectangular lattice. Therefore, the conversion from rectangular lattices to polar-like coordinate has been discussed [1]. Reversely, the samples in polar-like coordinate can also be converted back to rectangular coordinate. For the latter conversion, the nearest-neighbor interpolation method is rather convenient to be applied. To calculate the interpolated value $Q(k_x, k_y)$ on the rectangular grid point (k_x, k_y), we only need to find the nearest neighbor points. In Fourier domain, all arc grids points (k_X, k_Y) can be convert into the rectangular coordinate using (5).

$$\begin{cases} k_x = k_X\cos\varphi - k_Y\sin\varphi \\ k_y = k_X\sin\varphi + k_Y\cos\varphi \end{cases} \tag{5}$$

where φ is the incident angle which varies from 0 to 2π. k_X varies from 0 to k_0.

For any point on circular arcs, it is easy to find the corresponding nearest point in the rectangular coordinate, and its value is decided by this nearest point. The accuracy of the nearest-neighbor interpolation method can be considerably improved by increasing the sampling density in the Fourier domain or by using the computationally-efficient method of zero-extending $Q(k_x, k_y)$ matrix.

Another commonly used 2-D interpolation technique is the bilinear interpolation. We need to covert rectangular lattice from rectangular coordinate to polar-like coordinate so as to avoid

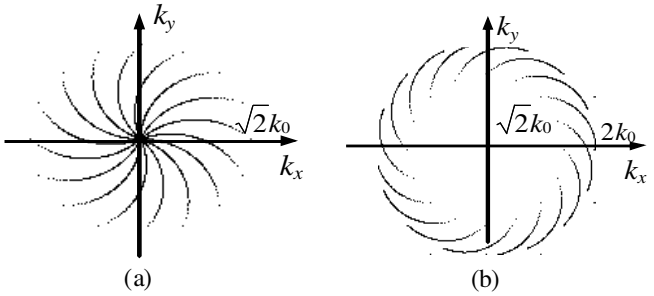

Figure 2: The Fourier domains of (a) front scattering and (b) back scattering with the plan wave illumination from 16 different views.

the non-uniform sampling on the quad circular arcs that happens in the rectangular coordinate as shown in Fig. 1(b). The known values on arc grids are donated by $P(k,\varphi)$, in which k is the distance from the origin to point B in Fig. 3. k varies from 0 to k_0. And r is the radial distance of P from origin. The angles θ and β are also shown in Fig. 3.

The relationship between (k,φ) and (k_x, k_y) is shown as (6)

$$\begin{cases} k = r\cos\beta = \sqrt{k_x^2+k_y^2}\cos\left(\arcsin\frac{\sqrt{k_x^2+k_y^2}}{2k_0}\right) \\ \varphi = \theta+\beta = \arctan\frac{k_y}{k_x} + \arcsin\frac{\sqrt{k_x^2+k_y^2}}{2k_0} \end{cases} \tag{6}$$

Given $M_k \times N_\varphi$ uniformly located samples $P(k_m,\varphi_n)$, we can calculate any interpolated value at the desired rectangular lattice point using the bilinear interpolation equation:

$$Q(k,\varphi) = \sum_{m=1}^{M}\sum_{n=1}^{N} P(k_m,\varphi_n)h(k-k_m)h(\varphi-\varphi_n) \tag{7}$$

where

$$h(x) = \begin{cases} 1-x/\Delta x & |x| \le \Delta x \\ 0 & \text{otherwise} \end{cases}$$

In order to get more precise result, the samples should be much denser, which means a larger $M\times N$ number and longer time in calculating interpolated values. Fortunately, we can choose another 2-D interpolation method which is based on sinc interpolation method to save computation time in interpolating values from truncated data. We name it the bi-sinc interpolation method.

As we know, if a function is band-limited, it can be fully recovered from its uniformly-spaced samples with a sampling frequency satisfying the Nyquist frequency. Therefore, interpolated value is calculated by two steps. First, we interpolate in k domain for a fixed φ.

$$F(k,\varphi) = \sum_{m=i-L}^{i+L} Q(m\Delta k,\varphi)w_1(k-m\Delta k) \tag{8}$$

where

$$\Delta k = \frac{2k_0}{M_k}, w_1(x) = \text{sinc}\left(\frac{x}{\Delta x}\right)$$

For any fixed k, $Q(k_x,k_y)$ is periodic to φ with a period of 2π. So we interpolate in φ domain with the periodic sinc function diric, w_2.

$$G(k,\varphi) = \sum_{n=j-L}^{j+L} Q(k,n\Delta\varphi)w_2(\varphi-n\Delta\varphi) \tag{9}$$

where

$$\Delta\phi = \frac{2\pi}{N_\varphi}, \quad w_2(x) = \text{diric}\left(\frac{x}{\Delta x}\right)$$

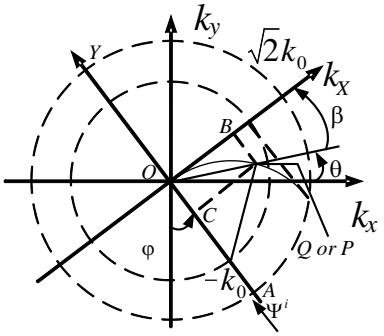

Figure 3: The relation of the rectangular coordinate lattice and polar-like coordinate and the defined variables.

Combining (8) and (9), we can get

$$Q(k,\varphi) = \sum_{m=i-L}^{i+L} \sum_{n=j-L}^{j+L} Q(m\Delta k, n\Delta\varphi) \cdot w_1(k - m\Delta k) w_2(\varphi - n\Delta\varphi) \tag{10}$$

where (i, j) is the nearest neighbor of the given (k, φ) on the arc grid, the interpolation involves the truncated $2L \times 2L$ points with the center of (i, j). When increasing L, the truncation error descends slowly but the time consumption ascends. So L may be 2, 4 or 8, optionally.

3. RESULTS

To study different interpolation methods mentioned above, it is necessary to apply them to reconstruct the image of an object. In the simulations a single plane wave is incident on a cylinder whose relative dielectric permittivity is 1.08 with a radius as λ (wavelength). The scattered field is measured along a line at a distance of 100λ from the origin. At the receiving line the received wave was measured at 512 points with a 0.5λ interval. The rectangular lattice is 128×128. Clearly, the image of the cylinder is successfully reconstructed, shown in Fig. 4. For the nearest-neighbor, bilinear and bi-sinc interpolation methods, the time consumptions are 0.8 s, 2.4 s, and 1.8 s respectively. The performance of the bi-sinc method is better because it balances the computation time and the imaging accuracy.

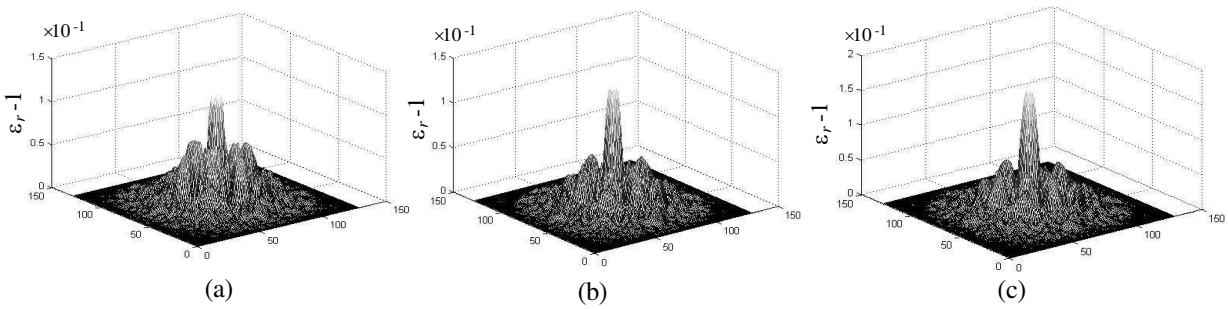

Figure 4: The reconstructed image of a 2-D object using (a) the nearest-neighbor method, (b) bilinear method, and (c) bi-sinc interpolation.

4. CONCLUSIONS

In this paper, diffraction-tomography-based microwave imaging has been studied. Different Fourier-domain interpolation methods between polar-like and rectangular coordinates are presented with corresponding transformations. Three methods, the nearest-neighbor, bilinear, and bi-sinc interpolation, are examined to show the algorithm efficiency by reconstructing the image of a 2-D cylindrical object. It is concluded that the nearest neighbor interpolation is more convenient in the rectangular coordinate, whereas the bilinear and bi-sinc interpolation methods are better in polar-like coordinate. The bi-sinc interpolation method is a good balance between time and accuracy.

ACKNOWLEDGMENT

The authors would like to thank Zhang Lu and Chufeng Hu for helpful discussions. They would also like to thank the reviewers for their comments and suggestions.

REFERENCES

1. Kak, C. and M. Slaney, *Principles of Computerized Tomographic Imaging*, IEEE Press, 1988.
2. Pichot, C., L. Jofre, and G. Peronnet, "Active microwave imaging of inhomogeneous bodies," *IEEE Trans. Antennas & Propagation*, Vol. 33, No. 4, 416–425, April 1985.
3. Pan, S. X. and A. C. Kak, "A computational study of reconstruction algorithms for diffractin tomography: Interpolation versus filtered backprojection," *IEEE Trans. Acoust., Speech & Signal Processing*, Vol. 31, No. 5, 1262–1275, October 1983.
4. Lin, H.-T. and Y.-W. Kiang, "Microwave imaging for a dielectric cylinder," *IEEE Trans. Microwave Theory & Tech.*, Vol. 42, No. 8, 1572–1579, August 1994.

5. Franchois, A. and C. Pichot, "Microwave imaging-complex permittivity reconstruction with a Levenberg-Marquardt method," *IEEE Trans. Antennas & Propagation*, Vol. 45, No. 2, 203–215, February 1997.

Surface Plasmon Resonance Absorption in a Multilayered Bigrating

T. Suyama[1], **Y. Zhang**[2], **Y. Okuno**[1], **Z. Luo**[1], **and T. Matsuda**[3]

[1]Graduate School of Science and Technology, Kumamoto University, Japan
[2]Department of Physics and Electronic Information, Wenzhou University, China
[3]Kumamoto National College of Technology, Japan

Abstract— We numerically analyze surface plasmon resonance absorption of incident light energy by a multilayered bigrating, which consists of dielectric and metallic thin-films corrugated periodically in two directions. We apply Yasuura's modal expansion method for solving the problem of plane-wave diffraction by a multilayered bigrating and evaluating the absorption, which is observed as dips in diffraction efficiency curves. Employing the numerical algorithm, we numerically examine characteristics of the surface plasmon resonance absorption in the multilayered bigrating.

1. INTRODUCTION

Metal film grating has an interesting property known as the resonance absorption [1], which causes partial or total absorption of incident light energy. The absorption is associated with the excitation of surface plasmons on a grating surface: an incident light couples with surface plasmons via an evanescent spectral order generated by the grating [2]. The resonance absorption in metal film grating has been the subject of many theoretical and experimental investigation in connection with chemical sensing, surface enhanced phenomena such as Ramman scattering, and photonic band gaps. Most of studies on the resonance absorption have mainly dealt with a thin metal film grating whose surfaces are periodic in one direction [3]. Doubly periodic metal film grating, i.e., periodic in two directions, also causes the plasmon resonance absorption as well as singly periodic grating [4]. The absorption in a doubly periodic metal grating has been of considerable interest since we can expect more complex behaviors in the absorption phenomena [5] by virtue of the presence of double periodicity and multilayer structure. In this paper we investigate the resonance absorption of a multilayered bigrating, which consists of dielectric and metallic thin-films corrugated periodically in two directions. We describe a numerical algorithm based on Yasuura's method [6] for analyzing diffraction of a plane-wave by a multilayered bigrating. Using the algorithm we numerically examine characteristics of the resonance absorption in the multilayered bigrating.

2. FORMULATION OF THE PROBLEM

Figure 1 shows the schematic representation of a mulatilayered bigrating and the ℓth thin-film layer. The bigrating consists of $(L-1)$ thin-film layers that are periodically corrugated in the X- and Y-directions with periods d_x and d_y, respectively. The corrugated multilayer is numbered starting from the incidence side and is denoted by V_ℓ ($\ell = 2, 3, \ldots, L$). The semi-infinite regions over and below the multilayer are V_1 and V_{L+1}. The regions V_ℓ ($\ell = 1, 2, \ldots, L+1$) are filled with isotropic and homogeneous media with refractive indices n_ℓ. The interface between V_ℓ and $V_{\ell+1}$ is denoted by S_ℓ ($\ell = 1, 2, \ldots, L$). The electric and magnetic fields of an incident light are given by

$$\begin{pmatrix} E^{\mathrm{i}} \\ H^{\mathrm{i}} \end{pmatrix}(P) = \begin{pmatrix} e^{\mathrm{i}} \\ h^{\mathrm{i}} \end{pmatrix} \exp(jk^{\mathrm{i}} \cdot P - j\omega t), \text{ with } h^{\mathrm{i}} = (1/\omega\mu_0)\, k^{\mathrm{i}} \times e^{\mathrm{i}} \tag{1}$$

Here, e^{i} and h^{i} are the electric- and magnetic-field amplitude, k^{i} is the incident wave vector and P is a position vector of an observation point P. The time factor is suppressed hereafter.

We denote the diffracted fields in the regions V_ℓ ($\ell = 1, 2, \ldots, L+1$) by $E^d_\ell(\mathrm{P})$ and $H^d_\ell(\mathrm{P})$, and explain briefly Yasuuras method [6] for finding the diffracted fields. We form approximate solutions for the diffracted field in each region in terms of a finite sum of Floquet modes with two spatial harmonic number m and n. In conical diffraction of plane-wave, the diffracted fields are decomposed into a TE and a TM components which mean the absence of Z-component in the relevant electric and magnetic field.

We therefore introduce the TE and TM vector modal functions defined in V_ℓ ($\ell = 1, 2, \ldots, L+1$):

$$\varphi^{\mathrm{TE}\pm}_{\ell mn}(\mathrm{P}) = e^{\mathrm{TE}\pm}_{\ell mn} \exp(ik^{\pm}_{\ell mn} \cdot P) \quad (m, n = 0, \pm 1, \ldots) \tag{2}$$

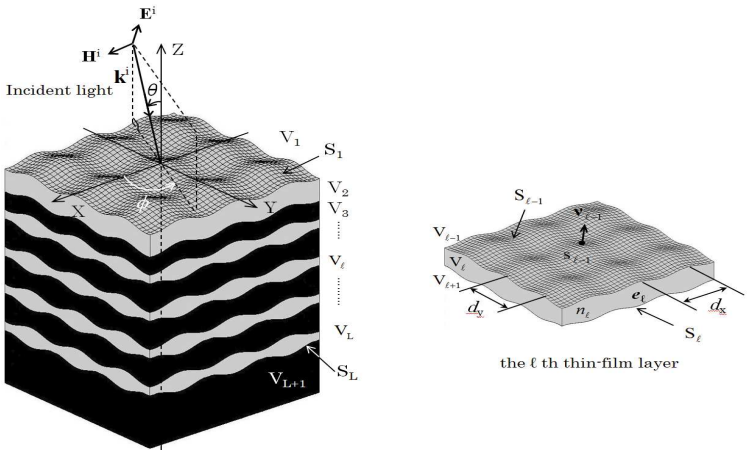

Figure 1: Schematic representation of diffraction by a mulatilayer bigrating and the ℓth thin-film layer.

with $e^{\mathrm{TE}\pm}_{\ell mn} = \frac{k^{\pm}_{\ell mn}\times i_Z}{\left|k^{\pm}_{\ell mn}\times i_Z\right|}$, and

$$\varphi^{\mathrm{TM}\pm}_{\ell mn}(\mathrm{P}) = e^{\mathrm{TM}\pm}_{\ell mn}\exp(ik^{\pm}_{\ell mn}\cdot P) \quad (m,n=0,\pm1,\ldots) \tag{3}$$

with $e^{\mathrm{TM}\pm}_{\ell mn} = \frac{e^{\mathrm{TE}\pm}_{\ell mn}\times k^{\pm}_{\ell mn}}{\left|e^{\mathrm{TE}\pm}_{\ell mn}\times k^{\pm}_{\ell mn}\right|}$. Here, i_Z is a unit vector in the Z-direction and $k^{\pm}_{\ell mn}$ is the wave vector of the (m,n)th order diffracted wave

$$k^{\pm}_{\ell mn} = [\alpha_m, \beta_n, \pm\gamma_{mn}], \tag{4}$$

where $\alpha_m = \alpha + \frac{2m\pi}{d}$, $\beta_n = \beta + \frac{2n\pi}{d}$ and $\gamma^2_{\ell mn} = (n_\ell k)^2 - (\alpha^2_m + \beta^2_n)$ with $\mathrm{Re}(\gamma_{\ell mn}) \geq 0$ and $\mathrm{Im}(\gamma_{\ell mn}) \geq 0$. Note that superscripts + and −, respectively, represent up- and down-going waves that travel in the positive and negative Z-direction.

In terms of linear combinations of the vector modal functions, we form approximate solutions for the diffracted electric and magnetic fields in V_ℓ:

$$\begin{aligned}\begin{pmatrix} E^{\mathrm{d}}_{\ell N} \\ H^{\mathrm{d}}_{\ell N}\end{pmatrix}(P) \;=\; &\sum_{m,n=-N}^{N} A^{\mathrm{TE}+}_{\ell mn}(N)\begin{pmatrix}\varphi^{\mathrm{TE}+}_{\ell mn}\\ \psi^{\mathrm{TE}+}_{\ell mn}\end{pmatrix}(\mathrm{P}) + \sum_{m,n=-N}^{N} A^{\mathrm{TM}+}_{\ell mn}(N)\begin{pmatrix}\varphi^{\mathrm{TM}+}_{\ell mn}\\ \psi^{\mathrm{TM}+}_{\ell mn}\end{pmatrix}(\mathrm{P}) \\ &+ \sum_{m,n=-N}^{N} A^{\mathrm{TE}-}_{\ell mn}(N)\begin{pmatrix}\varphi^{\mathrm{TE}-}_{\ell mn}\\ \psi^{\mathrm{TE}-}_{\ell mn}\end{pmatrix}(\mathrm{P}) + \sum_{m,n=-N}^{N} A^{\mathrm{TM}-}_{\ell mn}(N)\begin{pmatrix}\varphi^{\mathrm{TM}-}_{\ell mn}\\ \psi^{\mathrm{TM}-}_{\ell mn}\end{pmatrix}(\mathrm{P})\end{aligned} \tag{5}$$

with

$$\psi^{\mathrm{TE,TM}\pm}_{\ell mn} = \frac{1}{\omega\mu_0}k_{\ell mn}\times\varphi^{\mathrm{TE,TM}\pm}_{\ell mn} \quad (\ell = 1,2,\ldots,L+1) \tag{6}$$

Here, $A^{\mathrm{TE}-}_{1mn}(N) = A^{\mathrm{TM}-}_{1mn}(N) = 0$ and $A^{\mathrm{TE}+}_{L+1mn}(N) = A^{\mathrm{TM}+}_{L+1mn}(N) = 0$ because of the radiation condition that the diffracted field in V_1 (or V_{L+1}) propagates or attenuates in the positive (or negative) Z-direction.

In Yasuura's method [6], the unknown coefficients are determined so that the solutions approximately satisfy the boundary conditions at each interface S_ℓ $(\ell = 1,2,\ldots,L)$ in the sense of weighted least-squares. Computational implementation of the least-squares problem is detailed in the literature [7].

The power reflection and transmission coefficient of the (m,n)th order diffracted mode in V_1 and V_{L+1} are given as follows:

$$\rho_{mn} = \rho^{\mathrm{TE}}_{mn} + \rho^{\mathrm{TM}}_{mn}\ [\mathrm{Re}(\gamma_{1mn}) \geq 0], \quad \rho^{\mathrm{TE}}_{mn} = \frac{\gamma_{1mn}}{\gamma}|A^{\mathrm{TE}+}_{1mn}|^2, \quad \rho^{\mathrm{TM}}_{mn} = \frac{\gamma_{1mn}}{\gamma}|A^{\mathrm{TM}+}_{1mn}|^2 \tag{7}$$

$$\tau_{mn} = \tau^{\mathrm{TE}}_{mn} + \tau^{\mathrm{TM}}_{mn}\ [\mathrm{Re}(\gamma_{L+1mn}) \geq 0], \quad \tau^{\mathrm{TE}}_{mn} = \frac{\gamma_{L+1mn}}{\gamma}|A^{\mathrm{TE}-}_{L+1mn}|^2, \quad \tau^{\mathrm{TM}}_{mn} = \frac{\gamma_{L+1mn}}{\gamma}|A^{\mathrm{TM}-}_{L+1mn}|^2 \tag{8}$$

The extinction power absorbed in the grating is calculated by

$$Abs = 1 - \sum_{mn}{}' (\rho_{mn} + \tau_{mn}) \tag{9}$$

where $\sum'$ is a summation over the propagating orders.

3. NUMERICAL RESULTS

As numerical examples we consider a bisinusoidal silver (Ag) film grating having common period $d = 0.556\,\mu\text{m}$ and a corrugation depth $h = 0.030\,\mu\text{m}$. And, a wavelength of a TM incidence is chosen as $\lambda = 0.650\,\mu\text{m}$. We take $n_{\text{Ag}} = 0.07 + i4.20$ [8] as the refractive index of silver at this wavelength. Using the present algorithm we calculate diffraction efficiencies and field distributions to make properties of coupled surface-plasmon modes clear.

First we consider a bisinusoidal silver-film grating. The grating is denoted by $L = 2$ (V/Ag/V). Fig. 2 shows (0, 0)th order power reflection ρ_{00} in V_1 (vacuum) (a) and the transmission coefficient τ_{00} in V_3 (vacuum) (b) as functions of the incidence angle θ for two e/d's when azimuth angle $\phi = 0°$ is fixed. e is the thickness of a silver-film. We observe partial absorption of incident light as the dips of efficiency curves in Fig. 2(a), in addition to the constant absorption corresponding to the reflectivity of silver. We assume that the dips are caused by excitation of surface plasmons. If this is the case, each of the dips can be related to one of the three types of plasmon modes: a single-interface surface plasmon (SISP) that is observed as the single dip at $\theta = 8.0°$ on the $e/d = 0.4$ curve; and a short-range and long-range surface plasmon (SRSP and LRSP) corresponding to the two dips of the $e/d = 0.08$ ($\theta = 6.54°$ and $8.8°$), respectively.

When the grating is thick ($e/d = 0.4$), the power can be seen in V_1 alone and no transmitted power exists in V_3 in Fig. 2. Increasing θ from 0°, we first observe the dip at $\theta = 8.0°$ corresponding to the absorption in Fig. 2(a). While if the grating is relatively thin ($e/d = 0.08$), the power exists in both V_1 and V_3. Although the power in V_3 is small in general, it becomes large at the incidence angles at which the absorption was observed in Fig. 2. This suggests coupled oscillations occur on the upper and lower surface of the grating.

We examine the same phenomena observing the modal coefficients in V_ℓ ($\ell = 1, 3$). Figs. 3 and 4 illustrate the $(-1, 0)$th order coefficients $A^{\text{TM}+}_{\ell,-10}$ for $e/d = 0.4$ and 0.08, respectively. We observe in Fig. 3(a) ($e/d = 0.4$) resonance characteristics (enhancement and rapid change in phase) of the coefficient $A^{\text{TM}+}_{1,-10}$ near $\theta = 8.0°$. While the coefficient $A^{\text{TM}-}_{3,-10} = 0$ remains unchanged as we see in Fig. 3(b). This means that the incident wave illuminating the grating at the angle causes a coupling between the $(-1, 0)$th order evanescent mode and some oscillation excited on the upper surface of the grating. The oscillation exists locally in the vicinity of the illuminated surface and, hence, does not have any influence on the field in V_3. In Fig. 4 ($e/d = 0.08$) we find the resonance characteristics in both $A^{\text{TM}+}_{1,-10}$ and $A^{\text{TM}-}_{3,-10}$. They, in addition, appear around two incidence angles: $\theta = 6.54°$ and $\theta = 8.8°$. This means that the oscillation in the vicinity of the upper surface causes another oscillation on the lower surface at this thickness. The oscillations interfere with each other and result in two coupled oscillating modes: the SRSP and LRSP.

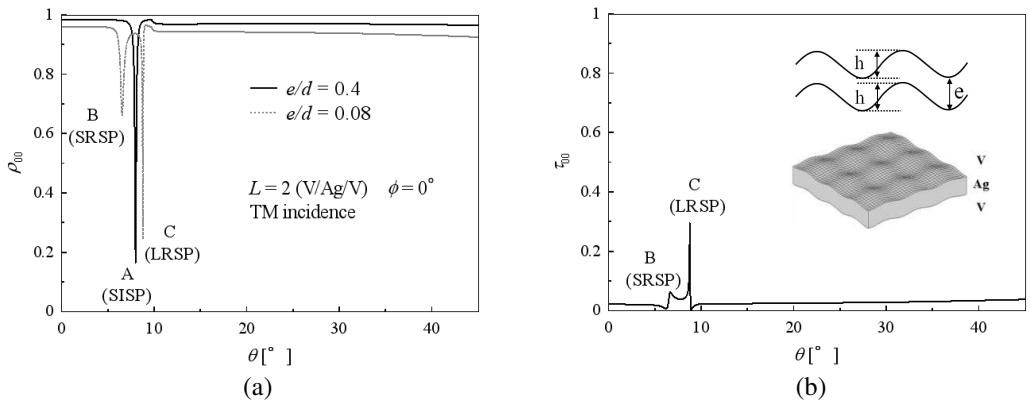

Figure 2: The (0, 0)th order diffraction efficiencies ρ_{00} (a) and τ_{00} (b) as functions of θ for two e/d's ($L = 2$).

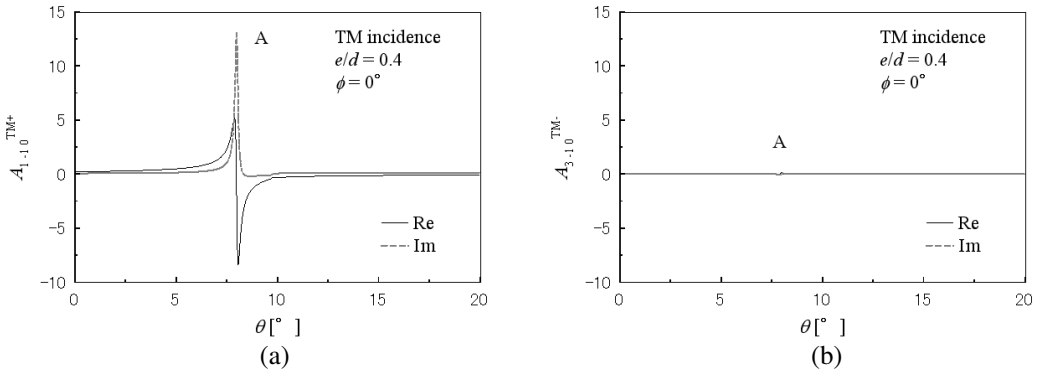

Figure 3: The $(-1, 0)$th order modal coefficients $A^{\mathrm{TM}+}_{1,-10}$ (a) and $A^{\mathrm{TM}-}_{3,-10}$ (b) as functions of θ at $e/d = 0.4$.

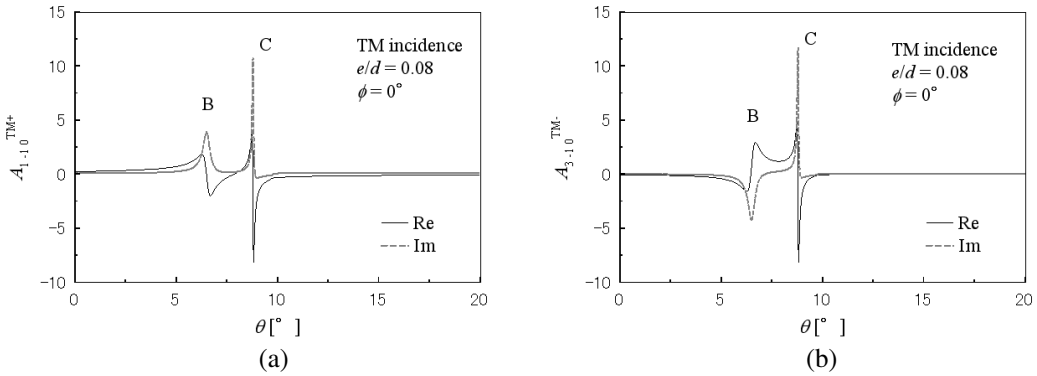

Figure 4: The $(-1, 0)$th order modal coefficients $A^{\mathrm{TM}+}_{1,-10}$ (a) and $A^{\mathrm{TM}-}_{3,-10}$ (b) as functions of θ at $e/d = 0.08$.

We consider the same phenomena observing field distribution near the grating surfaces. Figs. 5∼7 show the field distributions of X- and Z-component of the total electric field E_X and E_Z in the vicinity of the silver-film grating at the incidence angles, which the absorption was observed in Fig. 2. The abscissa and ordinate show the magnitude and distance in the Z direction normalized by the wavelength λ. The parallel broken lines are the grating surfaces. Fig. 5 shows E_X and E_Z for the case of $e/d = 0.4$ at $\theta = 8.0°$, which corresponds to the single dip in Fig. 2(a). Figs. 6 and 7 show the same thing for the $e/d = 0.08$ case. Fig. 6 illustrates the results at $\theta = 6.54°$ where the left dip is observed in Fig. 2(a). While Fig. 7 depicts the results at $\theta = 8.8°$, the right dip in Fig. 2(a). In Figs. 5∼7 we observe strong enhancement of E_X and E_Z (Note that the magnitude of incident radiation is 1), the enhancement which is observed at the incidence angles where the absorption occurs.

Figure 5 shows the total field above the grating surface decays exponentially in Z and the magnitude of total filed is almost E_Z. The state of affairs is nearly the same in the metal region except for the rapid decay. Because the grating is thick, the oscillation near the upper surface does not reach the lower surface and, hence, the field below the grating is zero. This is commonly observed when a SISP is excited.

In Figs. 6 and 7 we again see the enhancement of the E_X and E_Z on the upper and lower surface of the silver-film grating. The rate of enhancement in Fig. 6 is not so large as that in Fig. 7. We can understand the difference assuming that the former and the latter are the results of the SRSP and the LRSP mode excitation.

Next we consider a multilayered bigrating which consists of a bisinusoidal SiO_2 film sandwiched in two silver-films graing fabricated practically. The multilayered bigrating is denoted by $L = 4$ (V/Ag/SiO_2/Ag/V). The parameters are the same as those of Fig. 2 except for $n_{SiO_2} = 1.5$, $e_{SiO_2}/d = 0.3$, $e_{Ag}/d = 0.08$, and $\phi = 45°$. In this example we observe the broad absorption besides ones by SRSP and LRSP in Fig. 8. This is related to the excitation of a guided wave supported by the SiO_2 film.

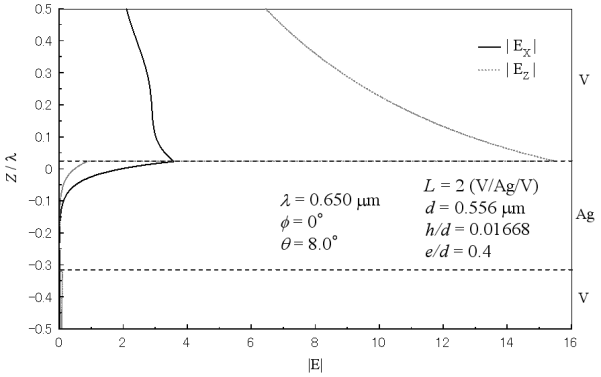

Figure 5: Field distribution at $\theta = 8.0°$.

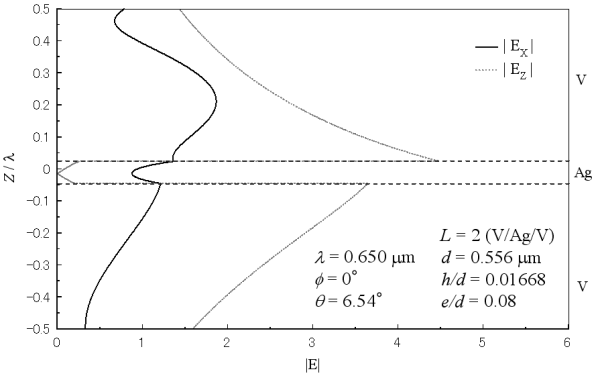

Figure 6: Field distribution at $\theta = 6.54°$.

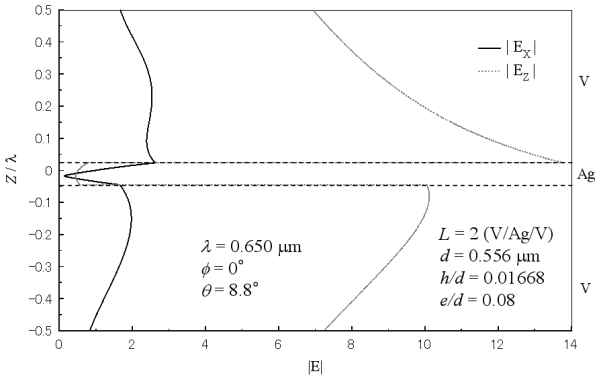

Figure 7: Field distribution at $\theta = 8.8°$.

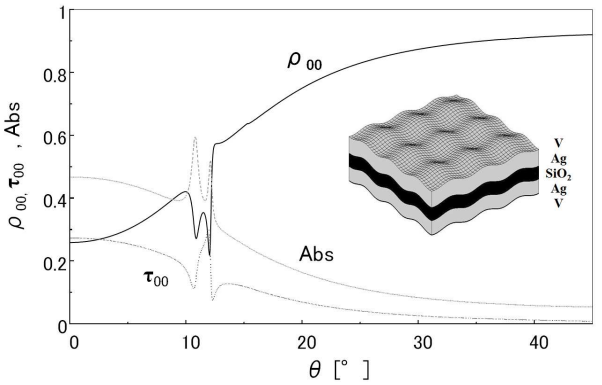

Figure 8: ρ_{00}, τ_{00}, and Abs as functions of θ ($L = 4$).

4. CONCLUSION

We have presented an efficient numerical algorithm for analyzing the resonance absorptions associated with the excitation of surface waves such as surface plasmons and guided waves by a multilayered bigrating. The results presented here facilitate our clear understanding of the coupled plasmon modes, SISP, SRSP and LRSP, excited in a silver-film bigrating. We observed strong field enhancement on the grating surface where surface plasmons excited.

REFERENCES

1. Raeter, H., "Surface plasmon and roughness," *Surface Polaritons*, V. M. Argranovich and D. L. Mills (eds.), 331–403, North-Holland, New York, 1982.
2. Kong, F. M., K. Li, B.-I. Wu, H. Huang, H. Chen, and J. A. Kong, "Propagation properties of the SPP modes in nanoscale narrow metallic gap, channel, and hole geometries," *Progress In Electromagnetics Research*, PIER 76, 449–466, 2007.
3. Chen, Z., I. R. Hooper, and J. R. Sambles, "Strongly coupled surface plasmons on thin shallow metallic gratings," *Phys. Rev. B*, Vol. 77, 161405, 2008.
4. Inagaki, T., J. P. Goudonnet, J. W. Little, and E. T. Arakawa, "Photoacoustic study of plasmon-resonance absorption in a bigrating," *J. Opt Soc. Am. B*, Vol. 2, No. 3, 433–439, 1985.
5. Matsuda, T., D. Zhou, and Y. Okuno, "Numerical analysis of plasmon resonance absorption in bisinusoidal metal gratings," *J. Opt Soc. Am. A*, Vol. 19, No. 4, 695–701, 2002.
6. Yasuura, K., "A view of numerical methods in diffraction problems," *Progress in Radio Science 1966–1969*, W. V. Tilson and M. Sauzade (eds.), 257–270, URSI, Brussels, 1971.
7. Lawson, C. L. and R. J. Hanson, *Solving Least-squares Problems*, Prentice-Hall, Englewood Cliffs, NJ, 1974.
8. Hass, G. and L. Hadley, "Optical properties of metals," *American Institute of Physics Handbook*, 2nd Edition, D. E. Gray (ed.), 6–107, McGraw-Hill, New York, 1963.

A Low-frequency RCS Measurement System in an Anechoic Chamber

C. F. Hu[1, 2], J. D. Xu[1], N. J. Li[2], and L. X. Zhang[2]

[1]Electronic Engineering Department, Northwestern Polytechnic University, China
[2]National Key Laboratory of UAV Specialty Technique, Northwestern Polytechnic University, China

Abstract— A practical RCS measurement system on low-frequency (VHF/UHF) is constructed in an anechoic chamber. Stepped-frequency signal generated by a network analyzer is transmitted by a log-periodic dipole antenna (LPDA). Another LPDA close to the transmitting antenna is applied to receive echoes. The rotation velocity of support and the interval of sample are controlled by a centre computer. With the revolving stage rotating, a trigger signal is sent to the network analyzer and the measurement begins. Many kinds of DSP techniques are employed to remove unwanted signals. Firstly, the frequency-domain data of background are subtracted from that of targets. Then high resolution time-domain response is got by inverse fast Fourier transform (IFFT), which reflects scattering distribution of the whole chamber. The energy of target area can be chosen by a time-domain gating which removes the coupling between antennas and other clutters. For expanding effective bandwidth, a low side lobe window function is adding to the frequency-domain data before gating. After scaling at the Rayleigh region of metal sphere, the accurate low-frequency RCS can be obtained. Experimental results show that the valid data waved less than ±1 dB can be got over UHF band for a metal sphere with 15 cm diameter, and the precision of ±2 dB is obtained on parts of VHF band.

1. INTRODUCTION

Generally, the radar cross section (RCS) of a certain target varies with frequency, especially at low-frequency band (VHF/UHF) [1]. Thus, the scattering characteristics of objects on these bands present more attention in microwave remote sensing and target recognition [2, 3]. Though there are several ways to calculate RCS, direct measurement is the most effective and accurate method.

RCS measured methods are divided into two ways of outdoor and indoor according to measurement fields. Testing in a controlled electromagnetic circumstance, more accurate results can be obtained in an anechoic chamber. However, the far-field condition is hard to meet for indoor RCS measurement, so a compact antenna test range (CATR) is used to transform sphere microwave into planar microwave, but when the frequency is low, severe diffraction exists at the margin of CATR, and the precision will be greatly degraded by this phenomenon [4]. Therefore, it's difficult to gain accurate RCS at low-frequency [5]. Luckily, the far-field condition can easily be met on these bands. In this paper, a remarkable system called stepped-frequency RCS measurement system is introduced, and some kinds of DSP techniques are applied [6]. The experiment results show that accurate RCS value can be obtained at low-frequency in the anechoic chamber.

2. DESIGN OF MEASUREMENT SYSTEM

The system is shown in Figure 1. Stepped-frequency signal is generated by a network analyzer Agilent E8363A, and then transmitted by a log-periodic dipole antenna (LPDA). Another LPDA close to the transmitting antenna is used to receive echoes. The rotation velocity of support and the interval of sample are controlled by a center computer. With the revolving stage rotating, a trigger signal is sent to the network analyzer when measurement begins. Comparing the echoes of target with scaling object, the RCS of target can be determined.

The steps of test are as follows:

Step 1: The frequency-domain data of anechoic chamber in all directions are collected.

Step 2: The frequency-domain data of target under the same background and angles are recorded.

Step 3: The frequency-domain data of a scaling object at one angle with the background unchanged are tested.

3. SIGNAL PROCESSING

As it is known, the echoes include many clutters that affect the precision of measurement system, such as residual reflections from the walls and floor as well as ceiling of the anechoic chamber,

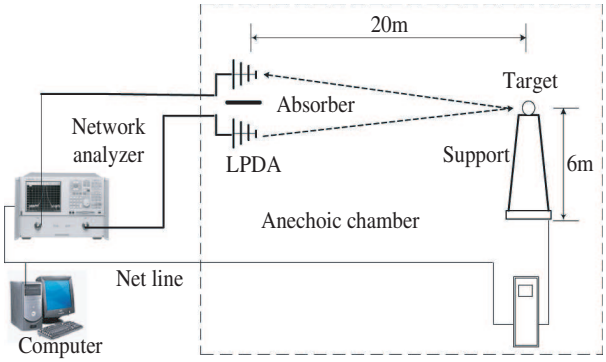

Figure 1: Stepped-frequency RCS measurement system.

and the mutual coupling between two antennas. So DSP techniques for clutters from the returns remove are in great importance. The flows of signal processing are described as follows.

3.1. Frequency-domain Cancellation

Subtracting frequency-domain data in step 1 from those in step 2 at the same angles, the frequency-domain response of target is obtained in Equation (1).

$$y(i) = y_{\text{target + background}}(i) - y_{\text{background}}(i) \tag{1}$$

If the target is a point one, the distance between target and radar is R. The echoes after frequency-domain cancellation can be expressed:

$$y(i) = \exp\left[-j2\pi\left(f_0 + i\Delta f\right) \times 2R/c\right], \quad i = 0, 1, \ldots, N-1 \tag{2}$$

where, c is the velocity of light, f_0 is the start frequency, Δf is the step of frequency. The frequency-domain cancellation can eliminate the effect of rotation and support, and reduce the clutters about 20 dB.

3.2. Fourier Transform

The phase of $y(i)$ is a linear sequence, so time-domain response can be got by inverse discrete Fourier transform (IDFT):

$$H_l = \frac{1}{N}\sum_{i=0}^{N-1} \exp\left[-j2\pi\left(f_0 + i\Delta f\right) \times 2R/c\right] \times \exp\left(j\frac{2\pi}{N}li\right) \tag{3}$$

Then, the amplitude of response is gained by a modular arithmetic, and we can see the location of target, and the other interferer resources, especially the mutual coupling between two antennas. Next, a time-domain gating will be used to remove them.

3.3. Time-domain Gating

The area of target can be chosen by an appropriate time-domain gating as Equation (4), therefore, the clutters of background is eliminated effectively.

$$|H_l|' = \begin{cases} |H_l| & l \in \text{ area of target} \\ 0 & \text{other area} \end{cases} \tag{4}$$

3.4. Window Function

The time-domain gating removes most of unwanted signals, meanwhile, the spectrum information of original echoes are lost. Moreover, the narrower gated, the less accurate data gained. If a suitable window function is added to the spectrum of returning echoes, the impact caused by cutting off time-domain data will be reduced [7]. The Hamming window is taken here as the following expression:

$$s(n) = 0.5 - 0.5\cos(2\pi n/N), \qquad n = 0, 1, \ldots, N-1 \tag{5}$$

3.5. Scaling

Metal sphere is often used for scaling because of its isotropy, as well as its theoretical RCS can be calculated [8]. However, when talking about scaling, we firstly consider employing the optical region of that. Actually, the Rayleigh or resonance region can also be made use of scaling. Compared of scattering mechanism in optical region, the returning echoes in Rayleigh or resonance region consist of mirror reflection and creeping wave, and the equivalent path is much longer in time-domain. Therefore, the time-domain gating must be wider to contain all of sphere's energy, and we can get the accurate characters of metal sphere.

The RCS of target is calculated by the following formula:

$$\sigma_{\mathrm{dBsm}} = S_{21} - S'_{21} + \sigma'_{\mathrm{dBsm}} \tag{6}$$

where, σ_{dBsm} is the RCS of target, σ'_{dBsm} is the RCS of scaling, S_{21}, $S'_{21}$are the measured value of target and scaling.

4. EXPERIMENTAL RESULTS IN AN ANECHOIC CHAMBER

The frequency of measurement starts from 200 MHz to 1200 MHz, which is divided into 201 points. The power given by a vector network analyzer is 10 dBm, and its IF bandwidth is 10 kHz. Two metal spheres are measured shown in Figure 2, the diameters of them are 40 cm and 15 cm respectively. The former is used for scaling, the latter is for target.

The results of all frequencies at a certain angle are given in Figure 3. The solid line is the value of measurement, while the dash line means the value of theory. We can see that the RCS of measurement is waved less than 1 dB around the center of frequency over 80%. The fluctuation on both sides of spectrum is about 4 dB because of the impact of time-domain gating. Wider the span of measurement gets, more accurate will be. The results in all directions at center frequency are shown in Figure 4. Waving 1.5 dB shows the high precision of measurement at each angle.

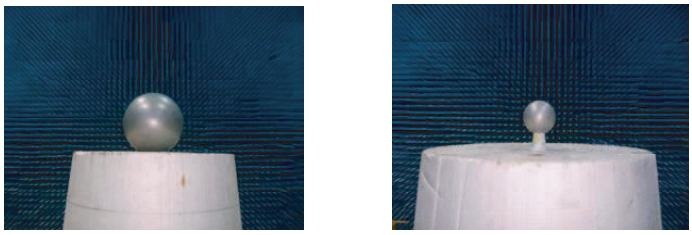

(a) (b)

Figure 2: Photos of metal spheres. (a) The diameter of 40 cm, (b) the diameter of 15 cm

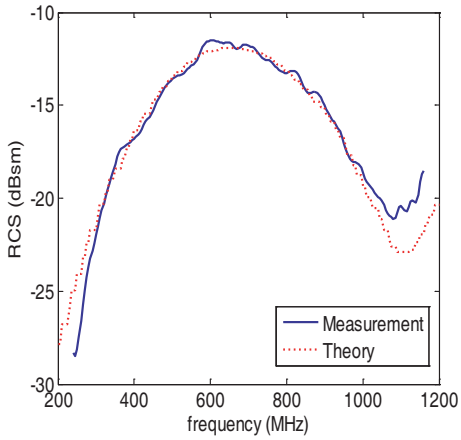

Figure 3: The line of all frequencies at a certain angle.

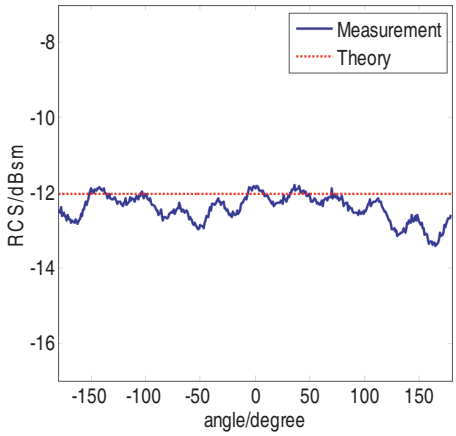

Figure 4: The RCS in all directions at center frequency.

5. CONCLUSION

Stepped-frequency system is a kind of high resolution RCS measurement system. By using some DSP techniques, the background will be improved, so the dynamic scope of system is expanded. The experimental results prove that accurate RCS can be obtained by this system. Moreover, if the antennas are changed, they can also be applied to the higher frequency RCS measurement.

ACKNOWLEDGMENT

This work is supported by the Doctorate Foundation of Northwestern Polytechnical University. I am grateful to Prof. W. L. Wang, National Key Laboratory of UAV Specialty Technique, for his helpful advice. Any errors are of course my responsibility.

REFERENCES

1. Knott, E. F., *Radar Cross Section*, Artech House Inc., Dedham, MA, 2004.
2. Pierce, L. and M. Moghaddam, "The MOSS VHF/UHF space borne SAR system tested," *IEEE International Geoscience and Remote Sensing Symposium*, Seoul, South Korea, July 25–29, 2005.
3. Ulander, L., et al., "The VHF/UHF-band LORA SAR and GMTI system," *Proceedings of the Society of Photo-optical Instrumentation Engineers*, 206–215, 2003.
4. Brumley, S. S., "Extending the low-frequency limits of the compact-range reflector," *IEEE Trans. Antennas and Propagation*, Vol. 38, 81–85, 1996.
5. Poey, P., et al., "Global analysis and realization of a wideband array (250–500 MHz) for RCS measurements in an anechoic chamber," *Microwave Opt. Technol.*, Vol. 34, 68–70, 2002.
6. Hu, C. F., C.-F. Hu, J.-D. Xu, N.-J. Li, and J. Cao, "Application of DSP in the step-frequency RCS measurement system," *PIERS Online*, Vol. 4, No. 1, 77–80, 2008.
7. Harris, F. J., "On the use of windows for harmonic analysis with the discrete fourier transform," *Proc. IEEE*, Vol. 66, 51–83, 1977.
8. Bowman, J. J., et al., *Electromagnetic and Acoustic Scattering by Simple Shapes*, North-Holland Publishing, Amsterdam, 1969.

Analytical Solutions of TD Scattering Fields from Parabolic Reflector Antenna Illuminated by Plane Waves and Gaussian Beams

Shih-Chung Tuan[1] and Hsi-Tseng Chou[2]

[1]Department of Communication Engineering, Oriental Institute of Technology
Taipei, Taiwan
[2]Department of Communication Engineering, Yuan Ze University
Chung-Li, Taiwan

Abstract— The increasing interests in the use of ultra-wideband or short pulse antennas for the target identification and remote sensing applications have driven the efforts to obtain direct time domain (TD) solutions in the electromagnetic (EM) analysis. This paper develops an Analytic Analysis of Transient Scattering from a parabolic reflector antenna illuminated by an Incident Plane Wave and electromagnetic (EM) fields of a general astigmatic Gaussian Beam (GB) respectively. The time domain transient analysis of Time Domain Physical Optical (TDPO) for parabolic reflector antenna illuminated by plane wave and TDPO with analytic time transform (ATT) for parabolic reflector antenna illuminated by Gaussian Beam (GB) are presented. It is obtained by analytically inverting, in closed-form, the corresponding frequency-domain (FD) solution based on physical optics (PO) integral, and coincidently can be decomposed in terms of reflection and diffraction effects as usually described in high-frequency asymptotic solutions. The ATT allows complex formulations with complex time variations in TD, and is thus able to treat the complex propagation phases resulted from a GB illumination on the reflector.

1. INTRODUCTION

The presented work is motivated by the needs of transient EM analysis in the booming applications of ultra-wide-band or short pulse antenna system for target identifications and remote sensing, where reflector antennas are apparently good candidates and have been widely used. In this paper, We develops an Analytic Analysis of Transient Scattering from a reflector antenna Illuminated by an Incident Plane Wave and electromagnetic (EM) fields of a general astigmatic Gaussian Beam (GB) respectively. A closed-form analytic solution is thus developed for predicting the early-time transient EM fields scattered from a second-order surface truncated with an arbitrary edge boundary when it is illuminated by a transient impulsive plane wave and addition analysis employs physical optics (PO) approximation and utilizes analytic time transform (ATT) to treat the complex time delays resulted from GB's complex phase variations along its propagation in a frequency domain (FD). First, a closed-form analytic solution is thus developed for predicting the early-time transient EM fields scattered from a second-order surface truncated with an arbitrary edge boundary when it is illuminated by a transient impulsive plane wave [1, 2]. A second-order surface is selected here because it is widely employed to approximate local surface profiles of many general scatters. Then a time domain (TD) transient analysis of the electromagnetic (EM) fields scattered from a perfectly conducting parabolic reflector antenna (truncated by the second-order surface), when it is illuminated by general astigmatic Gaussian Beam (GB) fields, is performed using TD physical optical (PO) approximation in this paper. By plane wave illuminated that the TD solution can be also employed via the convolution theorem to obtain the early time transient scattering fields generated by the same scatter when illuminated by a realistic astigmatic finite-energy pulse. A GB is used here to assemble a feed's radiation that illuminates the reflector surface because its Gaussian amplitude taper may realistically model the fields radiated from most of the practical feed's antennas.

In the past development of TD solutions, most efforts naturally consider either direct TD numerical techniques or frequency domain (FD) solutions with Fast Fourier Transform (FFT) to obtain their TD correspondences. Those solutions, such as finite-difference time-domain (FDTD) and TD integral approaches, were popularly employed in treating small scattering objects, and appear computationally inefficient when the sizes of scattering objects increase or the pulse widths of the incident wave are very narrow in comparison with the sizes of scattering objects as interested in this paper for a large reflector analysis. Quasi-analytical TD solutions with tremendously

simplified formulations become more attractive because they may perform the analysis directly in TD and provide more physical-appealing interpretations of wave behaviours. This paper presents a quasi-analytic TD analysis, based on a TD-PO approximation, of a reflector illuminated by an incident GB, where ATT is employed to transform its FD formulation into a TD correspondence. Then ATT allows complex formulations with complex time variations in TD, and is thus able to treat the complex propagation phases resulted from a GB illumination on the reflector.

2. FORMULATIONS DEVELOPMENT

2.1. Parabolic Reflector Antennas Illuminated by the Transient Step Incident Plane Wave, Scattering Field by a PO Analysis and Interpretations of the Scattering Mechanisms

The scattering problem is illustrated in Figure 1, where a second-order surface described by

$$z'(x',y') = z_0 + \frac{(x'-x_0)^2}{2R_1} + \frac{(y'-y_0)^2}{2R_2} \tag{1}$$

the electrical field of the incident plane wave in FD is expressed by

$$\bar{E}_i\left(\vec{r}',s\right) = \bar{E}_0 \frac{1}{s} e^{-\frac{s}{c}\hat{k}_i\cdot\bar{r}'} \tag{2}$$

thus the electrical field in TD obtained via an inverse Laplace transform over (2) with respect to s can be expressed by

$$\bar{\mathcal{E}}_i\left(\bar{r}',t\right) = \bar{E}_0 U\left(t - \frac{\hat{k}_i\cdot\bar{r}'}{c}\right) \tag{3}$$

and the TD solution can be obtained via an inverse Laplace transform of by

$$\bar{\mathcal{E}}_s^u(\bar{r},t) \cong \frac{1}{2\pi r c}\hat{r}\times\hat{r}\times\left\{\iint_{S_a}\hat{n}\cdot\delta\left(t - \frac{(\hat{k}_i-\hat{r})\cdot\bar{r}'+r}{c}\right)ds'\right\}\times\hat{k}_i\times\bar{E}_0 \tag{4}$$

Utilizing delta function's characteristic of

$$\delta\left(t - \frac{(\hat{k}_i-\hat{r})\cdot\bar{r}'}{c} - \frac{r}{c}\right) = \frac{\delta(\rho-\rho_t)}{\frac{\partial}{\partial\rho}\left(t - \frac{r}{c} - \frac{(\hat{k}_i-\hat{r})\cdot\bar{r}'}{c}\right)\Big|_{\rho=\rho_t}} \tag{5}$$

allows one to simplify the double integration in (5) into a line integral by

$$\bar{\mathcal{E}}_s^u\left(\vec{r},t\right) = \left\{\frac{\hat{r}\times\hat{r}}{2\pi r}\times\int_{C_\phi}\frac{\hat{n}|\bar{r}'_\rho\times\bar{r}'_\phi|}{(\hat{r}-\hat{k}_i)\cdot\bar{r}'_\rho}\Bigg|_{\rho=\rho_t}d\phi\times\hat{k}_i\times\bar{E}_0\right\}\left[U(t-t_1)-U(t-t_2)\right] \tag{6}$$

the integral in (6) can be found in a closed form by

$$\bar{P} \equiv \int_{\phi_b}^{\phi_e}\frac{\hat{n}|\bar{r}'_\rho\times\bar{r}'_\phi|}{(\hat{r}-\hat{k}_i)\cdot\bar{r}'_\rho}\Bigg|_{\rho=\rho_i}d\phi = \left\{\frac{\sqrt{R_1R_2}\left[\hat{r}-\hat{k}_i\right]}{a_3^2}\right\}(\phi_e-\phi_b) + \frac{1}{a_3}\left\{y_e\hat{x}-x_e\hat{y}\right\} - \frac{1}{a_3}\left\{y_b\hat{x}-x_b\hat{y}\right\} \tag{7}$$

The analytical interpretations start with the decomposition of (7) in terms of three components, which is addressed in a form of

$$\bar{P} = \bar{P}_r\cdot T(t) + \bar{P}_e + \bar{P}_b \tag{8}$$

If S_a is infinite in extent without any edge present, $\phi_e-\phi_b = 2\pi$ and $\bar{r}_b = \bar{r}_e$, which results in $T(t)\to 1$, $\bar{P}_b = -\bar{P}_e$ and thus $\bar{P}\to\bar{P}_r$ that is independent of t. Thus (8) reduces to the reflected field with a transient step response by substituting into (8) because in this case $t_2\to\infty$ and only $U(t-t_1)$ exists with t_1 being the time delay due to the reflected field propagation. $T(t)$ behaviours as a transition function that accounts for the contribution weighting of the reflected field.

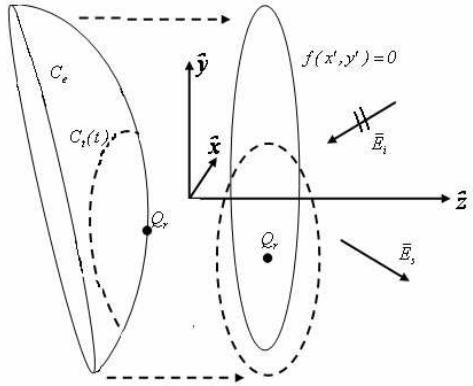

Figure 1.

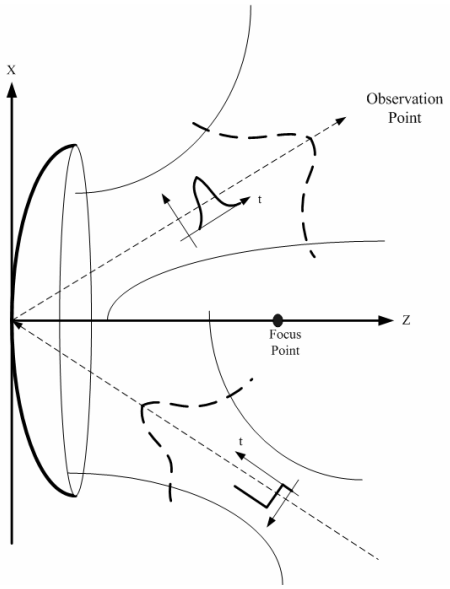

Figure 2.

2.2. Transient Analysis of the Electromagnetic (EM) Fields Scattered from Parabolic Reflector Antennas Illuminated by Gaussian Beam (GB) Using TD Physical Optical (PO) Approximation

The analytical time transformation (ATT) allows complex formulations with complex time variations in TD, and is thus able to treat the complex propagation phases resulted from a GB illumination on the reflector. Let the magnetic field of incident Gaussian Beam (GB) expressed in a Laplace domain by [3–5], the impulsive Gaussian beam propagation in a free space can be expressed as

$$\underset{\delta}{\overset{+}{h}}(t) = \bar{H}_i(O)\sqrt{\frac{|Q^i(z_i)|}{|Q^i(0)|}}\overset{+}{\delta}\left(t - \frac{1}{v}\left[z_i + \frac{1}{2}\left[\xi_i\right]^T Q^i(z_i)\left[\xi_i\right]\right]\right) \tag{9}$$

The scattering problem is illustrated in Figure 2 where a parabolic surface described by

$$z(x,y) = -\frac{1}{2}\left[\frac{x^2}{R_1} + \frac{y^2}{R_2}\right] \tag{10}$$

applying ATT to obtain an analytic TD step response for a GB gives

$$\vec{\mathcal{E}}_s^u(\vec{r},t) \cong \frac{Z_0}{2\pi r v}\hat{r}\times\hat{r}\times\left\{\iint_{S_a}\hat{n}\cdot\overset{+}{\delta}(t+\frac{f(x',y')}{v})dS'\right\}\times\vec{H}_i(O) \tag{11}$$

can be written closed forms as

$$\begin{aligned}\bar{P}_\phi(\phi) \;=\; & \frac{-j}{\pi A\rho}\left(\hat{z}\times\hat{z}\times\left(\bar{r}'_\rho\times\bar{r}'_\phi\right)\right)\Big|_{\rho=\rho_e} \\ & +\frac{j}{2\pi AD}\left\{\left[\left(\bar{r}'_\rho\times\bar{r}'_\phi\right)\ln\left(\frac{\rho-\rho_e}{\rho}\right)\right]_{\rho=\rho_2} - \left[\left(\bar{r}'_\rho\times\bar{r}'_\phi\right)\ln\left(\frac{\rho-\rho_e}{\rho}\right)\right]_{\rho=\rho_1}\right\}\end{aligned} \tag{12}$$

3. NUMERICAL EXAMPLES

(A). Numerical examples consider a convex parabolic surface where $(x_0, y_0, z_0) = (0, 0, 0)$ and $(R_1, R_2) = (-10\,\text{m}, -5\,\text{m})$. The surface is truncated at $z' = z_t = -1\,\text{m}$ with S_a described by $z' \geq z_t$, and is a very large surface of an almost 9 m diameter with a smooth elliptical edge truncation. A truncated second-order surface is illuminated by a transient-step plane wave, where C_e is the edge contour of truncation and $f(x', y') = 0$. The scattering fields' responses to a transient impulsive plane wave normally incident to a convex parabolic surface as shown in Figure 3.

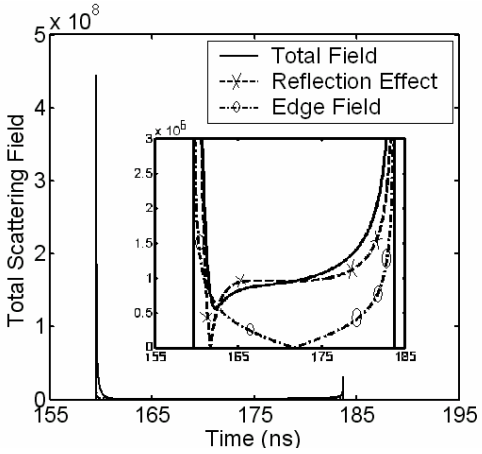

Figure 3.

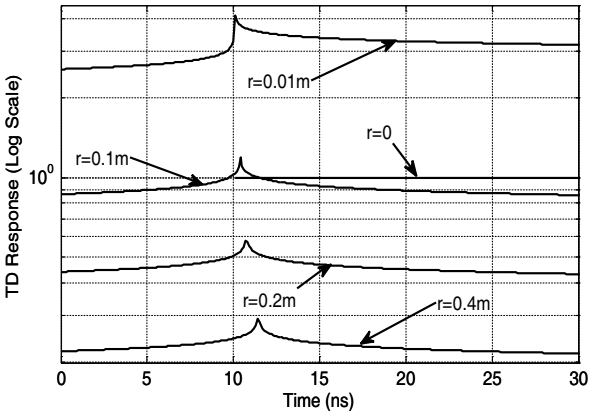

Figure 4.

(B). The TD characteristics of GB's propagation in a free space as well as the scattering fields when it is used as a feed to illuminate a reflector antenna are investigated in this section. Transient variations of a GB propagation in a free space, which is responded to a transient step excitation at GB's waist, $\theta = 40^\circ$ as shown in Figure 4.

4. CONCLUSIONS

A closed-form analytic solution is thus developed for predicting the early-time transient EM fields scattered from a second-order surface truncated with an arbitrary edge boundary when it is illuminated by a transient impulsive plane wave and a quasi-analytic TD solution is presented to perform a transient analysis of scattering from a parabolic reflector antenna when it is illuminated by a general GB. This solution is quite useful in practical applications of reflector antennas since the GB can be flexibly used to model a variety of antenna feeds.

REFERENCES

1. Duan, D.-W. and Y. Rahmat-Samii, "A generalized diffraction synthesis technique for high performance reflector antennas," *IEEE Transactions on Antennas and Propagation*, Vol. 43, No. 1, 27–40, Jan. 1995
2. Chou, H.-T. and P. H. Pathak, "Analytic solution for early-time transient radiation from pulse-excited parabolic reflector antennas," *IEEE Transactions on Antennas and Propagation*, Vol. 45, No. 5, 829–836, May 1997.
3. Chou, H.-T., P. H. Pathak, and R. J. Burkholder, "Novel Gaussian beam method for the rapid analysis of large reflector antennas," *IEEE Transactions on Antennas and Propagation*, Vol. 49, No. 6, 880–893, June 2001.
4. Chou, H.-T. and P. H. Pathak, "Uniform asymptotic solution for the EM reflection and diffraction of an arbitrary Gaussian beam by a smooth surface with an edge," *J. Radio Sci.*, Vol. 32, No. 4, 1319–1336, July–August 1997.
5. Hasselmann, F. J. V. and L. B. Felsen, "Asymptotic analysis of parabolic reflector antennas," *IEEE Transactions on Antennas and Propagation*, Vol. 30, 677–685, 1982.

THz Bessel Beams Generated by BOEs

Yanzhong Yu
School of Science, Quanzhou Normal University
Quanzhou, Fujian 362000, China

Abstract— Diffractive optical elements (DOEs) are designed for producing Bessel beams at THz frequencies in this paper. To lessen the computational burden and therefore improve the design efficiency, the design tool, which is to connect a microgenetic algorithm (MGA) for optimal design of DOEs with a body-of-revolution finite-difference time-domain (BOR-FDTD) method for rigorous analysis the fields diffracted by DOEs, has been adopted to acquire the profiles of the DOEs. Simulation results show that the field distributions generated by the designed DOEs are in good agreement with those of the desired on the output plane.

1. INTRODUCTION

Bessel beams, which are one family of diffraction-free beams, were discovered for the first time by Durnin in 1987 [1]. In the cylindrical coordinates system an ideal Bessel beam can be given by:

$$E_n(\rho, \phi, z) = E_0 J_n(k_\perp \rho) \exp(ik_z z) \exp(in\phi)$$

where E_0 is a constant, J_n denotes the nth-order Bessel function of the first kind, $\rho^2 = x^2 + y^2$, $k_\perp^2 + k_z^2 = (2\pi/\lambda)^2$, $k_\perp$ and k_z are the radial and longitudinal wave numbers, respectively, λ is a wavelength in free space. The central spot of the zero-order Bessel beam (denoted by J_0) is always bright; whereas that of all the higher-order Bessel beams (denoted by J_n, n is an integer and ≥ 1) is always dark on axis surrounded by concentric rings whose peak intensities decrease as ρ^{-1} [2]. Since perfect Bessel beams own lots of novel characteristics and therefore have many promising applications, such as imaging, alignment and measurement, the study of generation and applications of these beams has been widely carried out in various fields, including optics [1–4], acoustics [5] and the relevant science of physics [6, 7]. Numerous methods for generating Bessel beams have been suggested and demonstrated. Examples can be found in Refs. [2–7]. One of which is using DOEs, whose diffractive fields are calculated by scalar diffraction theory, to convert an incident beam into Bessel light beam [3, 4].

In view of the high diffraction efficiencies of DOEs, they are thus used to create Bessel beams at THz frequencies in our design. The conventional design approaches, based on scalar theory, are no longer suitable, as the feature sizes of DOEs used are on the order of or smaller than the submillimeter wavelengths. Accordingly, the rigorous electromagnetic analysis method, such as MOM, FEM and FDTD, should be employed to calculate the fields diffracted by DOEs. However, it is known that the full three-dimensional (3-D) analysis demands excessive computational memory and time. So the optimization design method is typically classified as computationally intensive [8] and becomes an intractable problem. Two measures are applied to conquer this difficulty in our design, that is, a BOR-FDTD method and a MGA.

2. BOR-FDTD METHOD

Many approaches referred to as body of revolution (BOR) have been developed to lessen the calculational burden of a full 3-D analysis. These methods take advantage of the symmetry structure and use a 2-D solution space instead of a full 3-D space, and therefore considerably reduce the needed computational resources [9]. It has been demonstrated that the BOR-FDTD method is computationally more efficient and suitable for analysis electrically large structures [10]. Accordingly, it is adopted in our design to analyse the fields diffracted by DOEs. A detailed description of BOR-FDTD method is presented in Refs. [10, 11]. So it will not be covered here.

Figure 1 illustrates schematically the calculational model of the BOR-FDTD method, where z_1 is the space between the input plane and the DOE, and the space between the DOE and the output plane is denoted by z_2; the aperture radius of the DOE, represented by R, is the same as that of the input and output planes; n_1 and n_2 indicate the refractive indices of the free space and the DOE, respectively; and z is the revolution symmetric axis.

The DOE shown in Fig. 1 is utilized to transform a normally incident Gaussian beam on the input plane into a Bessel beam on the output plane. Note that the aim of our design is to obtain a

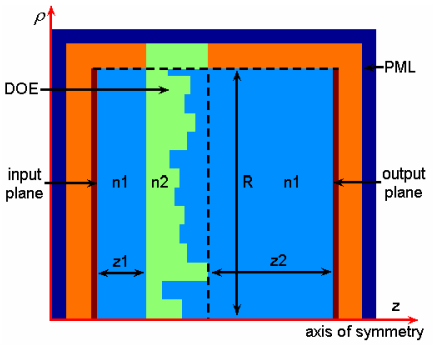

Figure 1: The computational model of the BOR-FDTD method.

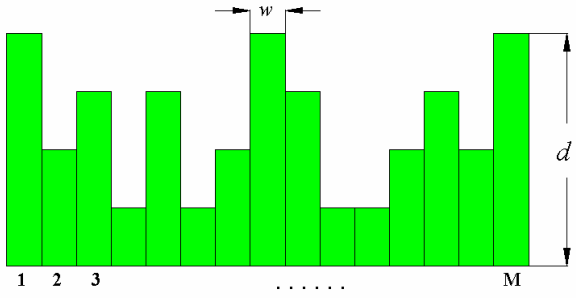

Figure 2: The profile of DOE. Each ring has the identical width w but different depth d.

desired Bessel beam in the near region (i.e., on the output plane). If one wants to acquire a desired Bessel beam in the far region, the techniques of near-to-far field transformation should be applied to calculate the fields in the far region.

3. MGA

In order to fabricate easily, the DOE with circular symmetry is usually split into concentric rings having identical width w but different depths d, as plotted in Fig. 2. The width w is determined by $w = R/M$, where R is the aperture radius of the DOE, M is a prescribed positive integer. The depth d of each ring is an integer multiple of some fixed depth Δd. The profile of the DOE can be characterized by a set of depth d, i.e., $D = \bigcup_{m=1}^{M} \{d_m\}$, where d_m represents the depth of the mth ring. Thus, the different combination D, represents the different profile of the DOE, and hence corresponds to the different field distribution. The design goal is to find the optimal combination D that generates the desired intensity pattern on the output plane. Thereupon, the global optimization algorithm should be employed to acquire the profile of the DOE.

Although the genetic algorithm (GA) has been used widely for the optimal design of DOEs [12], a main drawback to the conventional GA is that a large population base and a great many generations are required to achieve optimal or near-optimal results, and this places a considerable burden on computational resources. To decrease the calculational load of optimization, an advanced version of the GA, i.e., microgenetic algorithm (MGA) [13, 14], is introduced to optimize the DOE profile in our study. It is demonstrated that using the MGA can decrease the computational run time by 50%, even for "best-case" problems for the conventional GA [8]. Although the MGA obeys the same principles as the conventional GA, it operates on a small population. The block diagram of the MGA optimizer is shown schematically in Fig. 3, in which the fitness function is simply defined as:

$$fitness = \sum_{u=-U}^{U} \sum_{v=-V}^{V} (|E^c_{u,v}| - |E^d_{u,v}|)^2$$

where $E^c_{u,v}$ and $E^d_{u,v}$ denote the calculated and desired field at the (u, v) sample point of the output plane, respectively.

4. NUMERICAL RESULTS

Two examples are presented herein to demonstrate the validity of the present optimization tool, in which a normally incident Gaussian profile beam is shaped into a zero-order and a second order Bessel beams, respectively. The forms of the incident Gaussian profile beam and the desire profile of Bessel beam can be given by: $E^i(\rho_1) = \exp(-\rho_1^2/\omega_0^2)$ and $E^d(\rho_2) = E_0 J_n(k_\perp \rho_2)$, respectively, where ω_0 is the waist size of the incident Gaussian beam, ρ_1 and ρ_2 represent the radial coordinates on the input and output planes, respectively, $k_\perp$ is the radial wave number, and E_0 is a constant and can be determined by the law of conservation of energy. The same parameters used in these two examples are as follows: $z_1 = \lambda$, $z_2 = 4\lambda$, $R = 8\lambda$, $M = 128$, $U = V = M$, $\omega_0 = 4\lambda$, and $n_1 = 1.0$. The refractive indices of the DOE are $n_2 = 1.449$ (teflon) and $n_2 = 1.944$ (quartz glass) in the first and second instance, respectively. And the incident wavelengths are set at $\lambda = 0.599\,\text{mm}$

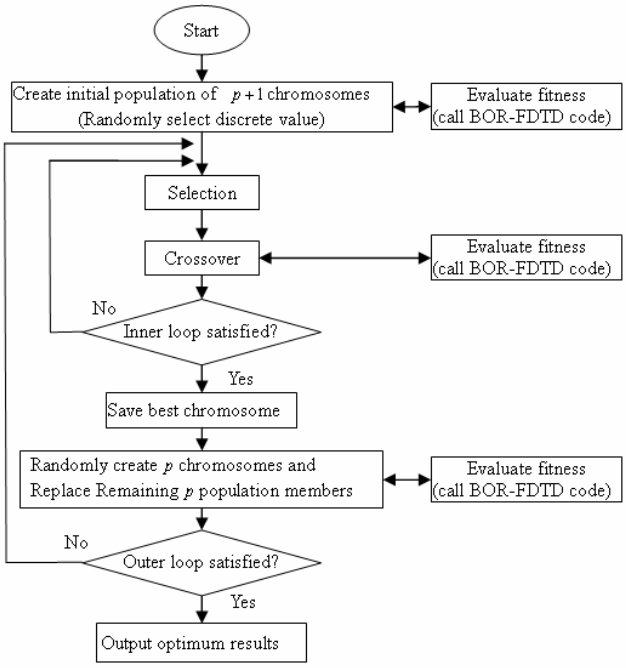

Figure 3: The block diagram of the MGA optimizer.

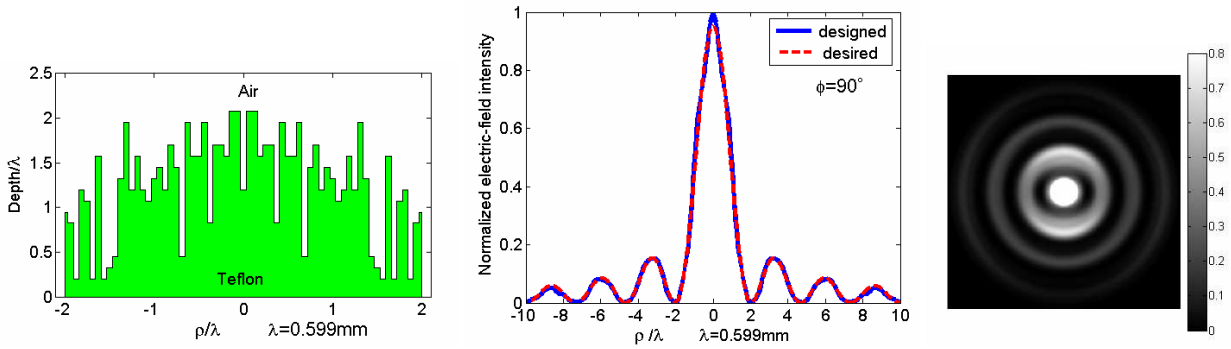

(a) (b) (c)

Figure 4: Normalized total electric-field intensity of J_0 Bessel beam on the output plane. $k_\perp = 1.9667\,\mathrm{mm}^{-1}$ and diffraction efficiency $\eta = 97.362\%$. (a) Part of the optimized DOE profile, (b) line scan of the desired and the designed transverse intensity distribution, and (c) the 2-D transverse intensity distribution.

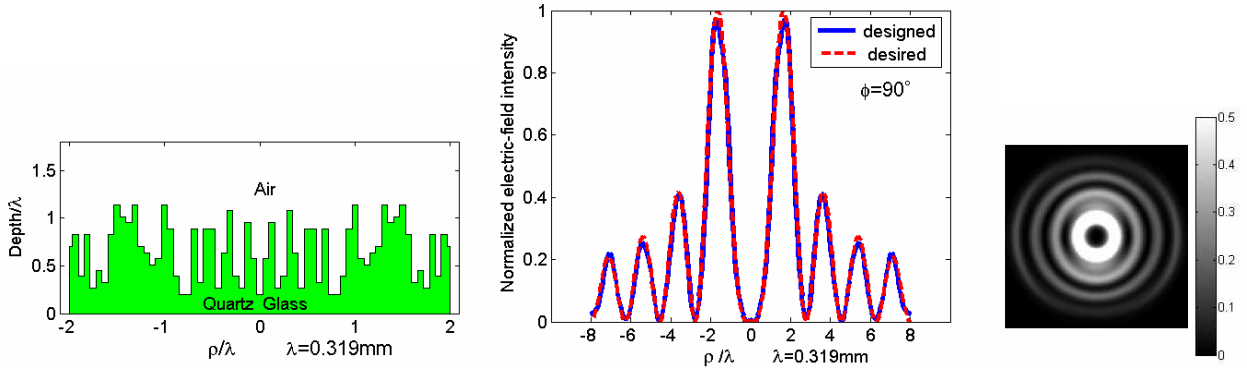

(a) (b) (c)

Figure 5: Normalized total electric-field intensity ofJ_2Bessel beam on the output plane. $k_\perp = 5.7991\,\mathrm{mm}^{-1}$ and $\eta = 96.773\%$. (a) Part of the optimized DOE profile, (b) line scan of the desired and the designed transverse intensity distribution, and (c) the 2-D transverse intensity distribution.

($f = 0.50\,\mathrm{THz}$) and $\lambda = 0.319\,\mathrm{mm}$ ($f = 0.94\,\mathrm{THz}$) in the first and second example, respectively. These frequency bands belong to a very important atmosphere window to propagation. It can be seen clearly from numerical results that the desired electric field intensity distributions are in good agreements with those diffracted by the designed DOEs on the output plane.

5. CONCLUSION

Using the design tool described above, we have designed several DOEs for producing arbitrary order Bessel beams at THz wavebands. Two measures are adopted in our design to save the computational resources and hence improve the design efficiency. The validity of the developed design approach is demonstrated by numerical results. The generated Bessel beams with long depth of field may be useful in THz imaging or measurement applications.

ACKNOWLEDGMENT

This work is supported by the Key Project of Quanzhou City Science and Technology Program (No. 2008G13).

REFERENCES

1. Durnin, J., "Exact solutions for nondiffracting beams. I. The scalar theory," *J. Opt. Soc. Am. A*, Vol. 4, 651–654, Apr. 1987.
2. Arlt, J. and K. Dholakia, "Generation of high-order Bessel beams by use of an axicon," *Opt. Commun.*, Vol. 177, 297–301, Apr. 2000.
3. Cong, W. X., N. X. Chen, and B. Y. Gu, "Generation of nondiffracting beams by diffractive phase elements," *J. Opt. Soc. Am. A*, Vol. 15, 2362–2364, Sep. 1998.
4. Zhou, G., X. Yuan, P. Dowd, Y. L. Lam, and Y. C. Chan, "Diffractive optical elements designed by hybrid algorithm for the generation of nondiffraction beams," *Proc. SPIE. Int. Soc. Opt. Eng.*, Vol. 4291, 148–156, Jan. 2001.
5. Lu, J. Y. and J. F. Greenleaf, "Nondiffracting X waves — Exact solutions to free-space scalar wave equation and their finite aperture realizations," *IEEE Transactions on UFFC*, Vol. 39, 19–31, Jan. 1992.
6. Monk, S., J. Arlt, D. A. Robertson, J. Courtial, and M. J. Padgett, "The generation of Bessel beams at millimetre-wave frequencies by use of an axicon," *Opt. Commun.*, Vol. 170, 213–215, Nov. 1999.
7. Meltaus, J., J. Salo, E. Noponen, et al., "Millimeter-wave beam shaping using holograms," *IEEE Trans. Microwave Theory Tech.*, Vol. 51, 1274–1279, Apr. 2003.
8. Chakravarty, S., R. Mittra, and N. R. Williams, "On the application of the microgenetic algorithm to the design of broad-band microwave absorbers comprising frequency-selective surfaces embedded in multilayered dielectric media," *IEEE Trans. Microwave Theory Tech.*, Vol. 49, 1050–1059, Jun. 2001.
9. Shi, S. and D. W. Prather, "Electromagnetic analysis of axially symmetric diffractive optical elements illuminated by oblique incident plane waves," *J. Opt. Soc. Am. A*, Vol. 18, 2901–2907, Nov. 2001.
10. Prather, D. W. and S. Shi, "Formulation and application of the finite-difference time-domain method for the analysis of axially symmetric diffractive optical elements," *J. Opt. Soc. Am. A*, Vol. 16, 1131–1142, May 1999.
11. Taflove, A. and S. C. Hagness, *Computational Electrodynamics: The Finite-Difference Time-Domain Method*, 2nd Edition, Artech House, Boston, Mass., 2000.
12. Zhou, G., Y. Chen, Z. Wang, and H. Song, "Genetic local search algorithm for optimization design of diffractive optical elements," *Appl. Opt.*, Vol. 38, 4281–4290, Jul.1999.
13. Krishnakumar, K., "Micro-genetic algorithms for stationary and non-stationary function optimization," *Proc. SPIE — Int. Soc. Opt. Eng.*, Vol. 1196, 289–296, 1989.
14. Johnson, E. G. and M. A. G. Abushagur, "Microgenetic-algorithm optimization methods applied to dielectric gratings," *J. Opt. Soc. Am. A*, Vol. 12, 1152–1160, May 1995.

Creation of Approximate Bessel Beams by Use of a Fractal Conical Lens

Yanzhong Yu
School of Science, Quanzhou Normal University, Quanzhou, Fujian 362000, China

Abstract— Increasing attention has been paid to axicons that are used to generate approximate Bessel beams. Recently many novel axicons, such as fractal conical lenses and Fresnel axicons, have been proposed and analyzed by scalar approximate theory. To accurately analyze the fields diffracted by a fractal conical lens (FCL), the rigorous electromagnetic analysis method, that is, a two-dimension finite-difference time-domain (2-D FDTD) method in conjunction with Stratton-Chu formulas, is adopted in our paper. The analysis results and conclusions are presented.

1. INTRODUCTION

An axicon, which was first introduced in 1954 by McLeod [1], is a specialized type of lens and has a figure of revolution. Generally speaking, axicons can be divided into three main types [2, 3], i.e., refractive axicons (conical lenses), reflective axicons (conical mirrors), and diffractive axicons (circular diffraction gratings). An axicon images a point source into a focal line along the optic axis, and this line can be approximated by a Bessel-type (nondiffracting) beam [4] that has extremely narrow intensity profile and yet possesses a very large depth of field [5]. These properties of an axicon have many potential applications in imaging, alignment, laser machining, etc, and the number of axicon applications has also increased significantly in the last few years [6]. Accordingly, much interest has been provoked in design and analysis of axicons [7]. Recently many novel axicons, such as fractal conical lenses [2], Fresnel axicons [4], and fractal axicons [8], have been proposed and investigated. However, all of these axicons are analysed by scalar approximate theory in optics. But at our interesting band, i.e., mm- and sub mm-wavelengths, it is known that the scalar-based analysis method is usually not suitable for calculating the fields diffracted by an axicon. Therefore, the present work applies 2-D FDTD method in conjunction with Stratton-Chu formulas to analyze the fields diffracted by a fractal conical lens. The analysis results and conclusions are given.

2. CANTOR-LIKE FRACTAL CONICAL LENSES

A FCL is a rotationally symmetric lens that is generated from a 1D Cantor set of a given stage of growth [2, 8]. As an example, the Cantor ternary set is shown in the upper part of Fig. 1(a). It is created by repeatedly deleting the open middle thirds of a set of line segments. One starts by deleting the open middle third $(1/3, 2/3)$ from the interval $[0, 1]$, leaving two line segments: $[0, 1/3] \cup [2/3, 1]$. Next, the open middle third of each of these remaining segments is deleted, leaving four line segments: $[0, 1/9] \cup [2/9, 3/9] \cup [6/9, 7/9] \cup [8/9, 1]$. Continuing this process, at stage S, there are 2^S segments of length 3^{-S} with $2^S - 1$ disjoint gaps located at the intervals $[p_{S,L}, q_{S,L}]$, with $L = 1, 2, ..., 2^S - 1$. In Fig. 1(a), only the first three stages of this process are illustrated for clarity.

The Cantor function, $F_S(x)$, based on the Cantor set, is defined in the interval $[0, 1]$ as [2]

$$F_S(x) = \begin{cases} \frac{L}{2^S} & \text{if } p_{S,L} \le x \le q_{S,L} \\ \frac{1}{2^S} \frac{x - q_{S,L}}{p_{S,L} - q_{S,L}} + \frac{L}{2^S} & \text{if } q_{S,L} \le x \le p_{S,L+1} \end{cases}$$

with $L = 1, 2, ..., 2^S - 1$. The Cantor function $F_3(x)$ is shown in the lower part of Fig. 1(a). The profile of FCL is matched to Cantor function $F_S(x)$ at a given stage, S, as illustrated in Fig. 1(b). Note that in order to keep a constant value of the open angles φ, at different stages S, the height of the FCL is $h_S = (2/3)^S h_0$, where h_0 is the height of a FCL at $S = 0$ corresponding to the conventional conical lens (CL).

3. RIGOROUS ELECTROMAGNETIC ANALYSIS METHOD

Because of rotational symmetry of FCL, a 2-D FDTD method can be employed to compute the fields diffracted by FCL in the near field. The computational model of a 2-D FDTD method is shown schematically in Fig. 2, in which the FCL, with open angle φ and aperture diameter D, is used to

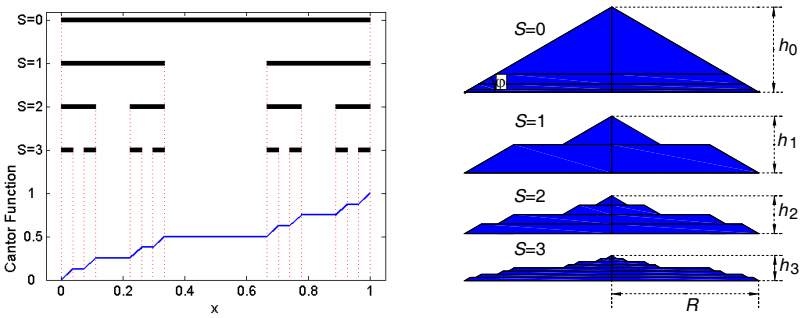

Figure 1: (a) The upper part shows Cantor ternary set for $S = 0, 1, 2$, and 3, and the Cantor function $F_3(x)$ is illustrated in the lower part. (b) The profiles of FCLs at stage $S = 0, 1, 2$, and 3, respectively.

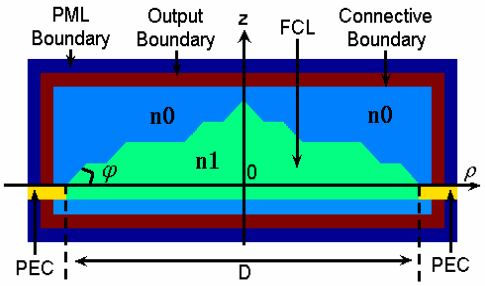

Figure 2: Schematic diagram of 2-D FDTD computational model.

convert an incident plane wave into Bessel beam. Duo to the limitation of computational time and memory, the computational rang of a 2-D FDTD method is restricted in the near field. Therefore, in order to accurately determine electromagnetic field distributions in the far field, Stratton-Chu formulas are applied and given by [9]

$$\vec{E}(\vec{r}) = \int_S \left\{ j\omega\mu \left[\vec{n} \times \vec{H}(\vec{r}')\right] G_0(\vec{r}, \vec{r}') - \left[\vec{n} \times \vec{E}(\vec{r}')\right] \times \nabla' G_0(\vec{r}, \vec{r}') - \left[\vec{n} \cdot \vec{E}(\vec{r}')\right] \nabla' G_0(\vec{r}, \vec{r}') \right\} dS'$$

$$\vec{H}(\vec{r}) = -\int_S \left\{ j\omega\varepsilon \left[\vec{n} \times \vec{E}(\vec{r}')\right] G_0(\vec{r}, \vec{r}') + \left[\vec{n} \times \vec{H}(\vec{r}')\right] \times \nabla' G_0(\vec{r}, \vec{r}') + \left[\vec{n} \cdot \vec{H}(\vec{r}')\right] \nabla' G_0(\vec{r}, \vec{r}') \right\} dS'$$

where $\vec{r} = (\rho, z)$ and $\vec{r}' = (\rho', z')$ denote an observation point in the far filed and an source point on the output boundary of 2-D FDTD method, respectively, $G_0(\vec{r}, \vec{r}') = -(i/4)H_0^{(2)}(k|\vec{r} - \vec{r}'|)$, ω is the angular frequency, ε and μ are permittivity and permeability, respectively.

4. NUMERICAL RESULTS AND ANALYSES

To investigate the properties of FCLs at different stages when illuminated by a plane wave, Fig. 3 displays the axial intensity distributions and corresponding transverse patterns at $z_{\max}$ planes for stage $S = 0, 1, 2$, and 3, respectively. Note that on the left side the z-axis is marked using logarithmic graduation for clarity in the near field. The parameters used in Fig. 3 are as follows: an incident wavelength is $\lambda = 3\,\text{mm}$, the open angle is $\varphi = 10°$, and the diameter is $D = 24\lambda$, the refractive indexes of axicon and air are $n_1 = 1.45$ and $n_0 = 1.0$, respectively. From the left side of Fig. 3, we can see visibly that the oscillation amplitudes of all these curves increase slowly, and reach their respective maximum values then decrease sharply, as the propagation distance z increase. Moreover, the higher the stage is, the larger is the average value of axial intensity, except the stage zero in which it reaches maximum value. This is interpreted as the increasing convergence while the stage increase, but except the stage zero in which the FCL has the largest convergence performance and therefore has the largest axial intensity. It is also found that the farther the propagation distance z is, the lower is the oscillation frequency.

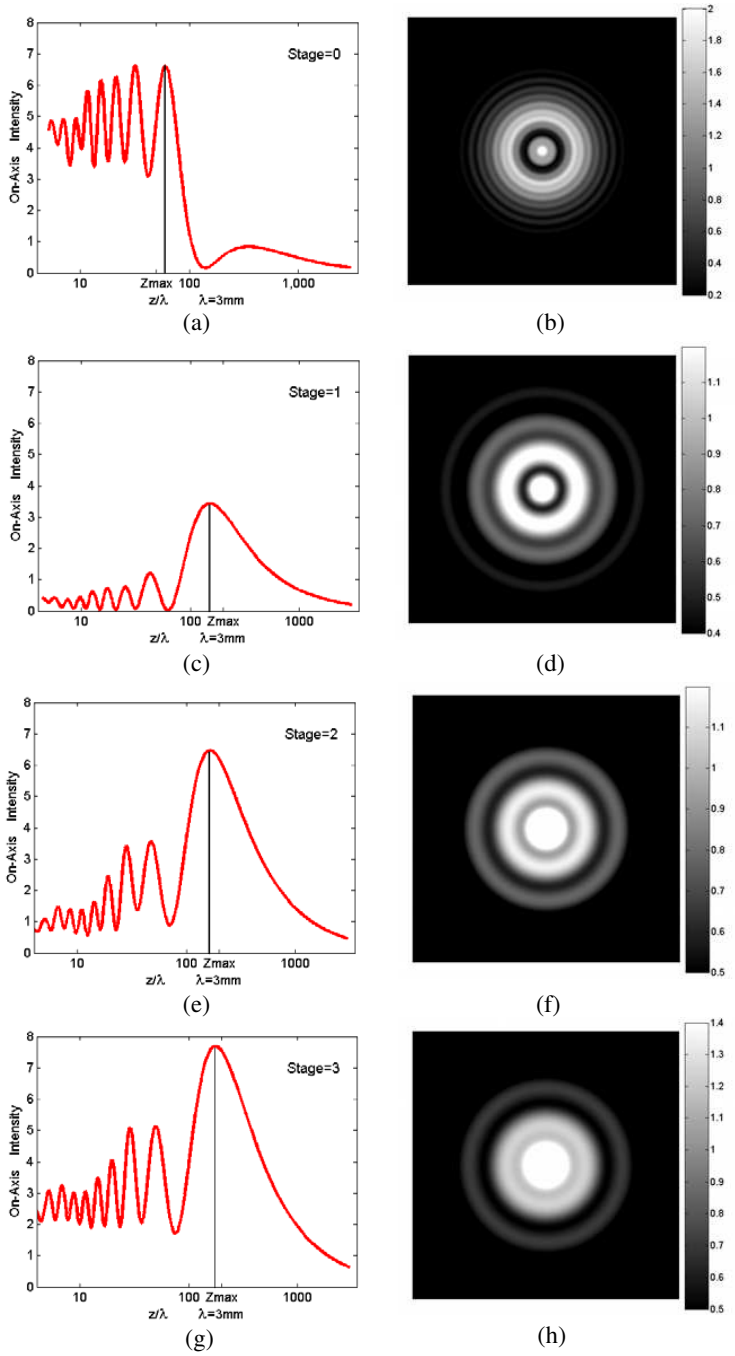

Figure 3: The axial intensity distributions and transverse patterns for stage $S = 0, 1, 2$, and 3, respectively. The axial intensity distributions are illustrated on the left side and corresponding transverse patterns at $z_{\max}$ planes are shown on the right side. Note that on the left side the z-axis is marked using logarithmic graduation for clarity in the near field.

In order to study the transverse patterns, we typically present them only at $z_{\max}$ planes on the right side of Fig. 3. Side bars illustrate the relative magnitudes. All of FCLs illuminated by a plane wave can generate Bessel beams that are only the approximations to the ideal. In addition, it can be seen clearly that the higher the stage is, the larger the diameter of central spot becomes.

5. CONCLUSION

The rigorous electromagnetic analysis method, which combines a 2-D FDTD method and Stratton-Chu formulas, has been applied to compute the axial intensity distributions and transverse patterns diffracted by FCLs at different stages. Not only the axial but also the transverse intensity distributions depend on the stage of growth. The different stage corresponds to different convergence

performance, and therefore there are different axial and transverse intensities. These results indicate that the desired millimeter-wave Bessel beams can be acquired by growing the FCL to a certain stage.

ACKNOWLEDGMENT

This work is supported by the Key Project of Quanzhou City Science and Technology Program (No. 2008G13).

REFERENCES

1. McLeod, J. H., "The axicon: A new type of optical element," *J. Opt. Soc. Am. A*, Vol. 44, 592–597, Aug. 1954.
2. Monsoriu, J. A., W. D. Furlan, P. Andres, and J. Lancis, "Fractal conical lenses," *Opt. Express*, Vol. 14, 9077–9082, Oct. 2006.
3. Anguiano-Morales, M., A. Martinez, M. D. Iturbe-Castillo, and S. Chavez-Cerda, "Different field distributions obtained with an axicon and an amplitude mask," *Opt. Commun.*, Vol. 281, 401–407, Feb. 2008.
4. Golub, I., "Fresnel axicon," *Opt. Lett.*, Vol. 31, 1890–1892, Jun. 2006.
5. Durnin, J., "Exact solutions for nondiffracting beams. I. The scalar theory," *J. Opt. Soc. Am. A*, Vol. 4, 651–654, Apr. 1987.
6. Jaroszewicz, Z., A. Burvall, and A. T. Friberg, "Axicon-the most important optical element," *Opt. Photonics News*, Vol. 16, 35–39, USA, Apr. 2005.
7. Pu, J. X. and S. J. Nemoto, "Design and analysis of diffractive axicons for gaussian beam illumination," *Chin. J. Lasers B*, Vol. 10, 228–232, Jun. 2001.
8. Monsoriu, J. A., C. J. Zapata-Rodriguez, and W. D. Furlan, "Fractal axicons," *Opt. Commun.*, Vol. 263, 1–5, Jul. 2006.
9. Stratton, J. A., *Electromagnetic Theory*, McGraw-Hill, NewYork, 1941.

Ku-band Balanced Resistive FET Mixer with Very Low IMD3

R. A. Sadeghzadeh[1], **A. R. Eskandari**[2], **and M. A. Honarvar**[3]

[1]Department Electrical Engineering, Khajenasirtoosi University, Tehran, Iran
[2]Islamic Azad University, East Tehran Branch, Tehran, Iran
[3]Islamic Azad University, Najafabad Branch, Isfahan, Iran

Abstract— This paper describes a practical realization of a mixer that achieves low 3rd-order intermodulation distortion (IMD3) by using the channel resistance of a GaAs MESFET to provide mixing. The IMD3 of the resistive mixer is 48.5 dBc with −10 dBm RF power at 14 GHz. In additional, the conversion loss and 3rd-order intercept point (IP3) are 7.7 dB and 19.8 dBm with 10 dBm LO power level, respectively. The isolation of LO/RF and LO/IF are 45 dB and 56 dB, respectively. The circuit was realized in microstrip on a Teflon substrate. For improvement of some parameters so as dynamic range, IP3, P1dB and isolation, balanced mixer structure was proposed.

1. INTRODUCTION

The most commonly used mixers in microwave systems employ Schottky-barrier diodes as the mixing elements. The active elements such as FETs which is used for fabrication of microwave mixers, not only can improve the conversion loss but also causes to appear conversion gain. Disadvantages of active mixers in comparison with Schottky-barrier mixers, are instability and more complicated bias circuits. Simplicity of bias circuits, is obtained by using the resistive region of FET, furthermore it decreases probability of instability. On the other hand, because of the very weak nonlinearity of channel resistance, the mixer generates very low intermodulation products and results in high 1-dB compression point.

In this paper, a resistive mixer for Ku-band designed and fabricated. The resistive mixer is one of gate mixer which employs drain-source resistance, which is channel resistance of the FET in order to obtain time-varying resistance in the saturated region. Due to the low nonlinearity, the resistive mixer has very low IMD3 and high output power [3]. In the case of the resistive mixer, the time-varying channel resistance, which is changed by LO cycle, plays as a switch. If the switch is ideal, IMD3 is nonexistent. Therefore, it is known that the resistive mixer has low IMD3. Also, the resistive mixer does not have shot noise due to the DC current, but ohmic noise which is thermal noise due to the channel resistance [2]. Since the shot noise of the mixer is not existence, the resistive mixer has superior noise characteristics comparing with drain mixers and/or gate mixers. The channel resistance of the MESFET is linear over the low drain-source voltage, and then this linear channel resistance can be changed by the depth of depletion layer under the gate. When the gate voltage is smaller than the turn-on voltage, practically, the resistance is infinite. On the other hand, the channel resistance is almost negligible when the gate voltage is reached at the point which causes the gate channel conduction. Typical value of the resistance is just several ohms and the small resistance is sufficient to perform superior conversion characteristics [4].

2. DESIGN AND FABRICATION OF THE ADVANCED MIXER

A block diagram of the mixer is shown in Fig. 1. The LO signal and negative DC bias voltage are applied in the gate, the RF signal is applied in the drain, and IF signal is measured at the drain. A matching network is designed to obtain minimum conversion loss at the drain, and a RF band-pass filter (BPF) is inserted to prevent the RF signal from flowing into the IF terminal. In addition, a $\lambda/4$ open stub is employed to improve the isolation characteristic between LO and RF. Matching circuits are also designed at the drain for LO signal and at the gate for RF signal to be short for IMD3 improvement. Tow filters and a matching circuit are used. A BPF is used at RF terminal for preventing IF and LO signal from flowing into the RF terminal. On the other hand, a low-pass filter (LPF) is used at IF terminal to block signals of high frequency band. Then a matching network is designed at the LO terminal. IMD3 can be measured from two RF input signals which are the same power level. The first RF signal (RF1) is −10 dBm at 14 GHz and the second RF signal (RF2) is −10 dBm at 14.01 GHz. There is 10MHz difference between RF1 and RF2.

The designed resistive mixer was fabricated on the Teflon substrate (RO4003). The dielectric constant is 3.38, height is 0.508 mm and height of copper substrate is 0.017 mm. 50 pF capacitors were used for the DC blocking. Fig. 2 shows a picture of the fabricated resistive mixer.

3. MEASUREMENT AND RESULTS

The RF an LO frequencies used for the measurement are 13 ∼ 15 GHz and 12 GHz, respectively. IF output power at band-center is −17.7 dBm with −10 dBm RF input power and +10 dBm LO power. Fig. 3 shows the measured IF output power at 12.5 ∼ 15.2 GHz RF frequency. The IMD3 characteristic of 48.5 dBc is measured with 10 dBm LO and −10 dBm RF input powers. Fig. 4 presents the characteristics of IF and IMD3 powers as a function of RF input power and shows the IP3 of 19.8 dBm at band-center and 10 dBm LO level. The LO to RF isolation is more than 30 dB in the full frequency band and it is 45 dB in band-center. Table 1 compare the difference between designed specifications and measurements of the resistive mixer.

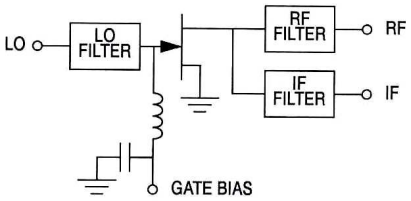

Figure 1: Block diagram of single mixer.

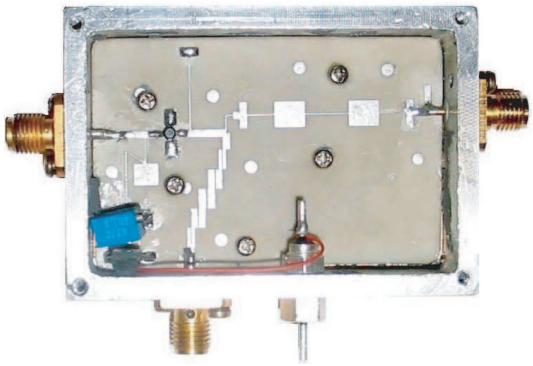

Figure 2: Picture of fabricated single mixer.

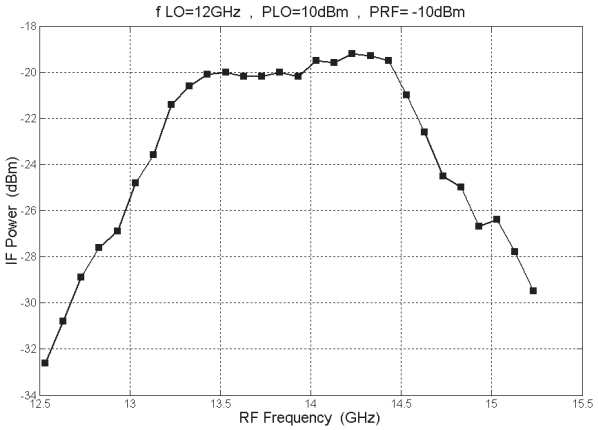

Figure 3: Measured IF output power.

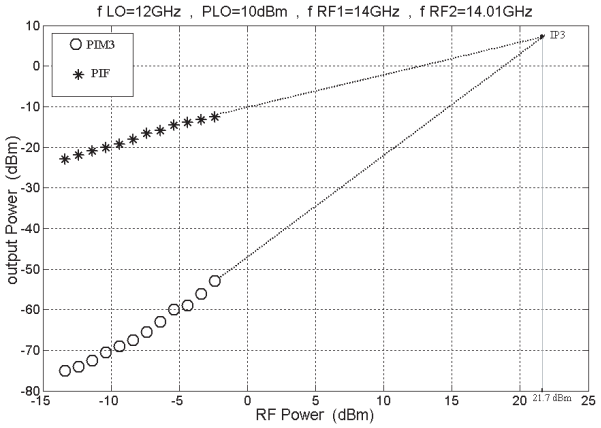

Figure 4: Measured IF power and IMD3 power and showing IP3.

Table 1: (fRF=14 GHz, fLO=12 GHz, PLO=10 dBm).

	Simulation	**Measurement**
conversion loss	6.3 dB	7.8 dB
IMD3	43 dBc	48.5 dBc
LO/RF isolation	20.3 dB	45 dB
IP3	16.7 dBm	19.8 dBm

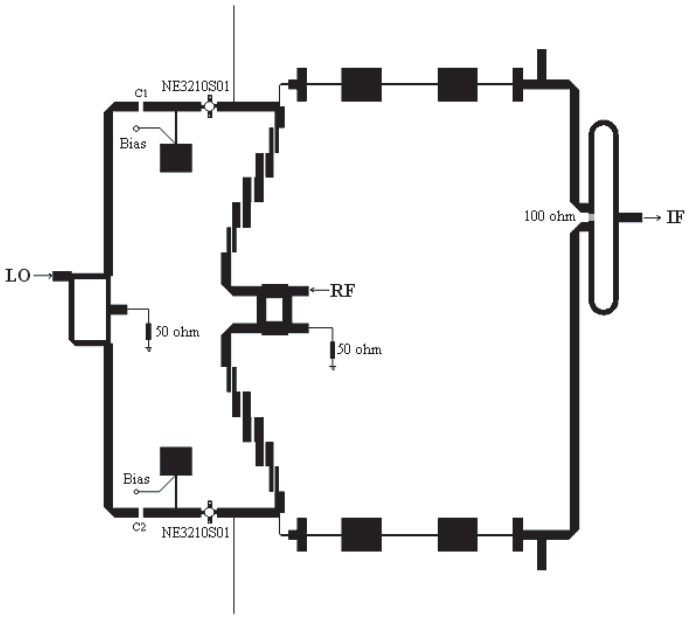

Figure 5: Layout of balanced mixer.

4. BALANCED MIXER

For improvement of some parameters so as dynamic range, IP3, P1dB and isolation balanced mixer structure was proposed and it was accomplished with design of suitable hybrids and combination them with single mixer. Fig. 5 present the layout of balanced mixer. The LO to RF isolation is very excellent.

5. CONCLUSION

In this paper, a resistive mixer for Ku-band was designed and fabricated. Good agreement between mixer's simulation and experimental results was demonstrated. The IMD3 characteristic of the fabricated resistive mixer is 48.5 dBc with −10 dBm RF power. The measured conversion loss is 7.8 dB with 10 dBm LO power. 45 dB isolation is measured for LO/RF isolation and 19.8 dBm IP3 is obtained. This mixer based on the resistance of a GaAs MESFET channel has significant advantages in noise, intermodulation, and power output capability over those based on a pumped Schottky-barrier diode junction. Such a mixer is easy to design and adjust and has characteristics which make it practical for use in low-noise receiver. Parameters of proposed balanced mixer so as dynamic range, IP3 and P1dB are improved.

REFERENCES

1. Maas, S. A., *Nonlinear Microwave and RF Circuits*, 2nd Edition, Artech House, 2003.
2. Maas, S. A., "A GaAs MESFET mixer with very low intermodulation," *IEEE Trans. MTT*, Vol. 35, No. 4, 425–429, April 1987.
3. Maas, S. A., "A GaAs MESFET balanced mixer with very low intermodulation," *IEEE MTT-S International Microwave Symposium Digest*, 895–898, 1987.
4. Virk, R. S. and S. A. Mass, "Modeling MESFETs for Intermodulation analysis in RF switches," *IEEE Microwave and Guided Wave Letters*, Vol. 4, No. 11, Novamber 1994.
5. Eskandari, A. R. and M. Ezoji, "Ku-band resistive FET mixer with very low IMD3," *The 13th Conference on Microwave Techniques, COMITE 2005*, September 2005.

Ultra-compact MMIC Chip Set Employing InGaP/GaAs HBT for Ku-band Receiver System

Young-Bae Park, Bo-Ra Jung, Jang-Hyeon Jeong, Jeong-Gab Ju, Suk-Youb Kang, and Young Yun
Department of Radio Communication Engineering, Korea Maritime University, Republic of Korea

Abstract— In this work, an ultra-compact receiver MMIC chip set employing heterojunction bipolar transistor (HBT) was developed for application to Ku-band receiver system. The receiver monolithic microwave integrated circuit (MMIC) includes mixer, filter, amplifier and input/output matching circuit. Especially, spiral inductor structures employing SiN film were used for a suppression of LO and its second harmonic leakage signals. The ultra-compact active 90° power divider employing InGaP/GaAs HBT was developed for highly integrated on-chip MMIC, and it used a novel composite structure employing common-emitter (CE) and common-collector (CC) circuits for 90° power splitting. The receiver MMIC showed a highly suppressed LO leakage power of −35 dBm and second harmonic LO leakage power of −53 dBm without external filters and the size of active 90° power divider was about 31.6% of conventional passive branch-line coupler. The active 90° power divider showed good RF performance comparable to passive divider at Ku-band.

1. INTRODUCTION

The Ku-band receiver MMICs and receiver chips have been reported in various literatures [1–5]. In conventional Ku-band receiver MMICs, however, mixer was fabricated using a high electron mobility field effect transistor (HEMT) for low noise characteristics, which prevented a realization of ultra-compact RF transceiver because power amplifier was fabricated using HBTs due to its high power and high efficiency characteristics [6]. In addition, for a suppression of LO leakage power at IF output, the conventional Ku-band receiver employed a bulky and complicated LO rejection filter, which was not integrated on a MMIC due to its large size [1–4]. This problem has been also an obstacle to a realization of ultra-compact RF transceiver. In this work, a ultra-compact receiver MMIC including filter, mixer and IF amplifier was realized using InGaP/GaAs HBT [8] for application to Ku-band one chip transceiver solution. Especially, for a suppression of LO leakage signals and its second harmonic, spiral inductor filter was integrated on MMIC. Owing to the realization of on-chip spiral inductor filter, bulky external IF filter (outside of MMIC) was not required for operation of the receiver MMIC.

90° power divider has been used for signal dividing at radio frequency (RF) input port of image rejection mixer [2, 8]. Until now, a passive branch-line coupler has mainly been employed for 90° power splitting [2, 4]. However, the branch-line coupler occupies a very large area in RF circuit. Therefore, passive power dividers can't be integrated on MMIC due to their very large size [8]. To reduce the size of the 90° power divider [7], it has to be fabricated using an active device. In this work, active 90° power divider was realized using the InGaP/GaAs HBT.

2. CIRCUIT DESIGN

The receiver MMIC was designed for the applications of Ku-band satellite system, and the RF and IF frequency are 12 and 1 GHz, respectively, with a LO frequency of 11 GHz. Fig. 1 shows a schematic circuit of the receiver MMIC proposed in this work.

As shown in this figure, a base-pumping mixer was employed using HBT, and the mixed RF and LO signals were applied to the base of the HBT of first stage mixer. Because only FET mixers (such as MESFET and HEMT) have been employed for most of Ku-band commercial wireless communication system [1–5], the operation mechanism of HBT mixer with base-pumping structure has not been theoretically analyzed to date. In all conventional Ku-band receiver system, IF filters have been used for a suppression of LO and its harmonic signal in IF output [6]. However, the IF filter occupies a very large area in transceiver of wireless communication system, and it has been fabricated outside of MMIC, which has been an obstacle to a realization of one chip transceiver [6]. For example, SAW filter, which has widely been used in wireless communication system, occupies 2.3×1.5 mm in an operation of Lband frequency [6]. In this work, a spiral inductor employing SiN film was used for application to filter, and LO and its second harmonic leakage signals were

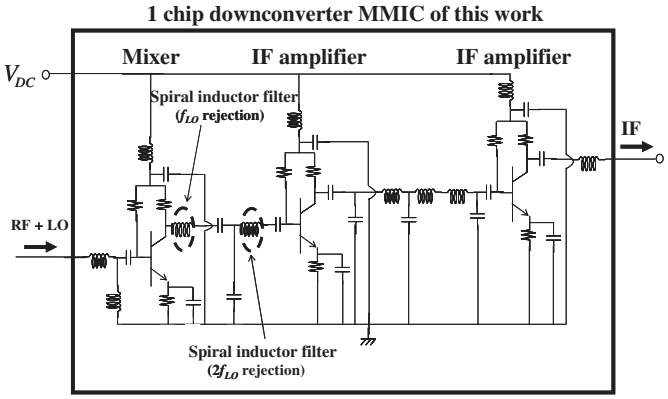

Figure 1: A schematic circuit of the receiver MMIC employing HBTs.

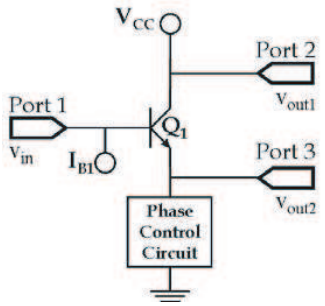

Figure 2: A schematic of active 90° power divider employing composite CE and CC circuit.

suppressed to a great extent by a sharp LC resonance characteristic originating from a parasitic capacitance of the SiN film. Using the parasitic capacitance of the spiral inductor employing SiN film caused a sharp and easily controllable LC resonance, which enabled the resonance frequency to exactly coincide with LO and its second harmonic frequency.

Figure 2 shows a schematic circuit of an active 90° power divider employing composite CE and CC circuit. As shown in Fig. 2, a novel composite structure employing common-emitter (CE) and common-collector (CC) circuits was used, and the output ports of the CE and CC circuits were connected to each other. To compensate for the insertion loss of the active 90° power divider, an amplifier was connected at each output port.

3. MEASURED RESULTS

Figure 3 shows a photograph of the receiver MMIC, and its schematic diagram is shown in Fig. 1. As shown in Figs. 1 and 3, the spiral inductors were connected at the collector of the HBT of the first stage mixer in order to suppress the LO and its second harmonic signal at IF output. The size of spiral inductors for a suppression of LO and its second harmonic signal is 0.2×0.2 mm and 0.16×0.16 mm, respectively. Therefore, the two spiral inductors occupy a size of $0.0656\,\text{mm}^2$ on MMIC, and total area is 1.9% of conventional IF filter with a size of 2.3×1.5 mm [6], which enabled an integration of spiral inductor on MMIC.

Figure 4 shows LO and its second harmonic leakage power at IF output, and their frequencies correspond to 11 and 22 GHz, respectively. As shown in this figure, the leakage powers for LO and its second harmonic signals were suppressed to a great extent by using the optimally designed spiral inductors. Concretely, at a LO power of −1 dBm, LO and its second harmonic leakage power are −35 and −53 dBm, respectively. Considering that a LO leakage power of less than −25 dBm is required for a normal operation of commercial DBS system including external IF

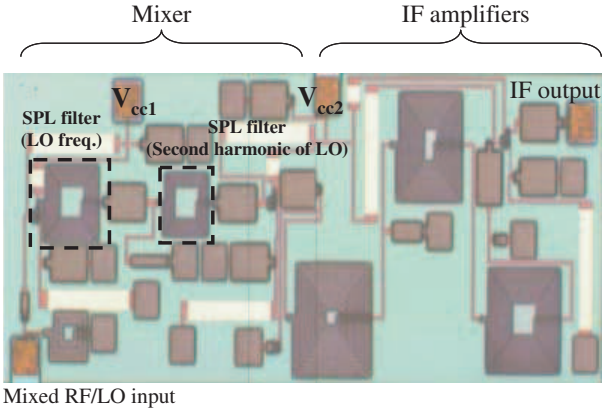

Figure 3: The photograph of the receiver MMIC.

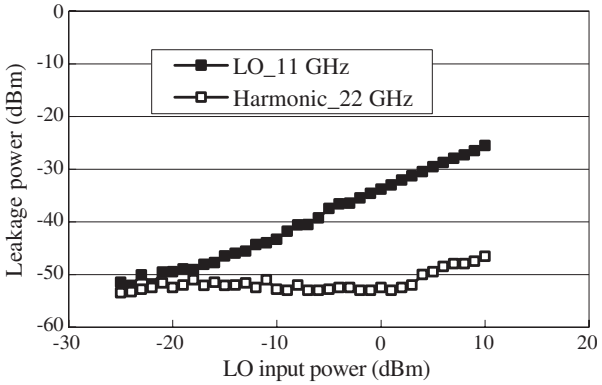

Figure 4: Measured LO and its second harmonic leakage power at IF output.

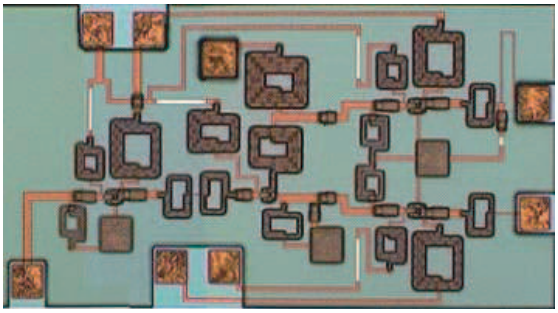

Figure 5: A photograph of the active 90° power divider employing InGaP/GaAs HBT.

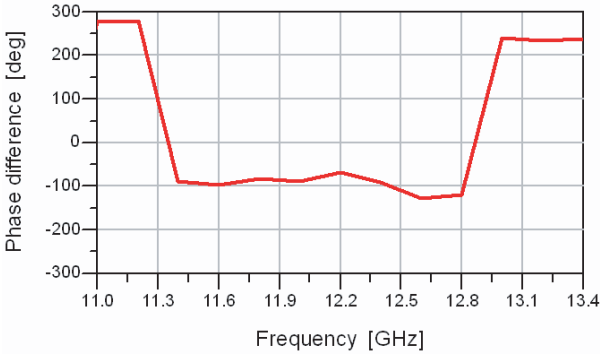

Figure 6: Measured phase difference between S_{21} and S_{31} of active 90° power divider for power division.

filter [1–5], above result indicates that the receiver MMIC including spiral inductors is sufficient for application to commercial DBS system and external filter is not required for normal operation of Ku-band communication system.

Figure 5 shows a photograph of the active 90° power divider employing CE and CC with InGaP/GaAs HBT, which was fabricated on GaAs MMIC. The size of the fabricated chip, including the active 90° power divider and amplifier, is 1.67×0.87 mm, which is 31.6% of the size of a conventional branch-line coupler fabricated on GaAs MMIC. (As mentioned before, the size of passive coupler is 2.11×2.18 mm).

Figure 6 shows a phase difference characteristic of the active 90° power divider employing CE and CC with InGaP/GaAs HBT. As shown in this figure, a phase difference characteristic of $-90 \pm 2.5°$ is observed at Ku-band.

4. CONCLUSION

In this work, we developed an ultra-compact receiver MMIC chip set employing HBT for application to Ku-band one chip transceiver solution. For a suppression of leakage signals for LO and its second harmonic, we used spiral inductor structures employing SiN film with parasitic capacitance. Considering that the spiral inductor has conventionally been used as matching element in much lower frequency range than the self-resonance frequency, the concept of filter application in this work is very challenging. The total size of spiral inductors for a suppression of LO and its second harmonic frequency was 1.9% of conventional IF filter, which enabled an integration of spiral inductor on receiver MMIC. Owing to the LC resonance characteristics of the spiral inductor structure employing SiN film, the receiver MMIC showed a highly suppressed LO leakage power of -35 dBm and second harmonic leakage power of -53 dBm without external filter, which made external filters unnecessary for normal operation of the Ku-band communication system. In addition, the LC resonance characteristics of the spiral inductors also led to a high suppression of RF and its second harmonic leakage signals. The design technology of spiral inductor filter in this work is also applicable to silicon devices as well as millimeter-wave III-V devices. And, we also fabricated an ultra-compact active 90° power divider employing CE and CC with InGaP/GaAs HBT on a GaAs MMIC. For a 90° phase difference and equal power splitting, we proposed a novel composite structure employing CE and CC circuits. The size of the active 90° power divider including amplifier was 1.67×0.87 mm, which was 31.6% of the conventional passive divider. The active 90° power divider showed good RF performances comparable to those of a conventional passive divider at the Ku-band.

ACKNOWLEDGMENT

This research was supported by the MKE (The Ministry of Knowledge Economy), Korea, under the ITRC (Information Technology Research Center) support program supervised by the NIPA (National IT Industry Promotion Agency)" (NIPA-2009-C1090-0903-0007). This work was financially supported by the Ministry of Knowledge Economy (MKE) and the Korea Industrial Technology Foundation (KOTEF) through the Human Resource Training Project for Strategic Technology. This work was partly sponsored by KETI (Korea Electronics Technology Institute). This work was

also partly supported by ETRI SoC Industry Promotion Center, Human Resource Development Project for IT SoC Architect.

REFERENCES

1. Camargo, E. and W. Kennan, "An E-mode GaAs FET operating as a single balanced gate mixer," *IEEE MTT-S Int. Microwave Symp. Dig.*, 951–954, 1996.
2. Sugiura, T., K. Honjo, and T. Tsuji, "12-GHz-band GaAs dual-gate MESFET monolithic mixers," *IEEE Trans. Microwave Theory Tech.*, Vol. 33, 105–110, Feb. 1985.
3. Hubbard, K., K. MacGowan, C. Kau, D. Smith, and S. Maas, "A family of low cost high performance HEMT MMICs for commercial DBS applications," *IEEE MTT-S Int. Microwave Symp. Dig.*, 1649–1652, 1995.
4. Kaneko, T., et al., "A Ku band converter IC," *IEEE MTT-S Int. Microwave Symp. Dig.*, 451–454, 1992.
5. Yun, Y., et al., "A low noise and low power dissipation downconverter MMIC for DBS applications," *Technical Journal of IEICE*, Vol. ED2001-198, 7–12, Jan. 2002.
6. Tanaka, S., et al., "High-power, high-efficiency cell design for 26 GHz HBT power amplifier," *IEEE MTT-S Int. Microwave Symp. Dig.*, 843–846, 1996.
7. Ida, M., K. Kurishima, and N. Watanabe, "Over 300 GHz f_T and $f_{\max}$ InP/InGaAs double heterojunction bipolar transistors with a thin pseudomorphic base," *IEEE Electron Device Lett.*, Vol. 23, 694–696, Dec. 2002.
8. Mass, S. A., *Microwave Mixer. Reading*, Artech House, MA, 1986.
9. Chongcheawchamnan, M., et al., "Design and performance of improved lumped-distributed Wilkinson divider topplogy," *Electron. Lett.*, Vol. 37, 501–503, 2001.

A X-band Duplexer Based on 3-D SICC Using LTCC Technology

Jian Gu, **Yong Fan**, **and Dakui Wu**
Extreme High Frequency Key Laboratory, UESTC, Chengdu, Sichuan 610054, China

Abstract— In this paper, two compact X-band band pass filters (BPFs) with low loss and narrow-band using low temperature co-fired ceramic (LTCC) technology are proposed, and then they are used to constitute the duplexer. The filters and duplexer are based on the substrate integrated circular cavity (SICC) resonators and fed by transmission lines. The duplexer exhibits low loss (IL $<$ 2.39 dB for the first channel and IL $<$ 2.65 dB for the second channel), high isolation (better than 51 dB for the first channel and 61 dB for the second channel), and narrow-band ($\sim$ 4.1% and $\sim$ 3.7% for two filters respectively).

1. INTRODUCTION

In modern microwave and millimeter-wave applications, various filters and duplexers have been developed based on integrated cavities, including rectangular substrate integrated waveguide (SIW) [1–4] and planar substrate integrated circular cavity (SICC) [5]. In this paper, a compact LTCC duplexer for X-Band narrow-band applications based on two multilayer SICC BPFs is developed. The merits of this novel SICC duplexer are as such: It is with compact size and simply structure, its insertion loss is very low and isolation is very high. Such kind of duplexer is suitable to be used in 3D LTCC RF and microwave front end modules.

2. DESIGN OF THE SICC RESONATORS AND COUPLING STRUCTURE

The TM_{010} mode is selected here as the operating mode in SICC. The field distribution of TM_{010} mode in SICC is axisymmetrical, so it has high flexibility in adjusting the position and angle of the input/output ports of the BPFs and duplexer. The designed duplexer has small size, and the size including whole pad is 18 mm $\times$ 10 mm $\times$ 1.78 mm.

Figure 1 shows the top views of the SICC resonator and coupling structure of BPFs presented here. Two identical quarter-wavelength axisymmetrical open stubs act as feeding structure, and rectangular slots serve as external and inner coupling structures. Positions and sizes of coupling slots are set to be optimal variables and fine-tuned to achieve the desired frequency response using 3D EM simulation software HFSS. These physical parameters are important factors to adjust insertion loss and bandwidth of filters.

The resonant frequency (unloaded) of circular cavities with metal via wall can be calculated by formula (1) as suggested in [6]:

$$f_{mnl} = \begin{cases} \dfrac{C}{2\pi\sqrt{\mu_r\varepsilon_r}}\sqrt{\left(\dfrac{p'_{mn}}{R}\right)^2 + \left(\dfrac{l\pi}{z}\right)^2} & \text{TE}_{mnl} \text{ mode} \\ \dfrac{C}{2\pi\sqrt{\mu_r\varepsilon_r}}\sqrt{\left(\dfrac{p_{mn}}{R}\right)^2 + \left(\dfrac{l\pi}{z}\right)^2} & \text{TM}_{mnl} \text{ mode} \end{cases} \tag{1}$$

where μ_r and ε_r are relative permeability and permittivity of the filling substrate material, and p_{mn} and p'_{mn} are the nth roots of mth Bessel function of the first kind and its derivative respectively. C is the speed of light in free space, and R is the radius of SICC.

Once the SICC height (H) satisfies $H < 2.1R$, TM_{010} mode is the dominate mode in SICC. Its field distribution is axisymmetrical, and the current of this mode has vertical direction. The TM_{010} mode is selected here as the operating mode in SICC on this condition. The corresponding resonant frequency of TM_{010} mode is given by (1), and once the resonant frequency is calculated, the radius of the SICC can be obtained according to the formula (2).

$$R = \frac{C}{2\pi\sqrt{\mu_r\varepsilon_r}} \cdot \frac{p_{01}}{f_{010}} \tag{2}$$

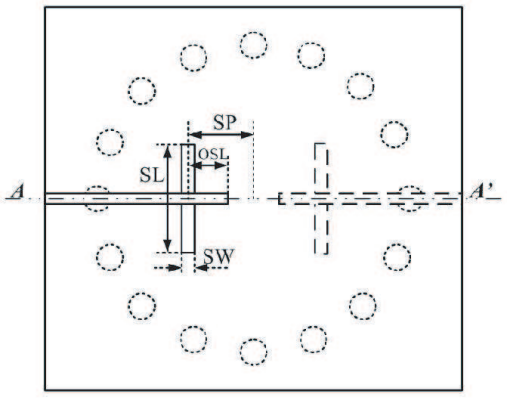

Figure 1: Top view of SICC resonator and coupling structure.

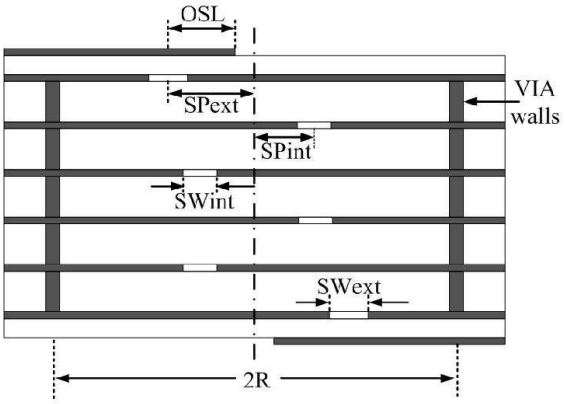

Figure 2: Side view of five-pole SICC BPF.

3. DESIGN OF THE SICC BPF AND DUPLEXER

Two five-pole filters for X-Band narrow-band applications that consist of five SICC resonators are designed in LTCC. The side view of these filters is shown in Fig. 2. These five-pole BPFs based on Chebyshev low-pass prototype filter are developed for 3-dB insertion loss, 0.1 dB in-band ripple, and their fractional bandwidth are designed to be 4.1% ($\sim$ 440 MHz) and 3.7% ($\sim$ 440 MHz) respectively. Center frequencies of these two BPFs are 10.86 GHz and 11.75 GHz. LTCC multilayer substrate Dupont943 is supposed to be used for the designing, the relative dielectric constant (ε_r) of the substrate is 7.4, and its loss tangent ($\tan\delta$) is 0.0009. The dielectric layer thickness per layer is 50 µm, and the metal thickness is 10 µm.

In the designing of a duplexer, a low insertion loss in the transmitter and receiver filters is the most fundamental requirement, because a low loss enhances the sensitivity of the receiver and prevents the excessive power consumption in the transmitter. In addition, the high channel-to-channel isolation is also an important requirement in order to minimize the electrical coupling level between two channels of duplexer.

A multilayer SICC duplexer for X-band application is designed here, and the top view of this structure is shown in Fig. 3. The duplexer consists of two five-pole SICC filters developed above and a microstrip T junction, which connects these two filters. The lengths of microstrip lines of T junction that connect the first and second channel filters are fine tuned to achieve good isolation between two channels of the duplexer. The final optimized lengths should compensate the fringing effects of the open stubs. Three ports of duplexer are described in Fig. 3, which the common port of T junction is port 1, the input transmission line of first channel BPF is port 2, and the input transmission line of second channel BPF is port 3.

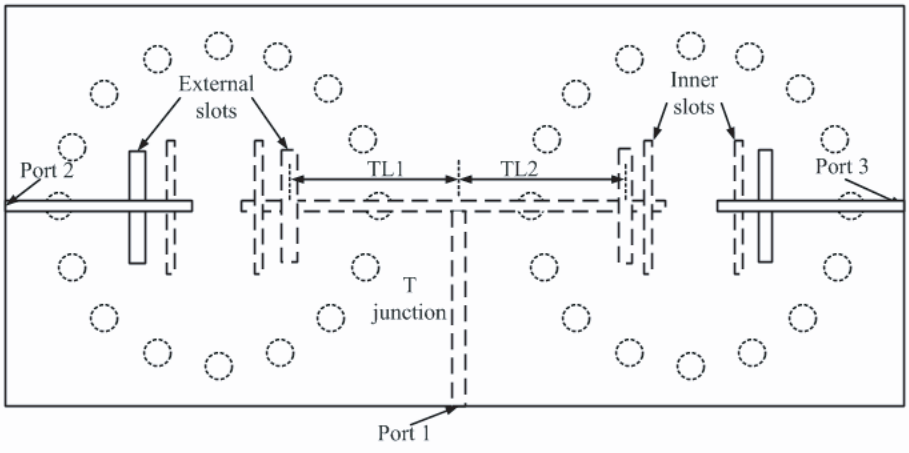

Figure 3: Top view of the duplexer structure.

Table 1: Physical parameters of SICC duplexer.

First channel BPF		Second channel BPF	
parameters	mm	parameters	mm
R_1	3.52	R_1	3.79
R_2	3.57	R_2	3.86
OSL_1	1.68	OSL_2	1.76
SPext_1	1.22	SPext_2	1.23
SLext_1	2.5	SLext_2	2.9
SWext_1	0.358	SWext_2	0.398
SPint_1	0.9	SPint_2	0.91
SLint_1	2.580	SLint_2	2.955
SWint_1	0.338	SWint_2	0.318
TL_1	2.750	TL_2	3.004

The final design parameters of the SICC duplexer depicted in Fig. 3 are summarized in Table 1. In each filter of duplexer, R_1 is the radius of top and bottom SICCs, and R_2 is the radius of three middle SICCs. TL_1 and TL_2 are the lengths of transmission lines in T junction for two BPFs respectively. OSL_1 and OSL_2 are the lengths of quarter-wavelength open stubs for two BPFs.

4. SIMULATION RESULTS

With the structure in Fig. 3, two narrow-band five-pole BPFs are designed and simulated in HFSS. The first channel filter exhibits an insertion loss 1.01 dB, and a 3-dB bandwidth of approximately 440 MHz ($\sim$ 4.1%) at the center frequency of 10.86 GHz. For the filter in second channel, the insertion loss is 0.99 dB at the center frequency 11.75 GHz, and a 3-dB bandwidth is approximately 440 MHz ($\sim$ 3.7%). The positions and lengths of coupling slots are major factors to decide the bandwidths of these filters.

The simulation results of duplexer are shown in Fig. 4–Fig. 6. Fig. 4 shows the insertion loss of the duplexer for two channels BPFs. The first channel exhibits an insertion loss $<$ 2.39 dB, and a bandwidth of about 440 MHz ($\sim$ 4.1%). The second channel exhibits an insertion loss $<$ 2.65 dB, and a bandwidth of about 440 MHz ($\sim$ 3.7%). Fig. 5 shows the return loss of the duplexer, and Fig. 6 shows the channel-to-channel isolation of the duplexer. The isolation is better than 51 dB across the first channel and better than 61 dB across the second channel.

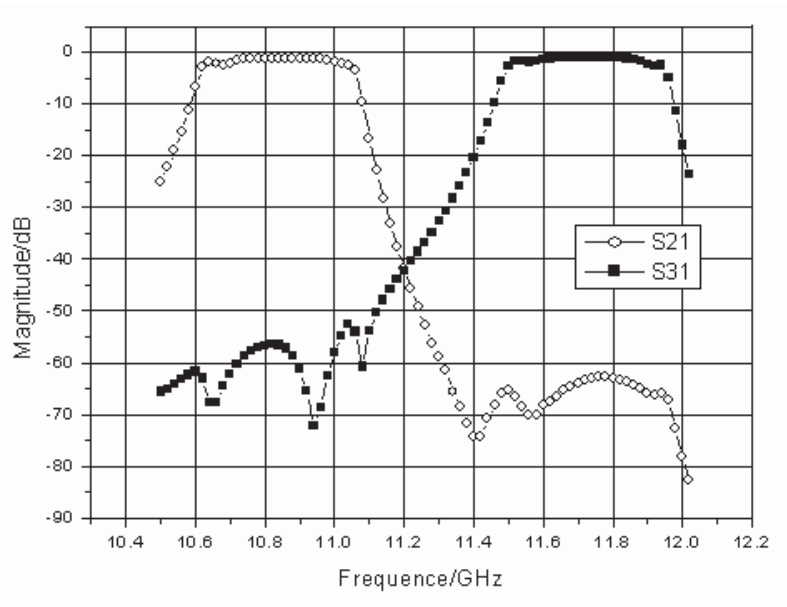

Figure 4: S_{21} and S_{31} transmission parameters of the duplexer.

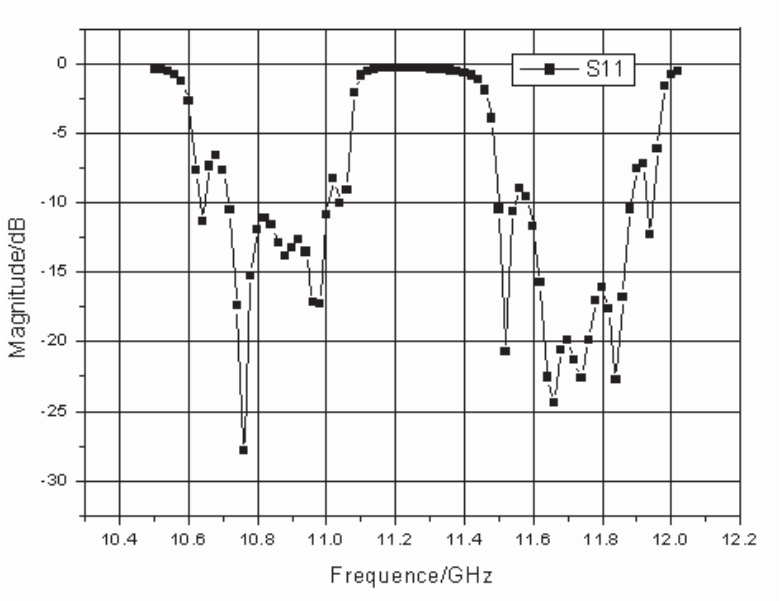

Figure 5: S_{11} parameter (common port) of the duplexer.

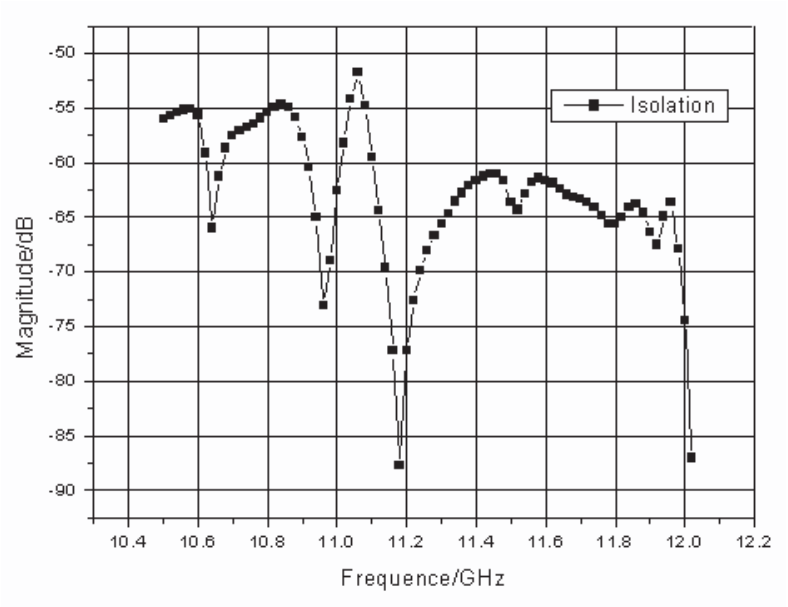

Figure 6: Isolation between two channels of the duplexer.

5. CONCLUSION

Advantages of this LTCC duplexer structure are low insertion loss, high isolation, very compact size and simple structure. It's suitable to be used in compact front end modules for microwave and millimeter-wave applications.

REFERENCES

1. Ruiz-Cruz, J. A., J. R. Montejo-Garai, J. M. Rebollar, and S. Sobrino, "Compact full ku-band triplexer with improved E-plane power divider," *Progress In Electromagnetics Research*, PIER 86, 39–51, 2008.
2. Lee, J.-H., S. Pinel, N. Kidera, J. Laskar, and M. M. Tentzeris, "A V-band front-end with 3-D integrated cavity filters/duplexers and antenna in LTCC technologies," *IEEE Trans. Microw. Theory Tech.*, Vol. 54, No. 7, 2925–2936, Jul. 2006.
3. Rosine, V., D. Baillargeat, and S. Verdeyme, "Q band duplexer design based on LTCC technology," *Proceedings of the 36th European Microwave Conference*, 129–132, Sep. 2006.

4. Cassivi, Y., et al., "Low-cost and high-Q millimeter-wave resonator using substrate integrated waveguide technique," *Proceedings of the 32nd European Microwave Conference*, Milan, Italy, Sep. 2002.
5. Potelon, B., J. C. Bohorquez, J. F. Favennec, C. Quendo, E. Rius, and C. Person, "Design of Ku-band filter based on substrateintegrated circular cavities (SICCs)," *IEEE MTT-S International Microwave Symposium Digest*, 1237–1240, Jun. 2006.
6. Pozar, D. M., *Microwave Engineering*, 2nd Edition, Wiley, New York, 1998.

The Solution and Simulation for the Stability of Active Receiving Antennas

Jing Li, **Lei Xing**, **Qian Xu**, **Jun Ding**, **and Chenjiang Guo**
School of Electronic and Information, Northwestern Polytechnical University, Xi'an 710129, China

Abstract— The stability of active receiving antenna is analyzed in this paper. The microstrip antenna with fast changing input impedance will lead to the instability of low noise amplifier (LNA) easily. By analyzing the S-parameters of amplifier and 3 dB Lange coupler, the stability condition of the balanced amplifier is derived. The results validate that the instability problem of the active receiving antenna can be solved by balanced amplifier efficiently. Finally, an active receiving patch antenna with Lange coupler and high mobility transistor FHX35LG is designed. The simulation results are obtained by ADS simulation software of Agilent Company. Compared with antenna without Lange coupler, the optimized antenna works in unconditional stability situation and the stability of active receiving antenna is improved greatly. (Stability factor is always greater than 1 in working frequency band).

1. INTRODUCTION

In recent years, the active antennas constitute a growing area of research [1]. By directly integrating active devices into antenna elements, feed line losses can be significantly reduced. Further advantages include size and weight reductions, enhanced reliability, and lower manufacturing costs [2]. Traditionally, antennas and low noise amplifier (LNA) integrated to be the receiving front-end. Usually, the bipolar junction transistor (BJT) and the high electron mobility transistors (HEMT) can be used to design LNA. The BJT are often preferred over HEMT at frequencies below 2–4 GHz because of higher gain and lower cost, but their noise figure is not as good as that of HEMT. The noise theory shows that the noise performance of the first stage is usually the most critical. In this way, we can see that LNA plays a very important role in noise performance of the whole receiving system. Thereby HEMT with lower noise figure can be chosen to design LNA. However potentially unstable of them exists when the input or output impedance change quickly at a lower frequency [3]. So how can the HEMT working stably at a low frequency become the key point of the active receiving antennas.

This paper describes a conjunction of the design processes for a microstrip antenna and balanced LNA constituted by Lange coupler and HEMT. Though theoretical analysis and derivation, this active receiving antenna works in unconditional stability. Finally, the simulation results are obtained by ADS simulation software of Agilent Company and show that the active receiving antenna is available.

2. ANALYSIS FOR STABILITY OF AMPLIFIER

Active receiving antenna is composed of microstrip antenna and LNA, so the stability of the active antenna depends on the stability of the LNA. In the LNA system of Fig. 1, oscillation is possible if either the input or output port impedance has a negative real part, which means $|\Gamma_{\text{in}}| > 1$ or $|\Gamma_{\text{out}}| > 1$. The network is unconditionally stable if $|\Gamma_{\text{in}}| < 1$ and $|\Gamma_{\text{out}}| < 1$ for all passive source and load impedances.

Some simpler tests can be used to determine unconditional stability. One of these is the $K - \Delta$ test [4], where it can be shown that a device will be unconditionally stable if Rollet's condition, defined as

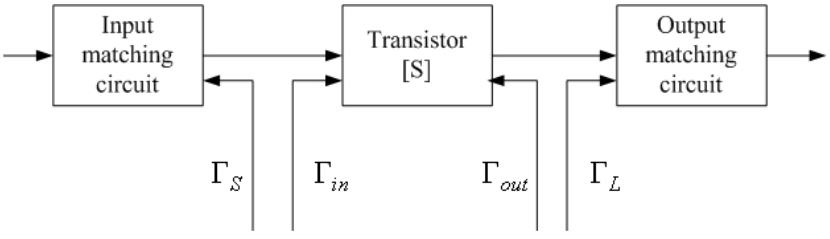

Figure 1: Block diagram of LNA with impedance matching.

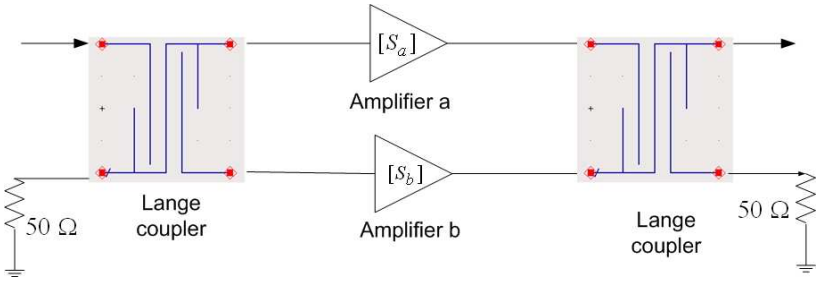

Figure 2: Balanced LNA with Lange coupler and two identical amplifiers.

$$K = \frac{1 - |S_{11}|^2 - |S_{22}|^2 + |\Delta|^2}{2\,|S_{12}S_{21}|} > 1 \tag{1}$$

along with the auxiliary condition that

$$|\Delta| = |S_{11}S_{22} - S_{12}S_{21}| < 1 \tag{2}$$

are simultaneously satisfied.

The basic circuit of a balanced LNA is shown in Fig. 2. The stability of the amplifiers has improved by using two Lange couplers to cancel input and output reflections from two identical amplifiers.

The relationship of S parameter between the every amplifier and the whole circuit is given by:

$$S_{11} = \frac{e^{-j\pi}}{2}(S_{11a} - S_{11b}) \tag{3}$$

$$S_{21} = \frac{e^{j\pi/2}}{2}(S_{21a} + S_{21b}) \tag{4}$$

$$S_{12} = \frac{e^{j\pi/2}}{2}(S_{12a} + S_{12b}) \tag{5}$$

$$S_{22} = \frac{e^{-j\pi}}{2}(S_{22a} - S_{22b}) \tag{6}$$

Because two amplifiers are identical, we get $S_{11} = S_{22} = 0$ and $|S_{12}S_{21}| = |S_{12a}S_{21a}|$. The $K-\Delta$ test (1), (2) can be written as:

$$K = \frac{1 + |S_{21a}S_{12a}|^2}{2|S_{21a}S_{12a}|}; \quad |\Delta| = |S_{12a}S_{21a}| \tag{7}$$

There is a condition of $|S_{12a}S_{21a}| < 1$ to most transistor amplifiers. So we can easily conclude $K > 1$ and $\Delta < 1$, which show that balanced LNA will meet the requirements of the unconditional stability when two LNAs are totally same. Hence the impedance of microstrip antenna changing greatly with the frequency has no influence on stability of the active receiving antenna system.

3. SIMULATION OF ACTIVE RECEIVING ANTENNA

We usually use an approach to matching the microstrip antenna to the LNA with the objective of minimizing the noise figure over the frequency range of interest while maintaining a useful overall gain [5]. In this paper, active receiving antenna works at the frequency of 2.4 GHz. In order to integrate conveniently, the design of microstrip antenna, Lange coupler and LNA should be on the same dielectric substrates. We choose FR4 substrate which thickness $h = 0.8$ mm, dielectric constant $\varepsilon_r = 4.4$.

3.1. Receiving Antenna Design

Because active antenna has small volume and can be easily integrated with other integrated circuit, the microstrip antenna is perfectly suitable for the front-end. Usually inset fed microstrip antenna can be used to produce perfect impedance matching [6] in Fig. 3.

In Fig. 3 we can conclude that the input impedance of the microstrip antenna is about 50 Ω at the resonant frequency. However, the input impedance changing greatly will cause the amplifier oscillate and make the instability of the system at the near resonant frequency.

3.2. LNA Design

Designing LNA are concerned more about its noise figure together with S parameter, bandwidth, gain and other performance index. Compared with other transistors, we choose FHX35LG HEMT

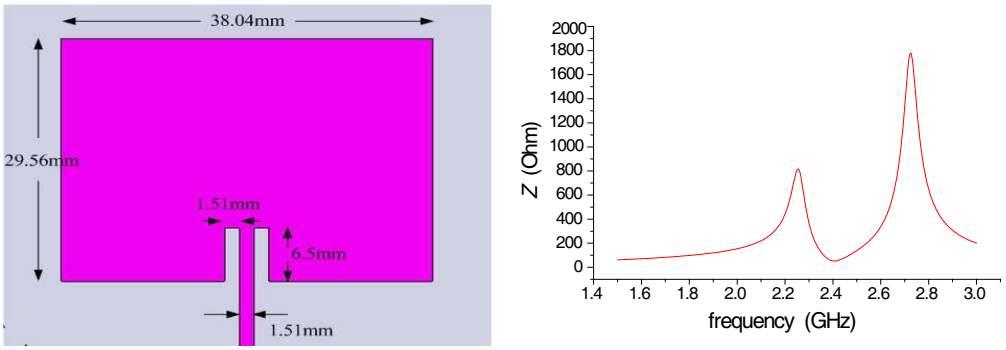

Figure 3: Inset fed microstrip antenna and the curve of input impedance with frequency.

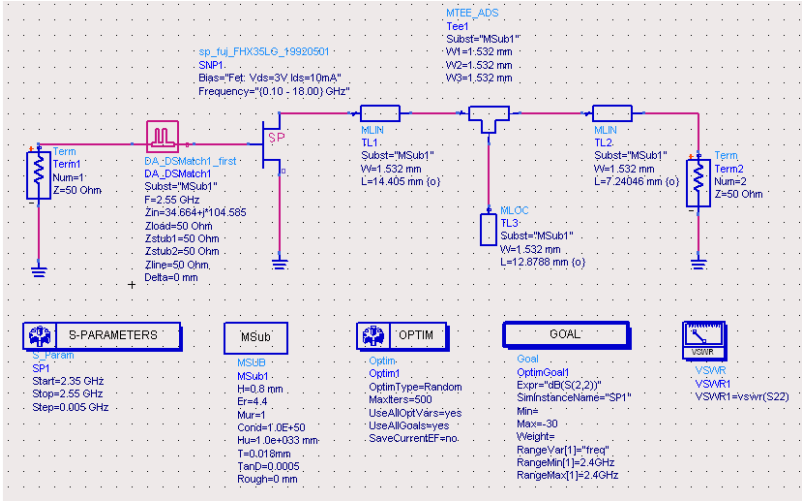

Figure 4: The LNA with the matching network of maximizing gain and minimizing noise figure.

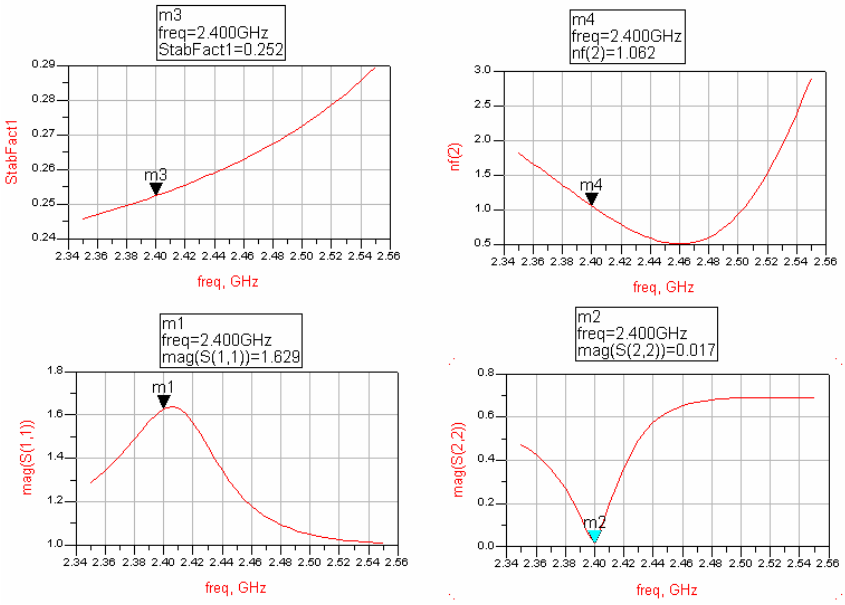

Figure 5: The curve of stability factor, noise figure, S_{11}, S_{22} of LNA simulated by Agilent ADS.

transistor with a much lower noise figure produced by Fujitsu corporation. In order to minimize the noise figure of the active antenna, the primary design objective is to transform the antenna impedance so that the antenna presents an input impedance to the LNA corresponding to the so called "optimum noise impedance". The output impedance of LNA can be matched to 50 Ω microstrip line. The circuit is shown in Fig. 4.

From the Fig. 5 we can see the LNA with FHX35LG maintains a better noise figure, however, the stability factor is less than 1 in the whole working frequency, which indicates that the amplifier work at potentially unstable region. Obviously $|\Gamma_{\text{in}}| > 1$ ($\Gamma_{\text{in}} = S_{11}$) at the working frequency, so the LNA work at instable range.

Two Lange couplers can be add to the input and output ports of the LNA, which can be component of balanced LNA as shown in Fig. 6. In the balanced LNA, Lange coupler's isolation is no more than −24 dB, input and output voltage standing wave radio (VSWR) is less than 1.5, coupling is equal to 3 dB.

From the Fig. 7 we can see that the stability coefficient of balanced LNA is always more than 1 and $|\Gamma_{\text{in}}| < 1$ ($\Gamma_{\text{in}} = S_{11}$) meanwhile the noise figure and Γ_{out} ($\Gamma_{\text{out}} = S_{22}$) are nearly unchanged at the working frequency range. The balanced LNA works stably unconditionally, which won't be affected by the fast changing impedance of the microstrip antenna with frequency.

Finally, the S parameter of antenna is imported into Agilent ADS to obtain final results.

The result in Fig. 8 suggests that system gain and bandwidth both get a well performance. The

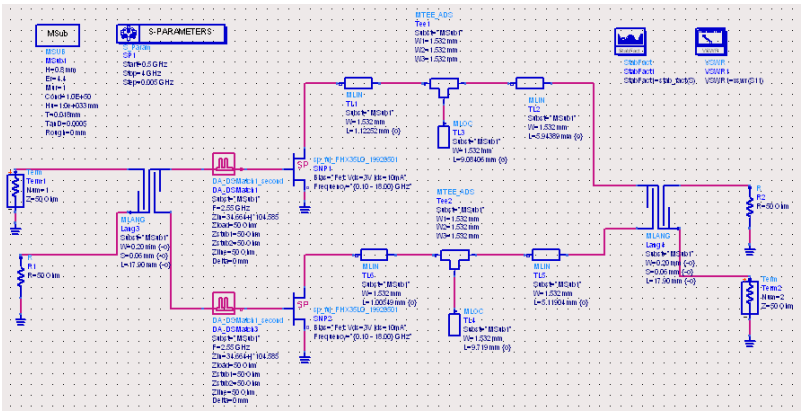

Figure 6: Balanced LNA with lange coupler.

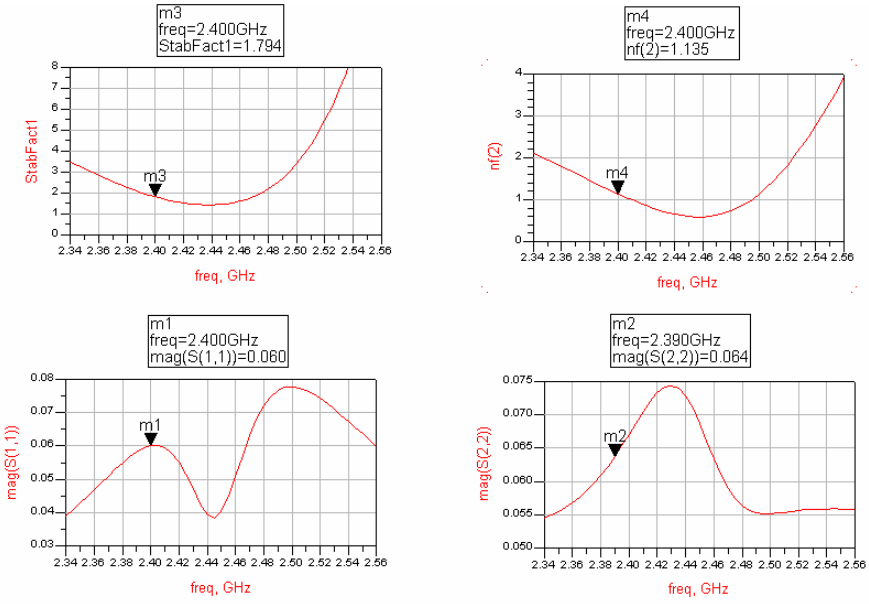

Figure 7: The curve of stability factor, noise figure, S_{11}, S_{22} of balanced LNA simulated by Agilent ADS.

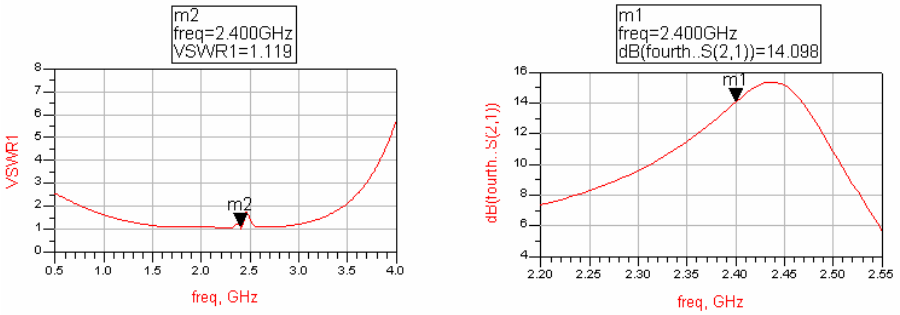

Figure 8: The curve of VSWR and system gain of the active receiving antenna.

active receiving antenna can be a good choice as the first stage of receiver.

4. CONCLUSIONS

In this paper, the instability of active receiving antenna consisted of HEMT transistor is analyzed. The Lange coupler together with LNA forming a balanced LNA is proposed. Theoretical derivation validate that active receiving antenna with balanced LNA can work in unconditional stability situation. (Stability factor is always greater than 1 in working frequency band). The simulation results are obtained by ADS simulation software of Agilent Company which verify the antenna can work in stable situation as well as achieve maximizing gain, bandwidth and minimizing noise figure. This paper only focus on the analysis of active receiver antenna stability, some other system performance of the active receiving antenna such as beam pattern, gain flatness are not discussed in detail.

ACKNOWLEDGMENT

This work is supported by graduate starting seed fund of Northwestern Polytechnical University.

REFERENCES

1. Chang, K., R. A. York, P. S. Hall, and T. Itoh, "Active integrated antennas," *IEEE Trans. Microw. Theory Tech.*, Vol. 50, No. 3, 937–944, Mar. 2002
2. Qian, Y. and T. Itoh, "Progress in active integrated antennas and their applications," *IEEE Trans. Microwave Theory*, Vol. 46, 1891–1900, Nov. 1998
3. Gonzalez, G., *Microwave Transistor Amplifiers: Analysis and Design*, 2nd Edition, Prentice Hall, Aug. 30, 1996.
4. Pozar, D. M., *Microwave Engineering*, House of Electronics Industry, Beijing, 2008.
5. Parfitt, A. and L. Milner, "The design of active receiving antennas for broadband low-noise operation," *CSIRO*.
6. Ramesh, M. and K. B. Yip, "Design formula for inset fed microstrip patch antenna," *Journal of Microwaves and Optoelectronics*, Vol. 3, No. 3, Dec. 2003.

Improved Design of a Compact Ultra-wideband Microwave Bandpass Filter Using a EBG Structure

Haiyan Chen, **Haipeng Lu**, **and Longjiang Deng**
State Key Laboratory of Electronic Thin Film Integrated Device
University of Electronic Science and Technology of China, Chengdu 610054, China

Abstract— A compact ultra-wideband microwave bandpass filter (BPF) is presented using a electromagnetic band-gap (EBG) structure for the microwave application. As a EBG structure, two linear arrays of metallic vias are used to generate shunt inductors, and the first two resonators with SIR structure are coupling to create a ultra-wide passband exceeding 87% at its center frequency of 3.76 GHz. Its characteristics are analyzed in terms of transmission line mode to exhibit the prosperities of ultra-wideband passband.

1. INTRODUCTION

High selectivity, low-cost, low insertion loss (IL), compact wideband bandpass filters for modern wireless communication systems have attracted much attention in recent years. Various wideband bandpass filters have been developed [1, 2]. Such filters are realized usually by parallel-coupled microstrip lines, and this requires smaller coupling gaps in order to enhance the coupling for wider bandwidths. Certainly, using existing parallel coupled microstrip techniques, filters with large FBW could be designed in principle [3]. However, filters with FBW $\geq 80\%$ that required enhance coupling have been difficult to realize because of the coupling between the resonators and limitation of the wet chemical-etching process. Therefore, the requirement for ultra-wideband applications has been deemed unachievable with conventional parallel coupling techniques, and the demand for large FBW applications has not been realized with coplanar waveguide (CPW). Stepped impedance resonators (SIR) have many attractive features and can be used in mobile communication, satellite communication, and other wireless communication systems. The main superiorities of the resonators lie in their compact size, easy fabrication, and low radiation loss. However, their bandwidths are usually not too wide.

In this paper, a planar bandpass filter with ultra-wideband large FBW is presented. Compact stepped impedance resonators are use to establish appropriate electromagnetic coupling among the resonators at the desired frequency. Metallic vias with EBG properties are incorporated in this stepped impedance resonators structure. The designed filter has a wideband, large FBW feature besides small size, easy fabrication, and low insertion loss. The proposed bandpass filter demonstrates an excellent properties, which are more than 87% fractional bandwidth (-3 dB bandwidth) at the center frequency 3.76 GHz and sharper rejection stopband at the lower passband edge, and low insertion loss at the passband range. The total circuit size is not more than $30 \times 3.2\,\mathrm{mm}^2$, which is a compact filter.

2. THEORY

In this section, the conditions of fundamental resonance of the SIR are discussed. The resonator structure to be considered here is shown in Fig. 1. The SIR structure is symmetrical and is composed of two coplanar microstrip lines with different characteristic impedances Z_1 and Z_2, or admittance Y_1 and Y_2 [4].

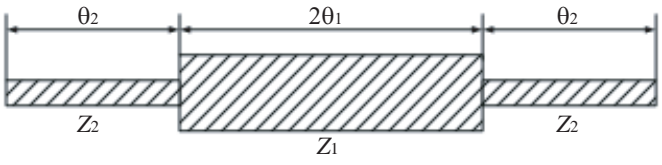

Figure 1: Structure of the SIR.

The admittance of the resonator from the open end, Y_i is given as:

$$Y_i = j\frac{1}{z_2} \cdot \frac{2\left(k\tan\theta_1 + \tan\theta_2\right) \cdot \left(k - \tan\theta_1 \tan\theta_2\right)}{k\left(1-\tan^2\theta_1\right)\left(1-\tan^2\theta_2\right) - 2\left(1+k^2\right)\tan\theta_1\tan\theta_2} \tag{1}$$

where k = impedance ratio = Z_2/Z_1, θ_1, θ_2, respectively, is electrical length of the coplanar microstrip line L_1 and L_2. The resonance condition can be obtained from the following:

$$Y_i = 0 \tag{2}$$

From (1) and (2), we can achieve the fundamental resonance condition:

$$k = \tan\theta_1 \tan\theta_2 \tag{3}$$

θ_T is defined as the electrical length of the SIR, $\theta_T = 2(\theta_1 + \theta_2)$. Then, the relationship between θ_T and θ_1 is gained from the (3) as:

$$\tan\frac{\theta_T}{2} = \frac{1}{1-k} \cdot \left(\frac{k}{\tan\theta_1} + \tan\theta_1\right) \quad (k \neq 1) \tag{4}$$

$$\theta_T = \pi \quad (k = 1) \tag{5}$$

As θ_1 is invariability, it is evident from (4) that the electrical length of the SIR θ_T has minimum value when $0 < k < 1$ and maximum value when $k > 1$. When $k = 1$, this corresponds to a uniform impedance line resonance. Similarly, as k is confirmed, the electrical length of the SIR θ_T has minimum or maximum value when θ_1 is variable.

Considering (1) and (2), we easily gain that the spurious response frequency or the corresponding is the function of the impedance ratio K. So we can draw a conclusion that the spurious response can be controlled by the impedance ratio K, and this is one of the special features of the SIR.

3. DESIGN

The proposed ultra-wideband bandpass filter is composed of hybrid microstrip and compact stepped impedance resonators with metallic vias and bottom CPW open-circuited/short-circuited resonators. The complete three-dimensional geometry structure of the BPF was given in Fig. 2 whereas the layout and geometry parameter definition of the top microstrip components and the bottom CPW element were demonstrated on Fig. 2(a) and Fig. 2(b) respectively. The microstrip cell of the structure consists of a series capacitor and the coupling stub inductors connected to the microstrip patch of two linear arrays of metallic vias. Considering that the extend bandwidths of the BPF required a more complicated arrangement, and in order to tune to bandwidths of the BPF, we prompt the microstrip structure of the ultra-wideband bandpass filter which is inserted by the metallic vias with EBG characteristic. Certainly, the insertion loss in the structure with metallic vias is much smaller than that in the structure without metallic vias. Moreover, the structure with metallic vias is difficult to be fabricated using the conventional printed circuit board technology when the vial diameter is too small. We remark that a good balance has been achieved between the vial diameter and the distance between two vias, which yields super-wide passbands.

We performed computer simulations using the commercial finite element method (FEM) solver HFSS version 10. The microstrip/CPW depicted in Fig. 2 were modeled as lossy copper with a conductivity of $\sigma = 5.80 \times 107\,\mathrm{S/m}$. The substrate was modeled as the RT/Duorid5880 with a dielectric constant of 2.2, a loss tangent of 0.009, and a thickness of 0.6 mm. After determining the approximate size of the unit by theoretically calculation, we will investigate the scattering or S parameters of the unit, that is to say, transmission coefficients (S_{21}) and reflection coefficients (S_{11}) of the unit. Based on the theory that was narrated in Section 2, inserted the structure with metallic vias for the sake of tunable properties of the bandwidths and the center frequency, the dimensions of designed ultra-wideband BPF can be obtained, as shown in the following: Microstrip input/output transmission lines width $w_1 = 0.2\,\mathrm{mm}$, the length of input/output transmission lines $L_1 = 12.4\,\mathrm{mm}$, CPW open-end-coupled gap $g_1 = 0.24\,\mathrm{mm}$, the width of CPW open–end-coupled transmission line $w_2 = 0.2\,\mathrm{mm}$, the length of CPW open-end-coupled transmission line $L_2 = 8.8\,\mathrm{mm}$, the width of microstrip main transmission line $w_3 = 3.2$, the length of microstrip main transmission line $L_3 = 17.2\,\mathrm{mm}$, and other parameters $g = 0.2\,\mathrm{mm}$, $w_4 = 2.8\,\mathrm{mm}$, $w_5 = 0.48\,\mathrm{mm}$, $L_4 = 16.8\,\mathrm{mm}$, $L_5 = 12.2\,\mathrm{mm}$. While performing the simulation, we must simultaneously consider the minimum

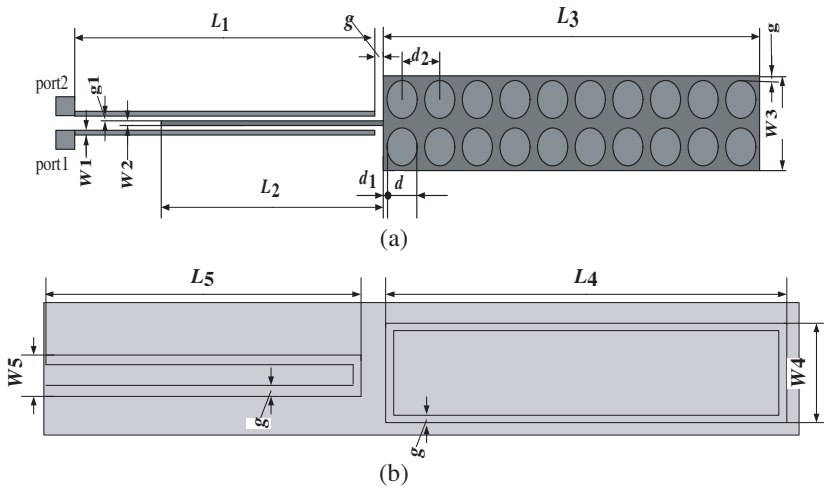

Figure 2: Layout and parameters definition for the proposed filter. (a) Top view (microstrip) and (b) bottom view (CPW).

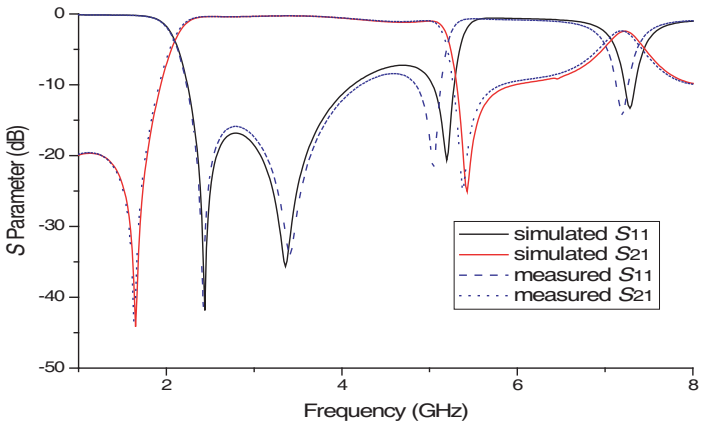

Figure 3: Simulated and measured S-magnitudes of the proposed filter.

line widths available to us and other various fabrication tolerances. We showed the results of lossless full-wave simulation and measurements for the reflection coefficient (S_{11}) and curves and the transmission coefficient (S_{21}) curves of designed ultra-wideband BPF, as shown Fig. 3.

Just as the results in Fig. 3, the frequency responses of the proposed BPF have shown good electrical performances. In the first, the presented BPF shows a ultra-wideband bandpass characteristics, whose FBW of -3 dB achieves 87% at the central frequency $f_c = 3.76$ GHz. In the second, the return loss of the designed BPF is greater than 8 dB over the whole passband range. In the third, there is several finite-frequency transmission zeros closer to each side of the passband edges. Moreover, the insertion loss of the proposed BPF exists no more than 1 dB over the whole passband range.

4. CONCLUSION

In summary, an ultra-wideband microwave bandpass filter with EBG structure has been designed and fabricated. The whole size of the designed BPF is 28 mm $\times$ 3.2 mm, which is more compact and larger bandwidth ratio in comparison of the previous works [5, 6]. The proposed BPF exhibits good electrical performances, such as more than 87% FBW (-3 dB bandwidth) at the center frequency, deep and wide stop-band property at the higher passband edge, sharp rejection slop at the lower passband edge, and deep return loss over the whole passband range. Moreover, the bandwidth of the proposed BPF may be adjusted expediently because of the tunable metallic vias with EBG properties. Therefore, the proposed BPF can be used to ultra-wideband radio frequency system.

REFERENCES

1. Chen, H. and Y.-X. Zhang, "A novel microstrip UWB bandpass filter with CPW resonators," *Microwave and Optical Technology Letters*, Vol. 51, No. 1, 24–26, January 2009.
2. Tang, C.-W. and M.-G. Chen, "A microstrip ultra-wideband bandpass filter with cascaded broadband bandpass and bandstop filters," *IEEE Transactions on Microwave Theory and Techniques*, Vol. 55, No. 11, 2412–2418, November 2007.
3. Hong, J.-S. and M. J. Lancaster, *Microstrip Filters for RF/Microwave Applications*, A Wiley-Interscience Publication, New York, 2001.
4. Makimoto, M. and S. Yamashita, "Bandpass filters using parallel coupled stripline stepped impedance resonators," *IEEE Transactions on Microwave Theory and Techniques*, Vol. 28, No. 12, 1413–1417, December 1980.
5. Chang, Y.-C., C.-H. Kao, and M.-H. Weng, "A compact wideband bandpass filter using single asymmetric SIR with low loss and high selectivity," *Microwave and Optical Technology Letters*, Vol. 51, No. 1, 242–244, January 2009.
6. Chiou, Y.-C., J.-T. Kuo, and E. Cheng, "Broadband quasi-Chebyshev bandpass filters with multimode stepped-impedance resonators (SIRs)," *IEEE Transactions on Microwave Theory and Techniques*, Vol. 54, No. 8, 3352–3358, August 2006.

Tuned Periodical Structures in THz Band Applied in Safety Applications

Pavel Fiala, **Radim Kadlec**, **and Petr Drexler**
Brno, FEEC BUT, UTEE, Kolejní 2906/4, Brno 612 00, Czech Republic

Abstract— The paper provides an insight into the issues of integration and application of non-lethal weapons and devices in the field of protection against special-type weapons. From the formal point of view, several perspectives are utilized to facilitate the topic analysis, and these aspects of evaluation can be identified within the regions of legal ethics, medicine, or military tactics as well as engineering and technology. In relation to the problem of protection against undesirable phenomena like terrorism, it is necessary to mention the fact that there exists long-term research focused on the institution of NATO and its member armies; this research mainly pertains to the determination and practical use of non-lethal or wounding methods and means in all constituent parts of protection and defence. The armies of European countries participate systematically in the process of non-lethal weapons development and integration within the respective armament systems. Significantly, one of the problems related to this broader issue consists in the elimination of snipers in the course of armed conflicts.

1. INTRODUCTION

Since 2001 discussions have been in full progress concerning legal adaptation to the newly emerged conditions or needs of finding methods and means that provide constrictive wounding effects [1]. Importantly, there have emerged several focus areas within the field. Firstly, let us turn our attention in this respect to legal conditions and ethics, where the problem is analyzed not only with a view to the question of how and when non-lethal weapons should be applied, but also from the perspective of the existing structures and regulations of international law as well as national legal systems. It is also important to note within this context that higher-order social functions have been taken into account, for example the maintenance of rights of individuals. In addition to this aspect, the overall discussion has involved the problem of an individual transgressing legal norms [2]. In the field of the operational-tactical outlook and tactical approaches to applying different classes of weapons, means and methods, the solution proposed in source [3] is of significant interest. Currently, psychological training or training conducted by a psychologist is being proven beneficial for various purposes in the province of tactics, where it has provided very good results. Yet, with a certain degree of contrast, the use of lethal means or methods can yield successful unravelling of local conflicts without causing major injuries to humans.

In the medicine-related sections of wounding effects and means evaluation [4, 5], methodology has been developed to evaluate the concrete effects on individual parts of the human body [6]. The ultimate province to be mentioned is the technical-technological field, where the potential and known physical principles are utilized to facilitate the designing of the means and principles of non-lethal effects.

One of the problematic aspects of various armed conflicts consists in the issue of snipers and their timely detection by protective forces. For this reason, full priority within the investigation into the problem of sniper position detection has been given to locating the sniper before the first shot; for the same reason, too, the applications of image recognition methods [11, 12] have emerged in the field of military tactics. Naturally, these methods are also utilized for several other purposes. Fig. 1 shows, according to [11], the analysis of the process of utilization of degrees of means and the application of image recognition as a sensor for the input evaluation of situation in the intervention process. Another sophisticated semiautomated system of intervention controlling consists in the procedure of identifying the physical characteristics of crowd behaviour [12] and, based on the evaluation of energy and behaviour of the crowd elements, the introduction of intervention with respect to the problem in the task. The task can be, for instance, loss minimization or the rapidity of crowd expansion inhibition. An example of the evaluation of necessary elements of image is shown in Fig. 2; here, the sources of crowd dynamics are found to provide the basis for evaluation of the crowd energy and for the identification of essential instruments to facilitate the ultimate controlling of the crowd, introduction of intervention, and intervention location recognition.

According to article [13], one of the options of sniper identification consists in the scanning of the required sector and the retrieval of the point that shows the corresponding optical characteristics.

Other ways of solution can be found in the process of further investigation from the perspective of physics into the problem of snipers and their identification.

2. TARGET CHARACTERISTICS WITH RESPECT TO THE ELECTROMAGNETIC FIELD

The electromagnetic field enables us to see the problem from a different perspective. In an analysis of the sniper location task we may assume that the identification of the sniper will only be possible in the ex post mode after a single gunshot. In this respect, it is necessary to note that the sniper's activity is very precise in distances above the range of 50 m and that, after the shooting action, the sniper will not show elements of movement that can be easily discernible or identified. Then, it is possible to focus from the perspective of physics on the characteristics of the target. With respect to the instruments or means of the sniper, the target can show different characteristics; thus, for example, in certain physical conditions the target does not have to be clearly visible or can be

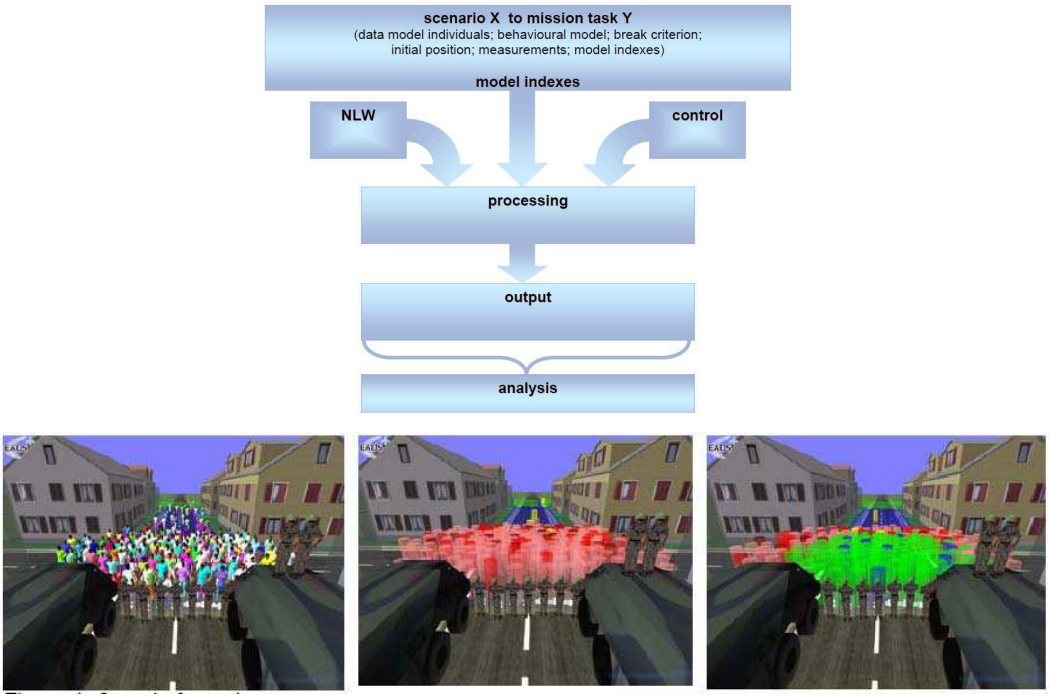

Figure 1: The procedure applied in the decision process concerning the utilization and deployment of instruments (means) based on input data and situation characteristics.

Figure 2: The evaluation of a crowd dynamics model based on image processing.

Figure 3: The evaluation of image with respect to the optical characteristics of the human eye retina.

visible in the light spectrum of white light with the wavelength of $\lambda \in \langle 400\,\mathrm{nm}, 700\,\mathrm{nm}\rangle$. Another possible solution consists in the situation when the image of the target from the observer-sniper shows, in the defined light spectrum, a position different from reality. Thus, there will not occur any fatal consequences in the absence of timely identification of the sniper position and, thanks to the fact, partial defensive actions to save the target will be made possible.

3. THE REFLECTION AND REFRACTION OF ELECTROMAGNETIC WAVES

In the DTEEE laboratories, an algorithm was derived and set up for the refraction and reflection of EMG wave on the interface by the help of the refraction coefficient the permeance coefficient. The algorithm was tested using the Matlab program, and an analysis of the issue was provided in [14]. The program generates a matrix of beams which propagate from the source. Intersections of the beams and objects in the model are evaluated and a new direction is determined of the reflected and the permeating beams. The program has been designed to facilitate the analysis and evaluation of any quantity of reflected beams. The number of reflections of each beam markedly increases the time exigence factor of the analysis. The reflections and permeation are solved on the basis of laws concerning electromagnetic waves. The reflection and permeation of a simple interface between two instances of the EMG wave environment is indicated in Fig. 4. It follows from the derivation of Snell's law [15, 16] that, for the calculation of refraction angle, there holds the equation

$$\frac{\sin\theta_0}{\sin\theta_2} = \frac{k_2}{k_1}, \tag{1}$$

where k is the wave number with the wave propagation data, and its shape is:

$$k = \sqrt{-j\omega\mu \cdot (\gamma + j\omega\varepsilon)}, \tag{2}$$

where ε is the environment permittivity, μ is the environment permeability, and γ the environment conductivity. Relation (1) is formulated only for the interface between two dielectrics which are not subject to the occurence of total reflection. In general, k_1 and k_2 are complex, and then also angle θ_2 is complex. The propagation of light as an electromagnetic wave is understood as the propagation of the electric and the magnetic field intensity, the electric constituent of the incident constituent, according to Fig. 4. This can be written as:

$$E_i = E_0 e^{-jk_1 u_{n0}\cdot r}, \tag{3}$$

where E_0 is the electric field intensity amplitude in the location of the interfaceí, r is the position vector, and u_{n0} is the unit vector of the propagation direction.. The reflected beams intensity and the permeated beams intensity are evaluated as:

$$E_r = E_1 e^{-jk_1\, u_{n1}\cdot r}, \quad E_t = E_2 e^{-jk_2\, u_{n2}\cdot r}, \tag{4}$$

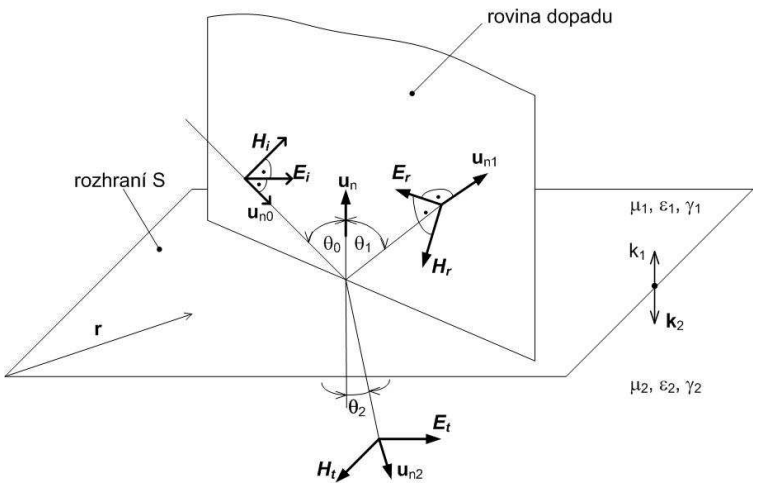

Figure 4: Reflection and refraction of a plane wave.

where E_1 is determined from the amplitude in the interface location and reflection coefficient $\underline{\rho}_E$, and $\underline{E}_2$ is determined from the amplitude in the location of the interface and transmission (permeation) factor $\underline{\tau}_E$.

The procedure is adjusted for a multilayer heterogeneous material (layers, metamateials structure). The EMG wave reflections from the heterogeneous material and its permeation are solved by the help of numerical methods. The multilayer environment is schematically indicated in Fig. 5. The algorithm only processes the reflection starting at the number of 10 layers. The reflection from n layers generates n of primary (only once reflected) EMG waves (in Fig. 6, an EMG wave impinges upon 5 layers and there are 5 reflected EMG waves on the surface), which reflect in a multilayer environment.

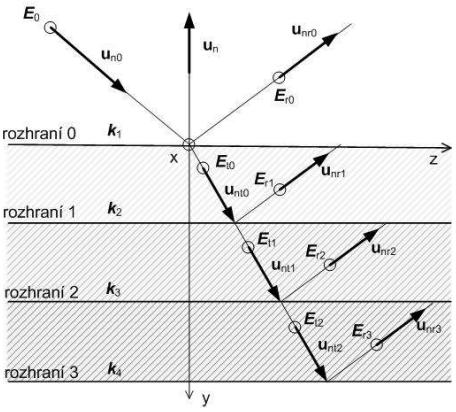

Figure 5: Multilayer environment of heterogeneous material.

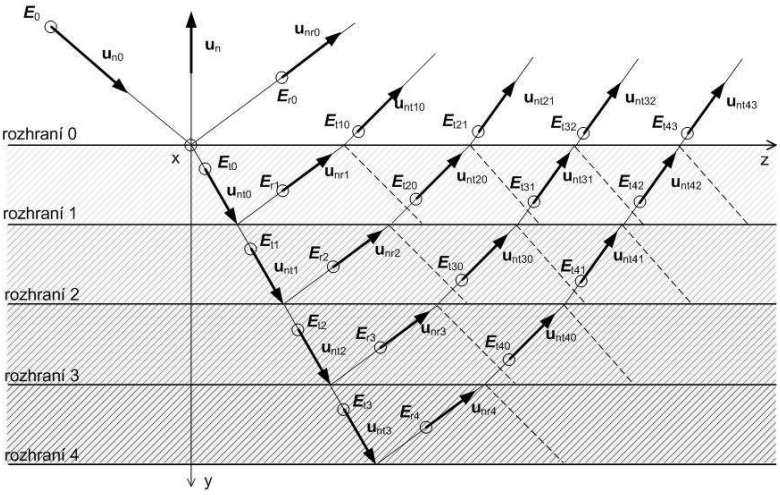

Figure 6: Waves on the surface of a heterogeneous material after the a reflection from several layers.

4. CONCLUSION

Both the basic and the applied types of research on optoelectronic systems and numerical modelling of wideband signals have led to conclusions in the field of multilayer and periodic structure optical materials.

The entire project was systematically guided by theoretical discussion and consideration, the results of modelling realized by the help of numerical models, and a large number of experiments. The main asset of the materialized work consists in the field of numerical modelling, in the proposed variants of models, and in the overall verification and calibration of the designed solutions using unique experiments. The activities have contributed significantly to the field of model design by proposing a combination of complementary yet different types of numerical models; these models then enabled marked acceleration of the calculation process while achieving and maintaining a satisfactory degree of accuracy. A valuable aspect consists in the methodology of a numerical model application and handling, where the correctness of the numerical analysis was verified by the experimental results.

ACKNOWLEDGMENT

The funding of the project was supported by the Ministry of Defence of the CR and Ministry of Industry and Trade of the CR (Diagnostics of superfast objects for safety testing, FR-TI1/368), Ministry of Education, Youth and Sports of the CR, and by insitutional resources from the Research Design — Electronic Communication Systems and New Generation Technologies (ELKOM) MSM0021630513, GAČR 102/09/0314.

REFERENCES

1. Krüger-Sprengel, F., "Legal adaptation of non-lethal capabilities in new conflict scenarious," *2nd European Symposium on Non-lethal Weapons*, Ettlingen, SRN, May 13–15, 2003.
2. Kim, B., "Between principles and absolutes: non-lethal weapons and the law of armed conflict," *2nd European Symposium on Non-lethal Weapons*, Ettlingen, SRN, May 13–15, 2003.

3. Janssen, W. J. H. and E. J. M. Jansen, "Decision-making processes: the choice between lethal an non-lethal force," *2nd European Symposium on Non-lethal Weapons*, Ettlingen, SRN, May 13–15, 2003.
4. David, E., "A effectiveness and risk during application of nlw from the medical point of view," *4th European Symposium on Non-lethal Weapons*, Ettlingen, SRN, May 10–12, 2005.
5. David, E., A. Fretz, J. Reissenweber, "Mortality following taser exposure," *4th European Symposium on Non-lethal Weapons*, Ettlingen, SRN, May 21–23, 2007.
6. Wolf, F., "Multi-spectral measurement of NLW effects," *4th European Symposium on Non-lethal Weapons*, Ettlingen, SRN, May 21–23, 2007.
7. Fiala, P., "Finite element method analysis of a magnetic field inside a microwave pulsed generator," *2nd European Symposium on Non-lethal Weapons*, Ettlingen, SRN, May 13–15, 2003.
8. Steinbauer, M., P. Drexler, and P. Fiala, "Measurement of vircator ultra-short solitary electromagnetic pulses," *3nd European Symposium on Non-lethal Weapons*, Ettlingen, SRN, May 10–12, 2005.
9. Fiala, P., M. Steinbauer, and R. Kubasek, "High power generator test, PGP-II," *4th European Symposium on Non-lethal Weapons*, Ettlingen, SRN, May 21–23, 2007.
10. Fiala, P. and P. Drexler, "Measurement methods of pulsed power generators," *4th European Symposium on Non-lethal Weapons*, Ettlingen, SRN, May 21–23, 2007.
11. Groll, J. H. and C. Pick, "Assessment of non-lethal-weapons (NLW)," *4th European Symposium on Non-lethal Weapons*, Ettlingen, SRN, May 21–23, 2007.
12. Kozyrev, V., V. V. Selivanov, V. V. Leonov, and A. A. Zverev, "Analysis of critical levels of physical effects on localized masses of people (CROWD)," *4th European Symposium on Non-lethal Weapons*, Ettlingen, SRN, May 21–23, 2007.
13. Langhans, D. and D. Meisterhans, "Sniper locating system," *2nd European Symposium on Non-lethal Weapons*, Ettlingen, SRN, May 13–15, 2003.
14. Kadlec, R., P. Fiala, and E. Kroutilová, "Improving of raytracing method for numerical modeling of lighting systems," *PIERS Proceedings*, 156–159, Beijing, China, March 23–27, 2009.
15. Dědek, L. and Dědková, *J. Elektromagnetismus*, 232, Students book, 2 vyd, Vutium, Brno, 2000.
16. Stratton, J. A., *Teorie Elektromagnetického Pole*, STNL, Praha, 1961.

The Application of a Novel Snake-like Gap Slanted DGS Structure in Microstrip Filter Design

Bin Dong, **Quanyuan Feng**, **and Lei Hou**
Institute of Microelectronics, Southwest Jiaotong University, Chengdu 610031, China

Abstract— By modifying the gap shape and dumbbell position of the traditional dumbbell DGS structure, more steep frequency characteristics and lower resonant frequency point were obtained, moreover, several decibels of attenuation can be obtained at the resonant frequency. At last the new DGS structure was introduced into design of microstrip filters, result shows good practicality and effectiveness.

1. INTRODUCTION

Microstrip filters have been widely used in modern microwave circuits designmilitaries and wireless communication fields. However, due to the cyclical frequency response of the transmission line, a second parasitic passband appears at a certain distance from the main center frequency passband, which makes against to the harmonic suppression. The electrical current distribution on the ground plane can be changed by etching certain shapes on the ground plane, and the characteristics of transmission line are consequently changed. Since 2000 when DGS structure is proposed by Korean professor Kim [1], variable DGS structures are brought forward and the design theory of microstrip filters with DGS structure is increasingly improved [2–7, 11]. The traditional dumbbell DGS unit is not suitable in the coupled microstrip filter design, the resonant frequency point and steep characteristic are supposed to be improved. This paper introduces a new snake-like gap slanted DGS structure, by modifying the gap shape and dumbbell position of the traditional dumbbell DGS structure, more steep frequency characteristics and lower resonant frequency point can be obtained.

2. DUMBBELL DGS STRUCTURE

The traditional dumbbell DGS structure is as follows in Fig. 1 [6], including two rectangle area and one gap line, looking like a dumbbell. Two rectangle area is generally regarded as inductance area and the gap capacitance area. In this structure, four variables a, b, g, w can be gained and its equivalent circuit is as Fig. 2. Influences of a and b to the whole structure is the same, so the inductance area is normally designed to be square in practice. Fig. 3 shows the transmission cave of dumbbell DGS structure(simulated in HFSS11).

In order to extract parameters of DGS equivalent circuits, 3-D EM platform is used to simulate the DGS structure to gain the transmission cave, then the resonant frequency f_0 and cutoff frequency f_C is achieved. Butterworth filter prototype circuit can be used to model the DGS equivalent circuit, then we get the inductance and capacitance of the equivalent circuit as follows [10]:

$$C = \frac{\omega_C}{Z_0 g_1} \frac{1}{\omega_0^2 - \omega_C^2} \tag{1}$$

$$L = \frac{1}{\omega_0^2 C} = \frac{1}{4\pi^2 f_0^2 C} \tag{2}$$

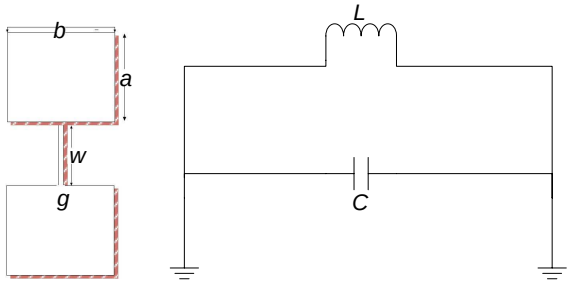

Figure 1: Dumbbell DGS and its equivalent circuit.

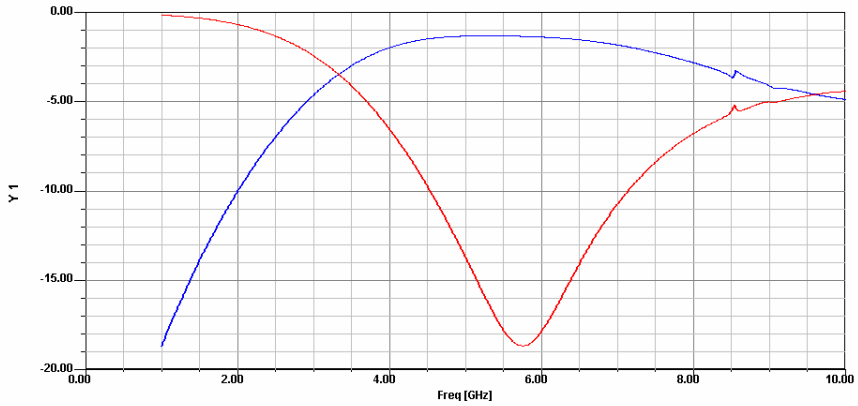

Figure 2: Transmission cave of dumbbell DGS structure ($a = b = 6.5\,\text{mm}$, $w = 2.84438\,\text{mm}$, $g = 0.5\,\text{mm}$).

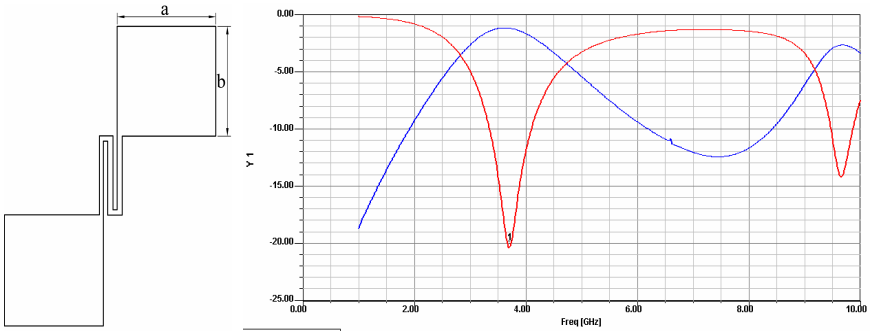

Figure 3: Snake-like gap slanted DGS and its transmission curve.

3. SNAKE-LIKE GAP SLANTED DGS STRUCTURE

By modifying the gap to be snake-like and dumbbell area to be slanted, the traditional dumbbell DGS structure's transmission characteristics can be improved [8]. Therebymore steep frequency characteristics and lower resonant frequency point were obtained by almost the same DGS area, as is shown in Fig. 3. Lower resonant frequency point makes the circuit size smaller, steeper frequency characteristics improves the stopband characteristics in microstrip filters.

Similar to traditional dumbbell DGS structure, the key factors to influence new structure include a, b, w, g and a new factor n, n represents the number of U-shape inflexions in the new DGS structure. Influence of variable n ($n = 0, 2, 4$) to the DGS structure is as the following Fig. 4:

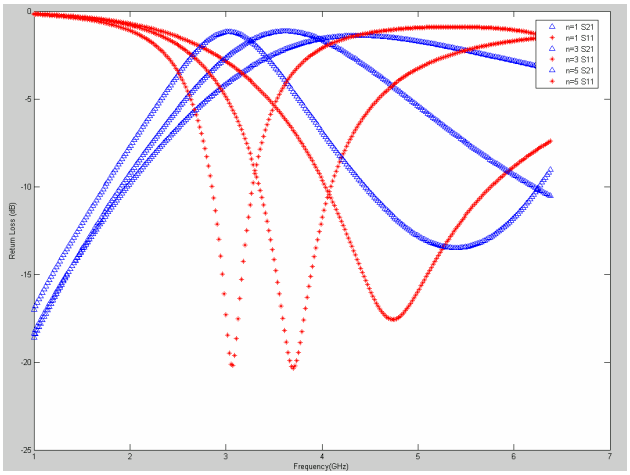

Figure 4: The influence of n to DGS unit.

Three resonant frequency points are 4.7 GHz, 3.8 GHz and 3 GHz. Therefore, by increasing the number of n, the resonant frequency becomes lower, this is because larger n means larger equivalent length of the gap. Moreover, steeper stopband characteristics and deeper attenuation at the resonant frequency point can be obtained.

4. APPLICATION OF THE NEW STRUCTURE TO MICROSTRIP FILTERS

The most important problem in parallel-coupled microstrip filter design is its velocity difference between even and odd mode phase, which is to cause cyclical responses, resulting in unwanted harmonic outputs at the terminal. The following Fig. 5 is a parallel-coupled microstrip filter working at 2 GHz [9, 10], using FR4 for its substrate medium:

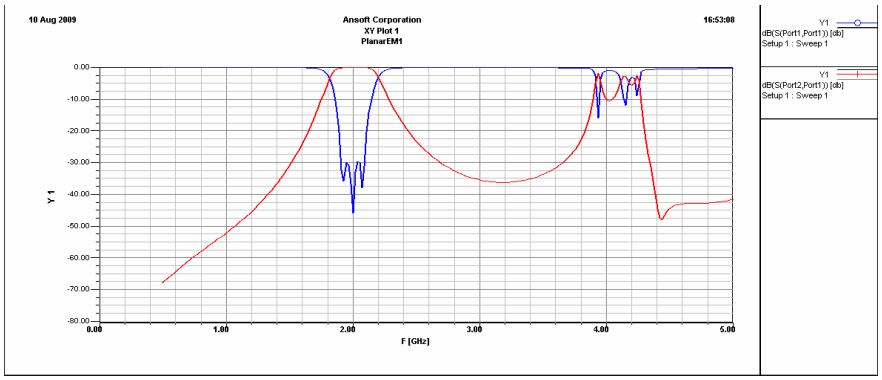

Figure 5: Transmission curve of parallel coupled microstrip filter.

Appearantly, there is a significant parasitic passband at twice the center frequency 4 GHz, the stopband attenuations on both sides of the center frequency are also not so good, reaching only -29 dB and -23 dB respectively.

In order to suppress this parasitic passband, four DGS cells are cascaded together to constitute a lowpass filter, allowing only the main passband frequency components to pass. The new filter with DGS structures used in both terminals of the filter is as shown below:

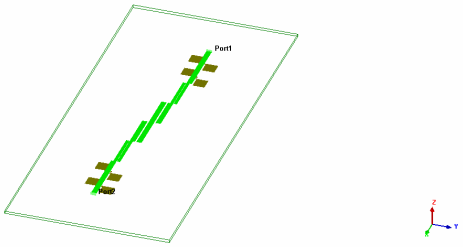

Figure 6: Cascade DGS applicated into microstrip filter.

The transmission characteristics of new filter is as follows:

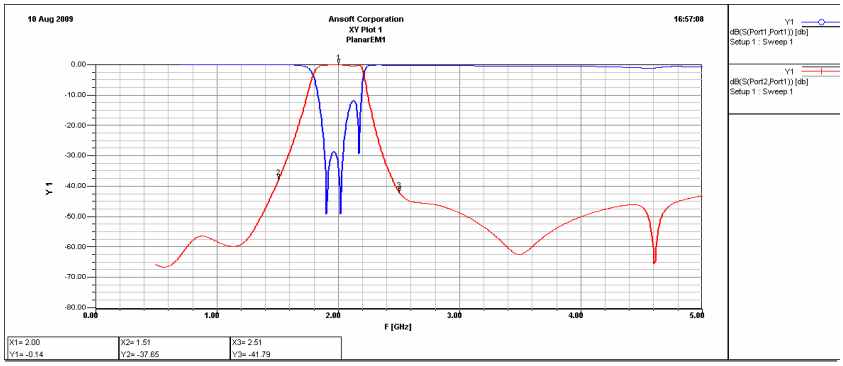

Figure 7: Transmission curve of microstrip filter with 4-order lowpass DGS structure.

It can be seen that, by adding new DGS structures, parallel-coupled filter succeeded in suppressing the harmonic response at 4 GHz, the attenuation achieves near −50 dB — a satisfying result. Meanwhile, the stopband characteristics become more steep outside 1.5 GHz and 2.5 GHz, attenuations decreased significantly to −38 dB and −42 dB respectively. Deficiencies of the filter is that the S_{11} curve performance of some part around the center passband has deteriorated which is because the introduction of DGS structure makes energy leak in the dielectric layer, this can be improved by factors such as the width of the microstrip line.

It is worth mentioning that, the two dumbbell-shaped inductor area adopt mutual slanted structure, so for the filters considering the coupling capacitance, this new DGS structure can be used to achieved the reduced size of the whole system.

5. CONCLUSIONS

This article analyzed the electromagnetic properties of DGS structure, presenting a snake-like slanted DGS structure, discussing the the impact of structural parameters to its transmission characteristics, by applying the new structure to microstrip filter design, the second harmonic response is suppressed significantly and the stopband became more steep, the new structure is expected to be more widely used in microwave field.

REFERENCES

1. Kim, C., et al., "A novel 2D periodic defected ground structure for planar circuits," *IEEE Microwave and Guided Wave Letters*, Vol. 10, No. 4, 131–133, 2000.
2. Boutejdar, A., et al., "A compact microstrip multilayer lowpass filter using triangle slots etched in the ground plane," *Proceedings of the 36th European Microwave Conference*, 271–274, 2006.
3. Boutejdar, A., et al., "Design of compact microstrip lowpass filters using a U shaped defected ground structure and compensated microstrip line," *Proceedings of the 36th European Microwave Conference*, 267–270, 2006.
4. Weng, T. S., et al., "Miniaturized microstrip lowpass filter with wide stopband using double equilateral U shaped defected ground structure," *IEEE Microwave and Wireless Components Letters*, Vol. 16, No. 5, 240–242, 2006.
5. Chen, J. X., et al., "Compact quasi-elliptic function filter based on defected ground structure," *IEE Proc. Microw. Antennas Propag.*, Vol. 153, No. 4, 320–324, 2006
6. Mandal, K. M. and S. Sanyal, "A novel defected ground structure for planar circuits," *IEEE Microwave and Wireless Components Letters*, Vol. 16, No. 2, 93–95, 2006.
7. Guha, D., et al., "Concentric ring shaped defected ground structures for microstrip app lications," *IEEE Antennas and Wireless Propagation Letters*, Vol. 5, 402–405, 2006.
8. Karshenas, F., A. R. Mallahzadeh, and J. Rashed-Mohassel, "Size reduction and harmonic suppression of parallel coupled-line bandpass filters using defected ground structure," *13th International Symposium on Antenna Technology and Applied Electromagnetics and the Canadian Radio Sciences Meeting*, 2009.
9. Cohn, S. B., "Parallel-coupled transmission-line_resonator filters," *IRE Transactions on Microwave Theory and Techniques*, Vol. 6, 223–231, April 1958.
10. Guan, X., G. Li, and Z. Ma, "Optimized design of a low-pass filter using defected ground structures," *APMC2005 Proceedings*, 2005.
11. Ting, S.-W., K.-W. Tam, and R. P. Martins, "Miniaturized microstrip lowpass filter with wide stopband using double equilateral U-shaped defected ground structure," *IEEE Microwave and Wireless Components Letters*, Vol. 16, No. 5, May 2006.

Millimetre Wave Beam Combiner Designed by a GA and the HFSS

Yanzhong Yu[1] and Mei Lin[2]

[1]School of Science, Quanzhou Normal University, Quanzhou 362000, China
[2]Department of Electronic Engineering, Jiangxi Polytechnic College, Pingxiang 337055, China

Abstract— A beam combiner, which can combine multiple gaussian beams into a single one, has many important applications, such as high power radar and weapon. In this paper, a high power beam combiner at millimeter wave is designed by utilizing wire grids. The design tool is to combine a genetic algorithm (GA) for global optimization and an Ansoft HFSS for rigorous electromagnetic computation. The process of designing a beam combiner is described in detail. The optimized results and conclusion are presented.

1. INTRODUCTION

The Polarization Beam Combiner is a high performance quasioptical component that combines two orthogonal polarization Gaussian beams into a single one. There are many practical applications. For example, a compact, millimeter wave high power radar can be obtained by combining the output of many corrugated horns. Currently, there are many technical schemes for constructing a beam combiner are proposed, such as diffractive optical element (DOE) [1, 2], frequency selective surface (FSS), and photonic crystal [3]. Because grids consisting of a number of parallel metallic wires are one of the earliest and simplest quasioptical components [4], they are thus used to make a high power beam combiner at millimeter wavelength in our design. Approximate expressions for wire grids reflection or transmission coefficients are well known theoretically [4, 5], but they are only suitable for thin wires, that is, the radius of the round wires is usually less than one percent of the wavelength of the incident radiation. For example, in our design, assuming that the incident wavelength of $\lambda = 10\,\text{mm}$, to satisfy above requirement, the radius a of the round wires is demanded that $a \leq 0.1\,\text{mm}$. Such wire is so thin that it can not bear high power and is therefore unfit to construct a high power beam combiner. To bear high power, in our design we demand that $a \geq 0.5\,\text{mm}$, under $\lambda = 10\,\text{mm}$. Therefore, under this condition, we should not apply approximate expressions to calculate reflection or transmission power of wire grids. Nevertheless, Ansoft HFSS is an excellent software package for calculating the electromagnetic behaviour of a structure, and can hence accomplish these tasks. Moreover, in order to improve the performance of a beam combiner, a GA is introduced. The design process and results are given in the following sections.

2. DESCRIPTION OF THE DESIGN PROCESS

2.1. Simulation Model Based on HFSS

The simplest one-dimensional (1D) wire grids are arrays of round wires, as shown schematically in Fig. 1(a). In the region $\lambda/g > 1$, where g is the spacing of the wires, the lD grids are nearly completely transparent for radiation polarized with the electric vector perpendicularly to the wires. Parallel polarized radiation is highly reflected. Thus it can be used as a beam combiner, whose principle diagram is shown schematically in Fig. 1(b).

Under the conditions that $\lambda \gg g$ and $g \gg a$, approximately analytical expressions for reflection or transmission coefficients of thin wire grids are well known theoretically. When the incident electric field parallel to the conductor direction, the reflectivity $R_{//}$and transmissivity $T_{//}$ are given by, respectively [4],

$$R_{//} = \frac{1}{|1 + x_L|^2} \tag{1}$$

$$T_{//} = \frac{1}{|1 + 1/x_L|^2} \tag{2}$$

where $x_L = \frac{2Z_{gL}}{Z_0}$, $Z_{gL} = jZ_{fs}(\frac{g}{\lambda})\ln(\frac{g}{2\pi a})$, $Z_{fs} = Z_0\cos\theta$, $Z_0 = 120\pi\,\Omega$, and θ is an incident angle. Likewise, while the incident radiation is polarized with the electric field vector perpendicularly to

the wires, the reflectivity $R_\perp$ and transmissivity $T_\perp$ are given by, respectively [4],

$$R_\perp = \frac{1}{|1+x_c|^2} \tag{3}$$

$$T_\perp = \frac{1}{|1+1/x_c|^2} \tag{4}$$

here $x_c = \frac{2Z_{gc}}{Z_0}$, $Z_{gc} = -\frac{jZ_{fs}}{4(\frac{g}{\lambda})(\frac{\pi a}{g})^2}$, and $Z_{fs} = Z_0/\cos\theta$.

Note that all of these formulas are valid only under the restriction of $\lambda \gg a$, i.e., thin wire relative to λ. In order to accurately calculate the reflectivity and transmissivity of thick wires, Ansoft HFSS v11 is therefore adopted in our design.

Two simulation models based on HFSS are illustrated in Fig. 2, which correspond to parallel and perpendicular polarized radiation respectively. The wire grids are enveloped by a box. Perfect E boundaries are set on the up, down, left and right surfaces of the box, respectively, and the wave port excitations are assigned on front and back surfaces of the box. Correctness of the simulation models is vital in design, and can be validated by comparing the results obtained from approximate expressions (1)–(4) and from HFSS. Assuming that $\lambda = 10\,\text{mm}$, $g = 1\,\text{mm}$, $a = 0.1\,\text{mm}$ and $\theta = 0$, the reflectivities and transmissivities are obtained easily from (1)–(4) and from HFSS respectively, as given in Table 1. It can be seen from Table 1 that the results obtained from approximate formulas coincide with the ones from HFSS within the permissible error level. Therefore, we confirm the validity of our simulation models. Furthermore, both of these simulation models are suitable not only for thin wires, but also for thick ones, so they can be credibly used to calculate the reflectivities and transmissivities of thick wires.

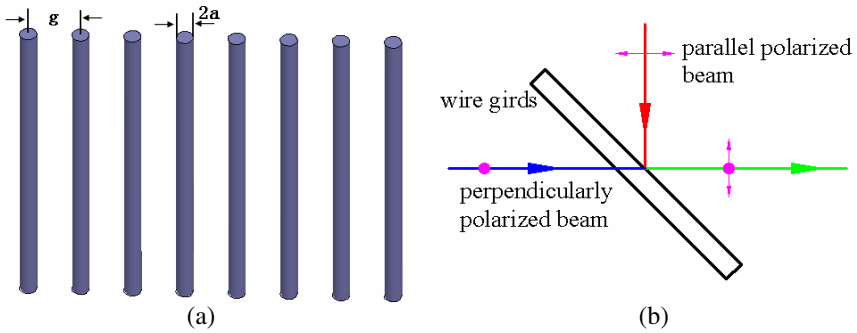

Figure 1: Schematic diagram of wire grids and a beam combiner. (a) The girds consist of round wires of diameter $2a$ and spacing g; (b) Wire grids are used to combine two beams with orthogonal polarizations.

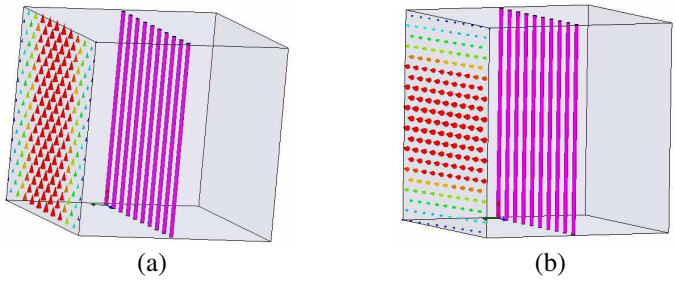

Figure 2: Simulation models. (a) Parallel polarized radiation; (b) Perpendicular polarized radiation.

Table 1: Reflectivities and transmissivities.

	$R_{//}$	$T_{//}$	$R_\perp$	$T_\perp$
Approximate formula	0.9914	0.0086	0.0004	0.9996
HFSS	0.9941	0.0059	0.0012	0.9988

2.2. Genetic Algorithm (GA)

It is known that the larger the parallel reflectivity $R_{//}$ and perpendicular transmissivity $T_{\perp}$ are, the higher is the performance of a beam combiner. When the incident wavelength λ and the radius a of the round wires are fixed beforehand, the reflectivities and transmissivities completely depend on the spacing g of the wire grids. This can be seen obviously from (1)–(4). The smaller the spacing g is, the larger is the parallel reflectivity $R_{//}$, and however the smaller is the perpendicular transmissivity $T_{\perp}$. Apparently, $R_{//}$ and $T_{\perp}$ are in contradiction to each other. Therefore, the main task in design is to find an optimal spacing g of the wire grids, where the $R_{//}$ and $T_{\perp}$ simultaneously reach the maximums and are mutual equilibriums (i.e., $R_{//} \approx T_{\perp}$). Obviously, this is an optimal problem which may be solved by GA. Although GA is provided by HFSS itself, it can not optimize two models simultaneously (i.e., parallel polarized and perpendicular polarized radiation). The feasible way to solve this problem is using independently external GA to optimize these models by calling HFSS scripts, as shown in Fig. 3. To evaluate fitness for each chromosome, GA should first execute HFSS script of parallel polarized radiation for calculating $R_{//}$, and then execute HFSS script of perpendicular polarized radiation for calculating $T_{\perp}$. The fitness function is simply defined as:

$$\text{fitness} = \left|R_{\parallel} + T_{\perp}\right| - \left|R_{\parallel} - T_{\perp}\right| \tag{5}$$

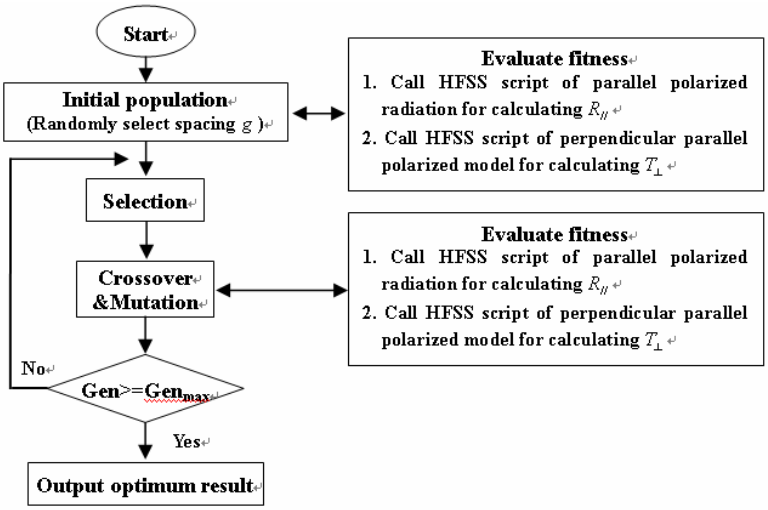

Figure 3: The flow chart of the GA procedure.

Table 2: The optimized results of spacing g ($\lambda = 10\,\text{mm}$).

a (mm)	g (mm)	$R_{//}$	$T_{\perp}$
0.1	0.5016	1	0.9994
0.2	1.4928	0.9929	0.9911
0.3	2.1985	0.9819	0.9822
0.4	2.8134	0.9692	0.9702
0.5	3.3870	0.9547	0.9511
0.6	3.9547	0.9341	0.9323
0.7	4.4823	0.9140	0.9142
0.8	4.9338	0.8971	0.8929
0.9	5.3072	0.8896	0.8762
1.0	5.7448	0.8620	0.8588

3. OPTIMIZED RESULTS AND CONCLUSION

Assuming that $\lambda = 10\,\text{mm}$ and a takes many fixed values, we apply the GA mentioned in Section 2 to search the optimum spacing g. The optimized results are listed in Table 2. A conclusion can be easily drawn from Table 2 that the larger the radius a is, the larger is the spacing g, and the lower are the reflectivity $R_{//}$ and transmissivity $T_{//}$. Therefore, under satisfaction of standing high power capacity, the small-diameter wires would better be applied to improve the performance of a beam combiner. For instance, in our case, to stand high power of 400 kW, we select the copper wires of radius $a = 0.7\,\text{mm}$ to form a beam combiner.

ACKNOWLEDGMENT

This work is supported by the Key Project of Quanzhou City Science and Technology Program (No. 2008G13).

REFERENCES

1. Sadovnik, L., A. Manasson, V. Manasson, and V. Yepishin, "Infrared/millimeter wave beam combiner utilizing holographic optical element," *Proc. SPIE Int. Soc. Opt. Eng.*, Vol. 3464, 155–163, Jul. 1998.
2. Shahriar, M. S., W. Weathers, and J. Riccobono, "Holographic beam combiner," *SBMO IEEE MTT S. Int. Microwave Optoelectron Conf. Proc.*, Vol. 2, 612–615, Aug. 1999.
3. Zhang, X. T. and P. F. Gu, "Design and fabrication of IR/mmW dichroic beam combiner," *Jiguang Yu Hongwai*, Vol. 32, 292–294, Oct. 2002.
4. Marcuvitz, N., *Waveguide Handbook*, McGraw-Hill Book Company, NewYork, 1986.
5. Goldsmith, P. F., *Quasioptical Systems Gaussian Beam Quasioptical Propagation and Application*, IEEE Press, New York, 1998.

Computer Aided Design of Depressed Collector for TWTs Using a New Numerical Methodology

Jianqiang Lai, **Yubin Gong**, **Hairong Yin**, **Yanyu Wei**, **and Wenxiang Wang**
National Key Laboratory of High Power Vacuum Electronics, School of Physical Electronics
University of Electronic Science and Technology of China, Chengdu 610054, China

Abstract— We employed a new numerical methodology-virtual boundary element (VBE) method for trajectory simulation in multistage depressed collector (MSDC) for traveling wave tubes (TWTs). The core idea of the VBE method is explained: expanding the real boundary as virtual boundary and setting virtual field sources on virtual boundary, the virtual field source distributed along the virtual boundary could substitute for the real source or physical quantity that can be regarded as field source on the real boundary [1]. The basic equations for VBE method and the numerical solution are given. The shape of virtual boundary, the distance between the real and virtual boundary, which are close related to the calculation precision are discussed. A new computer aided design (CAD) codes-CCAD is developed utilizing VBE method to design and analyze the MSDC system for TWTs. Simulation results are compared with EGUN [2]. Numerical results demonstrate that the advantages of VBE method mainly lie in fast and precise calculation.

1. INTRODUCTION

Multistage depressed collector (MSDC) can effectively improve the overall efficiency of traveling wave tubes (TWTs). Computer numerical simulation is a significant means to study MSDC and it mainly focus on two parts: the calculation of electromagnetic field and electron trajectory. For traditional regional-type method such as finite difference method (FDM) and finite element method (FEM), a large memory is needed and the calculation speed is greatly limited. Moreover for a system with complex boundary, the inevitable approximate treatment may cause unexpected error [3]. However the boundary-type method such as boundary element method (BEM) can avoid the above defects. It is not necessary to solve the whole field but only discretize the field boundary and it can deal with the boundary problems with complex field boundary [4].

The BEM overcomes the drawbacks of FDM and FEM successfully although it is not widely accepted in precise calculation for the disadvantage of the inevitable singular integral. To search a method with the advantages of BEM but without singular integral, a new methodology-virtual boundary element method (VBE) was proposed by H. C. Sun [5] in 1991. The VBE method is based on BEM which can avoid two types of singular integral [6]. Moreover the calculation for all points in field region is not necessary and it does not need special treatment for unclosed field [3]. This made it applicable for fast and precise calculation.

2. CORE IDEA AND BASIC EQUATIONS OF VBE METHODOLOGY

The VBE method based on BEM and BEM can be classified into surface charge method and boundary integral equation method. Its fundamental idea of the later is the calculation of steady electromagnetic field by solving the boundary problem of Poisson equations. In homogeneous medium the potential function on any point in the field can be expressed as:

$$U(x,y,z) = \frac{1}{4\pi\varepsilon}\int_v \frac{\rho}{\mathbf{r}}dv + \frac{1}{4\pi}\oint_\Gamma \left[\frac{1}{\mathbf{r}}\frac{\partial U}{\partial n} - U\frac{\partial}{\partial n}\left(\frac{1}{\mathbf{r}}\right)\right]ds \tag{1}$$

This is also the basic equation for calculation of electromagnetic field by the boundary integral method.

The remarkable advantages of the method are fast and precise calculation while the biggest drawback of this method is the singular integral which can cause a large calculation error and can not be eliminated. The singular integral happens under the following circumstances: 1) when field point is close to electrode; 2) when space charge is close to electrode; 3) when space charge is very close to each other. Therefore the boundary integral equation method is extremely limited for the existence of singular integral [7].

To maintain the advantages of BEM but eliminate the first two types of singular integral, another method was proposed by setting an imaginary boundary. The potential and the boundary

conditions caused by the virtual charge distribution along the imaginary boundary are equivalent to the real boundary caused. The imaginary boundary is called virtual boundary and this method is called virtual boundary element (VBE) method.

In homogeneous medium, there are the following potential government equations and boundary conditions:

$$\Delta U(r) = b, \quad r \in \Omega \tag{2}$$

$$U(r) = u_0|_{\Gamma_1}, \quad \frac{\partial U(r)}{\partial n} = q_0|_{\Gamma_2} \tag{3}$$

where $U(r)$ is potential function, b is field source function in the problem field Ω, the boundary of the field is $\Gamma(\Gamma = \Gamma_1 + \Gamma_2)$, Γ_1 and Γ_2 are Dirichlet and Neumann boundaries respectively

Reference [1] has proved a theorem: in a region Ω, if two harmonic functions are equal in a sub-region Q which is include in region Ω (see Figure 1), thus they are also equal in region Ω. This demonstrates that any harmonic function $U(r)$ in region Ω can be completely determined by the value on the sub-region Ω.

Suppose there is an expanded boundary Γ' outside $\Gamma(\Gamma = \Gamma_1 + \Gamma_2)$, Γ' is called virtual boundary and the region be enclosed is Ω' and $\Omega' \supset \Omega$, as also can be seen in Figure 1. A virtual field-source function $Q(r)$ distributes along the virtual boundary. Assume potential and the boundary conditions caused by $Q(r)$ are equivalent to the real boundary caused. According to superposition principle, the potential of any point on the virtual boundary and its derivative along n can be expressed as:

$$U(r) = \int_{\Gamma'} U^*(r, r')Q(r')d\Gamma'(r') + \int_{\Omega} U^*(r, r'')b(r'')d\Omega(r'') \tag{4}$$

$$\frac{\partial U(r)}{\partial n} = \int_{\Gamma'} \frac{\partial U^*}{\partial n}(r, r')Q(r')d\Gamma'(r') + \int_{\Omega} \frac{\partial U^*}{\partial n}(r, r'')b(r'')d\Omega(r'') \tag{5}$$

where U^* represents the fundamental solution of potential government equations, r is field point, r' and r'' are virtual source point on virtual boundary and source point in the real field respectively, Γ' is virtual boundary, Ω is the field inside the real boundary, n is the outward normal of boundary.

According to extremum principle of harmonic function, if the solutions of (4) and (5) exist and are continuous, the harmonic function $U(r)$ in Ω can be surely extended into $U'(r)$ in a larger region Ω' and $U'(r)$ can be uniquely determined by the value on the boundary of sub-region Ω. The essence of VBE method is the transformation of the solving of harmonic function of the boundary value problem into solving the harmonic function in a larger region and the solution of the VBE equation is unique if the transform exists.

Potential and its normal derivative on real boundary can also be expressed as the form of (4) and (5). If the real boundary is discretized intro N segments, the potential of each segment and its normal derivate is regarded as constant, thus (4) and (5) will be decomposed into N equations. Similarly, discretize the virtual boundary into N segments and regard the values of source function on the segments as constants, or set N nodes on virtual boundary and replace the source value between nodes with the interpolation of the two adjacent nodes. There will be N unknown $Q(r_i)$ of virtual source in N equations and each of them can be solved. According to the equations and the solved $Q(r_i)$, potentials of any point in the field can be obtained. The potential of any point in field (include boundary) is given by:

$$U(r) \int_{\Gamma'} \left[U^*(r, r') \frac{\partial U(r')}{\partial n} - U(r') \frac{\partial U^*(r, r')}{\partial n} \right] d\Gamma'(r') \tag{6}$$

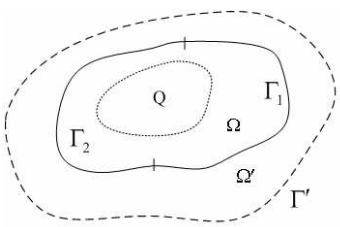

Figure 1: Boundary condition and virtual boundary.

where

$$U(r') = \int_{\Gamma} \left[U^*(r, r'') \frac{\partial U(r'')}{\partial n'} - U(r'') \frac{\partial U^*(r, r'')}{\partial n'} \right] d\Gamma(r'') \tag{7}$$

$$U(r'') = \int_{\Gamma'} \left[U^*(r', r'') \frac{\partial U(r')}{\partial n} - U(r') \frac{\partial U^*(r', r'')}{\partial n} \right] d\Gamma' \tag{8}$$

r represents field point, r' represents point on virtual boundary, r'' is the point on real boundary, n' is unit vector of outward normal on real boundary, Γ and Γ' are the real and virtual boundaries.

The above equations implies that it is correct to build equations for virtual boundary as the same principle as real boundary. The field with qualities equal on the virtual boundary will also equal in the whole field enclosed by virtual boundary.

3. THE ESTABLISHMENT OF VIRTUAL BOUNDARY

The potential in the field can be expressed by either the charge distribution on real boundary or the virtual charge distribution on virtual boundary.

Considering a point P in the field, drawing N radial-lines across the point (see as in Figure 2). Consequently, the virtual and real boundaries are divided into N segments. On condition that N is big enough, we can get the following conclusion after analyzing: the less distance between virtual and real boundary, the higher accuracy of this method is, while its lower limit is limited by singular integral (too small the distance may cause singular integral). That is to say there is a lower limit for D but without an upper limit,

$$D = |r_i - r_i'|, \quad (D \geq d) \tag{9}$$

where d is the minimum distance between virtual and real boundary, r_i and r_i' are the position vector of real and virtual source respectively.

If the distance between virtual and real boundary is not too large, thus the potential varies not too intensely, we consider approximately that the potential generated by virtual source and by real source are equal ($U_i' \approx U_i$). Then the following two expressions can be deduced

$$\frac{\partial r}{\partial n} \approx 1 \qquad \text{for convex boundary} \tag{10}$$

$$\frac{\partial r}{\partial n} \approx -1 \qquad \text{for concave boundary} \tag{11}$$

The above two expressions imply that for both concave and convex boundary, the normal line of any point on the real boundary should parallel with the normal line of the corresponding point on virtual boundary (see as in Figure 3). And only in this case, the operation of virtual boundary element method can go on without any approximation. In practice, to minimize the calculation error, we should make the angle between the two normal lines θ (in Figure 3) as small as possible when setting the virtual boundary.

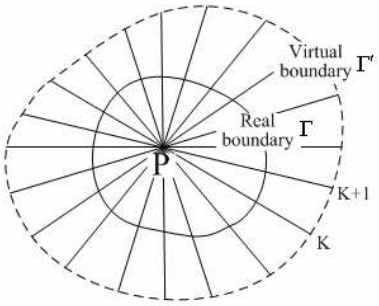

Figure 2: Discretization of the virtual and real boundaries by N half-lines originate from point P.

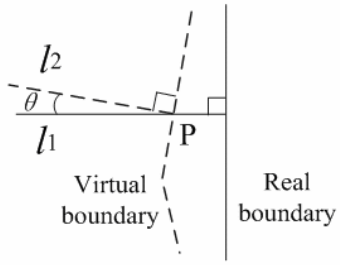

Figure 3: The relationship between the normal of real and virtual boundaries.

4. SIMULATIONS AND NUMERICAL RESULTS

Based on VBE method, we have developed a MSDC simulation code-CCAD. The code is now only two-dimensional axisymmetric and a three-dimensional one is in studying and will soon been in developing. A four stage depressed collector is designed by both CCAD and EGUN. The potential on slow wave structure is fixed on 9014 V. The size of mesh for EGUN is 3 mm. The number of boundary element (be called electrode element in CCAD) is 500.

The voltages on electrodes are fixed. Four groups of entrance beam are used for the simulation. The voltages on the 4 electrodes and the simulation results were assigned as in Table 1. The profile of the collector model and the visible electron trajectory and numerical results are plotted in Figure 4. According to the figures given in Table 1, the result efficiency from CCAD are generally higher than that of EGUN, however the error between the two is acceptable.

Table 1: Efficiency and time consumption comparison.

Potentials on stages:	Entrance Beam	Eff.-CCAD	Eff.-EGUN	CCAD-Time consumed	EGUN-Time consumed
$U_1 = 4500$ V,	Group a	83.25%	82.07%	75 s	138 s
$U_2 = 3200$ V,	Group b	82.57%	81.34%	70 s	132 s
$U_3 = 2100$ V,	Group c	77.96%	78.18%	76 s	141 s
$U_4 = 200$ V.	Group d	58.16%	53.35%	77 s	139 s

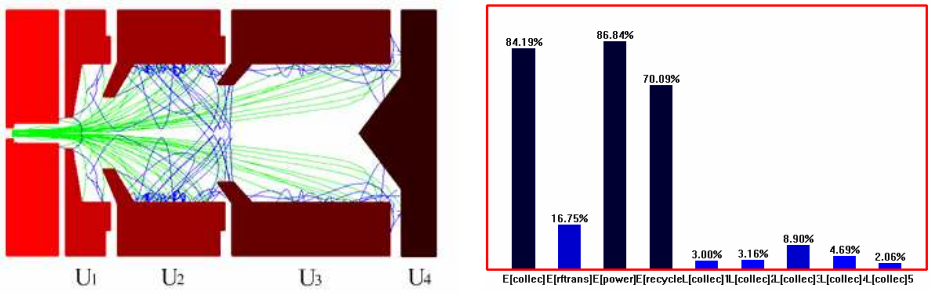

(a) (b)

Figure 4: (a) Trajectories of primary and secondary electron in collector simulated by CCAD. The trajectories of both primary electron and secondary electron are given. (b) Numerical results. The first column represents the collector efficiency, the second represents RF conversion efficiency, the third represents energy conversion efficiency, the forth represents energy recycle efficiency.

5. CONCLUSION

Virtual boundary element method is a promising approach to calculate the electromagnetic field which has the following prominent advantages:

1) It can avoid two types of singular integral.
2) As a boundary-type method, it reduced the computational complexity, so shorten the CPU time.
3) It is fit for open boundary problem and no need for special treatment to unclosed field.
4) It has high solution stability and calculation precision for a well chosen virtual boundary.

The basic idea of VBE method is setting virtual field sources on virtual boundary, and the virtual field source could substitute for the real source or physical quantity that can be regarded as field source on the real boundary. The shape of the virtual boundary, the distance between the virtual and real boundaries are the main factors that affect the calculation precision. To get precise solutions, the shape of virtual boundary must satisfy, a) the angle between the corresponding normal lines on real and virtual boundary should be as small as possible or equal to zero; b) the minimum distance between virtual and real boundary should ensure the singular integral does not occur. Numerical simulation results demonstrate the validity of VBE method applying in MSDC

system. The VBE method for three-dimensional collector is attractive and now under studying and a code will soon be in developing.

ACKNOWLEDGMENT

This work was partially supported by the State Key Program of National Natural Science Foundation of China under Grant No. 60532010 and partially supported by the University of Electronic Science and Technology of China Fund for Youth Scholar under Grant No. L08010401JX0736.

REFERENCES

1. Zhang, Y. M., H. C. Sun, and J. X. Yang, "Theoretical analysis for virtual boundary element method," *Chinese J. of Comput. Mechs.*, Vol. 17, No. 1, 56–62, Feb. 2000.
2. Herrmannsfeldt, W. B., "EGUN-An electron optics and gun design program," *SLAC-331*, Stanford, CA, Oct. 1988.
3. Yin, H.-R., Y.-B. Gong, Y.-Y. Wei, et al., "Virtual boundary method and electron trace in a power electron gun," *Chinese J. of Comput. Phys.*, Vol. 23, No. 6, 647–654, Nov. 2006.
4. Rucker. W. M. and K. R. Richter, "Three-dimensional magnetostatic field calculation using boundary element method," *IEEE Trans. Magn.*, Vol. 24, No. 1, 23–26, Jan. 1988.
5. Sun, H. C., X. H. Li, and L. Z. Zhang, "Virtual boundary element-collocation method for solving problems of elasticity," *Chinese J. of Comput. Mechs.*, Vol. 8, No. 1, 15–23, 1991.
6. Burgess, G. J. and E. A. Mahajerin, "A comparison of the boundary element and superposition methods," *Comput. & Strut.*, Vol. 19, No. 5–6, 697–702, 1984.
7. Liu, J. and J.-M. Jin, "A novel hybridization of higher order finite element and boundary integral methods for electromagnetic scattering and radiation problems," *IEEE Antennas and Propag. Soc. Int. Symp.*, Vol. 4, No. 8–13, 330–333, Jul. 2001.

Study on Circularly Polarized Traveling Wave Tube

Xiong Xu, **Yan-Yu Wei**, **Wen-Xing Liu**, **Jian-Ping Wei**,
Wen-Xiang Wang, **and Yu-Bin Gong**
National Key Laboratory of High Power Vacuum Electronics
University of Electronic Science and Technology of China
Chengdu 610054, China

Abstract— An interesting vacuum microwave power amplifier, named circularly polarized traveling wave tube (CPTWT), is introduced. It is supposed to have high efficiency and good linearity of phase frequency characteristics so that can be used to improve the performances of many microwave systems such as radar, satellite communication and electronic countermeasure (ECM). The simulation results indicate that CPTWT is a promising device.

1. INTRODUCTION

In 1996, at the IEEE International Conference on Plasma Science, Professor Vladimir A. Vanke of Lomonosov Moscow State University firstly used the CPTWT, abbreviation for Circularly Polarized Traveling Wave Tube, to call a kind of high efficiency traveling wave tube with a transverse field [1]. Different from traditional O-type traveling wave tube, CPTWT works on the interaction between circularly polarized electromagnetic wave and electron beam transverse wave.

The theory of electron beam transverse waves was put forward by Professor A. E. Siegman of Stanford University in 1960 [2]. Until 1972, the first prototype model based on that theory was fabricated by V. I. Yur'yev and his co-workers of Lomonosov Moscow State University. And they had obtained the actual gain of 13 dB and the output power of 140 W [3]. Subsequently, a detailed numerical analysis predicts that such tube have an electron efficiency on the order of 40% and a high linearity of the phase frequency response along with the output power of 3–4 kW and the gain of 20 dB [4]. However, these results have not been achieved because no experiment has been carried out for further study. So the authors want to do some simulations instead.

2. PRINCIPLE

The interaction process in a CPTWT is the process that electron beam transverse wave be excited by circularly polarized electromagnetic wave [5].

Distribution of the electric field of the circularly polarized electromagnetic wave is illustrated in Figure 1. It consists of a uniform transverse electric field component and a reversed-phase longitudinal electric field component. The magnitude of the reversed-phase longitudinal electric field at the center axis is zero.

When the longitudinal velocity of the electron is equal to the phase velocity of the circularly polarized electromagnetic wave, the electron will feel a static electric field. Therefore, under the effect of uniform longitudinal magnetic field and uniform transverse electric field, the electron will drift into the region of the retarding longitudinal electric field, and its trajectory is common cycloid.

However, with time went on, different electrons feel different phase of the static electric field due to the rotation of the uniform transverse electric field vector at the entrance of the retarding

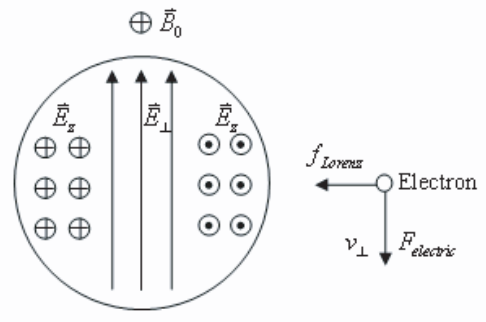

Figure 1: Distribution of electric field and the force on the singular electron.

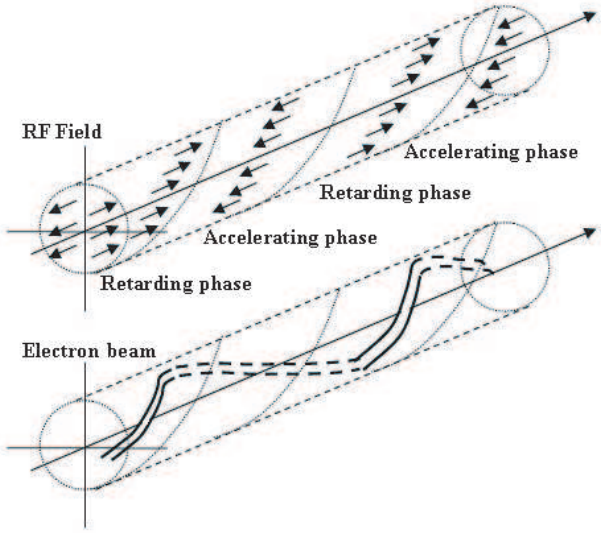

Figure 2: Distribution of longitudinal electric field and the shape of the filamentary electron.

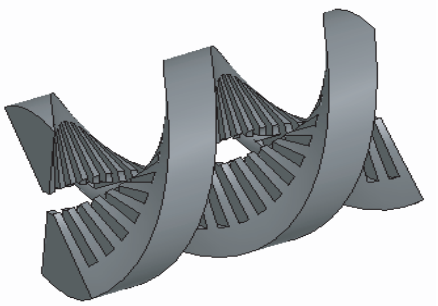

Figure 3: Spiral twinned comb.

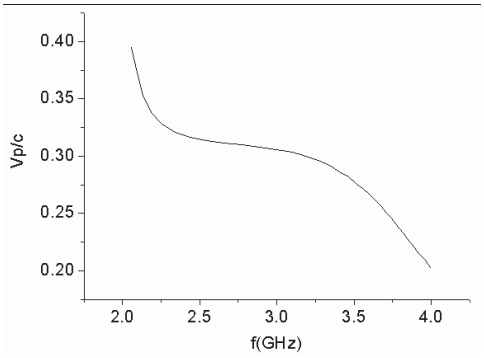

Figure 4: Dispersion characteristics of STC.

system. Then, the positions of the different electrons form a helical structure whose radius is increasing along the longitudinal direction. And the helix, shown in Figure 2, is entirely immersed in the region of the retarding longitudinal electric field. This is just the reason why the CPTWT has high efficiency.

3. SIMULATION RESULTS

A special slow wave structure illustrated in Figure 3, called spiral twinned comb (STC), which circularly polarized electromagnetic wave can propagate through, has been deeply studied by Professor Vanke [6]. Figure 4 shows the dispersion characteristics of spiral twinned comb by simulation with HFSS. The cold bandwidth achieves 30%.

According to the Figure 4, we can set the working voltage of the tube at the 25.6 kV. Then, the process of interaction is showed with our partial-in-cell software CHIPIC 3.0 [7]. And we can see from Figure 5 that electron beam is rotated on the center axis. That is to say, electron beam transverse wave has been excited. Of course, the phenomenon is not well accord with the results of the above theoretical analysis. That is because the helical structure mentioned in the theoretical analysis is just in allusion to a filamentary beam, and yet the practical electron beam has finite cross section. Moreover, the transverse electric field in the STC is not uniform. The uniform transverse electric field is present just as one of the spatial harmonics in the STC. Thus, in actual device, this will lead to a longitudinal velocity spread in the electron beam, thereby restricts the efficiency of the amplification.

Figure 6 shows the amplitude characteristics of the CPTWT at S band. The output power increases linearly with the input power increasing. The saturation power is not attained. The phenomenon is accord with the experimental results [3]. But the gain of this tube is not as good

Figure 5: The profile of electron beam.

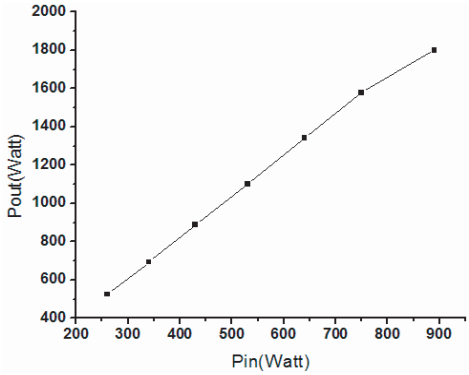

Figure 6: Amplitude characteristics of CPTWT.

as we expected.

4. CONCLUSION

The above simulation results show us two interesting things. One is circularly polarized electromagnetic wave can interacts with electron beam transverse wave, and this mechanism is different from that of the theory of space charge wave. It may have high electron efficiency. The other is the amplification in CPTWT is nearly linear, and this is different from that of the existing microwave power amplifiers.

Thus, these results indicate that CPTWT may have some excellent characteristics. Though none of any excellent characteristics had been developed well at present, we still conclude that CPTWT is a promising device. So many efforts should be made in future.

ACKNOWLEDGMENT

The authors would like to acknowledge the enlightening discussion with Prof. Vladimir A. Vanke and Dr. Aleksandr V. Konnov of Lomonosov Moscow State University. This work was supported by the State Key Program of National Natural Science Foundation of China under Grant No. 60532010.

REFERENCES

1. Vanke, V. A. and V. L. Savvin, "On some microwave physics research at Moscow State University and Russian Industries," *IEEE Int. Conf. on Plasma Science*, 226, New York, Jun. 1996.
2. Siegman, A. E., "Waves on a filamentary electron beam in a transverse field slow wave circuit," *J. Appl. Phys.*, Vol. 31, No. 1, 17–26, Jan. 1960.
3. Yur'yev, V. I., V. N. Dobrynchenko, V. A. Shestiperov, and U. A. Nigmatullin, "Experimental investigation of the interaction between the synchronous waves of the electron beam and the traveling wave of an electrodynamic structure," *Radio Engineering and Electronic Physics*, Vol. 17, No. 4, 648–651, Apr. 1972.
4. Vanke, V. A., A. A. Zaytsev, V. M. Lpukhin, A. V. Moshkov, and V. L. Savvin, "Numerical analysis of a transverse-field TWT," *Radio Engineering and Electronic Physics*, Vol. 24, No. 9, 115–123, Sep. 1979.
5. Vanke, V. A., "Transverse electron-beam waves for microwave electronics," *Physics-Uspekhi*, Vol. 48, No. 9, 917–937, Sep. 2005.
6. Vanke, V. A. and A. V. Konnov, "Retard electromagnetic waves in a spatially twisted two-row comb," *Soviet Journal of Communications Technology & Electronics*, Vol. 31, No. 8, 1–8, Aug. 1986.
7. Zhou, J., D. Liu, C. Liao, et al., "CHIPIC: A highly efficient code for electromagnetic PIC modeling and simulation," *17th International Conference on High-Power Particle Beams (BEAMS'08)*, Xi'an, China, Jul. 6–11, 2008.

A Ka-band Power Amplifier Based on Double-probe Microstrip to Waveguide Transition

Yi-Hong Zhou, **Jia-Yin Li**, **Bo Zhao**, **and Hai-Yang Wang**
School of Physical Electronics, University of Electronic Science and Technology of China
Chengdu, Sichuan 610054, China

Abstract— In this paper, a Ka-band power amplifier based on double-probe microstrip to waveguide transition is presented. The advantages of this power-combining/dividing structure are its low profile, ease of fabrication, as well as its potential for high power-combining efficiency. In addition, efficient heat sinking of monolithic microwave integrated circuit (MMIC) devices is achieved. In contrast with the traditional waveguide T combiner, the double-probe structure doubles the number of the combining branches. The measured results demonstrate a power-combining efficiency higher than 72% in 33–37 GHz band, especially higher than 80% in 34.5–35 GHz band.

1. INTRODUCTION

Conventional hybrid-type power-combining circuits, such as Wilkson power divider, Lange coupler and branch-line coupler, suffer from low power efficiency at millimeter frequencies [1]. Due to the low transmission loss of the waveguide, especially at millimeter frequencies, the waveguide T (magic-T, E-T and H-T) is usually employed as divider and combiner for power dividing/combining. In the ka-band 30 W amplifier [2], phase and amplitude balance was obtained by the use of 8 : 1 WR-28 waveguide magic-T combiner. In the W-band MMIC high power sources [3], the output power was combined using an 8-way waveguide hybrid junction combiner, and an output power of 2.4-watts was achieved at W-band.

Using the waveguide T as power divider/combiner, the microstrip to waveguide transition must be use to transfer the RF energy from the waveguide to the microstrip. The full band waveguide-to-microstrip probe transition is usually used to do this [4, 5]. However, using this probe type of transition, one waveguide can only be transited into one microstrip, and the number of waveguide-to-microstrip transitions must be equal to the number of combining branches. Another type of waveguide to microstrip line transition has been presented [6–9], and this type of transition can divide the input power from waveguide into two ways equally, as well as couple the RF energy from waveguide to microstrip.

In this paper, using the waveguide-to-microstrip transition with power divider, we propose a new power divider/combiner, which is designed in 33–37 GHz. The simulated and measured results are presented.

2. DESIGN

As shown in Figure 1, the combining circuit consists of input and output waveguide T, double-probe waveguide-to-microstrip transitions and Ka-band monolithic microwave integrated circuit (MMIC) amplifiers. In the power-dividing section, the input power is divided into two ways through the input waveguide T, and then each waveguide branch is divided into two ways through the double-probe waveguide-to-microstrip transition with RF energy transferred from waveguide to microstrip. In the power-combining section, each RF signal of the four microstrip branches is amplified by the MMIC amplifier and coupled to the power combiner, whose mechanism is the same as the power divider using waveguide T and double-probe waveguide-to-microstrip transitions.

Figure 2(a) and Figure 2(b) show the schematic and E-field distribution of the waveguide T respectively. Phase and amplitude balance can be obtained between the two H arms with a good return loss in the input port. Figure 3(a) and Figure 3(b) show the geometry of the double-probe waveguide to microstrip transition. As shown in Figure 3(a) and Figure 3(b), the transition consists of two microstrip probes, and each one is composed of a probe section extended into the waveguide and a high impedance matching section inserted between the probe and the standard 50 Ω microstrip line. This transition can transfer RF energy between waveguide and microstrip with the input power divided into two ways equally. The distance between the two probes must be wide enough to accommodate the two MMIC amplifiers. So the first step of the design of transition is to determine the minimal distance (the value of D3) between the two probes according to the

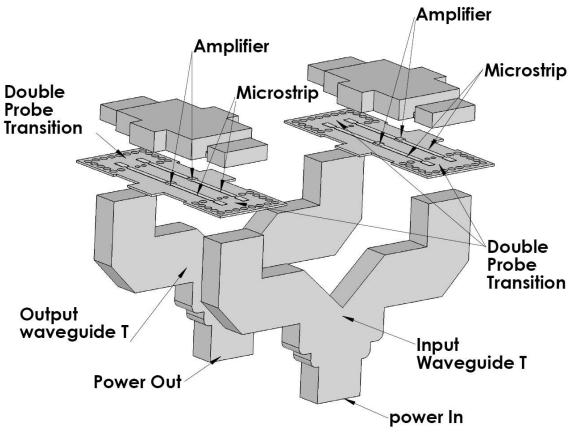

Figure 1: Configuration of four-way power-combining amplifier using double-probe waveguide to microstrip transition.

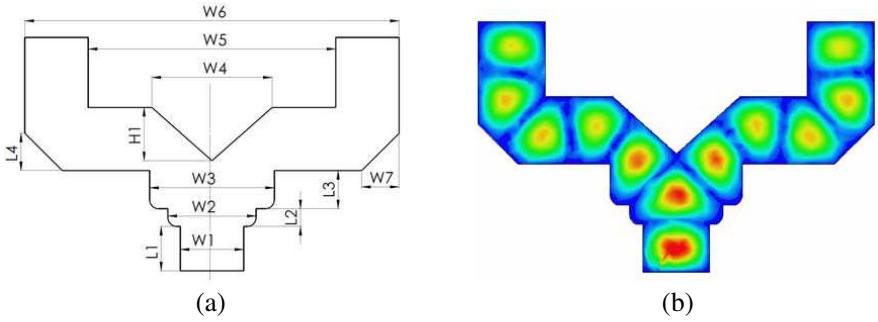

Figure 2: (a) The dimension illustration of waveguide T and (b) E-field distribution of waveguide T.

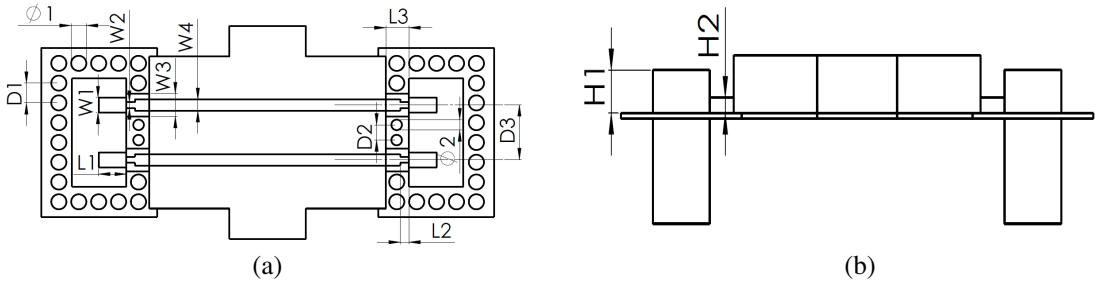

Figure 3: Double-probe waveguide to microstrip transition and power divider geometry. (a) Top view. (b) Cross-section view.

dimensions of MMIC amplifier. The challenge, however, is to achieve a good input return loss at the waveguide port and amplitude and phase balance at the two microstrip ports with the value of D3 larger than the minimal distance. We can optimize the RF performance of the transition by adjusting the width W_1, W_2 and W_3, the height H_1 and H_2, and the length L_1 and L_2 respectively. Figure 4 shows the E-field distribution of the overall power divider/combiner.

3. SIMULATED AND EXPERIMENT RESULTS

After optimization using Ansoft HFSS, the accurate dimensions and S-parameters of the waveguide T and double-probe waveguide to microstrip transition were obtained. The dimensions of the waveguide T are shown in Table 1, and the dimensions of the designed double-probe transition are shown in Table 2.

For the proposed power divider/combiner, Rogers 5880 with a dielectric constant of 2.2 and thickness of 0.254 mm was used as the substrate for the microstrip line. As shown in Figure 5(a), equal power division (-6.1 ± 0.1 dB) is achieved at the microstrip port 2, 3, 4 and 5 in 32–37 GHz

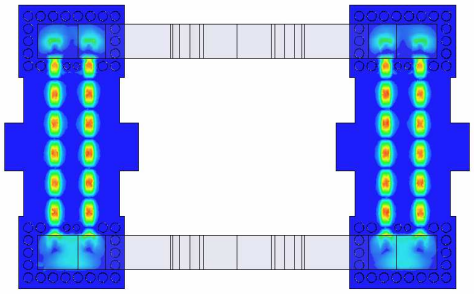

Figure 4: E-field distribution of four-way power divider/combiner.

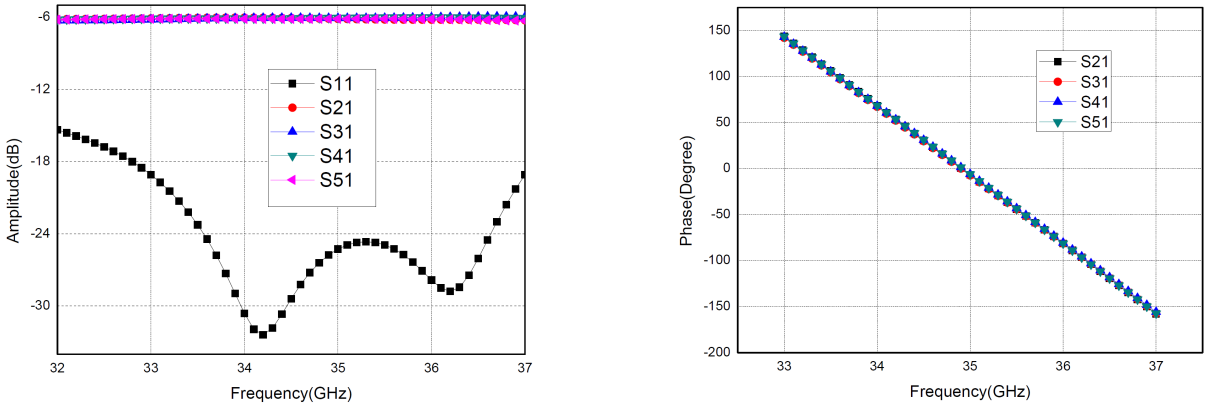

Figure 5: Simulated results of the four-way power divider/combiner. (a) Magnitude. (b) Phase.

Table 1: The dimensions of waveguide T (unit: mm).

W_1	W_2	W_3	W_4	W_5	W_6	W_7	L_1	L_2	L_3	L_4	H_1
7.112	9.9	14	13.5	27.78	42	4.2	5	2	4.3	4.2	6

Table 2: The dimensions of double-probe waveguide to microstrip transiton (unit: mm).

W_1	W_2	W_3	W_4	L_1	L_2	L_3	D_1	D_2	D_3	Φ_1	Φ_2
0.98	0.39	1.5	0.75	1.81	0.56	1.5	1.3	1	3.6	1	0.7

band, which is very close to the expected value of −6 dB. Also, the phases of the coupling coefficients are found to be uniform [see Figure 5(b)]. A passive divider/combiner was built by placing two identical circuits back to back. Figure 6 shows the simulated and measured results of the passive power divider/combiner. The measured results show a good agreement with the simulated results. The measured minimum insertion loss of 1.08 dB was achieved with a return loss of 25.2 dB [see Figure 6] at 34.8 GHz, which indicates a maximum expected power-combining efficiency of 89% for the combining circuit. At 35 GHz, the measured insertion loss is 1.28 dB, corresponding to a power-combining efficiency of 86%. A slight frequency shift was noted between the measured and HFSS simulation results.

Based on the passive power dividing/combining circuit, the ka-band double-probe power amplifier using four Agilent AMMC-5040 MMIC chips was fabricated and measured [see Figure 7]. The MMIC are biased at 4.5 V with a total dc current of 1.2 A. To measure the power combining efficiency, the power compression for the amplifier has been measured. At 34.7 GHz, the four-device double-probe power amplifier provides a saturated output power of 27.7 dBm. Since the measured single MMIC chip saturated output-power level (Psat) is 22.5 dBm, the ideal four-device power combiner would provide output power of 28.5 dBm. This translates into the power-combing efficiency of approximately 83%, close to the 89% [see Figure 8]. In 33–37 GHz band, the saturated output power is higher than 27 dBm, which indicates that the power combining efficiency is higher

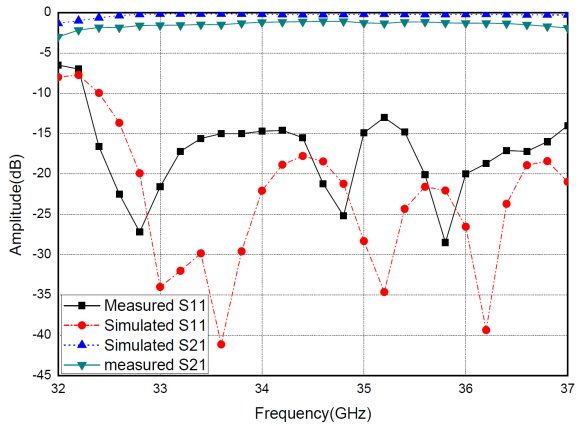

Figure 6: Simulated and measured results of the passive power divider and combiner placed back to back.

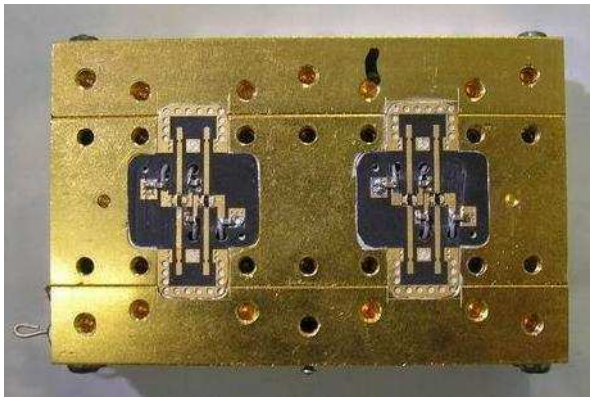

Figure 7: Perspective view of the four-device power amplifier.

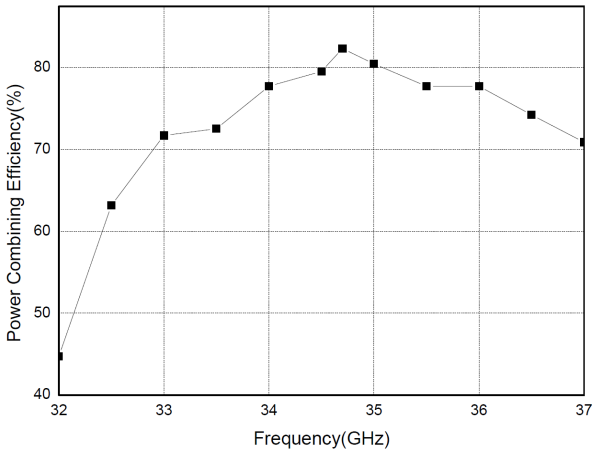

Figure 8: Power combining efficiency of the four-device power amplifier at different frequencies.

than 72%. In addition, in 33–37 GHz band, the saturated output power is higher than 27.5 dBm, which indicates that the power combining efficiency is higher than 80%. We believe it is possible to achieve a better power-combining efficiency by reducing the length of the microstrip lines in the existing circuits and through more accurate construction of double-probe power divider/combining.

4. CONCLUSIONS

A four-way Ka-band power amplifier has been designed based on a power-dividing/combining structure using double-probe waveguide to microstrip transitions. Low loss and high power-combining efficiency have been achieved at millimeter-wave frequencies. The measured power-combing efficiency is higher than 72% in 33–37 GHz band, especially higher than 80% in 34.5–35 GHz band. In addition, this power-combining/dividing structure is characterized by its low profile, ease of fabrication and efficient heat sinking of MMIC. In contrast with the traditional waveguide T combiner, the double-probe structure doubles the number of the combining branch.

REFERENCES

1. Chang, K. and C. Sun, "Millimeter-wave power-combining techniques," *IEEE Trans. Microwave Theory Tech.*, Vol. 31, 91–107, Dec. 1983.
2. Escalera, N. and W. Boger, "Ka-band, 30 watts solid state power amplifier," *IEEE MTTS Int. Microw. Symp. Dig.*, Vol. 6, 561–563, 2000.
3. Ingram, D., Y. C. Chen, and I. Stones, "Compact W-band solid-state MMIC high power sources," *IEEE MTTS Int. Microw. Symp. Dig.*, Vol. 6, 955–958, 2000.

4. Leong, Y.-C. and S. Weinreb, "Full band waveguide-to-microstrip probe transitions," *IEEE MTTS Int. Microw. Symp. Dig.*, Vol. 6, 1435–1438, 1999.
5. Shih, Y.-C., T.-N. Ton, and L. Q. Bui,"Waveguide-to-microstrip transitions for millimeter-wave applications," *IEEE MTTS Int. Microw. Symp. Dig.*, Vol. 5, 473–475, 1988.
6. Davidovitz, M., "Wide-band waveguide-to-microstrip transition and power divider," *IEEE Microwave and Guided Wave Letters*, Vol. 6, 13–15, 1996.
7. Wu, D. and K. Seo, "Waveguide to microstrip line transition and power divider," *Electronics Letters*, Vol. 43, 169–170, Feb. 2007.
8. Stones, D. L., "Analysis and design of a novel microstrip-to-waveguide transition/combiner," *IEEE MTTS Int. Microw. Symp. Dig.*, 217–220, 1994.
9. Deslands, D. and K. Wu, "Integrated transition of coplanar to rectangular waveguides," *IEEE MTTS Int. Microw. Symp. Dig.*, Vol. 2, 619–622, 2001.

A 3.5 GHz High-efficiency CMOS RF Power Amplifier with Adaptive Bias

Yi-Chen Chen and Jeng-Rern Yang
Microwave Laboratory, Department of Communication Engineering, Yuan Ze University
No. 135, Yuan-Dong Rd., Jhong Li City, Taoyuan County 320, Taiwan, R.O.C.

Abstract— This paper proposes a high-efficiency 3.5 GHz CMOS power amplifier that uses an improved linearizer as an adaptive bias control circuit. The proposed circuit is simulated by TSMC 0.18 µm RF CMOS process. At the 1-dB compression point (P1dB), the power amplifier exhibits 25.5 dBm of output power with a high power-added-efficiency (PAE) of 39% and sufficient gain (25.5 dB) at a supply voltage of 3.3 V. At the output power 6-dB back-off from P1dB, the PAE remains at 15%. The proposed structure improves PAE by 5%∼6% more than the resistor bias.

1. INTRODUCTION

Modern wireless communication systems impose stringent requirements on power amplifiers (PAs). The World Interoperability for Microwave Access (WiMAX) standard uses orthogonal frequency division multiplexing (OFDM) to offer high high-speed data and strong immunity to multi-path fading and narrow-band interference [1]. However, the multi-carrier characteristic of OFDM signals can lead to a large peak-to–average power ratio (PAPR) and dynamic range. This high PAPR poses a design challenge for power amplifiers [2]. WiMAX technology has matured quickly, and the advantages of WiMAX over WLAN include a larger wireless coverage area and mobile internet access. A PA used in a WiMAX system must be highly efficient to conserve battery power. However, the linearity specifications are often achieved by backing off the output power, which causes a large reduction in efficiency. Because the PA is the most power consuming block in a WiMAX transceiver, efficiency is a critical issue in PA design.

This study proposes a high-efficiency power amplifier that uses an improved linearizer as an adaptive bias control circuit. The proposed circuit is simulated by TSMC 0.18 µm RF CMOS process. Operated on a 3.3 V supply, the proposed structure improves the PAE by 5%∼6% more than the resistor bias.

This paper is organized as follows. Section 2 briefly introduces the architecture of the proposed RF power amplifier and the adaptive bias. Section 3 describes the simulation results and compares them to conventional results. Section 4 provides the conclusion.

2. DESIGN ARCHITECTURE

2.1. Design of Power Amplifier

Figure 1 shows a schematic of the proposed power amplifier with adaptive bias. This power amplifier consists of a power device, adaptive bias, and drive device. The power device was in cascode format, consisting of M3 and M4, whose unit gate widths are 6 µm * 64 µm to increase the breakdown voltage. The scaling ratio between the sizes of the power and drive devices is 2 : 1. This high-efficiency design, replaces the conventional resistor bias with adaptive bias.

2.2. Adaptive Bias

Figure 2 shows the schematic of adaptive bias. Since the linearizer acts as a variable resistor, the gate bias change depends on the input power. The resistor R1 stabilizes the operation of the linearizer. To avoid the gain compression of R1, C1 and R2 act as a bypass circuit for R1. Due to the adaptive bias, this design improves the efficiency by 5%∼6%, as Fig. 4 illustrates.

3. SIMULATION RESULT

This section summarizes the simulation results of the ADS and the TSMC 0.18 µm RF CMOS process. Fig. 3 shows that the proposed power amplifier produces 25.5 dBm of output power with high power-added-efficiency (PAE) of 39% at the 1-dB compression point (P1dB), and achieves a linear gain of 25.5 dB at a supply voltage of 3.3 V. At the output power 6-dB back-off from P1dB, the PAE remains 15%. The proposed structure improves the PAE by 5 ∼ 6% more than the resistor bias, as Fig. 4 illustrates.

Figure 5 shows the simulation result of third order inter-modulation (IMD3) for the proposed circuit, and compares it to resistor bias work. Simulation results show that the adaptive bias

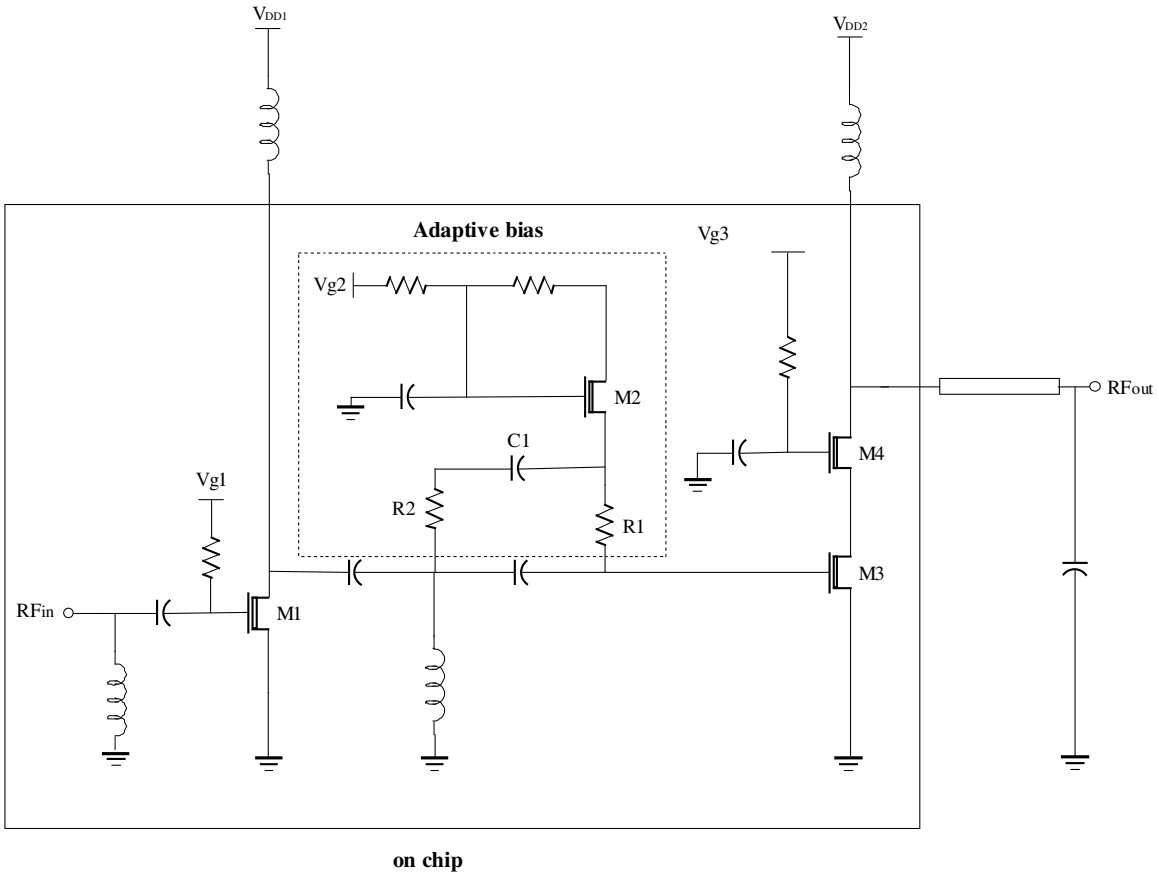

Figure 1: Schematic of the proposed power amplifier.

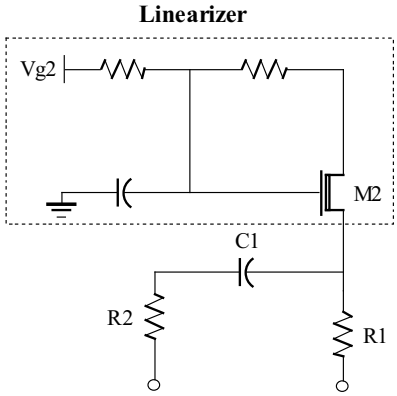

Figure 2: Schematic of adaptive bias.

Table 1: Summarized and compare to publish power amplifiers.

Ref.	Technology	year	VDD (V)	Gain (dB)	Pout@P1dB (dBm)	PAE@P1dB (%)	OIP3 (dBm)
* [4]	0.18 µm CMOS	2009	3.3	20	27	33	
[5]	0.18 µm CMOS	2009	2.4	18	20.6	24	35
This work	0.18 µm CMOS	2009	3.3	25.5	25.5	39	37

*PA1

improves the PAE without sacrificing the linearity of the power amplifier. IMD3 simulation results show that the reduction from the P1dB point to 6 dB is almost the same as resistor bias. Fig. 6 shows that the output power of the third order inter modulation is 37 dBm. Fig. 7 shows the system simulation of ACPR and EVM test using an IEEE 802.16e OFDM modulation signal. The

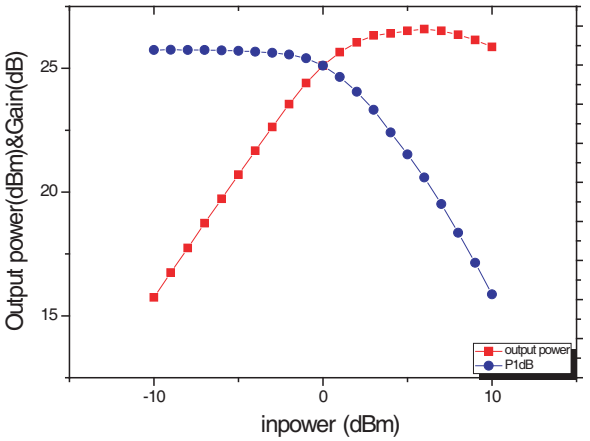

Figure 3: Simulation results of linear gain and output power.

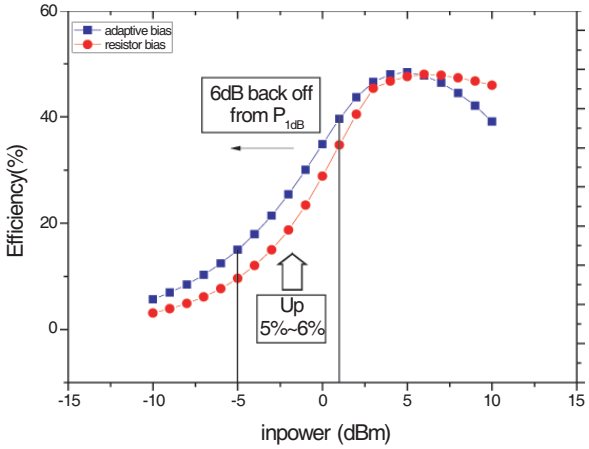

Figure 4: Simulation result of PAE and compare to the result by resistor bias.

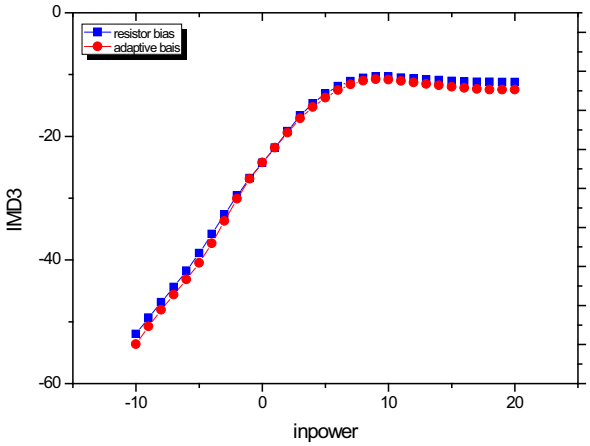

Figure 5: Simulation result of IMD and compare to the result by resistor bias.

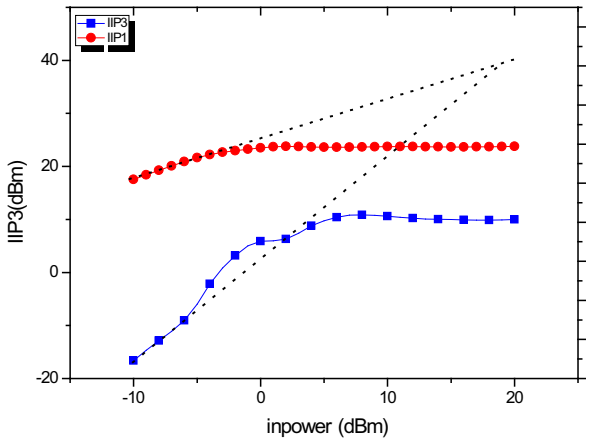

Figure 6: Simulation of third order inter modulation.

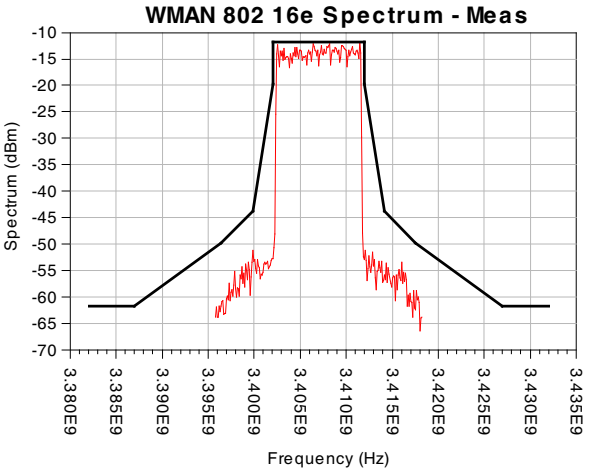

Figure 7: ACPR and EVM simulation uses using an IEEE 802.16e OFDM modulation signal.

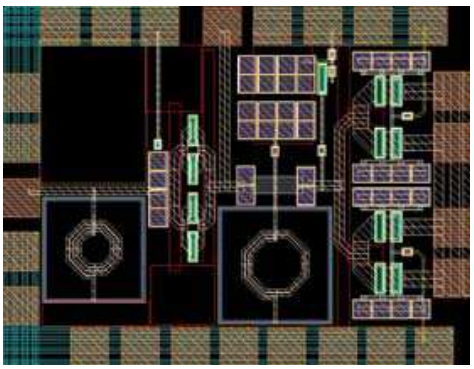

Figure 8: Layout of the proposed PA (1 mm * 0.75 mm).

output power of 3.5 GHz at EVM < -30 dB is 19.5 dBm (6 dB back-off). Table 1 summarizes these simulation results and compares them to those of previous PA designs.

Figure 8 shows the layout of the proposed circuit, in which the transistor gate and drain lines are placed on Metal 6, and ground plane is introduced on the Metal 1 to shield the RF signal lines from substrate coupling. The total chip size is 0.75 mm^2.

4. CONCLUSIONS

The proposed power amplifier was simulated in ADS and the TSMC 0.18 μm CMOS processes. The adaptive bias successfully improved the PAE of the power amplifier without sacrificing the linearity. The average efficiency improvement was nearly 5%. The maxima efficiency achieved 39%, and the PAE remains 15% after 6 dB back off.

ACKNOWLEDGMENT

The authors would like to thank the Chip Implementation Center (CIC) of the National Science Council, Taiwan, R.O.C., for supporting the TSMC 0.18 μm 1P6M CMOS process.

REFERENCES

1. Masse, C., "A 2.4 GHz direct conversion transmitter for Wimax applications," *IEEE Radio Frequency Integrated Circuits (RFIC) Symposium*, San Francisco, CA, June 2006.
2. Ochiai, H. and H. Imai, "On the distribution of the peak-to-average power ratio in OFDM signals," *IEEE. Trans. Commun.*, Vol. 49, No. 2, 282–289, Feb. 2001.
3. Chen, Y.-J. E., C.-Y. Liu, T.-N. Luo, and D. Heo,"A high efficient CMOS RF power amplifier with automatic adaptive bias control," *IEEE Microwave and Wireless Components Letters*, Vol. 16, No. 11, 615–617, Nov. 2006.
4. An, K. H., D. H. Lee, O. Lee, H. Kim, J. Han, W. Kim, C.-H. Lee, H. Kim, and J. Laskar, "A 2.4 GHz fully integrated linear CMOS power amplifier with discrete power control," *IEEE Microwave and Wireless Components Letters*, Vol. 19, No. 7, 479–481, Jul. 2009.
5. Huang, C.-C. and W.-C. Lin, "A compact high-efficiency CMOS power amplifier with built-in linearizer," *IEEE Microwave and Wireless Components Letters*, Vol. 19, No. 9, 587–589, Sept. 2009.
6. Shinjo, S., K. Totani, H. Tokunaga, K. Mori, and N. Suematsu, "Pre-distortion linearizer using self base bias control circuit," *Asia-Pacific Microwave Conference 2006, APMC 2006*, 879–882, Dec. 12–15, 2006.
7. Cui, X., P. Roblin, J. Lee, W. R. Liou, Y. G. Kim, "A 3.5 GHz CMOS Doherty power amplifier with integrated diode linearizer targeted for WiMax applications," *50th Midwest Symposium on Circuits and Systems 2007, MWSCAS 2007*, 465–468, Aug. 5–8, 2007.

A Novel Four-way Ka-band Power Divider/Combiner Based on Finline

Yi-Hong Zhou, **Jia-Yin Li**, **and Hai-Yang Wang**
School of Physical Electronics, University of Electronic Science and Technology of China
Chengdu 610054, China

Abstract— In this paper, a resonant four-way divider/combiner based on finline is presented. This divider/combiner is composed of four units coupling power from finline to microstrip lines. Coupling is achieved through the microstrip probe on the top side of the dielectric substrate with the finline on the bottom side. The advantages of this divider/combiner are ease of fabrication, efficient heat sinking of MMIC, as well as its potential for high power-combining efficiency. Experiments on the four-way passive divider/combiner back-to-back design demonstrate a minimum overall insertion loss of 0.96 dB at 35.2 GHz, and the inserting loss in 34–36 GHz band is less than 1.8 dB.

1. INTRODUCTION

With the rapid advancements of military and commercial communications systems in the last decade, the demand for high-power solid-state power amplifiers with high efficiency and wide bandwidth has greatly increased. For microwave and millimeter-wave systems, output power from an individual solid-state device is often not enough, therefore, it is necessary to combine power from multiple devices to obtain the desired power levels. Several techniques, such as quasi-optical and waveguide-based spatial power-combining approaches, have been proposed to address this issue [1–5]. The power-combining technology using slotted-waveguide has also been proposed [6–11]. This slotted-waveguide structure has several advantages, such as high efficiency, low profile, low complexity, and efficient heat sinking for active devices. In [7], a waveguide power combiner at X-band was demonstrated with a power-combining efficiency of 88%.

In this paper, based on finline, a novel four-way Ka-band power divider/combiner designed in 34–36 GHz band is presented, as shown in Figure 1. In this design, the finline, rather than the waveguide, is employed as main transmission line, and the microstrip probe placed above the finline, rather than the slot located at the top wall of the waveguide, is used to couple the RF energy between finline and microstrip. The simulated and measured results are presented.

2. DESIGN

The power-combining technique herein is based on a resonant finline configuration. As illustrated in Figure 1, the circuit consists of input and output finlines coupled to microstrips through microstrip probes on the top side of the dielectric substrate with finline on the bottom side. The input power is divided into 4 ways through identical microstrip probes. These probes are separated by half-guide wavelength of finline to achieve an equal power division. The input and output ports of the finline divider/combiner can either be on the same or the opposite sides of the finlines, with the other two finline ports terminated with shorts. This offers more flexibility in feeding the circuits without degenerating the performance.

Several finline to microstrip transitions have been proposed [12]. Among these transitions, the transition using uniform $\lambda/4$ open microstrip and uniform $\lambda/4$ finline is usually employed in the planar circuit. However, due to the great difference between the characteristic impedance of the two types of transmission line, the impedance matching between them is difficult. Furthermore, the coupling coefficient is too high to divide the power at each microstrip ports equally. So this type transition must be change to meet the demand for equal power division. As shown in Figure 2, the microstrip probe is employed to coupling power from finline to microstrip. This probe consists of microstrip probe placed above the finline and high impedance matching microstrip inserted between the probe and the standard 50 Ω microstrip line. The coupling coefficient is determined by the probe offset, probe length and probe characteristic impedance. The resonant frequency of the divider/combiner is dictated by the periodicity of the probes.

The analysis of the entire multiple ports' dividing/combining structure can be performed using full-wave electromagnetic (EM) simulations, but this approach is very time consuming. Since all finline-to-microstrip coupling units are identical, one can consider a single finline to microstrip

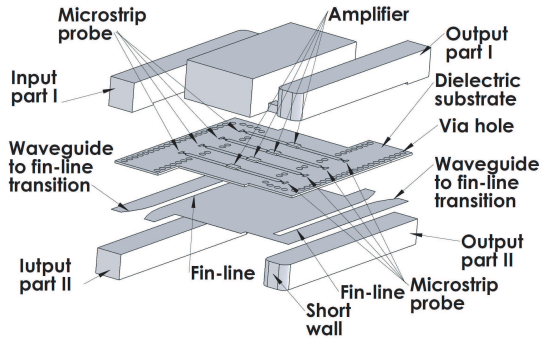

Figure 1: Configuration of four-way power-combining divider/combiner using fin-line.

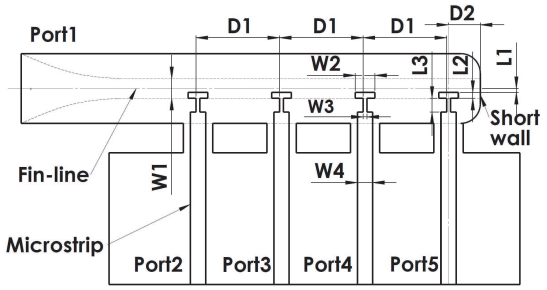

Figure 2: Geometry of the four-way dividing/combining structure and its port numbering.

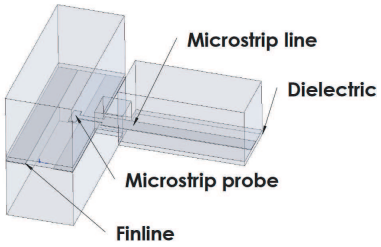

Figure 3: Single finline to microstrip transition.

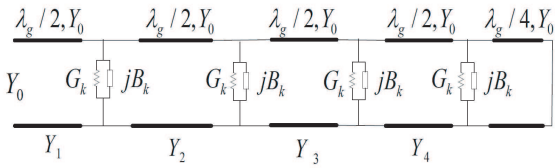

Figure 4: Equivalent circuit of a four-way resonant power-divider structure.

transition [see Figure 3]. As shown in Figure 4, the microstrip probe is modeled as a shunt element along a transmission line. The conductance G_k and susceptance B_k represent the discontinuity due to the probe. Y_0 is the characteristic admittance for the finline. All adjacent probes are spaced approximately one-half guide wavelength apart, and a short circuit placed $\lambda_g/4$ beyond the last probe presents an open circuit to the last probe. Assuming that the coupling between the adjacent probe and the finline losses are negligible, the admittance looking into the divider is $4 \times (G_k + jB_k)$. To achieve an equal power division, the probe conductance G_k must be $Y_0/4$.

As shown in Figure 3, to terminate the finline, a load is placed half wavelength away from the center of the probe. The load is equal to the characteristic wave impedance of the finline. The power is coupled to microstrip through the probe, and the $50\,\Omega$ microstrip line is also terminated by its characteristic impedance. The admittance G_k of the single probe can then be extracted from the reflection coefficient seen at the input port of the finline. The probe admittance is a function of the probe offset, probe length, probe characteristic impedance and dielectric constant of the substrate. Subsequently, an four-way finline divider was designed.

3. SIMULATED AND EXPERIMENT RESULTS

After optimization using Ansoft HFSS, the accurate dimensions and S-parameters of four-way finline divider were obtained. Figure 5 shows the E-field distribution of the overall finline divider/combiner. The dimensions of the finline divider are shown in Table 1.

Table 1: Dimensions of four-way finline divider/combiner (Unit: mm).

W_1	W_2	W_3	W_4	L_1	L_2	L_3	D_1	D_2
1	1	0.2	0.78	0.2	0.3	0.7	4.27	1.625

For the proposed power divider/combiner, Rogers 5880 with a dielectric constant of 2.2 and thickness of 0.254 mm was used as the substrate for the microstrip line. As shown in Figure 6(a), equal power division (-6.2 ± 0.3 dB) is achieved at the microstrip port 2, 3, 4 and 5 in 34–36 GHz band, which is very close to the expected value of -6 dB. Also, the phases of the coupling coefficients are found to be uniform [see Figure 6(b)]. A passive divider/combiner was built by placing two

identical circuits back to back. Figure 7 shows the simulated and measured results of the passive power divider/combiner. The measured results show a good agreement with the simulated results. The measured minimum insertion loss of 0.96 dB was achieved with a return loss of 29 dB [see Figure 7] at 35.2 GHz, which indicates a maximum expected power-combining efficiency of 89.5% for the combining circuit. The measured maximum insertion loss is 1.8 dB at 36 GHz, corresponding to a power-combining efficiency of 80%. So the maximum expected power-combining efficiency is higher than 80% in 34–46 GHz band. The increased insertion loss compared with the simulation results is most likely due to the fabrication errors and the slight mismatches in each branch's phase.

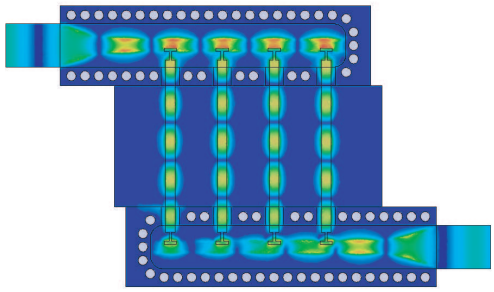

Figure 5: E-field distribution of four-way finline divider/combiner.

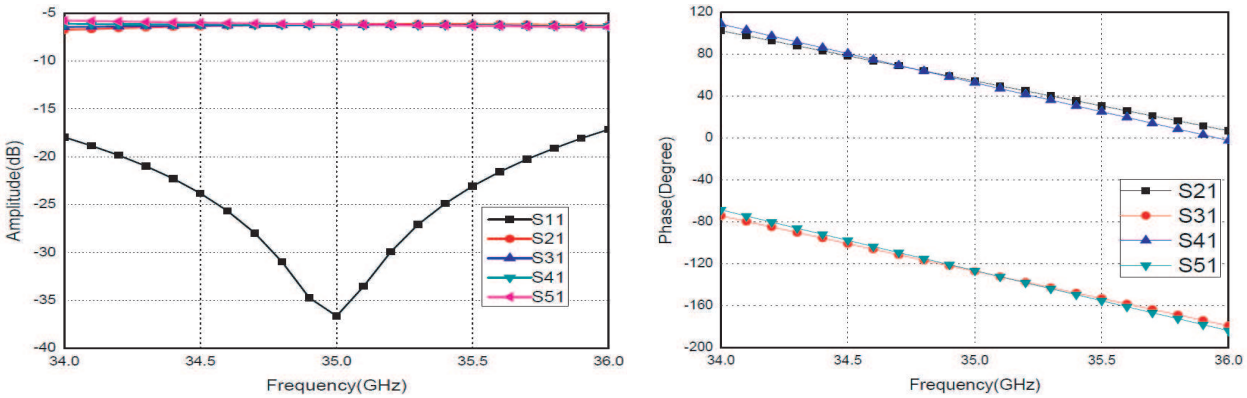

(a) (b)

Figure 6: Simulated results of the four-way power divider/combiner. (a) Magnitude, (b) phase.

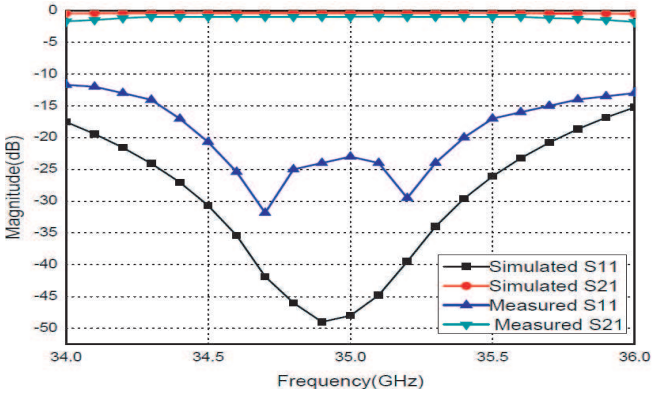

Figure 7: Simulated and measured results of the passive power divider and combiner placed back to back.

4. CONCLUSION

The design of a novel four-way finline power divider/combiner at Ka-band is presented in this paper. Experiments on the four-way passive divider/combiner back-to-back design demonstrate a minimum insertion loss of 0.96 dB at 35.2 GHz, and the inserting loss in 34–36 GHz band is less than 1.8 dB. As well as low insertion loss, this passive power divider/combiner offers an efficient heat sinking structure for the design of solid-state power amplifiers.

REFERENCES

1. Hollung, S., A. E. Cox, and Z. B. Popovic, "A bi-directional quasi-optical lens amplifier," *IEEE Trans. Microwave Theory Tech.*, Vol. 45, 2352–2357, Dec. 1997.
2. Ortiz, S., J. Hubert, L. Mirth, E. Schlech, and A. Mortazawi, "A high-power Ka-band quasi-optical amplifier array," *IEEE Trans. Microwave Theory Tech.*, Vol. 50, 487–494, Feb. 2002.
3. Sanada, A., K. Fukui, and S. Nogi, "A waveguide type power divider/combiner of double-ladder multi-port structure," *IEEE Trans. Microwave Theory Tech.*, Vol. 42, 1154–1161, Jul. 1994.
4. Cheng, N.-S., P. Jia, D. B. Rensch, and R. A. York, "A 120-W X-band spatially combined solid-state amplifier," *IEEE Trans. Microwave Theory Tech.*, Vol. 47, 2557–2561, Dec. 1999.
5. Jeong, J., Y. Kwon, S. Lee, C. Cheon, and E. A. Sovero, "1.6- and 3.3-W power-amplifier modules at 24 GHz using waveguide-based power-combining structures," *IEEE Trans. Microwave Theory Tech.*, Vol. 48, 2700–2708, Dec. 2000.
6. Bashirullah, R. and A. Mortazawi, "A slotted waveguide quasi-optical power amplifier," *IEEE MTT-S Int. Microw. Symp. Dig.*, 671–674, 1999.
7. Bashirullah, R. and A. Mortazawi, "A slotted-waveguide power amplifier for spatial power-combining applications," *IEEE Trans. Microwave Theory Tech.*, Vol. 48, 1142–1147, Jul. 2000.
8. Jiang, X., L. Liu, S. C. Ortiz, R. Bashirullah, and A. Mortazawi, "A Ka-band power amplifier based on a low-profile slotted-waveguide power-combining/dividing circuit," *IEEE Trans. Microwave Theory Tech.*, Vol. 51, 144–147, Jan. 2003.
9. Jiang, X., S. C. Ortiz, and A. Mortazawi, "A ka-band power amplifier based on the traveling-wave power-dividing/combining slotted-waveguide circuit," *IEEE Trans. Microwave Theory Tech.*, Vol. 52, 633–639, Feb. 2004.
10. Jiang, X., S. C. Ortiz, and A. Mortazawi, "A novel ka-band 1 to 8 power divider/combiner," *IEEE MTT-S Int. Microw. Symp. Dig.*, 35–38, 2001.
11. Eswarappa, C., T. Hongsmatip, N. Kinayman, R. Anderson, and B. Ziegner, "A compact millimeter-wave slotted-waveguide spatial array power combiner," *IEEE MTT-S Int. Microw. Symp. Dig.*, 1439–1442, 2003.
12. Shuppert, B., "Microstrip/slotline transitions: Modeling and experimental investigation," *IEEE Trans. Microwave Theory Tech.*, Vol. 36, 1272–1282, Aug. 1988.

The Design a LNA of 3.1∼10.6 GHz UWB Receive System

Chao-Hsu Chen and Jeng-Rern Yang
Microwave Laboratory, Department of Communication Engineering, Yuan Ze University
No. 135 Yuan-Dong Rd., Jhong LI City, Taoyuan County 320, Taiwan, R.O.C.

Abstract— The TSMC 0.18 µm CMOS Process is used to design a 3.1 GHz∼10.6 GHz Low Noise Amplifier for UWB system. The circuit adopts the Current Reuse structure and resistive feedback technology. The measure results demonstrate the following performances of the design: The total power consumption is 14.4 mW under 1.8 V supply voltage, the forward gain is 9.7 ± 1.1 dB for 3.1∼10.6 GHz wideband frequency, the noise figure is 3.4∼3.84 dB, and the P1dB is $-15 \sim 10.5$ dBm. The chip area is $0.78\,\text{mm} * 0.82\,\text{mm}$.

1. INTRODUCTION

In the field of wireless communications, demand for high transmission rates have continually increased even while bandwidth has remained limited. Many new technologies are constantly being implemented in real life. Ultra-Wideband (UWB) wireless technologies are a wireless communications method. The Federal Communications Commission's (FCC) definition of UWB is: UWB systems with central frequencies higher than 2.5 GHz must have at least 500 MHz of −10 dB bandwidth, while UWB systems with central frequencies lower than 2.5 GHz must have at least 20% fractional bandwidth; the frequency range used is 3.1 GHz∼10.6 GHz.

Low-noise amplifiers constitute an important component in wireless communications receivers. Lownoise amplifiers must have low noise indices, high gain, low power, and high linearity in order for receivers to have good reception capabilities.

2. MAIN CONTENT

Traditional current reuse frameworks are as shown in Figure 1. In a DC current operating mode, this framework is as shown in Figure 2; M1 and M2 are cascode amplifiers. In a small signal mode, as in Figure 3, Lm and C2 will divide M1 and M2, forming a two common-source amplifier series structure. In this way, a common current can be achieved to reduce power consumption. However, small signals are amplified over two grades; using this framework does not require connecting a second-grade amplifier in order to achieve a two-grade amplification effect. This setup constitutes a low-power consumption, high-gain approach.

The circuit framework designed in this study, as shown in Figure 4, is based on using a current re-use framework and electrical impedance and capacitance return to achieve a UWB low-noise amplifier. This circuit adjusts the parameters of L1, C1, and R2 and selecting M1 in an appropriate

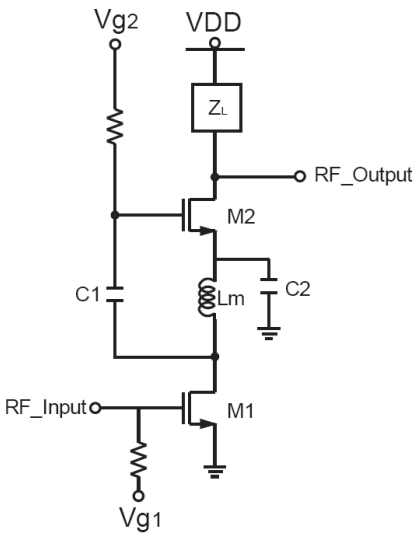

Figure 1: Traditional current reuse framework.

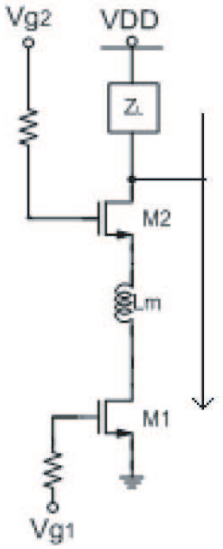

Figure 2: DC current operating mode.

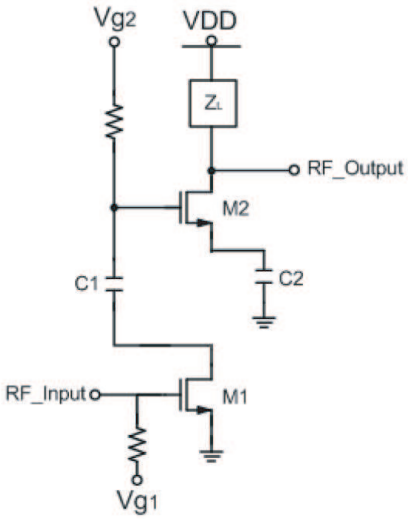

Figure 3: Small signal mode.

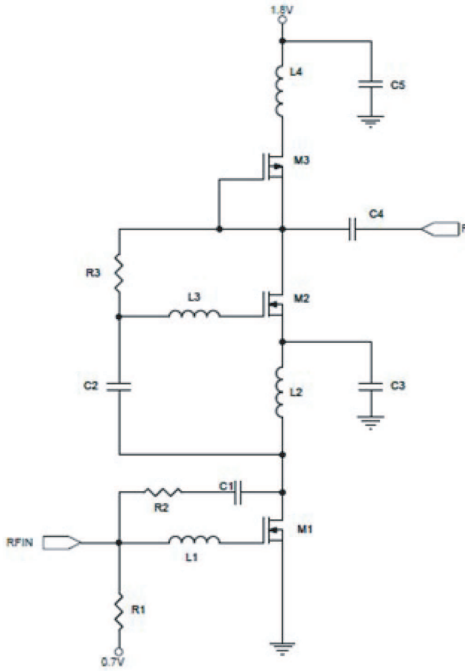

Figure 4: Circuit framework design.

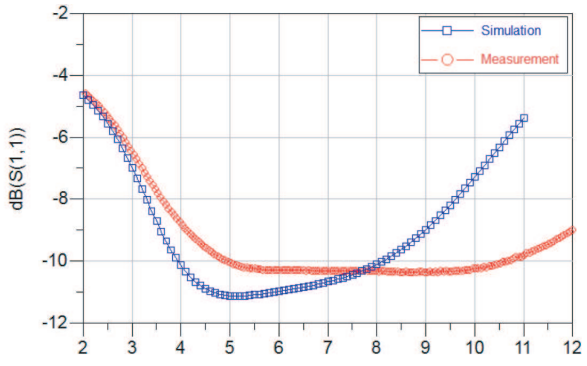

Figure 5: Input S parameter (dB).

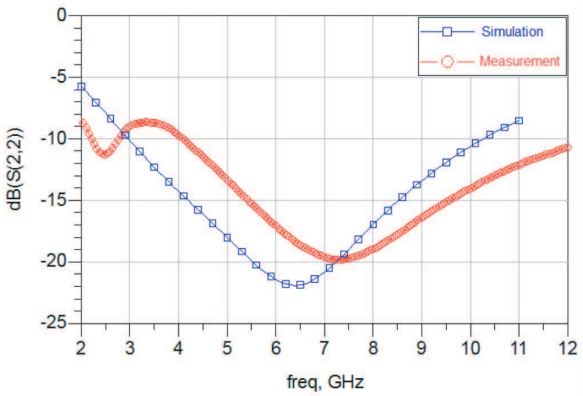

Figure 6: Output S parameter (dB).

width and bias to achieve good input impedance in 3.1∼10.6 GHz channels and to obtain a minimized noise index. Good impedance matching is obtained through adjusting the RLC harmonic vibration circuit (C4, L4 and M3 active loading). In addition, L3 can to raise the high-frequency gain of M2; a good gain flatness can be obtained in the operating frequency range in this way. In order for the circuit to have lower power consumption, a 1.8 V power source and a 0.7 V bias; overall power consumption was only 14.4 mW.

3. MEASURED RESULTS

As the design of this circuit was applied to a UWB (3.1∼10.6 GHz) receiver system, measure results are for the 3.1∼10.6 GHz range. The results for the various parameters of the designed circuit are shown below.

S_{11} (Figure 5) was less than −6.7 dB in the operating frequency range. S_{22} (Figure 6) was less than −8.5 dB in the required frequency range. It can be seen from Figure 7 that the gain within 3.1∼10.6 GHz is approximately 9.7 ± 1.1 dB. The NF (Figure 9) with in the operating frequency range was 3.4∼3.84 dB.

It can be seen from Table 1 that, compared to other studies, we indeed reached our goals in this study: low noise index, high gain flatness and low power consumption.

The chip microphotograph is shown in Figure 10, the total area was approximately $0.78 \times 0.82\,\text{mm}^2$.

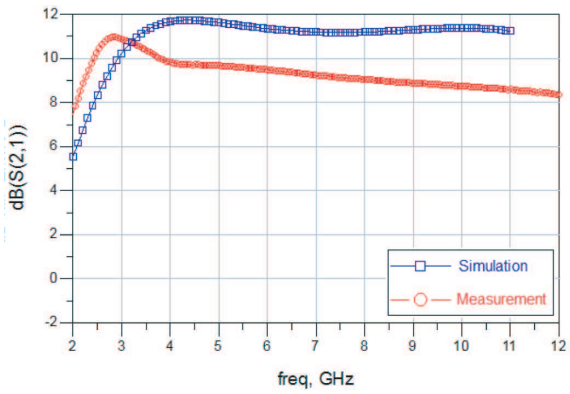

Figure 7: Gain (dB).

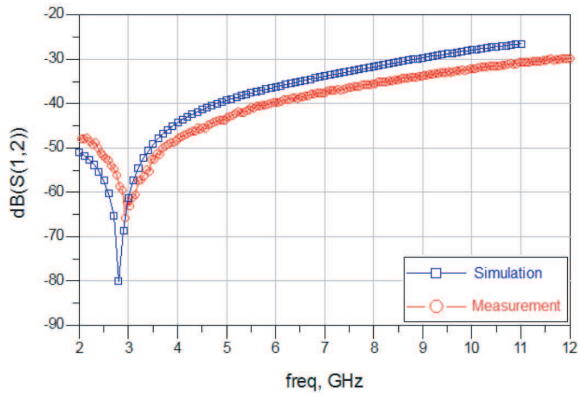

Figure 8: Isolation S_{12} (dB).

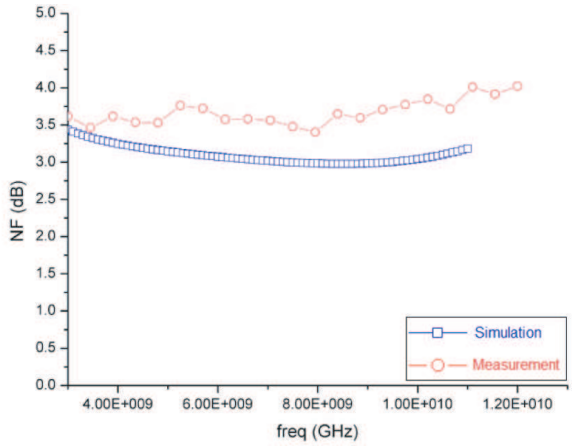

Figure 9: NF (dB).

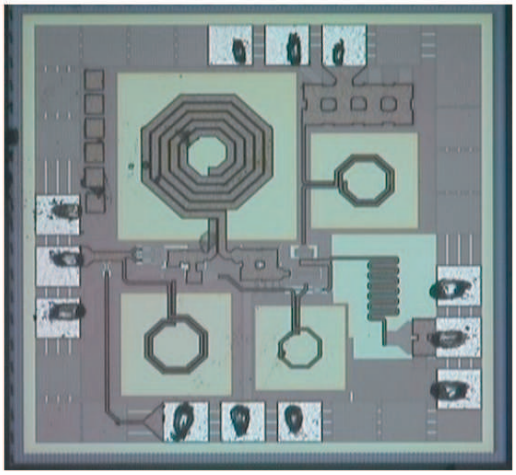

Figure 10: Microphotograph of UWB LNA.

Table 1.

	This Work (0.18 µm CMOS)	[1] (0.18 µm CMOS)	[2] (0.18 µm CMOS)
Frequency band (GHz)	3.1∼10.6	3.1∼10.6	3.1∼10.6
S_{11} (dB)	<-6.7	<10	<-10
S_{22} (dB)	<-8.5	<10	<-7
S_{21} (dB)	9.7 ± 1.1dB	9.7	10∼21.5
S_{12} (dB)	<-31	<-35	NA
NF (dB)	3.4∼3.84	4.5∼5.1	4∼6.2
P1dB (dBm)	−13 @ 7 GHz	−16	NA
IIP3 (dBm)	−3.5 @ 7 GHz	−6.2	−10.8 @ 5.5 GHz
Chip area (mm^2)	0.639	0.59	1.2
Power consumption (mW)	14.4	20	26

ACKNOWLEDGMENT

We thank National Laboratory Chip Implementation Center for providing helping to provide TSMC 0.18 µm 1P6M CMOS production process.

REFERENCES

1. Liao, C.-F. and S.-I. Liu, "A broadband noise-canceling CMOS LNA for 3.1–10.6-GHz UWB receiver," *IEEE Custom Integrated Circuits Conference*, 161–164, Sept. 18–21, 2005.

2. Gao, Y., Y. Zheng, and B.-L. Ooi, "A 0.18-μm CMOS UWB LNA with 5 GHz interference rejection," *2007 IEEE Radio Frequency Integrated Circuits (RFIC) Symposium*, 2007.
3. Wang, R.-L., M.-C. Lin, C.-F. Yang, and C.-C. Lin, "A 1 V 3.1–10.6 GHz full-band cascoded uwb lna with resistive feedback," *IEEE Conference*, 1021–1023, Dec. 20–22, 2007.
4. Lin, Y.-J., S. S. H. Hsu, J.-D. Jin, and C. Y. Chan, "A 3.1–10.6 GHz ultra-wideband CMOS low noise amplifier with current-reused technique," *IEEE Microwave and Wireless Components Letters*, Vol. 17, No. 3, 232–234, Mar. 2007.
5. Chen, K.-H., J.-H. Lu, B.-J. Chen, and S.-I. Liu, "An ultrawide-band 0.4–10-GHz LNA in 0.18-μm CMOS," *IEEE Transactions on Circuits and Systems. II, Express Briefs*, Vol. 54, No. 3, 217–221, Mar. 2007,

Design of Fully Integrated RF Power Amplifier for WLAN Applications

Cheng-Tang Liu and Jeng-Rern Yang
Microwave Laboratory, Department of Communication Engineering, Yuan Ze University
No. 135, Yuan-Dong Rd., Jhongli City, Taoyuan Country 320, Taiwan, R.O.C.

Abstract— To meet the demands of new generation wireless networks and the future requirements of wireless communications, we present the design of a fully integrated RF power amplifier for WLAN applications implemented in 0.18 µm CMOS technology. The proposed inductor improves the current density, increases the Q factor, and changes the output matching network to reduce the chip area. Operated with a 3.6 V supply, the characteristics of the output power were: P1dB = 22.2 dBm, linear gain = 20.1 dB, and power added efficiency (PAE) = 21.2%. The power amplifier draws 0.846 W with a chip size of 1.38 mm^2.

1. INTRODUCTION

Designing a fully integrated power amplifier (PA) in deep sub-micron CMOS technology with high output power (i.e., over 20 dBm) and reasonable efficiency is a difficult challenge. The integration and development of wireless local area networks (WLAN) is an important focus for communication industries and designing the RF circuit in a low cost 0.18 standard CMOS process is a good choice.

The PA is the most important block in the traditional transmitter system, which typically uses an off chip design. This produces such a large chip area that it is unpractical. The process is complicated, that is not easy to take load-pull and measure on PCB. For this reason, we want to design a fully integrated RF power amplifier.

The challenges are how to integrate an RF circuit in a finite chip area and provide high output power. We want to devise an inductor to reduce current density, improve its Q factor, and change the output matching network to reduce the chip area requirements.

This paper is organized as follows. Section 2 briefly introduces the architecture of the RF transmitter. Section 3 discusses the simulations. Section 4 provides the conclusion.

2. CIRCUIT DESIGN AND CONFIGURATION

2.1. Design of a Fully Integrated RF Power Amplifier

Figure 1 shows the schematic of a fully integrated Class AB RF power amplifier.

2.2. Improving the Output Matching Network

Consider the choke (L_3) inductor. The PA requires a high inductance, which uses a great deal of chip area, making it difficult to realize a fully integrated PA. Adding C_5 and L_5 to the drain of M_2, as shown in Fig. 2(a), can decrease the size of the inductor and increase its Q factor.

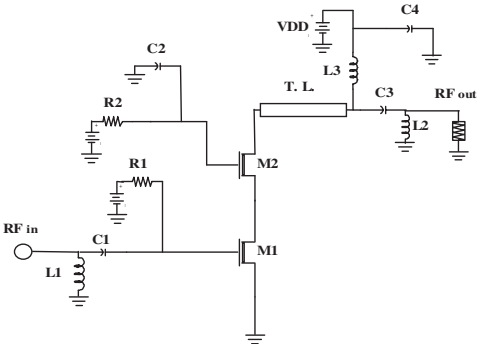

Figure 1. Architecture of the RF transmitter.

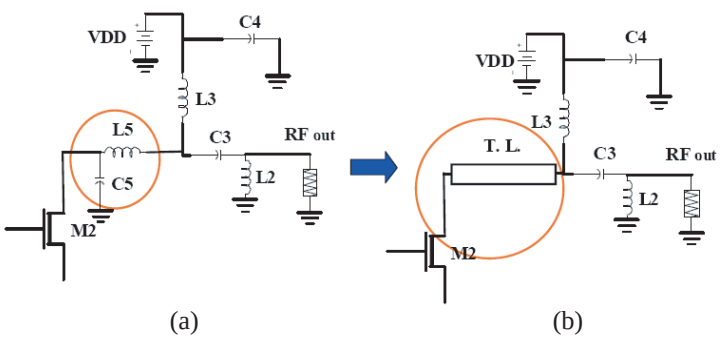

Figure 2.

This decrease in the value of inductor (L_3) by adding C_5 and L_5 is helpful, but the area required for L_5 presents another problem. To solve this, we connect the drain of M_2 to a transmission line and use its LC characteristics to reduce the required inductance of L_3, as shown in Fig. 2(b), making it possible to create a fully integrated RF power amplifier.

2.3. Design of the Proposed Inductor

A traditional PA usually uses the method of bond wire, it combines transistor drains with PADs to distribute the current and reduce the current density as shown in Fig. 3.

To use L_3 in the chip, we must be careful about the current density and chip area. For DC's analysis as Fig. 5 shows, L_3 is a component of the DC network. The output matching network consists of C_3, L_2, and L_3 for small signal network analysis. That is to say, the Q factor of inductor L_3 affects the performance of the whole circuit. What's more, the current density depends on the coil width, but it hasn't appropriate inductor's model by TSMC offers. Therefore, I want to design an inductor to satisfy the demand for current density as shown in Fig. 4 and provide full integration. Using a Taiwan Semiconductor Manufacturing Company (TSMC) model and using an Agilent ADS simulator to calculate the value of the inductor, we used the SONET simulator to design the improved inductor and simulate the whole circuit.

We find that the Q factor of the proposed inductor is higher than that in the TSMC module for the same inductor value, which is helpful in promoting the circuit performance. The simulated comparison between the TSMC module and the proposed inductor in Figs. 8–13, (Color: blue, TSMC module; red, proposed inductor).

The simulated comparison between the TSMC module and the proposed inductor.

3. SIMULATION

All simulation results for this circuit design are shown as Figs. 14–20.

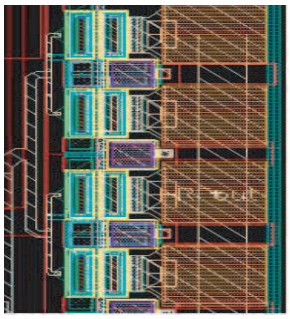

Figure 3.

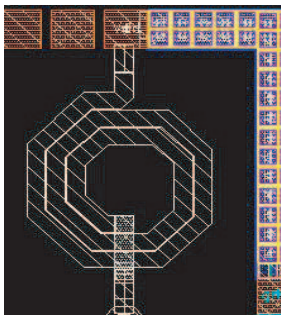

Figure 4.

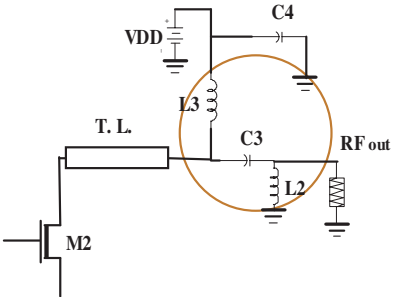

Figure 5.

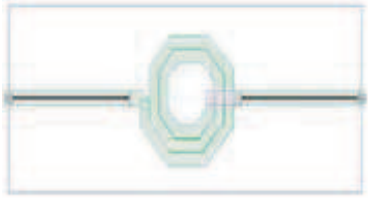

Figure 6.

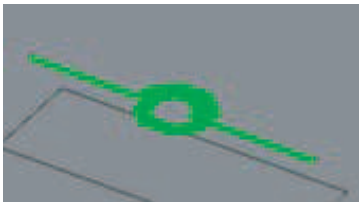

Figure 7.

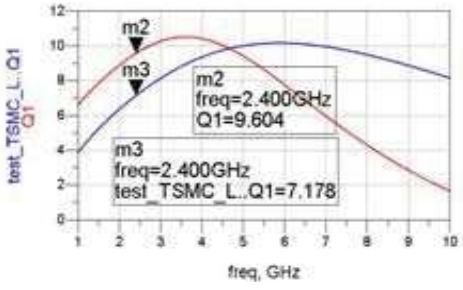

Figure 8. Comparison of Q factors.

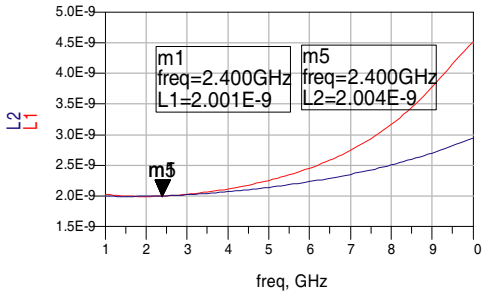

Figure 9. Comparison of inductor values.

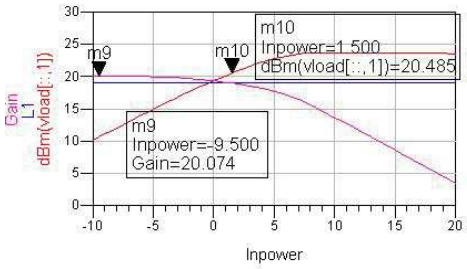

Figure 10. TSMC module.

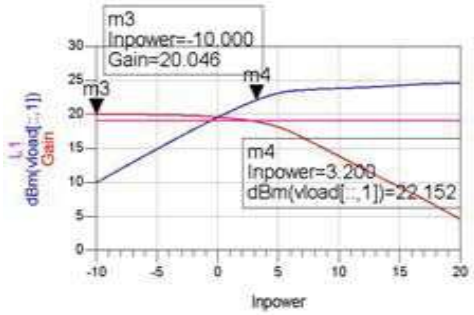

Figure 11. The proposed inductor.

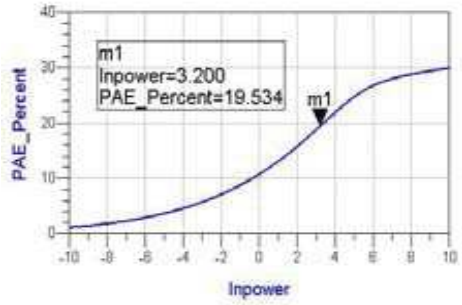

Figure 12. The TSMC module.

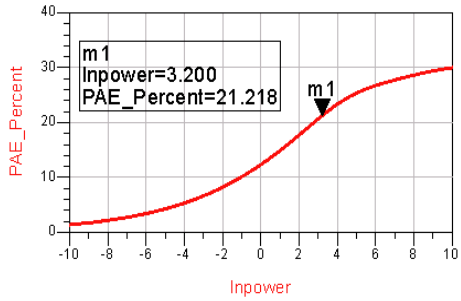

Figure 13. The proposed inductor.

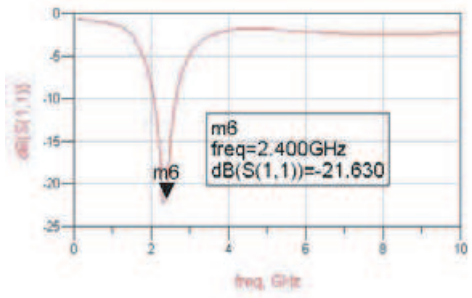

Figure 14. S-parameter (S_{11}) is -21.63 dB at 2.4 GHz.

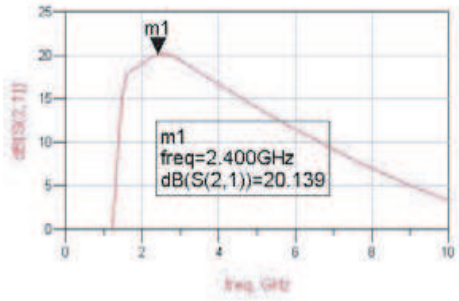

Figure 15. S-parameter (S_{21}) is 20.14 dB at 2.4 GHz.

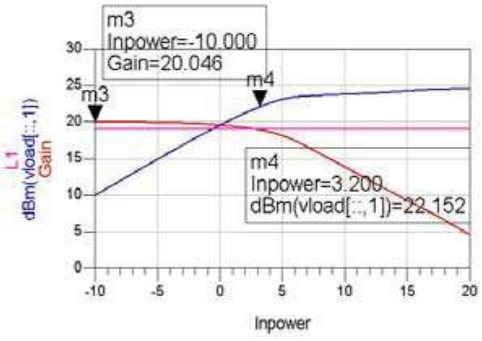

Figure 16. P1dB vs. Gain, P1dB = 22.2 dBm with linear gain = 20.1 dB.

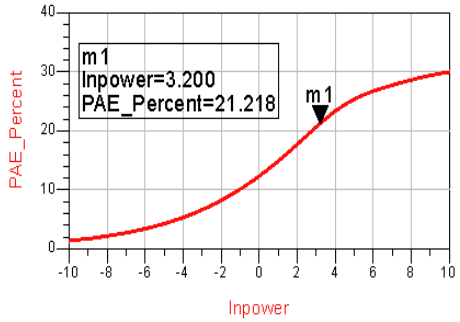

Figure 17. PAE @ 1 dB, PAE is 21.22% at 2.4 GHz.

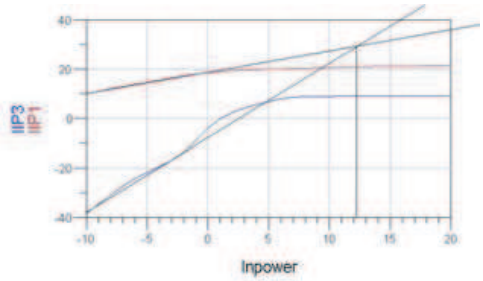

Figure 18. IIP3 is 12.3 at 2.4 GHz.

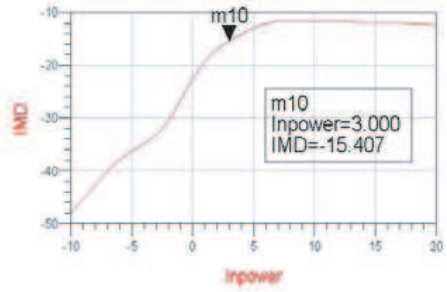

Figure 19. IMD3 (3rd inter-modulation) is −15.41 at 2.4 GHz, IM_dBc = dBm (Vload, {2, 1}) − dBm (Vload, {1, 0}).

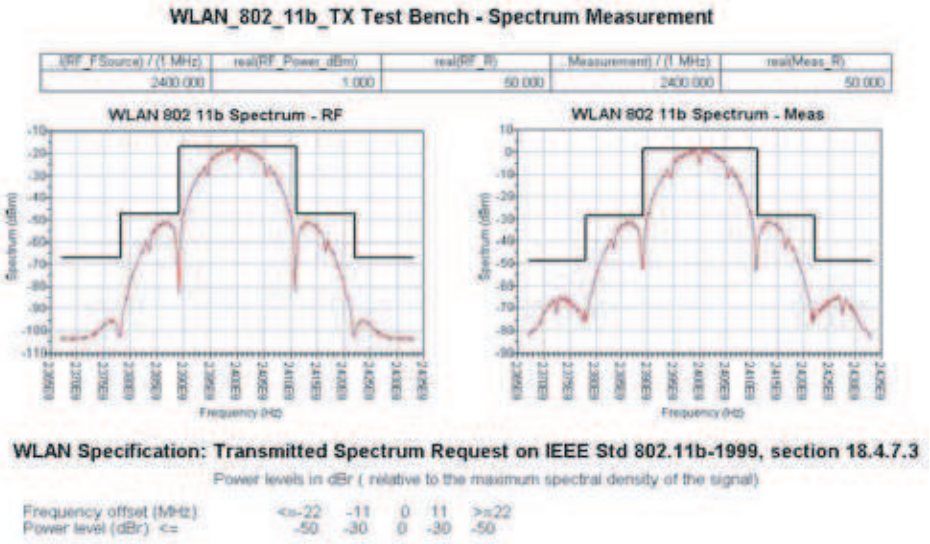

Figure 20. Spectrum @ 2.4 GHz, spectrum with mask Pin = 0.2 dBm (back-off 3 dB). The circuit design conforms to the 802.11 b communication protocol.

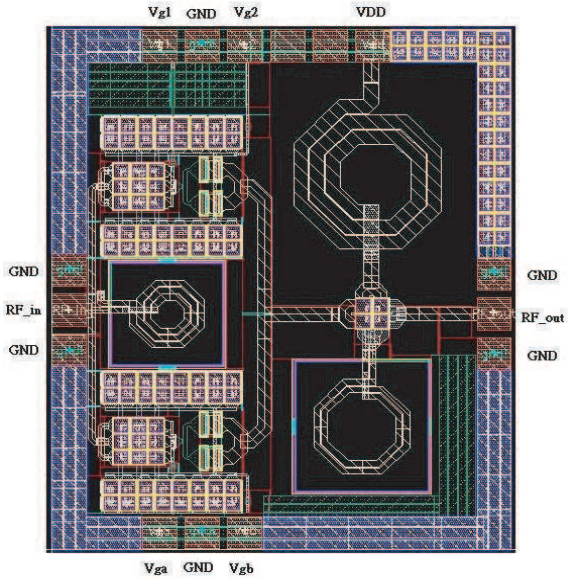

Figure 21. Layout of the fully integrated PA ($1.08 \times 1.28\,\mathrm{mm}^2$).

Table 1.

	[8]	[12]	[10]	This Work
Technology	0.25 CMOS	0.18 CMOS	0.18 CMOS	0.18 CMOS
Operation Frequency	2.4 G	2.4 G	2.4 G	2.4 G
Gain [dB] (numbers of cascade stage)	11.2 (2)	12 (2)	19 (1)	20.1 (1)
Output Power @ P1dB [dBm]	20	21.5	20.2	22.2
PAE @ P1dB	12	14	21	21.2
Area	N/A	2.76 mm^2	1.53 mm^2	1.38 mm^2
Note	Off-Chip	Fully-Integrated	Fully-Integrated	Fully-Integrated

4. CONCLUSION

This paper discusses WLAN applications, focusing on a proposed inductor that improves the current density, increases the Q factor, and changes the output matching network to reduce the required chip area. Table 1 summarizes the previously published RF Power Amplifier for WLAN applications. All the circuits in this study use the TSMC 0.18 µm 1P6M CMOS process.

ACKNOWLEDGMENT

The authors would like to thank the Chip Implementation Center (CIC) of the National Science Council, Taiwan, R.O.C., for supporting the TSMC 0.18 µm 1P6M CMOS process.

REFERENCES

1. Oka, T., M. Hasegawa, M. Hirata, Y. Ama, Y. Ishimaru, H. Kawamura, and K. Sakuno, "A high-power low-distortion GaAs HBT power amplifier for mobile terminals used in broadband wireless applications," *IEEE Journal of Solid-state Circuits*, Vol. 42, No. 10, Oct. 2007.
2. Lee, O., K. S. Yang, K. H. An, Y. Kim, H. Kim, J. J. Chang, W. Woo, C.-H. Lee, and J. Laskar, "A 1.8-GHz 2-Watt fully integrated CMOS push-pull parallel-combined power amplifier design," *IEEE*, 2007.
3. Kim, J. H., K. Y. Kim, Y. H. Park, Y. K. Chung, and C. S. Park, "A 2.4 GHz bipolar power amplifier with integrated diode linearizer for WLAN IEEE 802.11 b/g application," *IEEE*, 2006.
4. Oh, H.-S., C.-S. Kim, H.-K. Yu, and C.-K. Kim, "A fully-integrated +23-dBm CMOS triple cascode linear power amplifier with inner-parallel power control scheme," *IEEE Radio Frequency Integrated Circuits (RFIC) Symposium*, 2006.
5. Jung, J., U. Kim, J. Kim, K. Kang, and Y. Kwon, "A new 'series-type' doherty amplifier for miniaturization," *IEEE RFIC Symp. Dig.*, 259–262, 2005.
6. Komijani, A. and A. Hajimiri, "A 24 GHz, +14.5 dBm fullyintegrated power amplifier in 0.18 m CMOS," *Proc. IEEE Custom Integrated Circuits Conf.*, 561–564, Oct. 2004.
7. Cui, X., P. Roblin, J. Lee, W. R. Liou, and Y. Kim, "A 3.5 GHz CMOS doherty power amplifier with integrated diode linearizer targeted for WiMax applications," *IEEE MWSCAS/NEWCAS 2007*, Montreal, Canada, Aug. 2007.
8. Yen, C.-C. and H.-R. Chuang, "A 0.25-µm 20-dBm 2.4 GHz CMOS power amplifier with an integrated diode linearizer," *IEEE Microwave Wireless Comp. Lett.*, Vol. 13, 45–47, Feb. 2003.
9. Ding, Y. and R. Harjani, "A CMOS high efficiency +22 dBm linear power amplifier," *Proc. IEEE Custom Integrated Circuits Conf.*, 557–560, 2004.
10. Oh, H.-S., C.-S. Kim, H.-K. Yu, and C.-K. Kim, "A fully-integrated +23-dBm CMOS triple cascode linear power amplifier with inner-parallel power control scheme," 2006.
11. Wang, A., X. Guan, H. Feng, Q. Wu, R. Zhan, and L.-W. Yang, "A 2.4 GHz fully integrated class-A power ampifier in 0.35 µm SiGe BiCMOS technology," *IEEE*, 2005.
12. Yang, L.-Y., H.-S. Chen, and Y.-J. Emery Chen, "A 2.4 GHz fully integrated cascode-cascade CMOS doherty power amplifier," *IEEE*, Mar. 2008.

The Analysis and Design of High Power Millimeter Wave Pulse Detector for 2 mm Frequency Band

Guangqiang Wang[1], **Jianguo Wang**[2,3], **Xingzhou Wang**[2], **and Ruyu Fan**[1,2]

[1]Department of Engineering Physics, Tsinghua University, Beijing 100084, China
[2]Northwest Institute of Nuclear Technology, Xi'an 710024, China
[3]School of Electronics and Information Engineering, Xi'an Jiaotong University, Xi'an 710049, China

Abstract— The research progress of a high power millimeter wave pulse detector for 2 mm frequency band is presented here. This power detector, so-called resistive sensor, is composed of a 2 mm standard waveguide and a semiconductor sensing sample within it. At first, the principle of the detector is analyzed theoretically, and the sensitivity of the detector in the warm-electron region is derived. Then the structural parameters of the detector are calculated and optimized to make the frequency response flat over the waveguide frequency band. A three-dimensional finite difference time domain (FDTD) method is used here. The results show that, while the biased voltage on the detecting element is 10 V, the sensitivity of the optimized detector is about 6 V/kW with a fluctuation less than 27% in the frequency range 113–173 GHz, especially less than 9.8% in the frequency range 130–160 GHz. Compared with the diode detectors in 2 mm frequency band, the designed semiconductor detector shows better performance in pulse power measurement.

1. INTRODUCTION

Due to the potential applications in radar, communication and so on, the high power microwave (HPM) sources are developing toward millimeter wave region rapidly, and a lot of works in the generation of high power millimeter waves have been done in some laboratories all over the world [1]. For example, our research team successfully designed [2] and tested Q-band high power relativistic surface wave oscillator in recent years. Along with the developments of the sources, the power measurement techniques should be improved to be used for HPM pulses with higher frequency.

In general, the main method to measure the peak power of HPM pulses is to use the calibrated diode detectors or semiconductor detectors, namely resistive sensors. As the diodes have small breakdown voltages, the HPM pulses should be strongly attenuated, which leads to the decrease of the measurement accuracy. But the semiconductor detector , composed of a standard waveguide and a semiconductor sensing sample, can convert the pulse power as high as kW to a DC voltage pulse directly without any attenuation based on the hot-carrier effect in semiconductor under high electric field [3]. Power measurements of nanosecond pulses using it have highlighted its advantages in centimeter wave region [4, 5]. Also it is anticipated to have good performance for the lack of accurate attenuators in millimeter wave region, which has been proved in the frequency band as high as W-band until now [6].

In this paper, the research progress of a high power millimeter wave pulse detector for 2 mm frequency band in our laboratory is presented. Though the window size of the detector is very small ($1.651 \times 0.8255\,\mathrm{mm}^2$), the new structure of the sensing sample and the development of the microfabrication technology make its fabrication possible. This detector will be used in the pulse power measurements of our Q-band source.

2. PRINCIPLE OF THE DETECTOR

2.1. Hot-carrier Effect in Semiconductor [7]

When the electric field applied to the semiconductor is not very high, the current density J of the semiconductor is proportion to the magnitude of the electric field $|E|$, e.g., $J = \sigma|E|$. However, as the electric field increases up to about 10^3 V/cm, the deviation of the proportion relation is found in experiments. Lots of studies indicated that the change of mobilities of carriers in semiconductor under high electric field, which was called hot-carriers, was the reason of the deviation. The energy that carriers gained from electric field is so much that the average energy of carriers is higher than in thermal equilibrium, so is the effective temperature T of the carriers. Thus, the mobilities of the carriers decrease, while the resistance of semiconductor increases. This is the hot-carrier effect in semiconductor under high electric field.

Taking n-type silicon (n-Si) as an example and considering the scattering between the electrons and crystal lattices, the proportion between the effective temperature of electrons with and without applied electric field is gained:

$$\frac{T_e}{T_0} = \frac{1}{2}\left[1 + \sqrt{1 + \frac{3\pi}{8}\left(\frac{\mu_0 |E|}{u}\right)^2}\right] = \alpha^2 \tag{1}$$

where T_e and T_0 are the effective temperature of electrons with and without applied electric field, respectively, u is the velocity of the phonon, and μ_0 is the mobility of unheated electron. If $\mu_0|E| \ll u$, the expression (1) can be expanded in power series, and ignores the quadratic term and terms with higher order, yielding that:

$$\alpha \approx 1 + \frac{3\pi}{64}\left(\frac{\mu_0 |E|}{u}\right)^2 \tag{2}$$

Obviously, the effective temperature of electrons always rises, though unconspicuous, even if the applied electric field is very small. Usually the electrons are called warm-electrons when the applied electric field coincides with this assumption.

2.2. Prototype and Sensitivity of the power detector

The typical structure of the power detector in millimeter wave region [6] is given in Figure 1. It is composed of a standard waveguide, a semiconductor sensing sample within it and a DC bias current source to supply a bias voltage U_0 on the sample. Propagating through the waveguide, the electric field of the HPM pulse is applied to the semiconductor sample by stimulating the TE_{10} mode, whose electric field is in the vertical direction. Due to the high electric field, the carriers of the sample are heated. As the effective temperature of the carriers rises, the resistance of the sample increases. Simultaneously, the bias voltage on the sample increases in a shape the same as the pulse measured, and this is the output voltage U_s of the detector. With carefully calibrated in the waveguide frequency band, the pulse power of the HPM pulse is determined.

Figure 2 shows the sketch map of the cross-section of the sensing sample, indicating some structural parameters of the semiconductor. Two same semiconductors with length of l are separated with a small distance (μm), and shorted with thin copper foil. The lower contact of one of the semiconductors is grounded with the waveguide while the other is isolated. Thus the two semiconductors and upper thin copper foil compose a DC circuit with a bias current source. The feeding and output of the voltage dropped on the sample are easily achieved through the small obstacle.

According to the circuit analysis, the output voltage in respect to HPM pulse can be written as

$$\frac{U_s}{U_0} = \frac{\Delta R}{R_0} = \sqrt{\frac{T_e}{T_0}} - 1 = \alpha - 1 \tag{3}$$

where R_0 is the initial resistance of the sensing sample. Substituting (1) to (3) and normalizing the average electric field $\langle E \rangle$ in vertical direction in the sensing sample to the maximum electric field E_0 in the centre of empty waveguide, one can obtain the relationship between the U_s and the

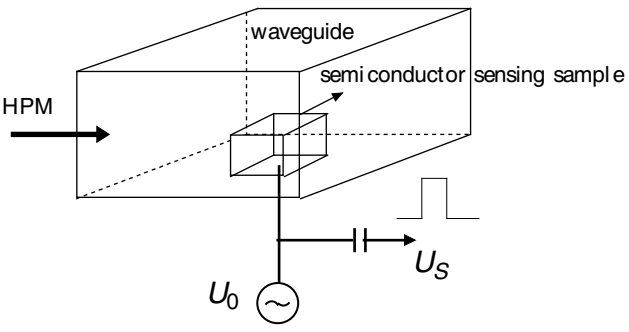

Figure 1: Sketch of semiconductor power detector.

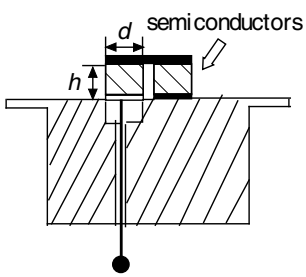

Figure 2: Cross-section of the sensing sample.

pulse power P_{in} as followed:

$$\left(\frac{U_s}{U_0}\right)^4 + 4\left(\frac{U_s}{U_0}\right)^3 + 5\left(\frac{U_s}{U_0}\right)^2 + 2\left(\frac{U_s}{U_0}\right) = \frac{45\pi^2(\frac{\mu_0}{u})^2\langle\frac{E}{E_0}\rangle^2}{ab\sqrt{1-(f_c/f)^2}}P_{in} \tag{4}$$

where a and b are the length of the long and short side of the waveguide, respectively, f is the frequency of the HPM pulse, and f_c is the cut-off frequency of the waveguide. Defining the relative sensitivity of the detector as $\xi = U_s/(U_0 \cdot P_{in})$, one can get ξ by solving the Equation (4). In the warm-electron region, the relative sensitivity is derived from Equation (2) and (3); that is,

$$\xi = \frac{45\pi^2(\frac{\mu_0}{u})^2\langle\frac{E}{E_0}\rangle^2}{2ab\sqrt{1-(f_c/f)^2}} \tag{5}$$

A proportion relation is found between the relative sensitivity and the pulse power under linear approximation. Denoting warm-electron coefficient in AC electric field as $\beta = \frac{3\pi}{64}(\frac{\mu_0}{u(f)})^2$, and according to the paper [4], the expression (5) is rewritten, yielding that:

$$\xi(f) = \frac{480\pi}{ab\sqrt{1-(f_c/f)^2}}\beta_{dc}\left[1/2 + 1/\left[1+(2\pi f\tau_\varepsilon)^2\right]\right]\left\langle\frac{E^2}{E_0^2}\right\rangle \tag{6}$$

where β_{dc} is the warm-electron coefficient in DC electric field, τ_ε is the phenomenological energy relaxation time.

3. DESIGN AND OPTIMIZATION OF THE PARAMETERS OF THE DETECTOR

3.1. Calculation Method

The pulse power detector for 2 mm frequency band is designed to be made up of a WR7 standard waveguide, whose window size is $1.651 \times 0.8225\,\text{mm}^2$, and a sensing sample including two same n-Si plates and a thin copper foil. It's suitable to be used in the frequency band of 113 GHz–173 GHz. The material of n-Si is chosen for its high time response and easily fabrication.

In expression (6) there is a dependence of the relative sensitivity on the frequency of the pulse measured in the linear region of the detector. To reduce the work of the calibration and increase the accuracy of the detector, this dependence should be avoided, that is, the parameters of the detector would be optimized to make the frequency response flat enough. Because of the disperse in the waveguide and the dependence of the warm-electron coefficient on the frequency, the relative sensitivity would decline. So the characteristic dimensions and the specific resistance ρ of the sample should be varied to make the average electric field in the sample increase to compensate it. Meanwhile, these parameters are restricted by that the voltage standing wave ratio (VSWR) is no more than 1.3.

A three-dimensional finite difference time domain (FDTD) method is used here to calculate the electric field in sensing sample. The simulated model is illustrated in Figure 3, where the length of the waveguide is 5 mm. An excitation of sinusoidal wave of TE_{10} mode is adopted all over the frequency band. There are two absorbing boundary conditions mathematically specified in both begin and end of the model. The sample is treated as a whole obstacle, and the thickness of the copper foil is neglected.

3.2. Results of the Optimization

Preliminary calculations are firstly performed to get moderate VSWR. Between the plane where microwave excited and the sample, a part standing wave is clearly seen in the distribution of electric field in y direction. When the transverse dimensions of sensing sample are $0.1 \times 0.2\,\text{mm}^2$ and the specific resistance is $\rho = 2\,\Omega\cdot\text{cm}$, the VSWR of the detector is about 1–1.25 in the waveguide frequency band. The length of the sample doesn't take much effect in VSWR, but in the average electric field in the sample.

Results of followed simulations are shown in Figure 4. The thick line is corresponding to ideal curve of $\frac{\langle E^2(f)/E_0^2(f)\rangle}{\langle E^2(f_l)/E_0^2(f_l)\rangle}$, which is calculated from expression (6) to make the relative sensitivity unchanged, and other curves are in respect to different length. Here f_l is 113 GHz, the lowest frequency in the waveguide frequency band. According to the analysis in 3.1, the optimized length is that the curve coincides with the thick line or the two have the same varying trend. Evidently $l =$

0.75 mm is the best choice, as both sides of its curve have contrary variation. Further computation of relative sensitivity in length of 0.75 mm is plotted in Figure 5. The sensitivity of 0.6 kW^{-1} is obtained with a fluctuation less than 27% in the frequency range 113–173 GHz, especially less than 9.8% in the frequency range 130–160 GHz, which means the frequency response is rather flat. Ultimately, all the parameters of the power detector are optimized and determined as follows: $a = 1.651$ mm, $b = 0.8225$ mm, $h = 0.1$ mm, $d = 0.1$ mm, $l = 0.75$ mm, and $\rho = 2\,\Omega$·cm.

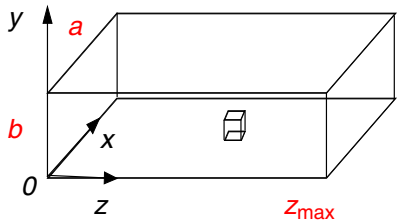

Figure 3: The calculation model of the detector.

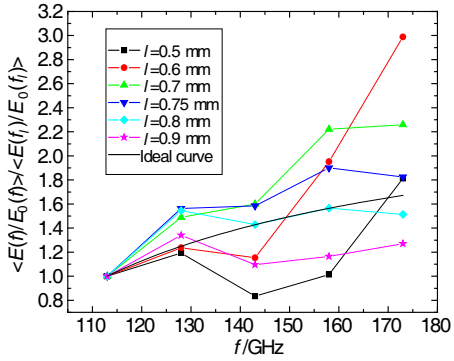

Figure 4: The dependence of the electric field on frequency.

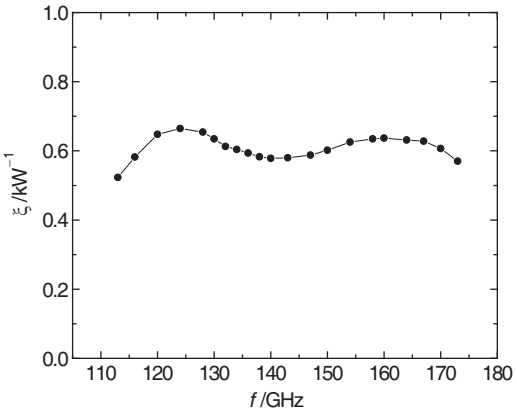

Figure 5: The relative sensitivity of detector with.

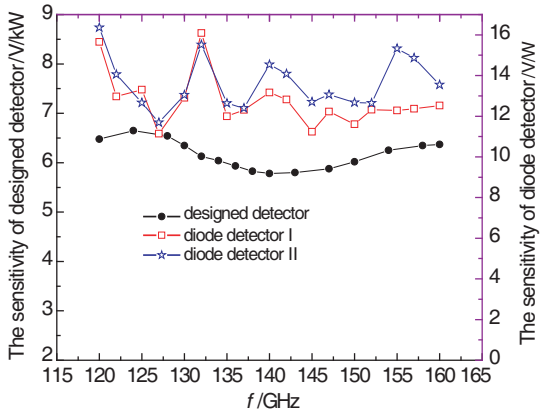

Figure 6: The sensitivities of designed detector the length of 0.75 mm of the sample and diode detectors.

4. CONCLUSION

Based on hot-electron effect in n-Si, a pulse power detector for 2 mm frequency band is analyzed theoretically and designed. Parameters of the detector are optimized to keep the relative sensitivity in warm-electron region flat with three-dimensional FDTD method. Compared with the purchased diode detectors in 2 mm frequency band, the advantages of our detector is obviously seen in Figure 6, where the designed detector is biased with a DC voltage of 10 V. Diodes have much higher sensitivities of about 13 V/W, fluctuating in a level of about 45.6% in the frequency range of 120 GHz–160 GHz. So the designed semiconductor detector has more flatter frequency response, and can measure pulse power with a magnitude of kW directly with an output signal of the order of a few tens of volts, which leads to less attenuation used in the high power measurements and good performances in high electromagnetic interference environments. The detector is seeking for fabrication, and will be used in the experiments of our Q-band HPM source if possible.

REFERENCES

1. Bratman, et al., "Millimeter-wave HF relativistic electron oscillators," *IEEE Trans. on Plasma Sci.*, Vol. 15, No. 1, 2–15, 1987.

2. Zhang, H., J. Wang, and C. Tong, "Optimization of high power terahertz surface wave oscillator," *Journal of Xi'an Jiaotong University*, Vol. 42, No. 12, 1531–1536, 2008 (in Chinese).
3. Dagys, M., et al., "High-power microwave pulse measurement using resistive sensors," *IEEE Trans. on Instru. and Measurement*, Vol. 46, No. 2, 499–502, 1997.
4. Dagys, M., et al., "The rsistive sensor: A device for high-power microwave pulsed measurements," *IEEE Antennas on Propagation Magazine*, Vol. 43, No. 5, 64–78, 2001.
5. Huang, W., et al., "New type of high power microwave detector," *High Power Laser and Particle Beams*, Vol. 14, No. 3, 449–452, 2002 (in Chinese),
6. Kancleris, Z., et al., "High power millimeter wave pulse sensor for W-band," *IET Microwave Antennas Propagation*, Vol. 1, No. 3, 757–762, 2007.
7. Liu, E., et al., *Physics of Semiconductors*, 105–110, Publishing House of National Defence Industry, Beijing, China, 2004 (in Chinese).

Interference Suppression in DC-DC Switch Converter By H∞ Controller

Yanhua Xian[1, 2] **and Jiuchao Feng**[1]

[1]School of Electronic and Information Engineering, South China University of Technology
Guangzhou 510641, China
[2]College of Electronic Engineering, Guangxi Normal University
Guilin 541004, China

Abstract— To suppress perturbations of input, output and external noise for a DC-DC switch converter, a new H∞ control scheme is proposed in this paper. A robust controller, guaranteeing stability and the desired closed-loop dynamical response, is designed. As an example, boost converter is used to illustrate the design procedure of the controller. Simulation results in frequency and time domain, by the controller, indicate that the controlled system is of a big phase margin, perfect tracking ability of the desired output voltage, and high immunity to perturbations.

1. INTRODUCTION

Switch converter is core of power supply, and study of its control is always a hotspot. It is required in applications of DC-DC converter that a converter is stable, its dynamical response under various disturbances is also fast. The main control methods of switch converter are voltage mode and current mode. The former presents slow response in front of load variations and input voltage perturbations [1]. The latter is added a current loop, which improves transient responses when input voltage varies. When loads varies, a converter do not work well by the two approaches [2]. In this paper, it is therefore a new H∞ controller is designed and used to control DC-DC converter.

The use of H∞ control in DC-DC converter can be found in [3], where H∞ control is applied to a boost converter, a converter has small output and error of steady-state tracking. In [4], H∞ controller is designed for non-minimal phase-switching converters that maximize the bandwidth control loop with zero steady-state error. A nonlinear H∞ controller for cuk converter in [5] and an H∞ loop-shaping control strategy for buck and boost converter were respectively reported in [6]. It was also reported in [7] that performance of a closed-loop system in time domain is stable. All above designed H∞ controllers are only considered disturbances of input voltage and/or load, exclusive of external noise. In this paper, three above-mentioned disturbances are totally taken into account to build a H∞ control scheme for DC-DC converter. Based the scheme, an H∞ controller is designed via the solution of two Riccati equations. Simulations in frequency and time domain demonstrate the excellent disturbance rejection and tracking ability of the proposed controller.

2. DESIGN OF H∞ CONTROLLER

2.1. Design of H∞ Control Scheme

Figure 1 shows the block diagram of a standard H∞ control scheme [8], in which P is the augmented plant, formed by combining controlled object and weight functions. Weight functions are chosen for reflecting the design objectives. $K\infty$ is the controller. w is the input vector containing all the input signals, and z is the output vector containing all system weighted outputs. The standard problem of H∞ control is to find a controller$K\infty$ that stabilizes the plant P minimizing the infinity norm of the close-loop transfer function T_{zw}, given: $\min ||T_{zw}(s)||_\infty \leq \gamma$, $0 < \gamma \leq 1$.

The minimizing sensitivity of interference suppression by H∞ control is to find a controller, which stabilizes the close-loop system and also minimizes the H∞ norm of the transfer function from disturbances to weighted outputs. This problem can be translated to the standard problem of H∞ control. In DC-DC converter, there exist disturbances mainly including input voltage perturbation at input port and load variation at output port. Also, external noise can not be ignored due to changing outside circumstance. When consider all these three disturbances, an H∞ control scheme is therefore built for DC-DC converter as showed in Fig. 2. All those in the dashed frame of Fig. 2 are compacted to form the argument plant $P(s)$, in which input vector w contains the perturbations input voltage variation v_{in}, load current variation i_o, external noise perturbation v. The $G(s)$ represents DC-DC converter, and $W_n(s)$ is the weighted function of external noise perturbation v, reflecting the capability of interference suppression within desired frequency band.

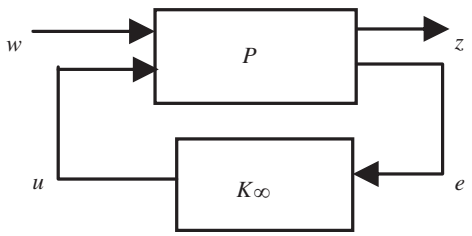

Figure 1: Standard problem of H∞ control.

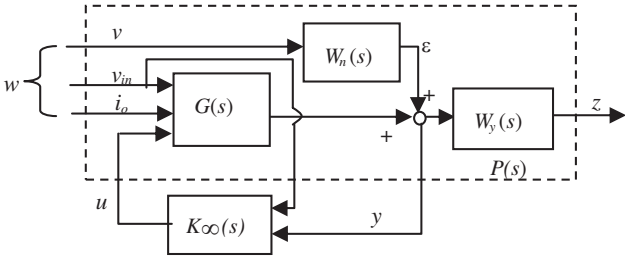

Figure 2: H∞ control scheme for DC-DC converter.

The $W_y(s)$ is the weighted function of the measurement output y, to define the desired behavior of y in some frequency domain.

Based on the scheme showed in Fig. 2, the transfer function of the plant $P(s)$ form $[v_{in}\, i_o\, v]^T$ to $[z\, y]^T$ can be described as follows:

$$P(s) = \begin{bmatrix} G_{11}W_y & G_{12}W_y & W_nW_y & G_{13}W_y \\ G_{11} & G_{12} & W_n & G_{13} \end{bmatrix} \tag{1}$$

where G_{11}, G_{12}, G_{13} are the transfer functions of out-input voltage, out-load current, out-control, respectively. For convenience of computation, the transfer function in (1) can be transformed into the following state-space equations

$$\begin{cases} \dot{x} = Ax + B_1w + B_2u \\ z = C_1x + D_{11}w + D_{12}u \\ y = C_2x + D_{21}w + D_{22}u \end{cases} \tag{2}$$

where x is the state vector of the converter, w corresponds to perturbations, u is the control input, z is weighted output and y is measurement output. A, B_1, B_2, C_1, C_2, $D_{11} \sim D_{22}$ are real matrixes with appropriate dimensions.

2.2. H∞ Controller

The plant $P(s)$ formed by (2) should satisfy the following assumptions [8]: 1) (A, B_1) is stabilizable, (C_1, A) is detectable; 2) (A, B_2) is stabilizable, (C_2, A) is detectable; 3) $D_{12}^T[C_1\ D_{12}] = [0\ I]$; 4) $D_{21}[D_{21}^T\ B_1] = [I\ 0]$, and 5) $D_{11} = 0$, $D_{22} = 0$.

In general, most $P(s)$ plants satisfy assumptions 1) and 2). If P(s) does not satisfy assumptions 3) $\sim$ 5), the loop shifting and scaling procedures [8] can transform $P(s)$ to satisfy the above assumptions. Another way is to modify the weight functions. For the plant satisfying the assumptions 1) $\sim$ 5), one can find an asymptotically stable controller $K\infty$ via solving the following pair of Riccati equations: $A^TX + XA + X(\gamma^{-2}B_1B_1^T - B_2B_2^T)X + C_1^TC_1 = 0$ and $AY + YA^T + Y(\gamma^{-2}C_1^TC_1 - C_2^TC_2)Y + B_1B_1^T = 0$. If and only if two solutions X, Y of Riccati equations satisfy: $X \geq 0$, $Y \geq 0$ and $\rho(XY) < \gamma^2$, the controller $K\infty(s)$ that guarantees $||T_{zw}(s)||_\infty \leq \gamma$ is expressed as

$$K_\infty(s) = \begin{bmatrix} A_\infty & -Z_\infty L_\infty \\ F_\infty & 0 \end{bmatrix}$$

where $A_\infty = A + \gamma^{-2}B_1B_1^TX_\infty + B_2F_\infty + Z_\infty L_\infty C_2$, $F_\infty = -B_2^TX_\infty$, $L_\infty = -Y_\infty C_2^T$, $Z_\infty = (I - \gamma^{-2}Y_\infty x_\infty)^{-1}$.

3. H∞ CONTROLLER FOR BOOST CONVERTER

As an example, a typical low-power boost converter (Fig. 3) operating in continuous conduction mode is studied. It transforms a 12 V input voltage into 24 V output. The output current source is inserted in the circuit to introduce load perturbation. The switching frequency is 20 kHz. The series resistance of the inductor, switch, diode, and capacitor are all shown in Fig. 2.

After averaging and linearizing procedure, the state-space equations of boost converter are

$$\begin{cases} \dot{x} = Ax + B_1w + B_2u \\ y = Cx + E_1w + E_2u \end{cases} \tag{3}$$

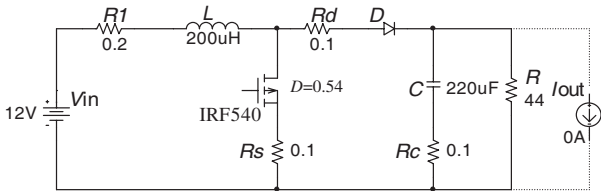

Figure 3: Boost converter.

where x is the state of the converter, $x = [i_L\ u_c]^T$, w is the perturbation vector $w = [v_{in}\ i_{out}]^T$, u is the control input and y is the load voltage. The matrices corresponding to (3) are given by

$$A = A_{on}D + A_{off}(1-D), \quad B_1 = B_{on}D + B_{off}(1-D), \quad B_2 = (A_{on} - A_{off})X + (B_{on} - B_{off})W$$
$$C = C_{on}D + C_{off}(1-D), \quad E_1 = E_{on}D + E_{off}(1-D), \quad E_2 = (C_{on} - C_{off})X + (E_{on} - E_{off})W,$$

where

$$A_{on} = \begin{bmatrix} -\dfrac{R_1 + R_s}{L} & 0 \\ 0 & -\dfrac{1}{(R + R_c)C} \end{bmatrix}, \quad B_{on} = \begin{bmatrix} \dfrac{1}{L} & 0 \\ 0 & -\dfrac{R}{(R + R_c)C} \end{bmatrix}, \quad C_{on} = \begin{bmatrix} 0 & \dfrac{R}{R + R_c} \end{bmatrix},$$

$$E_{on} = \begin{bmatrix} 0 & -\dfrac{RR_c}{R + R_c} \end{bmatrix}, \quad A_{off} = \begin{bmatrix} -\dfrac{RR_c + (R_1 + R_d)(R + R_c)}{(R + R_c)L} & -\dfrac{R}{(R + R_c)L} \\ \dfrac{R}{(R + R_c)C} & -\dfrac{1}{R + R_c)C} \end{bmatrix},$$

$$B_{off} = \begin{bmatrix} \dfrac{1}{L} & \dfrac{RR_c}{(R + R_c)L} \\ 0 & -\dfrac{R}{(R + R_c)C} \end{bmatrix}, \quad C_{off} = \begin{bmatrix} \dfrac{RR_c}{R + R_c} & \dfrac{R}{R + R_c} \end{bmatrix},$$

$$E_{off} = E_{on}, \quad X = -A^{-1}B_1W, \quad Y = \left(-CA^{-1}B_1 + E_1\right)W, \quad D = 0.54, \quad W = [120]^T.$$

Equation (3) is the state-space form of $G(s)$ in this H∞ control scheme.

Due to high gain of disturbance at low frequencies, a low-pass transfer function as the external noise weight function W_n is chosen, and given by $W_n = 100/(s + 2\pi \cdot 1000)$. To obtain a good tracing performance as well as satisfy solution conditions of the H∞ controller, the weight function is chosen as $W_y = 0.3(s + 2\pi \cdot 2500)/(s + 2\pi \cdot 100)$. By combining (3), W_n and W_y, one can obtain the plant $P(s)$.

By using MATLAB platform, we can obtain the controller:

$$K_\infty(s) = \begin{bmatrix} \dfrac{2.0207 \cdot 10^6 (s - 5.7139 \cdot 10^5)(s + 14227)(s + 1635.9)}{(s - 2.1503 \cdot 10^{11})(s + 45455)(s + 628.23)} & \dfrac{-8.5264 \cdot 10^9}{s - 2.1503 \cdot 10^{11}} \end{bmatrix} \tag{4}$$

There exists a big positive pole in (4), and it will lead to the instability of the closed-loop system. To overcome this problem, the unstable pole is approximated by

$$\frac{1}{s - a} \sim -\frac{1}{a} \qquad \text{for} \quad |s| \ll |a| \tag{5}$$

A similar approximation is used to get rid of the big zero in (4). Equation (4) can be then rewritten as $K_\infty(s) = \begin{bmatrix} \dfrac{5.37(s + 14227)(s + 1635.9)}{(s + 45455)(s + 628.23)} & 0.0397 \end{bmatrix}$.

4. SIMULATION RESULTS

A step signal with amplitude 10 V is introduced to boost converter as external noise signal. Simulation in time domain is executed to test the transient and static performances of the boost converter with the H∞ controller. Figs. 4(a)–(c) show the output voltage responses after introducing a 50% perturbation for different disturbances. In the three cases, the output response exhibits a fast

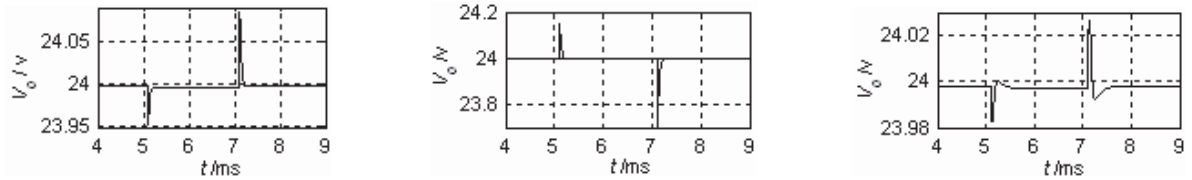

Figure 4: Output voltage. (a) Input voltage perturbation, (b) load perturbation, (c) external noise perturbation.

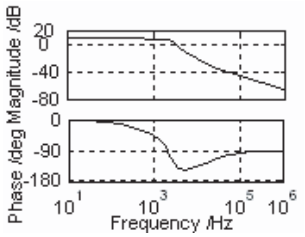

Figure 5: Loop gain in the H∞ control.

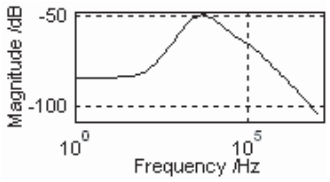

Figure 6: Input-output function.

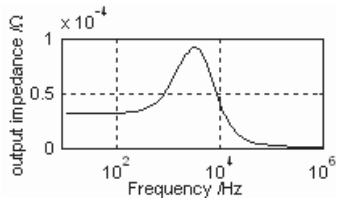

Figure 7: Output impedance.

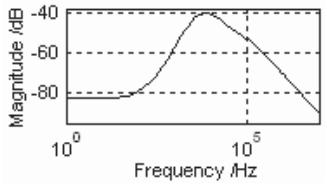

Figure 8: External noise-output function.

recovery procedure with little steady-state error and small overshoots. The overshoot for load variation is the biggest one, which is 1.25% as shown in Fig. 4(b), and the smallest one is for external noise perturbation, which is 0.1125% as shown in Fig. 4(c).

Simulation in frequency domain is also executed to test the dynamic performances of the H∞ controlled boost converter. Considering a descriptive function of $1/3\,\mathrm{V}^{-1}$ for the PWM, the resulting loop gain exhibits a phase margin of 49.6° as shown in Fig. 5., Figs. 6–8 show the frequency characteristics of the input-output function, output impedance and external noise-output function. In Figs. 6–8, we can see the low gain at low frequencies, the H∞ controlled boost converter is affected lightly by the perturbations of input voltage, load and external noise.

5. CONCLUSION

A H∞ control scheme is proposed and realized for rejecting perturbations of input voltage, load and external noise in DC-DC converter. The proposed H∞ controller is applied to boost converter. Simulation results obtained in the controlled boost show fast recovery, good tracing ability and stable frequency performance under different perturbations.

ACKNOWLEDGMENT

This work was supported by the National Natural Science Foundation of China (No. 60872123), and by the Joint Fund of the National Natural Science Foundation and the Guangdong Provincial Natural Science Foundation, China (No. U0835001).

REFERENCES

1. Erickson, R. W. and D. Maksimovic, *Fundamentals of Power Electronics*, Kluwer Academic Publishers Group, 2000.
2. Wang, F. Y. and J. P. Xu, "Comparison of small signal models for dc/dc switching mode power supply's control," *Journal of Power Electronics*, Vol. 41, 75–77, 2007 (in Chinese).
3. Naim, R, G. Weiss, and B. Y. Shmuel, "H∞ control applied to boost power converters," *IEEE Trans. Power Electron.*, Vol. 12, No. 2, 677–683, 1997.

4. Idiarte, E. V., L. M. Salamero, H. V. Blavi, F. Guinjoan, and J. Maixe, "Analysis and design of H∞ Control of nonminimum phase-switching converters," *IEEE Trans. Circuits Syst. I: Fund. Theor. Appl.*, Vol. 50, No. 10, 1316–1323, 2003.
5. Kugi, A. and K. Schlacher, "Nonlinear H∞-controller design for a dc-to-dc power converter," *IEEE Trans. Contr. Syst. Technol.*, Vol. 7, No. 2, 230–237, 1999.
6. Loannides, G. C. and S. N. Manias, "H∞ loop-shaping control schemes for the buck converter and their evaluation using μ–analysis," *IEE Proc. Electr. Power Appl.*, Vol. 146, No. 2, 237–246, 1999.
7. Patnaik, S. K. and B. Umamaheswari, "H∞ loop-shaping controller for a boost converter with harmonic reduction," *J. Circuits Systems Comp.*, Vol. 17, No. 2, 279–295, 2008.
8. Jia, Y. M., *Robust H∞ Control*, Science Press, Beijing, China, 2007.

Investigation of Detector Responsivity in the "Water Window" Wavelength Range

J. Mikołajczyk, Z. Bielecki, M. Nowakowski, and J. Wojtas
Institute of Optoelectronics, Military University of Technology, 2 Kaliskiego Str., Warsaw 00-908, Poland

Abstract— The paper presents a laboratory setup for investigation of spatial non-uniformity of detector responsivity in the wavelength range from 2 nm to 4 nm. The spectrum is of great interest in biology. In the water-window spectra, where water is rather transparent, microscopic observation of living objects is possible. Accurate determination of the responsivity of photodetectors used in this application is highly desired. The change of responsivity over the surface, so-called the spatial non-uniformity, causes error of power measurements especially in detectors with large active areas or in imaging ones. At the described setup, the laser-plasma source with a gas-puff target is used. The preliminary results of the silicon photodiode investigations are also presented and discussed.

1. INTRODUCTION

Soft X-ray microscopy is advancing as a perspective technology due to recent development of optical elements and high brightness sources. This technology can fill gap in optical and electron ones [1]. The currently technologies are limited by a spatial resolution of imaging. They also require a special procedure for preparation of investigated structure. During this procedure the structure is usually changed. Application of radiation in the "water window" range could minimize such problems (Fig. 1).

The photodetectors responsivity is one of the most important parameter in microscopy [2]. In a standard testing procedure, the whole active area of the photodetector is irradiated. An ideal detector should have a spatially uniform responsivity. It is mean, the responsivity is characterized by the same value over the active area regardless of the position of radiation spot [3]. In the case of uniform responsivity, for the beam irradiated a detector at different locations of its sensitive surface, the same level of output signal is generated. But, due to various effects, such as crystal structure of detector, fabrication quality, high level of radiation, heat conduction and convection losses, the photometers suffer from spatial non-uniformities [4]. At shorter wavelengths, the detector non-uniformity is reflected by the surface recombination centers [5]. Therefore, extra uncertainties have to be evaluated for an effective calibration of these devices.

2. LABORATORY SETUP FOR DETECTOR INVESTIGATION

The lab setup consists of a radiation source, a metrology chamber, and a scanning mechanism. In the source, the gas puff target is irradiated with the radiation generated by Nd : YAG laser [6]. The spectrum of source emission depends on the used gas. For the generation of water-window spectrum, the N_2 or Ar gases can be used (Fig. 2). The investigations show that N_2 gas spectrum

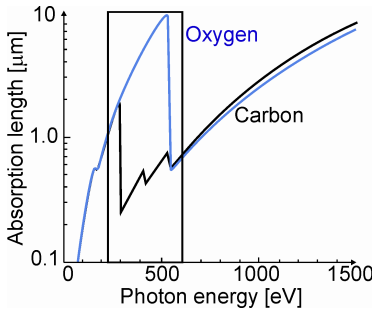

Figure 1: The water-window wavelength range.

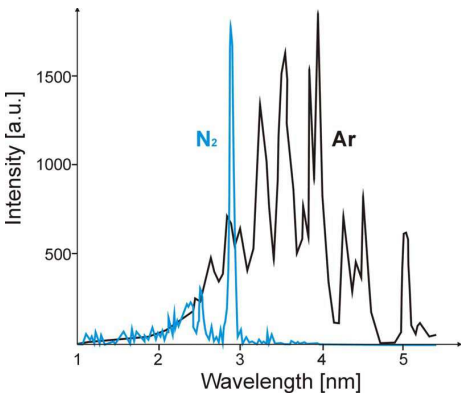

Figure 2: Emission spectrum of the laser-plasma source for different gas targets.

is characterized by a single strong emission line at the wavelength of 2.88 nm. In the case of *Ar* gas, the spectrum is widen in the wavelength range of 2–4.5 nm [7].

The preliminary investigations of the source showed that the efficiency and stability depend on conditions of plasma generation. The measured stability of the source radiation influences on the accuracy of the detector testing procedure. For this reason, a special metrology chamber with an optical beam splitter was constructed (Fig. 3). The setup makes it possible to control radiation level using monitoring detector.

The main elements of the optical beam splitter are two Cr/Ti multilayer mirrors produced at the Fraunhofer Institute for Applied Optics (Jena, Germany) [8]. The mirrors are characterized by reflectance of above 20% for incidence angle of 70 degree and wavelength of (2.85 ± 0.03) nm. The reflectance of the mirrors strictly depends on incident angle (Fig. 4). These features provide possibility of use the testing procedure in another wavelength ranges. However, the diagnostic spectrum can not be tuned so wide.

The beam of the source radiation is separated into two chamber flanges. In the flanges, the model detector and the tested one (photodiode, CCD etc.) are mounted. As the monitoring instrument, a AXUV-100HYB1 amplifier with calibrated AXUV 100 photodiode is applied [9]. The transfer characteristics of the preamp is linear in the wide range of the photocurrent changes (Fig. 5(a)). The photodiode is characterized by high quantum efficiency (Fig. 5(b)).

At the end of the control flange a pinhole holder is mounted. The holder provides the pinhole exchange. In the setup, the pinholes with different diameter sizes from Standa are used. Moreover, the scanning procedure is carried out using XYZ translation stages, and a stepper motor controller [11]. The pinhole is combined with the stage via special prepared holder. The construction of the mechanism makes it possible to set both the position and the size of irradiated spot on the detector surface. It is very useful during the testing procedure of image detectors, for example CCD

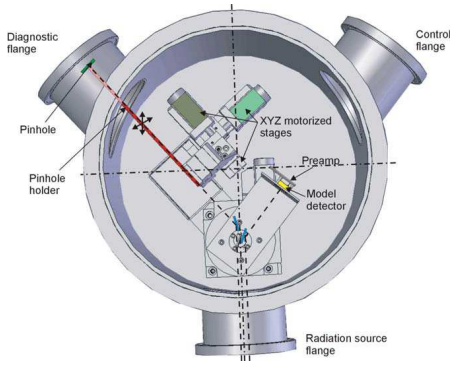

Figure 3: Scheme of the metrology chamber.

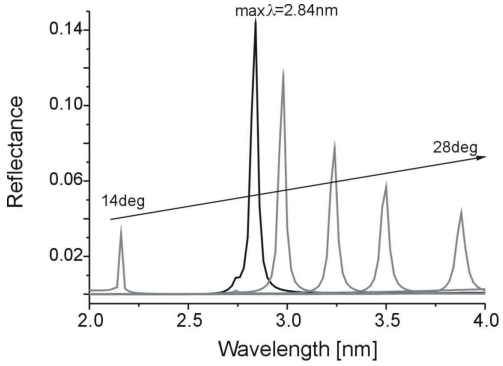

Figure 4: Spectral reflectivity of Cr/Ti multilayer mirrors.

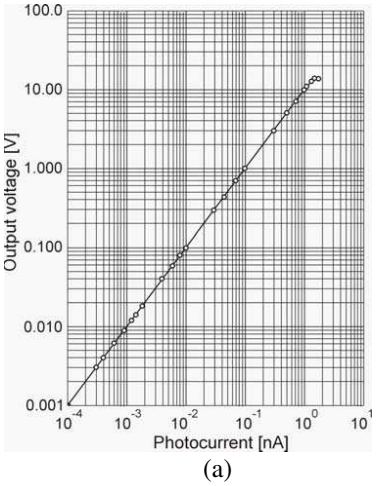

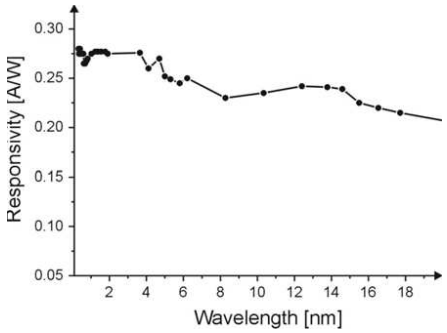

Figure 5: (a) Transfer characteristics of the preamp and (b) photodiode responsivity.

cameras. The minimum available pinhole size of 10 µm is comparable with the smallest camera pixel size.

3. EXPERIMENTAL RESULTS

The preliminary research of the scanning mechanism was made at the special relevant laboratory setup. The main task of the investigations was to verify the measurement procedure and mechanism operation. A stroboscope lamp was applied as a source. The diagnostic wavelength range is formed by optical filter 3C11 type manufactured by Standa ($\lambda = 525$ nm). As the tested detector, the AXUV 100 silicon photodiode manufactured by IRD Inc. was applied. The photodiode responsivity and the lamp spectra is presented in Fig. 6.

The investigated photodiode areawas 10 mm×10 mm with 1 mm steps in both directions. The spatial uniformity was measured by moving pinhole at equal steps in both directions perpendicular to beam direction. The stability of the lamp intensity was independently controlled by a model photodiode. The output signals of the tested photodiode and the model one were amplified with calibrated transimpedance amplifiers connected to digital voltmeters (DVM). A spatial filter consists of 1 mm pinhole, which provides a spot with a clean profile. Basing on the measurements, the arbitrary non-uniformity of the photodiode responsivity was determined (Fig. 7). The characteristic is normalized to the responsivity value measured in the case of whole detector surface irradiation.

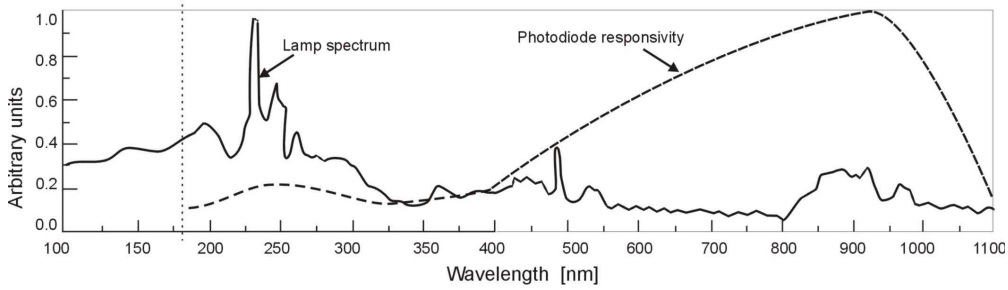

Figure 6: Emission spectra of xenon stroboscope lamp and spectral responsivity of silicon photodiode.

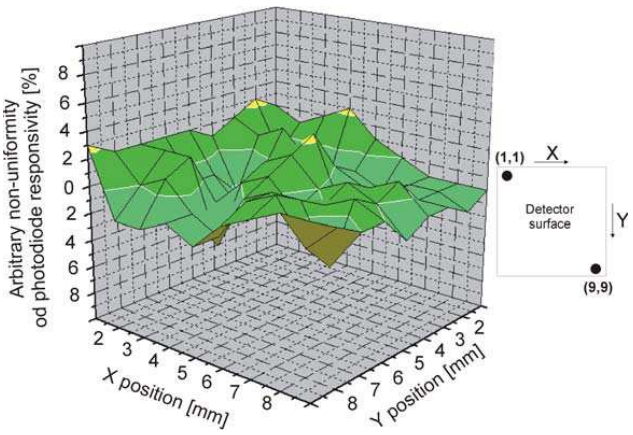

Figure 7: The non-uniformity of the photodiode responsivity determined with developed system.

4. CONCLUSIONS

The paper presents a project of the system desined to investigation of the photodetectors in thewater-window wavelength range. The experimental results give an opportunity to determine optimal parameters of the source operation. The results showed that the source efficiency and stability depend on conditions of plasma generation. For this reason, a special construction of the optical beam splitter was designed. The system is able to measure spatial non-uniformity of detector responsivity. Basing on the measurements made at the wavelength of 525 nm, no direct

formulation was observed as a relation between the local responsivity and the distance from the detector centre due to the non-uniform changing of responsivity over the photodiode surface.

ACKNOWLEDGMENT

This work was financially supported by the Polish Ministry of Science and Higher Education in the frame of research project No. O N515 005034.

REFERENCES

1. Majima, T., "Soft X-ray imaging of living cells in water: Flash contact soft X-ray microscope," *Trends in Analytical Chemistry*, Vol. 23, No. 7, 520–525, 2004.
2. Durak, M., et al., "Spatial non-uniformity measurements of large area silicon photodiodes," *Turk. J. Phys.*, Vol. 26, 375–379, 2002.
3. Nettleton, D. H., T. R. Prior, and T. H. Ward, " Improved spectral responsivity scales at NPL, 400 nm to 20 µm," *Metrologia*, Vol. 30, 425–432, 1993.
4. Larason, T. C., S. S. Bruce, and A. C. Parr, "Spectroradiometric detector measurements," *NIST Spec. Publ.,* Vol. 250, 41, 1998.
5. Zalewski, E. F. and J. Geist, "Silicon photodiode absolute spectral response self-calibration," *Appl. Opt.,* Vol. 19, 1214–1216, 1980.
6. Stock, K. D., "Internal quantum efficiency of Ge photodiodes," *Appl. Opt.*, Vol. 27, 12–14, 1998.
7. Fiedorowicz, H., et al., "Compact laser plasma EUV source based on a gas puff target for metrology applications," *Journal of Alloys and Compounds*, Vol. 401, 99–103, 2005.
8. Fiedorowicz, H. et al., "Investigation of soft X-ray emission from a gas puff target irradiated with a Nd : YAG laser," *Optics Communications*, Vol. 163, No. 1–3, 103–114, 1999.
9. Uspenskii, Y., et al., "Optimal design of multilayer mirrors for water-window microscope optics," *Optical Review*, Vol. 14, No. 1, 64–73, 2007.
10. Fonck, R. J., et al., "Low noise photodiode detector for optical fluctuation diagnostics," *Rev. of Sci. Instr.*, Vol. 63, 4924–4926, 1992.
11. Mikolajczyk, J., et al., "System for calibration of EUV detectors," *Photonics Letters of Poland*, Vol. 1, No. 2, 70–72, 2009.

The Novel Active Mode-locking 402.5 MHz Repetition Rate Pico-second Laser Based on PLL Structure

Yan Zhou[1, 2]

[1]The Department of Electronic Information Engineering, Beihang University, Beijing, China
[2]The Department of Electronic Engineering, University of California-Santa Cruz, Santa Cruz, USA

Abstract— The novel active mode-locking Pico-second Laser (PSL) system with 402.5 MHz repetition rate based on Phase Locked Loops (PLL) has been present in this paper. The complete PSL system configuration was been introduced, while suitable PLL structure has been used to get phase noise and jitters' decreasing. At the same time, the better pulse output feature been got. Agreement of the theoretical and experimental results confirms the applicability of this 402.5 MHz repetition rate Pico-second Laser system design.

1. INTRODUCTION

High speed Pico-second laser resource is used widely in modern communication system, such as high speed component and transmission network testing system, the short pulse width communication equipments, atmospheric photo-detectors, absorption photography research, and so on. Active mode-locking PSL enables users to have greater control over pulse repetition rate. Based on different repetition rates, users could use Active mode-locking PSL to realize many applications [1, 2]. For Active mode-locking PSL, how to get a stable and accurate RF controlling which will keep stable pulse performance and phase noise is still a research hot point. Using Phase Locked loop (PLL) to realize more perfect controlling for Active mode-locking PSL is a new method in mode locking laser. As higher performance is achieved, the complexity of verification of the complete PLL feedback circuit is needed. Based on traditional PLL technique, mixer and frequency synthesizer [3–6], a novel PSL system with complete PLL microwave system has been figured out.

This paper proposes novel 402.5 MHz repetition rate PSL system based on PLL. The remainder of this paper is organized as following. A description of active mode-locking Pico-second laser will be given after introduction. And following we will provides complete 402.5 MHz repetition rate PSL system based on Phase Locked Loops design. The experiment and result conclusion will be given finally.

2. ACTIVE MODE-LOCKING PICO-SECOND LASER

The ultra short pulses with their high peak power density Pico-second laser pulses achieve prefect application in industry and laboratory at present. Fig. 1 shows the schematic diagram of the Active Pico-second Laser system which is constructed in a basic ring cavity configuration consisted of a segment of erbium-doped fiber (EDF) pumped by 1480 nm laser diode.

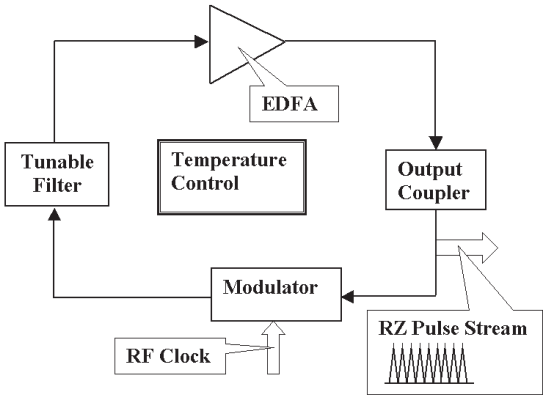

Figure 1: Schematic diagram of active mode locking Pico-second Laser system.

The active mode-locking function is driven by an external outside RF clock. While the adjustments to the frequency of the RF clocking signal affect the modulator which used to achieve

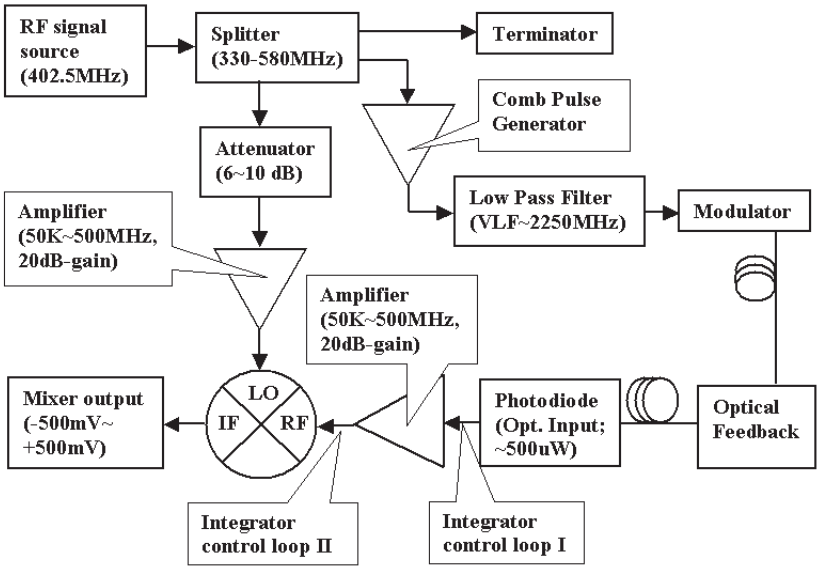

Figure 2: The schematic diagram of RF Phase Locked Loop structure for 402.5 MHz repetition rate PSL.

mode-locking level. Tunable filter generates needed pulse width optical signal with weak amplitude. Then after the amplifying by EDFA, we could get stable optical signal output. RF clock unit is important part for the reality of active mode-locking function. The key part of RF clock controlling is Phase locked loops structure.

3. THE PSL SYSTEM WITH 402.5 MHz REPETITION RATE PLL

In order to assess the performance of our Pico-second laser system, effective phase locked loop had to be constructed. The approach we adopted was based on traditional PLL technique and frequency synthesizer. In relative low frequency band such as VHF, it can be divided into two parts by splitter. One part signal pass through attenuator and amplified with 20 dB gain, enter into mixer as LO port. Another part signal will be put into discrete sequence by comb pulse generator, then pass through low pass filter (LPF), enter into optical modulator and optical cycle. In here, comb pulse generator and LPF are used to sort up analog signal and provide pure discrete sequence to modulator, see Fig. 2.

After optical feedback cycle, the same frequency RF signal will be generated from photodiode which will exchange optical signal to relative frequency RF signal. For there are some active devices like modulator and amplifiers used in the PLL system, thermal noise and flicker noise will be generated. However, comb pulse generator and LPF decrease the pre-phase noise's level and keep the pulse width into an acceptable standard level from pulse shaping and analog-digital conversion function. While the shaped RF signal will be send to optical modulator for optical circuit's processing after a low pass filter which will get rid of useless side band signal. In optical circuit, the controlling fiber's length define the repetition rate's value, while the optical pulse output's feature depend on the RF signal's controlling and timing jitter's level.

Two integrator loops release the voltage feedback function by calculating voltage changing range and estimating feedback factor. This part supports the whole system under stable optical-electric signal conversion used for final mixer. The middle frequency RF signal could be used as control and monitoring signal. While the controlled signal will control the electric-optical conversion device and do a additional affect to optical feedback part, and finally adjust the fiber's length in optical network. So the stable and low jitter optical signal will be got with above controlling.

4. EXPERIMENT RESULTS ANALYSIS

An analysis schematic of the actively stabilized 402.5 MHz repetition rate picoseconds laser optical output signal could be achieved. Through jitter test and numerical analysis, we can see that the pulse width is at 80 ps, timing jitter have been squeezed in a relative low level, 1.4 ps, Fig. 3. On the other hand, the pulse have deep and clear shape and curse which demonstrate the phase noise and jitter have been decreased to a very low level, while the RF signal has been successfully synthesized in PLL system.

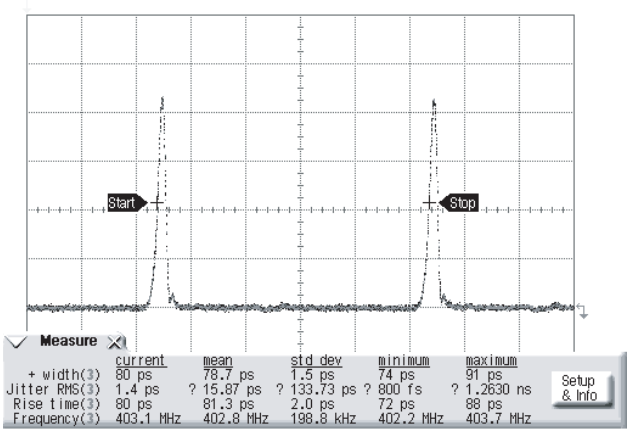

Figure 3: 402.5 MHz repetition rate active mode locking PSL output signal analysis result.

5. CONCLUSION

The novel active mode locking 402.5 MHz repetition rate Pico-second laser system based on PLL structure have been presented in this paper. Effective PLL design based on mixer realize the RF synchronization and signal control for Pico-second laser pulse. The theory and experiment have demonstrated the ability to reduce timing jitter, improves performance of pulse output and phase noise. This design of PSL based on PLL will show its special merit and application future in reducing the time jitter and optimizing output pulse.

ACKNOWLEDGMENT

The paper supported by University of California-Santa Cruz post-doctorial program funding: FOA-PAL#45121-444000 (2007–2009).

REFERENCES

1. Breglio, G. and A. Cutolo, "Optoelectronic measurement of voltage pulse repetition frequency by picosecond laser diodes," *IEEE Transactions on Instrumentation and Measurement*, Vol. 43, No. 1, 7–12, 1994.
2. Izzo, A. D., J. T. Walsh, E. D. Jansen, M. Bendett, J. Webb, H. Ralph, and C. P. Richter, "Optical parameter variability in laser nerve stimulation: A study of pulse duration, repetition rate, and wavelength," *IEEE Transactions on Biomedical Engineering*, Vol. 54, No. 6, 1108–1114, 2007.
3. Waldow, P. and A. Beyer, "Advanced phase-locked-loop oscillators," *Microwave Magazine*, 70–76, 2001.
4. Pan, C.-L. and H.-H. Wu, "Microwave applications of a laser-diode-based photoconductive harmonic mixer," *IEEE MTT-S International Microwave Symposium Digest*, Vol. 3, 1621–1624, 1992.
5. Ramond, T. M. and A. Bartels, "Low instability, low phase-noise femtosecond optical frequency comb microwave synthesizer," *Proceedings of the 2003 IEEE International Frequency Control Symposium and PDA Exhibition Jointly with the 17th European Frequency and Time Forum*, 168–171, 2003.
6. Sancho, S., A. Suarez, and T. Fernandez, "Nonlinear dynamics of microwave synthesizers-stability and noise," *IEEE Transactions on Microwave Theory and Techniques*, Vol. 49, No. 10, 1792–1783, 2001.

Accurate Evaluation of RF Coil-tissue Interactions Using a Hybrid FDTD-MoM Method

Wenlong Xu[1], **Feng Liu**[2], **Ling Xia**[3], **and Stuart Crozier**[2]

[1]Department of Biomedical Engineering, China Jiliang University, China
[2]School of Information Technology and Electrical Engineering, The University of Queensland, Australia
[3]Department of Biomedical Engineering, Zhejiang University, China

Abstract— A comprehensive consideration of loading effects is essential to the design/analysis of high-frequency MRI radio frequency (RF) coils. In this study, a hybrid finite difference time domain (FDTD)-method of moments (MoM) simulation method is implemented for the accurate evaluation of RF coil-tissue interaction. Using this approach, the RF coil is modelled using the MoM algorithm, and the biological load is handled with the FDTD algorithm. Effective communication between these two approaches is realized through a Huygence equivalent surface. The algorithm has been successfully validated and applied to a loaded coil study and the simulation demonstrated the potential of the hybrid algorithm for high frequency RF coil designs.

1. INTRODUCTION

In high field MRI, the dimensions of the RF coil are comparable to, or less than that of, the operational wavelength, causing the RF field inside the biological load to exhibit prominent wave behaviour. In addition, the RF field and source currents in the RF coil are strongly perturbed by the biological load. For the high frequency RF coil design, it needs to address these complex coil-tissue interactions. Quasi-static approximations are no longer an appropriate methods and the calculation of the electromagnetic (EM) fields requires full-wave solution of involved Maxwell's equations [1–5]. There are a number of full-wave numerical techniques available, including the finite difference time domain (FDTD) [1–5], finite element and the method of moments (MoM) [6]. Each numerical technique has its own strengths and limitations. Recently, hybrid numerical methods, which integrate the desirable features of two or more different full-wave EM numerical techniques [7], have been developed. The combination can usually enhance the overall efficiency and numerical accuracy of the algorithm. In the study a hybrid FDTD/MoM method is performed to evaluate the RF coil-tissue interaction. Although this hybrid approach has been reported for antenna applications, little investigation has been done in solving the EM problems in MRI and this work demonstrated that the FDTD/MoM approach is very useful for the analysis and design of high frequency RF coils with load.

1.1. FDTD

The FDTD method [8] belongs to a class of grid-based time-domain numerical techniques, which solve Maxwell's equations directly in their partial differential equation form. Central-difference approximations are used to discretize the partial differential form of Maxwell's time dependent equations into space and time partial derivatives. This results in replacing Maxwell's equations by a set of finite difference equations, which are solved in a time-stepping manner. To implement the FDTD method, the desired computational domain is first discretized into appropriately sized unit cells (Yee's cells), and dielectric properties of each cell are specified. Once this is established, excitation sources are also specified. At any given instant in time and space, the FDTD algorithm will calculate both electric and magnetic fields. This process is repeated until the desired transient or steady-state electromagnetic field behaviour is obtained. The behaviour of the field components over the problem space gives an essentially complete characterization of the behaviour of the initially assigned source so that it can be post-processed appropriately for its application.

FDTD has the advantage of simplicity and efficiency in analyzing heterogeneous dielectric samples such as the human body, but it suffers from the inconvenient way in which the 3D space has to be discretized into regular box-shaped cells and an absorbing boundary has to be used. Usually 3D perfectly matched layers (PMLs) [8] with a parabolic conductivity profile are used in the FDTD simulation. The PML is applied as an EM field absorbing boundary condition, and its inclusion is essential in the FDTD simulation to avoid having to compute large regions of free space, thereby saving considerable computing time and memory resources. Using the staircasing approach, the FDTD method discretizes 3D space in to cubic cells to model dielectric samples and RF coils, and this can sometimes lead to unacceptable numerical errors.

1.2. MoM

MoM is a numerical technique that solves Maxwell's equations in the integral form and in the frequency domain [6]. For a given RF structure with an arbitrary excitation source, MoM first discretizes all of the wire structures into segments, and conducting surfaces into small triangular patches. The task is then to determine the current distribution on these discretized segments and triangular patches when excited. The formulation begins with the development of an integral equation, which defines the electric field resulting from an arbitrary excitation source. This integral equation is formulated using the Green function, which relates the electric field at an arbitrary observation point to the current, at the source. The boundary condition of the total electric field is then forced on the surfaces of the discretized wire segments and triangular patches. Basis functions are used to expand the current distribution, and testing functions are used to enforce the electric field boundary condition on the wire and patch surfaces. This translates the integral equation into a system of simultaneous linear equations, which are then solved for the expansion coefficients associated with the basis functions. The current distribution is then constructed from the expansion coefficients. Once the current distribution is known, the feed point impedance and the radiation characteristics of the RF structure can be calculated.

MoM is very efficient at solving unbounded problems because it only requires the discretisation of the domain where the current flows. MoM does not need to analyse the space surrounding the source, hence the process of discretisation of the complete 3D space is not required, it is therefore very well suited for modeling complex coil structures, such as a cylindrical shield, but is not readily suited for modelling complex and arbitrary shaped dielectric samples. This is because it needs to either use a complicated Green function or the solution of large matrix equations necessary to accurately model the essentially lossy, dielectric loads, which can be practically very difficult for large-scale biomedical applications.

2. HYBRID FDTD/MOM BASED ON HUYGENCE EQUIVALENT SURFACE

A Huygence equivalent surface method [7] was used to effectively link MoM and FDTD together. To show the implementation of this hybrid approach for MRI RF coil modelling applications, a loop coil-spherical phantom interaction case is investigated (see Fig. 1).

As demonstrated in Fig. 1, the computational domain is first divided into two zones: an FDTD zone considers a total-field region including biological loads, where the dielectric sample was located and where coil-tissue interactions were explicitly evaluated; a MoM zone represents the RF coils region, containing the MoM-modelled circular surface coil only. The circular coil was firstly tuned to the desired resonance frequency and matched to the 50 Ω system impedance, without loading. Thereafter, the Huygence equivalent surface sources, generated by the MoM-calculated currents in free space, were determined. This first set of MoM-calculated Huygence equivalent sources are the six surfaces that bounded the spherical phantom (Huygence box) and this is the interface that efficiently hybridised the MoM and FDTD zones together. These equivalent surface sources were the electric and magnetic current elements that were mapped on to FDTD cell grids (cell size: 4 mm). With these equivalent surface sources, the FDTD method used a total/scattered formulation to calculate the RF field inside the spherical phantom excited by the mapped MoM-

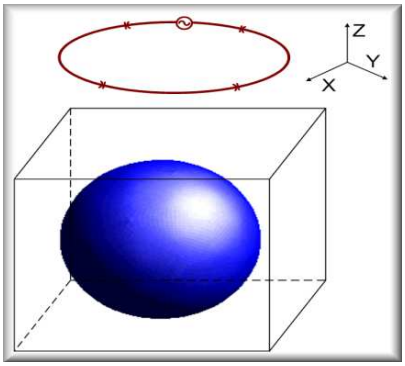

Figure 1: Decomposition of the computational domain for the hybrid fdtd/MoM approach. The rectangular box is the huygence surface, outside of the box is the MoM domain, and inside the box is the FDTD domain. Here a circular surface coil loaded with a homogeneous spherical phantom at 470 MHz is considered.

calculated Huygence equivalent sources. The total field region was inside the box, and the scattered field regions truncated by suitable PMLs were outside of the box. The scattered fields from the modelled phantom perturbed the values of the initial mapped MoM-calculated Huygence equivalent sources. These modified Huygence equivalent sources were recorded and handed back to the MoM domain for a recalculation of the currents on each wire segment of the surface coil resulting from the FDTD-updated Huygence equivalent sources. With the recalculated MoM currents, a new set of MoM-derived Huygence equivalent surface sources was obtained and again mapped back on to the FDTD discrete domain for another round of evaluation of the coil-tissue interactions. This process was iterated until convergence was achieved (that is, no further changes to the Huygence equivalent surface sources, the RF fields inside the phantom and the currents on the coil were observed), resulting in a steady solution.

3. RESULT

The hybrid algorithm was implemented and Fig. 2 demonstrates the convergence of the algorithm. It can be seen that the steady solution can be obtained within three or four iterations.

Once convergence was achieved, the RF field inside the spherical phantom was calculated. For validation, the same experiment was also numerically simulated using the well-established hybrid Green function/MoM solution [7]. Fig. 3 shows the scattered field pattern during the simulation. It is easy to see that the biological load introduce scattered field which will induce currents on the RF coils. The sample induced current will disturb the RF field in the sample again. This interaction will be simulated by the hybrid approach in an iterative fashion (see Fig. 2). Fig. 4 shows the accuracy of the proposed algorithm and also the field distortions inside the phantom at 470 MHz.

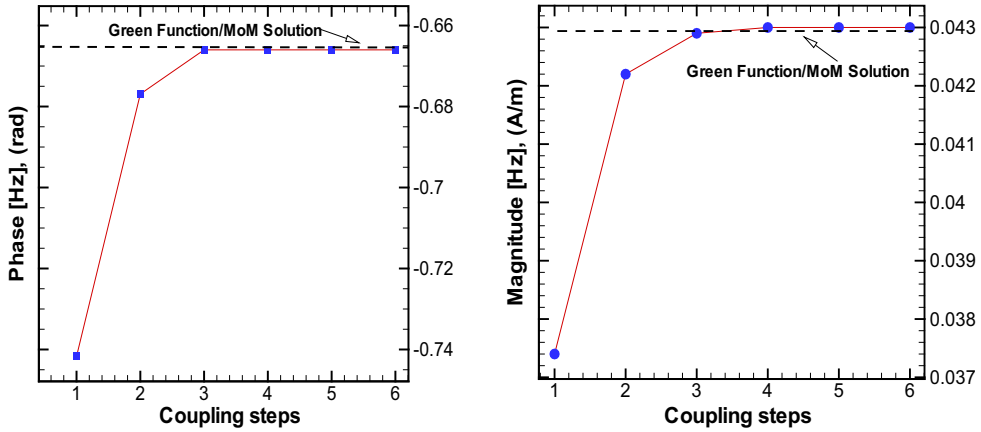

Figure 2: Convergence of the hybrid algorithm. It can be seen that FDTD/MoM coupling reached a steady solution within $3 \sim 4$ iterations.

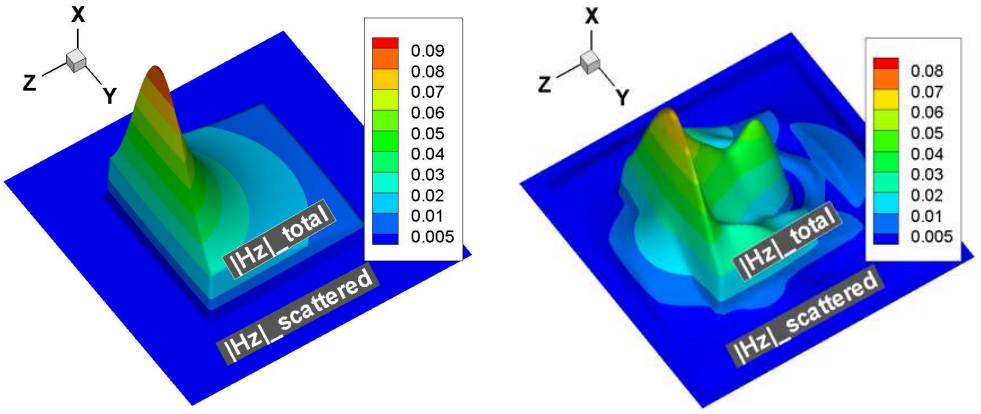

Figure 3: Hz profile in $x = 0$ plane. Left panel: without load; right panel: with load. In FDTD, Total/scattered formulation has been used, inside the Huygence box is the total-field region and outside is the scattered-field region.

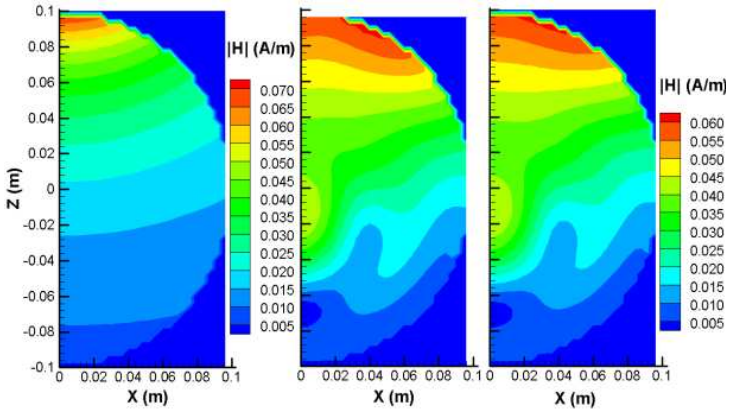

Figure 4: $|H|$ profile in $y = 0$ plane. Left panel: without load, middle panel: FDTD/MoM solution with load; right panel: MoM/Green function solution with load.

we noted that there was a 13.6% change of current on the coil before and after loading.

4. DISCUSSION

From the simulations, field-sample interactions are clearly more pronounced in these high frequency experiments than at lower frequencies [3]. Accurate assessment of the field-sample interaction phenomenon in high-field MRI should help with our understanding of the phenomenon and therefore provide invaluable insight into possible paths to alleviate the effect [1–6]. For example, from the simulation example, it can be seen that the coil current has been disturbed to a large amount; however the conventional simplified EM approaches will hardly provide such detailed information, and it indicates that the presented hybrid approach is more suitable for solving high frequency RF problems. Importantly, safety effects can also be accurately evaluated using this hybrid field calculation approach. In addition, the parallel computing of the FDTD and MoM algorithms will enhance the performance and capacity of the proposed methods.

5. CONCLUSION

In this study, a hybrid FDTD/MoM solver, using a Huygen's equivalent surface method, offers a high-performance computing platform for accurate evaluation of RF coil-tissue interactions. In the algorithm, the complex coil/tissue interactions have been explicitly accounted for, and in particular, this method does not make any compromise for RF coil modelling (simplified current/voltage source, staircase assumption, etc), and it enables us to consider more sophisticated coil structures and particularly the mutual coupling between coil-coil & coil-load in an accurate way, which is important for high field RF technology.

REFERENCES

1. Vaughan, T., L. DelaBarre, C. Snyder, J. F. Tian, C. Akgun, D. Shrivastava, W. Z. Liu, C. Olson, G. Adriany, J. Strupp, P. Andersen, A. Gopinath, P. F. van de Moortele, M. Garwood, and K. Ugurbil, "9.4 T human MRI: Preliminary results," *Magn. Reson. Med.*, Vol. 56, No. 6, 1274–1282, 2006.
2. Beck, B. L., K. Jenkins, J. Caserta, K. Padgett, J. Fitzsimmons, and S. J. Blackband, "Observation of significant signal voids in images of large biological samples at 11.1 T," *Magn. Reson. Med.*, Vol. 51, No. 6, 1103–1107, 2004.
3. Ibrahim, T. S., C. Mitchell, P. Schmalbrock, R. Lee, and D. W. Chakeres, "Electromagnetic perspective on the operation of RF coils at 1.5–11.7 Tesla," *Magn. Reson. Med.*, Vol. 54, No. 3, 683–690, 2005.
4. Liu, F. and S. Crozier, "Electromagnetic fields inside a lossy, multilayered spherical head phantom excited by MRI coils: Models and methods," *Phys. Med. Biol.*, Vol. 49, No. 10, 1835–1851, 2004.
5. Collins, C. M., W. Liu, B. J. Swift, and M. B. Smith, "Combination of optimized transmit arrays and some receive array reconstruction methods can yield homogeneous images at very high frequencies," *Magn. Reson. Med.*, Vol. 54, No. 6, 1327–1332, 2005.

6. Chen, J. H., S. K. Jeng, F. H. Lin, and W. P. Kuan, "Quantitative analysis of magnetic resonance radio-frequency coils based on method of moment," *IEEE Trans. Magn.*, Vol. 35, No. 4, 2118–2127, 1999.
7. Huang, Z., K. R. Demarest, and R. G. Plumb, "An FDTD/MoM hybrid technique for modeling complex antennas in the presence of heterogeneous grounds," *IEEE Trans. Geoscience and Remote Sensing*, Vol. 37, No. 6, 2692–2698, 1999.
8. Yee, K. S., "Numerical solution of initial boundary value problems involving Maxwells equations in isotropic media," *IEEE Transactions on Antennas and Propagation*, Vol. 14, No. 3, 302–307, 1966.
9. Berenger, J. P., "A perfectly matched layer for the absorption of electromagnetic-waves," *J. Comp. Phys.*, Vol. 114, Vol. 2, 185–200, 1994.

Choice of Suitable Wavelets for MR Image Processing

Karel Bartusek[1] and Eva Gescheidtova[2]

[1]Institute of Scientific Instruments, Academy of Sciences of the Czech Republic v.v.i
Kralovopolska 147, Brno 612 00, Czech Republic
[2]Faculty of Electrical Engineering and Communication, Brno University of Technology
Kolejni 2906/4, Brno 612 00, Czech Republic

Abstract— Magnetic nuclear resonance is used in particular as a diagnostic imaging method. Images of selected parts of organs must be of sufficient quality for doctors to be able to not miss any details and to make reliable diagnoses. The detected images are often of low contrast and resolution. They are mainly subjected to noise, whose level depends, among other things, on the level of the signal being detected, local proton density, voxel size, bandwidth, system design, quality of RF coil, and detection parameters [1–3]. Noise is in the same frequency band as the image spectral components that carry the details. Suppressing noise without knowing its properties must be a compromise between the desired smoothing and improvement of signal to-noise-ratio (SNR) on the one hand and the loss of details on the other hand. If the filtering method is applied in order to remove noise from MR images, a correct choice of individual filtering parameters is important.

In the paper, the selection is described of wavelets suitable for improving the quality of MR images of temporomandibular joint [4] and their evaluation according to three criteria: Increased SNR, steepness of the change in signal intensity in the image, and the change in contrast.

1. INTRODUCTION

Classical linear filtering methods (Fourier and Wiener filtering) remove noise from useful signal by suppressing the chosen frequency bands without distinguishing its usefulness. They are not suitable when suppressing broadband noise and they do not adapt to the noise level in useful signal, which results in insufficient effectiveness of modern digital signal processing and thus new solutions have to be looked for. One of the new solutions consists in using wavelet non-linear methods, which make use of the thresholding techniques and are able to better suppress wideband noise and thus partially distinguish useful signal from noise, and which adapt to the useful signal in any of its segments and at any level of decay. The result of filtering is influenced by the wavelet choice and decay level. Finding optimum decay levels and threshold magnitudes for the individual images being processed is a matter of extensive experiments.

The basis of wavelet transform is the application of a wavelet, a signal limited in time, to a part or to the whole of the signal being processed. This is the main difference in comparison with the other transforms, where harmonic signals of infinite length were used.

The basic wavelet is also referred to as the mother wavelet because further wavelets of the same shape but extended (compressed) and shifted are derived from it via changing the scale and shifting along the time axis. The mother wavelet must have zero mean value. It can have a non-zero mean value only on a finite time interval, which is fulfilled in the case of wavelets with compact carrier. An important property that the wavelet function bases should possess is orthogonality. Today there are over 400 types of wavelet in use, whose properties more or less meet the requirements of the task to be solved.

Rules for the selection of a suitable wavelet can be summed up in the following recommendations: Complex wavelets detect oscillations well but are not suitable for the detection of isolated singularities; pure real wavelets with few oscillations detect well the peaks and singularities in the signal; asymmetrical wavelets are suitable for the detection of changes in the gradient; symmetrical wavelets do not cause any phase shift between the peak, singularity and oscillation in the signal and the respective manifestation in wavelet coefficients; to detect amplitude and phase simultaneously the complex wavelet must be used.

2. EXPERIMENTAL METHOD

Selecting the criteria for the assessment of filtering effectiveness is very important. The following criteria were chosen for the selection of wavelets that are suitable for processing the MR images of temporomandibular joint:

- Subjective assessment by the physician, depending on the quality of details in the image.
- SNR — noise is determined in an image area that is free from signal; such an area is frequently found in MR images. The useful signal is the mean intensity value in a homogeneous area of the image.
- The steepness of image intensity. It is determined by differentiating the intensity of a selected area in the image, in which the steepness of the change is maximal.

To evaluate the criteria chosen a test MR magnitude image of a coronal slice of the head with SNR = 22 dB was chosen. The MR images of head (with TMJ) were acquired on the Philips ACHIEVA MRI system (DS = 1.5 T) in the Faculty Hospital Brno-Bohunice. The measurement parameters are: T2W-FSE pulse sequence, TE = 20 ms, TR = 1600 ms, MA = 256 × 256, FOV = 160 × 160 mm, sagital slice 2 mm. The Marevesi program was used to display the images and subsequently to evaluate the magnitude of SNR.

First, a group of wavelet functions was experimentally selected which best suppress noise in the image. Orthogonal wavelets: Haar, Coiflet4, Symlet4, Daubechies6. Biorthogonal wavelets: Bior2.4, Rbio2.6. The other currently used wavelets exhibited visible image distortion. The threshold values in each stage of decay are set by a comprehensive universal threshold because after the wavelet function is selected the same thresholds are set in each stage of decay. The threshold values can additionally be re-set manually in each stage of decay [1].

For the subjective assessment of the results of wavelet filtering a detail of an MR image in the area of temporomandibular joint was selected. Based on earlier experience, two-dimensional wavelet digital filtering with optimum wavelet function was used. The following wavelet functions were used: Haar, db6, Bior2.4, Rbio2.6 version 2, Coiflet4, Symlet3, Symlet4, and Dmey. The result of filtering, which is shown in Fig. 1, was assessed visually according to the details of a slice of an MR image of human brain near the temporomandibular joint. In the physician's opinion the image filtered by the Coif4 wavelet was of optimum quality. This image contains the greatest number of details with high contrast, although the differences in comparison with the other functions were minimal.

The effectiveness of the filtering based on the value of SNR was assessed on a sagital slice of the head in the area of temporomandibular joint (Fig. 2). In the area marked 1 the mean signal value was examined; its square expresses the root mean square of signal, $\mathrm{RMS}_{\mathrm{signal}}$. In the area free from

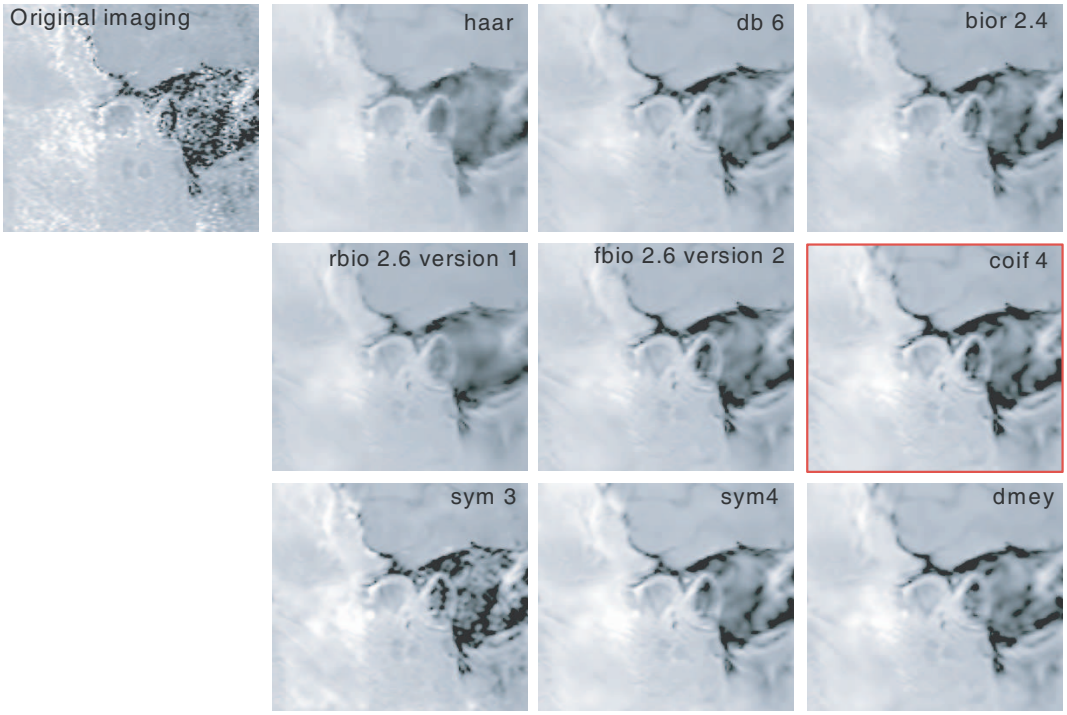

Figure 1: Selection of optimum wavelet function for digital filtering of a detail of MR image in the area of temporomandibular joint, after physician's assessment.

Figure 2: Areas for determination of signal RMS (1) and noise RMS (2).

signal, marked 2, the standard deviation of noise was determined, which corresponds to $\mathrm{RMS}_{\mathrm{noise}}$ on the assumption of zero mean value, which means that the noise has Gaussian distribution.

The SNR in the image is given by the relation

$$\mathrm{SNR} = 10 \log \frac{\mathrm{RMS}_{\mathrm{Signal}}}{\mathrm{RMS}_{\mathrm{Noise}}} \tag{1}$$

The assessment of filtering effectiveness is given in Table 1.

Table 1: SNR of image for selected wavelets.

Wavelet used		Orthogonal				Biorthogonal	
	None	Haar	Coiflet4	Symlet4	Daubechies6	Bior2.4	Rbio2.6
Mean signal values	1664.64	1662.33	1602.33	1655.8	1681.46	1673.97	1671.28
Effective noise	10.55	4.78	3.07	3.38	3.43	2.87	3.13
SNR [dB]	**21.98**	25.41	27.17	26.90	27.30	**27.66**	27.28

The SNR value of the original, non-processed image is 21.98 dB. The most suitable wavelet for filtering the test image is the biorthogonal wavelet Bior2.4 with SNR = 27.66 dB; from among the orthogonal wavelets it is the Daubechies wavelet of 6th order. Other suitable wavelets are: Biorthogonal wavelet Rbio2.6 with SNR = 27.28 dB, orthogonal wavelet Coiflet of 4th order with SNR = 27.17 dB, and orthogonal wavelet Symlet of 4th order with SNR = 26.90 dB. The least suitable for our purpose is the Haar wavelet with SNR = 25.41 dB. It should be emphasized that the degree (success) of noise suppression depends on image details and on the organs imaged.

Further but not so current criteria for the selection of suitable wavelets are the steepness of the change in signal intensity in the image at the site of step change. It is necessary to find in the image the sites of step changes in intensity magnitude and, via differentiation, to assess at these sites the steepness of intensity changes in the image being filtered.

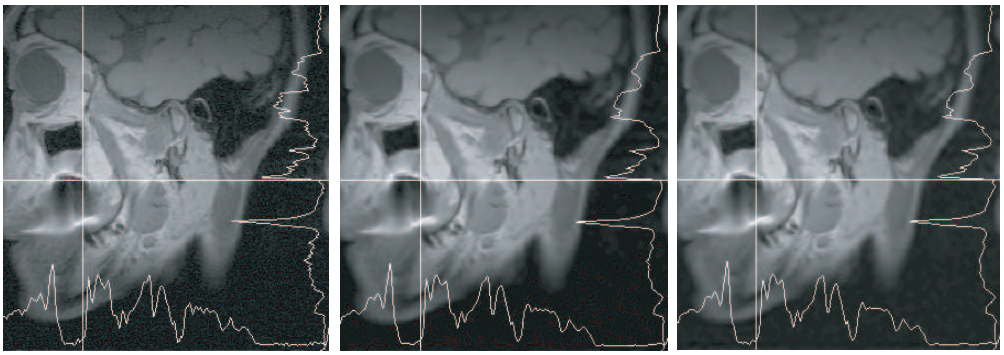

(a) (b) (c)

Figure 3: Signal intensity in the image being processed. (a) original image, (b) image filtered by Coiflet4 wavelet, and (c) image filtered by Bior2.4 wavelet.

Figure 3 gives an example of the area selected for the assessment of the steepness of intensity changes in a head image. The resultant values of the change in steepness for different wavelets are given in Table 2.

Filtering an image entails changes in its contrast. Changes in the contrast are pronounced particularly in images with a low SNR. In our case the changes of contrast in the head image are minimal and the contrast is the same for all the types of wavelet.

Table 2: Values of steepness of intensity changes in image being filtered, for different wavelets.

Wavelet used	None	Coiflet4	Daubechies6	Bior2.4	Rbio2.6
Steepness of intensity change	398	379	380	383	374

3. CONCLUSION

After evaluating, according to selected criteria, the results of filtering MR images of the head in the area of temporomandibular joint with typical contrast and numerous details we have come to the conclusion that for our purpose it is of advantage to use biorthogonal wavelets, the Bior2.4 wavelet in particular. For this wavelet we have obtained the highest SNR values and also the steepest changes of intensity in the image. The change in contrast in the test image chosen was negligible.

ACKNOWLEDGMENT

This work was supported within the framework of projects No. 102/07/0389 and 102/07/1086 of the Grant Agency of the Czech Republic and the research plan MSM 0021630513.

REFERENCES

1. Gescheidtova, E., R. Kubasek, Z. Smekal, and K. Bartusek, "Digital filter banks in MR measurement of gradient magnetic fields," *Applied Magnetic Resonance*, Vol. 33, No. 4, 399–417, 2008.
2. Semmlow, J. L., *Biosignal and Medical Image Processing*, CRC Press, 2008.
3. Gescheidtova, E., *Increasing the Diagnostic Yield While Processing MR Tomography Data*, VUTIUM, BUT, Brno, 2009.
4. Bartusek, K., E. Gescheidtova, and Z. Smekal, "MR Image noise suppression using wavelet filtering," *31st International Conference TSP*, 167–169, Budapest, Asszisztencia Szervezo, 2008.

Criteria for Wavelet Selection in MR Image Filtering

Eva Gescheidtova[1] and Karel Bartusek[2]

[1]Faculty of Electrical Engineering and Communication, Brno University of Technology
Kolejni 2906/4, Brno 612 00, Czech Republic
[2]Institute of Scientific Instruments, Academy of Sciences of the Czech Republic v.v.i
Kralovopolska 147, Brno 612 00, Czech Republic

Abstract— Magnetic resonance is made use of in particular as a diagnostic imaging method. To be able to reliably establish a diagnosis, the doctors must have at their disposal images of selected parts of human organs that are of sufficient quality, with no details missing. The detected images are frequently of very low contrast and resolution. Similar to MR signals, the images are degraded by noise, the level of which depends, among other things, on the level of the signal being detected, local proton density, voxel size, bandwidth, system design, quality of the RF coil, and the detection parameters. The introduction of wavelet transform provided an efficient tool for processing not only MR signals but also MR images. For a successful processing of images it is important to select from the many currently used types of wavelet. An inappropriate choice of the wavelet can lead to the loss of important information contained in the image or, on the contrary, filtering can be less efficient.

In the paper the selection criteria are described and their importance in the selection of wavelets suitable for MR image processing is evaluated.

1. INTRODUCTION

In the early 1980s, transformations were reported that describe in a novel way a suitable combination of time and frequency information about signals, in other words transformations that are more local than the Short Time Fourier Transform (STFT). A marked advance in methods for selecting the useful signal from non-stationary signals degraded by additive noise (MR signal) came with the definition of *lossless wavelet transforms*, e.g., transforms based on the Daubechies [1], and the Haar, Shannon [2] wavelets. The discrete implementation of wavelet transform is closely connected with digital filtering via filter banks [3–5] where the wavelet can be the pulse characteristic of a suitable FIR digital filter of the type of high-pass filter. These short-time signals can better adapt to real signals than infinitely long cosine and sine curves used, for example, in the Fourier transforms. In combination with digital filter banks with perfect signal reconstruction the wavelets define the pulse characteristics of reconstruction filters. Using the wavelet transform, a marked suppression of wideband noise can be obtained via adapting individual parts of the system during filtering to the level of useful signal and distinguishing it from noise [4–6].

The introduction of wavelet transform provided an efficient tool for processing not only MR signals but also MR images. For a successful processing of images it is important to select from the many currently used types of wavelet. An inappropriate choice of the wavelet can lead to the loss of important information contained in the image or, on the contrary, filtering can be less efficient.

In medicine it is problematic to evaluate the quality of filtered images. MR images are of various degrees of contrast; the doctor makes diagnoses on the basis of many details in the image or assesses large homogeneous areas. The selection of wavelets therefore corresponds to the number of details in the image. Image quality must be assessed in the case of images with a low signal-to-noise ratio (SNR). To assess the quality of image filtering and to compare the quality of images detected using different devices, several criteria must be used. We regard as suitable criteria the SNR, steepness of brightness changes in the image, and contrast in the image.

2. SIGNAL-TO-NOISE RATIO

When removing noise from signals, a common criterion for wavelet selection is the SNR, defined as a ratio of the spectral power densities of the useful signal S_j and the noise contained in the signal n. SNR can also be accepted as the main criterion in image filtering but here its formulation is, for the time being, not unique.

Sample dispersion σ^2 can be expressed using the well-known relation

$$\sigma^2 = \frac{1}{N-1}\sum_{i=1}^{N}(x_i - \bar{x})^2. \tag{1}$$

The average value is usually subtracted from the samples — we obtain data with zero average value if x_i is a sample from the Gaussian distribution. Normalizing the standard deviation $1/N-1$ yields the best estimate of the dispersion. Similarly, normalizing the dispersion $1/N$ yields the second moment of data around x_i. The dispersion can be considered the equivalent of the RMS of data if they have the zero average value.

$$\mathrm{RMS} = \frac{1}{N}\sum_{i=1}^{N} x_i^2. \tag{2}$$

In multiple measurements several random variables are generated. If these variables are combined or added up, their average values will also be added up. The resulting random variable is simply the average value of individual average values. The same holds true for dispersion. In other words, averaging the noise from different sensors or multiple observations reduces the standard deviation of noise with the square root of the number of observations N, according to the relation

$$\sigma_{\mathrm{eff}} = \frac{\sigma_0}{\sqrt{N_{\mathrm{acq}}}}. \tag{3}$$

The calculation of SNR in images has come to be interpreted as a ratio of signal root mean square and noise root mean square

$$\mathrm{SNR} = 10\log\frac{\mathrm{RMS}_{\mathrm{Signal}}}{\mathrm{RMS}_{\mathrm{Noise}}}. \tag{4}$$

An MR image is the spatial distribution of spectral components of the signal being detected. For this reason the intensity of a point in the image is the spectral component of the signal being detected. In the evaluation it is suitable to use the average value of the signal at the image site with maximum magnitude of intensity. The level of image intensity S_i at the site where the mean value is being established must be constant. The spectral power densities of useful signal are the square of the average value. If noise is present in the image $(S_i + n_i)$, the signal root mean square of image magnitude will be given by the expression

$$\mathrm{RMS}_{\mathrm{Signal}} = \frac{1}{N}\sum_{i=1}^{N}(S_i+n_i)^2 = \frac{1}{N}\sum_{i=1}^{N}\left(S_i^2 + 2S_in_i + n_i^2\right)^2. \tag{5}$$

For a low SNR the term $2S_in_i$ will be significant and causes an error. SNR can be increased by raising the level of MR signal, i.e., by increasing the induction of basic magnetic field B_0 in the tomograph and averaging the signals detected, at the cost of longer measurement time.

The magnitude of power spectral density of noise determined according to

$$\mathrm{RMS}_{\mathrm{Noise}} = \frac{1}{N}\sum_{i=1}^{N} n_i^2 \tag{6}$$

can conveniently be determined from an image area without signal presence. Such an area can usually be found in MR images.

To evaluate the chosen criteria, a test MR image of a coronal slice of the head was chosen. The MR images of head (temporomandibular joint) were acquired on the Philips ACHIEVA MRI system (DS = 1.5 T) in the Faculty Hospital Brno-Bohunice. The measurement parameters are: T2W-FSE pulse sequence, TE = 20 ms, TR = 1600 ms, MA = 256 × 256, FOV = 160 × 160 mm, sagital slice 2 mm. The MR image of the head is shown in Fig. 1, the SNR at selected sites after filtering by the Haar and Bior2.4 wavelets can be seen in the following Table 1.

Table 2: Steepness values at selected image sites for Coiflet4 and Bior2.4 wavelets.

Wavelet used	None	Coiflet4	Bior2.4
Steepness of intensity change	398	379	383

Wavelet used	None	Coiflet4	Bior2.4
RMS_{Signal}	1664,64	1602,33	1673,97
RMS_{Noise}	10,55	3,07	2,87
SNR [dB]	21.96	27.1	27.66

Table 1: Evaluation of SNR at selected image sites for filtering by the Haar and Bior2.4 wavelets.

Figure 1: Areas for establishing signal RMS (1) and noise RMS (2).

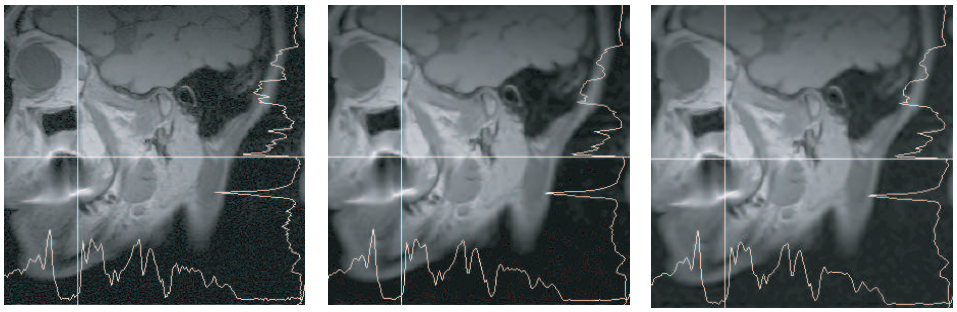

(a) (b) (c)

Figure 2: Signal intensity in the image being processed (a) original image, (b) filtered by Coiflet4 wavelet, and (c) filtered by Bior2.4 wavelet.

3. STEEPNESS OF CHANGE IN SIGNAL INTENSITY

The basic problem of simple filtering methods is the loss of image sharpness. Noise occurs in the same frequency band as the spectral components, which carry the details. Suppressing noise without knowing its properties must be a compromise between the desired smoothing and enhancement of SNR on the one hand and the loss of details on the other hand. It is necessary to find in the image the sites of step changes in intensity magnitude and evaluate the steepness of its change at these sites. The waveforms of intensities in the image at sites of steep changes are given in Fig. 2 while the calculated steepness values at selected image sites for the Coiflet4 and Daubechies6 wavelets are given in Table 2.

4. CHANGE IN CONTRAST

A third criterion for the selection of suitable wavelets is the contrast in image I defined as

$$c_{\mathrm{AB}} = I_{\mathrm{A}} - I_{\mathrm{B}}. \tag{7}$$

The relative contrast is contrast relative to reference image intensity I_{ref} $(I_{\mathrm{ref}} = (I_A + I_B)/2)$

$$\left(\frac{c_{\mathrm{AB}}}{I_{\mathrm{ref}}}\right) = 2\frac{|I_{\mathrm{A}} - I_{\mathrm{B}}|}{I_{\mathrm{A}} + I_{\mathrm{B}}}, \tag{8}$$

where I_{A} and I_{B} are the mean image intensities of the A and B image areas.

Filtering the image results in changes in its contrast. These changes are pronounced in particular in images with a low SNR. In the head image used the changes in contrast are minimal, and the contrast is the same for all the wavelet types applied.

5. CONCLUSIONS

To assess the effectiveness of filtering MR images using the wavelet transform three criteria were used. The basic criterion for the selection of wavelet functions is SNR. The differences in SNR when different wavelets are used are significant. In the test image the SNR is increased from 22 dB to 27 dB for the Coiflet4 wavelet, and to 27.6 dB for the Bior2.4 wavelet. Using the wavelet filtering,

the steepness of the intensity change in the image changed from 398 to 379 for the Coiflet wavelet, and the 383 for the Bior2.4 wavelet. It is obvious from the results that the above criteria for the assessment of the effectiveness of filtering can be applied when selecting suitable wavelet filtering functions.

ACKNOWLEDGMENT

This work was supported within the framework of projects No 102/07/0389 and 102/07/1086 of the Grant Agency of the Czech Republic and the research plan MSM 0021630513.

REFERENCES

1. Daubechies, I., "The wavelet transform, time-frequency localization and signal analysis," *IEEE Transactions on Information Theory*, Vol. 36, No. 5, 961–1005, 1990.
2. Fliege, N. J., *Multirate Digital Signal Processing*, John Wiley & Sons, Chichester, 1996.
3. Strang, G. and T. Nguyen, *Wavelets and Filter Banks*, Wellesley-Cambridge Press, 1996.
4. Gescheidtova, E., R. Kubasek, Z. Smekal, and K. Bartusek, "Digital filter banks in MR measurement of gradient magnetic fields," *Applied Magnetic Resonance*, Vol. 33, No. 4, 399–417, 2008.
5. Kubasek, R., E. Gescheidtova, and K. Bartusek, "Wavelet denoising of signal using QMF filter bank designed by Remez algorithm," *Advances in Electrical and Electronic Engineering*, Vol. 3, 13–16, 2004.
6. Bartusek, K., E. Gescheidtova, and Z. Smekal, "MR Image noise suppression using wavelet filtering," *31st International Conference TSP*, 167–169, Budapest, Asszisztencia Szervezo, 2008.

Diffusion Characteristics of Accumulators Electrode Materials

P. Marcon[1, 2], **P. Drexler**[1], **and K. Bartusek**[2]
[1]Department of Theoretical and Experimental Electrical Engineering
Brno University of Technology, Kolejni 2906/4, Brno 612 00, Czech Republic
[2]Institute of Scientific Instruments, Academy of Sciences of the Czech Republic
Kralovopolska 147, Brno 612 64, Czech Republic

Abstract— This contribution deals with a study of relaxation times measurement and diffusion constants of electrolyte accumulator materials using nuclear magnetic resonance method. This is important for understanding of electrodes material behavior in electrolytes. Magnetic resonance phenomenon is applied to increase particles energy by means of RF pulse with Larmor frequency. The RF pulse adds energy to the electrode material which is placed in the static magnetic field with flux density B_0.

The Inversion Recovery method was used for longitudinal relaxation time T_1 measurement. The Spin Echo method was used for the transverse relaxation time T_2 measurement. And the Spin Echo method with gradient field was used for the measurement of material diffusion. The samples of gels consisted of PMMA, PC and $NaClO_4$.

1. INTRODUCTION

The present investigation of polymer gel electrolytes is a very important for many branches of electrochemical devices such as accumulators, supercapacitors, electrochromic windows and sensors. The polymer gel electrolytes have lot of advantages in compare to liquid electrolytes. The value of interest of polymer gel electrolytes is not only the conductivity, but also the longitudinal relaxation time — T_1, transverse relaxation time — T_2 time and diffusion constant.

It is possible to measure the properties of gel electrolytes by means of nuclear magnetic resonance methods (NMR) in nondestructive way. In this paper T_1 and T_2 relaxation times and diffusion were measured using PMMA aprotic based gel electrolytes with $NaClO_4$ conducting agent. This is helpful for study of electrolyte chemical processes and ions migration.

2. EXPERIMENT

The samples of gels were based on polymethylmethacrylate (PMMA). Its preparation consists of mixing three convenient components:

1) Liquid monomer methylmethacrylate (MMA 99%).
2) Solid oligomer, including an initiator and a matter for polymer netting.
3) Optional components ensuring conductivity of the ions 1.0 M solution of waterless salt as sodium perchlorate in waterless propylenecarbonate (PC 99.7%).

Three samples were prepared from these components as Table 1 shows.

Table 1: Samples of gels.

Sample Number	Components
1	$NaCl + H_20$
2	1M $NaCl0_4 + PC$
3	1M $NaCl0_4 + PC + MMA$

Relaxation time T_1 was measured by the Inversion Recovery method (IR). This method uses sequences of 180° and 90° RF pulses for the measurement. Relaxation time T_2 was measured by use of the Spin Echo method (SE). This method uses 90° RF pulse and next series of 180° RF pulses for the measurement. T_2 has been determined from the half-width of the spectral line, according to

$$T_2 = \frac{1}{\pi \cdot \Delta v} \tag{1}$$

where Δv is the half-width of the spectral line which has been measured.

Diffusion constants were measured by the Pulsed Field Gradient Spin-Echo (PFG SE) [3] in every axis. Results of the measurement are in Table 2.

Table 2: Measured relaxation times of the samples.

Sample Number	T_1 [ms]	T_2 [ms]
1	45.2	10.0
2	2.2	1.8
3	5.3	3.6

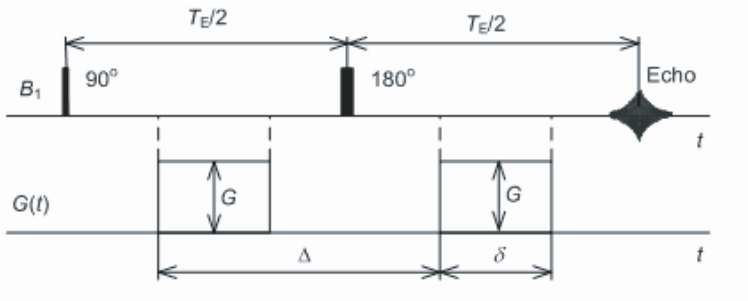

Figure 1: The RF pulse and gradient field waveforms of the Pulsed Field Gradient Spin-Echo method.

Table 3: Diffusion constants of the samples.

Sample Number	D (^{23}Na) [m^2/s]	D (^{1}H) [m^2/s]
1	8.02e-9	2.39e-009
2	3.05e-4	1.919e-009
3	2.74e-4	7.381e-010

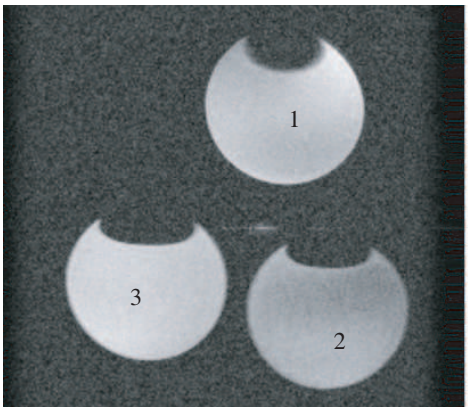

Figure 2: Slice images of nuclei ^{1}H measurement in all samples.

3. RESULTS AND DISCUSSION

The above described methods were experimentally tested on a MR tomograph at the Institute of Scientific Instruments, Academy of Sciences of the Czech Republic (ISI ASCR). The MR tomograph dispose of static field flux density $B_0 = 4,7\,\mathrm{T}$, nuclei resonance frequency is 200 MHz. The nuclei

of ^{23}Na resonate on frequency of 51 MHz. The specimen was a glass phial of 11 ml cubature filled by either 4 ml of liquid electrolyte, or 10 ml gel electrolyte.

The PFG SE method for diffusion measurement is illustrated in Figure 1.

Table 3 shows the results of the diffusion measurement. The pulse values of each diffusion measurement were: Sample 1: $\delta = 1\,\text{ms}$, $\Delta = 8.32\,\text{ms}$, $G = \pm 25000 \approx 161\,\text{mT/m}$, $T_E = 14\,\text{ms}$; Sample 2: $\delta = 0.2\,\text{ms}$, $\Delta = 7.2\,\text{ms}$, $G = \pm 1500$, $T_E = 14\,\text{ms}$; Sample 3: $\delta = 0.2\,\text{ms}$, $\Delta = 7.2\,\text{ms}$, $G = \pm 1500$, $T_E = 14\,\text{ms}$.

As you can see, the measured values of ^{23}Na diffusion constants are false in the case of Samples 2 and 3. To obtain better results the new sequence must be created. The Figure 2 shows the slice images of nuclei ^{1}H measurement in all samples.

Relaxation times of the samples are in ones of milliseconds. The sensitivity of the measurement is low, because of the low SNR in case of 50 signal accumulations. In time domain the SNR is 1, in frequency domain the SNR is 5.

4. CONCLUSION

Experimental results indicate the problems in the measurement of relaxation times and diffusion constants for gel electrolytes. The problems consist in very low SNR and short relaxation times simultaneously. At the same time the short value of echo time T_E is necessary for the diffusion constant measurement. The measurements which have been performed will be the basis for ongoing experimental work.

ACKNOWLEDGMENT

The research described in the paper was financially supported by FRVŠ (a fund of university development) by research plan No. MSM 0021630513 and GACR 102/09/0314.

REFERENCES

1. Vlaardingerbroek, M., *Magnetic Resonance Imaging*, 470, 3rd Edition, Springer-Verlag, New York, 2003.
2. Mikotova, E., K. Bartušek, and E. Gescheidtová, "Measuring of relaxation times of natrium ions by magnetic resonance methods," *Proceedings of Advanced Batteries and Accumulators International Conference*, Brno, 2006.
3. Bartušek, K., "Special methods of diffusion coefficients measurement by use of nuclear magnetic resonance," Inaugural Thesis, Brno Univeristy of Technology, Brno, 2007.
4. Vognar, J., M. Macalík, P. Špičák, J. Vondrák, V. Novák, O. Krejza, and K. Bartušek, "A study of PMMA based gel electrolytes containing Na^+ ions by nuclear magnetic resonance," *Proceedings of Advanced Batteries and Accumulators International Conference*, Brno, 2008.

Measurement of X-ray Radiation in Airplanes and the Related Methods of Protection

M. Al-Khaddour and R. Kubasek
Department of Theoretical and Experimental Electrical Engineering, Brno University of Technology
Kolejni 2906/4, Brno 612 00, Czech Republic

Abstract— The investigation into the sources of radiation, its control, and identification of the forms of radiation disintegration as well as the study of its interaction with particles (α, β, δ) are among the prominent aspects of general research on the problem of protection of humans against radiation risks. For the purpose of analyzing the effect of radiation on living cells and for the facilitation of proper protection it is of vital importance to have good knowledge of the procedures of ionizing radiation measurement. The amount of radiation on board the plane is featured in images of X-ray film, photographs, and film release of solid and clear technical specifications of the augmentation-sensitive screens for medical imaging. Further, it is important to mention dose mammography systems (the film) which radiate spherical ionizing radiation when dealing with materials and products.

1. INTRODUCTION

1.1. Cosmic Rays

Approximately a quarter of the total amount of difficulties or predicament caused to humans by natural radiation comes from outer cosmic rays. Most of the rays within this group arise out of distant space, but still some of them originate in the sun during solar flares. Naturally, Earth is affected by these rays, which interact with the atmosphere to produce other types of radiation and different radioactive materials. With respect to the rays' nomenclature, it is important to note that there exists some difference: Cosmic rays can be referred to as primary (before interaction with the atmosphere) or as secondary (after the interaction).

1.2. Primary Cosmic Rays

The rays are composed as follows:

- 87% protons
- 12% alpha particles
- 1% heavy nuclei such as carbon, nitrogen, oxygen, calcium, iron.

1.3. Secondary Cosmic Rays

A Cosmic rays falling within this group are generated after the interaction of primary rays with certain components of the atmosphere which follow hereafter.

- Light components such as electrons, mesons, and photons.
- Heavy components such as neutrons and protons. Generally, the density of primary cosmic rays decreases with the approach of the Earth's surface while the density of secondary cosmic rays increases with the approach, The components and type of the rays vary depending on the altitude in the manner given below.
- At 20 km or less, cosmic rays are only secondary (therefore, the levels or altitudes of aviation are within their reach).
- At 50 km or more, the rays are only primary.
- Cosmic rays ranging between the two elementary altitudes are a mixture of both the primary and the secondary type.

2. RADIATION DOSE IN AIRPLANES: CIVIL AVIATION

The radiation dose in civil aviation airplanes is given invariably and cannot be changed or eliminated, therefore any counteraction ought to be considered only within the limits of observing the norms of radiation protection.

At this point, let us recall the fact that the radiation dose in airplanes is the result of the interactions stimulated by solar and cosmic rays from the galaxy. In this respect, then, it is appropriate to note that there are four key factors affecting the radiation dose in airplanes (the description follows).

1. Flight time recorded: As the exposure to radiation is cumulative, with any increases in flight time duration there occurs the growth of radiation potential and deposition rate in the airplane.
2. Latitude: The incurrence increases with higher latitudes. At the poles, radiation increases about twice compared with the equator, and this fact is important especially for air crews and passengers in flying polar track.
3. Altitude: More intensive rates of exposure occur in higher altitudes as the atmosphere, which performs the function of a fundamental element of protection from cosmic rays, becomes thinner.
4. Solar activity: The sun contributes to the investigated radiation problem mainly during the highest peaks of solar activity, which occur in regular 11-year periods and are referred to as Great peak periods of solar activity (solar storms). The latest peak was the last solar cycle from 1999 to 2001, but more recently (there was a solar storm of a normal degree of potency), a significant activity was recorded also in October 2003.

Table 1: Shows the relationship between the equivalent dose to the whole body and levels of altitude.

Equivalent dose to the whole body (mSv /day)	Altitude (m)
0.17	7500
0.24	15000
0.29	30000
0.32	45000
0.35	60000
0.40	90000
0.46	120000

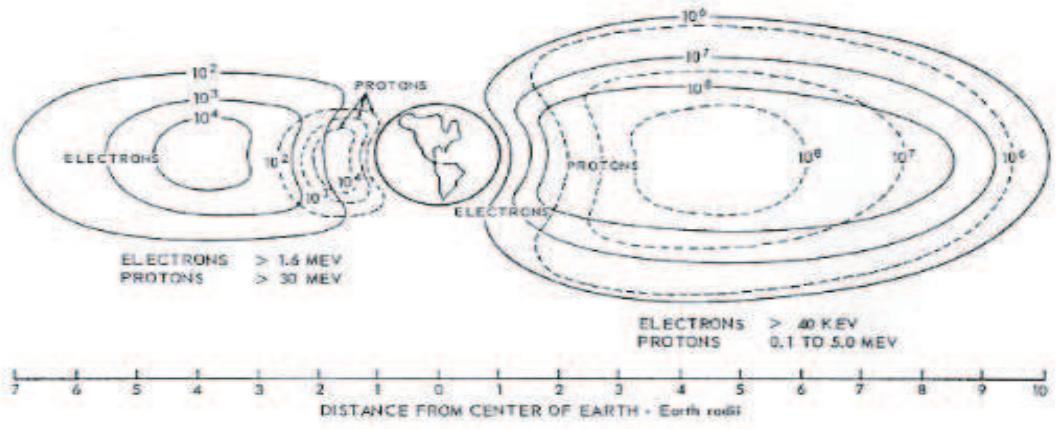

Figure 1: Trapped radiation belts as a function of energy and their distance from the earth.

3. PRACTICAL ESTIMATION OF THE DOSE RECEIVED IN AN AIRPLANE

The rate of dose received in an airplane was estimated practically using detectors of thermal luminescence (TLD). Thermal luminescence (TLD) is the thermal heating version of the way the light from insulating materials or semi-tankers was exposed to radiation before heating.

4. THE PRINCIPLES OF WORK

The principle of how this version uses the model of transport in bands and isolators is the semi-tanker. The related materials are exposed to radiation; then, their electrons gain enough energy to

lift the parity of the band to the band of transport. Some of the electrons belonging to a band of parity traps are captured (wells latency) and exist in the forbidden energetic region.

These electrons will remain captive in the trap till they receive some external power (usually through thermal heating) sufficient to free the captive electron, which is transmitted within the substance to combine with a charge inert from the counter wave; the electrons lose their capacity through the emission of a photon which is called Thermal Luminescence Photon (TL photon), and the centers where the photon is released is called Luminescence Centers (TL centers). The quantity of photons reborn during the heating process is commensurate with the radiation which had been reborn before the heating took place, so the materials of TLD are used as a detector.

One of the functions of the curve characteristics is to allow us to predict the amount of change required for the correction of an error of exposure. For example, we can infer from the curve that the average density at the bottom of the curve is 0.35 and the relative exposure is 4. If the exposure is doubled or if the relative exposure increases to 8, we can expect that the average density will increase to 0.8.

5. THE METHODS OF PROTECTION

1. Occupational exposure this aspect is considered in workers who are exposed to an annual dose of more than 1 mSv of cosmic radiation and therefore must take action to manage this problem.
2. The level of interference Specific types of action must be taken that will lead to the prevention of exposure to the level of annual dose. The related consideration level: 6 mSv, modify the list of works to get close to this value.
3. Application limit dose the management of occupational exposure to cosmic rays requires intervention when the annual exposure is more than 1 mSv.
4. Overexposure the n source of exposure is relatively constant, with the sole exception being the above-mentioned rare instances of the glow of the sun, during which n displays in the air and the environment of an airplane acquires a very high level of radiation doses. Any airplane flying at a high altitude should be provided with devices for dose rate n measurement or receive the necessary information from satellites or ground stations. In the occurrence of sudden solar flares, the number of night flight(s) must be reduced, which will in turn lead to the dose reduction.
5. Monitoring Information must be provided concerning the "dose" path leading to the maintenance of expected dose levels in workers. If it is useful to control the received doses during each journey, it is also important to use computer programs to harmonize the dose of the trip and the recorded group air. For aircraft flying at an altitude of more than 50,000 feet (15 kilometers), the related equipment must be provided to facilitate monitoring of the area. Alternatively, it is possible to communicate to the airplane the necessary information by satellite or ground stations.

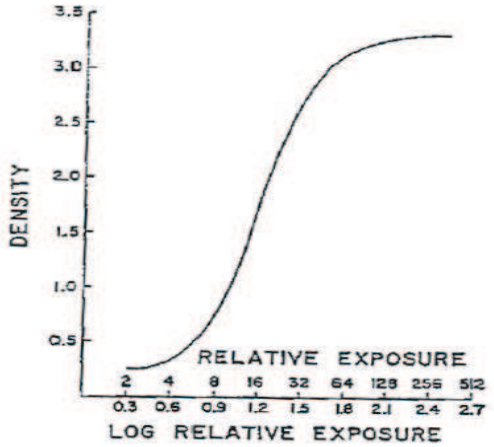

Figure 2: The relationship between the density and the log relative exposure.

6. Passengers due attention must be paid to travelers who are subject to an annual dose exceeding 1 mSv of cosmic radiation in fulfilling their professional duties (regular exposure experienced by professionals).
7. The dose received by workers returning from their air trips and by those at the top of their work during the return trip should be added to the individual records.
8. Pregnant women Pregnant must provide sufficient advice about their condition well in advance. During pregnancy, only minimum level doses should be received in order to protect the fetus, who is very sensitive to radiation. Ideally, any exposure to cosmic radiation should be excluded, which means that pregnant women ought to be assigned professional tasks other than those that may cause exposure.
9. Professionals working in the air need to know that the employer must inform the staff or the company management about any possible risk stemming from the exposure to cosmic rays.

6. CONCLUSION

Calculate the dose received from the air during the work period of five years assuming that the working hours are equal to 700 hours of flight per year of the entire period of five years. Further, assume the stress of the flight path from Jeddah to Damascus and the value of the estimated dose is 0.0037 mg Sv.

$$y \cdot h \cdot f = 5 \cdot 700 \cdot 0.0037 = 13\,\text{mSv} \tag{1}$$

ACKNOWLEDGMENT

This work was supported by/within the project of the Grant Agency of the Czech Republic No. 102/09/0314, ELCOM, No. MSM 0021630513 and FR-TI1/368.

REFERENCES

1. The publication of X-ray Radiation Specifications of the Syrian Arabian Republic Standards Organization (SASMO), Ministry of Industry, Syria.
2. The publication of X-ray Radiation Specifications of the Saudi Arabian Standards Organization (SASO).
3. L'Annunziata, M. and M. Baradei, *Handbook of Radioactivity Analysis*, 58, Academic Press, 2003, ISBN 012-43-6603-1.
4. Burattini, E. and A. Ballerna, "Biomedical applications of synchrotron radiation," *Proceedings of the 128th Course at the International School of Physics, Enrico Fermi*, 15, IOS Press, Varenna, Italy, July 12–22, 1994, ISBN 905-19-9248-3.

Computation of SAR Distribution in a Human Exposed to Mobile Phone Electromagnetic Fields

Luan Ahma, **Mimoza Ibrani**, **and Enver Hamiti**
Faculty of Electrical and Computer Engineering, University of Prishtina, Kosovo

Abstract— The most important dosimetric parameter used to assess human exposure to RF electromagnetic fields is SAR. Since SAR depends from dielectric properties of biological tissues and induced electric field, dielectric properties of human body tissues are addressed. At mobile communication frequencies biological tissues may be considered as lossy dielectrics. Radiation from mobile phone on talk position mostly covers human head.

In order to assess human exposure to mobile phone electromagnetic fields we have run simulations with SEMCAD (FDTD code) for model: human head + mobile phone.

Obtained result of Spatial Peak SAR averaged over 1 g of biological body tissues is 2.1 mW/g for typical transmitting power of mobile phone 250 mW, while obtained result for Spatial Peak SAR averaged over 10 g of biological body tissue is 1.35 mW/g.

Visually SAR distribution is presented. As noticed Peak SAR appears near human ear.

1. INTRODUCTION

Even though mobile phone is considered by many as fundamental of their lifestyle, exposure to cellular mobile communication electromagnetic fields has raised individual and public concern regarding possible adverse effects to people exposed to such radiation.

In developed countries more than half of population owns and uses on daily basis a mobile phone. Moreover increased usage among all age groups including children and elders is being reported.

Exposure of humans to electromagnetic field of mobile phone is being followed by many governments, research projects, industries and general population that are concerned regarding potential biological and health effects caused by mobile phone radiation.

At frequencies above 100 MHz, including here frequencies of mobile telephony the most important dosimetric parameter used to assess human exposure to electromagnetic fields is SAR (Specific Absorption Rate).

Dosimetric studies are performed to quantify the interactions of electromagnetic fields with biological tissues.

Whether they are numerical or experimental the SAR distribution has to be determined. For this reason almost all national and international safety guidelines and recommended limits on human exposure to electromagnetic fields are given in terms of SAR.

Radiation from mobile phone in talk position covers mostly human head. Determination of induced electrical field inside a human head exposed to mobile phone radiation is a complicated issue having in mind a near distance between phone and human head, dielectrical properties of head biological tissues etc.

Due to sensitivity and ethics on experiments with humans in order to calculate SAR in human head different numerical methods may be used. Finite Time Difference Domain is shown as very appropriate [1] thus software SEMCAD Jungfrau that is based on this method is used for simulations and SAR calculation in this paper.

The SAR, time rate of RF energy absorbed per unit mass of body biological tissue is given as:

$$\mathrm{SAR} = \frac{(\sigma + \omega\,\varepsilon_0\,\varepsilon_r'')\;E^2}{\rho} \quad (\mathrm{W/kg}) \tag{1}$$

where E — induced electrical field; σ — conductivity of biological tissue, ω — angular frequency, ε_r'' — imaginary part of complex permittivity, ρ — density of tissue.

As noticed SAR depends from induced electrical fields and electric properties of human body biological tissues. So before doing any SAR calculations the electrical properties of human body biological tissues should be addressed.

2. ELECTRICAL PROPERTIES OF HUMAN BODY HEAD BIOLOGICAL TISSUES

Comparing with other non-living materials used in applied electromagnetics, human body is composed by many biological tissues each with specific electrical properties.

Biological tissues of humans may be considered as diamagnetic materials with permittivity equal to permittivity of free space ($\mu_r = \mu_0$), thus having in mind Maxwell equation for continuation of magnetic flux we can conclude that human body is transparent to magnetic field.

Dielectrical properties of human body are strong function of frequency. At mobile phone frequencies analyzing ratio $\omega\varepsilon/\sigma$ as given on [2] we can conclude that human body biological tissues, including here head tissues, may be considered lossy dielectric.

Even though lately there have been many studies showing that dielectric properties of biological tissues are also age dependent [4], in paper SAR is calculated for human of middle age, no gender or age distinction.

Analyzing penetration depth at RF we can say that most critical organs are external biological tissues while comparing permittivity of body biological tissues can be concluded that on eyes, gallbladder, and body liquids will have stronger induced flux for same exposure conditions.

Running application [3] values of permittivity and conductivity of biological tissues will be obtained for different frequencies. Thus human eyes are among most sensitive organs as they are external and have big values of relative permittivity. Of course, this has to be considered if we place phone near eyes.

As model of human head for calculating SAR is used SAM (Specific Anthropomorphic Mannequin) phantom that represents 90 percentile of male head.

SAM is composed from two tissues: SAM shell with permitivity of 3.7 and SAM liquid with relative permitivity of 41.5 and conductivity of 0.97 (S/m), that coresponds to mean values of properties of biological tissues that comprise human head.

3. SAR DISTRIBUTION IN A HUMAN HEAD

There are few algorithms for SAR calculation during human exposure to electromagnetic fields. Whole body averaged SAR is not an appropriate one while calculating SAR distribution on specific parts of human body.

In order to assess SAR distribution on human head exposed to mobile phone radiation, we have simulated exposure scenario modeling mobile phone as perfectly conducting box with monopole antenna and as head model using SAM.

SAR is calculated as Spatial Peak SAR as per IEEE 1529 recommendation. Head is exposed to 900 MHz electromagnetic fields.

Obtained result of Spatial Peak SAR averaged over 1 g of body tissues is 2.1 mW/g for typical transmitting power of mobile phone 250 mW [5]. Surface distribution of SAR in SAM phantom is given on Figure 1.

As European safety standards give Spatial Peak SAR averaged over 10 g of body tissues we have run the simulations for the same model with unchanged parameters. Obtained value for Spatial Peak SAR averaged over 10 g of biological body tissue is 1.35 mW/g. Spatial Peak SAR averaged over 10 g, cut with slice $z = 0.033$, is illustrated on Figure 2.

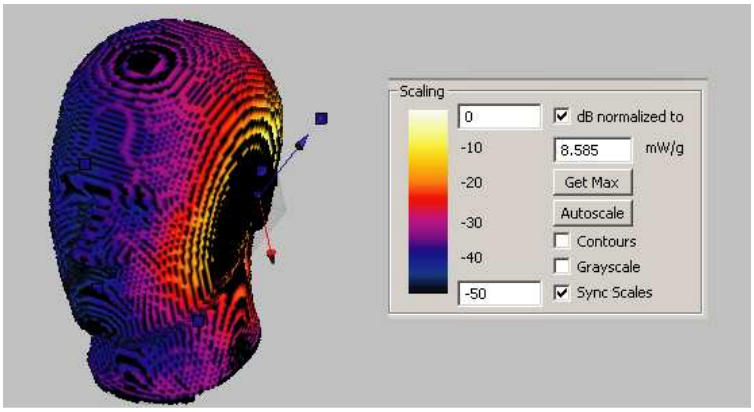

Figure 1.

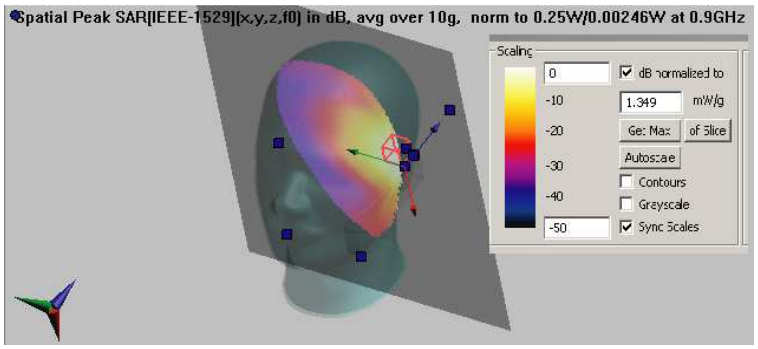

Figure 2.

4. CONCLUSIONS

Simulation of exposure scenario provides a solid way to compute SAR distribution on human during exposure to mobile phone electromagnetic fields.

At GSM 900 MHz, obtained results for Spatial Peak SAR averaged over 1 g of body tissues is 2.1 mW/g for typical transmitting power of mobile phone 250 mW.

Obtained value for Spatial Peak SAR averaged over 10 g of biological body tissue is 1.35 mW/g. As noticed Peak SAR appears near human ear.

Still, age dependence of dielectrical properties of human biological tissues and SAR computation for different age groups should be further studied while human eyes should be considered as sensitive organs to electromagnetic fields

REFERENCES

1. Schmidt, S., "Finite-difference time-domain methods for electromagnetic problems involving biological bodies," Doctoral thesis, 2005.
2. Interactions Between Electromagnetic Fields and Biological tissues, Questions, Some Answsers and Future Trends, http://www.cmap.polytechnique.fr/∼poignard/Ics_cegely.pdf.
3. Compilation of Dielectric Properties of Body Tissues at RF and Microwave Frequencies, Camelia Gabriel and Sami Gabriel, 1997
4. Gernot, S., et al., "Age dependence of dielectric properties of bovine brain and ocular tissues in the frequency range of 400 MHz to 18 GHz," *Phys. Med. Biol.*, Vol. 50, 4711–4720, 2005.
5. Ahma, L., M. Ibrani, and E. Hamiti, "Assessment of SAR in a human exposed to GSM electromagnetic fields," *Proceedings of the 13th WSEAS International Conference on Communications*, 131–135, Rodos, Greece, 2009.
6. Furse, C., C. Durney, and D. Christensen, *Basic Introduction to Bioelectromagnetics*, 2nd Edition, CRC, March 9, 2009.
7. Poljak, D., *Human Exposure to Electromagnetic Fields*, Witt Press, 2004.

Effects of Heliogeomagnetic Disturbances on Haemorheological Parameters of Human

Yu. Ya. Varakin[1], **V. G. Ionova**[1], **G. V. Gornostaeva**[1], **E. A. Sazanova**[2, 3], **and N. P. Sergeenko**[2]

[1]Scientific Center of Neurology RAMS, Moscow, Russia
[2]Pushkov Institute of Terrestrial Magnetism, Ionosphere and Radio Wave Propagation RAS Troitsk, Moscow, Russia
[3]Clinical Hospital of Russian Academy of Sciences, Troitsk, Moscow, Russia

Abstract— The changes of characteristics of blood at the healthy people during 23 geomagnetic disturbances were studied. The analysis of dynamics of haemorheological parameters of both human groups has shown that the most of parameters are beginning statistically authentically to fall outside the normal limits already prior the beginning of the magnetic disturbance, others — per day of a beginning of disturbance. Such effect can be caused by as direct and indirect action of an electromagnetic field of the Earth on the cells of blood. The influence of geomagnetic disturbances on rheological property of blood can be associated with the action of electromagnetic fields through synchronization of rhythms of electromagnetic cells oscillations in central nervous system.

1. INTRODUCTION

In recent decades, it was accumulated many new facts indicating on action geomagnetic storms on cardio-vascular system, on the course of already existing respiratory organs disease and on psychoemotional status of man [1]. Heliogeomagnetic disturbances influence on a functional status of system of a hemostasis and rheological property of a blood [2–5]. The infringements of rheological property of a blood have significant influence on macro- and microcirculation, tissue exchange.

The participation of catecholamins in a regulation of cell functions, including, as separately rheological characteristics of erythrocytes, and plateletely-vascular interactions was established. Hormones of a stress-catecholamins is directly or indirectly impact on the lipases activity, phospolipases, intensity of peroxide oxidizing of lipids. The above specified biochemical processes can be implemented in pinch of aggregation activity of blood cells, platelets, causing activation of enzymes of a hemostasis system and vasospasm of microvasculature [5].

The purpose of the present work was the analysis of features of haemorheological detrusions, platelets activity — vascular link of a hemostasis and performances of changes of concentration of catecholamins in a blood of the people in conditions of heliogeomagnetic perturbations which represents the scientific and practical interest.

2. MATERIAL AND METHODS

Haemorheological parameters of 62 practically healthy men examined in process of screening of the population of Moscow, were received in Scientific center of neurology RAMS in quiet conditions and in time of heliogeomagnetic perturbations. It was not observed scerebro-vascular pathology, attributes of ischemic illness of heart in examined subjects (according to the data from examination and ECG). The subjects were of follows age: 40–49 years — 42 %, 50–59 years — 48.4 % and 60–64 years — 9.6 %. The work of the examined persons was not connected to a professional harmfulness (chemical and toxic manufacture, the action of electromagnetic fields and radio-frequency radiations were excluded). In all examined persons defined viscosity of an integral blood (VC), hematocrit (HT), concentration of Fibrinogenum (FG), ability of erythrocytes to aggregation (AE), and ADF (an adenosinediphosphatase acid) — induced platelet aggregation. (ADF-AT).

Variation of catecholamins of plasma: Noradrenalin (OA), adrenalin (A), dofamin (DA) were measured in 73 men in different heliogeomagnetic conditions.

For an estimate of a geomagnetic situation was used a K-coefficient of IZMIRAN observatory (Moscow, Russia), and also hourly Dst, and AE coefficients. The K-coefficient represents the numerical performance of a degree of disturbance, expressed in numbers, where to each number corresponds to amplitude of a geomagnetic field (in nTl) for a three-hour. Dst — the coefficient characterizes occurrence and development large-scale planetary geomagnetic storm. On the Earth

also there are shorttime perturbations — substorms. Their beginning and the intensity describes AE — coefficient. In the Moscow region they are shown as well as world storms, but last usually 5–7 hours.

At mathematical processing the Student criterion was used, reliable considered differences at $p < 0.05$.

3. THE RESULTS OF EXAMINATION

The results of examination have shown, that investigated haemorheological parameters tend to increase in periods of heliogeomagnetic perturbations. In a Fig. 1 dynamics of medial values haemorheological parameters per quiet days, for one–two days before storm, during perturbations and three days after storm are submitted.

As it is visible from a figure, all parameters per quiet days did not overstep the bounds of normal oscillations, while the majority of the viewed parameters begins to change already before the beginning magnetic storm. Per days of perturbations the medial quantity of an aggregation of erythrocytes at the people in 1.6 times exceeds its value per quiet days, and the aggregative activity of platelets grows in 1.4 times. The statistical analysis has shown, that in these cases the considerable excess of upper parameter of norm of AE and ADF-AT is accompanied by double magnification of a root-mean-square deviation. It specifies on major variation of functional activity of blood cells in time of heliogeomagnetic perturbations.

The viewing of changes of catecholamins in a blood of the healthy people has revealed detrusions of investigated parameters in periods of heliogeomagnetic paroxysms in comparison with quiet days (Fig. 2).

During perturbations, 2 days prior to storm and in 2 days after storm a level NA raises from 343.3 pg/ml to 577.3 pg/ml and from 516.2 pg/ml to 537.9 pg/ml ($p < 0.05$). In the disturbances periods the level A at the healthy persons also grows, with more grown until storm from 136.3 pg/ml to 185.8 pg/ml ($p < 0.05$), at the moment of storm its concentration has increased by 30.5 %, and after-on 8.2 % in comparison with a quiet period. Thus the concentration DA 2 days prior to storm and in time of storm decreases, accordingly on 51.7 % and 60.6 %. And in 2 days after storm grows more than in 2 times.

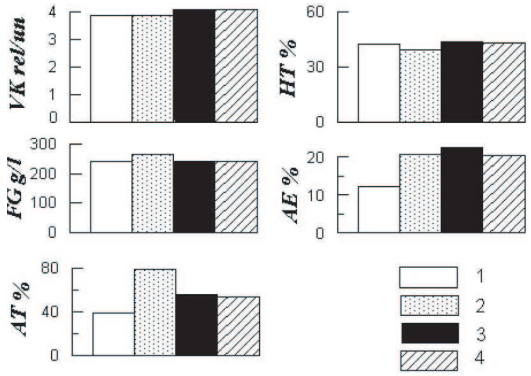

Figure 1: Dynamics of medial values haemorheological parameters of healthy men per quiet days (1), one–two days before storm (2), during perturbations (3) and three days after storm (4).

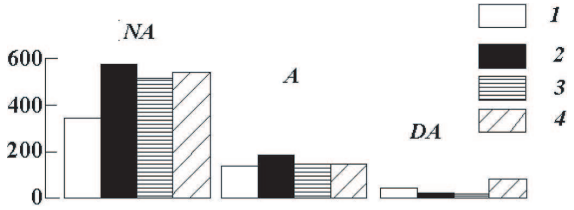

Figure 2: Dynamics of changes of concentrations of catecholamins of a blood plasma at the healthy people in per quiet days (1), one–two days before storm (2), during perturbations (3) and three days after storm (4).

4. DISCUSSION

Haemorheological shifts and changes of neurotransmitter concentrations in a blood, associated with increased heliogeophysigal activity, allow to suggest, that under the circumstances a human organism is exposed a number of physical factors. These factors are associated with magnetospheres activity caused by action solar corpuscular streams. As these changes of parameters of a blood begin to occur prior to the beginning of magnetic storm and before any changes of an amplitude of a geomagnetic field, it may be safely suggested that one of the basic physical mechanisms at initial stages of perturbations can be a stochastic resonance. The exterior oscillations can synchronize or desynchronize rhythms of humoral systems of a human organism. It appears that the development of the resonant phenomena probably may lead a stress reaction with activation sympathoadrenal system, that can result in increased aggregation of cell elements of a blood and increased of intensity of processes hemocoagulation.

From all spectrum of an electromagnetic field on a surface of the Earth, the biologically effective factor is in that frequency rang, where a level of a field is greatest, and the differences of its intensity from quiet conditions to disturbances are great enough. To such requirements satisfies a range of superlow frequencies, in which low-frequency "transparency window" of an ionosphere is situated. The electromagnetic waves with such frequencies freely reach the Earth, and the intensity of this low-frequency radiation increases 10–100-fold during disturbances [6].

In a low-frequency range, beside for micropulsations generated by processes in a magnetosphere of the Earth, and Shuman resonances, in a region of the Earth — the ionosphere is formed the resonator for Alfven waves. The resonancet structure of a spectrum of an atmospheric noise phon is regularly apparent feature of background electromagnetic noise within the frequency range 0.1–10 Htz. The Alfen's ionospheric resonancet structure of a spectrum is the fundamental characteristic of an electromagnetic field in a region of the Earth — ionosphere. The parameters of resonancet structure are controlled by a structure and degree of disturbance of an ionosphere in a point of observation.

In period after of a beginning geomagnetic storm and increase variations of amplitude of a geomagnetic field it appears to be a direct action of a geomagnetic field. Now it is reliably established, that inside of alive organisms it can be present nano crystals of ferromagnetic minerals, in particularly Fe_3O_4 [7]. It is defined, that they have a biogenic origin, i.e., are formed as a result of a crystallization directly in cell medium. The biogenic magnetite is found out in a brain and in the other human organs, also in birds, insects and bacteria. The presence of a magnetite in alive organisms is one of the possible reasons of their sensitivity to feeble magnetic fields and variations of a geomagnetic field.

The blood, due to erythrocytes, also can be considered as magnetic medium. The haemoglobin of erythrocytes is included atoms of iron having a non-zero magnet. moment Therefore medium containing such particles, is capable to show properties proper which are common to magnetics. In the disturbances conditions of an electromagnetic field with frequencies from several hertz up to several kilohertz increases, so the spontaneous magnetization of particles can lead to occurrence groups with oriented particle packing due to a parallel alignment of their magnet moments. Moving in a vasculature, this group represents soliton object or S-object. The vector of a magnetic flux of S-object is defined by product of a vector of a magnetic induction on a cross-sectional area of the channel, on which it moves. In his motion the S-object can influences on a lumen of a vasculature. Simultaneously, according to law of electromagnetic induction, there will be electrical currents arising to compensate the changes of a magnetic flux. The Lenz's rule demands, that these currents should be circular and circulated in a plane, of a perpendicular axis of the channel [8]. The presence in a blood plasma of a plenty of ions does it electroconductive. It is known, that the rheological property of a blood and its flow properties are caused not only by the viscosity characteristics, but also by the autoregulative control mechanism, including also vasculomotor autoregulation. It is proved, that the local control of a diameter of arterias is based on ability of endothelial cells to feel a voltage of shift, the changes of which characteristics are closely associated with variabilites of values of blood velocity and blood viscosity at different levels of hemocirculation. The quantity of viscosity of a blood is defined by integrated interaction of a variety of factors: First of all by viscosity of plasma, by hematocrit, deformability and by aggregative ability of erythrocytes. Increasing of the viscosities characteristic of a blood (statistically significant increase of average parameters of viscosity of a blood, hematocrit, level of fibrinogenum), and also increase of agregation of erythrocytes, which are marked by us during geomagnetic disturbances probably, are guided on optimization of delivery of oxygenium to tissues, thus, carrying out compensative

function. At the same time the existence of a particular coordination of dynamics of increasing of catecholamins concentrations in a blood with changes of values of fibrinogenum and agregative activity of thrombocytes and erythrocytes in periods of heliogeophysical perturbations can be considered as reflection of the answer on stressful action of the heliogeophysical factors. Thus, the moderate increasing of the viscosities characteristics of a blood at the healthy persons induced by heliogeophysical perturbations, can lead to increasing of coagulation potential manifesting by activation of functions of thrombocytes and increasing of concentrations of fibrinogenum at various levels of a blood circulation system. Mentioned haemorheological shifts, contributing to activations of a haemostasis, are accompanied by turning-on of mechanisms of a physiological hemodilution at a level of microcirculation, that promotes increase of efficiency of giving of oxygenium to tissues.

5. CONCLUSION

Submitted above data on changes of the haemorheological parameters and humoral shifts at healthy men are specific for stressful responses, which, as it was shown, can be, to some extent connected with changes of a geomagnetic field. The results our study let us to suggest, that, probably, one of main mechanisms of action of heliogeophysical perturbations capable to influence on hemoscirculation of the healthy man is as direct actions, and indirect (in particular, through catecholamins) effects on reological property of a blood. It is obvious, that response of composite nonlinear systems, what the human organism is, on feeble exterior actions of heliogeophysical character depends not only on properties of the influencing factor, but also from a state of the system. At integrity interior paving of a vascular channel at the healthy people of change of rheological properties of a blood and activation of platelets-vascular hemostasis connected with perturbations wear reversible, adaptative character.

REFERENCES

1. Komarov, F. I., T. K. Breus, S. I. Rapoport, V. N. Oraevskii, Y. L. Gurfinkel, F. Halberg, G. Cornelissen, and S. I. Chibisov, "Medicobiological effects of solar activity," *Vestn. Ross. Akad. Med. Nauk*, No. 11, 37–49, 1994.
2. Ionova, V. G., E. A. Sazanova, N. P. Sergeenko, G. V. Gornostaeva, and K. D. Kanonidi, "Response of the human organism to heliogeophysical disturbances," *Biophysics*, Vol. 48, No. 2, 361–365, 2003.
3. Varakin, Y. Y., V. G. Ionova, E. A. Sazanova, and N. P. Sergeenko, "The wavelet analysis at heliobiological connection," *Biophysics*, Vol. 49, No. 4, 684–687, 2004.
4. Ionova, V. G., E. A. Sazanova, and N. P. Sergeenko, "Influence of heliogeophysical disturbances on the haemorheological characteristics of the people," *Aerospace and Ecological Medicine*, Vol. 38, No. 2, 33–37, 2004 (in Russian).
5. Baluda, V. P., M. V. Baluda, I. I. Deyanov, and I. K. Tlepshukov, "Fiziologiya sistemy gomeostaza," *Physiology of Homeostasis System*, 243, Moscow, 1995.
6. Akasofu, S.-I. and S. Chapman, *Solar-terrestrial Physics: An Account of the Wave and Particle Radiations from the Quiet and the Active Sun, and of the Consequent Terrestrial Phenomena*, Clarendon Press, Oxford, 1972. Translated under the title *Solnechno-zemnaya Fizika*, Mir, Moscow, 509, 1975.
7. Bingi, V. N., D. S. Chernavsky, and A. B. Rubin, "The factor of temperature and magnetic hum in conditions of a stochastic resonance of magnetosoms," *Biophysics*, Vol. 51, No. 2, 274–277, 2006.
8. Rodionov, Y. Y., A. A. Yaknovets, A. A. Naumenko, and V. I. Shebeko, "Electromagnetic fields in hemodynamics physical mechanisms of interrelationship. Electromagnetic fields and human heals," *Proceeding of the Second International Conference "Problems of Electromagnetic Safety of the Human Being. Fundamental and Applied Research. Development of EMF Standards: Philosophy, Criteria and Harmonization*, 40–41, Moscow, 1999.

Improvement of the Confidence Interval Level of Multi-frequency Microwave Radiometer System for Measuring Deep Brain Temperature in New Born Infants

T. Sugiura[1], **N. Umehara**[1], **S. Mizushina**[2], **and H. Hirata**[1]

[1]Research Institute of Electronics, Shizuoka University, 3-5-1 Johoku, Hamamatsu 432-8011, Japan
[2]Hamamatsu Science Promotion Financial Group, 3-5-1 Johoku, Hamamatsu 432-8561, Japan

Abstract— Clinical trials of hypothermic brain treatment for newborn babies are currently hindered by the difficulty in measuring brain temperature non-invasively. As one of the possible methods for non-invasive temperature sensing and monitoring that is completely passive and inherently safe is passive microwave radiometry (MWR). Five-band microwave radiometer system and its feasibility were reported and then confidence interval level of the temperature estimation at 5 cm depth from the surface was 1.6 K. This result was not good enough for clinical application because clinical requirement is less than 1 K. This paper describes the improved result of temperature resolutions of the five radiometer receivers, and shows the new confidence interval obtained by the same simulation method. Obtained better temperature resolutions are 0.103, 0.129, 0.138, 0.105 and 0.111 K for each receiver and new confidence interval level is 0.70 K at 5 cm. We believe that the system takes a step closer to the clinical hypothermic treatment.

1. INTRODUCTION

Although cooling the brain of newborn baby can reduce neuro-developmental impairment after a hypoxic-ischemic insult [1], clinical trials are currently hindered by the difficulty in measuring brain temperature non-invasively as well as continuously. Currently there are few experimental data on the temperature distribution within the brains of newborn infants. MRI and MR spectroscopy methods have been used to measure temperature changes in the brain, however, these require access to complex equipment and they are not suitable for routine measurements repeated over a prolonged period of time. Invasive methods for direct measurement of deep brain temperature have not been applied for ethical reasons, and correlations between deep brain temperature and surrogate measures such as tympanic membrane, nasopharyngeal, oesophageal or rectal temperatures are uncertain, particularly in an infant undergoing active therapeutic cooling.

As one of the possible alternative methods for non-invasive temperature sensing and monitoring that is completely passive and inherently safe is microwave radiometry (MWR). The first temperature measurement study for an agar-phantom temperature-profile-model by MWR have been reported in PIERS 2006 [2] especially on 2-σ confidence interval (temperature sensing accuracy) at 5 cm depth from the surface. Then temperature resolutions were 0.280, 0.321, 0.155, 0.113 and 0.122 K for 1.2, 1.65, 2.3, 3.0, and 3.6 GHz receivers, respectively. Using these resolutions, the confidence interval level at 5 cm depth was simulated to be 1.6 K. Because the clinical requirement is less than 1 K, further improvements of MWR system were essential for a successful hypothermia treatment. We have done a couple of actions to reduce background noise in order to obtain the better temperature resolutions and tried to retrieve the temperature profile by using the same brightness temperature data and the microwave radiometric weighting functions used in the previous study [2]. This paper describes the feasibility of MWR system for clinical hypothermic treatment.

2. METHODS

2.1. Microwave Radiometry

MWR involves measuring the power in the microwave region of the natural thermal radiation from body tissues to obtain the so-called brightness temperature of the tissue under observation. Brightness temperature T_B is defined as

$$T_B = \frac{P}{k\Delta f} \tag{1}$$

where P is the thermal radiation power received by the radiometer's antenna in a bandwidth of Δf around a frequency f, and k is Boltzmann's constant. The antenna is a short waveguide-type

which is in contact with the head surface. Therefore, not all of the thermal radiation power from the tissues, P_{tissue}, reaches the radiometer because of reflections at the boundary between the tissue and dielectric material in the antenna. Brightness temperature, T_B, thus is expressed as

$$T_B = \frac{(1-R)\,P_{\text{tissue}}}{k\Delta f} = (1-R)\,T_{B,\text{tissue}} \tag{2}$$

where R is the unknown reflection coefficient at the tissue-antenna interface at f. The unknown reflection power can be cancelled by the thermal power of the reference noise source (RNS) in the radiometer in the balance mode operation [3].

Since the thermal radiation intensity at microwave frequency range is proportional to the absolute temperature, T_B may be expressed as

$$T_B = \iiint\limits_{afv} W(r)T(r)\,dV \tag{3}$$

where $T(r)$ is the absolute temperature in an incremental volume of tissue dV located at the distance r from the center of antenna aperture, $W(r)$ is the radiometric weighting function which links the tissue temperature and the measured brightness temperature. The integration is over the antenna's field of view (afv). $W(r)$ is obtained using the electromagnetic power density distributions which is calculated by the finite difference time domain (FDTD) method [2].

2.2. System Improvement

System noise temperatures are in the range of 325–455 K while the target brain temperature is about 310 K. Though the structure of radiometer is almost the same as that of a radio-telescope whose noise is usually minimized by cooling the receiver to cryogenic temperatures, the present microwave radiometers need to operate in a room temperature as might be expected. Therefore low noise microwave components have been used in the system. In this work, in addition to low noise componets, an analog to digital converter with input-output ports, which controls the system and gathers temperature data, T_{Bi} (T_{RNS}) and T_{water}, is changed to a low-noise type. Cables around an isolating transformer and primary power source circuits are doubly shielded and the water-bath is also shielded by fine woven metal wires.

2.3. Calibration Experiment

Five receivers ($f_i = 1.2, 1.65, 2.3, 3.0$ and 3.6 GHz) are calibrated by measuring the brightness temperatures of water. Actually, the water temperature is gradually increased so that there is enough time to balance T_{Bi} and T_{RNS}. When the balance is achieved, both temperatures are recorded in a PC and calibration curves are obtained for the five receivers.

2.4. Temperature Retrieval Simulation

Because finding an estimate for the temperature distribution from a set of measured brightness temperatures (five brightness temperatures in our system) is an inverse problem, we have previously reported a method to use a priori knowledge of the temperature profile in the brain [4]. Thus estimated temperature profile is achieved by minimizing the error function below,

$$\text{Error} = \sum_{n=1}^{5} \left(T_{B,\text{model},i} - T_{B,\text{measured},i}\right)^2 \tag{4}$$

where $T_{B,\text{measured},i}$ is the measured brightness temperature, i is the center frequency of the each receiver and $T_{B,\text{model},i}$ is the "model" brightness temperature at f_i calculated by using a priori temperature profile and radiometric weighting functions. A priori temperature profile in the brain is expressed as

$$T(z) = T_0 + \Delta T \cdot SF(z) \tag{5}$$

where T_0 is the surface temperature (cooling bolus temperature), ΔT is the differential temperature between the surface and the center of the brain and $SF(z)$ is the shape function which is the normalized temperature profile. Simulations of the temperature profile retrieval and 2-σ confidence interval were made using the same temperature distribution used in the previous work and the temperature resolutions obtained in this study.

3. RESULTS AND DISCUSSION

One example of calibration results is shown in Fig. 1 (3.6 GHz receiver). Abscissa is the water temperature and ordinate is the brightness temperature (RNS temperature). A regression line is drawn on those points and the temperature resolution of the receiver is defined from the standard deviation. The resolution of the receiver is 0.111 K. Thus obtained receiver resolutions are compared to those previously reported and listed in Table 1. Resolutions of five receivers have been successfully improved in this study. Temperature resolutions of radiometer receivers have direct effects on the estimation accuracy or confidence interval of the estimated temperature.

Table 1.

Receiver (GHz)*	Resolution (K) [2]	Resolution (K)
1.2	0.280	0.103
1.65	0.321	0.129
2.3	0.155	0.138
3.0	0.113	0.105
3.6	0.122	0.111

*Center frequency.
**Each receiver has 0.4 GHz bandwidth.

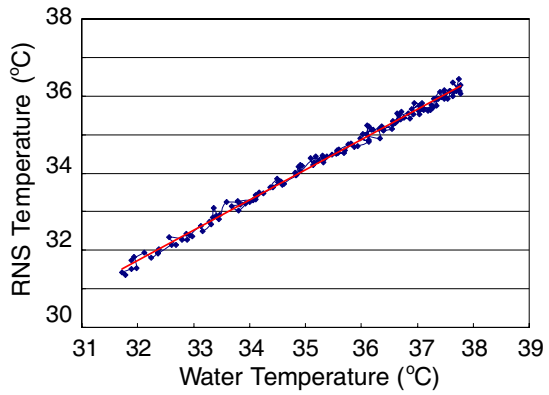

Figure 1. Calibration line of 3.6 GHz receiver. Dots are balanced points and a linear curve is a regression line. Temperature resolution of the receiver is defined from the standard deviation, and 0.111 K for this receiver.

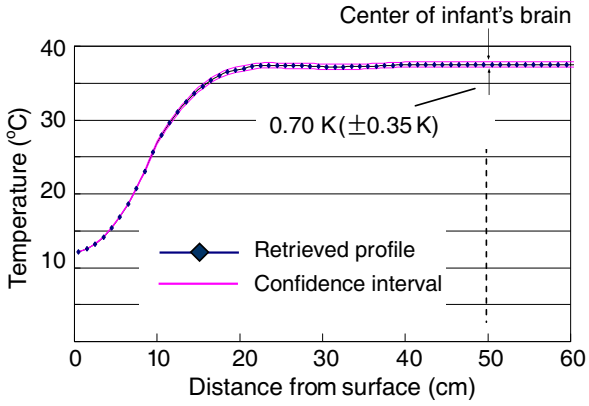

Figure 2. Temperature profile and 2-σ confidence interval retrieved from previously obtained brightness temperatures with improved temperature resolutions of five receivers.

A temperature profile and the 2-σ interval are retrieved from the simulated brightness temperature data and the radiometric weighting functions which were used in the previous work [2] using the temperature resolution data obtained in this work is shown in Fig. 2. Confidence interval of the estimation is 0.70 K compared to the previous interval of 1.6 K. Since the clinical requirement of estimation accuracy is less than 1 K, the present result is very promising and encouraging for the realization of a clinical equipment. This technology is also expected in the case of hypothermia neuroprotection in adults after cardiopulmonary resuscitation [5].

4. CONCLUSIONS

Temperature estimation accuracy has improved from 1.6 K to 0.7 K. This amelioration is a crucial step toward the realization of non-invasive and continuous measurement of deep brain temperatures in infants. We seek further improvements of signal to noise ratio for the first attempt of measuring an actual brain temperature.

REFERENCES

1. Perlman, M. and P. Shah, "Time to adopt cooling for neonatal hypoxic-ischemic encephalopathy: Response to a previous commentary," *Pediatrics*, Vol. 121, 616–618, 2008.

2. Sugiura, T., S. Hoshino, Y. Sawayama, et al., "Five-band microwave radiometer system for non-invasive measurement of deep brain temperature in newborn infants: First phantom study," *PIERS Proceedings*, 395–398, Tokyo, Japan, August 2–5, 2006.
3. Hamamura, Y., S. Mizushina, and T. Sugiura, "Non-invasive measurement of temperature-versus-depth profile in biological systems using a multiple-frequency-band microwave radiometer system," *Automedica*, Vol. 8, 213–232, 1987.
4. Van Leeuwen, G. M. J., J. W. Hand, J. J. W. Lagendijk, et al., "Numerical modeling of temperature distri-butions within the neonatal head," *Pediatrics*, Vol. 48, 351–356, 2000.
5. Cheung, K. W., R. S. Green, K. D. Magee, et al., "Systematic review of randomized controlled trials of therapeutic hypothermia as a neuroprotectant in post cardiac arrest patients," *Can. J. Emerg. Med.*, Vol. 8, 329–337, 2006.

Validity of Inverse Coupler to Improve Temperature Resolution of One-band Microwave Radiometer for Non-invasive Brain Temperature Monitoring

H. Hirata[1], **T. Ishii**[1], **Y. Okita**[2], **and T. Sugiura**[1]

[1]Research Institute of Electronics, Shizuoka University
3-5-1 Johoku, Hamamatsu 432-8011, Japan
[2]Graduate School of Science and Technology, Shizuoka University
3-5-1 Johoku, Hamamatsu 432-8011, Japan

Abstract— Clinical requirement of the confidence interval level of temperature estimation at 5 cm depth from head surface is less than 1 K. This requirement is a tough goal because the microwave radiometer measures average power of noise coming from inside the brain and indistinguishable from background noise and/or by receiver electronics. Though the structure of radiometer is almost the same as that of a radio-telescope whose noise is usually minimized by cooling the receiver to cryogenic temperatures, the present microwave radiometer needs to operate in a room temperature as might be expected. In order to reduce the background noise, an inverse coupler was inserted at the input to the receiver (1.4 GHz) and the temperature resolution was compared with that without the coupler by measuring the noise power of water. Thus obtained temperature resolution of the receiver was improved from 0.400 K to 0.125 K (68% amelioration) though further actions are fundamental to the practical implementation of the technique.

1. INTRODUCTION

Microwave radiometer has been proposed as a viable noninvasive thermometer for monitoring substrate tissue temperatures. With the evolution of technology, microwave radiometry (MWR) devices have been developed for this application [1, 2]. The problem posed is that such medical MWR thermometers are mostly non-invasive devices and observe the extremely weak thermal noise power emitted by the lossy material at about 310 K (body temperature). Reducing the unwanted thermal noise (background noise) is thus critical for the accuracy and stability of data obtained by the thermometer. We have been developing a five-band MWR system for monitoring deep brain temperatures in newborn infants and have already shown its feasibility in the first temperature measuring experiment using an agar phantom [3]. However, further reduction of the background noise is required to actualize the clinical equipment. This paper describes the attempt of an inverse coupler to improve the temperature resolution of MWR system using one-band MWR receiver.

2. ONE BAND MICROWAVE RADIOMETER

Oneband MWR, shown in Fig. 1, consists of a single cross-polarized, rectangular waveguide antenna, a cable, a PIN switch, a circulator, an isolator, an RF amplifier (1–2 GHz), a reference noise source (RNS), a mixer, an attenuator, a local oscillator. The receiver operates in the radiation balance mode [4] which provides the insensitivity to variations in the gain of the radiometer and compensates for power reflections at the tissue/antenna interface. This enables the brightness temperature to be determined independently of the reflection coefficient at the interface.

A 180 degree hybrid coupler (PN BL31-6331-00) is inserted at the PIN switch input in order to cancel the background noise as much as possible A contact type waveguide antenna and an antenna cable with 50-Ω.

The system consists of the Dicke-type radiometer, a single dual-polarized rectangular waveguide antenna dilled with high permittivity (low loss) material, a termination, a PC and a hybrid coupler (180 degree). It operates in the radiation balance mode. Termination are connected to the input ports of the coupler. Output of the coupler is fed to the PIN switch and is processed in one-band MWR (center frequency: 1.1 GHz, bandwidth: 0.3 GHz).

3. SYSTEM CALIBRATION

The antenna was placed on the surface of water in a water-bath and a 50-Ω termination was located in the vicinity of the antenna. Water temperature was increased very slowly (about 20 degrees for 4 hours) and both RNS and water temperatures were measured for calibration. Calibration curves

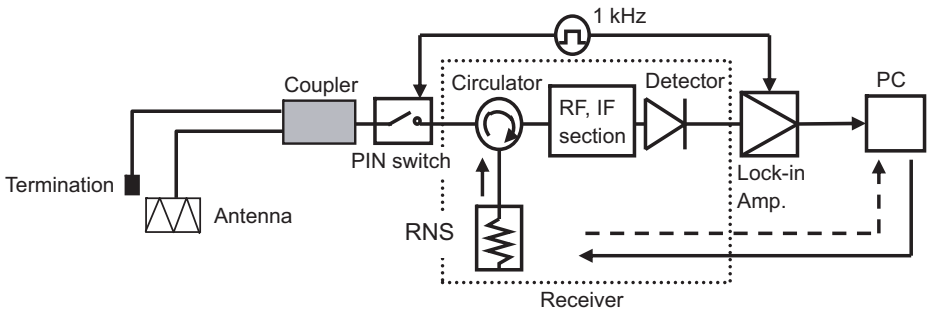

Figure 1: One-band microwave radiometer.

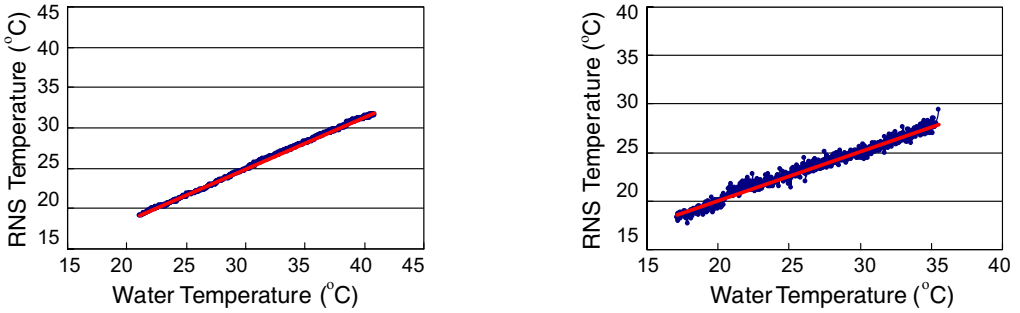

Figure 2: Calibration results (a) with and (b) without a directional coupler.

with and without the directional coupler are shown in Fig. 2. Horizontal axis is the water temperature while vertical axis is the RNS temperature. Dots are the balanced points in the radiation balance mode operation [4]. Lines are the regression lines. Standard deviation obtained from those data is used as the confidence interval level which proves the credibility of the measurement [5]. Thus obtained standard deviations are 0.125 K (with a coupler) and 0.400 K, respectively.

Horizontal axis is the water temperature in a water-bath and vertical axis is the RNS temperature. The noise power of RNS resistor is controlled to keep a balance with input thermal noise power in radiation balance mode. Regression lines are used as calibration lines. Standard deviation gives an indication of measurement accuracy.

4. DISCUSSION

The feasibility of using multi-frequency microwave radiometer to measure deep brain temperature in newborn infants was previously demonstrated [5]. The next study built on that work and reported the first experimental demonstration of the temperature measurement on the phantom [3]. The results of these feasibility studies of non-invasive measurement of deep brain temperature in infants show that the proposed technique is expected to provide an acceptable estimate of the temperature profile within the cooled baby-head. However, further reduction of unwanted thermal noise power is an essential requirement to realize the confidence interval less than 1 K in the radiometer system. As one of the actions, we have made an attempt to use a hybrid directional coupler at the input of a PIN switch and to compare the calibration results of the radiometer. The result shows that the coupler successfully reduced (but not satisfactory at present) the adverse affect of ambient thermal noise on the standard deviation of estimated temperature. Future work will include the application of the same technique to the five-band radiometer system and compare the accuracy of the estimated temperature. Optimization of its practical implementation will rely on future experimental data.

ACKNOWLEDGMENT

This work was supported in part by Grant-in Aid for Scientific Research, No. 20560394, the Ministry of Education, Culture, Sports, Science and Technology.

REFERENCES

1. Hand, J. W., G. M. Van Leeuwen, S. Mizushina, et al., "Monitoring of deep brain temperature in infants using multi-frequency microwave radiometry and thermal modeling," *Phys. Med. Biol.*, Vol. 46, 1885–1903, 2001.
2. Arunachalam, K., P. R. Stauffer, R. F. Maccarini, et al., "Characterization of a digital microwave radiometry system for noninvasive thermometry using temperature controlled homogeneous test load," *Phys. Med. Biol.*, Vol. 53, 3883–3901, 2008.
3. Sugiura, T., S. Hoshino, Y. Sawayama, et al., "Five-band microwave radiometer system for non-invasive measurement of deep brain temperature in newborn infants: First phantom measurement study," *PIERS Proceedings*, 395–398, Tokyo, Japan, August 2–5, 2006.
4. Lüdeke, K. M., B. Schiek, and J. Kohler, "Radiation balance microwave thermograph for industrial and medical applications," *Electronic Letters*, Vol. 14, 194–196, 1978.
5. Maruyma, K., S. Mizushina, T. Sugiura, et al., "Feasibility of non-invasive measurement of deep brain temperature in new-born infants by multi-frequency microwave radiometry," *IEEE Trans. Microwave Theory Tech.*, Vol. 48, 2141–2147, 2000.

Influence of Effective Mode Area on Stimulated Brillouin Scattering Slow Light in Optical Fibers

Shang-Lin Hou, **Zhong-Yi Wang**, **Suo-Ping Li**, **and Jing-Li Lei**
School of Science, Lanzhou University of Technology
Lanzhou 730050, China

Abstract— The SBS model was described based on Brillouin fiber amplifier and the SBS coupled equations were solved numerically. The influence of effective mode area on time delay and pulse broadening was studied within the gain range of 0–16. For smaller effect mode area, the Stokes pulse reaches gain saturation at a smaller gain, the time delay and pulse broadening factor also decrease with increasing gain more quickly in the gain saturation regime. Both the time delay and pulse broadening factor decrease with the increasing effective mode area at a given pump power whose gain is in the small signal regime.

1. INTRODUCTION

Slow light based on stimulated Brillouin scattering (SBS) in optical fibers has attracted wide attention for its potential applications in optical buffering, data synchronization, optical memories and optical signal processing. Compared with previously demonstrated slow-light techniques such as electromagnetically induced transparency (EIT) [1] and coherent population oscillations (CPO) [2], slow light based on SBS has a lot of advantages: the simple, flexible and easy-to-handle SBS can be realized in room temperature; the optical fiber components based on it can be easily integrated with the existing telecommunication infrastructure; the slow-light resonance can be tuned to any wavelength within the optical communication windows; the use of optical fiber allows for a relaxed pump-power requirement owning to long interaction length, small effective mode area and so on.

Kwang Yong Song et al. first demonstrated SBS slow light experimentally using single-mode fiber (SMF) and dispersion shift fiber (DSF) [3]. They achieved the time delay in the range of tens of nanoseconds in several kilometer-length fibers. Then they find the delay is limited by pump depletion (gain saturation) and amplified spontaneous Brillouin emission (ASBE), which can be avoided by cascaded fiber segments joined by unidirectional optical attenuators [4]. So they achieved time delay within the range of 150 ns, much larger than the 40 ns signal pulse. In the mean time, a large amount of pulse broadening is observed. Pulse distortion is an inevitable phenomenon in all SBS slow light experiments, it can be reduced by using a variety of pump modulating schemes [5–7] or various gain profiles [8–10]. To overcome the narrow band spectral resonance of SBS which limits the maximum data rate of the optical system, a simple and inexpensive pump spectral broadening technique is used in broadening the SBS slow light bandwidth to hundreds of MHz [11], and 12 GHz [12]. Song et al. further extended the SBS bandwidth up to 25 GHz by using a double pump method [13], which paves the way towards real applications based on SBS slow light.

Numerical studies of SBS slow light under different Stokes pulse widths and pump parameters were also studied [14, 15], which provide an insight into the SBS slow light process. However, optical fiber structure also has a strong influence on the SBS coupling process, leading the time delay and pulse distortion differently. Better design of the optical fiber structure will make it possible the realization of slow light devices with a much high efficiency. Considering the intensities of three coupled waves have a relationship with the effective mode area which plays an important role in the SBS process, the influence of effective mode area on time delay and pulse broadening is discussed in this paper.

2. NUMERICAL MODEL AND DISCUSSION

The process of SBS is the interaction of two counter-propagating waves, a strong pump wave and a weak Stokes wave. If a particular frequency relation is satisfied

$$v_{pump} = v_{Stokes} + v_B \tag{1}$$

where v_{pump} and v_{Stokes} are the frequency of pump wave and Stokes wave respectively, v_B is the Brillouin frequency. Then an acoustic wave is generated which scatters photons from the pump to the Stokes wave and the interference of these two optical waves in turn stimulates the process [16].

From a practical point of view, the process of SBS can be viewed as a narrowband amplification process, in which a pump wave produces a narrowband gain in a spectral region around $v_{pump} - v_B$. According to Kramers-Kronig relation, the amplification will result in a sharp transition in the refractive index of the material. Consequently, the group index will experience a strong transition, which is responsible for the pulse delay. If the Stokes pulse is set on the SBS gain line center, the maximum delay is achieved.

Considering a Brillouin amplifier where the pump wave counter-propagates through the fiber with respect to the Stokes pulse, the SBS process can be described by one-dimensional coupled wave equations involving a backward pump wave ($-z$ direction), a forward Stokes wave ($+z$ direction), and a backward acoustic wave. Under the slowly varying envelope approximation (SVEA) and neglecting the transverse field variations, the equations are written as follows [17]:

$$-\frac{\partial A_p}{\partial z} + \frac{n}{c}\frac{\partial A_p}{\partial t} = -\frac{\alpha}{2}A_p + ig_2 A_s Q \tag{2}$$

$$\frac{\partial A_s}{\partial z} + \frac{n}{c}\frac{\partial A_s}{\partial t} = -\frac{\alpha}{2}A_s + ig_2 A_p Q^* \tag{3}$$

$$\frac{\partial Q}{\partial t} + \left(\frac{\Gamma_B}{2} - i\Delta\omega\right) Q = ig_1 A_p A_s^* \tag{4}$$

where A_p, A_s, and Q are the amplitudes of the pump wave, the Stokes wave, and the acoustic wave, respectively; n is the group refractive index when SBS is absent; c is the velocity of the light in vacuum; α is the loss coefficient of the fiber; $\Gamma_B/2\pi$ is the bandwidth (FWHM) of the Brillouin gain; $\Delta\omega = (\omega_p - \omega_s) - \Omega_B$ is the detuning from the SBS gain line center; Ω_B is the SBS frequency shift; ω_p and ω_s are the center angular frequency of the pump wave and Stokes wave, respectively; g_1 is the coupled coefficient between the pump wave and the Stokes wave, g_2 is the coupled coefficient between the pump (Stokes) wave and the acoustic wave, $g_0 = 4\frac{g_1 g_2}{\Gamma_B}$ is the peak value of the Brillouin gain coefficient.

According to the small signal steady state theory of stimulated Brillouin scattering, the pump power $P_{critical}$ required to reach Brillouin threshold in a single pass scheme is related to the Brillouin gain coefficient g_0 by the following equation [16]:

$$g_0(P_{critical}/A_{eff})L_{eff} \cong 21 \tag{5}$$

where $P_{critical}$ is the power corresponding to the Brillouin threshold, A_{eff} is the effect mode area, L_{eff} is the effective length defined as $L_{eff} = \alpha^{-1}[1 - \exp(-\alpha L)]$, from Eq. (5) we can obtain the threshold pump intensity:

$$I_{critical} = P_{critical}/A_{eff} \cong 21/(g_0 L_{eff}) \tag{6}$$

Once reaching the threshold pump intensity, a large part of the pump power is transferred to the Stokes wave, resulting in the generation of Stokes wave at the output that depletes the pump seriously and leads to serious Stokes pulse distortion. In our simulations, we consider the pump intensity is near the Brillouin threshold and obtain the Stokes gain around 16 using the parameters described in Section 3, here the Stokes gain is defined as:

$$Gain = \log\left(\frac{P_{out}}{P_{in}}\right) \tag{7}$$

where P_{out} and P_{in} are the output and input of the Stokes peak power, respectively.

The time delay ΔT_d is defined as the peak difference between the output Stokes pulse with and without SBS in time domain:

$$\Delta T_d = t_{p-SBS} - t_{p-noSBS} \tag{8}$$

where t_{p-SBS} and $t_{p-noSBS}$ are the peak time of the out Stokes pulse with and without SBS, respectively.

The pulse broadening factor B is defined as the ratio of the output Stokes pulse width τ_{out} (FWHM) to input Stokes pulse width τ_{in} (FWHM):

$$B = \frac{\tau_{out}}{\tau_{in}} \tag{9}$$

3. NUMERICAL SIMULATION RESULTS

In order to study the situation where the pump is depleted, we solve the Eqs. (2)–(4) numerically using the method of implicit finite difference with prediction-correction [18] to determine how effective mode area influence SBS slow light.

In our simulation, the parameters are considered from the common single-mode fiber, and select: fiber length $L = 25\,\mathrm{m}$, pump wavelength $\lambda = 1550\,\mathrm{nm}$, group refractive index $n = 1.45$, effect mode area $A_{eff} = 50\,\mu\mathrm{m}^2$, loss coefficient $\alpha = 0.2\,\mathrm{dB/km}$, gain bandwidth (FWHM) $\Gamma_B/2\pi = 40\,\mathrm{MHz}$, gain coefficient $g_0 = 5 \times 10^{-11}\,\mathrm{m/W}$. We assume the pump wave is CW and the Stokes wave is Gaussian shaped with the peak power of $0.1\,\mu\mathrm{W}$ and the FWHM pulse width of 120 ns (its FWHM bandwidth in frequency domain is around 3.7 MHz which is much smaller than that of SBS gain bandwidth we use). The Stokes pulse is set on the SBS gain line center to achieve the maximum time delay ($\Delta\omega = 0$). The previous parameters are kept unchanged unless the influence of parameter itself on time delay and pulse broadening is involved.

As can be seen from Fig. 1(a), in the small signal regime, the time delay increases with the gain linearly for different effective mode areas when the gain is small (≤ 10), that's because the pump isn't completely affected when the gain is small. For larger gain, pump depletion becomes more and more seriously, the time delay increases slowly with gain and reaches its maximum before decreasing with gain. However, the pulse with smaller effective mode area reaches the gain saturation at a smaller gain, and the maximum time delay is accordingly smaller. Once reaching the gain saturation, the pulse with smaller effective mode area also decreases with the increasing gain more quickly than the others. The reason is: for pulse with the same peak power, the smaller the effective mode area is, the more optical power is injected into the optical fiber core, the pulse with smaller effective mode area is easier to reach the gain saturation.

Figure 1(b) shows the pulse broadening factor versus gain, the pulse broadening factor increases linearly with the increasing gain in the small signal regime, which is the same as the time delay versus gain. As has been said before, the pulse with larger effective mode area reaches the gain saturation at a larger gain and its maximum pulse broadening factor is accordingly larger. In the gain saturation regime, the pulse with smaller effective mode area narrows more seriously than the others at a fixed gain, which shows that the smaller effective mode area has a stronger influence on gain saturation, the pulse broadening factor even begins to increase at the gain around 16 for the smallest effective mode area.

We also investigate the time delay and pulse broadening factor as a function of effective mode area at a given pump power 0.125 W. As shown in Fig. 2, both the time delay and pulse broadening factor decrease with the increasing effective mode area. It indicates that smaller effective mode area could reduce the pump requirement and has a higher time delay efficiency (defined as time delay per unit pump power and per unit optical fiber length). Note that the maximum gain is 7.6 occurring at $A_{eff} = 20\,\mu\mathrm{m}^2$, which satisfies the small signal condition.

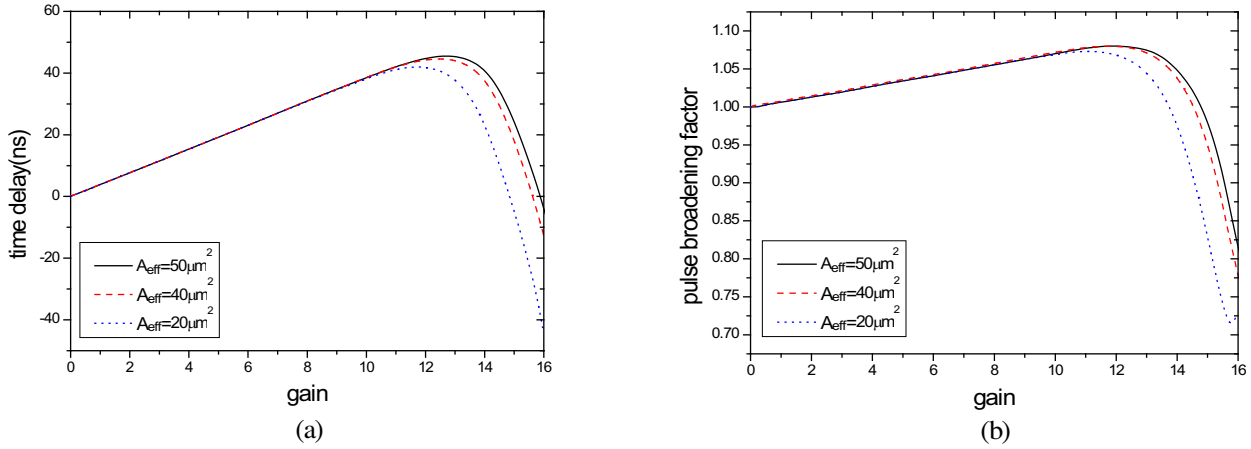

Figure 1: (a) Time delay and (b) pulse broadening factor as a function of gain with different effective mode areas.

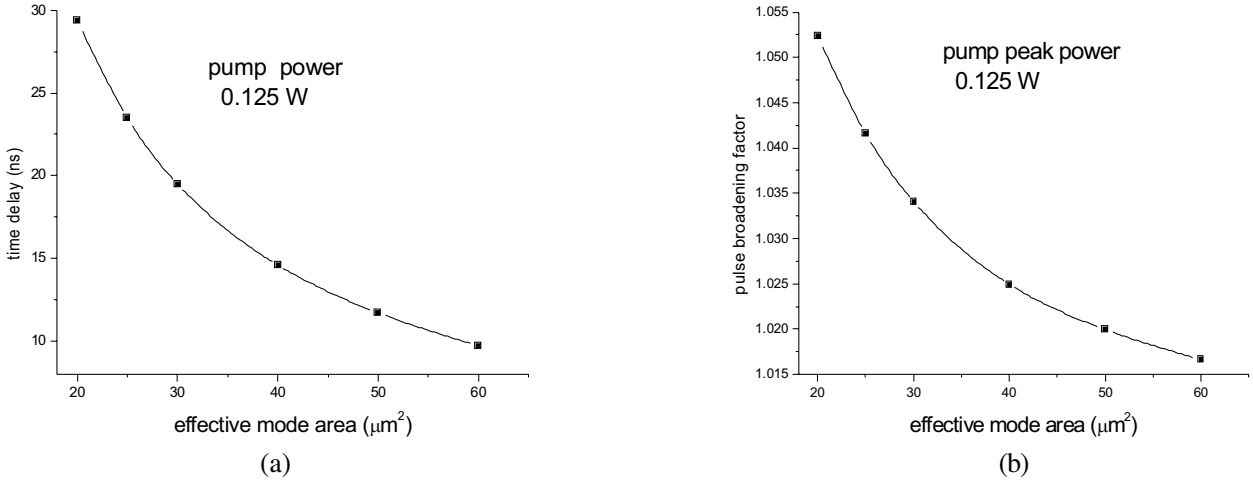

Figure 2: (a) Time delay and (b) pulse broadening factor as a function of effective mode area at a given pump power.

4. CONCLUSIONS

We make a numerical study of the SBS slow light in optical fibers, and consider the influence of effective mode area on time delay and pulse broadening in the gain range of $0 \sim 16$. In the small signal regime, the time delay and the pulse broadening factor increase with the increasing gain. The Stokes pulse with larger effective mode area reaches the gain saturation at a larger gain. In the gain saturation regime, the Stokes pulse with smaller effective mode area begins to decrease more quickly. We also investigate the time delay and pulse broadening factor vary with the increasing effective mode area at a given pump power whose gain parameter is in the small signal regime, and find that the time delay and pulse broadening factor decrease with the increasing effective mode area.

ACKNOWLEDGMENT

This work was supported by Natural Science Fund of Gansu Province (3ZS062-B25-036), China and the Outstanding Young Teacher Training Plan of Lanzhou University of Technology, Lanzhou, China.

REFERENCES

1. Hau, L. V., S. E. Harris, Z. Dutton, and C. H. Behroozi, "Light speed reduction to 17 metres per second in an ultracold atomic gas," *Nature*, Vol. 397, 594–598, 1999.
2. Bigelow, M. S., N. N. Lepeshkin, and R. W. Boyd, "Superluminal and Slow-light propagation in a room-temperature solid," *Science*, Vol. 301, 200–202, 2003.
3. Song, K. Y., M. G. Herráez, and L. Thévenaz, "Observation of pulse delaying and advancement in optical fibers using stimulated Brillouin scattering," *Opt. Express*, Vol. 13, No. 1, 82–88, 2005.
4. Song, K. Y., M. G. Herráez, and L. Thévenaz, "Long optically-controlled delays in optical fibers," *Opt. Lett.*, Vol. 30, No. 14, 1782–1784, 2005.
5. Minardo, A., R. Bernini, and L. Zeni, "Low distortion Brillouin slow light in optical fibers using AM modulation," *Opt. Express*, Vol. 14, No. 13, 5866–5876, 2006.
6. Zadok, A., A. Eyal, and M. Tur, "Extended delay of broadband signals in stimulated Brillouin scattering slow light using synthesized pump chirp," *Opt. Express*, Vol. 14, No. 19, 8498–8505, 2006.
7. Yi, L. L., L. Zhan, W. S. Hu, and Y. X. Xia, "Delay of broadband signals using slow light in stimulated Brillouin scattering with phase-modulated pump," *IEEE Photon. Technol. Lett.*, Vol. 19, No. 8, 619–621, 2007.
8. Stenner, M. D. and M. A. Neifeld, "Distortion management in slow-light pulse delay," *Opt. Express*, Vol. 13, No. 25, 9995–10002, 2005.
9. Schneider, T., M. Junker, K. U. Lauterbach, and R. Henker, "Distortion reduction in cascaded slow light delays," *Electron. Lett.*, Vol. 42, No. 19, 1110–1111, 2006.

10. Lu, Z. W., Y. K. Dong, and Q. Li, "Slow light in multi-line Brillouin gain spectrum," *Opt. Express*, Vol. 15, No. 4, 1871–1877, 2007.
11. Herráez, M. G., K. Y. Song, and L. Thévenaz, "Arbitrary-bandwidth Brillouin slow light in optical fibers," *Opt. Express*, Vol. 14, No. 4, 1395–1400, 2006.
12. Zhu, Z., A. M. C. Dawes, D. J. Gauthier, L. Zhang, and A. E. Willner, "12-GHz-bandwidth SBS slow light in optical fibers," *Optical Fiber Communication Conference and Exposition and the National Fiber Optic Engineers Conference*, paper PDP1, Anaheim, CA, March 2006.
13. Song, K. Y. and K. Hotate, "25 GHz bandwidth Brillouin slow light in optical fibers," *Opt. Lett.*, Vol. 32, No. 3, 217–219, 2007.
14. Zhu, Z., D. J. Gauthier, Y. Okawachi, J. E. Sharping, A. L. Gaeta, R. W. Boyd, and A. E. Willner, "Numerical study of all-optical slow-light delays via stimulated Brillouin scattering in an optical fiber," *J. Opt. Soc. Am. B*, Vol. 22, No. 11, 2378–2384, 2005.
15. Kalosha, V. P., L. Chen, and X. Bao, "Slow and fast light via SBS in optical fibers for short pulses and broadband pump," *Opt. Express*, Vol. 14, No. 26, 12693–12703, 2006.
16. Agrawal, G. P., *Nonlinear Fiber Optics*, Academic Press, San Diego, 2001.
17. Damzen, M. J., V. I. Vlad, V. Babin, and A. Mocofanescu, *Stimulated Brillouin Scattering: Fundamentals and Applications*, IOP Publishing, London, 2003.
18. Dane, B., W. A. Neuman, and L. A. Hackel, "High-energy SBS pulse compression," *IEEE J. Quantum Electro.*, Vol. 30, No. 8, 1907–1915, 1994.

Characterization of InP Based SAGCM Avalanche Photodetector for Single Photon Fiber Optic Communications

Wen-Jeng Ho, **Jheng-Jie Liou**, **and Cheng-Ju Chen**
Institute of Electro-Optical Engineering, National Taipei University of Technology
1, Sec. 3, Chung-Hsiao E. Rd., Taipei 106, Taiwan

Abstract— This paper presents fabrication and characterization of InP-based separate absorption, grading, charge, and InP/InAlAs hetro-multiplication (SAGCM) single photon avalanche photo-detectors (SPADs) for application of single photon fiber optic communications. The dark current (I_D) of SPAD at 90% of the breakdown voltage (V_{BR}) was 37.8 pA and 18.8 nA at 200 K and 300 K, respectively. Under −40°C and gate repetition frequency of 10 kHz with pulse width of 2 ns, the performance of dark count probability $P_{dc} = 0.02$, single-photon detection efficiency $\eta_{det} = 11.5\%$, noise equivalent power NEP $= 5 \times 10^{-14}$ W/(Hz)$^{1/2}$, a factor of quantum bit-error rate of $P_{dc}/\eta_{det} = 0.16$ were simultaneously achieved. In addition, both the dark current and the dark count exhibited activation energy of 0.24 eV in temperature below 240 K which shown the dominant generation sources were band-to-band tunneling and field-enhanced band-traps-band tunneling.

1. INTRODUCTION [1–3]

Recently, single photon communications, i.e., quantum key distribution (QKD), have received much interest due to their confirmed security. InP-based avalanche photodiodes operating in Geiger-mode at low temperature as single-photon avalanche detectors (SPADs) have emerged as a key component for 1550 nm QKD system application. However, SPADs for single photon detection are demanded to have a high single-photon detection efficiency (SPDE, η_{det}) and a low dark count probability (P_{dc}). For quantum key distribution, single-photon detection efficiency is proportional to bit rate. The ratio of P_{dc} to η_{det} is a factor of quantum bit-error rate of a detector (QBER$_{det}$), which a low QBER$_{det}$ was required for single photon fiber optic communications.

In this paper, we report the fabrication of InP-based separate absorption, grading, charge, and InP/InAlAs hetro-multiplication (SAGCM) single photon avalanche photo-detectors, and investigated the device performance of dark current (I_d), dark count probability (P_{dc}), single-photon detection efficiency (η_{det}), noise equivalent power (NEP), afterpulsing effect, and quantum bit-error rate of a detector (QBER$_{det}$).

2. EXPERIMENTAL

2.1. Device Fabrication

Figure 1 shows the schematic diagram of a SAGCM- SPAD. The device epitaxial layers grown on a (100) S-doped InP substrate by metal-organic chemical vapor deposition (MOCVD) consists of an InP buffer layer (0.5 µm, n $\sim 2 \times 10^{16}$ cm^{-3}), an undoped $In_{0.53}Ga_{0.47}As$ absorbing layer (1.0 µm, $n < 2 \times 10^{15}$ cm^{-3}), three undoped InGaAsP grading layers ($\lambda = 1.5, 1.3, 1.2$ µm, 1000Å each), an unintentionally doped InP charging layer (0.2 µm, $n \sim 6 \times 10^{16}$ cm^{-3}), an undoped $In_{0.52}Al_{0.48}As$ partly hetro-multiplication layer (30 nm, $n \sim 2 \times 10^{16}$ cm^{-3}), an undoped InP cap layer (3.0 µm, $n < 1 \times 10^{16}$ cm^{-3}), and an undoped $In_{0.53}Ga_{0.47}As$ diffusion control layer (0.2 µm, $n < 1 \times 10^{16}$ cm^{-3}). Before the fabrication of SAGCM-SAPD, the quality of epitaxial film was characterized by using double-crystal X-ray diffractometer (DCD) and electrical capacitance-voltage (EC-V). The electrical field profile in epitaxial structure would be expected close to $E \sim 1.5 \times 10^5$ V/cm at absorbing layer and $E > 5 \times 10^5$ V/cm at multiplication layer.

Device fabrication begins with a selective etching to removal InGaAs with a widow of 80 µm diameter. Following a 1500Å SiNx film was deposited by plasma-enhanced chemical vapor deposition (PECVD) and a 90 µm diameter SiNx central window was opened by reactive ion etching (RIE) which covers an inner annulus of InGaAs ring for the next Zn-diffusion process. During the Zn-diffusion, an elevated temperature with an longer duration was applied to control p^+-InP depth of central active junction to 0.4 µm away from the $In_{0.52}Al_{0.48}As$ layer. At the same time, under the InGaAs ring, Zn diffusion through InGaAs into InP formed a shallow p-InP junction relative to the central junction due to the diffusion coefficient of InGaAs was smaller than the diffusion coefficient of InP, as shown in Figure 1. The shallow p-InP junction ring at the edge of central active

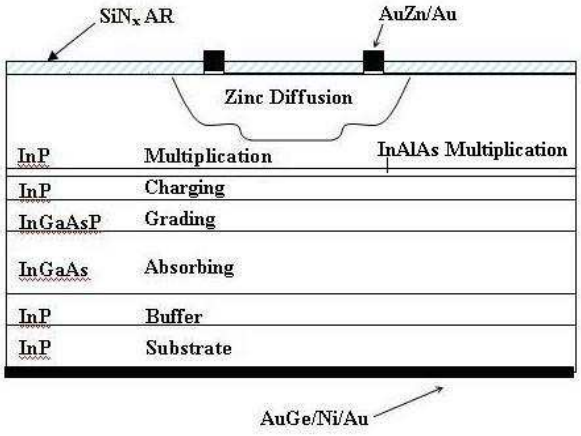

Figure 1: The schematic diagram of a SAGCM-SAPD.

junction served as a guard ring to suppress edge breakdown. This optimized diffusion process can improve the device characteristics and reduce the edge breakdown. After diffusion, all the surface InGaAs film was removed and a $\lambda/4$ thick SiNx film was deposited as an anti-reflection coating (ARC). Finally, P and N electrode contacts using AuZn/Au and AuGe/Ni/Au were deposited on the front-side and back-side of the substrate, respectively. We packaged an SPAD chip in a TO-46 fiber pigtail module for further device performance characterization.

3. CHARACTERIZATION IN LINEAR-MODE AND IN GEIGER-MODE

In the linear mode, the dark current-voltage (I-V) characteristics of SPAD at different temperature were measured by using the HP 4145B which show the dark current (I_D) and breakdown voltage (V_{BR}). However, the punch through voltage (V_{th}) and multiplication factor (M) were obtained when the device illuminated with a 1550 nm light source. Furthermore, the 3-dB bandwidth (f_{3-dB}) as a function of multiplication factor to deduce gain bandwidth product (GB) was measured by HP8703B also study in this work.

In Geiger mode operation, the experimental setup of SPAD characterization is illustrated in Figure 2. The SPAD device was biased below V_{BR} with a *dc* power supply. It was pulse-biased above breakdown through capacitor (C_g) with the pulse generator. The quenching circuit and SPAD were mounted inside a vacuum chamber with a water cooled two stage thermoelectric controller (TEC). The temperature on SPAD can be tuned by supplying different currents to the TEC. In additionally, SPAD was illuminated with 1550 nm light through optical fiber for η_{det} measurements. The light source was DFB laser that produced 500 ps optical pulses at 1550 nm. To produce short pulses of light, the DFB laser was triggered by a pulse generator and light intensity was attenuated

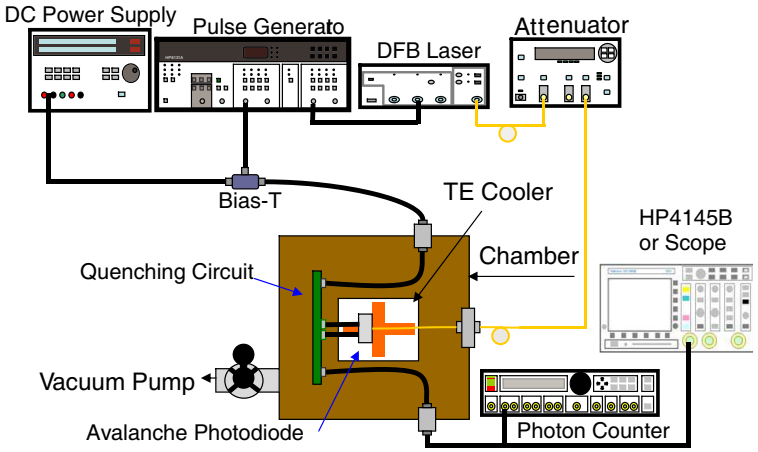

Figure 2: The experimental setup of SPAD characterization.

to single photon level using an optical attenuator. The output signal of SPAD was amplified with a noise amplifier and connects to SR 400 photon counter and Tektronix oscilloscope. Then, the dark count probability (P_{dc}), single-photon detection efficiency (η_{det}), afterpulsing , activation energy (E_a), noise equivalent power (NEP), and quantum bit-error rate of a detector (QBER_{det}) were obtained.

4. RESULTS AND DISCUSSION

Figure 3 presents a DCD spectrum of epitaxial layers on InP substrate. The lattice mismatch ($\Delta = a - a_0/a_0$) between InP and epitaxial layer was 85 ppm, which indicates a nearly perfect lattice-matched. However, there are stilly few defects at hetro-interface. The interface defect suggests an original source of dark carrier generated. Dark currents as a function of bias voltage and temperature were shown in Figure 4. The breakdown voltage (V_{BR}, defined as the voltage at 10 µA of dark current) at 25°C and −70°C were 62.5 V and 52.1 V, respectively. The temperature dependence of the breakdown voltage was measured to be only 0.11 mV/°C. However, the dark current of SPAD at 90% of the breakdown voltage was 37.8 pA and 18.8 nA at −70°C and 25°C, respectively.

The 3-dB bandwidth as a function of multiplication factor is shown in Figure 5. The maximum bandwidth is 3.0 GHz between the ranges of multiplication factor from 3 to 20. The gain-bandwidth product (GB) deduced from the inverse linear relationship is 56 GHz. The value of GB can be evaluated the effective transit time ($\tau^* = M/2\pi\,\mathrm{GB}$) and the average number of dark carriers generated was given by $N_d = I_D M\tau^*/q$ [2].

Dark count probability (P_{dc}) and single photon detection efficiency (η_{det}) as a function of excess bias voltage at temperature −40°C are illustrated in Figure 6. $P_{dc} = 0.02$ and $\eta_{det} = 11.5\%$ at

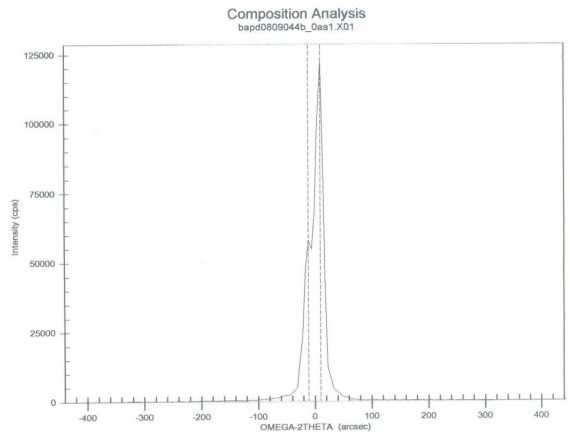

Figure 3: DCD spectrum of epitaxial layers on InP substrate.

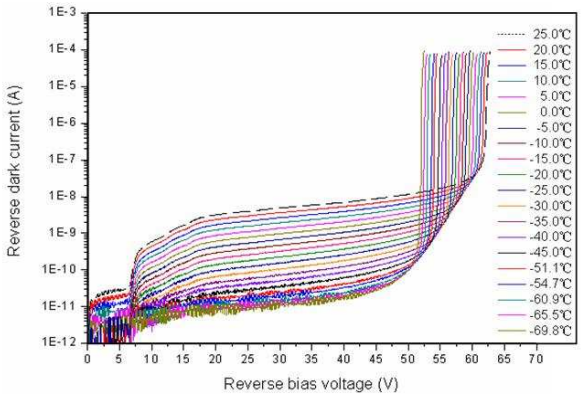

Figure 4: I_d-V-T curves.

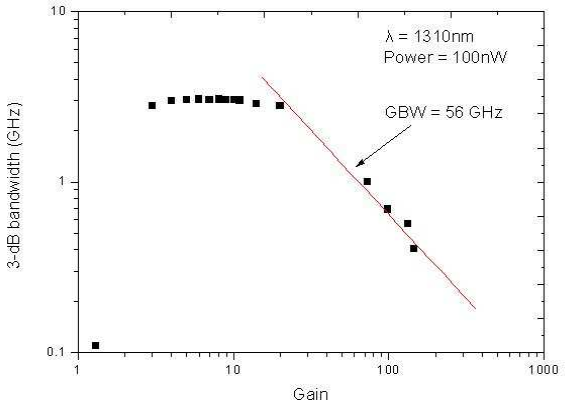

Figure 5: The f_{3-dB} as a function multiplication gain.

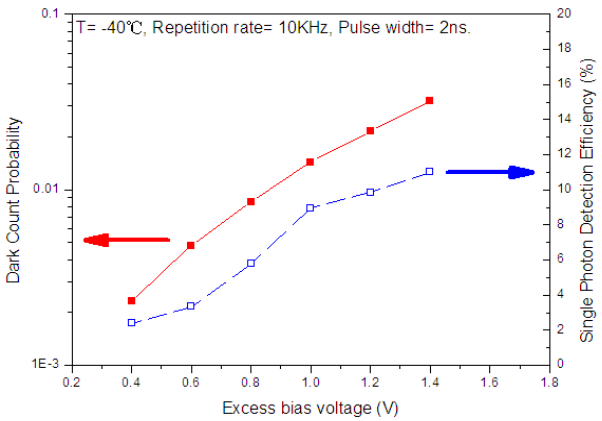

Figure 6: P_{dc} and η_{det} as a function of excess bias voltage.

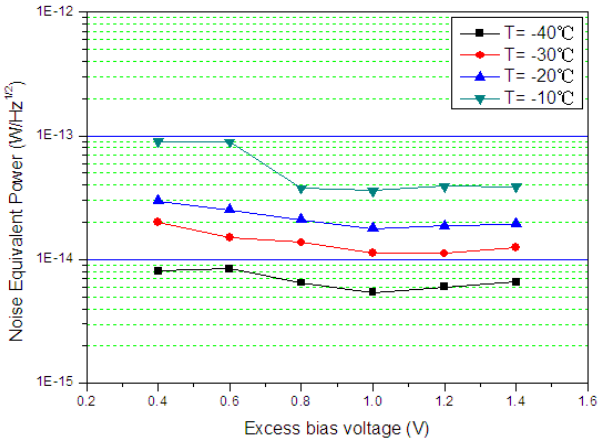

Figure 7: NEP versus excess bias voltage.

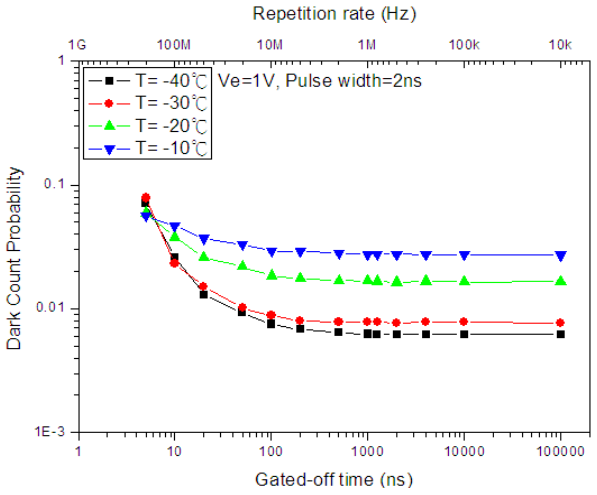

Figure 8: Dark count probability versus gate off time.

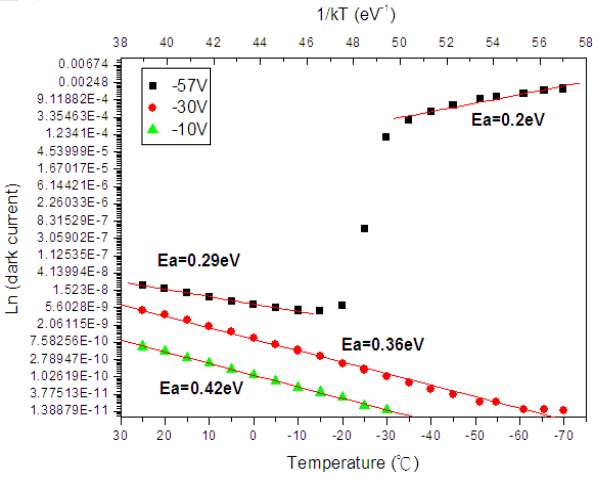

Figure 9: Arrhenius plot of dark current.

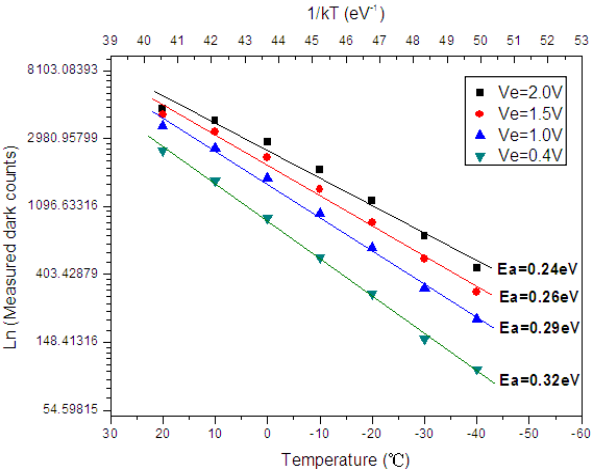

Figure 10: Arrhenius plot of dark count.

excess bias voltage of 1.4 V with gate frequency of 10 kHz and 2 ns pulse width were achieved. The ratio of P_{dc} to η_{det} is a factor of quantum bit-error rate of a detector (QBER_{det}), which a low QBER_{det} was required for single photon fiber optic communications in this work we obtained $P_{dc}/\eta_{det} = 0.16$.

Figure 7 shows the NEP versus excess bias voltage, the operating temperature from -10°C to -40°C. NEP value increases at lower excess bias due to the reduced in detection efficiency, while at higher excess bias it increases also due to the increasing in dark count probability. The lowest NEP of $5 \times 10^{-14}\,\mathrm{W/(Hz)}^{1/2}$ at excess bias voltage of -1 V and -40°C was obtained. In Figure 8, it is observed as an increase in the dark count probability as the repetition rate increases due to afterpulse effect. The onset of afterpulsing depends on a number of parameters such as temperature, trap density, and the total charge that flows through the device during an avalanche event. In this experiment, afterpulsing was negligible at gate frequencies up to 800 kHz.

Because the dark current variation versus temperature follows an Arrhenius law $I_D(T) = I_0 \exp(-E_a/kT)$ and the temperature dependence of the total dark counts can be expressed as $N_d(T) = N_0 \exp(-E_a/kT)$, from which we can extracted the activation energies (E_a) for discrete bias voltages. The dark current of SPAD at -57 V and 240 K (as shown in Figure 9), $E_a = 0.2$ eV was obtained. When the excess bias = 2 V and at 240 K, as shown in Figure 10, E_a also be 0.24 eV, which explained by the band-to-band tunneling or the field-enhanced band-traps-band tunneling [3] dominantly in InP multiplication layer was the same source for dark count sand dark current.

5. CONCLUSION

Planar SAGCM-SAPDs grown by MOCVD have been have successfully fabricated and characterized. The fabricated SAPD operating in Geiger-mode at low temperature $(-40°)$C are suited for gate frequencies up to 800 kHz QKD system.

ACKNOWLEDGMENT

The authors would like to thank the financial support from the National Science Council of Republic of China under Grant NSC-97-2221-E-027-008-MY2.

REFERENCES

1. Liu, M., et al., "High-performance InGaAs/InP single-photon avalanche photodiode," *IEEE Journal of Selected Topics in Quantum Electronics*, Vol. 13, 887–894, 2007.
2. Kang, Y., et al., "Dark count probability and quantum efficiency of avalanche photodiodes for single-photon detection," *Appl. Phys. Lett.*, Vol. 83, No. 14, 2955–2957, 2009.
3. Ang, K. W. et al., "Impact of field-enhanced band-traps-band tunneling on the dark current generation in germanium p-i-n photodetector," *Appl. Phys. Lett.*, Vol. 94, No. 223515, 1–3, 2009.

Design of a Novel Voltage Sensor Based on Fiber Bragg Grating with Electro-optic Crystal Material Cladding

Shang-Lin Hou, **Bo Chen**, **Zhong-Yi Wang**, **Yan-Jun Liu**, **and Jing-Li Lei**
School of Science, Lanzhou University of Technology, Lanzhou 730050, China

Abstract— Influence of the electric field on the reflectivity and Bragg wavelength of the fiber gratings with cladding made of uniaxial electro-optic crystal material whose optical axis is parallel to the axis of fiber was investigated and a novel voltage sensor based on fiber Bragg grating with $LiNbO_3$ electro-optic crystal material cladding was designed. The calculated results indicate that when the electric field varies from 0 to 100×10^7 V/m, the Bragg wavelength decreases from 1566.13 nm to 1542.80 nm, and the maximal reflectivity increases from 3.19% to 99.12%. These conclusions provided a theoretical basis for designing novel optical sensors.

1. INTRODUCTION

Fiber gratings have been studied extensively since the optical sensitivity was described in 1978 [1] and have become the key components of optical fiber communication system, such as dispersion compensator, density wavelength division multiplexer (DWDM), fiber laser, fiber sensors and so on [2–5]. In 2007, a new type of Bragg fiber grating with cladding made of uniaxial crystal materials was proposed [6], and the calculated results indicated that the parameter K_{cl}, i.e., the ratio of the extraordinary ray refractive index to the ordinary ray index, has a strong impact on the reflectivity and Bragg wavelength. Before this, Stevenson [7] and Cozens [8] proposed the characteristics of transmission and cut-off of the optical fiber with uniaxial crystal materials core. Electro-optic effect and elasto-optic effect in a chirped fiber grating [9] with cladding made of uniaxial crystal material are theoretically investigated in 2005 and the results indicated that the reflected spectra of the chirped grating could be changed by the electric field and the strain. The characteristics of a new type of fiber Bragg gratings with cladding made of uniaxial crystal material were predicted in 2007 and the calculated results indicated that parameter K_{cl} had a strong impact on the reflectivity and the Bragg wavelength. A new tunable wavelength selector with fiber Bragg gratings with cladding made of electro -optic materials was proposed in 2008 [10].

In the work, a novel voltage sensor based on fiber Bragg grating with electric-optic crystal material cladding was proposed, the influence of electric field on the reflectivity and Bragg wavelength of the fiber gratings were demonstrated. Firstly, the electro-optic effect of uniaxial electro-optic crystal material, i.e., $LiNbO_3$ was presented, and then the wave equations were solved in both the cladding and the core, at last, the reflectivity of the fiber Bragg grating was investigated using coupling theory. The calculated results indicate that the reflectivity and Bragg wavelength of the fiber Bragg grating with cladding made of uniaxial electro-optic crystal materials. It provided a basis for designing novel electric fields or voltage optical sensors.

2. THRORETICAL ANALYSIS

2.1. The Electro-optic Effect of Uniaxial Anisotropic Electro-optic Crystral Material

Supposing the electric field running along the axis of the optical fiber with cladding made of uniaxial electro-optic crystal material whose optical axis is parallel to the axis of fiber, for 3 m point group uniaxial material of trigonal system, the index ellipsoid equation in the principal dielectric axis is:

$$\left(\frac{1}{n_o^2}+\gamma_{13}E_3\right)\left(x^2+y^2\right)+\left(\frac{1}{n_e^2}+\gamma_{33}E_3\right)z^2=1 \tag{1}$$

where $E_3 = E$ is the electric field, γ_{ij} is the electro-optic coefficients. n_o and n_e are the ordinary ray refractive index and the extraordinary ray refractive index of the uniaxial material,respectively.

For $LiNbO_3$ crystal material, the index can be approximately expressed as

$$n(E)\approx n-\frac{1}{2}rn^3E \tag{2}$$

When the electric field is running along the axis of the fiber, the cladding is still uniaxial crystal which has same principal axis. But its ordinary ray refractive index and extraordinary ray refractive index are amended as:

$$\begin{cases} n_o(E) = n_o - r_{13}n_o^3 E/2 \\ n_e(E) = n_e - r_{13}n_o^3 E/2 \end{cases} \tag{3}$$

Thus the parameter K_{cl}, i.e., the ratio of the extraordinary ray refractive index to the ordinary ray index and the normalized core-cladding index difference can be expressed as

$$K_{cl} = n_e(E)/n_o(E) \tag{4}$$

$$\Delta = (n_0 - n_o(E))/n_0 \tag{5}$$

where n_0 is the core index, $n_o(E)$ and $n_e(E)$ are respectively the ordinary ray refractive index and the extraordinary ray index which is function of electric field intensity E, n_o and n_e are respectively the initial values of its ordinary and extraordinary ray refractive index.

2.2. The Characteristic Equation of the Ideal Normal Mode

Assuming the fiber Bragg grating with cladding made of uniaxial electro-optic crystal material has a core radius a and a core refractive index n_0. The optical axis of the uniaxial electro-optic crystal material is taken to be parallel to the axis of the fiber, i.e., z-axis, and the principal axis of cladding indices is n_x, n_y and n_z respectively, which satisfy: $n_x = n_y \neq n_z$. Through matching the relationship between axial and tangential field components, and using the boundary conditions of electromagnetic field, the characteristic equation of the ideal normal mode, i.e., the mode in an ideal waveguide without grating perturbation can be obtained as follows:

$$F\left[\frac{n_0^2}{n_o^2 K_{cl}}\frac{\mathrm{J}'_m(U)}{U\,\mathrm{J}_m(U)} + \frac{\mathrm{K}'_m(K_{cl}W)}{W\,\mathrm{K}_m(K_{cl}W)}\right] = \frac{m^2 Q}{K_{cl}}\left(\frac{n_0^2}{n_o^2 U^2} + \frac{1}{W^2}\right) \tag{6}$$

where $n_o = n_x = n_y$ and $n_0 > n_o$. If $\beta < k^2 n_0$, the parameters are defined as follows:

$$F = \frac{\mathrm{J}'_m(U)}{U\,\mathrm{J}_m(U)} + \frac{\mathrm{K}'_m(W)}{W\,\mathrm{K}_m(W)} \quad Q = \frac{1}{U^2} + \frac{1}{W^2}$$

$$U = a\sqrt{k_0^2 n_0^2 - \beta^2} \quad W = a\sqrt{\beta^2 - k_0^2 n_o^2(E)} \quad U = ak\sqrt{n_0^2 - n_o^2(E)}$$

where k_0 is the wave number in vacuum and β is the propagation constant, U is transversely normalized phase-constant, W is transversely normalized attenuation constant, V is normalized frequency. J_m, K_m are the Bessel and modified Bessel functions respectively.

2.3. The Reflectivity of the Fiber Bragg Grating

We only study unchirped uniform grating and assume that a perturbation to the core refractive index of the grating can be described as follows:

$$\delta n_{co}(z) = \overline{\delta n_{co}}\left[1 + \nu\cos\left(\frac{2\pi}{\Lambda}z\right)\right] \tag{7}$$

where $\overline{\delta n_{co}}$ is "dc" index change spatially averaged over a grating period and $\overline{\delta n_{co}} = 1.0 \times 10^{-4}$. ν is the fringe visibility of the index change and $\nu = 1$ in this work. Λ is the grating period, L is the grating length, N is the total numbers of the grating periods and $\Lambda = L/N$.

According to coupled-mode theory and the boundary condition of the fiber Bragg grating, the amplitude reflectivity can be shown as follows [11]:

$$\gamma = |\rho|^2 = \sinh^2\left(\sqrt{\kappa^2 - \hat{\sigma}^2}L\right) \Big/ \left[\cosh^2\left(\sqrt{\kappa^2 - \hat{\sigma}^2}L\right) - \frac{\hat{\sigma}^2}{\kappa^2}\right] \tag{8}$$

where $\hat{\sigma} = \delta + \sigma$ is a general "dc" self-coupling coefficient. The detuning δ is defined as:

$$\delta = \beta - \frac{\pi}{\Lambda} = 2\pi n_{eff}\left(\frac{1}{\lambda} - \frac{1}{\lambda_B}\right) \tag{9}$$

where $\lambda_B \equiv 2n_{eff}\Lambda$ is the Bragg wavelength.

3. CALCULATED RESULTS AND ANALYSIS

According to the previous theory, we simulated the curves of n_e, n_o, K_{cl} and Δ of the $LiNbO_3$ crystal. Setting $a = 900\,\text{nm}$, $n_0 = 2.33$, $L = 1.6416\,\text{cm}$, $N = 48000$, $n_o = 2.29$, $n_e = 2.20$, $\gamma_{13} = 8.6 \times 10^{-12}\,\text{m/V}$ $\gamma_{33} = 30.8 \times 10^{-12}\,\text{m/V}$ [12]. The curves of the reflective coefficient γ is function of the wavelength λ, i.e., γ-λ curves can been obtained from Eq. (8) for $E = 0, 10, 20, 30, 40, 60, 80, 100$ ($\times 10^7\,\text{V/m}$). It can be seen that the bandwidth and the maximal reflectivity of reflected spectra increase with E increasing, the reflected spectra moves toward the short wavelength when the electric field increase, when $E = 0, 10, 20, 30, 40$ ($\times 10^7\,\text{V/m}$), the variation of λ_B is nearly equal, i.e., it is approximatively linear variation. But when $E > 40$ ($\times 10^7\,\text{V/m}$), its variation is smaller.

In order to further study the influence of electric field on Bragg wavelength, we simulated Fig. 2. From it, we can see that the Bragg wavelength λ_B decreases from 1566.13 nm to 1542.80 nm along with the variation of the electric field intensity E from 0 to 100 ($\times 10^7\,\text{V/m}$). The slope of the curve is gradually decreasing, the influence of E on λ_B is gradually weaker.

In addition, we can see that the reflectivity γ will increase along with the increasing of E as shown in Fig. 3. It is accordant with the conclusion of Fig. 1. The range of the maximal reflectivity is from 3.19231% to 99.1157%.

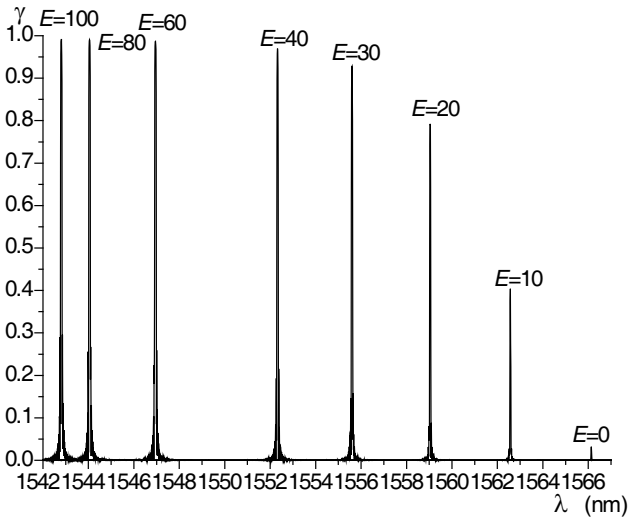

Figure 1: Variation of the reflective spectrum with electric field intensity.

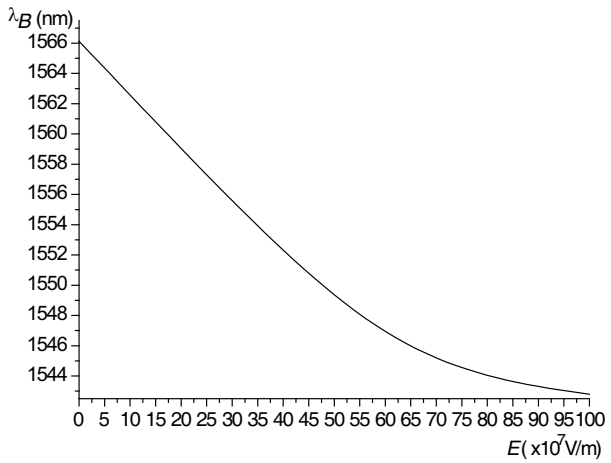

Figure 2: Influence of electric field on the Bragg wavelength λ_B.

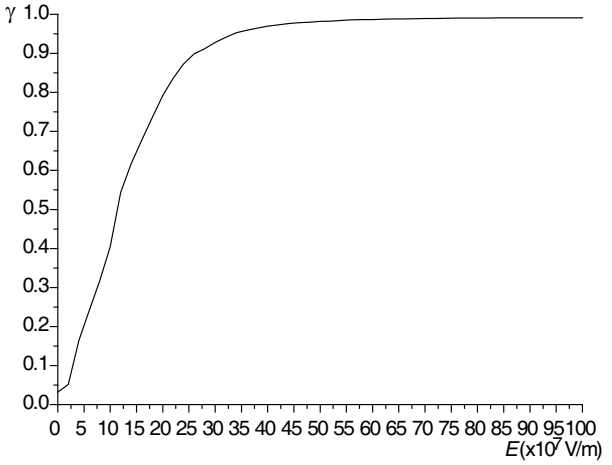

Figure 3: Effect of electric field on the maximal reflectivity.

4. CONCLUSIONS

In the work, we designed a novel voltage sensor based on fiber Bragg grating with cladding which is made of uniaxial anisotropic electro-optic crystal material i.e., $LiNbO_3$. The calculated results indicate that with the variation of electric field intensity from 0×10^7 V/m to 100×10^7 V/m, the Bragg wavelength λ_B has the decrease of 23.33 nm which varies from 1566.13 nm to 1542.80 nm, and the maximal reflectivity γ increase from 3.19% to 99.12%. Every one λ_B and γ is corresponding to an exclusive electric field intensity E, and the variation regularities of them provide us with the theoretical basis which we design a voltage sensor.

ACKNOWLEDGMENT

This work was supported by Natural Science Fund of Gansu Province (3ZS062-B25-036), China and the Outstanding Young Teacher Training Plan of Lanzhou University of Technology, Lanzhou, China.

REFERENCES

1. Hill, K. O., Y. Fujii, and D. C. Johnson, "Photosensitivity in optical fiber waveguides: Application to reflection filter fabrication," *Applied Physics Letters*, Vol. 32, 647–649, 1978.
2. Li, P., S. Jian, and F. Yan, "The dispersion compensation of optical fiber grating laser," *Acta Optica Sinica*, Vol. 24, No. 2, 220–224, 2004.
3. Bilodeau, F., D. C. Johnson, and S. Theriault, "An all-fiber-dense-wavelength-division multiplexer/demultiplexer using photo imprinted Bragg gratings," *Photonics Technology Letters, IEEE*, Vol. 7, No. 4, 388–390, 1995.
4. Chi, R., K. Lv, and S. Chen, "Research on lasing wavelength of fiber gratings," *Acta Optica Sinica*, Vol. 23, No. 11, 1315–1319, 2003.
5. Kersey, A. D., "A review of recent developments in fiber optic sensor technology," *Optic Fiber Technology*, Vol. 2, 291, 1996.
6. Hou, S., C. Hu, and X. Ren, "Influence of uniaxial crystal material cladding on reflectivity and dispersion of uniform fiber Bragg grating," *Optics Communication*, Vol. 271, 109–115, 2007.
7. Stevenson, J. L. and R. B. Dyott, "Optical fiber waveguide with a single-crystal core," *Electronics Letters*, Vol. 10, No. 22, 449–450, 1974.
8. Cozens, J., "Propagation in cylindrical fibres with anisotropic crystal cores," *Electronics Letters*, Vol. 12, No. 16, 413–415, 1976.
9. Lv, D. and X. Zhang, "Theoretical study on electro-optic effect and elasto-optic effect in chirped fiber grating with uniaxial crystal cladding," *Optical and Quantum Electronics*, Vol. 36, No. 5, 469–481, 2004.
10. Hou, S.-L., B. Chen, and Z.-X. Chen, "Design of tunable wavelength selector with fiber Bragg gratings with cladding made of electro-optic materials," *Asia-Pacific Optical Communications (SPIE), 2008, Proc. SPIE*, Vol. 7134, 71343K, Hangzhou, 2008.
11. Kogelnik, H. and T. Tamier, (Ed), *Guided-wave Optoelectronics*, Springer-Verlag, New York, 1990.
12. Pressley, R. J., Ed., *Handbook of Lasers*, The Chemical Rubber Co., 1971.

Modeling and Simulation of Large-scale Rectangular Surface-wave Plasma Source

Chaohui Lan, **Wendou Wang**, **Qiang Wang**, **Long Xie**, **Jihao Jiang**, **and Caihua Wei**
Institute of Fluid Physics, CAEP, Mianyang 621900, China

Abstract— A self-consistent and three-dimensional model of argon discharge in a large-scale rectangular Surface-wave plasma (SWP) source is presented, which is based on the finite-difference time-domain (FDTD) approximation to Maxwell's equations self-consistently coupled with a time-stepping fluid diffusion model for plasma evolution. The spontaneous outspread of plasma towards quartz edge under the drive of surface wave can be simulated by this model, and the final steady states of electron density and electron temperature distributions can be obtained. The numerical simulation results reveal the electromagnetic wave distribution in the whole device and confirm the existence of surface wave. The results also show that the electron density has a characteristic profile such that the peak is located several centimeters from quartz boundary, while the electron temperature monotonously increases toward the boundary.

1. INTRODUCTION

Surface-wave plasma (SWP) source can produce high-density and large-scale uniform plasma through microwave without use of external electrodes or magnets. In recent years, SWP source has been developed to be a competitive processing tool for ultra-large-scale integrated (ULSI) circuit devices, flat panel displays etc. To date, significant progress has been made in this field. [1–3] But most of these works mainly focus on the cylindrical configuration of SWP source. In Ref. [4], a novel structure of slot-antenna array for a rectangular SWP source has been reported. However, some problems like the antenna-surface wave coupling mechanism and the optimum design of the slot antenna have not been satisfactorily resolved yet. Furthermore, the large-scale spatial uniformity of plasma is the most important target but very difficult to carry out only by experience. Thus we urgently need the assistance of computer numerical simulation in the design of SWP device. In this paper, we introduce a numerical method which is based on the finite-difference time-domain method (FDTD) and fluid diffusion model for evolution plasma.

2. CONFIGURATION AND PHYSICAL MODEL

Figure 1 shows the configuration of the rectangular SWP source structure, the configuration is similar to the experimental setup under operation. The SWP source consists of a R22 rectangular waveguide connected to a metallic rectangular chamber with a size of 44 cm × 22 cm × 15 cm. The top wall of the chamber is a quartz dielectric with a thickness of 14 mm and relative permittivity $\varepsilon = 3.78$. Slot antennas are placed just at the bottom wall of the waveguide. The plasma is sustained through the injection of microwave energy at 2.45 GHz from the waveguide (TE_{10} mode) into the chamber.

The Maxwell's equations and cold plasma-electron equations of motion are given by

$$\varepsilon \frac{\partial \mathbf{E}}{\partial t} = \nabla \times \mathbf{H} - \mathbf{J} \tag{1}$$

$$\mu \frac{\partial \mathbf{H}}{\partial t} = -\nabla \times \mathbf{E} \tag{2}$$

$$m_e \frac{\partial \mathbf{u}}{\partial t} = -e\mathbf{E} - \boldsymbol{\nu}_{en}\mathbf{u} \tag{3}$$

$$\mathbf{J} = -en_e\mathbf{u} \tag{4}$$

where $\mathbf{E}$ and $\mathbf{H}$ are the electric and magnetic field, $\mathbf{J}$ is the plasma current density induced by microwaves, e is the electron charge, m_e is the mass of electron, n_e is the plasma electron density, v_{en} is the electron-neutral collision frequency, $\mathbf{u}$ is the electron velocity, μ and ε are the permeability and permittivity in free space or in quartz dielectric, respectively. Here, $v_{en} = n_n\sigma_{en}u$ is a function of gas pressure and electron temperature, where $n_n = p_n/(k_B T_n)$ is the neutral gas density with the gas pressure p_n and temperature T_n, and Boltzmann's constant k_B; σ_{en} is the electron-neutral collision cross section and assumed to be constant $5\times10^{-20}\,\mathrm{m}^2$. It is noted that in Equation (3)

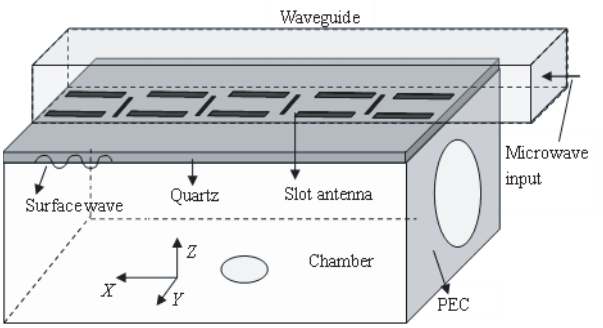

Figure 1: Three-dimensional model of SWP source.

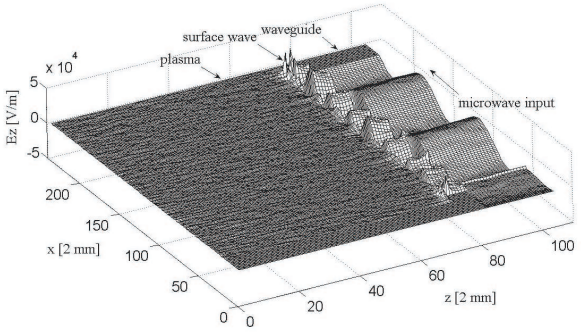

Figure 2: E_z field in x-z section of the SWP source.

the terms of nonlinear convection and pressure gradient are both ignored due to the high frequency and power of input microwave and the thin layer of surface wave zone.

Within one period of microwave, the plasma electron density and temperature can be viewed as in quasi-steady-state in comparison to the time scale of the microwave oscillation. So the electron fluid continuity and energy balance equations in plasma can be written as

$$\nabla \cdot \mathbf{\Gamma}_e = K_i n_e n_n \tag{5}$$

$$\nabla \cdot \mathbf{q}_e = P_{abs} - P_{coll} \tag{6}$$

where

$$\mathbf{\Gamma}_e = -\mu_e n_e \mathbf{E}_b - \frac{k_B}{m_e \boldsymbol{\nu}_{en}} \nabla (n_e T_e) \tag{7}$$

is the electron flux, and

$$\mathbf{q}_e = \frac{5}{2} \mathbf{\Gamma}_e k_B T_e - \frac{5 n_e k_B T_e}{2 m_e \boldsymbol{\nu}_{en}} \nabla k_B T_e \tag{8}$$

is the electron energy flux, P_{abs} is the power density deposited into electrons, and T_e is the electron temperature. The bipolar diffusion electric field can be expressed as

$$\mathbf{E}_b = \frac{D_i - D_e}{\mu_e + \mu_i} \cdot \frac{\nabla n_e}{n_e} - \frac{1}{\mu_e + \mu_i} \frac{k_B \nabla T_e}{m_e \nu_{en}} \tag{9}$$

where $\mu_\alpha = e/m_\alpha \nu_{\alpha n}$ and $D_\alpha = k_B T_\alpha / m_\alpha \nu_{\alpha n}$ $(\alpha = i, e)$ are the mobilities and diffusion constants of ion and electron, respectively.

Consider a single-ionized argon plasma with the assumption of charge neutrality, and besides, we take into account the excited $4s$ and $4p$ states of argon atom. The power density of energy losses due to electron-neutral inelastic collisions can thus be expressed as

$$P_{coll} = n_e n_n K_i U_i + n_e n_n K_{4s} U_{4s} + n_e n_n K_{4p} U_{4p} \tag{10}$$

where K_i, K_{4s} and K_{4p} denote the rate coefficients for ionization and excitation [5]. $U_i = 15.76\,\text{eV}$, $U_{4s} = 11.5\,\text{eV}$ and $U_{4p} = 13.2\,\text{eV}$ are the corresponding threshold energies for ionization and excitation to the states $4s$ and $4p$. The period-averaged electromagnetic deposited power density in Equation (6) is given by

$$P_{abs} = \frac{1}{T} \int_t^{t+T} \mathbf{J} \cdot \mathbf{E} dt \tag{11}$$

where T ($\approx 0.408\,\text{ns}$) is the period of 2.45 GHz microwave. The boundary conditions for Equations (5)–(6) are

$$\Gamma_{e\perp} = n_e u_B = 0.605 n_e \sqrt{k_B T_e / m_i} \tag{12}$$

$$q_{e\perp} = k_B T_e \left(2.5 + \ln \sqrt{m_i / 2\pi m_e}\right) \Gamma_{e\perp} \tag{13}$$

where $\Gamma_{e\perp}$, $q_{e\perp}$ are the respective components of $\mathbf{\Gamma}_e$ and $\mathbf{q}_e$ perpendicular to the walls, u_B is the Bohm velocity. Here we assume that there is a plasma sheath at the plasma-wall interface where the plasma contacts solid material.

3. SIMULATION RESULTS

The Maxwell's Equations (1)–(2) are solved using the finite-difference time-domain (FDTD) method [6], while the motion Equation (3) is discretized by the auxiliary difference equation (ADE) method. [7] Gauss-Siedel iteration is used to solve the discretized nonlinear difference equations of (5) and (6). The overall procedure of time-stepping self-consistent solution is as follows. At the beginning, electron density and temperature in the whole chamber are initialized to be constants, i.e., $T_{e0} = 2\,\mathrm{eV}$, $n_{e0} = 10^{18}\,\mathrm{m}^{-3}$. By performing the FDTD simulations of Equations (1)–(4), we obtain the steady-state electromagnetic field in 15–25 microwave periods. Then we calculate Equation (11) to obtain the spatial distribution of deposited power density, which as an input is transferred to plasma fluid subloop to solve the electron density and temperature. Typically in 1750–2000 Gauss-Siedel iterations, a converged solution of the electron density and temperature is reached. Then we use the electron density and temperature obtained as the inputs of the FDTD subloop. By reciprocally iterating of these two subloops, the main loop reaches a converged solution in approximately 6–15 iterations. In the current numerical simulation the gas pressure and input power are set to be 50 Pa and 1200 W, respectively.

Figure 2 shows the snapshot of E_z field distribution in x-z section of the SWP source, including the fields in the waveguide and in the chamber. It is clear to see the existence of a standing wave pattern in the x direction and an evanescent behavior in the z direction. The SW attenuates rapidly away from the plasma-dielectric interface, and the penetration depth is about 3 mm. From this figure, the existence of surface wave along the plasma-dielectric interface can be confirmed.

Figure 3 depicts the time-stepping evolution of electron density 2D distribution. The sampled plane is located at a distance of 1.2 cm from the quartz window. At the beginning, as shown in Fig. 3(a), four y-direction slots play a main role and build a plasma channel for the propagation of surface wave along the x direction. After that, the plasma starts to spread out along the y direction under the excitation of ten x-direction slots, which is indicated in Figs. 3(b) and (c). With the increase of uniformity and density of plasma, the absorption efficiency of injected microwave power

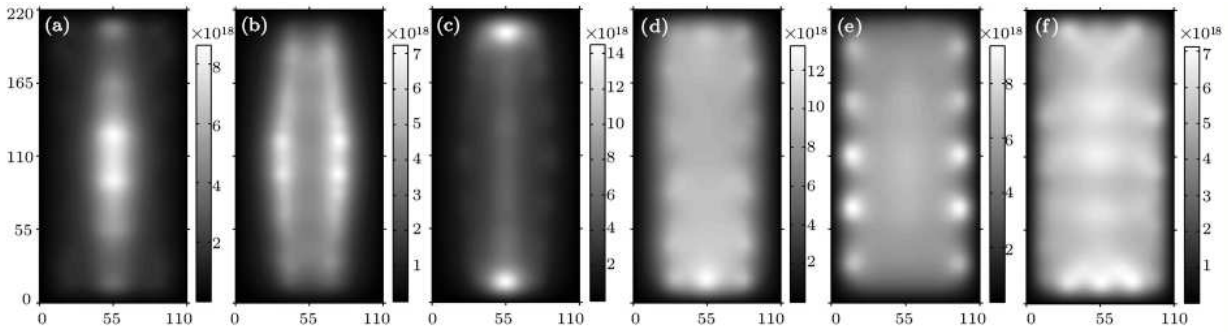

Figure 3: Time stepping of 2D electron density distribution, (a)∼(f) respectively represent the results of the 1∼6th main loop iterations.

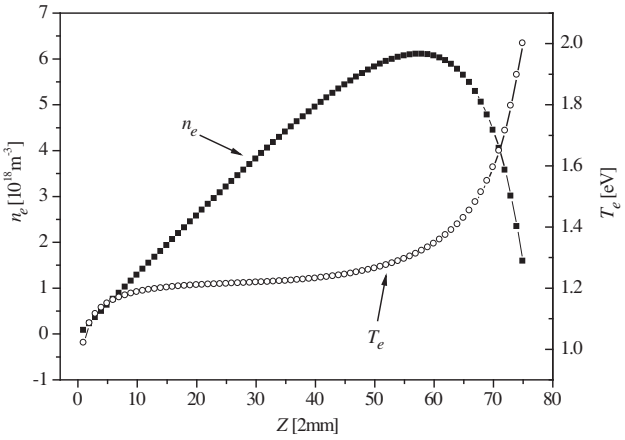

Figure 4: Electron density and temperature distributions along the vertical center axis of the chamber.

also tends to increase. As a result shown in Fig. 3(f), the high density plasma can completely spread out and cover the whole quartz window under the drive of surface wave. It is interesting to note that the whole process is totally spontaneous, and only depends on external conditions such as input power, gas pressure and the structure of slot antennas.

Figure 4 shows the n_e and T_e distributions along the vertical center axis of the rectangular chamber. For injected microwave power $P_{in} = 1200\,\mathrm{W}$ and gas pressure $p_n = 50\,\mathrm{Pa}$, the maximal values of n_e and T_e can reach about $6 \times 10^{18}\,\mathrm{m}^{-3}$ and $2\,\mathrm{eV}$. The distributions of n_e and T_e are nonuniform in the z direction owing to diffusion, and the distribution of n_e has a peak at around $z = 12\,\mathrm{cm}$ or a vertical distance of $3\,\mathrm{cm}$ from the quartz window. From $z = 12\,\mathrm{cm}$ to $z = 15\,\mathrm{cm}$, the distributions of T_e and n_e are quite different, one monotonously and steeply rises and the other rapidly drops down after reaching its peak.

4. CONCLUSIONS

In this paper, we have presented a self-consistent three-dimensional FDTD/fluid model for the large-scale rectangular surface wave source. The model employs the finite-difference time-domain (FDTD) method to solve the electromagnetic equations and at the same time employs plasma fluid model to self-consistently obtain steady-state plasma spatial distributions. We have simulated the time evolution of argon surface-wave discharge at an input microwave power of 1200 W and a gas pressure of 50 Pa. The results show that the electron density has a characteristic profile such that the peak is located several centimeters from the boundary, while the electron temperature monotonously increases toward the boundary. The tendencies and the orders of magnitudes of the results show good agreement with existing experiment data. Further investigations are now in progress to validate the FDTD/fluid simulation by comparing the numerical results with experimental investigations.

REFERENCES

1. Ghanashev, I. and H. Sugai, "Multiple eigenmode analysis and density jumps in planar surface-wave plasmas with slot-antenna excitation," *Phys. Plasmas*, Vol. 7, 3051–3061, 2000.
2. Sugai, H., I. Ghanashev, and M. Nagatsu, "High-density flat plasma production based on surface waves," *Plasma Sources Sci. Technol.*, Vol. 7, 192–205, 1998.
3. Kousaka, H. and K. Ono, "Numerical analysis of the electromagnetic fields in a microwave plasma source excited by azimuthally symmetric surface wave," *Jpn. J. Appl. Phys.*, Vol. 41, 2199–2206, 2002.
4. Chen, Z. Q., P. Q. Zhou, W. Chen, et al., "A novel structure of slot-antenna array for producing large-area planar surface-wave plasmas," *Plasma Sci. and Technol.*, Vol. 10, No. 6, 655–660, 2008.
5. Ashida, S., C. Lee, and M. A. Lieberman, "Spatially averaged (global) model of time modulated high density argon plasmas," *J. Vac. Sci. Technol. A*, Vol. 13, 2498–2507, 1995.
6. Taflove, A., *Computational Electrodynamics: The Finite-difference Time-domain Method*, Artech House, Boston, 1995.
7. Takayama, Y. and W. Klaus, "Reinterpretation of the auxiliary differential equation method for FDTD," *IEEE Microwave Wireless Components Lett.*, Vol. 12, 102–104, 2002.

Property of Subwavelength Resonator with DNG Metamaterials by FDTD Method

Kui-Song Zheng, **Chang-Ying Wu**, **Jia-Dong Xu**, **and Gao Wei**
School of Electronics and Information, Northwestern Polytechnical University, Chang'an Campus
Xi'an, Shaanxi 710129, China

Abstract— A novel designing subwavelength resonator loaded with metamaterials has been investigated both analytically and numerically. Based on constitutive equations of DNG materials modeled by Drude model, the updated equations in the DNG materials are deduced and determined with the FDTD scheme. In the one-dimensional case, a subwavelength cavity resonator with metamaterials of negative permeability and negative permittivity is proposed. Numerical results show that the resonator with DNG materials has two resonances: one is a normal resonance; the other one is a subwavelength resonance. The proposed subwavelength resonator overcomes the diffractive limitation. By analyzing the numerical results, the physical dimensions of the subwavlength cavity resonator with operating in the subwavelength frequency can reduce to 0.083 times the operating wavelength in comparison to 0.5 times the operating wavelength for the conventional resonator. A new avenue has supplied for manufacturing the subwavelength resonators.

1. INTRODUCTION

The permittivity ε and the permeability μ are the fundamental characteristic quantities which determine the propagation of the electromagnetic wave in mater. In 1968, V. G. Veselago states that a material with both negative permittivity and negative permeability has unusual electromagnetic properties different from one with positive permittivity and positive permeability [1], such as the reversed Doppler effect, the reversed Snell law and the vavilov-cerenkov effect and so on. Several recent papers have been reported the special properties of double negative (DNG) material, i.e., metamaterials having negative permittivity and negative permeability. Pentry's team and other research groups have reported that artificial complex materials and some structures with arrays of thin metallic lines could produce metamaterials with negative permittivity and negative permeability [2, 3]. D. R. Smith has proposed that using metallic lines and split ring resonators could also construct DNG metamaterials [4]. In recent years, several theoretical and numerical study results have been expressed by many literates at home and abroad [5–9]. As far as I know, a lot of study results of metamaterials have been focused on aspects of the antenna radiations, while in this paper the subwavelength effect of resonators due to introducing metamaterials are mainly discussed. A one-dimensional cavity resonator partially loaded by metamaterials has the subwavelength resonance, which overcomes the diffraction limitation and reduces the transversal physical dimensions.

2. FDTD FORMULATION

For lossy DNG metamaterials, negative permittivity and permeability are realized using the Drude medium model as follows:

$$\varepsilon(\omega) = \varepsilon_0 \varepsilon_r(\omega) = \varepsilon_0 \left(1 - \frac{\omega_{pe}^2}{\omega(\omega - j\Gamma_e)}\right) \tag{1}$$

$$\mu(\omega) = \mu_0 \mu_r(\omega) = \mu_0 \left(1 - \frac{\omega_{pm}^2}{\omega(\omega - j\Gamma_m)}\right) \tag{2}$$

where ω_{pe}, ω_{pm} and Γ_e, Γ_m denote the corresponding plasma and damping frequencies, respectively. For modelling SNG metamaterial, either the dispersive permittivity or permeability is replaced by a frequency independent constant. The Drude model can be implemented into the FDTD scheme by introducing the associated electric and magnetic current densities into the equations that govern their temporal behaviours. The time domain equations solved with the FDTD for the

DNG metamaterials can be presented by

$$\nabla \times \mathbf{H} = \varepsilon_0 \frac{\partial \mathbf{E}}{\partial t} + \mathbf{J} \tag{3}$$

$$\frac{\partial \mathbf{J}}{\partial t} + \Gamma_e \mathbf{J} = \varepsilon_0 \omega_{pe}^2 \mathbf{E} \tag{4}$$

$$\nabla \times \mathbf{E} = -\mu_0 \frac{\partial \mathbf{H}}{\partial t} - \mathbf{K} \tag{5}$$

$$\frac{\partial \mathbf{K}}{\partial t} + \Gamma_m \mathbf{K} = \mu_0 \omega_{pm}^2 \mathbf{H} \tag{6}$$

where $\mathbf{J}$ and $\mathbf{K}$ stand for the electric and magnetic current densities. By replacing the derivatives with their central finite difference counterparts, the discretized equations of the electric field E_x and current J_x components in (3) and (4) are written as follows:

$$\begin{aligned} E_x^{n+1}(i+1/2,j,k) = {} & E_x^n(i+1/2,j,k) - \frac{\Delta t}{\varepsilon_0} J_x^{n+1/2}(i+1/2,j,k) \\ & + \frac{\Delta t}{\varepsilon_0 \Delta y \Delta z} \left\{ \left[H_z^{n+1/2}(i+1/2,j+1/2,k) - H_z^{n+1/2}(i+1/2,j-1/2,k) \right] \Delta z \right. \\ & \left. - \left[H_y^{n+1/2}(i+1/2,j,k+1/2) - H_y^{n+1/2}(i+1/2,j,k-1/2) \right] \Delta y \right\} \end{aligned} \tag{7}$$

$$J_x^{n+1/2}(i+1/2,j,k) = \frac{1-0.5\Gamma_e \Delta t}{1+0.5\Gamma_e \Delta t} J_x^{n-1/2}(i+1/2,j,k) + \frac{\varepsilon_0 \omega_p^2 \Delta t}{1+0.5\Gamma_e \Delta t} E_x^n(i+1/2,j,k) \tag{8}$$

Similar expressions can be derived for the remaining finite-difference expressions based on Yee's algorithm for the E_y and E_z field components and the J_y and J_z current components given by Maxwell's equations (3) and (4). Referring again to (3) $\sim$ (6), the time-stepping expressions having a form similar to that of the $\mathbf{E}$ equations above can be derived to update the magnetic $\mathbf{H}$ components. Similarly, three equations for the magnetic current $\mathbf{K}$ can be also derived using the same approach.

3. SUBWAVELENGTH RESONATOR

3.1. Geometry of Resonator

For a resonator closed by metallic walls at its two ends, the conditions of causing a stable resonance is to produce a stable standing wave within the cavity. That is to say that the distance l between two metallic walls is going to equal the integral multiple of half the operating wavelength λ_g, i.e., $l = p\lambda_g/2$ $(p = 1, 2, \ldots)$. In this paper, due to the phase compensation of metamaterials with negative permittivity and negative permeability, a proposed resonator loaded with double negative materials can operate at a subwavelength resonant frequency.

In the following, a designing one-dimensional resonator is described in Fig. 1. The antenna is embedded in a suitable Cartesian coordinate system, as defined in the figure. The length of the resonator along z axis is set as $l = 50\,\text{mm}$. In the figure, the unit of x coordinate axis is defined by numbers of spacing, i.e., $z/\Delta z$. The spatial step is $\Delta z = 0.5\,\text{mm}$. The origin point of the coordinate system is set as the center of the one-dimensional resonator along z axis. This resonator is fed by a gaussian pulse source located by the position $z = -10\Delta z$ as

$$E_i(t) = \exp\left[\frac{-4\pi(t-t_0)^2}{\tau^2}\right] \tag{9}$$

where $t_0 = 0.8\tau$ and $\tau = 0.5\,\text{ns}$. The observation point is defined as the position $z = -15\,\text{mm}$.

3.2. Numerical Results

In the Fig. 1, the designing resonator is filled with two materials: one is a material with negative permeability and negative permittivity (DNG: $\varepsilon_2 < 0$ and $\mu_2 < 0$); another is a material with positive permittivity and positive permeability ($\varepsilon_1 > 0$ and $\mu_1 > 0$). The DNG metamaterial is applied in the spatial interval $(-50, 0)$ (unit is numbers of grids), and the double positive (DPS) materials is set in the interval (0, 50). Based on the electromagnetic wave propagation theorem,

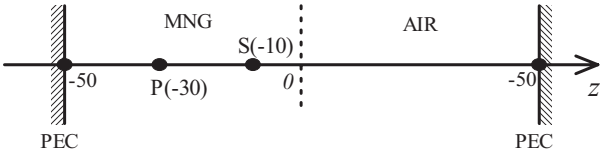

Figure 1: Sketch of subwavelength resonator.

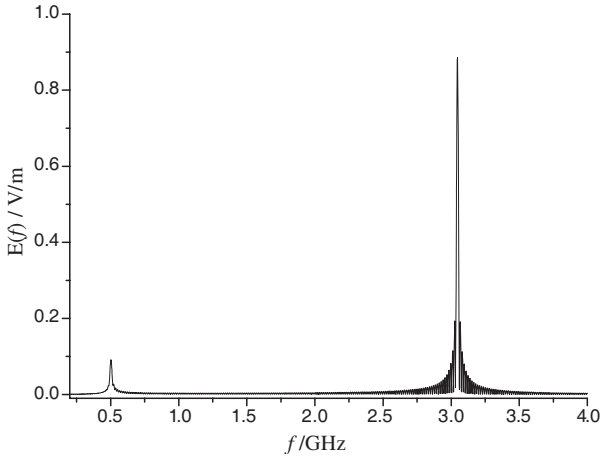

Figure 2: Resonant frequency of subwavelength resonator with DNG material.

the dispersive equations of the cavity resonator can be derived as follows [10]:

$$\frac{n_2}{\mu_2}\tan(n_1 k_0 d_1) + \frac{n_1}{\mu_1}\tan(n_2 k_0 d_2) = 0 \tag{10}$$

where $k_0 = \omega\sqrt{\varepsilon_0\mu_0}$. The symbols n_1 and n_2 denote the refraction index of these two materials, respectively. The symbols d_1 and d_2 stand for the thickness along z axis for these two materials.

Assuming that the variable ω, d_1 and d_2 are chosen such that the small-argument approximation can be used for the tangent function, the above relation can be simplified as

$$\frac{d_1}{d_2} \simeq -\frac{\mu_2}{\mu_1} \tag{11}$$

This relation shows even more clearly that d_1 and d_2 should be related to d_1/d_2, not $d_1 + d_2$ in order to have a non-trivial one-dimensional solution with frequency ω for a cavity resonator. If the second material is set as a metamatrial with negative permeability and the ratio d_1/d_2 satisfies the above condition, one can obtain a thin subwavelength resonator for the given frequency. Therefore, if the second slab is constructed by a metamaterial with negative permittivity $\varepsilon_{2r} = -1$ and negative permeability $\mu_{2r} = -1$ and if the conventional material is assumed to be air with ε_0 and μ_0, and thus the required ratio d_1 over d_2 should be approximately equal to 1, the cavity resonator can be resonated at a subwavelength frequency. Blow this point can be also proved by calculating an analogous cavity resonator model with FDTD method, as sketched by Fig. 1.

In the numerical calculation, the DNG material is properly modeled by the dispersive Drude model with $\omega_p \approx 4.44 \times 10^9$ rad/s and $\Gamma = 50$ MHz. Therefore, the relative permeability μ_{2r} can be approximately equal to -1 at $f = 0.5$ GHz. The first slab is defined as air with ε_0 and μ_0. The thickness d_1 is set as $d_1 = 25$ mm, and in order to produce a subwavelength resonance and satisfy the constrained condition as expressed in (11), the thickness d_2 is also equal to 25 mm. By simulating the cavity model with FDTD method determines that there are two resonances for the one-dimensional cavity resonator, as shown in Fig. 2. One is the subwavelength resonance at $f = 0.5$ GHz, and the other one is the normal resonance at $f = 3.08$ GHz. Numerical results are in good agreement with theoretical analysis results of using dispersive equation (10). When the cavity resonator operates at the normal resonant frequency $f = 3.08$ GHz, the relative permeability is $\mu_{2r} \approx 0.95$. Meanwhile, this case is equivalent to the cavity resonator with approximately totally filled with air. By comparing these two resonant frequencies depicted in the figure, when the resonator is operated at the subwavelength frequency the transversal physical dimension of the resonator can be reduced from $0.5\lambda_g$ to $0.083\lambda_g$.

4. CONCLUSION

A new designing model of subwavelength cavity resonator loaded by metamaterials with negative permittivity and negative permeability has been proposed in this paper. The update equations have been derived by introducing metamaterials with negative constitutive parameters into the

computation domain. By comparing numerical calculation results with FDTD method with theoretical analysis results using dispersive equations, there is a subwavelength resonance of the cavity resonator partially loaded with metamaterials. Due to the property of phase compensation of negative material, the proposed subwavelength cavity resonator can overcome the limitation of diffraction condition and reduce the transversal volume of the cavity resonator. It is a new avenue of miniaturizing the cavity antennas.

ACKNOWLEDGMENT

The project is supported by the Science Research Starting Foundation of Northwestern Polytechnical University of China.

REFERENCES

1. Veselago, V. G., "The electrodynamics of substance with simultaneously negative value of ε and μ," *Sov. Phys. Usp.*, Vol. 10, No. 4, 509–514, 1968.
2. Pendrv, J. B., A. J. Holden, W. J. Stewart, and I. Youngs, "Extremely low frequency plasmons in metallic mesostructrue," *Phys. Rev. Lett.*, Vol. 76, No. 25, 4773–4776, 1996.
3. Pendry, J. B., I. J. Holder, D. J. Robbins, et al., "Low frequency plasmons in thin-wire structures," *J. Phvs. C*, Vol. 10, 4785–4808, 1998.
4. Smith, D. R., W. J. Padilla, D. C. Vier, S. C. Nemat-Nasser, and S. Schultz, "Composite medium with simultaneously negative permeability and permittivity," *Phys. Rev. Lett.*, Vol. 84, No. 18, 4184–4187, 2000.
5. Valanju, P. M., R. M. Walser, and A. P. Valanju, "Wave refraction in negative-index media: Always positive and very inhomogeneous," *Phys. Rev. Lett.*, Vol. 88, No. 18, 187401, 2002.
6. Sui, Q., L. Li, and F. Li, "Simulation of media with negative permittivity and negative permeability," *Science of China* (*Series G*), Vol. 33, No. 5, 416–427, 2003.
7. Wan, G.-B., S. Jing, W. Wan, et al., "Simulation and experimental studies on cavity backed microstrip antennas with DNG substrates," *Chinese Journal of Radio Science*, Vol. 23, No. 4, 679–693, 2008.
8. Richard, W. Z. and D. K. AllIson, "Causality and double-negative metamaterials," *Physical Review E*, Vol. 68, No. 2, 026615–026624, 2003.
9. Ziolkowski, R. W. and E. Heyman, "Wave propagation in media having negative permittivity and permeability," *Physics Review E*, Vol. 64, No. 5, 056625–056640, 2001.
10. Engheta, N., "An idea for thin subwavelength cavity resonators using metamaterials with negative permittivity and permeability," *IEEE Antennas and Wireless Propagation Letters*, Vol. 1, No. 1, 10–13, 2002.

Experimental Verification of Anisotropic Three-dimensional Left-handed Metamaterial Composed of Jerusalem Crosses

Jiafu Wang[1], **Shaobo Qu**[1], **Hua Ma**[1], **Song Xia**[2], **Yiming Yang**[1], **Lei Lu**[1], **Xiang Wu**[1], **Zhuo Xu**[2], **and Qian Wang**[3]

[1]College of Science, Air Force Engineering University, Xi'an, Shaanxi 710051, China
[2]Electronic Materials Research Laboratory, Key Laboratory of the Ministry of Education
Xi'an Jiaotong University, Xi'an, Shaanxi 710049, China
[3]College of Environment and Planning, Liaocheng University, Liaocheng, Shandong 252000, China

Abstract— An anisotropic three-dimensional (3D) left-handed metamaterial (LHM) was proposed in this paper. The LHM is composed of unit cells with metallic Jerusalem crosses etched correspondingly on both sides of dielectric substrates. 3D left-handed property is realized by the couplings between neighboring metallic Jerusalem crosses. The LHM was fabricated and experimentally measured. The results show that the LHM always exhibits left-handed bands for incident plane waves along x, y, and z directions. Because of the symmetry of the unit cell, left-handed properties of the proposed 3D LHM in x and y directions are the same but are different from that in z direction. This verifies the validity of the proposed anisotropic 3D LHM.

1. INTRODUCTION

Left-handed metamaterials (LHMs) have become a hot international research topic since the pioneering work of J. B. Pendry and D. R. Smith [1, 2]. Nowadays, the realization of broad-band, low-loss LHMs is still the main task of LHM research. A great variety of LHMs have been designed and fabricated. Generally speaking, presently existing LHMs fall roughly into three categories. The LHMs in the first category are based on metallic patterns and both negative μ and ε are realized by the resonances of metallic patterns in response to incident waves. LHMs composed of S-shaped [3], Ω-shaped [4], crossing resonator unit cells [5] and the planar LHMs [6–9] fall into this category. LHMs in the second category are based on transmission line [10, 11]. LHMs in the third category are called all-dielectric LHMs. Many all-dielectric LHM unit cells, such as the disk-like unit cell [12], were proposed. These unit cells are based on different resonance modes in all-dielectric unit cells. Under a certain resonance mode, the effective μ or ε is negative.

The above-mentioned LHMs are mostly one-dimensional or two-dimensional. Comparatively, there are few literatures about the realization of 3D LHMs. 3D LHMs composed of a 3D network of reactively loaded transmission lines were proposed by G. V. Eleftheriades et al. [13 ,14]. Th. Koschny et al. [15] investigated 3D LHMs by using SRRs and 3D inter-crossing conducting wires. The afore-mentioned two kinds of 3D LHMs are isotropic under the condition that all the six sides of the 3D cubic unit cells are identical. However, in practice, it is very difficult to fabricate them, especially LHMs using SRRs and 3D inter-crossing conducting wires. A candidate 3D LHM was proposed by J. F. Wang et al. by using coplanar resonators [16], which is comparatively easier to be fabricated. All-dielectric 3D LHMs using dielectric spheres [17] and cubes [18] were proposed, which are easier to be fabricated and have isotropic left-handed property. However, left-handed bands of all-dielectric 3D LHMs are rather narrow, which limits their practical applications.

In this paper, an anisotropic 3D LHM is presented. Unit cell of the LHM is composed of a dielectric substrate with metallic Jerusalem crosses etched on it. 3D left-handed property is realized by the couplings between neighboring metallic Jerusalem crosses. We fabricated the LHM and measured its scattering parameters as well as effective permeability and permittivity. The LHM always exhibits left-handed bands for incident plane waves along x, y, and z directions. Because of the symmetry of the unit cell, left-handed properties of the proposed 3D LHM in x and y directions are the same but are different from that in z direction. The experiment results verify the proposed anisotropic 3D LHM.

2. SAMPLE FABRICATION AND EXPERIMENT SETUP

2.1. Sample Fabrication

Figure 1 shows the unit cell of the proposed 3D LHM and the fabricated LHM layers. Metallic patterns of the Jerusalem cross is etched on both sides of a square dielectric substrate. In practical

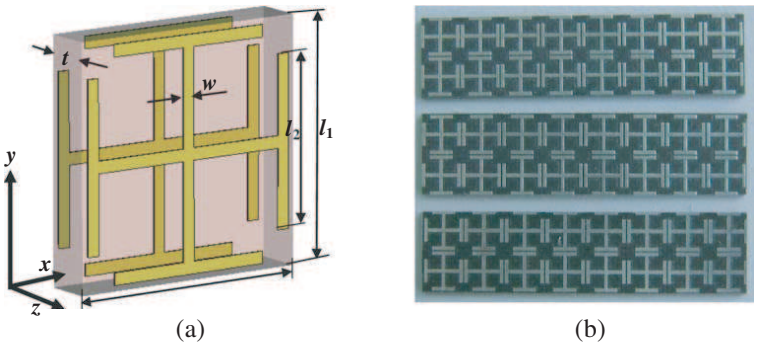

(a) (b)

Figure 1: (a) Unit cell of the proposed 3D LHM composed of metallic Jerusalem crosses and (b) the fabricated LHM layers.

fabrication, periodic arrays of copper (conductivity $\sigma = 5.8 \times 10^7\,\mathrm{S/m}$, thickness $t_1 = 0.017\,\mathrm{mm}$) Jerusalem cross patterns were etched on Rogers5880 substrates (dielectric constant $\varepsilon_r = 2.2$, loss tangent $\tan\delta = 0.0009$, thickness $t = 0.787\,\mathrm{mm}$). The side length of the square substrate board is $a = 5\,\mathrm{mm}$. Geometrical dimensions of the copper Jerusalem cross are: $w = 0.5\,\mathrm{mm}$, $l_1 = 4.8\,\mathrm{mm}$, $l_2 = 2.8\,\mathrm{mm}$.

In the two cases that a plane wave is incident onto the LHM along x or y direction with its magnetic field threading through the substrate plane (along z direction), the LHM has always equal electric and magnetic resonant frequencies [19] due to the couplings between neighboring Jerusalem crosses on the same side of the substrate. Thus, there is always a left-handed band for the two cases. While, in the case that a plane wave is incident onto the LHM along z direction, according to the working principle of planar LHMs [5, 9], the coupling between the two fore-and-aft corresponding Jerusalem crosses of each unit cell as well as that between two up-and-down neighboring Jerusalem crosses provide the magnetic and electric resonances, respectively. Thus, simultaneously negative permeability and permittivity (and hence a left-handed band) can be realized.

2.2. Experiment Setup

Figure 2 shows the measured sample and the measurement system. For the sake of practical measurement, the LHM layer must be put together and fixed. To fix the LHM layers with a spacing $s = 5\,\mathrm{mm}$, the MM layers were put inside a foam. Since permittivity of foam is quite close to that of the free space, the fixed LHM layers can be considered approximately to be in free space. Fig. 2(a) shows the fabricated sample for measurement. The sample was put into a standard waveguide of the measurement system (shown in Fig. 2(b)). Scattering parameters (S_{11} and S_{21}) of the fabricated LHM sample were measured by the Agilent network analyzer HP8720ES. By a standard algorithm [20, 21], effective permeability and permittivity can be extracted from the measured scattering parameters.

3. EXPERIMENT RESULTS AND ANALYSIS

3.1. Left-handed Properties in x and y Directions

Left-handed properties in x and y directions were firstly investigated. Figs. 3(a), (b) and (c) give the measured magnitudes of scattering parameters, real part of effective permittivity and real part of effective permeability, respectively. As shown in Fig. 3(a), there is a transmission peak and

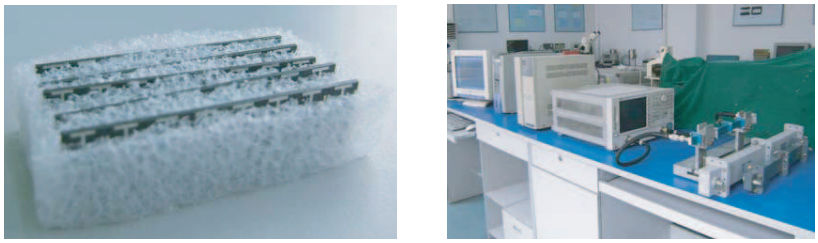

(a) (b)

Figure 2: (a) The LHM sample used for measurement and (b) the measurement system used in experiments.

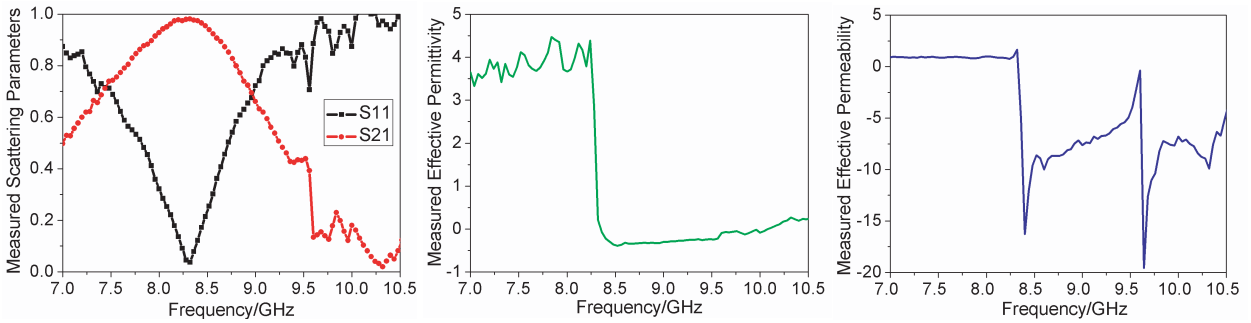

Figure 3: Measured results in x and y directions: (a) Measured scattering parameters, (b) measured real part of effective permittivity, (c) measured real part of effective permeability.

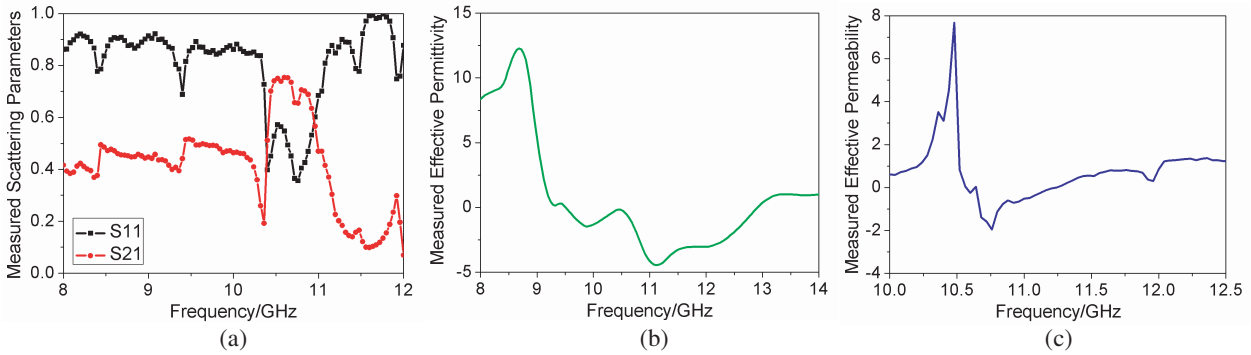

Figure 4: Measured results in z directions: (a) Measured scattering parameters, (b) measured real part of effective permittivity, (c) measured real part of effective permeability.

correspondingly a reflection dip around 8.3 GHz, which indicates a possible left-handed pass-band. Fig. 3(b) show that the effective permittivity drops and becomes negative at 8.3 GHz. The negative permittivity frequency range is 8.3–10.1 GHz. The effective permeability also becomes negative at 8.3 GHz, which verifies that the electric and magnetic resonant frequencies of the proposed LHM are indeed the same for the two cases. Correspondingly, the real part of effective permeability is negative in 8.3–9.6 GHz, as shown in Fig. 3(c). Thus, the left-handed band with simultaneously negative permittivity and permeability is 8.3–9.6 GHz.

3.2. Left-handed Properties in z Direction

The measured magnitudes of scattering parameters, real part of effective permittivity and real part of effective permeability for the case with incident waves along z direction are given in Figs. 4(a), (b) and (c), respectively. Fig. 3(a) shows that there is a transmission peak and a corresponding reflection dip around 10.7 GHz. Figs. 3(b) and (c) show that the real part of effective permittivity is negative in 9.5–12.9 GHz and the negative effective permeability range is 10.63–11.25 GHz. Thus, the corresponding left-handed band is 10.63–11.25 GHz.

Note the bandwidth is about 0.62 GHz, much narrower than 1.3 GHz in the x and y direction cases. This is because the coupling between the two corresponding Jerusalem crosses of one unit cell is usually quite weak and hence the induced magnetic resonance is quite weak, too. As a result, the resonance strength is weak and the negative permeability range is narrow. This results in a much narrower left-handed band.

4. CONCLUSION

In this paper, we proposed, fabricated and measured a 3D LHM composed of Jerusalem crosses. The experiment results show that the LHM exhibits different left-handed bands in different directions. Compared with other 3D LHMs, the proposed 3D LHM owe its advantage to its simple structure and easy fabrication. Moreover, since the left-handed bands can be tuned downward or upwards by carefully adjusting geometrical parameters of the metallic patterns, the proposed 3D LHM can be such that its left-handed bands in three directions are the same.

ACKNOWLEDGMENT

This work is supported in part by the National Natural Science Foundation of China under Grant Nos. 50632030 and 60871027 and in part by the 973 Project of Science and Technology Ministry of China under Grant No. 2009CB613306. The Natural Science Foundation of Shaanxi Province (Grant No. SJ08F01) also supports this work.

REFERENCES

1. Pendry, J. B., A. J. Holden, D. J. Robbins, and W. J. Stewart, "Magnetism from conductors and enhanced nonlinear phenomena," *IEEE Trans. Microw. Theory Tech.*, Vol. 47, 2075–2084, 1999.
2. Smith, D. R., W. J. Padilla, D. C. Vier, S. C. Nemat-Nasser, and S. Schultz, "Composite medium with simultaneously negative permeability and permittivity," *Phys. Rev. Lett.*, Vol. 84, 4184–4187, 2000.
3. Wang, D. X., L. X. Ran, H. S. Chen, M. K. Mu, J. A. Kong, and B.-I. Wu, "Experimental validation of negative refraction of metamaterial composed of single side paired S-ring resonators," *Appl. Phys. Lett.*, Vol. 90, 254103, 2007.
4. Huangfu, J. T., L. X. Ran, H. S. Chen, X. M. Zhang, K. S. Chen, T. M. Grzegorczyk, and J. A. Kong, "Experimental confirmation of negative refractive index of a metamaterial composed of Ω-like metallic patterns," *Appl. Phys. Lett.*, Vol. 84, 1537–1539, 2004.
5. Wang, J. F., S. B. Qu, Z. Xu, J. Q. Zhang, Y. M. Yang, and H. Ma, "The design of left-handed metamaterials composed of magnetic resonators and electric resonators," *Acta. Phys. Sin.*, Vol. 57, 5015–5018, 2008.
6. Zhou, J. F., L. Zhang, G. Tuttle, T. Koschny, and C. M. Soukoulis, "Negative index materials using simple short wire pairs," *Phys. Rev. B*, Vol. 73, 041101, 2006.
7. Alici, K. B. and E. Ozbay, "A planar metamaterial: polarization independent fishnet structure," *Photonics Nanostruct.: Fundam. Appl.*, Vol. 6, 102–107, 2008.
8. Kafesaki, M., I. Tsiapa, N. Katsarakis, T. Koschny, C. M. Soukoulis, and E. N. Economou, "Left-handed metamaterials: the fishnet structure and its variations," *Phys. Rev. B*, Vol. 75, 235114, 2007.
9. Wang, J. F., S. B. Qu, Z. X, J. Q. Zhang, H. Ma, Y. M. Yang, and C. Gu, "Broadband planar left-handed metamaterials using split-ring resonator pairs," *Photon Nanostruct: Fundam Appl.*, Vol. 7, 108–113, 2009.
10. Ozbay, E., K. Aydin, E. Cubukcu, and M. Bayindir, "Transmission and reflection properties of composite double negative metamaterials in free space," *IEEE Trans. Antennas Propagat.*, Vol. 51, 2592–2595, Oct. 2003.
11. Anthony, L., C. Caloz, and T. Itoh, "Composite right left-handed transmission line metamaterials," *IEEE Microwave Magazine*, Vol. 9, 34–50, 2004.
12. Ahmadi, A. and H. Mosallaei, "Physical configuration and performance modeling of all-dielectric metamaterials," *Phys. Rev. B*, Vol. 77, 045104, 2008.
13. Iyer, A. K. and G. V. Eleftheriades, "A three-dimensional isotropic transmission-line metamaterial topology for free-space excitation," *Appl. Phys. Lett.*, Vol. 92, 261106, 2008.
14. Grbic, A. and G. V. Eleftheriades, "An isotropic three-dimensional negative-refractive-index transmission-line metamaterial," *J. Appl. Phys.*, Vol. 98, 043106, 2005.
15. Koschny, T., L. Zhang, and C. M. Soukoulis, "Isotropic three-dimensional left-handed metamaterials," *Phys. Rev. B*, Vol. 71, 121103, 2005.
16. Wang, J. F., S. B. Qu, Z. Xu, J. Q. Zhang, Y. M. Yang, H. Ma, and C. Gu, "A candidate three-dimensional GHz left-handed metamaterial composed of coplanar magnetic and electric resonators," *Photon Nanostruct: Fundam Appl.*, Vol. 6, 183, 2008.
17. Holloway, C. L., E. F. Kuester, J. Baker-Jarvis, and P. Kabos, "A double negative (DNG) composite medium composed of magnetodielectric spherical particles embedded in a matrix," *IEEE Trans. Antennas Propgat.*, Vol. 51, No. 10, 2596–2603, 2003.
18. Kim, J. and A. Gopinath, "Simulation of a metamaterial containing cubic high dielectric resonators," *Phys. Rev. B*, Vol. 76, 115126, 2007.
19. Wang, J. F., S. B. Qu, Z. Xu, Z. T. Fu, H. Ma, and Y. M. Yang, "A robust left-handed metamaterial using Jerusalem crosses," *Photon Nanostruct: Fundam Appl.*, Vol. 7, 2009 (Submitted).

20. Chen, X. D., T. M. Grzegorczyk, B.-I. Wu, J. Pacheco, Jr., and J. A. Kong, "Robust method to retrieve the constitutive effective parameters of metamaterials," *Phys. Rev. E*, Vol. 70, 016608, 2004.
21. Smith, D. R., D. C. Vier, T. Koschny, and C. M. Soukoulis, "Electromagnetic parameter retrieval from inhomogeneous metamaterials," *Phys. Rev. E*, Vol. 71, 036617, 2005.

Application of Optimization Algorithm to Designing Absorber Composed of RHM and LHM

Dan Lv[1, 2], **C. M. Tong**[1, 2], **and Y. Geng**[3]

[1]25 Letter Box, China
[2]State Key Lab. of Millimeter Waves, China
[3]Satellite Control Center, China

Abstract— When electromagnetic wave is propagating in LHM, electric field, magnetic field and wave vector conform to the left-hand screw rule. In this paper, the reflection characteristics of an absorber composed of RHM and LHM are analyzed by transmission line model. A hybrid algorithm based on improved PSO and SA algorithm is derived to optimize the parameters of the absorber. With the optimal permittivity, permeability and thickness of LHM and optimal thickness of RHM, the minimum reflectivity will be attained. Then the reflectivity is also computed when one parameter is changeable and the other parameters are unchangeable.

1. INTRODUCTION

There are two very important parameters for describing the materials properties: permittivity and permeability. In nature, the permittivity, permeability and refractive index of materials are mostly positive. When plane wave is propagating in these materials, electric field, magnetic field and wave vector are conformed to right-hand screw rule. So they are named for "right-handed materials (RHM)". If the permittivity and permeability are both negative, the refractive index will be negative. Additionally the electric field, magnetic field and wave vector will be conformed to left-hand screw rule. Although, the materials with negative permittivity and negative permeability have not been found in nature, they were produced in 2001 for the first time [1]. Then they are named for "left-handed materials (LHM)".

LHM are used to design ultrathin resonant cavity, energy beam splitter, flat lens with ultrahigh resolution, leaky wave antenna [2] and so on. In the field of military, aircraft or other targets can be coated with LHM and the reflected wave will not be received from the front direction.

In this paper, reflectivity of an absorber composed of RHM and LHM is analyzed by transmission line model. A hybrid algorithm based on Particle Swarm Optimization (PSO) and simulated annealing (SA) algorithm is derived. Then parameters of absorber are optimized by the optimization algorithm.

2. REFLECTIVITY OF LHM

Relative permittivity and relative permeability of lossy LHM can be expressed as $\varepsilon_r = \varepsilon_r' - j\varepsilon_r''$ and $\mu_r = \mu_r' - j\mu_r''$. Both LHM and RHM are of positive ε_r'' and μ_r''. ε_r' and μ_r' of RHM are positive, however they are negative in LHM.

The wave number $k = k' - jk''$ is given by [3]

$$\begin{aligned} k' &= \frac{-\omega\sqrt{\varepsilon_r'\mu_r'}}{c}\sqrt{0.5\left[1-\tan\delta_e\tan\delta_m+\sqrt{(1+\tan\delta_e^2)(1+\tan\delta_m^2)}\right]}, \\ k'' &= \frac{\omega\sqrt{\varepsilon_r'\mu_r'}}{c}\sqrt{0.5\left[\tan\delta_e\tan\delta_m-1+\sqrt{(1+\tan\delta_e^2)(1+\tan\delta_m^2)}\right]} \end{aligned} \tag{1}$$

where $\tan\delta_e = \varepsilon_r''/\varepsilon_r'$, $\tan\delta_m = \mu_r''/\mu_r'$.

The impedance $Z = Z' - jZ''$ is given by

$$\begin{aligned} Z' &= \sqrt{\frac{\mu_0\mu_r'}{\varepsilon_0\varepsilon_r'}}\frac{1}{\sqrt{1+\tan\delta_e^2}}\sqrt{0.5\left[1+\tan\delta_e\tan\delta_m+\sqrt{(1+\tan\delta_e^2)(1+\tan\delta_m^2)}\right]}, \\ Z'' &= \sqrt{\frac{\mu_0\mu_r'}{\varepsilon_0\varepsilon_r'}}\frac{1}{\sqrt{1+\tan\delta_e^2}}\sqrt{0.5\left[-1-\tan\delta_e\tan\delta_m+\sqrt{(1+\tan\delta_e^2)(1+\tan\delta_m^2)}\right]} \end{aligned} \tag{2}$$

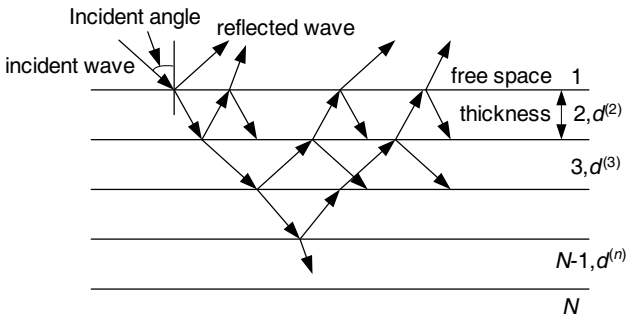

Figure 1: Multilayered coating backed by a perfectly conducting panel.

Figure 1 depicts the multilayered coating backed by a perfectly conducting panel. The total number of layers is N. $\varepsilon_r^{(n)}$ and $\mu_r^{(n)}$ are the relative permittivity and permeability of nth layer. $d^{(n)}$ and $\alpha^{(n)}$ are the thickness and incident angle of nth layer. ε_0 and μ_0 are permittivity and permeability of free space.

When plane wave is propagating in the multilayered coating, the reflection would be analyzed by transmission line model. Parallel and perpendicular polarization reflection coefficients $R_{||}$ and $R_\perp$ are given by [4]

$$R_{||} = \frac{Z^{(1)}\cos\alpha^{(1)} - Z_{i||}^{(2)}\cos\alpha^{(2)}}{Z^{(1)}\cos\alpha^{(1)} + Z_{i||}^{(2)}\cos\alpha^{(2)}}, \quad R_\perp = \frac{Z_{i\perp}^{(2)}\cos\alpha^{(1)} - Z^{(1)}\cos\alpha^{(2)}}{Z_{i\perp}^{(2)}\cos\alpha^{(1)} + Z^{(1)}\cos\alpha^{(2)}} \tag{3}$$

where $Z_{i||}^{(n)}$ and $Z_{i\perp}^{(n)}$ stand for the parallel and perpendicular polarization input impedance of nth layer, given by

$$\begin{aligned} Z_{i||}^{(n)} &= \frac{Z_{i||}^{(n+1)}\cos\alpha^{(n+1)} - jZ^{(n)}\cos\alpha^{(n)}\tan\left(c^{(n)}d^{(n)}\right)}{Z^{(n)}\cos\alpha^{(n)} - jZ_{i||}^{(n+1)}\cos\alpha^{(n+1)}\tan\left(c^{(n)}d^{(n)}\right)}Z^{(n)}, \\ Z_{i\perp}^{(n)} &= \frac{Z_{i\perp}^{(n+1)}\cos\alpha^{(n)} - jZ^{(n)}\cos\alpha^{(n+1)}\tan\left(c^{(n)}d^{(n)}\right)}{Z^{(n)}\cos\alpha^{(n+1)} - jZ_{i\perp}^{(n+1)}\cos\alpha^{(n)}\tan\left(c^{(n)}d^{(n)}\right)}Z^{(n)} \end{aligned} \tag{4}$$

where $Z^{(N)}$ and $k^{(n)}$ stand for the impedance and wave number of nth layer, $c^{(n)} = k^{(n)}\cos\alpha^{(n)}$. Especially, if n is equal to N, $Z^{(N)} = Z_{i||}^{(N)} = Z_{i\perp}^{(N)}$.

It shall be marked that the results of $Z^{(N)}$, $k^{(n)}$ and $\cos\alpha^{(n)}$ in LHM is different from the results in RHM.

The reflectivity id defined as

$$r = 20\lg\left(|R|\right) \tag{5}$$

3. INTELLIGENT ALGORITHM

3.1. PSO

PSO has been applied to optimization design broadly since it was presented in 1995 [5–7]. In this paper, an improved PSO is derived from the standard algorithm. The main procedure is given by

1) A population of particles with random positions and velocities is initialized by chaos algorithm in the N dimensional space. $\vec{x}_i = (x_1^i, x_2^i, \ldots x_N^i)$ and $\vec{v}_i = (v_1^i, v_2^i, \ldots v_N^i)$ stand for the position and velocity of ith particle, respectively. The population of particles is equal to M, and the current iterative degree k is equal to zero. A chaotic variable is ergodic, stochastic and regular [8]. If the positions are initialized by chaos algorithm, the initialization of PSO will still keep random and the diversity of population will be enhanced. Because there are more initial particles, a better population of particles can be chosen to enhance the convergence velocity. Logistic equation is a typical chaotic system, given by

$$z_{n+1} = \mu z_n(1 - z_n) \qquad n = 0, 1, \ldots \tag{6}$$

where μ is the control parameter. A deterministic time series will be derived from a random initial value, and then the chaotic series is transformed into position $\vec{x}$. The fitness value of every chaotic variable is computed. Through comparison, M variables whose fitness values are better are substituted for the initial positions of M particles.

2) Fitness value of each particle is computed. $\vec{p}_i$ stands for the best previous position of ith particle, and $\vec{p}_G$ stands for the best position of a population. $\vec{p}_i$ is set to the position and the index of ith original particle, and $\vec{p}_G$ is set to the position and the index of the best previous position whose fitness value is best.
3) If criterion is met, the result will be shown. Otherwise the next step will be executed.
4) The positions and velocities will be changed by the following equations

$$\begin{aligned} \vec{v}_i(k+1) &= \omega\vec{v}_i(k) + c_1r_1[\vec{p}_i - \vec{x}_i(k)] + c_2r_2[\vec{p}_G - \vec{x}_i(k)], \\ \vec{x}_i(k+1) &= \vec{x}_i(k) + \vec{v}_i(k+1) \qquad i = 1, 2, \ldots M \end{aligned} \tag{7}$$

where c_1 and c_2 are two learning parameters which are positive constants. ω stands for the inertia weight. r_1 and r_2 are hypodispersion random numbers in the range $[0, 1]$.

The fitness value of each particle with new position is recomputed. Additionally, it is compared with the previous fitness value of $\vec{p}_i$. If the new fitness value is better than the previous fitness value, $\vec{p}_i$ will be set to the new position, and the fitness value of $\vec{p}_i$ will be recomputed. Then fitness value of $\vec{p}_i$ (i =1, 2, ..., M) is compared with the fitness value of $\vec{p}_G$. If the fitness value of $\vec{p}_i$ is better than fitness value of $\vec{p}_G$, $\vec{p}_G$ will be set to the position and the index of $\vec{p}_i$.

5) The positions and velocities of all particles are re-initialized if the period $Ie = k/n$ is met, where n is a positive integer. The fitness values of all particles are computed. Half of the particles whose fitness values are better are saved, and the others are re-initialized. But $\vec{p}_i$ and $\vec{p}_G$ keep unchangeable.
6) If criterion is met, the result will be shown. Otherwise all the best previous positions are mutated except the $\vec{p}_i$ whose index is equal to the index of $\vec{p}_G$.
7) Iterative degree k will become $k + 1$, and the fourth step will be executed.

3.2. SA

SA simulates the physical annealing process. By adjusting the control parameter, the optimum will be found in the given range at less cost of calculation [9, 10]. A worse state may be accepted when SA is applied to optimization. The main procedure of SA algorithm is given by

1) An original state is initialized. The original temperature and final temperature are T_0 and T_f, respectively. The outer iterative degree k is equal to zero, and the current temperature T_k is equal to T_0.
2) A new state is presented in the neighborhood range. Then the fitness value of current state f and fitness value of new state f' are computed. The inner iterative degree l is equal to zero.
3) If f' is better than f, current state will be set to the new state. But if f' is worse than f, a hypodispersion random number ξ will be initialized. If ξ is less than a definite value $\exp(-(f' - f)/T_k)$, current state will still be set to the new state.
4) If inner criterion is met, the fifth step will be executed. Otherwise inner iterative degree l will become $l + 1$ and the second step will be executed.
5) If outer criterion is met, the result will be shown. Otherwise the current temperature will be decreased. Additionally, the outer iterative degree k will become $k + 1$ and the second step will be executed.

4. RESULTS

A perfectly conducting panel is coated with two kinds of materials. The first material is RHM, and the second one is LHM. The relative permittivity and permeability of RHM are $\varepsilon_{r1} = 22.6 - j2.9$ and $\mu_{r1} = 1.69 - j1.18$. The relative permittivity and permeability of lossless LHM will be optimized in the range $\varepsilon_{r2} \in (-25, -1)$ and $\mu_{r2} \in (-5, -1)$. In addition, the thickness of RHM will be optimized in the range $d_1 \in (0.5, 1.5)$ mm, and the thickness of LHM will be optimized in the range $d_2 \in (2.5, 3.5)$ mm.

The design goal is to determine the permittivity, permeability and thickness of coating which exhibits a low reflection in the frequency band $f \in (8, 12)$ GHz with 90 degree incident angle. The objective function F which attains a maximum for the optimal coating is given by

$$F = \min_i \{1 - \left|R_{||/\perp}(f_i)\right|\} \tag{8}$$

After optimization, the parameters are obtained. $\varepsilon_{r2} = -25$, $\mu_{r2} = -1.04391$, $d_1 = 0.854893$, $d_2 = 2.57048$.

Figure 2 depicts the reflectivity with changeable relative permittivity of LHM. Fig. 3 depicts the reflectivity with changeable relative permeability of LHM. Fig. 4 depicts the reflectivity with changeable thickness of RHM. Fig. 5 depicts the reflectivity with changeable thickness of LHM.

Results in Fig. 2 show that as relative permittivity of LHM is increased, the reflectivity minimum is increased and the location of minimum moves to high frequency section at the early stage. But it is reduced at a later stage. In addition, the location of minimum becomes clear at the early stage. The results also show that with the optimal parameters the reflectivity is mostly less than -10 dB in the frequency band. When the frequency is equal to 9.13 GHz, the reflectivity would reach the maximum. Results in Fig. 3 show that as relative permeability of LHM is increased, the reflectivity minimum is increased and the location of minimum moves to high frequency section at the early stage. With a deterministic permeability the location of minimum begins to move to low frequency section. Then reflectivity minimum is reduced and the location of minimum still moves to high frequency section at a later stage. In addition, the location of minimum becomes unclear at the middle stage. Results in Fig. 4 show that as thickness of RHM is increased, the reflectivity minimum is reduced at the early stage, but it is increased at a later stage. The location of minimum mostly keeps unchangeable. In addition, the location of minimum becomes clear at the middle stage. Results in Fig. 5 show that as thickness of LHM is increased, the reflectivity minimum is reduced at the early stage but it is increased at a later stage. The location of minimum always moves to low frequency section. In addition, the location of minimum becomes clear at the early stage.

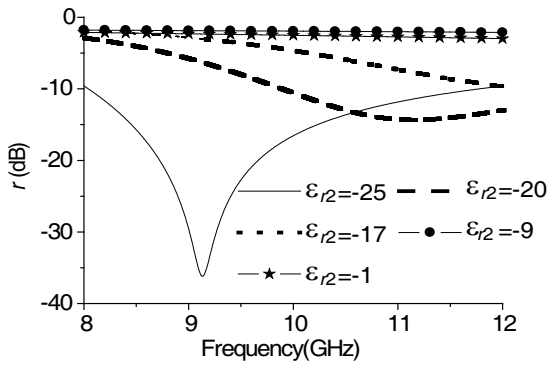

Figure 2: Reflectivity with changeable permittivity of LHM.

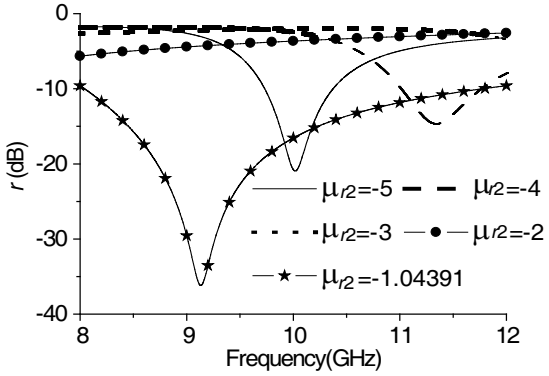

Figure 3: Reflectivity with changeable permeability of LHM.

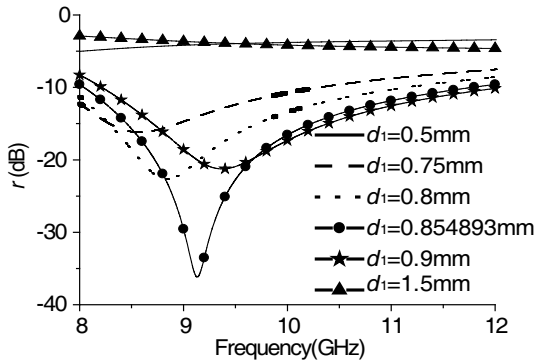

Figure 4: Reflectivity with changeable thickness of RHM.

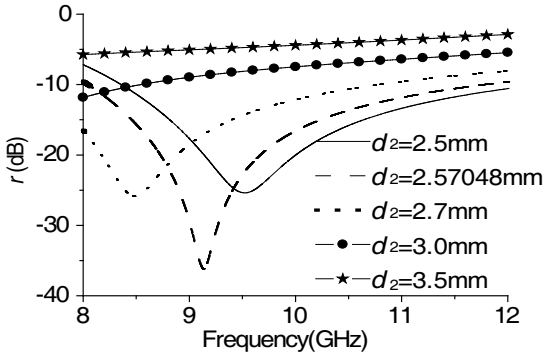

Figure 5: Reflectivity with changeable thickness of LHM.

5. CONCLUSIONS

LHM has been applied to designing coating broadly. Targets can be coated with LHM only, and the coating also can be composed of LHM and other materials. In this paper, a panel coated with RHM and LHM is presented, and some parameters are optimized by hybrid algorithm based on PSO and SA. Depending on the optimal parameters, minimum reflection in the frequency band is obtained. Additionally, when one parameter is changeable but the others keep unchangeable, there are some different characteristics.

REFERENCES

1. Smith, D. R., W. Padilla, and D. C. Vier, "Composite medium with simultaneously negative permeability and permittivity," *Physics Review Letters*, Vol. 84, No. 18, 4184–4187, 2000.
2. Engheta, N., "An idea for thin, subwavelength cavity resonators using metamaterials with negative permittivity and permeability," *IEEE Antennas and Wireless Propagation Letter*, Vol. 1, No. 1, 10–13, 2002.
3. Wang, X. X., "Research on absorbing properties of wave-absorbers with LHM and RHM structures," Harbin Engineering University, Harbin, China, 2006.
4. Dieter, K., P. Jürgen, and V. Stein, "Special problems in applying the physical optics method for backscatter computations of complicated objects," *IEEE Transaction on Antennas and Propagation*, Vol. 36, No. 2, 228–237, 1998.
5. Kennedy, J. and R. Eberhart, "Particle swarm optimization," *IEEE Int. Conf. Neural Network*, Vol. 4, 1942–1948, 1995.
6. Shi, Y. and R. Eberhart, "Empirical study of particle swarm optimization," *IEEE Proc. Cong. Evol. Comput.*, Vol. 3, 1945–1950, 1999.
7. Eberhart, R. and Y. Shi, "Particle swarm optimization: Developments, applications, and resources," *IEEE Proc. Cong. Evol. Comput.*, Vol. 1, 81–86, 2001.
8. Tang, X. L., "The theory and application of particle swarm optimization algorithm based on chaos," Chongqing University, Chongqing, China, 2007.
9. Wang, D. W., J. W. Wang, and H. F. Wang, *Intelligent Optimization Methods*, Beijing, 2007.
10. Kou, X. L. and S. Y. Liu, "Particle swarm algorithm based on simulated annealing to solve constrained optimization," *Journal of Jilin University (Engineering and Technology Edition)*, Vol. 37, No. 1, 136–140, 2007.

The Transmission Properties of Electromagnetic Wave in Three-dimensional Plasma Photonic Crystals

J.-W. Xu and J.-M. Shi
State Key Laboratory of Pulsed Power Laser Technology
Key Laboratory of Infrared and Low Temperature Plasma of Anhui Province
Electronic Engineering Institute, Hefei 230037, China

Abstract— The transmission properties of electromagnetic wave in three-dimensional plasma photonic crystals (PPCs) were studied by the Finite Difference Time Domain (FDTD) method in this paper. The results were presented that the plasma frequency, plasma collision frequency, layer number, and ratio of radius to crystal lattice constant can influence the transmissivity in the face-centered cubic (fcc) and face-centered tetragonal (fct) lattice woodpile structure PPCs.

1. INTRODUCTION

Photonic crystals are novel, artificially created materials, in which refractive index is periodically modulated in a scale compared to the wavelength of operation [1, 2]. Similarly, the plasma photonic crystals (PPCs) are defined as a periodic arrangement of plasma column and other dielectric materials, including vacuum, which were first proposed by H. Hojo et al. [3]. Plasma has the complex frequency dependent permittivity and it is the frequency dispersive medium. Due to the unique characters of plasma, there are many special electromagnetic properties with PPCs. The studies on the electromagnetic wave propagating properties in one and two dimensional PPCs were carried out in recent years [4–7]. With the convenience of controlling the plasma parameter, the PPCs can be used in many potential fields. So the study of the PPCs is of a practical significance. Nowadays, there is little literatures studied on the three-dimensional PPCs, and the different structures of the three-dimensional PPCs may cause different electromagnetic properties compared with the one- and two-dimensional PPCs. In this paper, the electromagnetic properties of three-dimensional PPCs are studied by the Finite Difference Time Domain (FDTD) method.

2. NUMERICAL METHOD

2.1. The Finite Difference Time Domain (FDTD) Method

The time-dependent Maxwell's curl equations in free space are

$$\frac{\partial \vec{D}}{\partial t} = \nabla \times \vec{H} \tag{1}$$

$$\vec{D}(\omega) = \varepsilon_0 \cdot \varepsilon_r(\omega) \cdot \vec{E}(\omega) \tag{2}$$

$$\frac{\partial \vec{H}}{\partial t} = -\frac{1}{\mu_0} \nabla \times \vec{E} \tag{3}$$

ε_0 is the permittivity of vacuum. $\varepsilon_r(\omega)$ is the relative permittivity of the dispersive media.

The FDTD method is a full-wave, dynamic, and powerful solution tool for solving Maxwell's equations, introduced by K. S. Yee in 1966. The algorithm involves direct discretization of Maxwell's equations by writing the spatial and time derivatives in a central finite difference form [8]. In this paper, the electromagnetic properties of three-dimensional PPCs are studied by the FDTD method. In Figure 1, the schematic diagram is given to show the calculation method. The plane wave irradiates the PPCs, and the output wave is recorded at the recording area. By the Fourier transformation, the amplitude of the incident and output wave can be calculated in the frequency domain. And then the transmissivity can be got from the results of the amplitude of the incident and output wave.

In the study on the electromagnetic properties of dispersive media such as plasma, it is convenient to calculate $\vec{D}$ instead of $\vec{E}$. And the expression (2) can be used to calculate $\vec{E}$ from $\vec{D}$ [9].

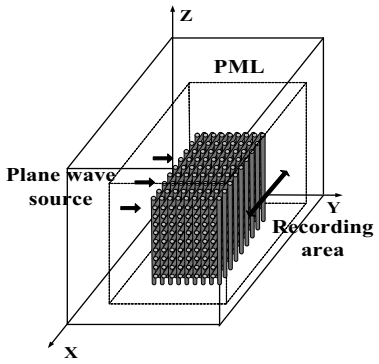

Figure 1: The schematic diagram of calculation model.

The relative permittivity of the unmagnetized plasma is

$$\begin{aligned}\varepsilon_r &= 1 + \frac{\omega_p^2}{\omega(jv_c - \omega)} \\ &= 1 + \frac{\omega_p^2/v_c}{j\omega} - \frac{\omega_p^2/v_c}{v_c + j\omega}\end{aligned} \tag{4}$$

where plasma angular frequency can be written as $\omega_p = 2\pi f_p$, f_p is the plasma frequency, v_c is the plasma collision frequency. The Z transformation of expression (4) can be written as

$$\varepsilon(z) = \frac{1}{\Delta t} + \frac{\omega_p^2/v_c}{1 - z^{-1}} - \frac{\omega_p^2/v_c}{(1 - e^{-v_c \cdot \Delta t})z^{-1}} \tag{5}$$

Then we can get

$$\vec{D}(z) = \varepsilon_0 \cdot \varepsilon(z) \cdot \vec{E}(z) \cdot \Delta t \tag{6}$$

The following expression can be got from expression (5) and (6)

$$\vec{D}(z) = \varepsilon_0 \vec{E}(z) \left\{ 1 + \frac{\omega_p \Delta t}{v_c} \left[\frac{1}{1 - z^{-1}} - \frac{1}{(1 - e^{-v_c \cdot \Delta t})\, z^{-1}} \right] \right\}. \tag{7}$$

Letting

$$\vec{S}(z) = \frac{\omega_p \Delta t}{v_c} \left[\frac{1}{1 - z^{-1}} - \frac{1}{(1 + e^{-v_c \cdot \Delta t}) z^{-1}} \right] \vec{E}(z) = \frac{\omega_p \Delta t}{v_c} \left[\frac{1 - e^{-v_c \cdot \Delta t}}{1 - (1 + e^{-v_c \cdot \Delta t}) z^{-1} + e^{-v_c \cdot \Delta t} z^{-2}} \right] \vec{E}(z), \tag{8}$$

gives

$$\vec{E}(z) = \frac{1}{\varepsilon_0} \vec{D}(z) - z^{-1} \vec{S}(z), \tag{9}$$

where $S(z)$ satisfies the following equation,

$$\vec{S}(z) = (1 + e^{-v_c \cdot \Delta t}) z^{-1} \vec{S}(z) - e^{-v_c \cdot \Delta t} z^{-2} \vec{S}(z) + \frac{\omega_p \Delta t}{v_c} (1 - e^{-v_c \cdot \Delta t}) \vec{E}(z). \tag{10}$$

Before the numerical simulation of the three-dimensional PPCs, the calculation program was proved accurate with the data in literature [10].

In this paper, the calculation parameters of plasma frequency are 10 GHz, plasma collision frequency is 5 GHz, layer number is 9, and the ratio of radius to crystal constant is 0.375.

2.2. The Calculation Model

In this calculation, the Gaussian pulse source is used as the incident wave,

$$E_i = \exp\left[-\frac{4\pi (t - t_0)^2}{\tau^2} \right] \tag{11}$$

where $t_0 = 16\,\text{ps}$, $\tau = 20\,\text{ps}$. The cell size of the FDTD method is 1 mm. According to the Courant condition, the time step Δt is 2 ps. The computational domain is subdivided into $88 \times 88 \times 88$ cells. Seven cells PML (Perfectly Matched Layers) absorbing boundaries are used at the terminations of the space. The other cells are free space. The total calculation time is 10000 time steps.

The two types of three-dimensional PPCs are calculated, which are face-centered cubic (fcc) and face-centered tetragonal (fct) lattice woodpile structure. In this paper, the transmissivity of electromagnetic wave in three-dimensional PPCs are studied by adjusting the plasma parameters and the crystal structures.

3. RESULTS AND DISCUSSION

3.1. Effect of Plasma Frequency

In this section, we changed the plasma frequency f_p from 10 to 16 GHz. In Figure 2, the relationship between electromagnetic wave frequency and transmissivity in fcc and fct lattice woodpile structure PPCs are shown respectively. It can be found easily that the higher plasma frequency causes the larger electromagnetic wave attenuation frequency band, and in the lower frequency band (frequency lower than 8 GHz) the transmissivity curves are almost the same. It could be explained by the plasma character of high pass filter.

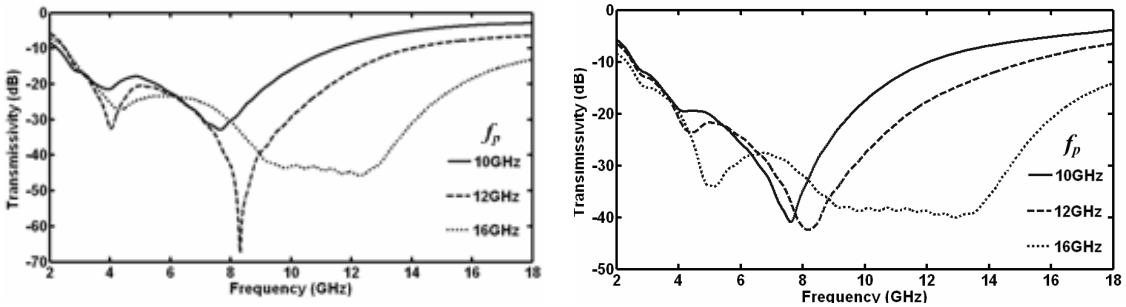

Figure 2: The transmissivity versus frequency in (a) fcc and (b) fct lattice woodpile structure PPCs with the changing of plasma frequency.

3.2. Effect of Plasma Collision Frequency

In Section 3.2, the plasma collision frequency is changed from 1 to 5 GHz. When the electromagnetic wave frequency f is lower than the plasma frequency f_p which is 10 GHz, the influence of the plasma collision frequency on the transmissivity is not obvious as shown in Figure 3. But the collision absorbent of the electromagnetic wave with the frequency larger than the plasma frequency may not be ignored, and the transmissivity decreases with the plasma frequency changing from 1 to 5 GHz.

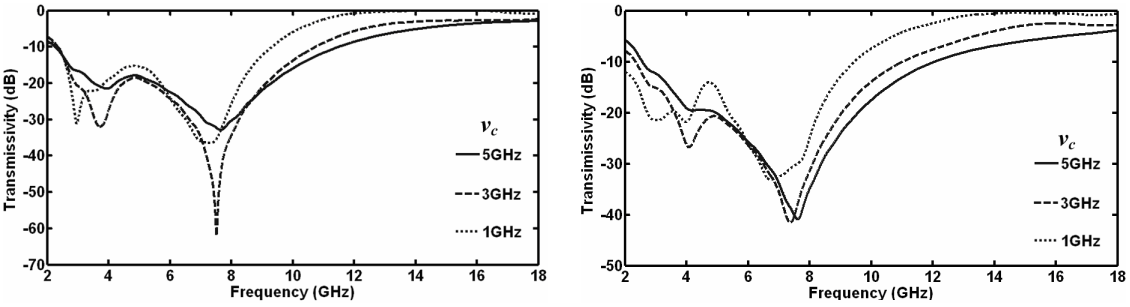

Figure 3: The transmissivity versus frequency in (a) fcc and (b) fct lattice woodpile structure PPCs with the changing of plasma collision frequency.

3.3. Effect of Layer Number

In Section 3.3, the layer number is changed from 3 to 9. It's obvious that the transmissivity increases when the layer number of PPCs decreases. But in Figure 4 we can also find that the electromagnetic frequency of the minimum transmissivity value becomes lower when the layer number decreases.

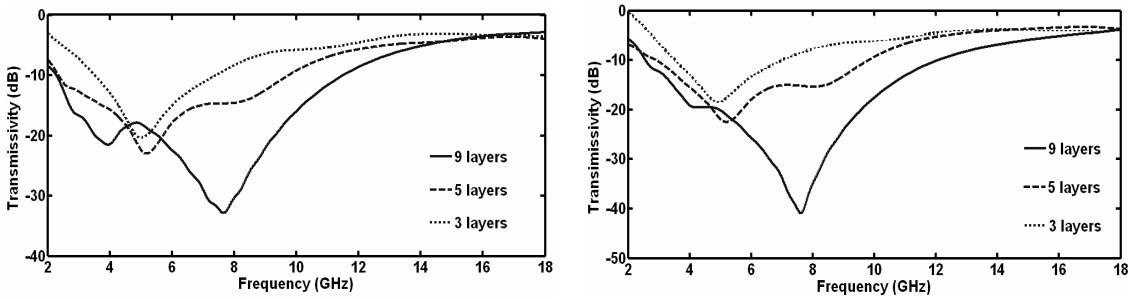

(a) (b)

Figure 4: The transmissivity versus frequency in (a) fcc and (b) fct lattice woodpile structure PPCs with the changing of layer number.

3.4. Effect of Ratio of Radius to Crystal Lattice Constant

In this section, the ratio of radius to crystal lattice constant (r/a) is changed from 0.125 to 0.375, as shown in Figure 5. When the value of r/a decreases, the plasma column is thinner and the influence of the plasma on the electromagnetic wave becomes weaker. The electromagnetic wave can transmit in the PPCs more easily. The frequency of the minimum transmissivity value becomes lower when the value of r/a decreases.

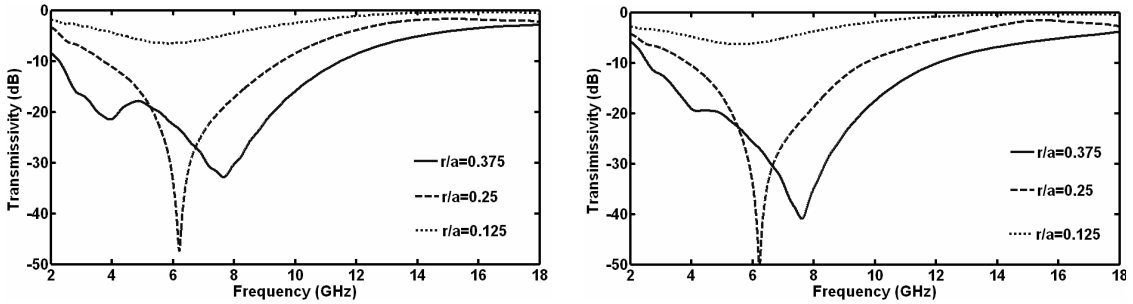

(a) (b)

Figure 5: The transmissivity versus frequency in (a) fcc and (b) fct lattice woodpile structure PPCs with the changing of ratio of radius to crystal lattice constant.

The Figures 2–5 show the influence of plasma frequency, plasma collision frequency, layer number , ratio of radius to crystal lattice constant on the transmissivity in both the fcc and fct lattice woodpile structure PPCs. As shown in corresponding figures, there's almost no significant difference between the electromagnetic properties in fcc and fct lattice woodpile structure PPCs. The frequency of the minimum transmissivity, the frequency range of the transmissivity attenuation, the shape of the curve are nearly the same in both fcc and fct lattice woodpile structure PPCs.

4. CONCLUSIONS

In this paper, the FDTD method, which is fit for modeling the isotropic dispersive unmagnetized plasma, is applied to simulate the three-dimensional PPCs. It can be concluded that the transmissivity of the electromagnetic wave in the PPCs can be influenced by the plasma frequency, the plasma collision frequency, the layer number, and the ratio of radius to crystal lattice constant. The plasma frequency can affect the frequency band of the transmissivity attenuation. And the magnitude of transmissivity attenuation can be influenced by the plasma collision frequency, the layer number, and the ratio of radius to crystal lattice constant. With the results of this paper, it might be feasible to utilize plasma photonic crystals in electromagnetic wave control in the future.

REFERENCES

1. Yablonovich, E., "Inhibited spontaneous emission in solid state physics and electronics," *Phys. Rev. Lett.*, Vol. 58, No. 20, 2059–2062, 1987.
2. John, S., "Strong localization of photons in certain disordered dielectric super lattice," *Phys. Rev. Lett.*, Vol. 58, No. 23, 2486–2489, 1987.
3. Hojo, H., "Dispersion relation of electromagnetic waves in one-dimensional plasma photonic crystals," *J. Plasma Fusion Res.*, Vol. 80, No. 2, 89–90, 2004.
4. Osamu, S., "Properties of electromagnetic wave propagation emerging in 2-D periodic plasma structures," *IEEE Trans. Plasma Science*, Vol. 35, No. 5, 1267–1273, 2007.
5. Osamu, S., "Characteristics of metamaterials composed of microplasma arrays," *Plasma Phys. Control. Fusion*, No. 49, 453–463, 2007.
6. Osamu, S., "Photonic bands in two-dimensional micro plasma arrays. I. Theoretical derivation of band structures of electromagnetic waves," *J. Appl. Phys.*, No. 101, 073304-1–9, 2007.
7. Osamu, S., "Photonic bands in two-dimensional micro plasma arrays. II. Theoretical derivation of band structures of electromagnetic waves," *J. Appl. Phys.*, No. 101, 073305-1–7, 2007.
8. Yee, K. S., "Numerical solution of initial boundary value problems involving Maxwell's equations in isotropic media," *IEEE Trans. Antennas Propaga.*. Vol. 14, No. 3, 1966.
9. Sullivan, D. M., "Electromagnetic simulation using the FDTD method," *IEEE Press Series on RF and Microwave Technology*, New York, 2000.
10. Liu, S. B., C. X. Zhu, and N. C. Yuan, "FDTD simulation for plasma photonic crystals," *Acta Physica Sinica*, Vol. 54, No. 6, 2804–2807, 2005.

The Non-constancy of Speed of Light in Vacuum for Different Galilean Reference Systems (Revisited)

Namik Yener
Technical Education Faculty, Umuttepe Campus, Kocaeli University
Izmit 41380, Kocaeli, Turkey

Abstract— It was established by the author in a previous article that the postulate of the constancy of speed of light of Special Relativity Theory is false for an electromagnetic system that consisted of a rest frame (denoted by K) constituted by a simple medium with loss (medium (I)), and a frame (denoted by K') in uniform rectilinear motion with respect to the first, wherein a perfectly conducting medium (medium (II)) fills the half space such that the interface of the two media is an infinite plane, perpendicular to the direction of motion of K'. In that system a plane wave was assumed to impinge on the boundary of the two media. In this paper we consider the same electromagnetic system but we add a point charge in uniform motion parallel to one of the rectangular axes perpendicular to the direction of motion of K'. Now it is this charge that is the source for the fields. However we find that the relationship that was found in the above mentioned article and that was the basis for arguing the falsity of the Special Relativity Theory does not change in the present system as well. The said relationship is an algebraic relationship between the relative speed of K' with respect to K, frequency measured from K', the constitutive parameters of medium (I) and the speed of light c in vacuum for reference system K. It is also remarked that, the falsity of Special Relativity Theory rises not only because of dependence of c on the frequency in this algebraic relationship, but also because of its dependence on the relative speed of K' with respect to K, which implies dependence of c on the reference systems.

1. INTRODUCTION

Consider two Galilean reference frames K and K', of which K' is in uniform rectilinear motion with speed v_1 with respect to K.

The three assumptions of Special Relativity Theory are [1]

i) The principle of relativity (i.e., that laws of physics are the same in all Galilean reference systems, there exists no preferred Galilean system),
ii) Assumption of homogeneity of space-time (to infer linearity of transform equations),
iii) Assumption of isotropy of space (to infer reciprocity also using the principle of relativity).

The author has established in [2] that the principle of constancy of speed of light in vacuum [3–6] that is a consequence of the above three assumptions, is false in the general case, by considering an electromagnetic system, wherein the above inertial frame K is attached to a medium which is simple but lossy, whereas inertial frame K' is attached to a medium which is a perfect electric conductor filling the half space, such that the interface of the two media is an infinite plane perpendicular to the velocity of K' with respect to K.

As a reminder, the arguments that have been used in [2] to conclude falsity of the principle of constancy of speed of light in vacuum are that ω' is a free variable in Equation (40) of [2] and if $c = c'$ is taken, the infinite number of values attained by the frequency ω', can not be satisfied in Equation (40), because all other parameters in (40) are constants. Therefore $c \neq c'$ must hold. However it must be remarked that the reason for assuming $c \neq c'$, is not only the infinite number of values attained by ω', but also the dependence of c on α hence on the speed of reference frame K' with respect to K. It should be noted that even if the 'modified Lorentz transformation' was not constructed in [2] and hence $c \neq c'$ was not utilized, Equation (40) of [2] would still stand as a contradiction of Special Relativity Theory with Maxwell's equations.

The objective of this paper is to show that Equation (40) of [2], on which the argument to negate the Special Relativity Theory is based, is the same for an electromagnetic system such as the one described above, but in which additionally there is a point charge in medium (I), in uniform motion parallel to one of the axes perpendicular to the direction of motion of K' with respect to K.

The presence of a planar surface (our boundary between medium (I) and medium (II)) near a cylindrical wave radiator (the point charge in our case) breaks the cylindrical symmetry and an approach based on cylindrical waves (CWs) seems less natural. However the problem can be

addressed efficiently, if use is made of the Fourier spectrum of the CWs [7]. This method has been used for the solution of the two dimensional scattering problem by a set of perfectly conducting parallel objects, with arbitrary size, buried in a dielectric lossless half space [8]. It has also been used to solve the scattering problem from a dielectric cylinder buried beneath a slightly rough surface [9].

The problem of radiation from a uniformly moving charge in an anisotropic plasma has been treated [10]. In this paper we follow the same steps except that our medium is a simple, lossy medium. So we have modified the analysis in [10] accordingly. After thus having reduced the problem to one of a two dimensional cylindrical wave, we decompose the cylindrical wave into plane waves. This problem has also been treated for simple, lossy media [7]. Next we utilize the phase invariance principle [5, 11, 12], and continuity of the tangential component of the electrical field on the boundary of the two media to arrive at the desired result. For conciseness we do not repeat here the transformation formulas derived in [2], between the coordinates (t, x, y, z) and (t', x', y', z') of a point as observed from K and K' respectively and which formulas incorporate two different speeds of light c and c' in vacuum for K and K'. For these formulas we have used the term 'modified Lorentz transformation' in [2]. These formulas can also be found in [6].

2. SOLUTION OF MAXWELL'S EQUATIONS IN TERMS OF CYLINDRICAL WAVES

Following the steps in [10], let

$$q = q_0 \frac{\delta(y - ut)\delta(\rho)}{2\pi\rho} \tag{1}$$

represent a point charge q_0 moving with arbitrary uniform speed u along the Oy axis in a cylindrical coordinate system which is formed by (ρ, ϕ, y) as indicated in Figure 1 [10]. The current density arising from this uniformly moving charge is

$$\vec{J}(\vec{r}, t) = q_0 u \frac{\delta(y - ut)\delta(\rho)}{2\pi\rho} \vec{e}_y, \tag{2}$$

where $\vec{r}$ represents the position vector of a point in (ρ, ϕ, y) space, and $\vec{e}_y$ is the unit vector along Oy axis.

Let $\vec{E}(\vec{r}, t)$ and $\vec{H}(\vec{r}, t)$, be respectively, the electric and magnetic field vectors. We shall also need the Fourier and inverse Fourier transforms defined by

$$f(\vec{r}, \omega) = \int_{-\infty}^{\infty} f(\vec{r}, t) e^{j\omega t} dt \tag{3}$$

$$f(\vec{r}, t) = \int_{-\infty}^{\infty} f(\vec{r}, \omega) e^{-j\omega t} d\omega \tag{4}$$

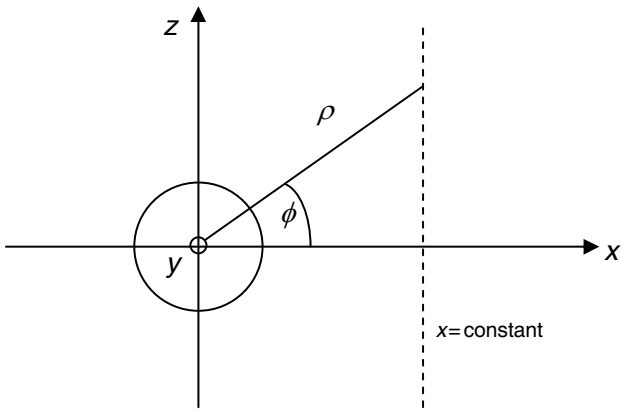

Figure 1: Coordinate system used for the electromagnetic system of paper.

The Fourier transform of the source expression (2) is

$$J_y(\vec{r},\,\omega) = q_0 u \frac{\delta(\rho)}{2\pi\rho} e^{j\omega y/u}. \tag{5}$$

The electric and magnetic fields $\vec{E}(\vec{r},\,\omega)$ and $\vec{H}(\vec{r},\,\omega)$ satisfy the following two Maxwell's equations in the frequency domain.

$$\nabla \times \vec{E}(\vec{r},\,\omega) = j\omega\mu_1 \vec{H}(\vec{r},\,\omega) \tag{6}$$

$$\nabla \times \vec{H}(\vec{r},\,\omega) = -j\omega\varepsilon_1 \vec{E}(\vec{r},\,\omega) + J_y(\vec{r},\,\omega)\vec{e}_y + \sigma_1 \vec{E}(\vec{r},\,\omega). \tag{7}$$

Here σ_1, ε_1, μ_1 are the conductivity, dielectric permittivity, and magnetic permeability coefficients of medium (I) measured from K.

It can easily be seen that the fields are independent of the ϕ coordinate, and they depend on y only through the factor of $e^{j\omega y/u}$. Hence one can write

$$\vec{E}(\vec{r},\,\omega) = \vec{E}(\rho,\,\omega)e^{j\omega y/u} \tag{8a}$$

$$\vec{H}(\vec{r},\,\omega) = \vec{H}(\rho,\,\omega)e^{j\omega y/u} \tag{8b}$$

$$J_y(\vec{r},\,\omega) = J_y(\rho,\,\omega)e^{j\omega y/u} \tag{8c}$$

Substitution of (8) in (6) and (7) yields

$$H_\rho(\rho,\,\omega) = -\frac{1}{u\mu_1} E_\phi(\rho,\,\omega), \tag{9}$$

$$H_y(\rho,\,\omega) = \frac{j}{\omega\mu_1}\frac{1}{\rho}\frac{\partial}{\partial\rho}[\rho E_\phi(\rho,\,\omega)], \tag{10}$$

$$E_\rho(\rho,\,\omega) = -j\frac{\omega}{u}\frac{1}{\sigma_1 - j\omega\varepsilon_1} H_\phi(\rho,\,\omega), \tag{11}$$

$$E_y(\rho,\,\omega) = \frac{1}{\sigma_1 - j\omega\varepsilon_1}\frac{1}{\rho}\frac{\partial}{\partial\rho}[\rho H_\phi(\rho,\,\omega)] - \frac{1}{\sigma_1 - j\omega\varepsilon_1} J_y(\rho,\,\omega). \tag{12}$$

We also have:

$$\frac{\partial}{\partial\rho}\left[\frac{1}{\rho}\frac{\partial}{\partial\rho}[\rho E_\phi(\rho,\,\omega)]\right] + \left[j\omega\mu_1(\sigma_1 - j\omega\varepsilon_1) - \left(\frac{\omega}{u}\right)^2\right] E_\phi = 0 \tag{13}$$

$$\frac{\partial}{\partial\rho}\left[\frac{1}{\rho}\frac{\partial}{\partial\rho}[\rho H_\phi(\rho,\,\omega)]\right] + \left[j\omega\mu_1(\sigma_1 - j\omega\varepsilon_1) - \left(\frac{\omega}{u}\right)^2\right] H_\phi = \frac{\partial}{\partial\rho}[J_y(\rho,\,\omega)] \tag{14}$$

The absence of a source term in (13) along with (9) and (10) yield the result,

$$H_\rho(\rho,\,\omega) = E_\phi(\rho,\,\omega) = H_y(\rho,\,\omega) = 0 \tag{15}$$

On the other hand (5) and (14) together give

$$\left[\frac{\partial^2}{\partial\rho^2} + \frac{1}{\rho}\frac{\partial}{\partial\rho} + \left(k^2 - \frac{1}{\rho^2}\right)\right] H_\phi(\rho,\,\omega) = \frac{\partial}{\partial\rho}\left[u q_0 \frac{\delta(\rho)}{2\pi\rho}\right] \tag{16}$$

where

$$k^2 = \omega^2\mu_1\varepsilon_1 + j\omega\mu_1\sigma_1 - \left(\frac{\omega}{u}\right)^2. \tag{17}$$

The solution to (16) can be obtained through the Hankel transform as [10],

$$H_\phi(\rho,\,\omega) = C H_1^{(1)}\left(\tilde{k}\rho\right) \tag{18}$$

where $H_1^{(1)}$ is the first kind Hankel function of order 1,

$$\tilde{k} = \pm k \tag{19}$$

and C is a multiplicative constant. The sign in (19) is chosen in order to satisfy the radiation condition which requires an outward flow of power at large distances from the source. The true field $H_\phi(\rho,\, \phi,\, y,\, \omega)$ will be

$$H_\phi(\rho,\, y,\, \omega) = CH_1^{(1)}\left(\tilde{k}\rho\right) e^{j\omega y/u}. \tag{20}$$

It is to be noted that fields for the electromagnetic system at hand constitute a cylindrical wave with rotational symmetry around the Oy axis.

3. DECOMPOSITION OF FIELDS INTO ELEMENTARY PLANE WAVES

The procedure to be followed after this point is to decompose this cylindrical wave into plane waves for a two dimensional (2D) problem and to impose the boundary conditions relevant for the moving interface on each of the elementary plane waves [7] that constitute the cylindrical wave. To this end we make use of the plane wave expansion of cylindrical functions in lossy media given in [7]. Indeed in [7] it is pointed out that any (2D) field can be represented in terms of a suitable superposition of cylindrical waves. The expansion coefficients of such linear combinations constitute the unknowns in a typical scattering problem and are determined by imposing the boundary conditions. The additional third dimension in our problem will be handled in the sequel by the addition of a third component (the $\vec{e}_y$ component) which is equal to $\frac{\omega}{u}\vec{e}_y$ due to Equation (8), to the (2D) $\vec{\mathbf{k}}$ vector which is to be derived by the analysis in Equations (21) through (25).

We quote below the basic result of [7] that we need for this expansion, namely Equation (10) of [7] which is for the (2D) problem:

$$LF_m(x,\, n_{||}) = \exp\left(-|x|\sqrt{1-n_{||}^2}\tan\varphi_k\right)\begin{cases} F_m(x,\, n_{||}) & (x \geq 0) \\ F_{-m}(x,\, n_{||}) & (x \leq 0) \end{cases} \tag{21}$$

where $LF_m(x,\, n_{||})$ is the elementary plane wave function in the lossy case and F_m is the counterpart for a lossless medium and is given by

$$F_m(x,\, n_{||}) = \int_{-\infty}^{\infty} CW_m(x,\, z)\exp(-jn_{||}z)dz \tag{22}$$

And which has the analytical expression [7]

$$F_m(x,\, n_{||}) = \frac{2}{\sqrt{1-n_{||}^2}}\exp(j|x|\sqrt{1-n_{||}^2})\begin{cases} \exp(-jm\arccos(n_{||})) & (x \geq 0) \\ \exp(jm\arccos(n_{||})) & (x \leq 0) \end{cases} \tag{23}$$

where CW_m is the cylindrical wave function propagating in a homogeneous, isotropic, lossless medium. Its explicit expression as given in [8] is $CW_l(n_1\xi_h, n_1\zeta_h) = H_l^{(1)}(n_1\rho_h)e^{j\theta_h}$ where $H_l^{(1)}$ is the first kind Hankel function of integer order l, $(\xi_h,\, \zeta_h)$ and $(\rho_h,\, \theta_h)$ are rectangular and polar coordinate pairs respectively. In our case (cf. Equation (20)), our cylindrical wave function is independent of the polar coordinate θ_h and $n_1 = \tilde{k}$.

In (22) and (23) $\vec{\mathbf{n}} = \vec{\mathbf{k}}/\mathbf{k}$ is the unit vector parallel to the wave vector $\vec{\mathbf{k}}$ of a typical wave composing the spectrum, moreover $||$ refers to the parallel component of $\vec{\mathbf{n}}$ with respect to z.

In (21) $\tan\varphi_k = \frac{k_I}{k_R}$ when $k = k_R + jk_I$, i.e., k_R and k_I are the real and imaginary parts of k respectively.

In the light of (21) and (23) we can write the phase of an elementary plane wave as

$$\Phi = x\left[\sqrt{1-n_{||}^2}k_R(1+j\tan\varphi_k)\right] + n_{||}zk_R(1+j\tan\varphi_k) - \omega t \tag{24}$$

The wave vector will have the following components:

$$k_x = \sqrt{1-n_{||}^2}k_R(1+j\tan\varphi_k) \tag{25a}$$

$$k_y = 0 \tag{25b}$$

$$k_z = n_{||}k_R(1+j\tan\varphi_k) \tag{25c}$$

It is assumed above that the plane wave field components have the factor $e^{j\Phi}$ in common and that $k = k_R(1 + j\tan\varphi_k) = \sqrt{j\omega\mu_1(\sigma_1 - j\omega\varepsilon_1)}$ [7].

Notice that our fields also had the factor $e^{j\omega y/u}$ as given by (8). Hence the overall wave vector for an elementary plane wave of our problem will have the following components:

$$k_x = \sqrt{1 - n_{||}^2}k_R(1 + j\tan\varphi_k) \tag{26a}$$

$$k_y = \frac{\omega}{u} \tag{26b}$$

$$k_z = n_{||}k_R(1 + j\tan\varphi_k) \tag{26c}$$

The wave number is defined by

$$k^2 = k_x^2 + k_y^2 + k_z^2 = k_R^2(1 + j\tan\varphi_k)^2 + \left(\frac{\omega}{u}\right)^2, \tag{27}$$

where

$$k_R^2(1 + j\tan\varphi_k)^2 = \omega^2\mu_1\varepsilon_1 + j\omega\mu_1\sigma_1 \tag{28}$$

Thus we have introduced the third dimension of our problem by including the k_y component of $\vec{\mathbf{k}}$.

It should be remarked that the k in (27) is different from the k in (17). Equation (27) is the dispersion relation for an elementary plane wave and is the equation we shall base the remaining arguments on.

4. DERIVATION OF EQUATION (40) OF [2]

Now from the phase invariance principle, off the boundary of the two media, we write the following equations for the phases of the incident and reflected waves respectively in frames K and K'. Here in line with Equation (4) a time dependence of $e^{-j\omega_i t}$, $e^{-j\omega_r t}$ have been assumed in the frame K and a time dependence of $e^{-j\omega' t'}$ has been assumed in the frame K'. The subscript i stands for 'incident' while the subscript r stands for 'reflected'.

$$\Phi_i = (k_{ix}x + k_{iy}y + k_{iz}z) - \omega_i t = (k'_x x' + k'_y y' + k'_z z') - \omega' t' = \Phi'_i \tag{29a}$$

$$\Phi_r = (-k_{rx}x + k_{ry}y + k_{rz}z) - \omega_r t = (-k'_x x' + k'_y y' + k'_z z') - \omega' t' = \Phi'_r \tag{29b}$$

In the stationary system observed from K', the phase angles Φ'_i and Φ'_r must have the same $y'$and z' dependences in Equations (29). This is because at $x' = 0$, the continuity of the tangential electrical field requires that the phases Φ'_i and Φ'_r be equal. Hence coefficients of y' and z' were selected equal. This implied that for the same wave number k' measured in K' for reflected and incident waves, the only option for the coefficients of x' was to choose them as negatives of each other.

Now recalling the 'modified Lorentz transformation' (see [2] or [6]), from (29) one will find

$$k_{ix} = \alpha\left(k'_x - \frac{\omega'}{c'}r\right) \tag{30a}$$

$$k_{iy} = \frac{\omega_i}{u} \tag{30b}$$

$$k_{iz} = k'_z \tag{30c}$$

$$\omega_i = \alpha\left(\frac{\omega'}{c'}c - k'_x rc\right) \tag{30d}$$

Here k'_x is the x component of $\vec{\mathbf{k}}'$ which is the wave vector of the same plane wave as observed from K', and ω' is the frequency corresponding to ω_i and ω_r and that is measured from K'.

Similarly for the reflected wave we can write

$$k_{rx} = \alpha\left(k'_x + \frac{\omega'}{c'}r\right) \tag{31a}$$

$$k_{ry} = \frac{\omega_r}{u} \tag{31b}$$

$$k_{rz} = k'_z \tag{31c}$$

$$\omega_r = \alpha\left(\frac{\omega'}{c'}c + k'_x rc\right). \tag{31d}$$

Note that

$$k_i^2 = k_{ix}^2 + k_{iy}^2 + k_{iz}^2 = \omega_i^2 \mu_1 \varepsilon_1 + j\omega_i \sigma_1 \mu_1 + \frac{\omega_i^2}{u^2}, \tag{32a}$$

$$k_r^2 = k_{rx}^2 + k_{ry}^2 + k_{rz}^2 = \omega_r^2 \mu_1 \varepsilon_1 + j\omega_r \sigma_1 \mu_1 + \frac{\omega_r^2}{u^2}. \tag{32b}$$

Hence using (30) through (32) we obtain,

$$k_r^2 - k_i^2 = 4\alpha^2 k_x' \omega' \frac{r}{c'} + \frac{\left(\omega_r^2 - \omega_i^2\right)}{u^2} = \left(\omega_r^2 - \omega_i^2\right)\left(\varepsilon_1 \mu_1 + \frac{1}{u^2}\right) + j\left(\omega_r - \omega_i\right)\sigma_1 \mu_1, \tag{33}$$

or we obtain

$$4\alpha^2 k_x' \omega' \frac{r}{c'} = \left(\omega_r^2 - \omega_i^2\right)\varepsilon_1 \mu_1 + j\left(\omega_r - \omega_i\right)\sigma_1 \mu_1. \tag{34}$$

But from (32d) and (33d) we observe that

$$\omega_r - \omega_i = 2\alpha k_x' r c. \tag{35}$$

Therefore using (35) in (34) we get

$$2\left(\omega_r - \omega_i\right)\alpha \frac{\omega'}{cc'} = \left(\omega_r^2 - \omega_i^2\right)\varepsilon_1 \mu_1 + j\left(\omega_r - \omega_i\right)\sigma_1 \mu_1. \tag{36}$$

Dividing both sides by $(\omega_r - \omega_i)$, we obtain,

$$2\alpha \frac{\omega'}{cc'} = (\omega_r + \omega_i)\varepsilon_1 \mu_1 + j\sigma_1 \mu_1. \tag{37}$$

However again from (30d) and (31d)

$$(\omega_r + \omega_i) = 2\alpha \omega' \frac{c}{c'} \tag{38}$$

can be seen. Thus,

$$2\alpha \frac{\omega'}{cc'}\left(1 - \varepsilon_1 \mu_1 c^2\right) = j\sigma_1 \mu_1, \tag{39}$$

which is the same result as Equation (40) of [2].

Therefore we can again follow the same arguments as in the Introduction section and conclude that Special Relativity Theory fails to account for the loss in this particular electromagnetic system also.

What must be pointed out here is that the relationship (39) that leads to this conclusion is the same for both the electromagnetic system in this paper and the one in [2].

5. CONCLUSION

It has been found that the basic relationship that leads to the negation of Special Relativity Theory and was found in [2] for a particular electromagnetic system that consisted of a rest frame (denoted by K) constituted by a simple medium with loss, and a frame (denoted by K') in uniform rectilinear motion with respect to the first,wherein a perfectly conducting medium fills the half space such that the interface of the two media is an infinite plane perpendicular to the direction of motion of K, does not change, if, as the source of fields there exists a point charge in the first medium in uniform motion parallel to one of the axes perpendicular to the direction of motion of K'.

REFERENCES

1. Berzi, V. and V. Gorini, "Reciprocity principle and the Lorentz transformations," *J. of Mathematical Phys.*, Vol. 10, No. 8, 1518–1524, 1969.
2. Yener, N., "On the non-constancy of speed of light in vacuum for different Galilean reference systems," *Journal of Electromagnetic Waves and Applications*, Vol. 21, No. 15, 2241–2255, 2007.
3. Einstein, A., *On the Electrodynamics of Moving Bodies*, The Principle of Relativity, Dover, New York, 1952.

4. Idemen, M., *Elektromagnetik Alan Teorisinin Temelleri*, Literatür Yayıncılık, Istanbul, 1996.
5. Jackson, J. D., *Classical Electrodynamics*, John Wiley & Sons, New York, 1975.
6. Yener, N., "Determination of speeds of light in vacuum for different Galilean reference systems," *PIERS Proceedings*, 115–119, Beijing, China, March 23–27, 2009.
7. Frezza, F., et al., "Plane-wave expansion of cylindrical functions in lossy media," *Optics Communications*, Vol. 265, 47–51, 2006.
8. Vico, M. D., et al., "Scattering by a finite set of perfectly conducting cylinders buried in a dielectric half-space: A spectral-domain solution," *IEEE Trans. on Antennas and Propagation*, Vol. 53, No. 2, 719–727, 2005.
9. Lawrence, D. E. and K. Sarabandi, "Electromagnetic scattering from a dielectric cylinder buried beneath a slightly rough surface," *IEEE Trans. on Antennas and Propagation*, Vol. 50, No. 10, 1368–1376, 2002.
10. Tuan, H. S. and S. R. Seshadri, "Radiation from a uniformly moving charge in an anisotropic plasma," *IEEE Trans. on Microwave Theory and Techniques*, Vol. 11, No. 6, 462–471, 1963.
11. Kong, J. A., *Electromagnetic Wave Theory*, EMW Publishing, Cambridge, 2005.
12. Censor, D., "Relativistic electrodynamics: Various postulate and ratiocination frameworks," *Progress In Electromagnetics Research*, PIER 52, 301–320, 2005.

Non-constancy of Speed of Light in Vacuum for Different Galilean Reference Systems in Case of an Impulsive Plane Wave

Namik Yener
Technical Education Faculty, Umuttepe Campus, Kocaeli University, Izmit 41380, Kocaeli, Turkey

Abstract— Previous work which negates Special Relativity Theory and which was carried out only for a monochromatic plane wave is extended to an impulsive plane wave. The media considered consist in a linear dispersive medium with absorption (the Lorentz medium) that fills the space $x > -\infty$ (medium (I)) and a simple but lossy medium (II) initially filling the half space $x > 0$. Medium (I) has frequency dependent conductance and dielectric permittivity in distinction from the original work for the monochromatic wave. Inertial frames K and K' are attached to medium (I) and (II), and the above description of these two media are true when they are observed from K and K' respectively. K and K' have coincident origins in space and time initially, and at $t = t' = 0$, K' starts a uniform rectilinear motion with respect to K. An impulsive in time plane wave is assumed to impinge on the plane $x = -x_0$, at the time t_0, when $-x_0$ and t_0 are both measured from K. Complex phase invariance principle is applied to the resulting elementary plane waves whose superposition yields the impulse response of the system. Transformation relations for the wave numbers and frequencies for incident and reflected waves for the interface of medium (I) and (II), are obtained using a 'modified Lorentz transformation' which incorporates different speeds of light in vacuum c and c' for K and K', as was done for the monochromatic plane wave case. Next using the dispersion relations for the incident and reflected waves an algebraic relation is derived between constitutive parameters of the Lorentz medium, the frequency, c and the relative speed of K' with respect to K. This result implies that the speed of light in vacuum c is dependent on the reference frame, a violation of the basic assumption of Special Relativity Theory.

1. INTRODUCTION

The author has proved in previous work [1–3] that when inertial frames K and K' are attached to simple but lossy media, Special Relativity Theory [4] can be shown to be incapable of accounting for the loss in medium (I) attached to frame K. This proof leads to compulsory assumption of anisotropy of space in contradistinction from Special Relativity Theory and incorporation of different speeds of light in vacuum c and c' for K and K' in a transformation law different from the Lorentz transformation between coordinates (x, y, z, t) an (x', y', z', t') of a point measured from K and K'. This new transformation is derived in [1] and named 'modified Lorentz transformation' in [1] again.

The above development was carried out for a monochromatic plane wave in [1–3]. In this paper we consider an impulsive wave and medium (I) is chosen as a Lorentz medium that is dissipative and temporally dispersive. In the monochromatic wave case we had frequency independent conductance and dielectric permittivity.

In this paper at the end of our analysis we come up with Equation (37) which points out to a dependence of c on the inertial frame which is a result contradicting the Special Relativity Theory.

2. PROPERTIES OF THE IMPULSIVE WAVE

This section is based on [5]. Let a linear homogeneous, isotropic, temporally dispersive medium occupy the space $x > -\infty$. Let $A(x + x_0, t)$ represent either the scalar potential or any component of the electric field, magnetic field, Hertz vector or vector potential. Consider together with the quantity $A(x + x_0, t)$ its Laplace transform also, namely $A(x + x_0, \omega)$, which pair is related by

$$A(x + x_0, t) = \int_C A(x + x_0, \omega) e^{-i\omega t} d\omega. \tag{1}$$

$A(x + x_0, \omega)$ satisfies the Helmholtz equation

$$\left[\nabla^2 + \tilde{k}^2(\omega)\right] A(x + x_0, \omega) = 0 \tag{2}$$

where the complex wave number $\tilde{k}(\omega)$ is given by,

$$\tilde{k}(\omega) = \frac{\omega}{c} n(\omega). \tag{3}$$

Here $n(\omega) = (1 - \frac{b^2}{\omega^2 - \omega_0^2 + i2\delta\omega})^{1/2}$ is the complex refraction index of the dispersive medium which is taken as a Lorentz medium. The symbols ω, b, ω_0 and δ stand for angular frequency of the monochromatic component of incident pulse, plasma frequency, resonant frequency, damping constant respectively.

Now let us consider the $A(0,t)$ field on the plane $x = -x_0$ which is known for all time t and is non-zero only after $t = 0$, so that

$$A(0,\, t) = f(t) \tag{4}$$

where $f(t)$ is chosen in particular as

$$f(t) = \delta(t - t_0) \tag{5}$$

whose Laplace transform is

$$\tilde{f}(\omega) = e^{i\omega t_0} \tag{6}$$

such that $A(x + x_0,\, t)$ is the impulse response of the system, and is given as

$$\begin{aligned} A(x + x_0,\, t) &= \frac{1}{2\pi} \mathrm{Re} \left\{ \int_{ia-\infty}^{ia+\infty} \tilde{f}(\omega) \exp\left[\frac{x + x_0}{c} \phi_{t_0}(\omega, \theta) \right] d\omega \right\} \\ &= \frac{1}{2\pi} \mathrm{Re} \left\{ \int_{ia-\infty}^{ia+\infty} e^{i\omega t_0} \exp\left[\frac{x + x_0}{c} \phi_{t_0}(\omega, \theta) \right] d\omega \right\} \end{aligned} \tag{7}$$

For $t_0 \neq 0$,

$$\begin{aligned} A(x + x_0,\, t) &= \frac{1}{2\pi} \mathrm{Re} \left\{ \int_{ia-\infty}^{ia+\infty} \exp\left(\frac{x + x_0}{c} i\omega \left[n(\omega) - \frac{c}{x + x_0}(t - t_0) \right] \right) d\omega \right\} \\ &= \frac{1}{2\pi} \mathrm{Re} \left\{ \int_{ia-\infty}^{ia+\infty} \exp\left[i\tilde{k}(x + x_0) - i\omega(t - t_0) \right] d\omega \right\} \end{aligned} \tag{8}$$

Hence the elementary plane wave component is $\exp([i\tilde{k}(x + x_0) - i\omega(t - t_0)]$ where $\tilde{k}$ and ω are in general complex. The following analysis is based on this elementary wave because results derived from it will also hold for $A(x + x_0,\, t)$, since due to (8), the latter is merely a superposition of such elementary waves for different frequencies.

3. APPLYING THE PRINCIPLE OF COMPLEX PHASE INVARIANCE OF PLANE WAVES

In Figure 1, the origins of K and K' in space and time are coincident initially when K' starts to move with velocity $\vec{v}_1$ with respect to K along the Ox axis. It will be assumed that medium (II) to which K' is attached, is a simple medium with loss when observed from K', while medium (I) to which K is attached is a Lorentz medium for $x > -\infty$ when observed from K. The interface between media (I) and (II) is an infinite plane perpendicular to direction of motion of K' with respect to K. Using the 'modified Lorentz transformation' and referring to Figure 1, the following relations will hold:

$$x_0' = \alpha(-x_0 + rct_0) \tag{9a}$$

$$t_0' = \alpha\left(-\frac{r}{c'} x_0 + \frac{c}{c'} t_0 \right) \tag{9b}$$

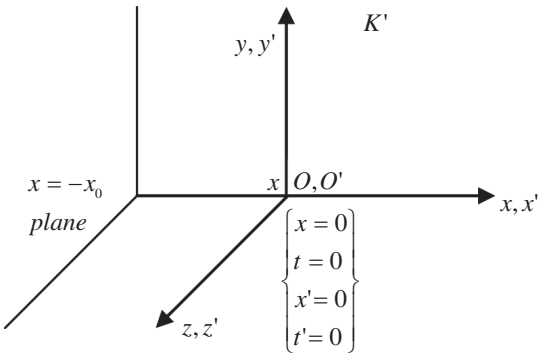

Figure 1: Initial coincidence of origins in space and time for K and K', and plane of $x = -x_0$.

$$-x_0 = \alpha(x'_0 - rc't'_0) \tag{10a}$$

$$t_0 = \alpha\left(-\frac{r}{c}x'_0 + \frac{c'}{c}t'_0\right) \tag{10b}$$

For the application of the principle of the invariance of the complex phase we shall use an argument similar to the one in [6], whereby the invariance is based on the transformation of the fields between K and K' using the Lorentz transformation. The difference of our argument will be that we shall use the 'modified Lorentz transformation' derived in [1] and not the classical Lorentz transformation.

Referring to [1] the two set of fields measured from K and K' are related by

$$\vec{E}' = \alpha\left(\vec{E} + \vec{v}\times\vec{B}\right) + (1-\alpha)\left(\vec{v}\cdot\vec{E}\right)\frac{\vec{v}}{v^2} \tag{11}$$

where $\alpha = [1-(v_1/c)^2]^{-1/2}$ and primed and unprimed quantities are relevant to K' and K respectively as in the entirety of this paper. In order that the above relation be true at all points in space and time, the complex phase factors ϕ and ϕ' defined as below on the basis of (8), and measured from K and K' must be the same for the incident wave indicated by a subscript i.

$$\phi_i = k_i(x+x_0) - \omega_i(t-t_0) = k'_1(x'-x'_0) - \omega'(t'-t'_0) = \phi'_i \tag{12}$$

The constant terms in ϕ and ϕ' constituted of a linear combination of t_0 and x_0 and a linear combination of t'_0 and x'_0 respectively must also be equal as we shall see in the sequel.

Rewriting (12) as follows after splitting real and imaginary parts and utilizing the 'modified Lorentz transformation' derived in [1] and which can also be found in [2]

$$\begin{aligned}\phi_{ir} &= k_{ir}\left[\alpha\left(x'-rc't'\right) - \alpha\left(x'_0 - rc't'_0\right)\right] - \omega_{ir}\left[\alpha\left(-\frac{r}{c}x' + \frac{c'}{c}t'\right) - \alpha\left(-\frac{r}{c}x'_0 + \frac{c'}{c}t'_0\right)\right] \\ &= k'_{1r}\left(x'-x'_0\right) - \omega'_r\left(t'-t'_0\right) = \phi'_{ir}\end{aligned} \tag{13}$$

will be found where the second subscript r stands for real part. Similarly for the imaginary part:

$$\begin{aligned}\phi_{ii} &= k_{ii}\left[\alpha\left(x'-rc't'\right) - \alpha\left(x'_0 - rc't'_0\right)\right] - \omega_{ii}\left[\alpha\left(-\frac{r}{c}x' + \frac{c'}{c}t'\right) - \alpha\left(-\frac{r}{c}x'_0 + \frac{c'}{c}t'_0\right)\right] \\ &= k'_{1i}\left(x'-x'_0\right) - \omega'_i\left(t'-t'_0\right) = \phi'_{ii}\end{aligned} \tag{14}$$

will be found where the second subscript i stands for imaginary part. Equating coefficients of x' in the two phase functions in the two Equations (13) and (14) yields:

$$\alpha k_{ir} + \alpha\frac{r}{c}\omega_{ir} = k'_{1r}$$

$$\alpha k_{ii} + \alpha\frac{r}{c}\omega_{ii} = k'_{1i}$$

Equating coefficients of t' in the two phase functions in the two Equations (13) and (14) yields:

$$\alpha r c' k_{ir} + \alpha \frac{c'}{c}\omega_{ir} = \omega'_r$$
$$\alpha r c' k_{ii} + \alpha \frac{c'}{c}\omega_{ii} = \omega'_i$$

From these four equations, we obtain

$$k_{ir} = \alpha k'_{1r} - \alpha \frac{r}{c'}\omega'_r \tag{15a}$$
$$\omega_{ir} = -\alpha r c k'_{1r} + \alpha \frac{c}{c'}\omega'_r \tag{15b}$$

$$k_{ii} = \alpha k'_{1i} + \alpha \frac{r}{c'}(-\omega'_i) \tag{16a}$$
$$\omega_{ii} = -\alpha r c k'_{1i} + \alpha \frac{c}{c'}\omega'_i \tag{16b}$$

Similarly the constant terms can be found to be equal in the two phase functions ϕ_i and ϕ'_i as seen below. To this end we make use of the results given in (15) and substitute expressions for k_{ir} and ω_{ir} from these into the real parts of the constant terms in ϕ_i and ϕ'_i as follows.

$$\begin{aligned} k_{ir}x_0 + \omega_{ir}t_0 &= x_0\left(\alpha k'_{1r} - \alpha\frac{r}{c'}\omega'_r\right) + t_0\left(-\alpha r c k'_{1r} + \alpha\frac{c}{c'}\omega'_r\right) \\ &= k'_{1r}\alpha\left(x_0 - rct_0\right) - \alpha\omega'_r\left(\frac{r}{c'}x_0 - \frac{c}{c'}t_0\right) = -k'_{1r}x'_0 + \omega'_r t'_0 \end{aligned}$$

will be found when we also observe (11). Similarly substitute expressions for k_{ii} and ω_{ii} from (16) into the imaginary parts of the constant terms in ϕ_i and ϕ'_i as follows.

$$\begin{aligned} k_{ii}x_0 + \omega_{ii}t_0 &= x_0\left(\alpha k'_{1i} - \alpha\frac{r}{c'}\omega'_i\right) + t_0\left(-\alpha r c k'_{1i} + \alpha\frac{c}{c'}\omega'_i\right) \\ &= k'_{1i}\alpha\left(x_0 - rct_0\right) - \alpha\omega'_i\left(\frac{r}{c'}x_0 - \frac{c}{c'}t_0\right) = -k'_{1i}x'_0 + \omega'_i t'_0 \end{aligned}$$

will be found when we also observe (9). This and above result for real part was expected as per (12).

Equation (12) must hold also for the reflected wave in the following form:

$$\phi_r = -k_r(x + x_0) - \omega_r(t - t_0) = -k'_1\left(x' - x'_0\right) - \omega'\left(t' - t'_0\right) = \phi'_r \tag{17}$$

Following the same steps as for the incident wave which are omitted for conciseness we arrive at

$$k_{rr} = \alpha k'_{1r} + \alpha \frac{r}{c'}\omega'_r \tag{18a}$$
$$\omega_{rr} = \alpha r c k'_{1r} + \alpha \frac{c}{c'}\omega'_r \tag{18b}$$

$$k_{ri} = \alpha k'_{1i} + \alpha \frac{r}{c'}\omega'_i \tag{19a}$$
$$\omega_{ri} = \alpha r c k'_{1i} + \alpha \frac{c}{c'}\omega'_i \tag{19b}$$

Similarly the constant terms can be found to be equal in the two phase functions ϕ_r and ϕ'_r in just the same way as was shown for the incident wave. We omit this part of the proof for conciseness.

Thus we have determined the transformation equations between k_i, k_r, ω_r, ω_i and k'_1, ω' which we summarize as below.

$$k_i = \alpha k'_1 - \alpha \frac{r}{c'}\omega' \tag{20a}$$
$$k_r = \alpha k'_1 + \alpha \frac{r}{c'}\omega' \tag{20b}$$

$$\omega_i = -\alpha r c k_1' + \alpha \frac{c}{c'}\omega' \tag{21a}$$

$$\omega_r = \alpha r c k_1' + \alpha \frac{c}{c'}\omega' \tag{21b}$$

In the above, quantities k_i, k_r, ω_r, ω_i and k_1', ω' are complex quantities incorporating real and imaginary parts given by (15), (16), (18) and (19). Similarly for the constant terms in ϕ_i, ϕ_i' and ϕ_r, ϕ_r'

$$\begin{aligned} k_i x_0 + \omega_i t_0 &= -k_1' x_0' + \omega' t_0' \\ -k_r x_0 + \omega_r t_0 &= k_1' x_0' + \omega' t_0' \end{aligned}$$

hold. The boundary condition $\phi_i' = \phi_r'$ at $x' = 0$ is due to continuity of tangential component of electric field on the interface of medium (I) and (II) and can be seen to be satisfied when the constant terms in the two phase factors are disregarded.

4. DERIVATION OF RELATION WHICH SHOWS C IS DEPENDENT ON INERTIAL FRAME

On the other hand, we can write the dispersion equation for medium (I) (the Lorentz medium) as observed from K as follows for the incident wave: $k_i^2 = \frac{\omega_i^2}{c^2}(1 - \frac{b^2}{\omega_i^2 - \omega_0^2 + i2\delta\omega_i})$ and for the reflected wave as $k_r^2 = \frac{\omega_r^2}{c^2}(1 - \frac{b^2}{\omega_r^2 - \omega_0^2 + i2\delta\omega_r})$. It is easy to obtain

$$k_i^2 - k_r^2 = \frac{\omega_i^2 - \omega_r^2}{c^2} - \frac{b^2}{c^2}\left(\frac{\omega_i^2}{\omega_i^2 - \omega_0^2 + i2\delta\omega_i} - \frac{\omega_r^2}{\omega_r^2 - \omega_0^2 + i2\delta\omega_r}\right) \tag{22}$$

$$k_i^2 + k_r^2 = \frac{\omega_i^2 + \omega_r^2}{c^2} - \frac{b^2}{c^2}\left(\frac{\omega_i^2}{\omega_i^2 - \omega_0^2 + i2\delta\omega_i} + \frac{\omega_r^2}{\omega_r^2 - \omega_0^2 + i2\delta\omega_r}\right) \tag{23}$$

Noting (20) and (21), from (22) one obtains,

$$\omega_i^2\left(\omega_r^2 - \omega_0^2 + i2\delta\omega_r\right) = \omega_r^2\left(\omega_i^2 - \omega_0^2 + i2\delta\omega_i\right) \tag{24}$$

Noting (20) and (21) from (23), we get,

$$\left(k_1'\right)^2 - \left(\frac{\omega'}{c'}\right)^2 = -\frac{b^2}{c^2}\left(\frac{\omega_i^2}{\omega_i^2 - \omega_0^2 + i2\delta\omega_i}\right). \tag{25}$$

From (21), we see that

$$\omega_i + \omega_r = 2\alpha\frac{c}{c'}\omega' \tag{26}$$

and

$$\omega_i\omega_r = \left(\alpha\frac{c}{c'}\omega'\right)^2 - \left(\alpha r c k_1'\right)^2 \tag{27}$$

From (24), we also obtain

$$\omega_0^2(\omega_i + \omega_r) = i2\omega_i\omega_r\delta. \tag{28}$$

Using (26) in (28), we find $2\omega_0^2\alpha\frac{c}{c'}\omega' = i2\omega_i\omega_r\delta$ or $\omega_i\omega_r = \omega_0^2\alpha\frac{c}{ic'\delta}\omega' = \omega_0^2\frac{\bar{b}}{i\delta}$ where $\bar{b} = \alpha\frac{c}{c'}\omega'$. Also $\omega_i + \omega_r = 2\alpha\frac{c}{c'}\omega' = 2\bar{b}$. Since we know the sum and product of ω_i and ω_r, these are roots of quadratic equation

$$W^2 - 2\bar{b}W + \bar{b}\frac{\omega_0^2}{i\delta} = 0 \tag{29}$$

Then

$$\omega_i^2 - 2\bar{b}\omega_i + \bar{b}\frac{\omega_0^2}{i\delta} = 0. \tag{30}$$

With some algebra, we can write (25) as

$$\left(k_1'\right)^2 - \left(\frac{\omega'}{c'}\right)^2 = -\frac{b^2}{c^2}\frac{\bar{b}}{\bar{b}+i\delta}. \tag{31}$$

On the other hand, the equality $2\omega_0^2\alpha\frac{c}{c'}\omega' = i2\omega_i\omega_r\delta$ can be written as follows using (21).

$$\omega_0^2\alpha\frac{c}{ic'\delta}\omega' = \left(\frac{\alpha c}{c'}\omega'\right)^2 - \left(k_1'\alpha r c\right)^2 \tag{32}$$

or

$$\omega_0^2\alpha\frac{1}{icc'\delta}\omega' = \left(\frac{\omega'}{c'}\right)^2 - \alpha^2 r^2\left[\left(k_1'\right)^2 - \left(\frac{\omega'}{c'}\right)^2\right]. \tag{33}$$

Using (25), we get

$$\omega_0^2\alpha\frac{c}{icc'\delta}\omega' = \left(\frac{\omega'}{c'}\right)^2 + \alpha^2 r^2\left(\frac{b^2}{c^2}\frac{\bar{b}}{\bar{b}+i\delta}\right). \tag{34}$$

Noting $\bar{b} = \alpha\frac{c}{c'}\omega'$, we finally can get

$$\left(\frac{\omega'}{c'}\right)^2 - \left(\frac{\omega'}{c'}\right)\left(\frac{\delta^2+\alpha^2\omega_0^2}{i\alpha c\delta}\right) + \frac{1}{c^2}\left(r^2b^2\alpha^2 - \omega_0^2\right) = 0 \tag{35}$$

If in this equation, we set $c = c'$

$$\alpha^2\left(\omega'\right)^2 - \omega'\left(\frac{\delta^2+\alpha^2\omega_0^2}{i\delta}\right) + \alpha\left(r^2b^2\alpha^2 - \omega_0^2\right) = 0 \tag{36}$$

will be found. If ω' is solved for

$$\omega' = \frac{1}{i2\alpha\delta}\left(\alpha^2\omega_0^2 + \delta^2 \pm \left|\alpha^2\omega_0^2 - \delta^2 + i2r^2b^2\alpha^2\delta\right|\right) \tag{37}$$

will be obtained where $|\cdot|$ stands for the absolute value of a complex number. This relation clearly points out to a dependence of c on α, hence on v_1, since as noted above $\alpha = [1-(v_1/c)^2]^{-1/2}$. Hence c is dependent on the choice of reference frames. If based on this result we foresee $c \neq c'$, then on condition that $c \neq c'$ is adhered to after (35), we get:

$$\omega'\frac{c}{c'} = \frac{1}{i2\alpha\delta}\left(\alpha^2\omega_0^2 + \delta^2 \pm \left|\alpha^2\omega_0^2 - \delta^2 + i2r^2b^2\alpha^2\delta\right|\right). \tag{38}$$

ACKNOWLEDGMENT

The author is indebted to Prof. Dr. Ari Henrik Sihvola for his suggestion to carry the result of [1] for a monochromatic wave to an impulsive wave in time.

REFERENCES

1. Yener, N., "On the non-constancy of speed of light in vacuum for different Galilean reference systems," *Journal of Electromagnetic Waves and Applications*, Vol. 21, No. 15, 2241–2255, 2007.
2. Yener, N., "Determination of speeds of light in vacuum for different Galilean reference systems," *PIERS Proceedings*, 115–119, Beijing, China, March 23–27, 2009.
3. Yener, N., "The non-constancy of speed of light in vacuum for different Galilean reference systems (revisited)," *Progress In Electromagnetics Research Symposium*, Xi'an, China, March 22–26, 2010.
4. Einstein, A., "On the electrodynamics of moving bodies," *The Principle of Relativity*, Dover, New York, 1952.
5. Oughstun, K. E. and G. C. Sherman, "Propagation of electromagnetic pulses in a linear dispersive medium with absorption (the Lorentz medium)," *J. of Opt. Soc. Am. B*, Vol. 5, No. 4, 817–849, 1988.
6. Ko, H. C., "On the relativistic invariance of the complex phase of plane waves," *Radio Science*, Vol. 12, No. 1, 151–155, 1977.

Non-constancy of Speed of Light in Vacuum for Different Galilean Reference Systems and Momentum and Energy of a Particle

Namik Yener
Technical Education Faculty, Umuttepe Campus, Kocaeli University, Izmit 41380, Kocaeli, Turkey

Abstract— The conservation of energy and momentum of a particle is investigated under a 'modified Lorentz transformation' which is a transformation law that emerges as compulsory after considering two lossy media to which inertial frames K and K' are attached. This emergence is an outcome of the failure of Special Relativity Theory to account for the mentioned loss in one of the media, as proved by the author in reported preceding work. This 'modified Lorentz transformation' incorporates different speeds of light in vacuum c and c' for K and K'. The velocity addition law under this transformation is given. Dependence of the relativistic expressions of momentum and energy for a particle which are relegated to their nonrelativistic values in the limiting case, on the magnitude of velocity is sought for. To this end collision and scattering of two identical particles are considered. A small scattering angle θ' is assumed in a glancing collision of the two particles, and the demanded dependences on the magnitude of the velocity of the particle are derived. This is achieved by considering a Taylor expansion of the conservation of energy equation around the point $\theta' = 0$. The results dictate a covariant but not invariant relation between the energy of a particle and its mass. This is due to the assumption of existence of different speeds of light in vacuum c and c' for frames K and K'. This development is identical with an existing one in the literature, but here the principle of constancy of speed of light is put aside on the basis of the falsity of Special Relativity Theory that was established previously.

1. INTRODUCTION

Consider two Galilean reference frames K and K', of which K' is in uniform rectilinear motion with speed v_1 with respect to K.

The three assumptions of Special Relativity Theory are [1]

i) The principle of relativity (i.e., that laws of physics are the same in all Galilean reference systems, there exists no preferred Galilean system),
ii) Assumption of homogeneity of space-time (to infer linearity of transform equations),
iii) Assumption of isotropy of space (to infer reciprocity also using the principle of relativity).

The author has established in [2, 3] that the principle of constancy of speed of light in vacuum [4–6] that is a consequence of the above three assumptions, is false in the general case, by considering an electromagnetic system, wherein the above inertial frame K is attached to a medium which is simple but lossy, whereas inertial frame K' is attached to a medium which is a perfect electric conductor filling the half space, such that the interface of the two media is an infinite plane perpendicular to the velocity of K' in direction of Ox axis with respect to K.

It is noted in [3] as the outcome of this finding that if $c \neq c'$ (inequality of speeds of light in vacuum for K and K') is assumed a 'modified Lorentz transformation' has to be derived that considers unequal c and c'. Derivation of this transformation is given in [2]. Using the results of this transform the following law of addition of velocities can be derived.

$$u_x = \frac{u'_x - v_2}{(c'/c - ru'_x/c)} \quad u_y = \frac{u'_y}{\alpha\,(c'/c - ru'_x/c)} \quad u_z = \frac{u'_z}{\alpha\,(c'/c - ru'_x/c)}$$

Here u_x, u_y, u_z and u'_x, u'_y, u'_z are respectively the velocity components of a moving object as observed from K and K'. Here $\alpha = (1 - r^2)^{-1/2}$ with $r = -v_1/c = v_2/c'$ and v_2 being the speed of K with respect to K'.

2. FUNCTIONAL FORM OF MOMENTUM AND ENERGY OF A PARTICLE

This section is exclusively based on [6] and only the changes called for by the non-constancy of speed of light in vacuum for different Galilean reference systems are implemented in the derivation of functional form of momentum and energy of a particle.

For a particle with speed small compared to speed of light in vacuum

$$\vec{p} = m\vec{u} \tag{1a}$$

$$E = E(0) + \frac{1}{2}mu^2 \tag{1b}$$

m is the mass of the particle, $\vec{u}$ is its velocity and $E(0)$ is a constant corresponding to the rest energy of the particle. We shall attempt to derive the momentum and energy of a particle in line with the 'modified Lorentz transformation' law of velocities. The modified Lorentz transformation is reported in [2, 3]. As stated above this transformation deviates from the Lorentz transformation in that it incorporates two different speeds of light for systems K and K'.

The only possible general versions of (1) in line with the principle of relativity are:

$$\vec{p} = M(u)\vec{u} \tag{2a}$$

$$E = E(u) \tag{2b}$$

where $M(u)$ and $E(u)$ are functions of the magnitude of the velocity $\vec{u}$. The relativistic momentum and energy of (2) must reduce to (1) in the nonrelativistic case. Hence

$$M(0) = m \tag{3a}$$

$$\frac{\partial E}{\partial u^2}(0) = \frac{m}{2} \tag{3b}$$

Our aim is to determine the functional dependence $M(u)$ and $E(u)$ on u. We make the assumption that $M(u)$ and $E(u)$ are well behaved monotonic functions of u. We then consider the elastic collision of two identical particles and utilize the conservation of momentum and energy which must hold in all equivalent inertial frames, commensurate with the relativity principle. In particular, we consider the collision in two frames K and K' related by the 'modified Lorentz transformation'.

Let the inertial frame K' have two identical particles having initial velocities $\vec{u}'_a = \vec{v}$, $\vec{u}'_b = -\vec{v}$ along the Ox axis. The particles collide and scatter after which they have final velocities $\vec{u}'_c = \vec{v}'$ and $\vec{u}'_d = \vec{v}''$. The particles and their velocities are depicted in Figure 1.

In K' the conservation of momentum and energy read:

$$\vec{p}'_a + \vec{p}'_b = \vec{p}'_c + \vec{p}'_d$$
$$E'_a + E'_b = E'_c + E'_d$$

Or with the form (2)

$$M(v)\vec{v} - M(v)\vec{v} = M\left(v'\right)\vec{v}' + M\left(v''\right)\vec{v}'' \tag{4a}$$

$$E(v) + E(v) = E\left(v'\right) + E\left(v''\right) \tag{4b}$$

Because the particles are identical, $E(v') = E(v'')$ must hold. Since we assumed monotonic behavior for $E(v)$, then $v' = v''$ is true. Then the second equation in (4) requires $v' = v'' = v$. The first equation requires $\vec{v}'' = -\vec{v}'$. All four velocities are the same in magnitude with the final velocities opposite in direction, just like the initial velocities. Assume θ' represents the scattering angle in K'.

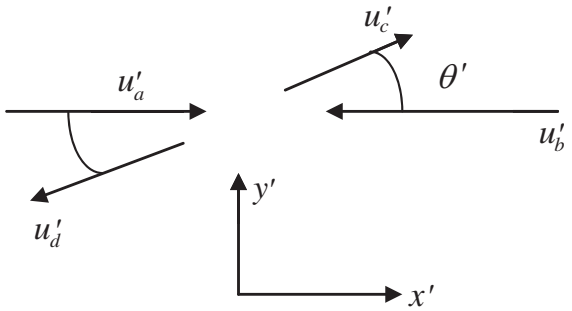

Figure 1: Initial and final velocity vectors in frame K' for the collision of two identical particles.

We now consider the same collision in another inertial frame K moving with a velocity $\vec{v}_2 = -\vec{v}$ in the Ox direction with respect to K'. From Section 1 where the transform equations for the velocity are given, we observe that particle a moves along the Ox axis with velocity given by

$$\begin{aligned} u_{ax} &= \frac{2v}{(c'/c - rv/c)} \quad u_{ay} = 0 \quad u_{az} = 0 \\ \vec{u}_a &= \frac{2\vec{v}}{c'\left(1 + v^2/c^2\right)/c} = \frac{2c\vec{\beta}}{(1+\beta^2)} \end{aligned} \tag{5}$$

where $\vec{\beta} = \frac{\vec{v}}{c'}$ and $\beta = \frac{v}{c'}$.

Similarly, because $\vec{u}'_c = \vec{v}' = v'\cos\theta'\vec{i} + v'\sin\theta'\vec{j}$ where $\vec{i}$ and $\vec{j}$ are unit vectors along $O'x'$ and $O'y'$,

$$u_{cx} = \frac{v'\left(1+\cos\theta'\right)}{c'\left(1+\beta^2\cos\theta'\right)} = \frac{c\beta\left(1+\cos\theta'\right)}{\left(1+\beta^2\cos\theta'\right)} \quad u_{cy} = \frac{c\beta\sin\theta'}{\alpha\left(1+\beta^2\cos\theta'\right)} \tag{6a}$$

Similarly because $\vec{u}'_d = -\vec{v}' = -(v'\cos\theta'\vec{i} + v'\sin\theta'\vec{j})$

$$u_{dx} = \frac{c\beta\left(1-\cos\theta'\right)}{\left(1-\beta^2\cos\theta'\right)} \quad u_{dy} = -\frac{c\beta\sin\theta'}{\alpha\left(1-\beta^2\cos\theta'\right)} \tag{6b}$$

with $\alpha = (1-\beta^2)^{-1/2}$.

The conservation of momentum and energy equations in K are:

$$M(u_a)\vec{u}_a + M(u_b)\vec{u}_b = M(u_c)\vec{u}_c + M(u_d)\vec{u}_d, \tag{7a}$$

$$E(u_a) + E(u_b) = E(u_c) + E(u_d). \tag{7b}$$

It can be seen from (5) and (6) that while particle b is at rest because

$$u_{bx} = \frac{u'_{bx}}{\left(c'/c - ru'_{bx}/c\right)} = \frac{-v+v}{(c'/c + rv/c)} = 0 \quad u_{by} = 0, \quad u_{bz} = 0,$$

the other three velocities are all different in general. Thus the determination of $M(u)$ and $E(u)$ from (7) looks complicated. We can however consider the limiting situation of a glancing collision in which θ' is very small. Then in the frame K, $\vec{u}_d$ will be nonrelativistic and $\vec{u}_c$ will differ only slightly from $\vec{u}_a$. We can therefore make appropriate Taylor series expansions around $\theta' = 0$ and obtain equations involving $M(u)$, $E(u)$ and perhaps their first derivatives.

Explicitly the y component of the momentum conservation equation in (7a) is:

$$0 = M(u_c)\frac{c\beta\sin\theta'}{\alpha\left(1+\beta^2\cos\theta'\right)} - M(u_d)\frac{c\beta\sin\theta'}{\alpha\left(1-\beta^2\cos\theta'\right)}$$

Canceling common terms and rearranging terms we have,

$$M(u_c) = M(u_d)\frac{\left(1+\beta^2\cos\theta'\right)}{\left(1-\beta^2\cos\theta'\right)},$$

This relation is valid for all θ', and in particular for $\theta' = 0$. Examination of (6) shows that in that limit $u_c = u_a$, $u_d = 0$. Thus we obtain

$$M(u_a) = M(0)\frac{1+\beta^2}{1-\beta^2}. \tag{8}$$

From (5) it can easily be observed that

$$\frac{1+\beta^2}{1-\beta^2} = \frac{1}{\sqrt{1-u_a^2/c^2}} = \alpha_a \tag{9}$$

will hold.

With the value $M(0) = m$ from (3) we thus have

$$M(u_a) = m\alpha_a$$

which implies that the momentum of a particle of mass m and velocity $\vec{u}$ is

$$\vec{p} = \alpha m\vec{u} = \frac{m\vec{u}}{\sqrt{1 - u^2/c^2}} \tag{10}$$

Determining the functional form of $E(u)$ needs examination of the conservation of energy equation for small θ' rather than at $\theta' = 0$. From (7) we have

$$E(u_a) + E(0) = E(u_c) + E(u_d) \tag{11}$$

where u_c and u_d are functions of θ'. From (6), we find correct to order θ'^2 inclusive,

$$\begin{aligned} u_c^2 &= u_a^2 - \frac{\eta}{\alpha_a^3} + O\left(\eta^2\right) \\ u_d^2 &= \eta + O\left(\eta^2\right) \end{aligned}$$

where α_a is given by (9) and η is defined as $\eta = \frac{c^2\beta^2\theta'^2}{1-\beta^2}$.

In Equation (7b), we equate coefficients of different powers of η. First order terms yield for $\eta \neq 0$

$$\frac{\partial E(u_c)}{\partial u_c^2}\left(-\frac{1}{\alpha_a^3}\right) + \frac{\partial E(u_d)}{\partial u_d^2} = 0 \tag{12}$$

$$\frac{\partial E(u_c)}{\partial u_c^2} = \frac{\partial E(u_a)}{\partial u_a^2} \tag{13}$$

But $\lim_{\eta \to 0} \frac{\partial E(u_d)}{\partial u_d^2} = \frac{\partial E}{\partial u^2}(0) = \frac{m}{2}$ as per Equations (3). Utilizing (13) one has

$$\frac{\partial E(u_a)}{\partial u_a^2} = \frac{\partial E(u_c)}{\partial u_c^2} = \alpha_a^3 \frac{\partial E(u_d)}{\partial u_d^2} = \alpha_a^3 \frac{m}{2} = \frac{m}{2\left(1 - u_a^2/c^2\right)^{3/2}}$$

Integration yields:

$$E(u_a) = \frac{mc^2}{\left(1 - u_a^2/c^2\right)^{1/2}} - mc^2 + E(0) \tag{14}$$

We have

$$\begin{aligned} p_0 &= \frac{m}{\sqrt{1 - u^2/c^2}}\, c \\ cp_0 &= \frac{mc^2}{\sqrt{1 - u^2/c^2}} \end{aligned}$$

Based on (14)

$$E(u_a) + mc^2 = E(0) + cp_0 \tag{15}$$

The solution to $E(0)$ from this equation is provided in the Appendix and is found to be $E(0) = mc^2$. Hence

$$E(u) = \frac{mc^2}{\left(1 - u^2/c^2\right)^{1/2}}.$$

The corresponding results derived for K' will read

$$\begin{aligned} E'(0) &= mc'^2 \\ E'\left(u'_a\right) &= \frac{mc'^2}{\left[1 - \left(u'\right)^2/c'^2\right]^{1/2}} = \frac{mc'^2}{\left(1 - u^2/c^2\right)^{1/2}}. \end{aligned}$$

Appendix: Determination of $E(0)$

We shall utilize the fact that $E(0)$ has to be the same in relativistic and nonrelativistic speeds and compute the quantity $E^2(u) - (pc)^2$, using the expressions $E(u) = E(0) + \frac{1}{2}mu^2$, $E(u) = \frac{mc^2}{(1-u^2/c^2)^{1/2}} - mc^2 + E(0)$ and $cp = \frac{mc^2}{\sqrt{1-u^2/c^2}}$. Then

$$\begin{aligned} E^2(u) - (pc)^2 &= E^2(0) + mu^2E(0) + \frac{1}{4}\left(mu^2\right)^2 - m^2\left(\frac{u^2c^2}{1-u^2/c^2}\right) \\ &= m^2c^4 + \frac{2mc^2}{\sqrt{1-u^2/c^2}}\left[E(0) - mc^2\right] + \left[E(0) - mc^2\right]^2 \end{aligned} \tag{A1}$$

must hold for nonrelativistic speeds u. We now claim that the solution for above equation is $E(0) = mc^2$. To see this we substitute this value for $E(0)$ in (A1). We get

$$m^2c^4 + mu^2mc^2 + m^2c^4\left[\frac{1}{4}\left(\frac{u^2}{c^2}\right)^2 - \left(\frac{u^2/c^2}{1-u^2/c^2}\right) - 1\right] = 0.$$

In this equation within the brackets, we neglect the term $\frac{1}{4}(\frac{u^2}{c^2})^2$ when compared with 1 and divide the equation by c^4 to get;

$$m^2 + m^2u^2/c^2 - m^2\left(\frac{u^2/c^2}{1-u^2/c^2}\right) - m^2 = 0.$$

Or

$$m^2\left[1 + \frac{u^2}{c^2} - \frac{u^2/c^2}{1-u^2/c^2}\right] - m^2 = 0.$$

This is equivalent to

$$m^2\left[\frac{\left(1-u^4/c^4\right) - u^2/c^2}{1-u^2/c^2}\right] - m^2 = 0.$$

We again neglect the term $(\frac{u^2}{c^2})^2$ when compared with 1.

$$m^2\left[\frac{1-u^2/c^2}{1-u^2/c^2}\right] - m^2 = 0$$

which shows that our solution $E(0) = mc^2$ is true.

REFERENCES

1. Berzi, V. and V. Gorini, "Reciprocity principle and the Lorentz transformations," *J. of Mathematical Phys.*, Vol. 10, No. 8, 1518–1524, 1969.
2. Yener, N., "On the non-constancy of speed of light in vacuum for different Galilean reference systems," *Journal of Electromagnetic Waves and Applications*, Vol. 21, No. 15, 2241–2255, 2007.
3. Yener, N., "The non-constancy of speed of light in vacuum for different Galilean reference systems," *Progress In Electromagnetics Research Symposium*, Xi'an, China, March 22–26, 2010.
4. Einstein, A., "On the electrodynamics of moving bodies," *The Principle of Relativity*, Dover, New York, 1952.
5. Idemen, M., *Elektromagnetik Alan Teorisinin Temelleri*, Literatür Yayıncılık, Istanbul, 1996.
6. Jackson, J. D., *Classical Electrodynamics*, John Wiley & Sons, New York, 1975.

Numberical Methods for Three-dimensional Electromagnetic Invisible Cloaks with Irregular Boundary Shapes

Xinhua Wang[1], **Shaobo Qu**[1, 2], **Song Xia**[2], **Binke Wang**[1], **Zhuo Xu**[2], **Hua Ma**[1], **Jiafu Wang**[1], **Chao Gu**[1], **Xiang Wu**[1], **Lei Lu**[1], **and Hang Zhou**[1]

[1]College of Science, Air Force Engineering University, Xi'an 710051, China
[2]Electronic Materials Research Laboratory, Key Laboratory of Ministry of Education
Xi'an Jiaotong University, Xi'an 710049, China

Abstract— The coordinate transformation theory is used to design invisible cloaks including the electromagnetic wave and the acoustic wave ones. By solving Laplace's equation that describes how the coordinates transform, three-dimensional (3-D) electromagnetic (EM) invisible cloaks with irregular boundary shapes can be designed provided the boundary conditions of the cloaks can be determined by the corresponding transformation. This design process is efficiency to design complicated and practical structures. Full wave simulations based on finite element method verified the designed 3-D EM invisible cloaks. The constitutive material parameters of the EM invisible cloaks can be calculated according to the coordinate transformation theory.

1. INTRODUCTION

The coordinate transformation method [1–6] for design invisible cloaks has attracted great attention in the scientific world. This method was firstly proposed by Pendry et al. [1] and the sphere analytic solution was obtained. Almost at the same time, Leonhardt et al. [2] gave the optical transformation method to design the invisible cloaks. These two papers brought the invisible theory from wave absorption mechanism to wave transmission mechanism. Full wave simulations [3] verified the invisible effects. A cylindrical electromagnetic cloaks [4] with metamaterials at microwave frequencies were designed and tested by experiment. Both simulation and experimental results illuminated the invisible effects.

By using the form-invariance coordinate transformations of Maxwell's equations, the electromagnetic wave cloaks and concentrators [5] were designed and verified. And ray tracing method [6] was also used to design the invisible cloaks and calculate the material properties. By analogy to the electromagnetic field, the acoustic equations [7] were transformed to design the acoustic cloaks.

All these cloaks are sphere and cylindrical cloak which have regular boundary shapes. In order to make the cloaks go near to the practical applications, complicated structure cloaks [8–20] were proposed and designed, such as the elliptical cylindrical cloaks [8–10], cloaks with arbitrary boundary shapes [11–20]. These cloaks are complicated structure cloaks but they are still the ideal ones because of the infinitely long in the perpendicularity direction. In other words, they are just two-dimensional (2-D) case. But in the real world, all objects are three dimensional (3-D) ones. In this paper, we use the Laplace equation to design the 3-D invisible cloaks with irregular boundary shapes. In the following sections, we will discuss the design theory for 3-D case.

2. LAPLACE EQUATION FOR THE DESIGN OF 3-D CLOAKS

For a given transformation, the component of the Jacobian transformation matrix [6] between the electromagnetic distorted space and the original physic space (flat space) is given by:

$$\Lambda_{\alpha}^{\alpha'} = \frac{\partial x^{\alpha'}}{\partial x^{\alpha}} \tag{1}$$

The constitutive material parameter tensors (the effective permittivity tensors and the effective permeability tensors) of the designed cloaks become:

$$\begin{aligned} \varepsilon^{i'j'} &= \left|\det\left(\Lambda_i^{i'}\right)\right|^{-1} \Lambda_i^{i'} \Lambda_j^{j'} \varepsilon^{ij} \\ \mu^{i'j'} &= \left|\det\left(\Lambda_i^{i'}\right)\right|^{-1} \Lambda_i^{i'} \Lambda_j^{j'} \mu^{ij} \end{aligned} \tag{2}$$

where, x' and x denote the coordinate in the transformed space and before the transformed space, respectively. ε and μ denote the effective permittivity tensors and the effective permeability tensors, respectively.

The component of the Jacobian transformation matrix must be ascertained firstly. Then the material parameter tensors of the cloaks can be obtained according to Eq. (2). Here, we use the Laplace equation [18] to get the component of the Jacobian transformation matrix.

The inverse form of the Laplace equation [18] are as follows:

$$\left(\frac{\partial^2}{\partial x_1'^2}+\frac{\partial^2}{\partial x_2'^2}+\frac{\partial^2}{\partial x_3'^2}\right)U_i=0, \quad i=1,2,3 \tag{3}$$

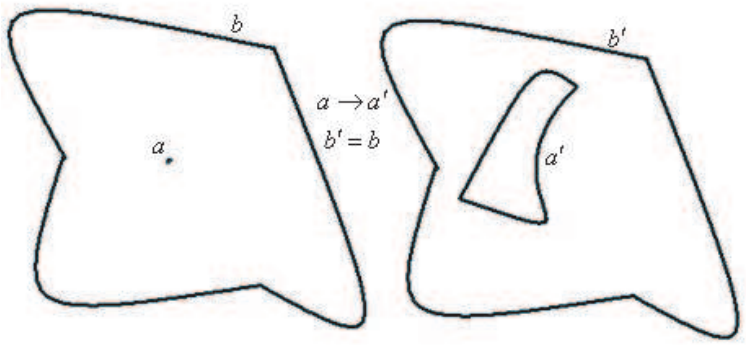

Figure 1: The illumination of constructing an invisible cloak.

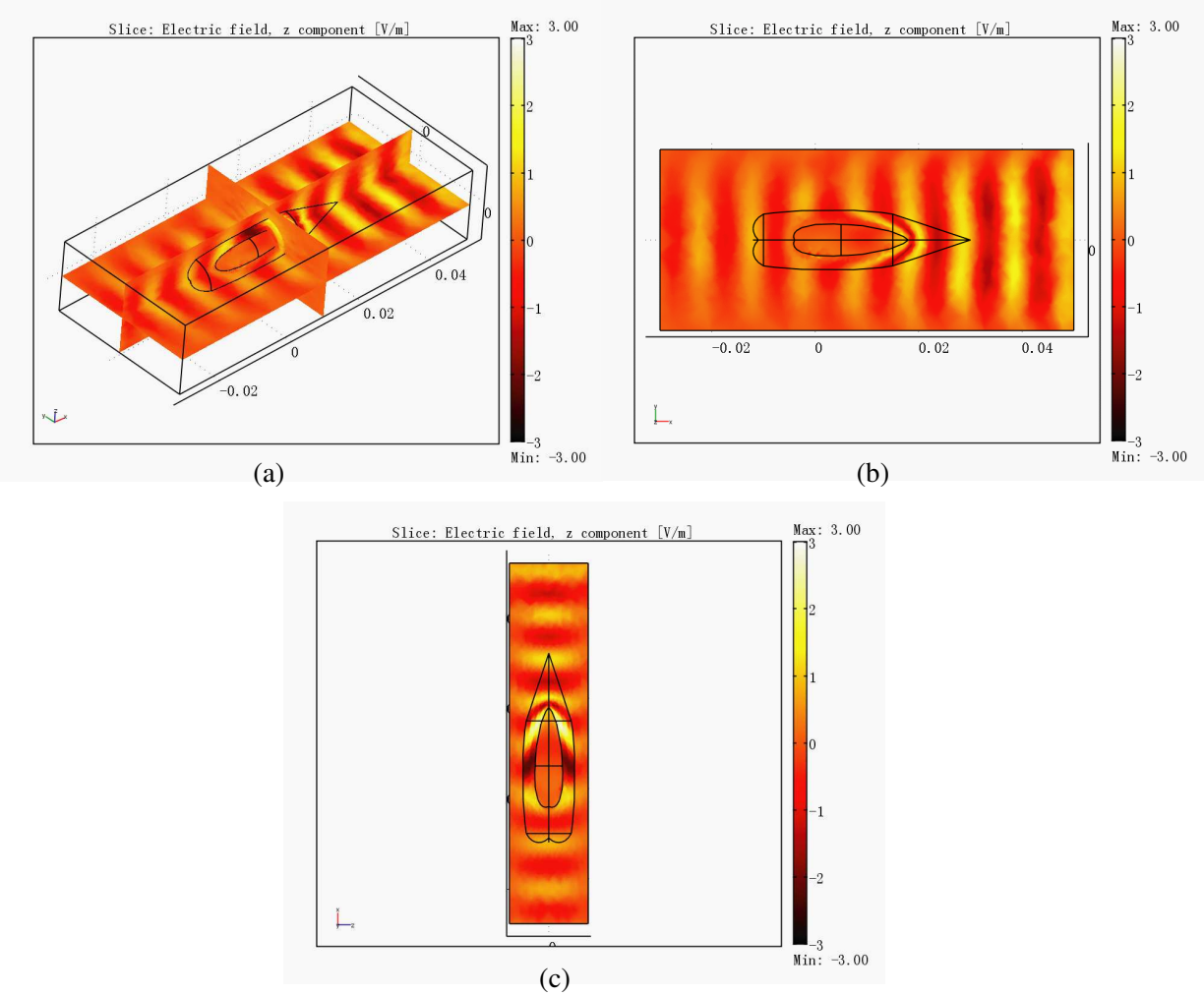

Figure 2: The z component of the electric field: (a) 3-D profile (b) XOY plane (c) XOZ plane.

where U_i denotes the coordinate in the original flat physic space. The corresponding of the boundary condition is as the following figure shown:

From Fig. 1, an arbitrary cloak [18] can be constructed by enlarging the point a to the inner boundary a', while keeping the outer boundary of the region fixed ($b = b'$). So this transformation process can be described by the Dirichlet boundary conditions:

$$U(a') = a \quad U(b') \ = b \tag{4}$$

By solving Eqs. (3) and (4), the deformation field inside of the cloak can be obtained. Then we can get the material parameter tensors of the cloaks.

This design process mainly concludes two processes. The first step is solving the Laplace equation with its corresponding boundary shapes to get the material parameter tensors of the cloaks. Then a plane wave will propagate through the cloaks to verify the invisible effects.

3. DESIGN OF 3-D CLOAKS WITH IRREGULAR BOUNDARY SHAPES

The commercial software Comsol Multiphysics is used to design the 3-D electromagnetic invisible cloaks with irregular boundary shapes. First of all, the PDE Module is used to set the boundary conditions and get the material parameters of the invisible cloaks. Then the RF Module is used to illuminate the cloaks by a plane wave. This modeling procedure is similar to that in Ref. [18].

In the computation domain, the inner boundary a' of the cloak is perfect electric conductor boundary condition, and the outer boundary b' of the cloak is continuity boundary condition. A time-harmonic uniform plane wave is incident onto the cloak, and then propagates along the cloak. This modeling is shown in Fig. 2.

From Fig. 2, we can see that the electromagnetic incident on the cloaks, the inner boundary of which has the structure as the stones, but does not enter into the cloaks. The wave shape does not change after the propagation. So the stones can be invisible from outside observers. This process just likes the case that water flows around the stones in the real world.

This design verifies the invisible effects. And the 3-D objects with irregular boundary shapes can be hidden in the cloak region. This design can bring the cloaks go to the real world.

4. CONCLUSION

By solving Laplace equation and the corresponding boundary conditions, the material parameter tensors of the 3-D electromagnetic invisible cloaks can be designed. Two steps are involved in the designed process. The full wave simulation based on the finite element method verified our design cloaks. The 3-D invisible cloaks with irregular boundary shapes make them go near to the practice. In the near future, the cloaks will be used to hide the objects inside it.

ACKNOWLEDGMENT

This work was supported partly by the National Natural Science Foundation of China (Grant Nos. 50632030, 10474077, and 60871027), partly by the 973-Project of the Ministry of Science and Technology of China (Grant No. 2009CB613306), and partly by the Natural Science Foundation of Shaanxi Province (Grant No. SJ08F01).

REFERENCES

1. Pendry, J. B., D. Schurig, and D. R. Smith, "Controlling electromagnetic fields," *Science*, Vol. 312, 1780–1782, 2006.
2. Leonhardt, U., "Optical conformal mapping," *Science*, Vol. 312, 1777–1780, 2006.
3. Cummer, S. A., B.-I. Popa, D. Schurig, D. R. Smith, and J. Pendry, "Full-wave simulations of electromagnetic cloaking structures," *Phys. Rev. E*, Vol. 74, 036621, 2006.
4. Schurig, D., J. J. Mock, B. J. Justice, S. A. Cummer, J. B. Pendry, A. F. Starr, and D. R. Smith, "Metamaterial electromagnetic cloak at microwave frequencies," *Science*, Vol. 314, 977–980, 2006.
5. Rahm, M., D. Schurig, D. A. Roberts, S. A. Cummer, and D. R. Smith, "Design of electromagnetic cloaks and concentrators using form-invariant coordinate transformations of Maxwell's equations," *Photon. Nanostruc. Fundam. Appl.*, Vol. 6, 87–95, 2006.
6. Schurig, D., J. B. Pendry, and D. R. Smith, "Calculation of material properties and ray tracing in transformation media," *Opt. Express*, Vol. 14, 9794–9804, 2006.

7. Cummer, S. A. and D. Schurig, "One path to acoustic cloaking," *New J. Phys.*, Vol. 9, 45, 2007.
8. Ma, H., S. B. Qu, Z. Xu, J. Q. Zhang, B. W. Chen, and J. F. Wang, "Material parameter equation for elliptical cylindrical cloaks," *Phys. Rev. A*, Vol. 77, 013825, 2008.
9. Kwon, D. and D. H. Werner, "Two-dimensional eccentric elliptic electromagnetic cloaks," *Appl. Phys. Lett.*, Vol. 92, 013505, 2008.
10. Jiang, W. X., T. J. Cui, G. X. Yu, X. Q. Lin, Q. Cheng, and J. Y. Chin, "Arbitrarily elliptical-cylindrical invisible cloaking," *J. Phys. D: Appl. Phys.*, Vol. 41, 085504, 2008.
11. Yan, W., M. Yan, Z. Ruan, and M. Qiu, "Coordinate transformations make perfect invisibility cloaks with arbitrary shape," *New J. Phys.*, Vol. 10, 043040, 2008.
12. Li, C. and F. Li, "Two-dimensional electromagnetic cloaks with arbitrary geometries," *Opt. Express*, Vol. 16, 13414–13420, 2008.
13. Ma, H., S. Qu, Z. Xu, and J. Wang, "Numerical method for designing approximate cloaks with arbitrary shapes," *Phys. Rev. E*, Vol. 78, 036608, 2008.
14. Ma, H., S. Qu, Z. Xu, and J. Wang, "Approximation approach of designing practical cloaks with arbitrary shapes," *Opt. Express*, Vol. 16, 15449–15454, 2008.
15. Jiang, W. X., J. Y. Chin, Z. Li, Q. Cheng, R. Liu, and T. J. Cui, "Analytical design of conformal invisible cloaks for arbitrarily shaped objects," *Phys. Rev. E*, Vol. 77, 066607, 2008.
16. Nicolet, A., F. Zolla, and S. Guenneau, "Electromagnetic analysis of cylindrical cloaks of an arbitrary cross section," *Opt. Lett.*, Vol. 33, 1584–1586, 2008.
17. Cai, W., U. K. Chettiar, A. V. Kildishev, and V. M. Shalaev, "Design of optical cloak with nonlinear transformation," *Opt. Express*, Vol. 16, 5444–5452, 2008.
18. Hu, J., X. Zhou, and G. Hu, "Design method for electromagnetic cloak with arbitrary shapes based on Laplace's equation," *Opt. Express*, Vol. 17, 1308–1320, 2009.
19. Chen, X., Y. Fu, and N. Yuan, "Invisible cloak design with controlled constitutive parameters and arbitrary shaped boundaries through Helmholtz's equation," *Opt. Express*, Vol. 17, 3581–3586, 2009.
20. Hua, M., S.-B. Qu, Z. Xu, J.-Q. Zhang, and J.-F. Wang, "Material parameter equation for rotating elliptical spherical cloaks," *Chinese Physics B*, Vol. 18, 179, 2009.

Millimeter-wave Signals Generated by Using Up-conversion for Radio-on-fiber System

C. C. Weng[1], **W. S. Tsai**[1], **Y. F. Lin**[1], **and H. H. Lu**[2]

[1]Department of Electrical Engineering, Ming Chi University of Technology
84 Gungjuan Rd., Taishan, Taipei 24301, Taiwan, R.O.C.
[2]Department of Electro-Optical Engineering, National Taipei University of Technology
1, Sec. 3, Chung-hsiao E. Rd., Taipei 10608, Taiwan, R.O.C.

Abstract— Recently, the microwave frequency of millimeter-wave band in 30 ∼ 300 GHz is most popular. In this article, we proposed an up-conversion system, make the use of semiconductor optical amplifier (SOA) to achieve the frequency multiplication for four-wave mixing (FWM) of nonlinear effects. The 7.5 GHz radio frequency (RF) signal will be fed and generated doubled frequency, tripled frequency even to quadruple frequency multiplications, it means that 15 GHz, 22.5 GHz and 30 GHz electrical signal can achieve. Finally this millimeter-wave signal is filtered out by using optical band pass filter (OBF). Comparing to traditional high-frequency signal generation system, this system is simple and lower cost.

1. INTRODUCTION

The traditional microwave frequency band of wireless network concentrates in 0.3 ∼ 30 GHz. Nowadays the millimeter wave (mm wave) is the most popular topic in the microwave frequency band. Comparing to the microwave signal, the size of mm wave electrical circuit and antenna is smaller, the bandwidth is wider and the efficiency is higher. It can promote the facility of antenna. For this reason, mm wave becomes a potential candidate of wireless communication in the future [1, 2]. The mm wave is referred to the radio wave which frequency situates between 30 ∼ 300 GHz. The mm wave frequency covers important frequency band of communication system. It can support the satellite communication, automobile radar, and optical fiber communication system [3].

In this research, FWM within SOA to generate the mm wave is applied in our proposed system. SOA has the advantages of simple configuration, small sealing, and easy integration. The most important is that it will not have any influence of Brillouin scattering. Because of its non-linear effects, for example, the self phase modulation (SPM), cross-phase modulation (XPM), self gain modulation (SGM), cross gain modulation (XGM), and four wave mixing (FWM) [4], applies these to the enlargement such as wavelength converter, amplification, chromatic dispersion compensation, and regenerator. FWM can be observed by the non-linear effect of SOA. The supposition is two wave frequencies its carrier frequencies are f_1 and f_2 respectively when they transmit by the optical fiber to the SOA. By the non-linear effect will produce third and fourth wave frequencies, f_3 and f_4, conform to $f_3 = 2f_1 - f_2$; relationship of the $f_4 = 2f_2 - f_1$. The supposition points out that N wave frequencies are inputted will produce $N^2 * (N-1)/2$ new members. As shown in Fig. 1, f_1 and f_2 are the wave frequencies originally, after SOA's four wave mixing effect produced new wave bands f_3 and f_4. In general situation, FWM is a bad noise disturbance item. However, in this research, uses this kind of non-linear effect in order to produce the different frequency optical beat. After suitable processing, can obtain many slip frequency items in the frequency spectrum from photo detector (PD) to perform electro-optical transformation. These optical beat signals are located in the microwave band, then using SOA's four wave mixing effect to obtain intended signal.

The millimeter wave signal which is produced by this way has broad line width. The wide bandwidth can hold more information and be used as the transmission signal of the millimeter wave optical fiber system.

2. EXPERIMENTAL

Figure 2 is an up-conversion system which shows using FWM to produce millimeter wave. 7.5 GHz electrical signal is output from the micro-wave signal generator and then feeds to the Mach-Zehnder modulator (MZM). The optical modulator's input light source is 1534.95 nm provided by a single mode laser diode, because the optical modulator has the sensitive characteristic regarding the input photo source's polarization state. In front of the MZM input section, needs to add on a polarization controller (PC). This function is to maintain the input light at the specific polarization state when

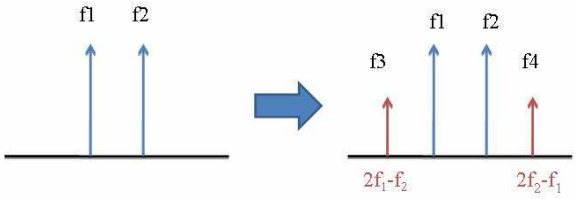

Figure 1: Four-wave mixing of nonlinear effects.

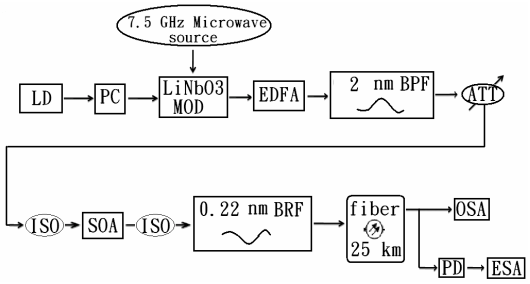

Figure 2: The up-conversion system architecture by using four-wave mixing to produce millimeter wave.

the laser gets into the optical modulator. In the MZM output port, the optical signal sends to the erbium doped fiber amplifier (EDFA). Because of the EDFA joined, may enable the optical signal which from the optical modulator output port overcomes the insertion loss. Optical modulator has enormous insertion loss, causes the optical signal passed optical modulator is weak, does not favor the optical signal transmission. Optical signal launches to 2 nm band-pass filter to filter out the noise which provided by EDFA. Passing through attenuator (ATT) to adjust the suitable input power, avoids the SOA output power saturation.

In the experiment construction, optical isolators (ISO) are added on in the SOA's input and output port respectively, the main function is to prevent the optical signal has the reflection to disturbance the system. After SOA's four wave mixing effect, the output optical signal produces many optical beats, then using optical spectrum analyzer (OSA) to measure optical spectrum. On the other hand, using PD to transform optical signal to electrical one, then measures the output frequency spectrum by using electrical spectrum analyzer (ESA).

3. RESULTS AND DISCUSSION

In FWM, three signals at frequencies f_k, f_l and f_m interact through the third order electric susceptibility to generate a new signal. When the generated signal wavelength coincides with the original signal wavelength, it results in interference. The number of generated signals grows rapidly as the number of transmitted signals/channels are increased. The generated signal power is expressed as [5].

$$P_{klm} = d^2 k \left(\frac{\alpha^2}{\alpha^2 + \Delta\beta^2} \right) L_{eff}^2 P_k P_l P_m \exp[-\alpha L] \cdot \left\{ \frac{(1-\exp[-\alpha L])^2 + 4\exp[-\alpha L]\sin^2\left(\frac{\Delta\beta L}{2}\right)}{(1-\exp[-\alpha L])^2} \right\} \quad (1)$$

where L_{eff} is the effective length of fiber, α the linear loss coefficient, L the fiber length and d the degeneracy factor. It takes a value of 3 when the products mixed are degenerates (i.e., $f_k = f_l \neq f_m$) and a value of 6 when the products are non-degenerates (i.e., $f_k \neq f_l \neq f_m$). In (1), the term P_k, P_l and P_m are launched signal powers at frequencies f_k, f_l and f_m respectively and k is given by

$$k = \frac{1024\pi^6}{n^4 \lambda^4 c^2} \left(\frac{\chi_{111}}{A_{eff}} \right)^2 \quad (2)$$

In (2), λ is the optical wavelength, c the speed of light in vacuum, χ_{111} represents the non-linear susceptibility and A_{eff} the effective cross-sectional area of fiber core.

In Fig. 2 construction, system is to use intensity modulation. Adjusting the bias voltage V_π of the modulator to suppress the central wavelength produces standard double sideband signals as shown in Fig. 3.

Enlarge the output signal by using the four wave mixing effect of the SOA. Fig. 4 shows two new wavelengths produced after passing through SOA. The two wavelengths f_3 $(2f_1 - f_2)$ and $f_4(2f_2 - f_1)$ are produced from the original signal. The signals in entire spectrum are shown in Fig. 5. Due to the beat signals are detected by PD, the original 7.5 GHz (−47.71 dBm), the double frequency 15 GHz (−37.46 dBm), and the triple frequency 22.5 GHz (−56.40 dBm) signals appear in the spectrum. The power of optical beat is detected by PD must to consider two points that

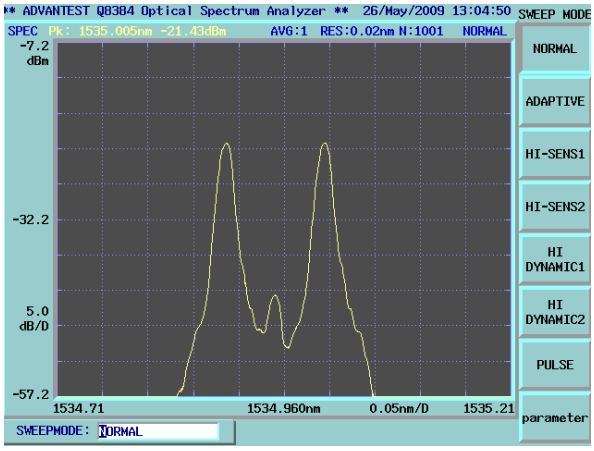

Figure 3: The spectrum at the output of Mach-Zehnder modulator.

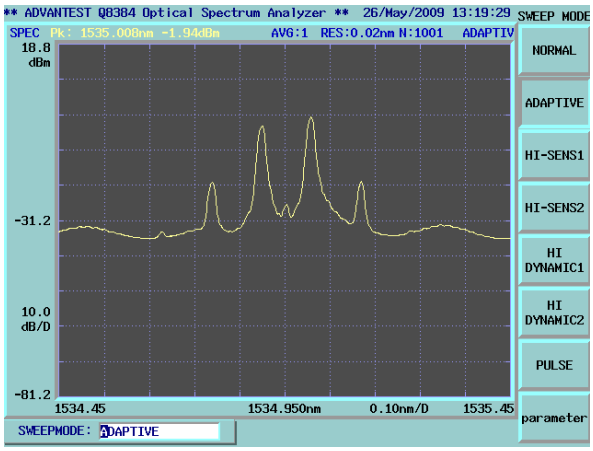

Figure 4: The Spectrum at the output of the SOA.

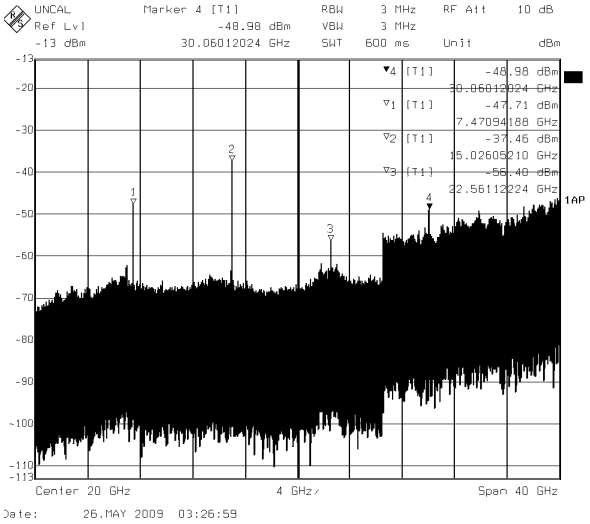

Figure 5: After four-wave mixing, the entire frequency spectrum.

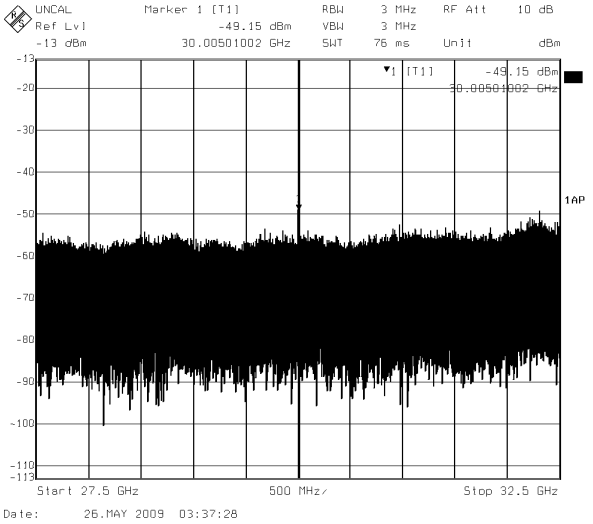

Figure 6: By inspection to detect quadruple frequency at 30 GHz.

are signal power can not be much difference between the optical beat and amount of optical beat. Large power at 15 GHZ observed in Fig. 5 is because that 3 beats detected by PD and optical power does not differ much from the optical beat signals. Finally, the quadruple frequency multiplication 30 GHz (−49.15 dBm) is shown in Fig. 6.

4. CONCLUSION

Make the use of SOA to achieve the frequency multiplication for FWM of nonlinear effects. We feed 7.5 GHz RF signal and generate frequency multiplications for 15 GHz, 22.5 GHz and 30 GHz. The structure of experiment succeeds in the frequency of microwave signal to perform up-conversion to millimeter-wave. The high-frequency signal in the output depends on the input RF signal frequency that is more flexible. Comparing to traditional high-frequency signal generation system, this system is simple and lower cost.

REFERENCES

1. Okamoto, Y., R. Miyamoto, and M. Yasunaga, "Radio-on-fiber access network systems for road-vehicle communication," *IEEE Intelligent Transportation Systems Conf. Proc.*, 1050–1055, 2001.
2. Kuri, T., K. I. Kitayama, and Y. Ogawa, "Fiber-optic millimeter-wave uplink system incorporating remotely fed 60-GHz-band optical pilot tone," *IEEE Trans. Microwave Theory Tech.*, Vol. 47, 1332–1337, 1999.

3. Kaminow, I. P. and T. Li, *Optical Fiber Telecommunications IV-B: Systems and Impairments*, Ch. 3, 57–153, Academic Press, San Diego, 2002.
4. Silveira, T., A. Teixeira, A. Ferreira, P. Monteiro, and P. André, "Influence of SOA based deviceson optical single sideband signals," *Proceedings of 2005 7th International Conference on Transparent Optical Networks*, Vol. 2, 234–237, 2005.
5. Singh, S. P., S. Kar, and V. K. Jain, "Novel strategies for reducing FWM using modified repeated unequally spaced channel allocation," *Fiber and Integrated Optics*, Vol. 6, No. 23, 415–437, 2004.

SVM-based Approach for Buried Object Detection

Qing He Zhang[1] and Jing-Jing Yao[2]

[1]School of Science, Three Gorges University, Yichang, Hubei 443002, China
[2]School of Electronics Information, Wuhan University, Wuhan 430079, China

Abstract— In this paper, a new method for the buried object detection is proposed. The center position and dielectric properties of 2-D buried object are estimated by means of a regression technique based on the use of support vector machines (SVMs). The proposed method, after a proper training procedure, is able to reconstruct the center position and dielectric properties of buried object inside a given investigation domain. Numerical results are provided for the validation of the approach.

1. INTRODUCTION

In the past, many methods have been proposed to solve the electromagnetic inverse scattering problem, in literature, lot of works are focused on the buried object detection. Civil applications (mapping of urban services, archaeological surveys, detection of polluting materials) as well as military applications (mapping of unexploded ordinances) may require, the goal is often not only to detect the object's position but also to get dielectric characteristics of the target. The inversion techniques that have been proposed are mostly based on the numerical inversion of the integral scattering equations in the spatial domain [1–3] or on iterative minimization technique [4, 5]. Unfortunately, all these methods often require a great amount of computational resources and long CPU times. In the last years, a new technique based on the use of neural networks (NNs) has been proposed to face inverse scattering problems [6–8]. As far as the reconstruction of buried targets is concerned. Methods based on both multilayer perceptron neural networks (MLPNNs) [6, 7] and radial basis function neural networks (RBFNNs) [8] have been successfully proposed.

In this paper, an algorithm based on the use of support vector machines (SVMs) is proposed. In particular, as in the case of the using of neural networks, SVMs are used to estimate the unknown function that relates the scattering field to the target's properties. After a proper learning phase, the SVMs can obtain reconstruction in real-time. Moreover, in SVMs, the original problem is recasted into a constrained quadratic programming (CQP) problem, and it avoids typical drawbacks as overfitting or local minima occurrence [9].

2. SUPPORT VECTOR MACHINES FOR REGRESSION PROBLEMS

A regression problem can be stated as follows. Given some training samples $(\{e_1, v_1\}, \ldots, \{e_l, v_l\}) \in \sum \times \Theta$ (in particular, in this work, $e_l = (E^s)_l$, v_l being the unknown properties of the target), the goal is to find a function that have a maximum fixed error (defined in the following) for all the samples belonging to the training set and that is as smooth as possible, in order to reduce the effects on the estimated values due to the perturbation of the input data.

In the SVM regression, the unknown function is constructed by linearly combining the results of a nonlinear transformation of the input samples [10]

$$\Phi(e) = \sum_{n=1}^{n_{sv}} (\alpha_n - \alpha_n^*) k(e_n, e) + b \tag{1}$$

where n_{sv} is the number of support vector, while functional parameters $(\alpha_n, \alpha_n^*, b)$ are unknown quantities and must be chosen in order to minimize the distance between the values predicted by the function and the known samples, where k is a kernel function, it is a nonlinear transformation function. In the literature, several kernel functions have been considered, such as polynomial kernels, hyperbolic tangent kernels and Gaussian kernels [11].

The structural parameters $(C, \sigma^2, \varepsilon)$, the parameter C measures the trade-off between the capability of to approximate the input samples and the error on the new samples, while σ^2 is the variance of the kernel function, when Gaussian function are taken into account. The ε is the so-called — insensitive loss, which is defined as [10]

$$c(e, v) = \begin{cases} 0 & \text{if } |v - \Phi| \le \varepsilon \\ |v - \Phi| - \varepsilon & \text{otherwise} \end{cases} \tag{2}$$

In the case, we are considering (the detection of buried object) the inputs of the SVMs are the date extracted from the scattered field by the object while at the output we expect to have the unknown parameters characterizing the target (i.e., the position, the dielectric properties). By training the SVMs to relate its input patterns of data to the corresponding outputs, the structural parameters (C, σ^2, ε) of the SVMs are configured. Once this phase is concluded and the SVM's parameters determined, the characterization of a buried target is achieved by extracting the input data from the scattered field and letting the SVMs to process them.

3. NUMERICAL RESULTS

In order to assess the effectiveness of the proposed approach, several numerical simulations have been performed.

The kernel function used for the SVM regression in this work is a radial kernel, which is given by

$$k(e_n, e) = e^{-\|e_n - e\|^2/\sigma^2} \tag{3}$$

where σ^2 is the variance of the radial function which has been chosen in training phase.

We analyze the capability of the SVM regression based on amplitude-only data to reconstruct dielectric parameters (ε_r, σ) of buried cylinder. The problem considered is illustrated as in Fig. 1. A TM uniform plane wave (with frequency $f = 1\,\mathrm{GHz}$) traveling in the y-direction and incident normally on the air-soil interface. A dielectric cylinder of known geometric property ($R = \lambda_0/6$) and unknown dielectric properties is buried in a lossy investigation domain having a side length equal to λ_0, and the target's buried depth is λ_0. The dielectric properties of the half space where the cylinder is buried are $\varepsilon_b = 4.0$ and $\sigma_b = 0.005\,\mathrm{S/m}$. Its magnetic permeability is that of the vacuum.

Exactly as in the previous example, 10 equally spaced observation points are used to measure the amplitude of the scattered electric field. The unknowns of the problem are, in this case, the relative dielectric permittivity ε_r and electric conductivity σ of the target and will be reconstructed by the SVM regression. The data sets used for the training phase have been obtained by using FDTD, and made up of 315 examples. In particular, 15 different values of ε_r ($\varepsilon_r = 4.5 + 0.25n,\ n = 0, 1, \ldots, 14$) and 21 values of σ ($\sigma = 0.001 + 0.00045n\,(\mathrm{S/m}),\ n = 0, 1, \ldots, 20$) have been used.

After the training phase, the structural parameters of the SVM regression are given in Table 1. Then, we evaluated the precision of the SVM regression by using a test set made up of $N = 108$ examples ($\varepsilon_r = 4.55, 4.80, 5.05, 5.30, 5.55, 5.76, 6.05, 6.30, 6.80, 7.30, 7.55, 7.90$, $\sigma = 0.00105 + 0.001n\,(\mathrm{S/m}),\ n = 0, 1, \ldots, 8$). The reconstruction of both the relative dielectric permittivity ε_r and the electric conductivity σ are reported in Figs. 2 and 3, respectively.

4. CONCLUSION

In this paper, a method for the localization and the dielectric characterization of buried cylindrical object has been proposed. The proposed approach is based on the use of support vector machine for

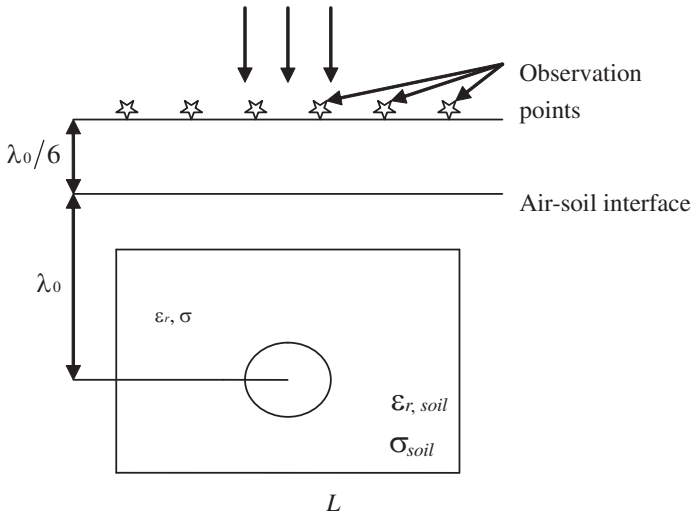

Figure 1: Problem geometry.

Table 1: The structural parameters of the SVM regression.

	C	σ^2	ε
ε_r	1000.2116	0.0028	0.001
σ	10000	1000	0.0001

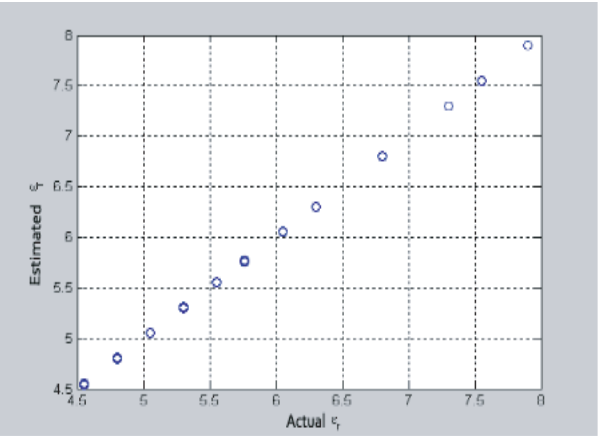

Figure 2: SVMs-based approach. Estimation of the buried cylinder's relative permittivity.

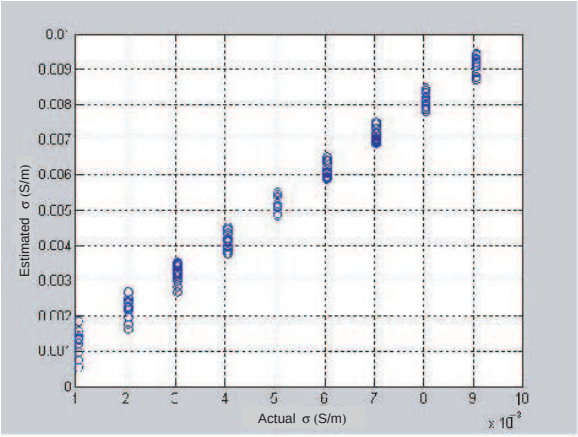

Figure 3: SVMs-based approach. Estimation of the buried cylinder's conductivity.

the solution of the regression problem. The efficiency of the proposed technique was illustrated in the case of the detection of the position and in the case of reconstruction of the dielectric properties of circular cylinder buried in a lossy half space. The training of SVM requires the solution of a constrained quadratic optimization problem. This is a key point of the proposed approach which allows to overcome the typical drawbacks as overfitting or local minima (with respect to NNs). The results obtained are by themselves encouraging, compared with those obtained by BPNNs approach. The proposed approach seems to be very attractive in many real applications because of the fast processing times and the possibility to work on field.

REFERENCES

1. Caorsi, S., G. Gragnani, and M. Pastorino, "Numerical electromagnetic inverse-scattering solutions for two-dimensional infinite dielectric cylinders buried in a lossy half-space," *IEEE Trans. on Microwave Theory and Techniques*, Vol. 41, No. 2, 352–356, 1993.
2. Joachimwicz, N., C. Pichot, and J. P. Hugonin, "Inverse scattering an iterative numerical method for electromagnetic imaging," *IEEE Trans. on Antennas and Propagation*, Vol. 39, No. 12, 1742–1753, 1991.
3. Chiu, T. J., W. C. Chew, A. A. Aydiner, and S. Y. Chen, "Inverse scattering of 2D dielectric objects buried in a lossy using the distorted Born iterative method," *IEEE Trans. Geosci. Remote Sens.*, Vol. 38, No. 6, 1–9, 2000.
4. Lobel, P., C. Pichot, L. Blanc-Feraud, and M. Barlaud, "A new regularization scheme for inverse scattering problems," *Inverse Problems*, Vol. 13, 403–410, 1997.
5. Caorsi, S., A. Massa, and M. Pastorino, "A computational technique based on a real-coded genetic algorithm for microwave imaging purposes," *IEEE Trans. Geosci. Remote Sens.*, Vol. 38, No. 4, 1697–1708, 2000.
6. Caorsi, S. and P. Gamba, "Electromagnetic detection of dielectric cylinders by a neural network approach," *IEEE Trans. Geosci. Remote Sens.*, Vol. 37, No. 2, 820–827, 1999.
7. Mydur, R. and K. A. Michalski, "A neural-network approach to the electromagnetic imaging of elliptic conducting cylinders," *Microwave Opt. Technol. Lett.*, Vol. 28, No. 5, 303–306, 2001.
8. Rekanos, I. T., "On-line inverse scattering of conducting cylinders using radis basis-functions neural networks," *Microwave Opt. Technol. Lett.*, Vol. 28, 378–380, 2001.
9. Vapnik, V., *Statistical Learning Theory*, Wiley, New York, 1998.
10. Cristianini, N. and J. S. Taylor, *An Introduction to Support Vector Machine*, Cambridge Univ. Press, Cambridge, UK, 2000.

11. Vapnik, V., S. Golowich, and A. J. Smola, "Support vector method for function approximation, regression estimation, and signal processing," *Neural Information Processing Systems*, MIT Press, Cambridge, MA, 1997.

Electronically Tunable Current Mode Second Order High Pass Filter with Variable Central Frequency f_0

G. N. Shinde[1] and D. D. Mulajkar[2]

[1]Indira Gandhi (SR) College, Nanded, Maharashtra 431603, India
[2]Dnyanasadhana College, Thane, Maharashtra 400604, India

Abstract— At present, there is a growing interest in designing capacitor-less, resistor-less current mode active only filters using only active elements such as Operational amplifier [OA], Operational transconductance amplifiers [OTAs]. Current mode filters have many advantages compared with their voltage mode counterparts. Current mode filters have large dynamic range, higher bandwidth, greater linearity, simple circuitry, low power consumption etc.

A novel single-input current-mode active-R filter using two operational amplifiers (OAs) and resistors is presented. The circuit is fully programmable and implements high pass (HP) functions. The availability of currents at high impedances facilitates cascadibility feature. The filter performance factors center frequency (ω_0), bandwidth (ω_0/Q), quality factor (Q) and gain (G) are electronically tunable. The SPICE simulation results are included to confirm the workability of the proposed circuit.

This circuit can realize quadratic transfer function. Paper includes theoretical frequency response of second order high pass filter for cut off frequency 50 k with variable Q. The circuit is suitable for high frequency operation and monolithic integration. The proposed second order high pass filter works ideal for $Q = 10$ and central frequency from 1 kHz to 50 kHz. The gain roll-off is 40 dB/decade. The designed filter has passive sensitivities less than unity magnitude and active sensitivities half in magnitude.

1. INTRODUCTION

At present, there is a growing interest in designing capacitor-less, resistor-less current mode active only filters using only active elements such as Operational amplifier [OA], Operational transconductance amplifiers [OTAs]. Current mode filters have many advantages compared with their voltage mode counterparts. Current mode filters have large dynamic range, higher bandwidth, greater linearity, simple circuitry, low power consumption etc. Many circuits for realizing voltage mode filters have been proposed by researchers. The realization of current mode transfer function is topic of considerable interest for researchers. Misami Higashimura proposed a synthesis of current mode high pass transfer function using op-amp pole [Higashimura, 1993]. Extensive work has been done employing active devices such as OAs and OTAs [2, 3]. Due to their many advantages there is growing interest in designing and implementing current mode active filters using second generation current conveyors [CCIIs]. Several implementations of current mode CCII-based filters are available in literature. Current mode active filters are also designed with second generation duel output current conveyors [DO-CCII] [10].

This paper focuses on second order current mode active-R filter with quadratic transfer function. The proposed circuit is solely designed with op-amps and resistors and hence suitable for high frequency operation. The filter has low passive sensitivities. The gain roll-off is 40 dB/decade.

2. CIRCUIT ANALYSIS AND ANALYTICAL TREATMENT

Figure 1 shows proposed circuit diagram of second order high pass filter. It consists of two op-amps (LF 356N) having gain bandwidth ratio of 6.392×10^6. The resistors g_{1a}, g_{1b}, g_{2a} and g_{2b} serves the voltage divider for op-amps.

The analysis gives the current transfer function $T_H = [I_{out}/I_{in}]$ as follows

$$T_H[S] = \frac{g_0 S^2}{(g_0 + g_1 + g_2 + g_{1b}k_1)\, S^2 + (g_1\beta_1 + g_2\beta_2)\, k_1 S + g_2\beta_1\beta_2 k_1 k_2} \tag{1}$$

where

$$k_1 = \frac{g_{1a}}{g_{1a} + g_{1b}}$$

and

$$k_2 = \frac{g_{2a}}{g_{2a} + g_{2b}}$$

If $g_{1b}k_1 \ll [g_0 + g_1 + g_2]$, Equation (1) becomes,

$$T_H[S] = \frac{g_0 S^2}{(g_0 + g_1 + g_2) S^2 + (g_1\beta_1 + g_2\beta_2) k_1 S + g_2\beta_1\beta_2 k_1 k_2}$$

3. THE PROPOSED CIRCUIT DIAGRAM

The frequency response for $Q = 10$ for different central frequency 50 kHz for different values of Q is as shown in the Figure 2.

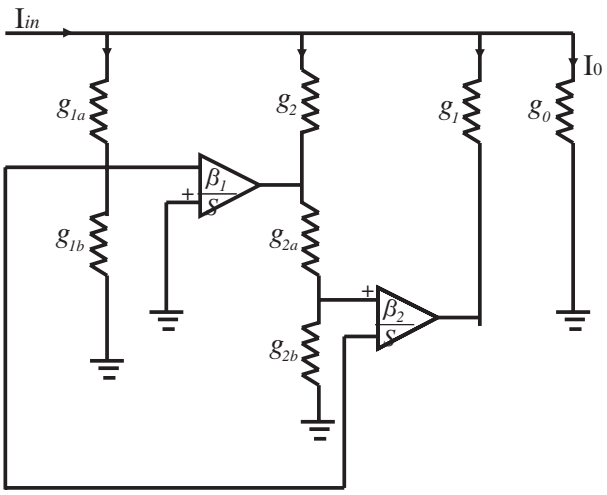

Figure 1: Circuit configuration for electronically tunable current mode second order high pass filter with variable central frequency f_0.

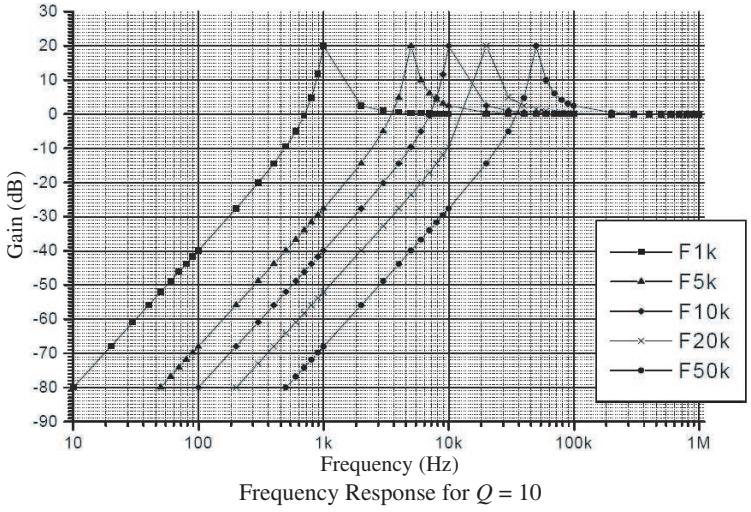

Figure 2: High pass response for electronically tunable current mode second order filter.

4. SENSITIVITIES

The practical solution is to design a network that has low sensitivity to element changes. The sensitivity must be less than limit i.e., unity [2, 4].

Table 1: Analysis of frequency response of the filter for $Q = 10$ with variable F_0.

F_0	F_{OH} Hz	F_0-F_{OH} Hz	Gain Roll-off in stop band		Gain Stabilization		Peak Gain of overshoot in the pass band dB	F_{OSH} (kHz)
			dB/decade	Decade Starting at (Hz)	dB	F_S (kHz)		
1 k	0.6 k	0.4 k	42	50 Hz	0	30 k	20	1 k
5 k	3.2 k	1.8 k	40	100 Hz	0	30 k	20	5 k
10 k	6.5 k	3.5 k	44	600 Hz	0	40 k	20	10 k
20 k	12 k	8 k	41	1 k	0	100 k	20	20 k
50 k	32 k	18 k	41	2 k	0	110 k	20	50 k

F_{OH}: -3 dB Frequency, F_{OSH}: Frequency at which overshoot occurs, F_S: Frequency at which gain stabilizes.

The equations of ω_0 and Q sensitivities of the filter transfer functions with respective parameters k_1, k_2, g_1, g_2, g_0 are as follows:

$$\begin{aligned}
S_{k_1}^{\omega_0} &= S_{k_2}^{\omega_0} = S_{\beta_1}^{\omega_0} = S_{\beta_2}^{\omega_0} = \frac{1}{2} \\
S_{g_0}^{\omega_0} &= -\frac{g_0}{2\,(g_0+g_1+g_2)} \\
S_{g_1}^{\omega_0} &= -\frac{g_1}{2\,(g_0+g_1+g_2)} \\
S_{g_2}^{\omega_0} &= \frac{(g_0+g_1)}{2\,(g_0+g_1+g_2)} \\
-S_{k_1}^{Q} &= S_{k_2}^{Q} = \frac{1}{2} \\
S_{g_0}^{Q} &= -\frac{g_0}{2\,(g_0+g_1+g_2)}
\end{aligned}$$

From these equations filter developed were successful in obtaining passive sensitivities less than unity in magnitude and active sensitivities half in magnitude.

5. RESULT AND DISCUSSION

We have proposed the circuit with $k_1 = k_2 = 0.5$ ms, $\beta_1 = \beta_2 = 6.392 \times 10^6$ for LF 356 N.

The frequency response for $Q = 10$ for different values of central frequencies is as shown in Figure 2. This second order high pass filter circuit works ideal for $Q = 10$ for all central frequencies which are tabulated. The gain-roll off of this configuration is 40 dB/decade. It is also observe that gain stabilizes at 0 dB.

High pass response of the filter for different values of f_0 is shown in Figure 2. Gain roll-off values varies between 41 to 44 dB/decade which is approaches to the ideal value 40 dB/decade for second order filter. The value of overshoot is 20 dB and small decreases with increase in the value of central frequency. The gain stabilizes at 0 dB after pass band for different values of center frequencies f_0.

Table 1 gives analysis of frequency response of the filter for $Q = 10$ with variable F_0.

6. CONCLUSION

The current mode active-R filter can realize quadratic transfer function. The proposed circuit works ideal for $Q = 10$ as second order High pass filter for variable central frequencies tabulated since the Roll-off is 40 dB/decade. Since the circuit is composed only of resistances, it is suitable for high frequency operation and monolithic implementation. The circuit is suitable for high frequency operation and monolithic integration. The proposed second order high pass filter works ideal for $Q = 10$ and central frequency from 1 kHz to 50 kHz. The gain roll-off is 40 dB/decade. The designed filter has passive sensitivities less than unity magnitude and active sensitivities half in magnitude.

REFERENCES

1. Higashimura, M., "Active-R realization of current-mode high pass filter," *Int. J. Electronics*, Vol. 6, 1279–1283, 1992.
2. Shinde, G. N. and P. D. Achole, "Multiple feedback third order active-R filter with varying tapping ratio," *Indian J. Physics*, Vol. 80, No. 2, 187–190, 2006.
3. Shinde, G. N. and P. B. Patil, "Third order active-R filter with feed forward input signal," *Sadhana Journal of Engineering Science*, Vol. 28, No. 6, 1919–1926, 2003.
4. Tsukutani, T., M. Higashimura, Y. Sumi, and Y. Fukui, "Electronically tunable current mode active-only biquadratic filter," *Int. J. Electronics*, Vol. 87, No. 3, 307–314, 2000.
5. Hsu, C. C. and W.-S. Feng, "Structural design of current-mode biquad filters," *Int. J. Electronics*, Vol. 88, No. 1, 41–51, 2001.
6. Nandi, R., "Active R realization of bilinear RL impedances and their applications in a high-Q parallel resonator and external oscillator," *Proceeding of the Institute of Electrical and Electronics Engineering*, 1978.
7. Mitra, A. K. and V. K. Aatre, "Low sensitivity high frequency active R filters," *IEEE Transactions on Circuits and Systems*, Vol. 23, 670–676, 1976.
8. Trkutani, T., M. Ishida, and Y. Fuksui, "Cancellation technique of parasitic poles for active-R high pass filter," *Transaction of the Institute of Electronics and Communication Engineering of Japan*, Pt. E, Vol. 75, 1083–1085, 1991.
9. Shah, N. A., M. F. Rather, M. A. Malik, and S. Z. Iqbal, "Cascadable electronically tunable SITO current-mode active-only universal filter," *Int. J. Electronics*, Vol. 8, No. 1, 141–151, 2005.
10. Shinde, G. N. and D. D. Mulajkar, *International Journal of Physical Sciences*, Vol. 3, No. 6, 148–151, Jun. 2008.

A SAR Superresolution Method Based on 2D Linear Prediction Extrapolation

Ping Zhang and Zhen Li
Center for Earth Observation and Digital Earth, Chinese Academy of Sciences
Kedian Tower F14, No. 9 Beiyitiao Road, Zhongguancun Haidian District, Beijing 100190, China

Abstract— A SAR (Synthetic Aperture Radar) bandwidth extrapolation method is presented to improve SAR image resolution based on two-dimensional linear prediction extrapolation. The method uses the SLC SAR image signal model and the measured data as the prior information to estimate the 2D AR (AutoRegression) parameters. A lap-to-lap approach is developed for the efficient bandwidth extrapolation to obtain a large dimension frequency domain spectrum. Simulation and real measured data experiments validate the effectiveness of the paper's method together with the quantitative analysis.

1. INTRODUCTION

Conventional radar imaging methods based on Fourier transform provide good resolution as long as the backscattered data is available over a large bandwidth and a sufficient aspect region. Wider transmitted bandwidth achieves higher range resolution. Either a higher centre frequency or wider aspect angle variation will improve azimuth resolution. But in many practical applications only limited frequency and limited aspect region are available. This leads to radar images with limited resolution.

The paper provides an efficient bandwidth extrapolation algorithm to reach a higher resolution in SAR (Synthetic Aperture Radar) imaging based on 2D AR (AutoRegression) linear prediction algorithm. The signal model is described in Section 2. The 2D AR parameters estimation method used in the paper is presented in Section 3. In Section 4, the SAR superresolution imaging method based on 2D AR linear prediction extrapolation is described and the method flow is given. Section 5 shows the experiments and the quality analysis. Section 6 gives the paper's conclusion.

2. SIGNAL MODEL

Based on the theory of synthetic aperture radar imaging, the signal model of SAR imagery is analyzed to be feasible by using data extrapolation methods to improve SAR image resolution in this section. Generally, SAR systems use linear FM signal as transmitted signal. After imaging processing, the form of scene echo can be represented as [1]

$$x\left(t_r,t_a\right)=\sum_{n=1}^{N}\sigma_n\mathrm{sinc}\left[B_r\left(t_r-t_1(R_{r,n})\right)\right]\times\mathrm{sinc}\left[B_a\left(t_a-t_2(R_{a,n})\right)\right]+n\left(t_r,t_a\right) \tag{1}$$

where t_r and t_a represent time in slant range and azimuth direction, respectively; $x_{r,n}$ and $x_{a,n}$ represent targets location in slant range and azimuth direction, respectively; B_r and B_a represent transmit signal bandwidth and Doppler bandwidth in azimuth, respectively; N is the number of scatter centers. Transforming (1) into phase history domain, we can see a rectangle support domain in the following expression

$$x\left(\omega_r,\omega_a\right)=\sum_{n=1}^{N}\sigma_n\mathrm{Rect}\left[\frac{\omega_r}{B_r}\right]\otimes\mathrm{Rect}\left[\frac{\omega_a}{B_a}\right]\times\exp\left(-jt_1(R_{r,n})\omega_r\right)\times\exp\left(-jt_2(R_{a,n})\omega_a\right)+v\left(\omega_r,\omega_a\right) \tag{2}$$

From the expression, we can see that SAR image signal model in phase history domain is a band-pass function with a main frequency support domain as the following expression

$$x\left(\omega_r,\omega_a\right)=\sum_{n=1}^{N}\sigma_n\times\exp\left(-jt_1(R_{r,n})\omega_r\right)\times\exp\left(-jt_2(R_{a,n})\omega_a\right)+v\left(\omega_r,\omega_a\right) \tag{3}$$

Thus, the problem of superresolution SAR imaging is transformed to solve the efficient bandwidth extrapolation.

3. ESTIMATION OF 2D AR PARAMETERS

To develop the 2D version AR model based on estimation of 2D AR parameters via the 2D covariance method of linear prediction, consider the case of quarter-plane linear prediction error filter. The linear prediction error filter of first-quarter plane is considered. $x(m,n)$ is the $M \times N$ dimension 2D measured data, and $a^1(l_1,l_2)$ is the coefficients of (p_1,p_2) order linear prediction error filter for $0 \le l_1 \le p_1$ and $0 \le l_2 \le p_2$. The linear prediction error filter is [2–5]

$$e^1(m,n) = \sum_{l_1=0}^{p_1} \sum_{l_2=0}^{p_2} a^1(l_1,l_2)\, x(m-l_1, n-l_2) \tag{4}$$

where $a^1(0,0) = 1$. Assume $e^1(m,n)$ is white noise process with the variance $\rho^1 = E\left\{\left|e^1(m,n)\right|^2\right\}$. In a similar manner, we can define the second, third, and fourth quarter plane linear prediction error filter outputs.

The two dimensional least squares normal equations of 2D covariance method of linear prediction are obtained by $M \times N$ measured data. The total sum of squared errors is

$$\rho^i = \sum_{m=p_1}^{M-1} \sum_{n=p_2}^{N-1} \left|e^i(m,n)\right|^2 = \mathbf{a}^i \left(\sum_{m=p_1}^{M-1} \sum_{n=p_2}^{N-1} \mathbf{x}(m,n)\, \mathbf{x}^H(m,n) \right) \mathbf{a}^{iH} = \mathbf{a}^i \mathbf{R} \mathbf{a}^{iH} \tag{5}$$

where $i = 1,2,3,4$. $\mathbf{R}$ is the $(p_1+1)(p_2+1) \times (p_1+1)(p_2+1)$ covariance variance matrix as follows

$$\mathbf{R} = \sum_{m=p_1}^{M-1} \sum_{n=p_2}^{N-1} \mathbf{x}(m,n)\, \mathbf{x}^H(m,n) = \mathbf{X}\mathbf{X}^H = \begin{bmatrix} \mathbf{R}(0,0) & \mathbf{R}(0,1) & \cdots & \mathbf{R}(0,p_2) \\ \mathbf{R}(1,0) & \mathbf{R}(1,1) & \cdots & \mathbf{R}(1,p_2) \\ \vdots & \vdots & \ddots & \vdots \\ \mathbf{R}(p_2,0) & \mathbf{R}(p_2,1) & \cdots & \mathbf{R}(p_2,p_2) \end{bmatrix} \tag{6}$$

where $\mathbf{R}(i,j) = \sum_{n=p_2}^{N-1} \mathbf{X}(n-i)\, \mathbf{X}^H(n-j)$, and $\mathbf{X}$ is a block-Toeplitz matrix.

$$\mathbf{X} = \begin{bmatrix} \mathbf{X}(p_2) & \mathbf{X}(p_2+1) & \cdots & \mathbf{X}(N-1) \\ \mathbf{X}(p_2-1) & \mathbf{X}(p_2) & \cdots & \mathbf{X}(N-2) \\ \vdots & \vdots & \ddots & \vdots \\ \mathbf{X}(0) & \mathbf{X}(1) & \cdots & \mathbf{X}(N-p_2-1) \end{bmatrix},$$

$$\mathbf{X}(i) = \begin{bmatrix} x(p_1,i) & x(p_1+1,i) & \cdots & x(M-1,i) \\ x(p_1-1,i) & x(p_1,i) & \cdots & x(M-2,i) \\ \vdots & \vdots & \ddots & \vdots \\ x(0,i) & x(1,i) & \cdots & x(M-p_1-1,i) \end{bmatrix}.$$

Minimize the total squared error.

$$\begin{aligned} \mathbf{a}^1\mathbf{R} &= \begin{bmatrix} \rho^1 & \cdots & 0 & 0 & \cdots & 0 & \cdots & 0 & \cdots & 0 \end{bmatrix}, \\ \mathbf{a}^2\mathbf{R} &= \begin{bmatrix} 0 & \cdots & 0 & 0 & \cdots & 0 & \cdots & \rho^2 & \cdots & 0 \end{bmatrix} \\ \mathbf{a}^3\mathbf{R} &= \begin{bmatrix} 0 & \cdots & 0 & 0 & \cdots & 0 & \cdots & 0 & \cdots & \rho^3 \end{bmatrix}, \\ \mathbf{a}^4\mathbf{R} &= \begin{bmatrix} 0 & \cdots & \rho^4 & 0 & \cdots & 0 & \cdots & 0 & \cdots & 0 \end{bmatrix} \end{aligned} \tag{7}$$

can compute the AR parameter $\mathbf{a}^i$.

4. METHODOLOGY

From the Equation (3), it is easy to see a stationary 2D backscattered field $x(\omega_r, \omega_a)$ may be predicted by a linear combination of its neighboring samples. The 2D AR parameters can be estimated using the efficient bandwidth data. According to the 2D AR linear prediction model, the lap-to-lap approach is used for the extrapolation of the efficient bandwidth to obtain a large

dimension frequency domain spectrum, i.e., the bandwidth of the SAR image is increased. The lap-to-lap approach can use more data of the efficient bandwidth. Then the new data in the frequency domain can be transformed to the time domain and better resolution can be achieved.

In the 2-D linear modeling, a stationary 2-D backscattered field $\hat{x}(m,n)$ may be predicted by a linear combination of its neighboring samples. There are several causal models depending on the prediction region. Using the quarter-plane model, the coefficient at the index (m,n) can be predicted by four different prediction filters of order L. The Cartesian frequency region defined by the extended data matrix $\hat{x}(m,n)$ is divided into several regions as shown in Fig. 1. In these regions, optimum quarter-plane prediction filter is used to predict the unmeasured samples.

Region A: The original $M \times N$ data matrix is conserved in the centre of the 2D extended data matrix as [6]

$$\hat{x}(m,n) = x(m - M_1, n - N_1) \tag{8}$$

where $N_1 \le n \le N_1 + N$, $M_1 \le m \le M_1 + M$.

Region B: The prediction obtains the backward prediction on f_x and f_y as

$$\hat{x}(m,n) = \sum_{\substack{i=0 \\ i=j\neq 0}}^{L} \sum_{j=0}^{L} a^*_{i,j}\, x(m+i, n+j), \quad \begin{cases} 1 \le m \le M_1, N_1 \le n \le N_1 + N/2 \\ 1 \le m \le M_1, 1 \le n \le N_1 \\ M_1 \le m \le M_1 + M/2, 1 \le n \le N_1 \end{cases} \tag{9}$$

Region C: The prediction obtains the backward prediction on f_x and forward prediction on f_y as

$$\hat{x}(m,n) = \sum_{\substack{i=0 \\ i=j\neq 0}}^{L} \sum_{j=0}^{L} b^*_{i,j}\, x(m+i, n-j), \quad \begin{cases} 1 \le m \le M_1, N_1 + N/2 \le n \le N_1 + N \\ 1 \le m \le M_1, N_1 + N \le n \le N_2 \\ M_1 \le m \le M_1 + M/2, N_1 + N \le n \le N_2 \end{cases} \tag{10}$$

Region D: The prediction obtains the forward prediction on f_x and on f_y as

$$\hat{x}(m,n) = \sum_{\substack{i=0 \\ i=j\neq 0}}^{L} \sum_{j=0}^{L} a_{i,j}\, x(m-i, n-j), \quad \begin{cases} M_1 + M \le m \le M_2, N_1 + N/2 \le n \le N_1 + N \\ M_1 + M \le m \le M_2, N_1 + N \le n \le N_2 \\ M_1 + M/2 \le m \le M_1 + M, N_1 + N \le n \le N_2 \end{cases} \tag{11}$$

Region E: The prediction obtains the forward prediction on f_x and the backward prediction on f_y

$$\hat{x}(m,n) = \sum_{\substack{i=0 \\ i=j\neq 0}}^{L} \sum_{j=0}^{L} b_{i,j}\, x(m-i, n+j), \quad \begin{cases} M_1 + M/2 \le m \le M_1 + M, 1 \le n \le N_1 \\ M_1 + M \le m \le M_2, 1 \le n \le N_1 \\ M_1 + M \le m \le M_2, N_1 \le n \le N_1 + N/2 \end{cases} \tag{12}$$

where $\hat{x}(m,n)$ is the extrapolated SAR data. $a_{i,j}$, $a^*_{i,j}$, $b_{i,j}$, and $b^*_{i,j}$ are the prediction coefficients of four one quarter plane models. L is the order of 2D prediction filters. The measured data is $M \times N$ dimension. M_2 and N_2 is the forward and backward extrapolated data.

Using the (8)–(12), the extrapolated data can be computed. The extrapolation order may be as Fig. 2, which is extrapolated form inside to outside through the lap-to-lap order. Then Fig. 3 shows the detailed process of the 2D AR linear prediction extrapolation superresolution SAR imaging algorithm.

5. EXPERIMENTS

To test the feasibility and validity of the SAR super resolution imaging algorithm based on 2D AR linear prediction extrapolation, we compared the results of traditional imaging algorithm and the paper's method using simulated data and real measured data.

The simulation of point target echo is used to validation the paper's SAR superresolution imaging algorithm based on 2D AR linear prediction extrapolation. Assume the chirp signal bandwidth is 150 MHz, the sample frequency is 180 MHz (I/Q), pulse repetition frequency is 1000 Hz, the velocity of aircraft is 250 m/s, the azimuth width of antenna is 2 m, the slant range in the scene center is 18km, and the signal noise ratio is 7 dB. Fig. 4 is the results comparison of two methods. (a) is the

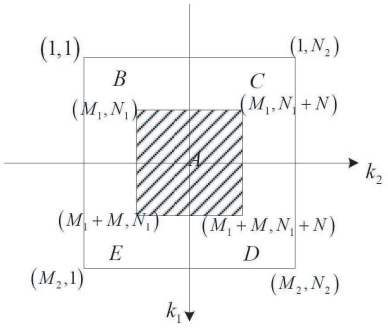

Figure 1: The extrapolation of 2D SAR data.

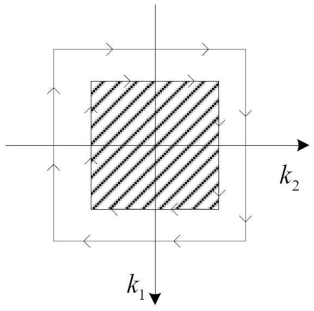

Figure 2: the extrapolation order.

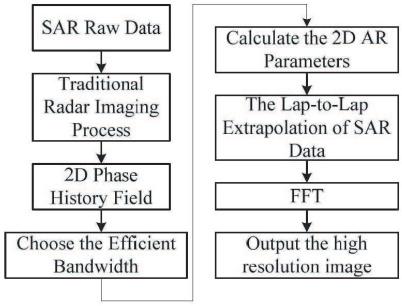

Figure 3: Flow of SAR superresolution imaging algorithm based on 2D AR linear prediction extrapolation.

Performace	RD method	The Paper's Method
Range resolution(m)	1.0473	0.6217
Range PSLR (dB)	−13.2699	−11.9431
Range ISLR (dB)	−10.8154	−8.9883
Azimuth resolution(m)	1.0652	0.6100
Azimuth PSLR (dB)	−11.8471	−9.0653
Azimuth ISLR (dB)	−10.1703	−6.4878

Table 1: The indexes comparison of point target performance.

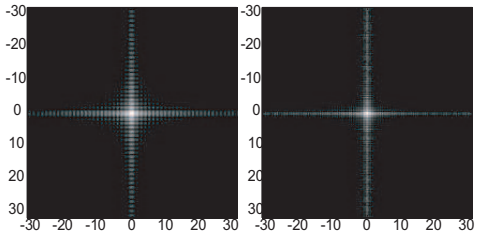

(a) RD Method (b) The Paper's Method

Figure 4: The results comparison of two methods.

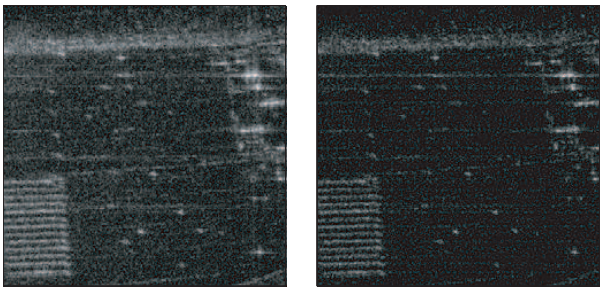

(a) RD Method (b) The Paper's Method

Figure 5: The results comparison of two methods.

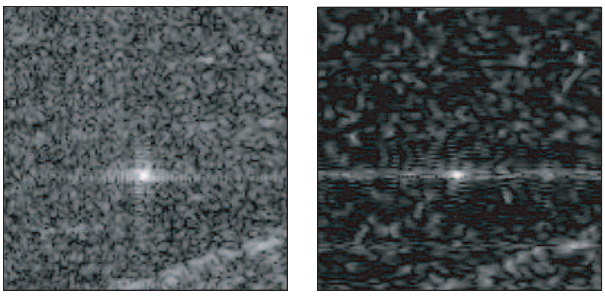

(a) RD Method (b) The Paper's Method

Figure 6: The results comparison of calibration point.

result of Range Doppler imaging method (RD) and (b) is the result of two times data extrapolation by the paper's method. Table 1 is the indexes comparison of point target performance. From the figure and the table, we can see the resolution improved for almost one time.

In order to validate the effectiveness of real measured data, the X band aircraft SAR data is used, of which the resolution is 2.5 m × 2.5 m and the height of aircraft is 10 km. Fig. 5 is the comparison of processing results. (a) is the result of range Doppler imaging method and (b) is the result of 2D AR linear prediction extrapolation. The calibration point is selected to analysis the performance quantitatively. Fig. 6 is the comparison of the calibration point. (a) is the result of RD imaging method and (b) is the result of 2D AR linear prediction extrapolation. Table 2 is the indexes comparison of point target performance. From the figure and the table, we can see the resolution improved obviously. However, for the sake of noise effect, the model is not accurate enough to lose the performance of PLSR and ISLR.

Table 2: The indexes comparison of point target performance.

Performace	RD method	The Paper's Method
Range resolution (m)	2.5886	1.4287
Range PSLR(dB)	−24.5681	−17.8467
Range ISLR(dB)	−16.4489	−15.1185
Azimuth resolution(m)	2.5423	1.5876
Azimuth PSLR(dB)	−11.4356	−8.7206
Azimuth ISLR(dB)	−7.0187	−6.2644

6. CONCLUSION

In this paper, we present a SAR bandwidth extrapolation method to improve SAR image resolution based on two-dimensional linear prediction extrapolation. The method uses the SLC SAR image signal model as the prior information to estimate the 2D AR parameters. According to the 2D AR linear prediction model, the lap-to-lap approach is used for the extrapolation of the efficient bandwidth to obtain a large dimension frequency domain spectrum. From the process of simulation and real measured data, we can obtain the better results using the paper's method after quantitative analysis.

REFERENCES

1. Curlander, J. C. and R. N. McDonough, *Synthetic Aperture Radar Systems and Signal Processing*, John Wiley & Sons, Inc., 1991.
2. Lawrence Marple, Jr., S., "A fast algorithm for the two-dimensional covariance method of linear prediction," *1995 International Conference on Acoustics, Speech, and Signal Processing, ICASSP-95*, Vol. 3, 1693–1696, Detroit, MI, USA, 1995.
3. Lawrence Marple, Jr., S., "Two-dimensional lattice linear prediction parameter estimation-method and fast algorithm," *IEEE Signal Processing Letters*, Vol. 7, No. 6, 164–168, 2000.
4. Aksasse, B. and L. Radouane, "Two-dimensional autoregressive (2-D AR) model order estimation," *IEEE Transactions on Signal Processing*, Vol. 47, No. 7, 2072–2079, 1999.
5. Aksasse, B., L. Badidi, and L. Radouane, "A rank test based approach to order estimation — Part I: 2-D AR models application," *IEEE Transactions on Signal Processing*, Vol. 47, No. 7, 2069–2072, 1999.
6. Erer, I., M. Kartal, and A. H. Kayran, "2-D data extrapolation for high resolution radar imaging using autoregressive lattice modelling," *IEE Proc. — Radar, Sonar Navig.*, Vol. 148, No. 5, 277–282, 2001.

Construction of a Global Database of Surface Reflectance and Emissivity at a Sub km Resolution

L. Gonzalez[1], **F.-M. Bréon**[2], **and X. Briottet**[3]

[1]LOA UFR de Physique, Université des Sciences et Technologies de Lille
F-59655 Villeneuve d'Ascq Cedex, France
[2]LSCE-Orme, point courrier 129, CEA-Orme des Merisiers, F-91191 Gif-sur-Yvette Cedex, France
[3]ONERA/DOTA, 2 Avenue E. Belin, BP 74025, F-31055 Toulouse, France

Abstract— The MODIS instruments have been flying onboard the Terra and Aqua platforms and acquire Earth observation data since early 2000 and mid 2002. Data processing allows the monitoring of the land cover dynamic. Here, a data processing scheme is described to generate Earth reflectance and emissivity time series at a sub-kilometer spatial resolution and with a period of 8 days. The data processing allows the identification of artifacts generated by clouds, aerosols or other unwanted effects that corrupt the time series. In addition, a bidirectional reflectance model, depending on the surface cover type, is applied to i) normalize the reflectance to a constant viewing geometry and ii) compute a land surface albedo.

A web-service tool has also been developed for an easy analysis of the reflectance images and their time-evolution. It is expected that the database and the tool will help researchers to identify and quantify the anthropogenic impact on the Earth surface cover, and the impact of naturally-induced disturbances such as fires, floods or droughts.

1. INTRODUCTION

The management of forest resources, the improvement of estimates of the Earth's water and energy cycles, and the modelling of climate and global carbon exchange among land, and the atmosphere need an accurate climatology of land cover. Furthermore, the design of new space mission requires also a precise land cover database which must cover the entire spectral optical range. The main request of such data set is its realism in a statistical sense. Remote sensing from space is the better alternative to build such global land cover. A first land cover at 1 km of resolution, with a period of 10 days, have been produced from data collected in 1992 and 1993 by the National Oceanic and Atmospheric Administration's Advanced Very High Resolution Radiometer (Global Land 1 km AVHRR http://edc2.usgs.gov/1KM/comp10d.php) but was limited by the limited number of bands and the number of soil type.

More recently the GlobCover, [http://postel.mediasfrance.org/en/PROJECTS/Preoperational-GMES/GLOBCOVER/] program using MERIS acquisitions, delivers a bimonthly composite at a 300 meter spatial resolution, along 1 year. Its main drawbacks are a limited spectral range, but also some artefacts introduced by the cloud filtering.

The Terra satellite was launched in December 1999 and the Aqua one in May 2002. Both of these NASA platforms carry the MODIS instrument. The high-resolution spectrometer acquires continuously images of the Earth at a resolution between 250 m and 1 km, depending on the spectral band, in the visible, solar infrared and thermal infrared. Their measurements serve many scientific and operational objectives. In this paper, we focus on the monitoring of land surfaces dynamics. MODIS [MOD09A1 product (http://modis.gsfc.nasa.gov/data/atbd/atbd_mod08.pdf)] has been developed to identify the surface cover type, to quantify the vegetation primary productivity, to monitor the surface snow cover, and to analyze the impact of natural and anthropogenic disturbances to the surface cover and the vegetation state. MODIS on board Terra and Aqua platforms are a good opportunity to refines global land cover. Boston University in Boston, Mass., developed maps based on a digital database of Earth images collected between November 2000 and October 2001. "These maps, with spatial resolution of 1 kilometer (6 mile), mark a significant step forward in global land cover mapping by providing a clearer, more detailed picture than previously available maps," says Mark Friedl, one of the project's investigators. Such global land cover is able to distinguished 17 different soil types.

MODIS acquisitions are routinely processed and the deduced top-of-atmosphere reflectance is corrected from atmospheric effects to generate their surface counterparts. The resulting products are distributed by NASA. Although these products have received a high interest and are very

widely used, some artifacts may be pointed out due to the unscreened atmospheric influence or other unwanted effects (see 2.2). Besides, the reflectance time-series show a large variability that is due to the anisotropic properties of land surface reflectance. This variability makes difficult the interpretation of time series by non specialists. In addition, data access is not straightforward and requires some experience. This paper aims to describe the processing on MODIS data set to build this database accessible through an easy-to-use web interface. It is built with a frequency of 8 days and re-projected on a "plate-carree" grid ($+-85°/+-180°$) and contains the spectral reflectance (respectively emissivity) in all the MODIS wavelengths at a resolution of 500 m (resp. 1 km). Original data is cleaned from all pixel anomalies. Moreover, ground reflectances are corrected from bi-directionality effects and normalized at a fixed sun and viewing geometry. From this data base, directional surface reflectance and albedo or integrated spherical albedo can be deduced.

In Section 2 the developed algorithm identifying corrupted measurements, correcting the data and normalizing the directional effects is described. Section 3 provides a comparison of this database to the standard MODIS products. Finally, conclusions are given in Section 4.

2. ALGORITHM DESCRIPTION

2.1. Input Data

The reflectance NASA MOD09A1 product constitutes the input of our processing chain, which also contains geophysical parameters. This product is available for the two instruments that are on board the TERRA and AQUA platforms. In particular, the product includes the surface reflectance, after atmospheric compensation, in 7 spectral bands ranging from 459 nm to 2155 nm with a spatial resolution of 500 meters and a temporal resolution of 8 days gridded by a sinusoidal projection. The temporal composite does not average the measurements but rather samples the best observation of the period. "Best" is defined as no significant aerosol or cloud, absence of cloud shadow, and low view angle.

For emissivity, the NASA MOD11 product (http://modis.gsfc.nasa.gov/data/atbd/atbd_mod1-1.pdf) is used which contains level 2 and 3 land surface temperature and emissivity retrieved from MODIS data at spatial resolutions of 1 km and 5 km over global land surfaces under clear-sky conditions.

The directional signature correction, described below, requires the knowledge of the surface type. To this end, the BOSTON university land cover product MOD12 is used to classify each pixel according to the International Geosphere-Biosphere Program (IGBP, http://www.igbp.net/) scheme. This set of cover types includes eleven categories of natural vegetation covers broken down by life form, three classes of developed and mosaic lands, and three classes of non-vegetated lands [1]. (http://modis.gsfc.nasa.gov/data/atbd/atbd_mod12.pdf).

2.2. Filter Algorithms and BRDF Corrections

Despite its overall quality, the MODIS products include many anomalous measurements due to:

- data transmission errors that have not been detected in pre-processing,
- anomalies in the cloud detection, presence of cloud shadows,
- anomalies in snow detection,
- strong directional effects.

A 4 steps algorithm is proposed which aims to keep the general dynamic of the original measurements, reject the contaminated measurements, and to rebuild the incomplete time series as close as possible to reality. These 4 steps are:

1. Filter the contaminated pixels from clouds and cloud shadows based on a contrast method,
2. Apply BRDF corrections and compute the mean values over 4 consecutive 8-days periods for both satellites.
3. Fill the missing measurements through either a simple temporal interpolation or by using data from a nearby pixel with a similar signature and classification.
4. Final generation and projection.

2.2.1. Step 1: Contaminated Pixel Filtering and Pixel Mean Value Computation

The analysis of MODIS products shows a large number of erroneous pixels. In most cases, the contamination can be traced back to clouds or cloud shadows directly affecting the signal level. To detect this artifact, a spectral contrast test is developed, refered to as the "pixel contrast ratio"

Figure 1: True color composite of land surface reflectances for an area located in Nigeria (−9.53W, −6.063E, 8.53N, 6.15S) (January 17). The reflectances are derived from a composite of 4 MOD09 periods. The magenta pixels are those rejected as definitely cloudy. On the left image, in orange, we can observe all the areas where the PCR test rejects at least one data among the 8 input values (scratch from bad inputs are clearly detected). On the right image, in yellow, we see all the areas where less than 5 pixels are available to compute the mean reflectance result.

(PCR). It is based, in the visible, that cloudy and shadow pixels have a lower spectral contrast than their uncontaminated counterpart. One therefore defines the contrast P as the standard deviation on the spectral reflectance in the three following bands: 0.459, 0.545, 0.620 µm, divided by the mean reflectance:

$$P = \frac{1}{\overline{x_\lambda}} \sqrt{\sum_{i=1}^{3} (x_{\lambda_i} - \overline{x_\lambda})^2}$$

where x_{λ_i} is the measured reflectance in band λ. A pixel is declared contaminated by a cloud if the contrast P is smaller than a threshold $T_{\text{cloud\_shadow}}$. This threshold, $T_{\text{cloud\_or\_shadow}} = 0.04$, is empirically estimated by selecting several mid latitudes and equatorial geographic areas, the threshold is increased until the extinction of all bad pixels clearly seen. Furthermore, the optimal number of pixels we can collect to determine the mean value is 8 (4 periods of 8 days and two satellites). However, after applying this test, a significant number of areas have just a few available pixels and the threshold must be auto adjusted to increase the number of data sets. In the case where less than 3 pixels fit the initial threshold condition, $T_{\text{cloud\_or\_shadow}}$ is decreased step by step, until finding enough pixels to compute the mean value. In this case, the corresponding pixels are flagged "suspicious" and will be kept or rejected by the times series analysis. Since, this test also rejects pixels naturally bright or dark, the further analysis of the time series will aim to recover these very non-common areas.

Figure 1 illustrates the impact of the PCR method over an area located in Nigeria. A true color composite is built using the mean value of the reflectance computed over 4 periods in January. In magenta are inlayed the definitely cloudy areas for the period. In orange appear all the pixels where the PCR test rejects at least one data from the 8 input values (Scratch from bad inputs are clearly detected). Yellow pixels in the right display the areas where less than 5 pixels are available to compute the mean values.

2.2.2. Step 2: Bidirectional Signature Correction

Land surface reflectances vary by a factor of more than two over the observation geometry range. For a good analysis of the time series, it is therefore essential to normalize the measurements to a reference observation geometry.

The BRDF correction depends on both the type of the landscape (or biome assuming it as homogeneous) and the viewing geometry (sun, satellite). The biome is defined from the IGBP product where 17 ones are identified. Thus, the corresponding BRDF correction is defined as follow:

$$\rho(40,\ 0,\ 0)^* = \rho(\theta_s,\ \theta_v,\ \Phi) \cdot \frac{\text{BRDF}(40,\ 0,\ 0)}{\text{BRDF}(\theta_s,\ \theta_v,\ \Phi)}$$

where $\rho(\theta_s,\ \theta_v,\ \Phi)$ represents a MODIS acquisition in a given band in the viewing conditions defined by the θ_s solar zenithal angle, the θ_v satellite zenithal angle and the Φ difference between the solar and instrument azimuths, $\text{BRDF}(\theta_s,\ \theta_v,\ \Phi)$ is the BRDF model attached to a given biome. The reference geometry is defined as $\theta_s = 40°$, $\theta_v = 0°$, $\Phi = 0°$.

For most of the biomes, the "*Ross-Li Hot Spot*" model is used [3].

$$\mathrm{BRDF}(\theta_s,\ \theta_v,\ \Phi)^* = k_0 \left[1 + \frac{k_1}{k_0} \cdot F_1(\theta_s,\ \theta_v,\ \Phi) + \frac{k_2}{k_0} \cdot F_2(\theta_s,\ \theta_v,\ \Phi)\right]$$

For a given biome, its corresponding parameters (k_0, k_1, k_2) are estimated with POLDER and PARASOL [2, 3] measurements over several soil type defined by their normalized difference vegetation index (NDVI). Four intervals of NDVI are considered: $[-0.2, 0.2]$, $[0.2, 0.5]$, $[0.5, 0.8]$, $[0.8, 1.0]$.

Over bright areas like desert, a low estimation of the reflectance appears which is corrected by an iterative algorithm where the initial Ross-Li coefficients are fitted using the measured reflectance: (B) $\frac{k_2}{k_0} = a_\lambda \cdot k_{0,\lambda\_\mathrm{typic}} + b_\lambda$ with the initial value $k_0 = \frac{\rho_{\mathrm{ref\_measure}}}{1+C\cdot F_1+\frac{k_2}{k_0}\cdot F_2}$, C being a constant.

For the snow biome, the reflectance model of A. Kokhanovsky & E. P. Zege [4] is used for this normalization process. By selecting the normalized clean pixels from a window of 4 periods, a mean value $\overline{\rho(40,\ 0,\ 0)^*_{\lambda_i t}}$ is then computed for each band:

$$\overline{\rho(40,\ 0,\ 0)^*_{\lambda_i t}} = \frac{1}{M} \sum_{j=t}^{t+M} \rho(40,\ 0,\ 0)^*_{\lambda_i j}$$

where M is the number of remaining pixels on the 4 periods of index j in a given band λ_i.

The operation is then repeated all year long with a shift of one period.

2.2.3. Step 3: Time Series Reconstruction

As discussed above, after the step one, each pixel is flagged (good, cloudy, snow or suspicious).

By studying along the year the variation of each pixel, the cloudy areas in the images is rebuilt and kept or rejected. The analysis of many areas enables us to classify the times series into specific patterns of missing data and then three main families are identified, each with a different correction protocol:

- **Ideal time series**: alternating cloudy and clear pixels. The pixels reconstruction is carried out by interpolating the missing cloudy level between the clear pixels. Note that in the case where the gap between two successive clear pixels is important the interpolation is based on the use of the closest similar biome. Around the pixel to rebuild, we search a similar biome containing the missing values with the best correlation for the common values. The missing values are then pick up from the similar biome and normalized by the ratio of the averaged signal of the two biomes.
- **Time series very cloudy:** The reconstruction is carried out by interpolation using a close similar biome.
- **Time series with permanent indetermination:** The flag suspicious is cleared and the reconstruction of the cloudy pixels is performed as above.

2.2.4. Step 4: Final Generation and Projection

The results expressed in the MODIS geographic coordinates (sinusoidal representation) are then projected in a plate-carrée representation in an HDF compressed format. Original 1 km data is remapped at 500 m by a near pixel interpolation. The land surface temperature and emissivity are provided by TERRA and AQUA. Some ancillary data as biome type and vegetation index allows estimating the reflectance in any geometry.

This new product, FDS, is implemented in an intuitive and simple interface able to browse the huge volume of data and to extract from an area of interest the information such as values, graphics or images. To this end, existing graphic packages (Mgraph, HDFLook...) are used to display the results with a reasonable delay. (http://www-loa.univ-lille1.fr/).

3. VALIDATION

This validation is conducted in two stages. The first one follows a qualitative procedure based on simple observations of the resulting time series over several landscapes. Such analysis allows detecting possible artifact introduced by our algorithm. As an illustration, a very cloudy area (Figure 2) in the Northwest of Argentina (W63.23°, S24.72°) is given where the temporal extension of a farm area and the seasonal vegetation changes, period by period of 8 days, may be pointed out.

In a second step, the reflectance product (FDS) is compared with a similar MODIS Land group product (MCD43A1 MODIS/Terra Albedo 8-Day L_3 Global 500 m SIN Grid Version 5). Over the same very cloudy Nigerian region of Figure 1 and the same period of time, we built a true color composite of the albedo products (Figure 3) without the time series reconstruction (step 3). As clearly seen in the left side, FDS results are less affected by cloudy or bad pixels.

In Figure 4 we divide the globe by 1×1 degree^2 boxes and we display the relative variation between both albedos at 620–670 nm for the period of January 17, 2006. The variation coefficient (v) is computed as

$$v_{=}1.0 - \frac{\bar{\alpha}_{mcd43a1}}{\bar{\alpha}_{fds}}$$

Figure 2: True color composite for 46 8-day periods in 2006 (sinusoidal projection). The images focus on a 50×35 km area in the North-West of Argentina. Note the appearance of clear pixels that indicates the extension of an agriculture area over the surrounding vegetation.

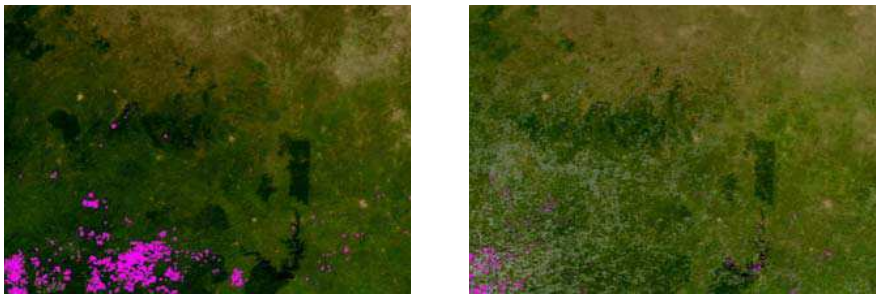

Figure 3: Impact of the pixel filtering over the same area of Nigeria as Figure 1. On the left the final FDS mean values before the time series reconstruction on the right the MCDA1 product result for the same period.

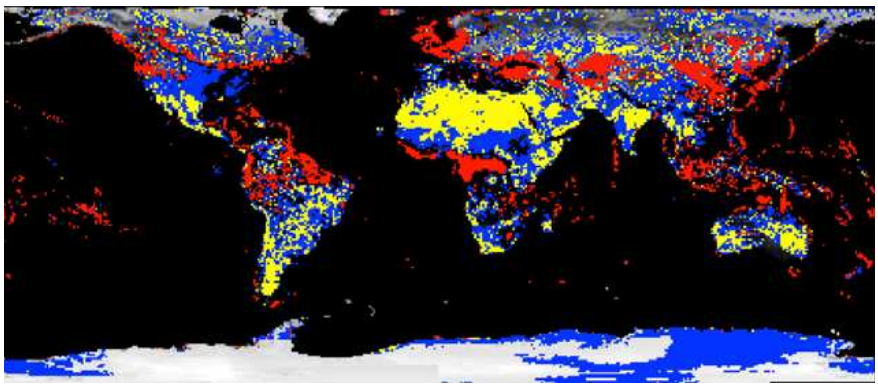

Figure 4: Relative variation between MCD43A1 albedo and FDS albedo at 620–670 nm for the period of January 17, 2006. Yellow pixels show the areas with ±3% of variation, blue pixels show a variation of ±10% and red pixels point to areas with an over estimation of 30% for MCD43A1 compared with FDS values. These regions correspond to very cloudy areas.

where $\bar{\alpha}$ is the mean albedo value within the box.

The result shows a very good agreement in the desert regions the yellow pixels show $\pm 3\%$ of variation and an huge difference over the frequently cloudy regions the red pixels point out areas with an over estimation of 30% of MCD43A1 compared to FDS.

4. CONCLUSION

A new and improved land cover data base is presented using MODIS measurements. The main improvements in comparison with the nominal MODIS product a better cloud filtering, an improved discrimination between cloud and snow and a temporal interpolation for screened pixels during an entire 8 days period.

The validation phase shows that most artifacts have been removed and that the time-series are very consistent with a reduced high frequency behavior.

However, the use of such FDS data base remains limited by a huge volume of data, a spectral reflectance only known in the MODIS bands and finally only one year of MODIS data has been processed. In the future, to make our database more statistically representative, we plan to process more years of MODIS acquisitions. Then, to reduce the volume of data a statistical approach will be taken into account. The main track, which will be investigated, is the evaluation and modeling of the temporal variability of every biome by band of latitude. At last, the spectral extension will be studied. Our purpose is to have a statistical estimation of every spectral reflectance whatever the wavelength in the entire optical domain. Finally, the ground reflectance climatology will be integrated in our 3D radiative transfer code MATISSE to improve the design of new remote sensing sensors.

ACKNOWLEDGMENT

The authors wish to thank Christine Deroo for her invaluable technical advice and web site development, Emilie Fedele for the BRDF algorithm development over bright surfaces.

This study was funded by the French Ministry of Defense under MIRA program.

Data was collected from the Land Process Distributed Active Archive Center (http://edcimswww.cr.usgs.gov/pub/imswelcome/).

REFERENCES

1. Friedl, M. A., D. K. McIver, Z. Y. hang, J. C. F. Hodges, A. Schnieder, A. Bacinni, A. H. Strahler, A. Cooper, F. Gao, C. Schaaf, and W. Liu, "Global land cover classification results from MODIS," *IEEE 2001 International Geoscience and Remote Sensing Symposium, IGARSS apos01*, Vol. 2, No. 2001, 733–735, 2001.
2. Bacour, C., F.-M. Bréon, and F. Maignan, "Normalization of the directional effects in NOAA/AVHRR reflectance measurements for an improved monitoring of vegetation cycles," *Rem. Sens. Env.*, Vol. 102, 402–413, 2006.
3. Maignan, F., F. M. Bréon, and R. Lacaze, "Bidirectional reflectance of earth targets: Analytical modeling and validation against a large data set of satellite observations," *Rem. Sens. Env.*, Vol. 90, 210–220, 2004.
4. Kokhanovsky, A. A. and E. P. Zege, "Scattering optics of snow," *Appl. Opt.*, Vol. 43, No. 7, 1589–1602, March 1, 2004.

A New Concept of Cold Atom Using Fast Optical Tweezers

B. Jakgoljun, **K. Srinuanjan**, **S. Kamoldilok**, **and P. P. Yupapin**
Advanced Research Center for Photonics, Faculty of Science
King Mongkut's Institute of Technology Ladkrabang, Bangkok 10520, Thailand

Abstract— We propose a new concept of a cold atom generation using a tiny optical device system. A system consists of a multi-stage nonlinear micro-ring system incorporating an add/drop filter, which the storage unit can be formed the fast tweezers and the cold atom concept presented. In operation, the optical tweezers can be generated by using a Gaussian pulse input into the microring system, where the amplified and tuned optical tweezers using a light pulse propagating within an add/drop filter. By using the suitable parameters such as ring radii, effective areas, coupling coefficients and refractive indices, an atom/particle can be trapped by the specific optical tweezers and propagating within a storage ring. Results obtained have shown that the fast tweezers time is approached the negligible value, where the terms of time independent motion of atom/particle can be performed by using the fast tweezers, and the cold atom concept is obtained. In application, such a technique can be used to form the similar manner for molecule, DNA, photon, or Ion, where the memory unit of them can be formed, which will be available for a hybrid memory or computer in the near future.

1. INTRODUCTION

A concept of cold atom or atom traps has been proposed world wide, such as Bose-Einstein Contestation (BEC), optical lattice or optical tweezers and laser cooling [1–3]. According to a concept of laser cooling, a laser beam was pointing opposite to the direction of the atoms. An atom will absorb photons and it will lose a momentum equal to the momentum of the photon. If the atom, which is now in the excited state, emits a photon spontaneously, it will be kicked by the same amount of momentum but in a random direction. The result of the absorption and emission process is to reduce the speed of the atom, provided its initial speed is larger than the recoil velocity from scattering a single photon. If the absorption and emission are repeated many times, the mean velocity, and therefore the kinetic energy of the atom will be reduced. Since the temperature of an ensemble of atoms is a measure of the random internal kinetic energy, this is equivalent to cooling the atoms. So we have an atom that is practically motionless (a "cold" atom). We can also use a concept of optical tweezers to cold an atom [2], by exerting extremely small forces via a highly focused laser beam. The beam is typically focused by sending it through a microscope objective. The narrowest point of the focused beam, known as the beam waist, contains a very strong electric field gradient. It turns out that dielectric particles are attracted along the gradient to the region of strongest electric field, which is the center of the beam. The laser light also tends to apply a force on particles in the beam along the direction of beam propagation. It is easy to understand why if one considers light to be a group of particles, each impinging on the tiny dielectric particle in its path. This is known as the scattering force and results in the particle being displaced slightly downstream from the exact position of the beam waist, so an atom can be guided along the optical path [4, 5]. There are several ways to achieve cold atom by those concepts, such as the concept of cold atom toolbox [6] to trap and control the atom but in this paper we propose a new concept of cold atom by using fast optical tweezers method. There for the source of laser was presented and designed by P. P. Yupapin et al. [7–9], which its intensity and wavelength can be adjust and controllable.

2. OPERATING AND PRINCIPLE

To generate the specific wavelength of light pulse, the simple device schematic diagram is as shown in Fig. 1, when light from a monochromatic light source is launched into each ring resonator with constant light field amplitude (E_0) and random phase modulation (ϕ_0), which results in temporal coherence degradation. Hence, the input light field (E_{in}) can be expressed as

$$E_{in}(t) = E_0 \exp^{j\phi_0(t)} . \quad (1)$$

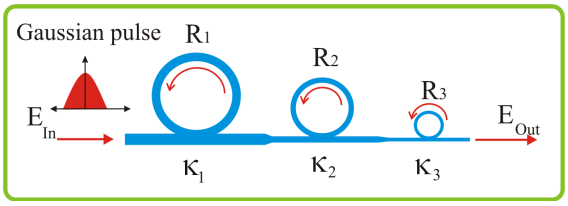

Figure 1: A schematic of the fast optical tweezers system.

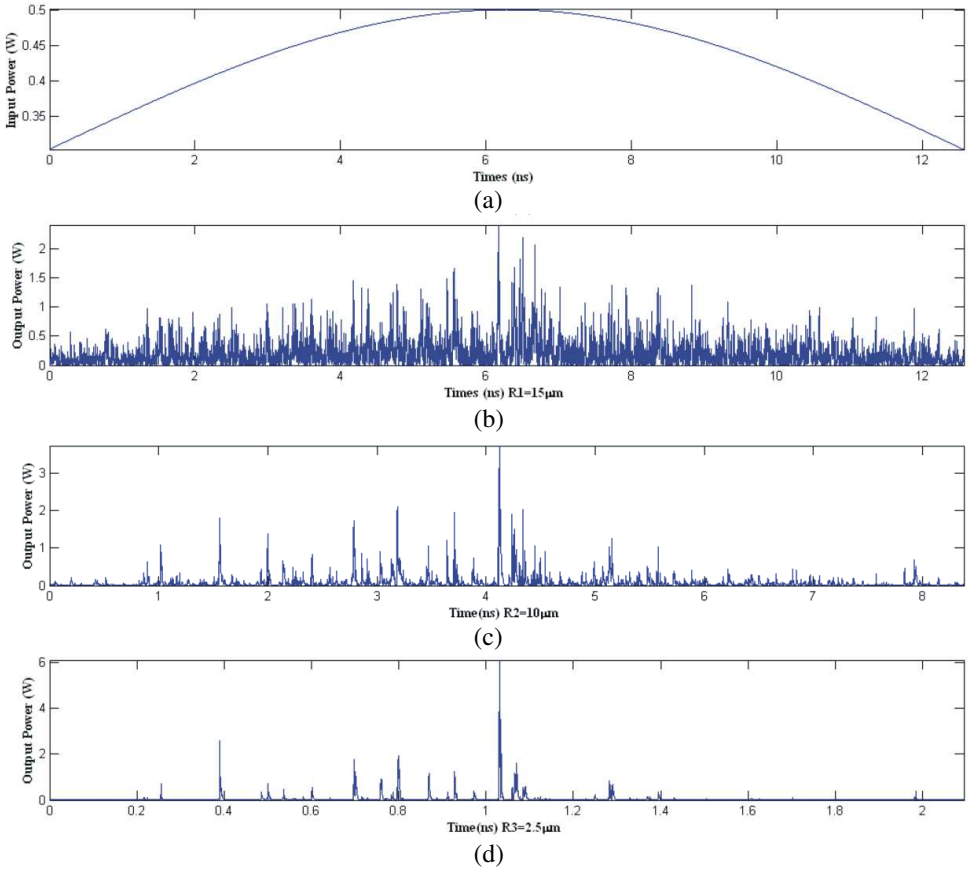

Figure 2: Simulation Result with Gaussian pulse is input into a micro-ring system.

We assume that the nonlinearity of the optical ring device is of the Kerr-type, i.e., the refractive index is given by

$$n = n_0 + n_2 I = n_0 + \left(\frac{n_2}{A_{eff}}\right) P, \tag{2}$$

where n_0 and n_2 are the linear and nonlinear refractive indexes, respectively. I and P are the optical intensity and optical field power, respectively. The effective mode core area of the device is A_{eff}. Thus, the normalized output of the light field can be expressed as

$$\left|\frac{E_{out}}{E_{in}}\right|^2 = (1-\gamma)^2 \left[1 - \frac{\kappa\left[1-(1-\gamma)^2\tau^2\right]}{1+(1-\gamma)^2(1-\kappa)\tau - 2(1-\gamma)\sqrt{1-\kappa}\tau\cos\phi}\right]. \tag{3}$$

The close form of Equation (3) indicates that a ring resonator in the particular case to very similar to a Fabry-Perot cavity, which has an input and output mirror with a field reflectivity, $1-\kappa$, and a fully reflecting mirror. where n_0 and n_2 are the linear and nonlinear refractive indices, the coupling coefficient is κ. Where $x = \exp^{-\frac{\alpha L}{2}}$ represents the one round-trip losses coefficient, $\phi_0 = kLn_0$ and $\phi_{NL} = kLn_2\left|E_1\right|^2$ are the linear and nonlinear phase shifts, $k = 2\pi/\lambda$ is the wave propagation number in a vacuum, respectively.

This nonlinear behavior of light traveling in a single ring resonator (SRR) is described. When the parameters of the system are fixed to optical input power = 500 mW, $\lambda_0 = 1.55\,\mu m$, $n_0 = 3.34$, $A_{eff} = 25\,\mu m^2$, where the waveguide ring resonator loss is $\alpha = 0.5\,dBmm^{-1}$. The propagation loss as low as $1.3 \pm 0.02\,dBmm^{-1}$ at $1.55\,\mu m$, where the fractional coupler intensity loss is $\gamma = 0.1$, and $R_1 = 15\,\mu m$, $R_2 = 10\,\mu m$ and $R_3 = 2.5\,\mu m$. The coupling coefficient of the fiber coupler κ is approximately 0.9. The nonlinear refractive index used is $n_2 = 2.2 \times 10^{-15}\,m^2W^{-1}$, and the data of 40,000 iterations of roundtrips inside the optical micro ring is plotted. We assume that $\phi_L = 0$ for simplicity, however, the change in phase is slightly altered the optical output, which means the dispersion can be neglected when the resonant output is occurred.

3. SIMULATION RESULT AND DISCUSSION

Figure 2(a) show the Gaussian input pulse and Figs. 2(b)–(d) show the output pulse from micro-ring system with ring radius of 15 μm, 10 μm, and 2.5 μm respectively. The maximum peak occurred at 6.15 ns for the first ring and the time it take for the other round trips, for second ring, is reduce to 4.1 ns, and finally for the third ring which smaller radius, the maximum peak is reduce to the minimum value at 1.0 ns. The simulation results show that the time for revolution is reduced when ring radius is deceased.

4. CONCLUSION

According to the integrated system the laser intensity and wavelength can be controlled to achieve the source of laser for optical tweezers, the laser was fired into a cloud of atoms that had been deep chilled into a slow-moving state known as a Bose-Einstein condensate. and then randomly the atom could be trapped, by mean of fast optical tweezers and the hold system, laser and atom, has been launched into the other optical ring resonator, even if the ring radius is small the time it takes for revolution is vary shot, approximately 1.0 ns and could be approach to zero value if the ring radius is sufficiently small. Then the system is adiabatic process, because it's no heat transfer between system and environment that mean cold atom concept has been achieved. In conclusion several concepts of cold atom have been shown and discussion, and also the new concept of cold atom. The results and discussion shows that it is possible to cold atom by using fast optical tweezers.

ACKNOWLEDGMENT

We would like to give our acknowledgement to the Faculty of Science, King Mongkut's Institute of Technology Ladkrabang, Bangkok 10520, Thailand for the partially supporting of this research project.

REFERENCES

1. Fioretti, A., J. Lozeille, C. A. Massa, M. Mazzoni, and C. Gabbanini, "An optical trap for cold rubidium molecules," *Optics Communications, Science Direct*, Vol. 243, 203–208, 2004.
2. Dong, G., W. Lu, P. F. Barker, and M. N. Shneider, "Cold molecules in pulsed optical lattices," *Progress in Quantum Electronics, Science Direct*, Vol. 29, 1–58, 2005.
3. Moiseyev, N., M. Šindelka, and L. S. Cederbaum, "Trapping of cold atoms in optical lattices by the quadrupole force," *Physics Letters A, Science Direct*, Vol. 362, 215–220, 2007.
4. Pruvost, L., D. Marescaux, O. Houde, and H. T. Duong, "Guiding and cooling of cold atoms in a dipole guide," *Optics Communications, Science Direct*, Vol. 166, 199–209, 1999.
5. Rhodes, D. P., G. P. T. Lancaster, J. Livesey, D. McGloin, J. Arlt, and K. Dholakia, "Guiding a cold atomic beam along a co-propagating and oblique hollow light guide," *Optics Communications, Science Direct*, Vol. 214, 247–254, 2002.
6. Jaksch, D. and P. Zoller, "The cold atom Hubbard toolbox," *Annals of Physics, Science Direct*, Vol. 315, 52–79, 2005.
7. Yupapin, P. P., N. Pornsuwancharoen, and S. Chiyasoonthorn, "Generalized fast, slow, stop and store light optically within a nano-ring resonator", *Microw., and Opt., Technol., Lett.*, Vol. 51, No. 4, 899–902, 2009.
8. Pornsuwancharoen, N., Y. Fujii, K. Srinuanjan, and P. P. Yupapin, "A novel system of the simulataneous trapping of dark-bright solitons within a nano-waveguide system," *Optik, Science Direct*, 2009.
9. Yupapin, P. P. and N. Pornsuwancharoen, "Proposed nonlinear micro-ring resonator arrangement for stopping and storing light," *IEEE Photon., Technol., Lett.*, Vol. 21, No. 4, 404–406, 2009.

Novel Nanoscale Signal Processing and Networking via a Wavelength Router

P. Youplao[1], **S. Mitatha**[1], **and P. P. Yupapin**[2]

[1]Hybrid Computing Research Laboratory, Faculty of Engineering
King Mongkut's Institute of Technology Ladkrabang, Bangkok 10520, Thailand
[2]Advanced Research Center for Photonics, Faculty of Science
King Mongkut's Institute of Technology Ladkrabang, Bangkok 10520, Thailand

Abstract— This paper presents the very fascinating simulation results of light pulse traveling within a ring resonator system that have shown the unexpected results with various applications. The design system consists of a nonlinear microring/nanoring resonator system incorporating an add/drop filter. The proposed fabricated material used is InGaAsP/InP, which can provide the required output behaviors. Three different forms of input light pulses are Gaussian pulse, dark and bright soliton, whereas the suitable simulation parameters are input power, pulse width, ring radii and the material refractive indices. Three different forms of the results have been interpreted, whereas the dominants behaviors are such as Gaussian soliton, multisoliton and tunable dark soliton, and the potential applications for new laser sources, new communication bands, dynamic optical tweezers and high frequency source THz technology. The use of the proposed system incorporating a nanoscale communication and networking via wavelength router is discussed.

1. INTRODUCTION

Nanotechnology has become the major role in modern technology today. The use of pulse laser in nano-device system has been the interesting aspects where many applications can be provided. A Gaussian pulse has been recognized in the form of a laser pulse that can be used in both theoretical and experimental investigation in many subjects. However, in some ways, the limit of laser power cause a problem. Optical soliton becomes a powerful tool that can overcome such a problem, i.e., for high power laser source. Furthermore, the non-dispersion of soliton in medium is the other advantage. Optical solitons can naturally be divided into classes of dark and bright solitons, whereas a dark soliton exhibits an interesting and remarkable behavior, when it is transmitted into an optical transmission system. It has the advantage of the signal detection difficulty, when the ambiguity of signal detection becomes a problem for the un-wanted users. In principle, the soliton generations and their behaviors in media are well analyzed and described by Agarwal [1]. Many earlier theoretical and experimental works on soliton applications can be found in the soliton application book by Hasegawa [2]. However, to make such a tool more useful, the problems of soliton-soliton interactions [3], collision [4], rectification [5], and dispersion management [6] must be solved and addressed. Therefore, in this work, we are looking for a powerful laser source with broad spectrum that can be used in many applications.

2. OPERATING PRINCIPLE

Light from a monochromatic light source is launched into a ring resonator with constant light field amplitude (E_0) and random phase modulation as shown in Fig. 1(a), which is the combination of terms in attenuation (α) and phase (ϕ_0) constants, which results in temporal coherence degradation. Hence, the time dependent input light field (E_{in}), without pumping term, can be expressed as [7] where L is a propagation distance (waveguide length).

$$E_{in}(t) = E_0 \exp^{-\alpha L + j\phi_0(t)} \tag{1}$$

We assume that the nonlinearity of the optical ring resonator is of the Kerr-type, the refractive index is given by

$$n = n_0 + n_2 I = n_0 + n_2 \left(\frac{P}{A_{eff}} \right) \tag{2}$$

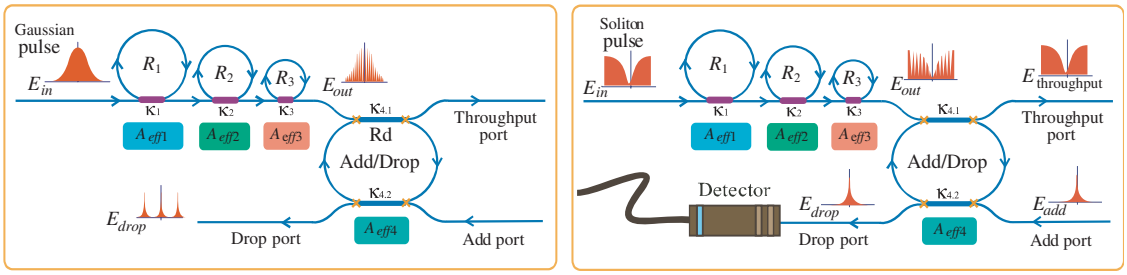

Figure 1: A schematic of a Gaussian soliton generation system (a), a dark-bright soliton conversion system (b), where R_s: ring radii, κ_s: coupling coefficients, R_d: an add/drop ring radius, A_{effs}: Effective areas.

where n_0 and n_2 are the linear and nonlinear refractive indexes, respectively. I and P are the optical intensity and optical power, respectively. The effective mode core area of the device is given by A_{eff}. For the microring and nanoring resonators, the effective mode core areas range from 0.10 to 0.50 μm^2 [8, 9].

When a Gaussian pulse is input and propagated within a fiber ring resonator, the resonant output is formed, thus, the normalized output of the light field is the ratio between the output and input fields ($E_{out}(t)$ and $E_{in}(t)$) in each roundtrip, which can be expressed as [10].

$$\left|\frac{E_{out}(t)}{E_{in}(t)}\right|^2 = (1-\gamma)\left[1 - \frac{\left(1-(1-\gamma)\,x^2\right)\kappa}{\left(1-x\sqrt{1-\gamma}\sqrt{1-\kappa}\right)^2 + 4\,x\sqrt{1-\gamma}\sqrt{1-\kappa}\sin^2\left(\frac{\phi}{2}\right)}\right] \tag{3}$$

Equation (3) indicates that a ring resonator in the particular case is very similar to a Fabry-Perot cavity, which has an input and output mirror with a field reflectivity, $(1-\kappa)$, and a fully reflecting mirror. k is the coupling coefficient, and $x = \exp(-\alpha L/2)$ represents a roundtrip loss coefficient, $\phi_0 = kLn_0$ and $\phi_{NL} = kLn_2(P/A_{eff})$ are the linear and nonlinear phase shifts, $k = 2\pi/\lambda$ is the wave propagation number in a vacuum. Where L and α are a waveguide length and linear absorption coefficient, respectively. In this work, the iterative method is introduced to obtain the results as shown in Equation (3), similarly, when the output field is connected and input into the other ring resonators.

Bright and dark soliton pulses are introduced into the multi-stage nano ring resonators as shown in Fig. 1(b), the input optical field of the bright and dark soliton pulses input are given by an Equations (4) and (5) [1], respectively.

$$E_{in}(t) = A\sec h\left[\frac{T}{T_0}\right]\exp\left[\left(\frac{z}{2L_D}\right) - i\omega_0 t\right] \tag{4}$$

$$\text{and} \quad E_{in}(t) = A\tan h\left[\frac{T}{T_0}\right]\exp\left[\left(\frac{z}{2L_D}\right) - i\omega_0 t\right] \tag{5}$$

where A and z are the optical field amplitude and propagation distance, respectively. T is a soliton pulse propagation time in a frame moving at the group velocity, T_0 is a soliton pulse propagation time at initial input, where t is the soliton phase shift time, and the frequency shift of the soliton is ω_0.

The input optical field is input into a nonlinear microring resonator. By using the appropriate parameters, the chaotic signal is obtained by using Equation (3). To retrieve the signals from the chaotic noise, we propose to use the add/drop device with the appropriate parameters. This is given in details as followings. The optical outputs of a ring resonator add/drop filter can be given by the Equations (6) and (7).

$$\left|\frac{E_t}{E_{in}}\right|^2 = \frac{(1-\kappa_1) - 2\sqrt{1-\kappa_1}\cdot\sqrt{1-\kappa_2}e^{-\frac{\alpha}{2}L}\cos(k_nL) + (1-\kappa_2)\,e^{-\alpha L}}{1+(1-\kappa_1)(1-\kappa_2)\,e^{-\alpha L} - 2\sqrt{1-\kappa_1}\cdot\sqrt{1-\kappa_2}e^{-\frac{\alpha}{2}L}\cos(k_nL)} \tag{6}$$

$$\text{and} \quad \left|\frac{E_d}{E_{in}}\right|^2 = \frac{\kappa_1\kappa_2 e^{-\frac{\alpha}{2}L}}{1+(1-\kappa_1)(1-\kappa_2)\,e^{-\alpha L} - 2\sqrt{1-\kappa_1}\cdot\sqrt{1-\kappa_2}e^{-\frac{\alpha}{2}L}\cos(k_nL)} \tag{7}$$

where E_t and E_d represents the optical fields of the throughput and drop ports respectively. The transmitted output can be controlled and obtained by choosing the suitable coupling ratio of the ring resonator, which is well derived and described by reference [10]. In the case of add/drop device, the nonlinear refractive index is neglected.

3. RESULTS

From Fig. 1(a), in principle, light pulse is sliced to be the discrete signal and amplified within the first ring, where more signal amplification can be obtained by using the smaller rings device. Finally, the required signals can be obtained via a drop port of the add/drop filter. In operation, an optical field in the form of Gaussian pulse from a laser source at the specified center wavelength is input into the system. From Fig. 2, the Gaussian pulse with center wavelength (λ_0) at 130 µm, pulse width of 20 ns, peak power at 2 W is input into the system as shown in Fig. 2(a). After light is input into the system, the Gaussian pulse is chopped (sliced) into a smaller signal spreading over the spectrum due to the nonlinear effects [11], The large bandwidth signals can be seen within the first, second microring and third nanoring device, and shown in Figs. 2(b), 2(c) and 2(d), respectively.

The suitable ring parameters are used, for instance, ring radii $R_1 = 15.0\,\mu m$, $R_2 = 10.0\,\mu m$, $R_3 = 5.0\,\mu m$, and $R_d = 155.0\,\mu m$. In order to make the system associate with the practical device [8, 9], the selected parameters of the system are fixed to $n_0 = 3.34$ (**InGaAsP/InP**), $A_{eff} = 0.50\,\mu m^2$ and $0.25\,\mu m^2$ for a microring and add/drop ring resonator, respectively, $\alpha = 0.5\,dBmm^{-1}$, $\gamma = 0.1$.

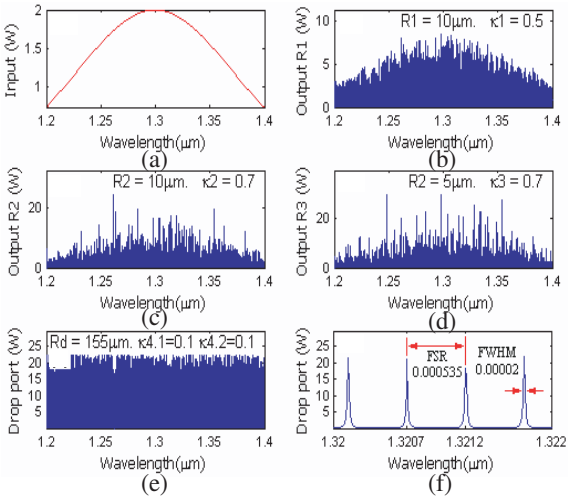

Figure 2: Result of the spatial pulses of Gaussian soliton generation system with center wavelength at 1.3 µm.

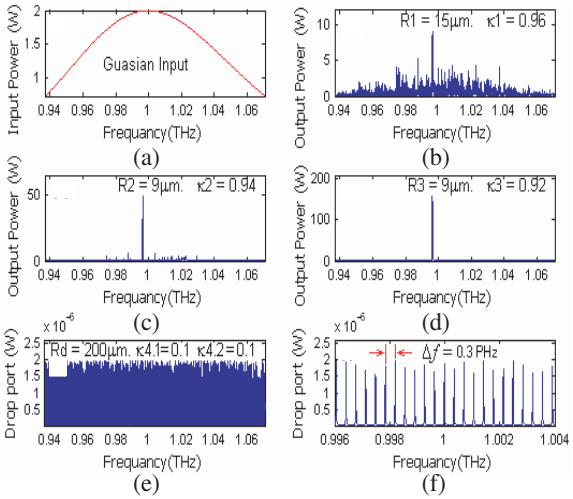

Figure 3: Result of the spatial pulses with center wavelength at 1 THz of Gaussian soliton generation system.

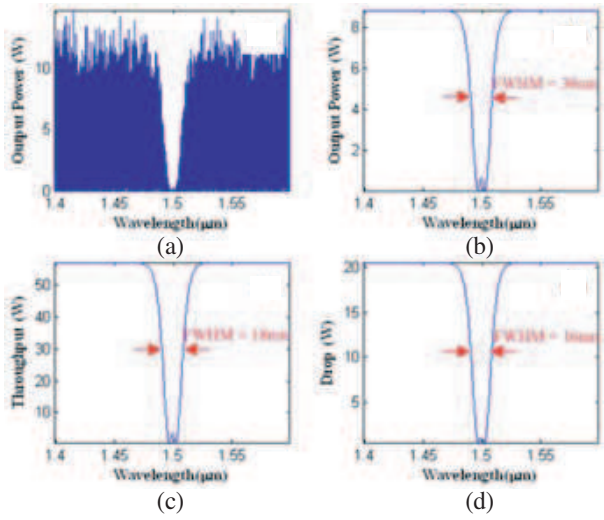

Figure 4: The dynamic optical tweezers within add/drop filter.

In this investigation, the coupling coefficient of the microring resonator is ranged from 0.55 to 0.90. The nonlinear refractive index of the microring used is $n_2 = 2.2 \times 10^{-17}\,\mathrm{m}^2/\mathrm{W}$. In this case, the attenuation of light propagates within the system (i.e., wave guided) used is $0.5\,\mathrm{dBmm}^{-1}$. Result of the spatial pulses with center wavelength at 1.30 µm, Fig. 2(e), the large bandwidth signals, Fig. 2(f), the filtering and amplifying signals from the drop port. The smallest free spectrum range (FSR) and spectral width ($\Delta\lambda$) of 535 and 20 pm are generated respectively. The maximum output power is 40 W which is available for high capacity and long distance communication link.

In operation of THz pulse, an optical field in the form of Gaussian pulse from a laser source at the specified center wavelength is input into the system. In practice, the maximum wavelength that can be confined within the optical waveguide has been increased by using the composite of materials known as meta-materials [12], which is shown that the wavelength close to few mm can be confined within the waveguide. From Fig. 3, the Gaussian pulse with center frequency (f_0) at 1.0 THz pulse width of 20 ns, peak power at 2 W is input into the system The large bandwidth signals can be seen within the ring resonator device. The suitable ring parameters are used. The smallest free spectrum range (FSR) of 0.3 PHz is generated.

From Fig. 1(b), a dark soliton pulse with 50-ns pulse width with the maximum power of 0.65 W is input into the dark-bright soliton conversion system. The suitable ring parameters are ring radii, where $R_1 = 10.0\,\mu\mathrm{m}$, $R_2 = 7.0\,\mu\mathrm{m}$, and $R_3 = 5.0\,\mu\mathrm{m}$. The selected parameters of the system are fixed to $\lambda = 1.50\,\mu\mathrm{m}$, $n_0 = 3.34$. $A_{eff} = 0.50$, 0.25, and $0.10\,\mu\mathrm{m}^2$ for a microring and nanoring resonator, respectively. The input dark soliton pulse is chopped (sliced) into the smaller output signals of the filtering signals within the rings R_2 and R_3. The soliton signals in R_3 is entered in the add/drop filter, when the bright soliton propagating into the add/drop system, the optical tweezers behavior is occurred the dark-bright soliton collision in add/drop system is seen as shown in Fig. 4.

4. NANOSCALE NETWORKING VIA A WAVELENGTH ROUTER

Let us consider that the case when the optical tweezers output is partially input into the quantum processor unit, the transportation of the trapped atom/molecule/photon is plausible, this concept is well described by the published work [13, 14], the transported atom with long distance link via quantum tweezer is realized. The transmission of atoms/molecules from dark soliton pulses via a wavelength router is plausible, which can be described: (i) a dark soliton pulse can propagate into the optical device/media, (ii) atom/molecule being trapped by tweezers force during the movement, the atom/molecule recovery can be realized by using the optical detection scheme [15]. From Fig. 5, the transmission atoms/molecules can be performed by the dark soliton pulse, the atoms/molecules recovery can be taken by using the add/drop filter incorporating in the wavelength router, i.e., optical network. However, the separation of atoms/molecules from light pulse is required to have the specific environment, which becomes the interesting research area, where light with the specific wavelength (λ_i) is detected by a detector, while the required molecule is absorbed by the specific environment. Where the corresponding states of the transmitted atom/molecule between input and output states can be recognized and formed the secret information. Therefore, in practice, the quantum processing unit is required to connect into the system, where the input and output states can be linked and obtained the required information.

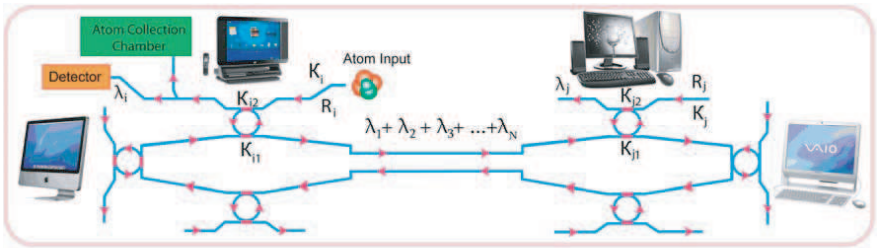

Figure 5: A schematic of atomic/molecular router and network system, where R_i, R_j: ring radii and κ_{is}, κ_{js} are the coupling coefficients.

5. CONCLUSION

We have demonstrated that some interesting results can be obtained when the laser pulse is propagated within the nonlinear optical ring resonator, especially, in microring and nanoring resonators,

which can be used to perform many applications. For instance, the broad spectrum of a monochromatic source with the reasonable power can be generated and achieved by using a Gaussian pulse. Moreover, the use of a Gaussian pulse can provide the non-dispersion soliton, where the generation of soliton communication bandwidth with the center wavelength at 1.30 µm is achieved. The dynamic optical tweezers can be generated by using a dark soliton and a bright soliton pulse with the ring resonator system incorporating the add/drop multiplexer. We have also proposed the simulation of THz carrier frequencies using the small device using a Gaussian beam propagating within the device system. We found that the generated output power with the THz frequency can be achieved. Moreover, the good frequency free spectrum range (FSR) results have shown that they can be used to separate the two adjacent outputs seen. The spatial simulation output is also demonstrated which is shown the use of the very high output power within the small device is plausible, which means that the security imaging by using the propose device which is a tiny system will be realized in the near future. Finally, the use of quantum tweezers for quantum-molecular networking via a wavelength router is also described.

ACKNOWLEDGMENT

The project was supported by Telecommunications Research and Industrial Development Institute. (TRIDI.), with National Telecommunication Commission of Thailand. (NTC.).

REFERENCES

1. Agarwal, G. P., *Nonlinear Fiber Optics*, 4th Edition, Academic Press, New York, 2007.
2. Hasegawa, Ed., A., *Massive, WDM and TDM Soliton Transmission Systems*, Kluwer Academic Publishers, 2000.
3. Simonov, Yu. A. and J. A. Tjon, "Soliton-soliton interaction in confining models," *Phys. Lett. B*, Vol. 85, 380–384, 1979.
4. Drohm, J. K., L. P. Kok, Yu. A. Simonov, J. A. Tjon, and A. I. Veselov, "Collision, and rotation of solitons in three space-time dimensions," *Phys. Lett. B*, Vol. 101, 204–208, 1981.
5. Iizuka, T. and Yu. S. Kivshar, "Optical gap solitons in nonresonant quadratic media," *Phys. Rev. E*, Vol. 59, 7148–7151, 1999.
6. Ganapathy, R., K. Porsezian, A. Hasegawa, and V. N. Serkin, "Soliton interaction under soliton dispersion management," *IEEE J. Quantum Electron.*, Vol. 44, 383–390, 2008.
7. Deng, D. and Q. Guo, "Ince-Gaussian solitons in strongly nonlocal nonlinear media," *Opt. Lett.*, Vol. 32, 3206–3208, 2007.
8. Kokubun, Y., Y. Hatakeyama, M. Ogata, S. Suzuki, and N. Zaizen, "Fabrication technologies for vertically coupled micro ring resonator with multilevel crossing busline and ultracompact-ring radius," *IEEE J. Sel. Top. Quantum Electron.*, Vol. 11, 4–10, 2005.
9. Su, Y., F. Liu, and Q. Li, "System performance of slow-light buffering, and storage in silicon nano-waveguide," *Proc. SPIE 6783*, 67832, 2007.
10. Yupapin, P. P., P. Saeung, and C. Li, "Characteristics of complementary ring-resonator add/drop filters modeling by using graphical approach," *Opt. Commun.*, Vol. 272, 81–86, 2007.
11. Yupapin, P. P. and W. Suwancharoen, "Chaotic signal generation and cancellation using a micro ring resonator incorporating an optical add/drop multiplexer," *Opt. Commun.*, Vol. 280, No. 2, 343–350, 2007.
12. Fujii, M., J. Leuthold, and W. Freude, "Dispersion relation and loss of subwavelength confined mode of metal-dielectri-gap optical waveguides," *IEEE Photon. Technol. Lett.*, Vol. 21, No. 6, 362–364, 2009.
13. Suchat, S., W. Khannam, and P. P. Yupapin, "Quantum key distribution via an optical wireless communication link for telephone network," *Opt. Eng. Lett.*, Vol. 46, No. 10, 100502-1-5, 2007.
14. Yupapin, P. P. and S. Suchat, "Entangle photon generation using fiber optic Mach-Zehnder interferometer incorporating nonlinear effect in a fiber ring resonator," *Nanophotonics (JNP)*, Vol. 1, 13504-1-7, 2007.
15. Sarapat, K., N. Sangwara, K. Srinuanjan, P. P. Yupapin, and N. Pornsuwancharoen, "Novel dark-bright optical solitons conversion system and power amplification," *Opt. Eng.*, Vol. 48, 045004-1-7, 2009.

Novel Molecular Networking via a Simultaneous Optical Wireless Up-down Link Systems

P. Udomariyasap[1], **S. Noppanakeepong**[1], **S. Mitatha**[2], **and P. P. Yupapin**[3]

[1]Department of Telecommunication Engineering, Faculty of Engineering
King Mongkut's Institute of Technology Ladkrabang, Bangkok 10520, Thailand
[2]Hybrid Computing Research Laboratory, Faculty of Engineering
King Mongkut's Institute of Technology Ladkrabang, Bangkok 10520, Thailand
[3]Advanced Research Center for Photonics, Faculty of Science
King Mongkut's Institute of Technology Ladkrabang, Bangkok 10520, Thailand

Abstract— In this paper, we present the interesting results of THz carrier frequency generation using the small device system for high frequency generation. Simulation results are obtained by using a Gaussian beam propagating within the nonlinear device system, which is required to use in the THz regime. A generated system consists of a micro and nano rings that can be integrated into a single system, which can be employed to generate the large bandwidth of high frequency bands by a Gaussian pulse propagating within the ring resonator system incorporating an add/drop filter. The multiplexed transporters are generated and multiplexed via add/drop filter, which can be used for high capacity molecular signal processing in the communication system. By controlling the ring parameters, add/drop filter to increase the input add port, the appropriate output power can be obtained, which can be modified to be suitable for nano-scale communication applications. Moreover, the very wide band of wavelength can be simultaneously generated and controlled for various applications. Moreover, we found that the generated output power with the THz frequency carrier regime can be achieved.

1. INTRODUCTION

Recently, Mitatha et al. [1] have shown that the up-link and down link carrier frequencies can be generated by using a single small device, where the advantage is that the simultaneous operation can be operated. Moreover, the generated signals can be stored within the system which is confirmed by Yupapin and Suwancharoen [2]. However, the problem of cut-off wavelength of light propagating within the proposed device is become a problem, which is become a problem of the continuous research works in the areas of meta-materials [3]. Up to date, light pulse with wavelength up to sub millimeter wave can be confined within such a device [4]. In this work, we propose the simulation of THz carrier frequencies using the small device, where a Gaussian beam is propagated within the device system. We found that the generated output power with the THz frequency can be achieved. Moreover, the Gaussian pulse exhibits the gain constant within the Gaussian period. Furthermore, the selected light pulse can be trapped and used to perform the multiplex channel, which is controlled by light. The adiabatic multiplex pulse process to preserve the coherent information encoded can also be performed. The multiplexed transporters [5] are generated and multiplexed via add/drop filter, which can be used for high capacity molecular signal processing via the communication system. The key advantages of the system are the reversely compress bandwidth and the maintaining power, which can be tuned to obtain the arbitrary pulse for high frequency generation, which can be modified to be suitable for nano-scale communication applications.

2. CURRENT RESULTS

Light from a monochromatic light source is launched into a ring resonator with constant light field amplitude (E_0) and random phase modulation as shown in Fig. 1, which is the combination of terms in attenuation (α) and phase (ω_0) constant, which results in temporal coherence degradation.

Hence, the time dependent input light field (E_{in}), without pumping term, can be expressed as [6]

$$E_{in}(t) = E_0 \exp^{-\alpha L + j\varphi_0(t)} \tag{1}$$

where L is a propagation distance (waveguide length).

We assume that the nonlinearity of the optical ring resonator is of the Kerr-type, i.e., the refractive index is given by

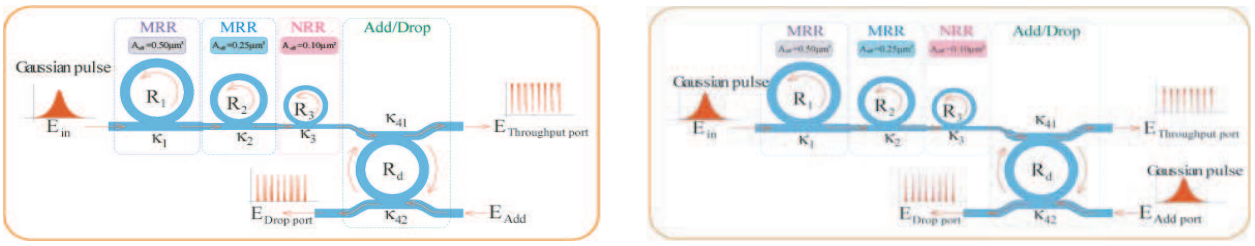

(a) (b)

Figure 1: A schematic of a Gaussian pulse generation system, where R_s: ring radii, κ_s and κ_{41} and κ_{42}: coupling coefficients, R_d: an add/drop ring radius, A_{eff}s: effective areas.

$$n = n_0 + n_2 I = n_0 + n_2 \left(\frac{P}{A_{eff}} \right) \tag{2}$$

where n_0 and n_2 are the linear and nonlinear refractive indexes, respectively. I and P are the optical intensity and optical power, respectively. The effective mode core area of the device is given by A_{eff}. For the micro ring and nano ring resonators, the effective mode core areas range from 0.10 to 0.50 μm^2

When a Gaussian pulse is input and propagated within a fiber ring resonator, the resonant output is formed, thus, the normalized output of the light field is the ratio between the output and input fields ($E_{out}(t)$ and $E_{in}(t)$) in each roundtrip, which can be expressed as [7]

$$\left| \frac{E_{out}(t)}{E_{in}(t)} \right|^2 = (1-\gamma) \left[1 - \frac{\left(1-(1-\gamma)\, x^2\right) \kappa}{\left(1 - x\sqrt{1-\gamma}\sqrt{1-\kappa}\right)^2 + 4\, x\sqrt{1-\gamma}\sqrt{1-\kappa} \sin^2\left(\frac{\varphi}{2}\right)} \right] \tag{3}$$

Equation (3) indicates that a ring resonator in the particular case is very similar to a Fabry-Perot cavity, which has an input and output mirror with a field reflectivity, (1-κ), and a fully reflecting mirror. κ is the coupling coefficient, and $x = e^{(-\alpha L/2)}$ represents a roundtrip loss coefficient, $\varphi_0 = kLn_0$ and $\varphi_{NL} = kL(n_2/A_{eff})P$ are the linear and nonlinear phase shifts, $k = 2\pi/\lambda$ is the wave propagation number in a vacuum. Where L and α are a waveguide length and linear absorption coefficient, respectively. In this work, the iterative method is introduced to obtain the results as shown in Equation (3), similarly, when the output field is connected and input into the other ring resonators.

The input optical field as shown in Equation (1), i.e., a Gaussian pulse, is input into a nonlinear micro ring resonator. By using the appropriate parameters, the chaotic signal is obtained by using Equation (3). To retrieve the signals from the chaotic noise, we propose to use the add/drop device with the appropriate parameters. This is given in details as followings. The optical output of a ring resonator add/drop filter can be given by the Equations (4) and (5) [7, 8]

$$\left| \frac{E_t}{E_{in}} \right|^2 = \frac{(1-\kappa_1) - 2\sqrt{1-\kappa_1} \cdot \sqrt{1-\kappa_2} e^{-\frac{\alpha}{2}L} \cos(k_n L) + (1-\kappa_2)\, e^{-\alpha L}}{1 + (1-\kappa_1)(1-\kappa_2)\, e^{-\alpha L} - 2\sqrt{1-\kappa_1} \cdot \sqrt{1-\kappa_2} e^{-\frac{\alpha}{2}L} \cos(k_n L)} \tag{4}$$

and

$$\left| \frac{E_d}{E_{in}} \right|^2 = \frac{\kappa_1 \kappa_2 e^{-\frac{\alpha}{2}L}}{1 + (1-\kappa_1)(1-\kappa_2)\, e^{-\alpha L} - 2\sqrt{1-\kappa_1} \cdot \sqrt{1-\kappa_2} e^{-\frac{\alpha}{2}L} \cos(k_n L)} \tag{5}$$

where E_t and E_d represents the optical fields of the throughput and drop ports respectively. The transmitted output can be controlled and obtained by choosing the suitable coupling ratio of the ring resonator, which is well derived and described by reference [8]. Where $\beta = kn_{eff}$ represents the propagation constant, n_{eff} is the effective refractive index of the waveguide, and the circumference of the ring is $L = 2\pi R$, here R is the radius of the ring. In the following, new parameters will be used for simplification, where $\varphi = \beta L$ is the phase constant. The chaotic noise cancellation can be managed by using the specific parameters of the add/drop device, which the required signals at the specific wavelength band can be filtered and retrieved. K_1 and K_2 are coupling coefficient of add/drop filters, $k_n = 2\pi/\lambda$ is the wave propagation number for in a vacuum, and the waveguide (ring resonator) loss is $\alpha = 0.5\,\mathrm{dBmm}^{-1}$. The fractional coupler intensity loss is $\gamma = 0.1$. In the

case of add/drop device, the nonlinear refractive index is neglected. In practice, the maximum wavelength that can be confined within the optical waveguide has been increased by using the composite of materials known as meta-materials [4], which is shown that the wavelength close to few mm can be confined within the waveguide, MRR (Micro Ring Resonator), NRR (Nano Ring Resonator).

In operation, light pulse is sliced to be the discrete signal and amplified within the first and second ring, where more signal amplification can be obtained by using the smaller ring device (third ring) as shown in Fig. 1(a). Finally, the required signals can be obtained via a drop port of the add/drop filter. An optical field in the form of Gaussian pulse from a laser source at the specified center wavelength is input into the system.

From Fig. 2, the Gaussian pulse with center wavelength (λ_0) at 3.0 mm, pulse width (Full Width at Half Maximum, **FWHM**) of 20 ns, peak power at 2 W is input into the system as shown in Fig. 2(a). The large bandwidth signals can be seen within the first micro ring device, and shown in Fig. 2(b). The suitable ring parameters are used, for instance, ring radii $R_1 = 15.0\,\mu\text{m}$, $R_2 = R_3 = 9.0\,\mu\text{m}$, and $R_d = 50.0\,\mu\text{m}$. In order to make the system associate with the practical device [6], the selected parameters of the system are fixed to $n_0 = 3.34$ (**InGaAsP/InP**), $A_{eff} = 0.50\,\mu\text{m}^2$ and $0.25\,\mu\text{m}^2$ for a micro ring and add/drop ring resonator, respectively, $\alpha = 0.5\,\text{dBmm}^{-1}$, $\gamma = 0.1$. In this investigation, the coupling coefficient (kappa, κ) of the micro ring resonator is ranged from 0.10 to 0.96. The nonlinear refractive index of the micro ring used is $n_2 = 2.2 \times 10^{-17}\,\text{m}^2/\text{W}$. In this case, the attenuation of light propagates within the system (i.e., wave guided) used is $0.5\,\text{dBmm}^{-1}$. After light is input into the system, the Gaussian pulse is chopped (sliced) into a smaller signal spreading over the spectrum due to the nonlinear effects [7], which is shown in Fig. 2(b). The large bandwidth signal is generated within the first ring device. In applications, the specific input or out wavelengths can be used and generated, where the suitable parameters are used and shown in the figures. Fig. 2 shows the results of the spatial pulses with the center wavelength at 3 mm, Fig. 3 shows the results of the 3 THz frequency band with the center frequency at 3 THz, where (a) the input Gaussian pulse, (b) the large bandwidth signal, (c) the filtering and amplifying signals, (d) output frequency band, (e) and (f) are the drop port signals, (g) and (h) are the through port signals.

Multi Channel by using the propose design as shown in Fig. 1(b), the Gaussian pulse generation system (E_{in} and E_{Add}) be used for multi frequency, which can be used employed via the simultaneous up link and down link system [1], the higher channel capacity can also be obtained by using

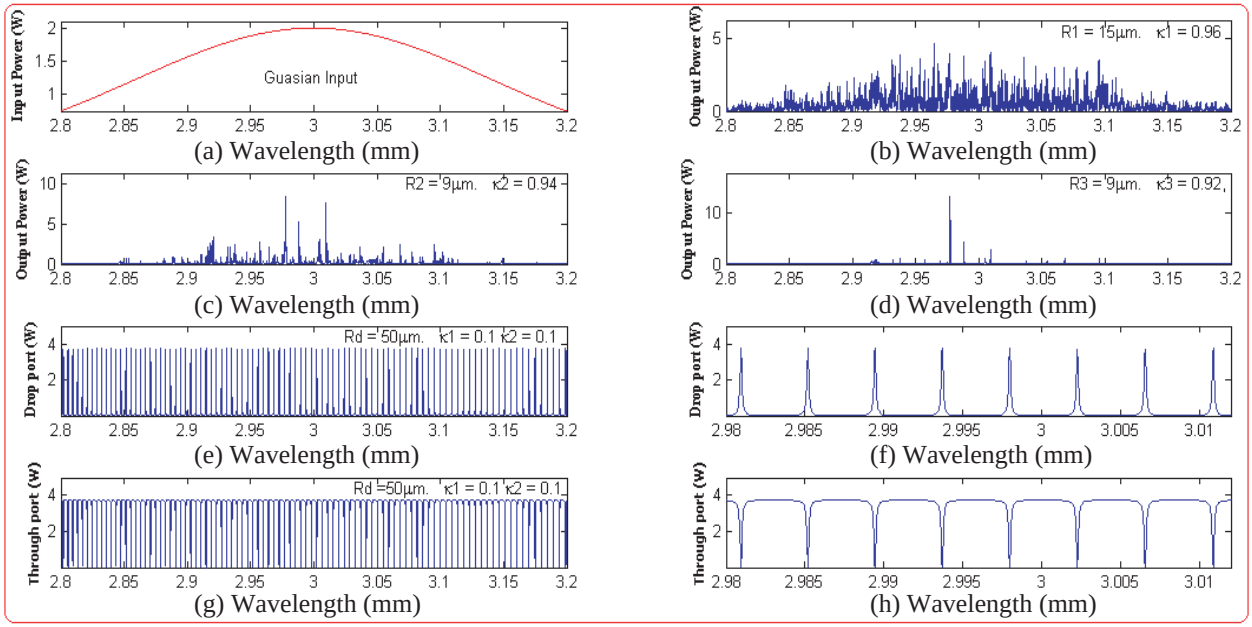

Figure 2: Results of the spatial pulses with the center wavelength at 3 mm, where (a) the input Gaussian pulse, (b) the large bandwidth signal, (c) the filtering and amplifying signals, (d) output frequency band, (e) and (f) are the drop port signals, (g) and (h) are the through port signals, with R_d and FSR are 50 μm and 5.0 μm.

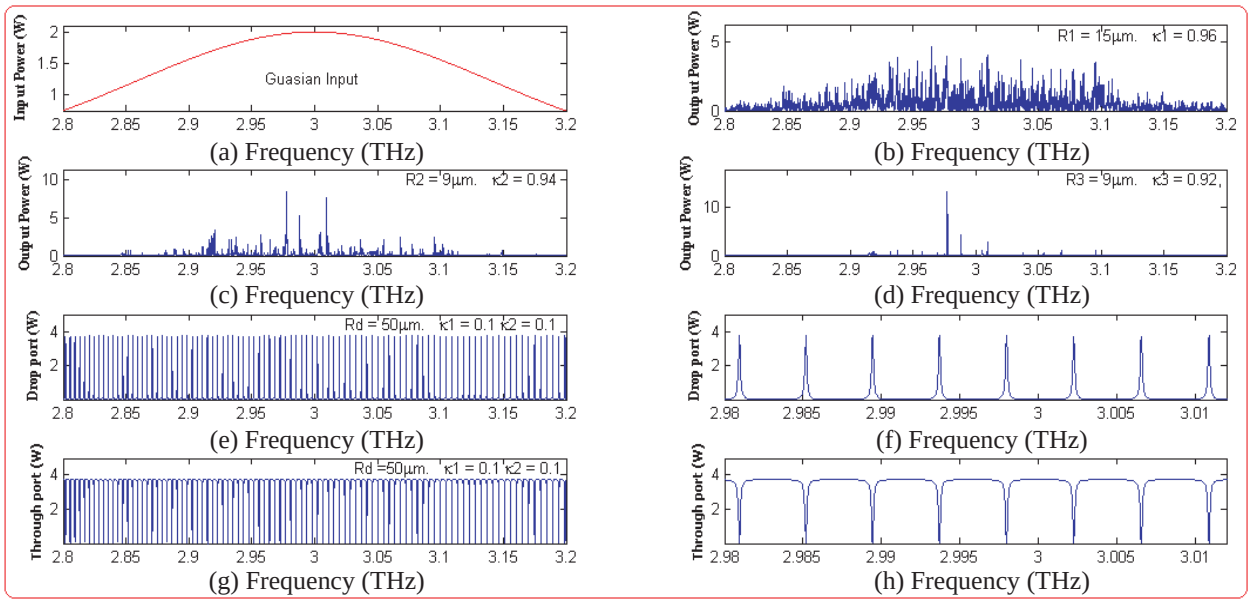

Figure 3: Results of the THz frequency band with the center frequency at 3 THz, where (a) the input Gaussian pulse, (b) the large bandwidth signal, (c) the filtering and amplifying signals, (d) output frequency band, (e) and (f) are the drop port signals, (g) and (h) are the through port signals, with R_d and FSR are 50 μm and 1.5 PHz.

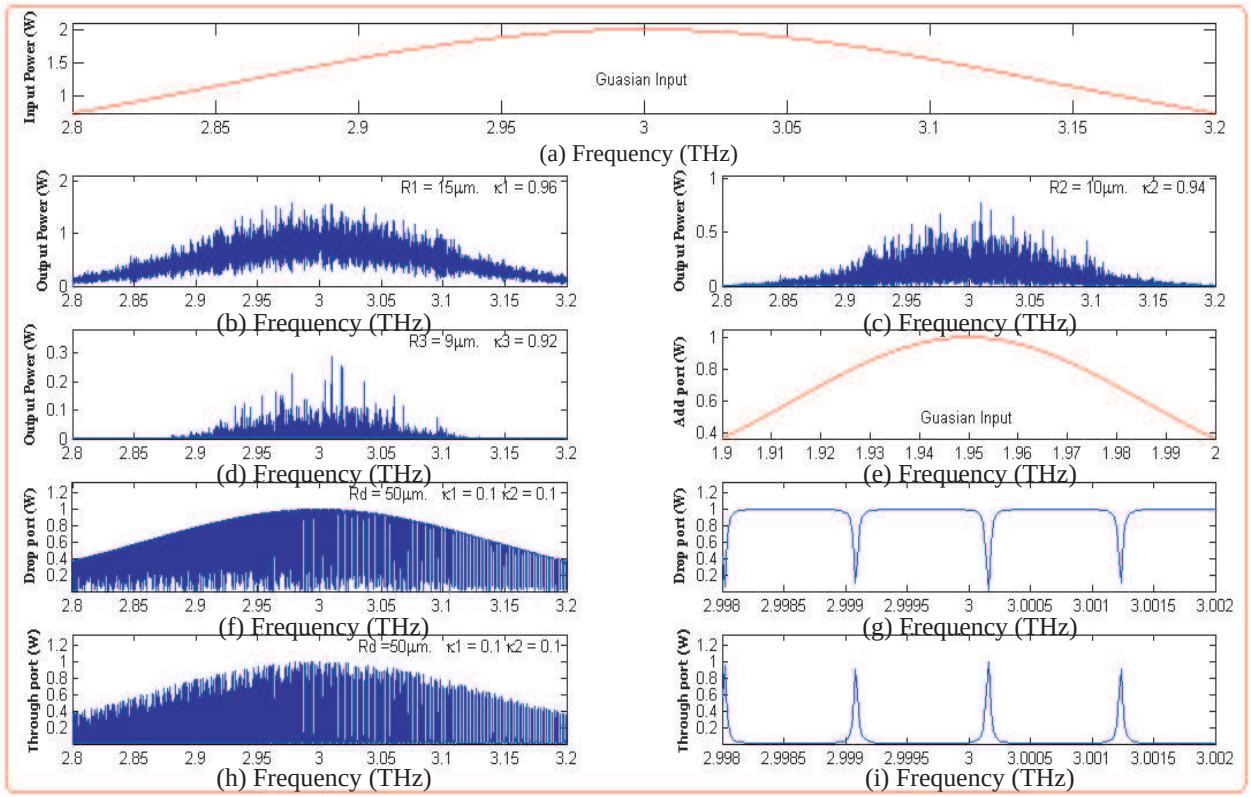

Figure 4: Results of the THz frequency band with the center frequency at 3 THz, where (a) the input Gaussian pulse, (b) the large bandwidth signal, (c) the filtering and amplifying signals, (d) output frequency band, (e) the Add port is Gaussian pulse with the center frequency at 1.95 THz (f) and (g) are the drop port signals, (h) and (i) are the through port signals, with R_d and FSR are 50 μm and 1 PHz.

FSR modification and more available frequency bands, for instance, the use of system different parameters can provide more frequency bands as shown in Fig. 4. Results of the THz frequency band with the Gaussian pulse center frequency at 3 THz and 1.95 THz, where (a), (e) the input and add

port, (b) the large bandwidth signal, (c) the filtering and amplifying signals, (d) output frequency band, (f) and (g) are the drop port signals, (h) and (i) are the through port signals. The generated carrier signals can be used as the modulated carrier that can be used to form the simultaneous up link, down link and multi channel, which is controlled by two input Gaussians pulse. This can be used with the control network applications. Furthermore, the new available frequency bands can be use to form the new multi channel, where more communication capacity can be performed.

The tunable spatial modes can be obtained by using the array waveguide as shown in Fig. 1(b) and Fig. 4, which means that the Gaussian pulse can be generation the large bandwidth signal by using the ring radii R_1, R_2 and R_3. After the Gaussian pulse (E_{in}, $E_{Add\,port}$) is amplified and reached the specified value. Finally, the required signals can be obtained via a drop port of the add/drop filter, which the coupling coefficients κ_{41} and κ_{42} are designed to output signal by controlling the ring parameters, add/drop filter.

3. CONCLUSION

The large bandwidth of the arbitrary wavelength of Gaussian pulse can be reversely compressed, expanded and tuned to generate and multiplex within a nano-waveguide, whereas the Gaussian pulse exhibits the gain constant within the Gaussian period. The selected light pulse can be trapped and used to perform the multiplex Gaussian pulse, which is controlled by light. The multiplexed transporters are generated and multiplexed via add/drop filter, which can be used for high capacity molecular signal processing and communication system.

ACKNOWLEDGMENT

This research project has been supported by Telecommunications Research and Industrial Development Institute (TRIDI.), with National Telecommunication Commission of Thailand (NTC).

REFERENCES

1. Mithata, S., N. Pornsuwancharoen, and P. P. Yupapin, "A simultaneous short wave and millimeter wave generation using a soliton pulse within a nano-waveguide," *IEEE Photon. Technol. Lett.*, Vol. 21, No. 13, 932–934, 2009.
2. Yupapin, P. P. and N. Pornsuwancharoen, "Porposed nonlinear micro ring resonator arrangement for stopping and storing light," *Photon. Technol. Lett.*, Vol. 21, No. 6, 404–406, 2009.
3. Mitatha, S. and P. P. Yupapin, "Novel continuous spectrum generation system using a nano-waveguide for white light, short and sub-millimeter waves use," *Microw. and Opt. Technol. Lett.*, Vol. 51, 2009, in press.
4. Fujii, M., J. Leuthold, and W. Freude, "Dispersion relation and loss of subwavelength confined mode of metal-dielectri-gap optical waveguides," *IEEE Photon. Technol. Lett.*, Vol. 21, No. 6, 362–364, 2009.
5. Carpentier, A. V., J. Belmonte-Beitia, H. Michinel, and V. M. Perez-Garcia, "Laser tweezers for atomic solitons," *J. of Mod. Opt.* Vol. 55, No. 17, 2819–2829, 2008.
6. Xu, Q. and M. Lipson, "All-optical logic based on silicon micro-ring resonators," *Opt. Exp.*, Vol. 15, No. 3, 924–929, 2007.
7. Yupapin, P. P. and W. Suwancharoen, "Chaotic signal generation and cancellation using a micro ring resonator incorporating an optical add/drop multiplexer," *Opt. Commun.*, Vol. 280, 343–350, 2007.
8. Yupapin, P. P., P. Saeung, and C. Li, "Characteristics of complementary ring-resonator add/drop filters modeling by using graphical approach," *Opt. Commun.*, Vol. 272. 81–86 2007.

Quantum Parallel Processing Manipulation Using Gaussian Pulses via an Optical Multiplexer

P. Pongwongtragull[1], **S. Suchat**[2], **S. Mitatha**[3], **and P. P. Yupapin**[1]

[1]Advanced Research Center for Photonics, Faculty of Science
King Mongkut's Institute of Technology Ladkrabang, Bangkon 10520, Thailand
[2]Faculty of Science and Technology, Phranakhon Rajabhat University, Bangkok 10220, Thailand
[3]Department of Computer Engineering, Faculty of Engineering
King Mongkut's Institute of Technology Ladkrabang, Bangkok 10520, Thailand

Abstract— We propose a new system of quantum signal and parallel processing using Gaussian pulses propagating within a nonlinear ring resonator system. To increase the channel capacity and security, the multiplexer is operated incorporating a quantum processing unit via an optical multiplexer. The transmitted part can be used to generate the high capacity packet of quantum codes within the series of micro ring resonators. The received part can be used to detect the quantum bits (qubits) via the optical link, which can be obtained via the end quantum processor. The reference states can be recognized by using the cloning unit, which is operated by the add/drop filter. Two add-drops that are in two parts can be used to be Alice and Bob, respectively, in quantum communication. Results obtained have shown that the multiplexed wavelengths can be formed by using the multiple operating systems, which is allowed the filtering at the end users (Bob). In application, the embedded system within the computer processing unit is available for quantum computer. Furthermore, such a concept is also available for hybrid communications, for instance, wire/wireless, satellite, which will be discussed in details.

1. INTRODUCTION

Quantum key distribution has been recognized as the very good candidate for information security. Many research works have been reported in the last decade. Recently, Suchat et al. [1] have reported the interesting concept of continuous variable quantum key distribution via a simultaneous optical-wireless up-down-link system, where they have shown that the continuous variable quantum key distribution (KQD) could be performed via the chaotic signals that generated by a nonlinear micro-ring resonator system, with appropriate soliton input power and micro-ring resonator. They have also shown that the different time slot entangled photons can be formed randomly, which can be used to select two different frequency bands for up-down-link converters within a single system. Yupapin et al. [2] have proposed a new technique for QKD that can be used to make the communication transmission security and implemented with a small device for such as mobile telephone hand set. This technique used Kerr nonlinear type of light in the microring resonator to generate the superposition of the chaotic signal via a four-wave mixing type that introduced the second-harmonic pulse. Up to date, there is no quantum parallel processing manipulation using a common laser (Gaussian pulse) via an optical multiplexer. In this paper, we have proposed the use of nonlinear microring resonator to form the high capacity quantum codes, where the packet of quantum codes can be generated by using Gaussian light pulse propagating with the series of microring resonator. In application, the device can be embedded within the computer processing unit with using to increase the capacity and the speed for quantum computer.

2. MULTI-LIGHT SOURCE GENERATION

Light from a monochromatic light source is launched into a ring resonator with constant light field amplitude (E_0) and random phase modulation, which is the combination of terms in attenuation (α) and phase (ϕ_0) constants, which results in temporal coherence degradation. Hence, the time dependent input light field (E_{in}), without pumping term, can be expressed as Equation (1) and we assume that the nonlinearity of the optical ring resonator is of the Kerr-type, i.e., the refractive index is given by Equation (2).

$$E_{in}(t) = E_0 \exp^{-\alpha L + j\phi_0(t)} \tag{1}$$

and

$$n = n_0 + n_2 I = n_0 + \left(\frac{n_2}{A_{eff}}\right) P \tag{2}$$

where L is a propagation distance(waveguide length). n_0 and n_2 are the linear and nonlinear refractive indexes, respectively. I and P are the optical intensity and optical power, respectively. The effective mode core area of the device is given by A_{eff}. For the microring and nanoring resonators, the effective mode core areas range from 0.10 to 0.50 μm^2 [3].

When a Gaussian pulse is input and propagated within a fiber ring resonator, the resonant output is formed, thus, the normalized output of the light field is the ratio between the output and input fields ($E_{out}(t)$ and $E_{in}(t)$) in each roundtrip, which can be expressed as [4]

$$\left|\frac{E_{out}(t)}{E_{in}(t)}\right|^2 = (1-\gamma)\left[1 - \frac{(1-(1-\gamma)x^2)\kappa}{(1-x\sqrt{1-\gamma}\sqrt{1-\kappa})^2 + 4\,x\sqrt{1-\gamma}\sqrt{1-\kappa}\sin^2(\frac{\phi}{2})}\right] \tag{3}$$

Equation (3) indicates that a ring resonator in the particular case is very similar to a Fabry-Perot cavity, which has an input and output mirror with a field reflectivity, $(1-\kappa)$, and a fully reflecting mirror. κ is the coupling coefficient, and $x = \exp(-\alpha L/2)$ represents a roundtrip loss coefficient, $\phi_0 = kLn_0$ and $\phi_0 = kL(n_2/A_{eff})P$ are the linear and nonlinear phase shifts, $k = 2/\pi\lambda$ is the wave propagation number in a vacuum. Where L and α are a waveguide length and linear absorption coefficient, respectively. In this work, the iterative method is introduced to obtain the results as shown in Equation (3), similarly, when the output field is connected and input into the other ring resonators.

The input optical field as shown in Equation (1), i.e., a Gaussian pulse, is input into a nonlinear micro ring resonator. By using the appropriate parameters, the chaotic signal is obtained by using Equation (3). To retrieve the signals from the chaotic noise, we propose to use the add/drop device with the appropriate parameters. This is given in details as followings. The optical outputs of a ring resonator add/drop filter can be given by the Equations (4) and (5) [5].

$$\left|\frac{E_t}{E_{in}}\right|^2 = \frac{(1-\kappa_1) - 2\sqrt{1-\kappa_1}\cdot\sqrt{1-\kappa_2}e^{-\frac{\alpha}{2}L}\cos(k_nL) + (1-\kappa_2)\,e^{-\alpha L}}{1+(1-\kappa_1)(1-\kappa_2)\,e^{-\alpha L} - 2\sqrt{1-\kappa_1}\cdot\sqrt{1-\kappa_2}e^{-\frac{\alpha}{2}L}\cos(k_nL)} \tag{4}$$

and

$$\left|\frac{E_d}{E_{in}}\right|^2 = \frac{\kappa_1\kappa_2 e^{-\frac{\alpha}{2}L}}{1+(1-\kappa_1)(1-\kappa_2)\,e^{-\alpha L} - 2\sqrt{1-\kappa_1}\cdot\sqrt{1-\kappa_2}e^{-\frac{\alpha}{2}L}\cos(k_nL)} \tag{5}$$

where E_t and E_d represents the optical fields of the throughput and drop ports respectively. The transmitted output can be controlled and obtained by choosing the suitable coupling ratio of the ring resonator, which is well derived and described by reference [5].

Where $\beta = kn_{eff}$ represents the propagation constant, n_{eff} is the effective refractive index of the waveguide, and the circumference of the ring is $L = 2\pi R$, here R is the radius of the ring. In the following, new parameters will be used for simplification, where $\phi = \beta L$ is the phase constant. The chaotic noise cancellation can be managed by using the specific parameters of the add/drop device, which the required signals at the specific wavelength band can be filtered and retrieved. κ_1 and κ_2 are coupling coefficient of add/drop filters, $k_n = 2/\pi\lambda$ is the wave propagation number for in a vacuum, and the waveguide (ring resonator) loss is $\alpha = 0.5\,\mathrm{dBmm}^{-1}$. The fractional coupler intensity loss is $\gamma = 0.1$. In the case of add/drop device, the nonlinear refractive index is neglected.

From Fig. 1, in principle, light pulse is sliced to be the discrete signal and amplified within the first ring, where more signal amplification can be obtained by using the smaller ring device (second ring). Finally, the required signals can be obtained via a drop port of the add/drop filter. In operation, an optical field in the form of Gaussian pulse from a laser source at the specified center wavelength is input into the system. After light is input into the system, the Gaussian pulse is chopped (sliced) into a smaller signal spreading over the spectrum due to the nonlinear effects [5]. The large bandwidth signal is generated within the first ring device. In applications, the specific input or out wavelengths can be used and generated. For instance, the center wavelength at 1.5 μm of the input pulse is shown in Fig. 2, where the suitable parameters are used and shown in the figures.

3. QUANTUM PARALLEL PROCESSING VIA AN OPTICAL MULTIPLEXER

Let us consider that the case when the photon output is input into the quantum processor unit. Generally, there are two pairs of possible polarization entangled photons forming within the ring device, which are represented by the four polarization orientation angles as [0°, 90°], [135° and

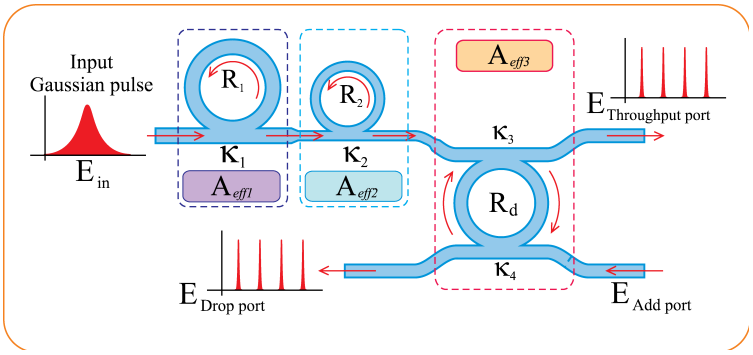

Figure 1: A schematic of a Gaussian soliton generation system, where R_s: ring radii, κ_s: coupling coefficients, R_d: an add/drop ring radius, A_{eff}s: Effective areas.

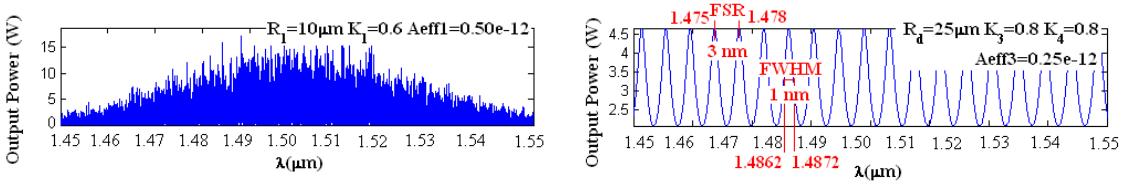

Figure 2: Results of the spatial pulses with center wavelength at 1.50 μm, where (a) large bandwidth signals, (b) filtering and amplifying signals from the drop port.

180°]. These can be formed by using the optical component called the polarization rotatable device and a polarizing beam splitter (PBS). In this concept, we assume that the polarized photon can be performed by using the proposed arrangement. Where each pair of the transmitted qubits can be randomly formed the entangled photon pairs. To begin this concept, we introduce the technique that can be used to create the entangled photon pair (qubits) as shown in Fig. 3, a polarization coupler that separates the basic vertical and horizontal polarization states corresponds to an optical switch between the short and the long pulses. We assume those horizontally polarized pulses with a temporal separation of Δt. The coherence time of the consecutive pulses is larger than Δt. Then the following state is created by Equation (6) [6].

$$|\Phi\rangle_p = |1, H\rangle_s |1, H\rangle_i + |2, H\rangle_s |2, H\rangle_i \tag{6}$$

In the expression $|k, H\rangle$, k is the number of time slots (1 or 2), where denotes the state of polarization [horizontal $|H\rangle$ or vertical $|V\rangle$], and the subscript identifies whether the state is the signal (s) or the idler (i) state. In Equation (6), for simplicity, we have omitted an amplitude term that is common to all product states. We employ the same simplification in subsequent equations in this paper. This two-photon state with $|H\rangle$ polarization shown by Equation (6) is input into the orthogonal polarization-delay circuit shown schematically. The delay circuit consists of a coupler and the difference between the round-trip times of the microring resonator, which is equal to Δt. The micro ring is tilted by changing the round trip of the ring is converted into $|V\rangle$ at the delay circuit output. Then Equation (6) is converted into the polarized state by the delay circuit and by the coincidence counts in the second time slot, we can extract the fourth and fifth terms. As a result, we can obtain the following polarization entangled state as

$$|\Phi\rangle = |2, H\rangle_s |2, H\rangle_i + \exp[i(\phi_s + \phi_i)] |2, V\rangle_s |2, V\rangle_i \tag{7}$$

We assume that the response time of the Kerr effect is much less than the cavity round-trip time. Because of the Kerr nonlinearity of the optical device, the strong pulses acquire an intensity dependent phase shift during propagation. The interference of light pulses at a coupler introduces the output beam, which is entangled. Due to the polarization states of light pulses are changed and converted while circulating in the delay circuit, where the polarization entangled photon pairs can be generated. The entangled photons of the nonlinear ring resonator are separated to be the signal and idler photon probability. The polarization angle adjustment device is applied to investigate the

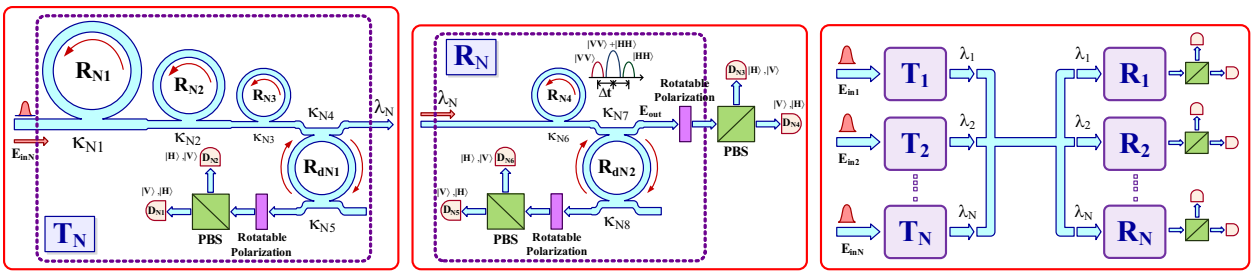

(a) (b) (c)

Figure 3: The schematic diagram (a) a quantum generation system at the transmission unit (T_N), where R_{NS}: ring radii, κ_{NS}: coupling coefficients, R_{dNS}: an add/drop ring radius, can be used to be the received part, PBS: Polarizing Beamsplitter, D_N: Detectors. (b) The quantum manipulation within a ring resonator at the receiver unit (R_N). The quantum state is propagating to a rotatable polarizer and then is split by a beam splitter (PBS) flying to detector D_{N3} and D_{N4}. (c) A schematic of a system of the transporters transmission system via an optical link.

orientation and optical output intensity, this concept is well described by the published work [6, 7]. The transporter states can be controlled and identified by using the quantum processing system as shown in Fig. 3.

The transmitter unit can be used to generate the quantum codes within the series of microring resonators and the cloning unit [8], which is operated by the add/drop filter (R_{dN1}) as shown in Fig. 3(a). The receiver unit can be used to detect the quantum bits via the optical link, which can be obtained via the end quantum processor and the reference states can be recognized by using the cloning unit, which is operated by the add/drop filter (R_{dN2}) as shown in the schematic diagram in Fig. 3(b). The remaining part of a system is the parallel processing system which can be combined the high capacity secret information via an optical multiplexer as shown in the schematic diagram in Fig. 3(c). The multiplexed quantum codes are allowed to form and transmit the secret information via the available link, where the quantum keys with different wavelengths (λ_N) can be generated and obtained, which is available for high capacity transmission of the secured information. In application, the packet switching of data can be secured by using the quantum codes which is known as quantum packet switching technique.

4. CONCLUSIONS

We have demonstrated that some interesting results can be obtained when the common laser pulse is propagated within the nonlinear optical ring resonator, especially, in microring and nanoring resonators, which can be used to perform many applications. For instance, the broad spectrum of a monochromatic source with the reasonable power can be generated and achieved. By using a Gaussian pulse, it can be converted to be a broad light source by using the ring resonator system incorporating the add/drop multiplexer, which can be configured as multi light sources. Results obtained have shown that the multiplexed sources with different wavelengths can be formed by using the multiple operating systems. In application, the embedded system within the computer processing unit is available for quantum computer to increase the channel capacity and security. Furthermore, such a concept is also available for hybrid communications, for instance, wire/wireless or satellite communication, where the use of quantum encoding for high capacity quantum communication/cryptography via a single photon based technology in the communication link in the network is plausible.

REFERENCES

1. Suchat, S., N. Pornsuwancharoen, and P. P. Yupapin, "Continuous variable quantum key distribution via a simultaneous optical wireless up-down-link system," *Int. J. Light Electron. Opt.*, 2009, doi:10.1016/j.ijleo.2008.11.012.
2. Yupapin, P. P., S. Thongme, and K. Sarapat, "Second-harmonic generation via microring resonators for optimum entangled photon visibility," *Int. J. Light Electron. Opt.*, 2009, doi:10.1016/j.ijleo.2008.09.017.
3. Su, Y., F. Liu, and Q. Li, "System performance of slow-light buffering, and storage in silicon nano-waveguide," *Proc. SPIE*, 6783, 67832P, 2007.

4. Yupapin, P. P., P. Saeung, and C. Li, "Characteristics of complementary ring-resonator add/drop filters modeling by using graphical approach," *Opt. Commun.*, Vol. 272, 81–86, 2007.
5. Yupapin, P. P. and W. Suwancharoen, "Chaotic signal generation and cancellation using a microring resonator incorporating an optical add/drop multiplexer," *Opt. Commun.*, 280/2, 343–350, 2007.
6. Suchat, S., W. Khannam, and P. P. Yupapin, "Quantum key distribution via an optical wireless communication link for telephone network," *Opt. Eng. Lett.*, Vol. 46, No. 10, 100502-1–5, 2007.
7. Yupapin, P. P. and S. Suchat, "Entangle photon generation using fiber optic Mach-Zehnder interferometer incorporating nonlinear effect in a fiber ring resonator," *Nanophotonics (JNP)*, Vol. 1, 13504-1–7, 2007.
8. Yupapin, P. P. and W. Suwancharoen, "Entangled photon states generation and regeneration using a nonlinear fiber ring resonator," *Int. J. Light Electron. Opt.*, 2008, doi:10.1016/j.ijleo.2008.03.004.

Molecular Transporters Generations Based on Ant Colony Algorithm for Molecular and Storage Applications

T. Taengtang[1, 2], **K. Praitoonwattanakit**[1], **and P. P. Yupapin**[2]

[1]Faculty of Engineering, King Mongkut's Institute of Technology Ladkrabang
Bangkok 10520, Thailand
[2]Advance Research Center for Photonics, Faculty of Science
King Mongkut's of Institute of Technology Ladkrabang
Bangkok 10520, Thailand

Abstract— We proposes a new method of molecular transporters generations based on ant colony algorithm for molecular classification and storage applications. The transportation network of molecules via multi tweezers inside the close system can be manipulated in the same way of ant colony algorithm relationship. In the proposed method, we assign each of ants represents an individual tweezer. By using ant colony system, the random codes can be used to communicate between ants inside swarm with pheromone being formed the random network. The quantum state of transporters (individual ant) with different states and wavelengths can be represented by the pheromone. In application, this proposal can be an alternative random networking which may be use for communication security, where the fast multiple access may be plausible.

1. INTRODUCTION

Recently, several research works have show that use of dark and bright soliton in various applications can be realized [1–6], where one of them has shown that the secured signals in the communication link can be retrieved by using a suitable an add/drop filter that is connected into the transmission line. The other promising application of a dark soliton signal [7] is for the large guard band of two different frequencies which can be achieved by using a dark soliton generation scheme and trapping a dark soliton pulse within a nanoring resonator [8]. Furthermore, the dark soliton pulse shows a more stable behavior than the bright solitons with respect to the perturbations such as amplifier noise, fiber losses, and intra-pulse stimulated Ramman scattering [9]. It is found that the dark soliton pulses propagation in a lossy fiber, spreads in time at approximately half the rate of bright solions.

2. THE ANT COLONY ALGORITHM [10]

In this section we explain the Ant Colony Algorithm is also called Ant Colony System (ACS), Italian Scholar M. Dorigo propose a bionic evolution algorithm, who is showed by path selection behavior of ant swarm in theirs finding food process. Ant swarm is able of finding the optimal path from a food source to their nest theirs are using exploiting pheromone information. While ant swarm is working it deposits pheromone on the ground, for pheromone previously deposited by other ants. The step of ACS applied to solve problem is as follows. 1. Problem analysis: Making the problem to be solved abstract, and giving the problem space parameters variables specific implication. 2. Initialization: Giving every variable the initial value, ants all wait in the hole for starting out to search food. 3. Optimal process: Ants make a dynamic selection in accordance with given path length and information hormone strength, and release information hormone during moving. 4. Cessation conditions: If given conditions are meet, the algorithm will case; otherwise step onto 3. Step 3 is an adaptive process, and it embodies the essence of ant colony algorithm: Selection mechanism and updating mechanism.

3. DARK SOLITON CONTROL THERY

We are looking for a stationary dark soliton pulse, which is introduced into the multistage microring resonators as shown in Fig. 1. The input optical field (E_{in}) of the dark soliton pulse input is given by [8]

$$E_{in}(t) = A \tanh\left[\frac{T}{T_0}\right] \exp\left[\left(\frac{z}{2L_D}\right) - i\omega_0 t\right] \tag{1}$$

where A and z are the optical field amplitude and propagation distance, respectively. T is a soliton pulse propagation time in a frame moving at the group velocity, $T = t - \beta_1 * z$ where β_1 and

β_2 are the coefficients of the linear and second-order terms of Taylor expansion of the propagation constant. $L_D = T_0^2/|\beta_2|$ is the dispersion length of the soliton pulse. T_0 in equation is a soliton pulse propagationtime at initial input (or soliton pulse width), where t is the soliton phase shift time, and the frequency shift of the soliton is ω_0. This solution describes a pulse that keeps its temporal width invariance as it propagates, and thus is called a temporal soliton. When a soliton peak intensity $(\beta_2/\Gamma T_0^2)$ is give, then T_0 is know. For the soliton pulse in the microring device, a balance should be achieved between the dispersion lengths (L_D) and the nonlinear lengths $(L_{NL} = 1/\Gamma_{\phi NL})$, where $\Gamma = n_2 * k_0$ is the length scale over which dispersive or nonlinear effects makes the beam become wider or narrower. For a soliton pulse, ther is a balance between dispersion and nonlinear lengths, hence $L_D = L_{NL}$. When light propagates within the nonlinear material (medium), the refractive index (n) of light within the medium is given by

$$n = n_0 + n_2 I = n_0 + \frac{n_2}{A_{eff}} P \tag{2}$$

where n_0 and n_0 are the linear and nonlinear refractive indexes, respectively. I and P are the optical intensity and optical power, respectively. The effective mode core area of the device is given by A_{eff}. For the micro-ring resonator (MRR) and nano-ring resonator (NRR), the effective mode core areas range from 0.5 to 0.1 μm^2 [9, 10]. When a soliton pulse is input and propagated within a MRR, as shown in Fig. 1, which consists of a series MRRs. The resonat output is formed, thus, the normalized output of the light field is the ration between the output and input fields in each roundtrip, which is given by [10].

$$\left|\frac{E_{out}(t)}{E_{in}(t)}\right|^2 = (1-\gamma)\left[1 - \frac{\left(1-(1-\gamma)x^2\right)k}{\left(1-x\sqrt{1-\gamma}\right)^2 + 4x\sqrt{1-\gamma}\sqrt{1-k\sin^2\left(\frac{\phi}{2}\right)}}\right] \tag{3}$$

The close form of Eq. (3) indicates that a ring resonator in this particular case is very similar to a fabry-perot cavity, which has an input and output mirror with a field reflectivity, $(1-\gamma)$, and a fully reflecting mirror. k is the coupling coefficient, and $x = \exp(-\alpha L/2)$ represents a roundtrip loss coefficient, $\phi_0 = kLn_0$ and $\phi_{NL} = kLn_2|E_{in}|^2$ are the linear and nonlinear phase shifts, $k = 2\pi/\lambda$ is the wave propagation number in avacuum, where L and α are waveguide length and linear absorption coefficient, respectively in this work, the iterative method is introduced to obtain the results as shown in Eq. (3), and similarly, when the output field is connected and input into the other ring resonators.

4. MOLECULE TRANSPORTER GENERATION

In operation, a dark soliton pulse with 50-ns pulse width with the maximum power of 0.65 W is input into the dark-bright soliton conversion system as shown in Fig. 1. The suitable ring parameters are ring radii, where $R_1 = 10.0\,\mu m$, $R_2 = 7.0\,\mu m$, and $R_3 = 5.0\,\mu m$. In order to make the system associate with the practical device the selected parameters of the system are fixed to $\lambda_0 = 1.50\,\mu m$, $n_0 = 3.34$ (InGaAsP/InP). The effective core areas are $A_{eff} = 0.50$, 0.25, and 0.10 μm^2

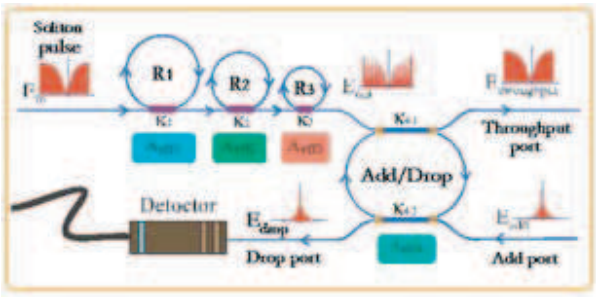

Figure 1: Schematic of a dark-bright soliton conversion system, where R_s is the ring radii, k_s is the coupling coefficient, and k_{41} and k_{42} are the add/drop coupling coefficients.

for a microring resonator (MRR) and nanoring resonator (NRR), respectively. The waveguide and coupling loses are $\alpha = 0.5\,\mathrm{dBmm}^{-1}$ and $\gamma = 0.1$, respectively, and the coupling coefficients κ_s of the MRR are ranged from 0.05 to 0.90. The nonlinear refractive index is $n_2 = 2.2 \times 10^{-13}\,\mathrm{m}^2/\mathrm{W}$. In this case, the waveguide loss used is 0.5 dBmm^{-1}. The input dark soliton pulse is chopped (sliced) into the smaller output signals of the filtering signals within the rings R_2 and R_3. We find that the output signals from R_3 are smaller than from R_1, which is more difficult to detect when it is used in the link. In fact, the multistage ring system is proposed due to the different core effective areas of the rings in the system, where the effective areas can be transferred from 0.50 to 0.10 $\mu\mathrm{m}^2$ with some losses. The soliton signals in R_3 is entered in the add/drop filter, where the dark-bright soliton conversion can be performed by using Eqs. (5) and (6). The dynamic dark soliton control can be configured to be an optical dynamic tool known as an optical tweezers, where more details of optical tweezers can be found in references. After the bright soliton input is added into the system via add port as shown in Fig. 1, the optical tweezers behavior is occurred. The parameters of system are used the same as the previous case. The bright soliton is generated with the central wavelength $\lambda_0 = 1.5\,\mu\mathrm{m}$, when the bright soliton propagating into the add/drop system, the dark-bright soliton collision in add/drop system is seen. The dark soliton valley dept, i.e., potential well is changed when it is modulated by the trapping energy (dark-bright solitons interaction) as shown in Fig. 2 The dynamic dark soliton (optical tweezers) occurs within add/drop tunable filter, when the bright soliton is input into the add port with the central wavelength $\lambda_0 = 1.5\,\mu\mathrm{m}$. (a) add/drop signals, (b) dark-bright soliton collision, (c) optical tweezers at throughput port, and (d) optical tweezers at drop port. The recovery photon can be obtained by using the dark-bright soliton conversion, which is well analyzed by Sarapat et al. [6], where the trapped photon or molecule can be released or separated from the dark soliton pulse, in practice, in this case the bright soliton is become alive and seen.

The optical tweezers probe can be trapped/confined atom/light by using the appropriate probe, which can be tuned to meet the specific requirement. The stability of the dual Brillouin is show Fig. 3 the dark soliton valley dept, i.e., potential well, is changed when it was modulated by the trapping energy (dark-bright solitons interaction) as shown in Fig. 2(b). The trapping of photon within the dark well is occurred and seen, the recovery photon can be obtained by using the dark-bright soliton conversion, which is well analyzed by Sarapat et al. [12], where the trapped photon or molecule can be released an seen separately from the dark soliton pulse, in practice, in this case the bright soliton is become alive and seen.

From the above reason, the transmission of atoms/molecules from dark soliton pulses via a wavelength router is plausible, which can be described by the following reasons: (i) A dark soliton pulse

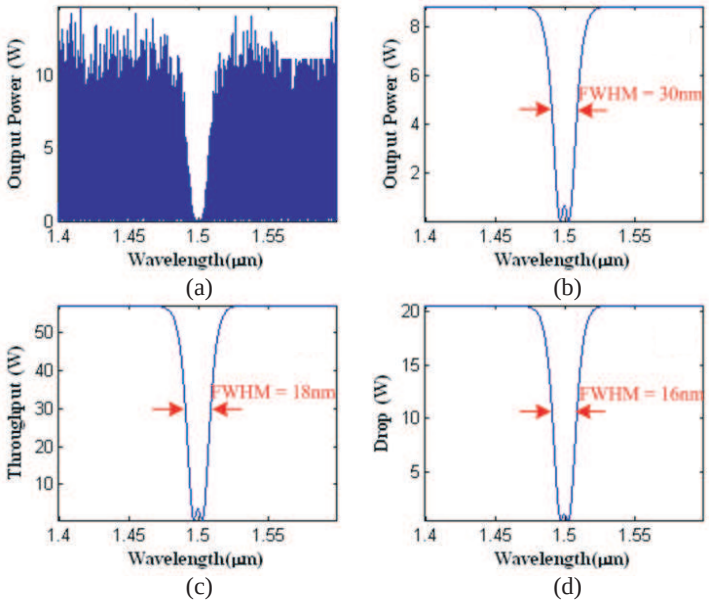

Figure 2: The dynamic dark soliton(optical tweezers) occurs within add/drop tunable filter, where (a) add/drop signals, (b) darkCbright soliton collision, (c) optical tweezers at throughput port, and (d) optical tweezers at drop port.

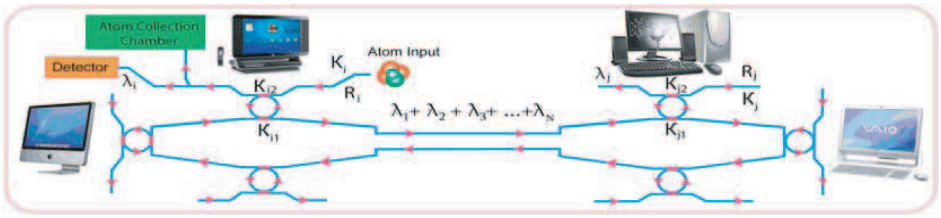

Figure 3: A schematic of atomic/molecular router and network system, where R_i, R_j: ring radii and κ_{is}, κ_{js} are the coupling coefficients.

can propagate into the optical device/media, (ii) atom/molecule being trapped by tweezers force during the movement, the atom/molecule recovery can be realized by using the optical detection scheme, where the dark-bright conversion technique is also available. From Fig. 3, the transmission atoms/molecules can be formed by the dark soliton pulse, the atoms/molecules from light pulse is required to have the specific environment, which becomes the interesting research area, where light with the specific wavelength (λ_i) is detected by a detector, while the required molecule is absorbed by the specific environment.

5. CONCLUSION

We have demonstrated that some interesting results can be obtained when the laser pulse is propagated with the nonlinear optical ring resonator, especially, in microring and nanoring resonators, which can be used to perform many applications. For instance, the broad spectrum of a monochromatic a source with the reasonable power can be generated and achieved by using a dark soliton can be converted to be a bright soliton by using the ring resonator system incorporation the add/drop multiplexer, which can be configured as a dynamic optical tweezers. The use of quantum tweezers for quantum-molecular communication/cryptography via a single photon based technology in the communication link is plausible.

REFERENCES

1. Pornsuwancharoen, N., U. Dunmeekeaew, and P. P. Yupapin, "Multi-soliton generation using a microring resonator system for DWDM base soliton communication," *Microw. and Opt. Technol. Lett.*, Vol. 51, No. 5, 1374–1377, 2009.
2. Yupapin, P. P., N. Pornsuwanchroen, and S. Chaiyasoonthorn, "Attosecond pulse generation using nonlinear microring resonators," *Microw. and Opt. Technol. Lett.*, Vol. 50, No. 12, 3108–3011, 2008.
3. Pornsuwancharoen, N. and P. P. Yupapin, "Generalized fast, slow, stop, and store lights optically within a nanoring resonator," *Microw. and Opt. Technol. Lett.*, Vol. 51, No. 4, 899–902, 2009.
4. Pornsuwancharoen, N., S. Chaiyasoonthorn, and P. P. Yupapin, "Fast and slow lights generation using chaotic signals in the nonlinear microring resonators for communication security," *Opt. Eng.*, Vol. 48, No. 1, 50005-1–5, 2009.
5. Yupapin, P. P. and N. Pornsuwancharoen, "Proposed nonlinear microring resonator arrangement for stopping and storing light," *IEEE Photon. Technol. Lett.*, Vol. 21, 404–406, 2009.
6. Sarapt, K., N. Sangwara, K. Srinuanjan, P. P. Yupapin, and N. Pornsuwancharoen, "Novel dark-bright optical solitons conversion system and power amplification," *Opt. Eng.*, Vol. 48, 045004-1–7, 2009.
7. Mitatha, S., N. Pornsuwancharoen, and P. P. Yupapin, "A simultaneous short-wave and millimeter-wave generation using a soliton pulse within a nano-waveguide," *IEEE Photon. Technol. Lett.*, Vol. 21, 932–934, 2009.
8. Agrawal, G. P., *Nonlinear Fiber Opitcs*, 4th Edition, Academic Press, New York, 2007.
9. Heidari, M. E., M. K. Moravvej-Farshi, and A. Zariffkar, "Multichannel wavelength conversion using fourth-order soliton decay," *J. Lightwave Technol.*, Vol. 25, 2571–2578, 2007.
10. Dorigo, M., V. Maniezzo, and A. Colorni, "The ant system: Optimization by a colony of cooperation agents," *IEEE Trans. on System, Man and Cybernetics*, Part B, Vol. 26, No. 1, 1–13, 1996.

Multi-photons Trapping Stability within a Fiber Bragg Grating for Quantum Sensor Use

H. M. Hairi[1], **T. Saktioto**[1,2], **S. Nafisah**[1], **M. Fadhali**[3], **Rabia Qindeel**[1], **P. P. Yupapin**[4], **and J. Ali**[1]

[1]Advanced Photonics and Science Institute, Universiti Teknologi Malaysia, Malaysia
[2]University of Riau, Pekanbaru, Riau 28293, Indonesia
[3]Ibb University, Yemen
[4]Advanced Research Center for Photonics, Faculty of Science
King Mongkut's Institute of Technology Ladkrabang, Bangkok 10520, Thailand

Abstract— We propose an interesting result of the trapped multi photons distribution within a fiber Bragg grating. The trapped photons are confined by the potential well, which introduce the motion of photons in a fiber Bragg grating affected by multi perturbations. The external perturbations are defined as series of nonlinear parametric in terms of potential energy. This investigation is developed by using the nonlinear couple mode equations and under Bragg resonance condition where the initial frequency of the light, ω_0 is the same value as the Bragg frequency, ω_B. The results show that the higher perturbation series represents the potential well is much indifferent of equilibrium. In applications, the perturbation can cause the trapped photons instability which introduces the escape photons from the potential well. The applications such as entangled photon source and quantum sensors can be performed.

1. INTRODUCTION

Periodically structured optical media have been in the clarity of research activity for many years, due to versatile technologies applications in the fields of telecommunications and sensor system [1], and also as a subject of fundamental studies [2]. At the early stage of the work in this area, the pioneering contribution by Winful et al. [3] laid the groundwork for extensive theoretical activities exploring nonlinear pulse propagating in one dimensional periodic structure known as fiber Bragg gratings. They have considered the role of the Kerr nonlinearity in the light transmission through the FBGs. Bragg gratings in optical fibers are excellent devices for studying nonlinear phenomena particularly based on the Kerr nonlinearity [4]. These structures are based on the periodic modulation of the local periodic modulation of the local refractive index in the axial direction. A characteristic feature of FBGs is a stopband, alias photonic bandgap, in their linear-propagation spectrum. The bandgap is induced by the resonant coupling between the forward- and backward-propagating waves due to the Bragg resonance [5]. The stationary properties of one-dimensional Bragg gratings were first analyzed by Winful et al. [6]. Research on the existence of soliton in FBGs has been reported [7]. Chen and Mills coined the term gap soliton in their numerical work covering the nonlinear optical super lattices [8]. Mills and Trullinger obtained an analytical solution for stationary gap solitary waves [9]. Sipe and Winful [10], Christoudolides and Joseph [11], Aceves and Wabnitz [12], de Sterke and Sipe [13] and recently, Senthilnathan et al. have derived the formation of bright and gap soliton solution for nonlinear coupled mode equation, which governs the pulse propagation in FBG [7].

The motion of a particle moving in FBG represents the pulse propagation in the grating structure of fiber optics exhibiting the existence of optical soliton. In order to describe the photon motion, the function of potential energy is depicted. Photon can be trapped by some parameters of potential energy such as α and γ. The other parameter, theta, θ is introduced to describe any disturbance effect of moving particle having specific energy. In this paper we further describe the effect of α and γ to obtain the optimized point of the potential well.

2. MULTI PHOTONS POTENTIAL ENERGY DISTRIBUTION

Wave propagation in FBG is analyzed by solving Maxwell's equation with appropriate boundary conditions. In the presence of Kerr nonlinearity, using the coupled-mode theory, the nonlinear coupled mode equation is defined under the absence of material and waveguide dispersive effects. The dispersion arising from the periodic structure dominates near Bragg resonance conditions and it

is valid only for wavelengths near to the Bragg wavelength. By substituting the stationary solution to the coupled mode equation and by assuming $E_{\pm}(z,t) = e_{\pm}(z)e^{-i\vec{\delta}ct/\bar{n}}$, we obtain

$$\text{and} \quad \begin{array}{l} i\frac{de_f}{dz} + \hat{\delta}e_f + \kappa e_b + \left(\Gamma_S |e_f|^2 + 2\Gamma_X |e_b|^2\right) e_f = 0 \\ -i\frac{de_b}{dz} + \hat{\delta}e_b + \kappa e_f + \left(\Gamma_S |e_b|^2 + 2\Gamma_X |e_f|^2\right) e_b = 0 \end{array}, \tag{1}$$

Equation (1) represents the time-independent light transmission through the gratings structure where e_f and e_b are the forward and backward propagating modes [1]. In order to explain the formation of Bragg soliton, consider the Stokes parameter [11] since it will provide useful information about the total energy and energy difference between the forward and backward propagating modes.

$$\begin{array}{l} A_0 = |e_f|^2 + |e_b|^2, \\ A_1 = e_f e_b^* + e_f^* e_b, \\ A_2 = i\left(e_f e_b^* - e_f^* e_b\right), \\ A_3 = |e_f|^2 - |e_b|^2 \end{array} \tag{2}$$

with the constraint $A_0^2 = A_1^2 + A_2^2 + A_3^2$. In the FBG theory, the nonlinear coupled-mode (NLCM) equation requires that the total power $P_0 = A_3 = |e_f|^2 - |e_b|^2$ inside the grating is constant along the grating structures. Rewriting the NLCM equations in terms of Stokes parameter gives

$$\frac{dA_0}{dz} = -2\kappa A_2, \quad \frac{dA_1}{dz} = 2\hat{\delta}A_2 + 3\Gamma A_0 A_2, \quad \frac{dA_2}{dz} = -2\hat{\delta}A_1 - 2\kappa A_0 - 3\Gamma A_0 A_1, \quad \frac{dA_3}{dz} = 0 \tag{3}$$

In Equation (3), we drop the distinction between the Self-Phase Modulation and cross effect modulation effects and hence it becomes $3\Gamma = 2\Gamma_x + \Gamma_s$. It can be clearly show that the total power, P_0 $(= A_3)$ inside the grating is found to be constant or conserved along the grating structure [2]. In the construction of the anharmonic oscillator type equation, it is necessary to use the conserved quantity, and it is obtained in the form $\hat{\delta}A_0 + \frac{3}{4}\Gamma A_0^2 + \kappa A_1 = C$, where C is the constant of integration and $\hat{\delta}$ is the detuning parameter. Using Equation (3), we obtain

$$\frac{d^2A_0}{dz^2} - \alpha A_0 + \beta A_0^2 + \gamma A_0^3 = 4\hat{\delta}C \tag{4}$$

where $\alpha = 2[2\hat{\delta}^2 - 2\kappa^2 - 3\Gamma C]$, $\beta = 9\Gamma\hat{\delta}$ and $\gamma = \frac{9}{4}\Gamma^2$. Equation (4) contains all the physical parameter of the NLCM equation.

In order to describe the motion of a particle moving with the classic anharmonic potential, where the external disturbance is involved then we have the solution as follows,

$$V(A_0) = -\alpha\frac{A_0^2}{2} + \beta\frac{A_0^3}{3} + \gamma\frac{A_0^4}{4} \tag{5}$$

It represents the potential energy distribution in the Fiber Bragg Grating structures.

3. MULTI PHOTONS TRAPPING INSTABILITY

Consider Equation (2) having a set of constraints which is introduced by $\phi_{(e)} = \sum_{n=0}^{\infty} A_0^n$ as a function of perturbation factor then

$$\frac{d^2A_0}{dz^2} = \phi_e''|_{n=0} \tag{6}$$

If Equation (4) is accumulated using external perturbation, then

$$\phi''|_{n=0} + \sum_{\substack{n=0 \\ m=1}}^{\infty} C_m A_0^n = \psi$$

where ψ is a function of $f(\delta, C, C_m)$, and $C_m = [\alpha, \beta, \gamma, \ldots]$.

The value of $m = 2n$ for $n = 1, 2, 3, \ldots$, $m = 2n + 1$ for $n = 0, 1, 2, \ldots$.

C is constant and $C = (C_1, C_2, C_3, \ldots, C_m)$. The value of C is linear to A_0 but not to V. Equation (5) can then be modified by

$$V(A_0) = \sum_{\substack{m=1 \\ n=0}}^{\infty} C_m A_0^n \tag{7}$$

Equation (7) represents the complete potential energy distribution in the Fiber Bragg Grating structure. We believe at this juncture, the potential function is modified from Conti and Mills [14]. Using well-known Duffing oscillator type equation, analogically it is written as

$$\phi_e'' + \sum_{\substack{m=1 \\ n=0}}^{\infty} C_m A_0^n = 0 \tag{8}$$

For multi perturbation of nonlinear parametric, two major shapes will be simplified in series term.

Figure 1 depicts the motion of photon in potential well changes when few nonlinear parameter is take into account as shown is Equation (5). There are theoretically some comments in this figure. Photon is trapped by α parameter which is depicted by legend V. When α is too large, the potential well produces A_0 an increase in and have a wider double well. γ parameter is shown by X legend. When γ is large, the potential well produces an increase in A_0. Suppose that the source that is imposed onto FBG than initial power is used to generate the particles. It shows that double well potential well is not symmetric and potential energy will decrease within the region at legend Y. The other effect is the perturbation of potential energy by legend Z where photon cannot be trapped symmetrically. It will tend to equilibrate but it is not stable where it will lead to losses.

In term of parametric function, we can describe it as follows. The change in α will affect the dip of the potential well. If α is approximately too small, the shape of the potential well will turn into a single potential well. The occurrence of β effect in the motion of photon will give effect to the negative region for $A_0 < 0$. The effect of γ shows that the width of potential well will decrease if we increased the value of γ. Therefore if we increased the value of γ, we can assume that the photon will be localized trapped. Another nonlinear factor, θ will turns the shape of potential well

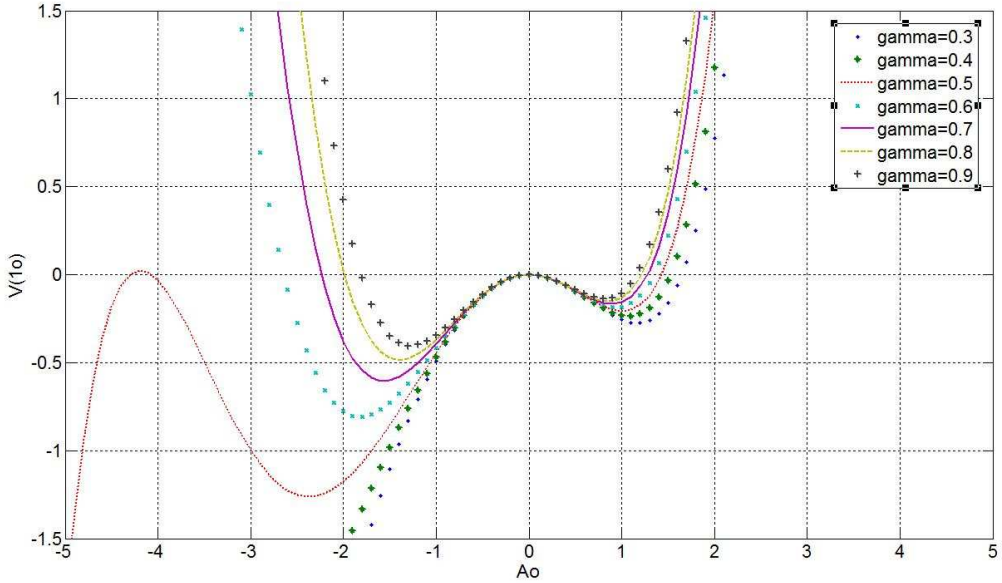

Figure 1: The motion of photon in potential well for $\alpha = 0.9$, $\beta = 0.3$, $\theta = 0.09$ and γ is varies from 0.3 to 0.9.

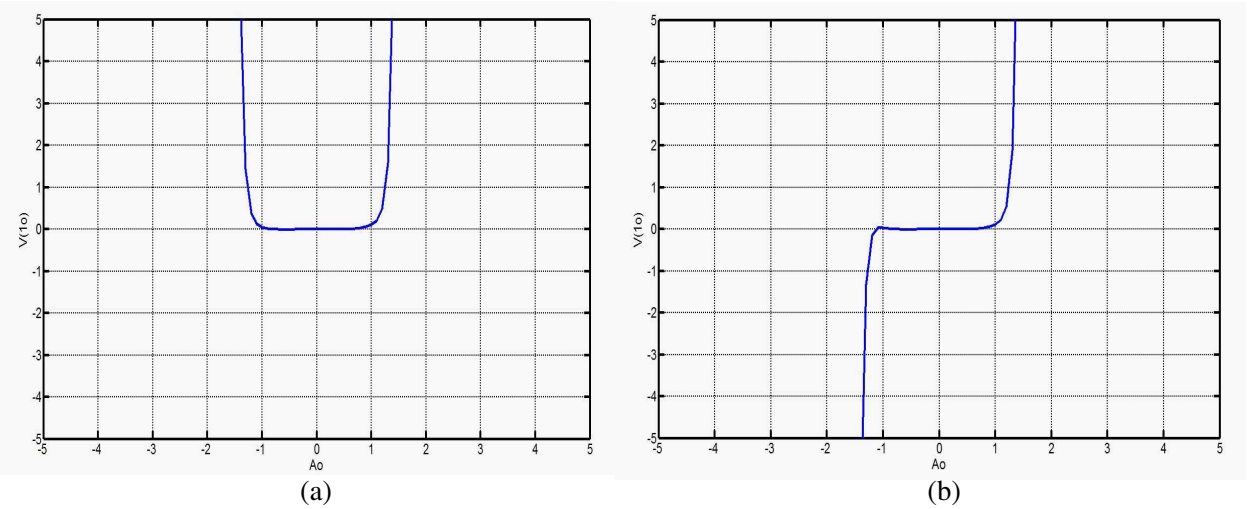

Figure 2: The disturbance factor that affect the shape of the potential well of the motion of photon.

rapidly. If we include the existence of θ, the shape of potential well becomes chaotic. The photon does not only move in certain region known as potential well but also can be termed as free moving particles. Figure 2 explains the extrapolation of the graph if more factors of perturbation added into Equation (7). The addition of parametric factors by the higher odd number (Figure 2(b)) will lead the photon to be untrapped and higher even number (Figure 2(a)) will allow the photon to move in a well. It is clearly shown in the graphs that as $n \gg \infty$, the value of $|A_0|$ will remain constant in the range of $-2 < A_0 < 2$. However, when the value of $V_{(0)}$ is equal to zero, there are many possibilities of A_0, meaning the exact value of intentsity, A_0 to trap the photon is difficult to determine in this condition. If the parametric factor is considered is too large then we may conclude that the photon is in indifferent state part of the equlibrium.

The stationary solutions of Equation (7) are applied neither for bright nor dark soliton solution since the dominant parameters in contributing A_0 is unknown. However, from Equation (7) we have

$$A_0 = A_0\left(C_m, z\right) \tag{9}$$

Under these conditions, the frequencies with photonic band gap keep forming an envelope after the exact balancing at grating-induced dispersion with nonlinearity. It either decays or increased with the forward and backward waves being transferred by Bragg reflection process. The total energy of the system, potential energy function is equal to zero having multi perturbation which is $-1 < A_0 < 1$ and if $V \to \infty$, $A_0 = 2$.

4. QUANTUM PROCESSING UNIT

Let us consider that the case when the photon output is input into the quantum processor unit. Generally, there are two pairs of possible polarization entangled photons forming within the ring device, which are represented by the four polarization orientation angles as $[0°, 90°]$, [135° and 180°]. These can be formed by using the optical component called the polarization rotatable device and a polarizing beam splitter (PBS). In this concept, we assume that the polarized photon can be performed by using the proposed arrangement. Where each pair of the transmitted qubits can be randomly formed the entangled photon pairs. To begin this concept, we introduce the technique that can be used to create the entangled photon pair (qubits) as shown in Figure 3, a polarization coupler that separates the basic vertical and horizontal polarization states corresponds to an optical switch between the short and the long pulses. We assume those horizontally polarized pulses with a temporal separation of Δt. The coherence time of the consecutive pulses is larger than Δt. Then the following state is created by Equation (10),

$$|\Phi\rangle_p = |1, H\rangle_s |1, H\rangle_i + |2, H\rangle_s |2, H\rangle_i \tag{10}$$

In the expression $|k, H\rangle, k$ is the number of time slots (1 or 2), where denotes the state of polarization [horizontal $|H\rangle$ or vertical $|V\rangle$], and the subscript identifies whether the state is the signal (s) or the idler (i) state. In Equation (10), for simplicity, we have omitted an amplitude term

that is common to all product states. We employ the same simplification in subsequent equations in this paper. This two-photon state with $|H\rangle$ polarization shown by Equation (10) is input into the orthogonal polarization-delay circuit shown schematically. The delay circuit consists of a coupler and the difference between the round-trip times of the micro ring resonator, which is equal to Δt. The micro ring is tilted by changing the round trip of the ring is converted into $|V\rangle$ at the delay circuit output. That is the delay circuits convert $|k, H\rangle$ to be

$$r\,|k, H\rangle + t_2 \exp(i\phi)\,|k+1, V\rangle + rt_2 \exp(i_2\phi)\,|k+2, H\rangle + r_2 t_2 \exp(i_3\phi)\,|k+3, V\rangle\,.$$

where t and r is the amplitude transmittances to cross and bar ports in a coupler. Then Equation (10) is converted into the polarized state by the delay circuit as

$$\begin{aligned}
|\Phi\rangle &= [|1, H\rangle_s + \exp(i\phi_s)\,|2, V\rangle_s] \times [|1, H\rangle_i + \exp(i\phi_i)\,|2, V\rangle_i] \\
&\quad + [|2, H\rangle_s + \exp(i\phi_s)\,|3, V\rangle_s] \times [|2, H\rangle_i + \exp(i\phi_i)\,|2, V\rangle_i] \\
&= [|1, H\rangle_s\,|1, H\rangle_i + \exp(i\phi_i)\,|1, H\rangle_s\,|2, V\rangle_i] + \exp(i\phi_s)\,|2, V\rangle_s\,|1, H\rangle_i \\
&\quad + \exp[i\,(\phi_s + \phi_i)]\,|2, V\rangle_s\,|2, V\rangle_i + |2, H\rangle_s\,|2, H\rangle_i + \exp\,(i\phi_i)\,|2, H\rangle_s\,|3, V\rangle_i \\
&\quad + \exp\,(i\phi_s)\,|3, V\rangle_s\,|2, H\rangle_i + \exp[i\,(\phi_s + \phi_i)]\,|3, V\rangle_s\,|3, V\rangle_i
\end{aligned} \tag{11}$$

By the coincidence counts in the second time slot, we can extract the fourth and fifth terms. As a result, we can obtain the following polarization entangled state as

$$|\Phi\rangle = |2, H\rangle_s\,|2, H\rangle_i + \exp[i\,(\phi_s + \phi_i)]\,|2, V\rangle_s\,|2, V\rangle_i \tag{12}$$

We assume that the response time of the Kerr effect is much less than the cavity round-trip time. Because of the Kerr nonlinearity of the optical device, the strong pulses acquire an intensity dependent phase shift during propagation. The interference of light pulses at a coupler introduces the output beam, which is entangled. Due to the polarization states of light pulses are changed and converted while circulating in the delay circuit, where the polarization entangled photon pairs can be generated. The entangled photons of the nonlinear ring resonator are separated to be the signal and idler photon probability. The polarization angle adjustment device is applied to investigate the orientation and optical output intensity, this concept is well described by the published works [15, 16].

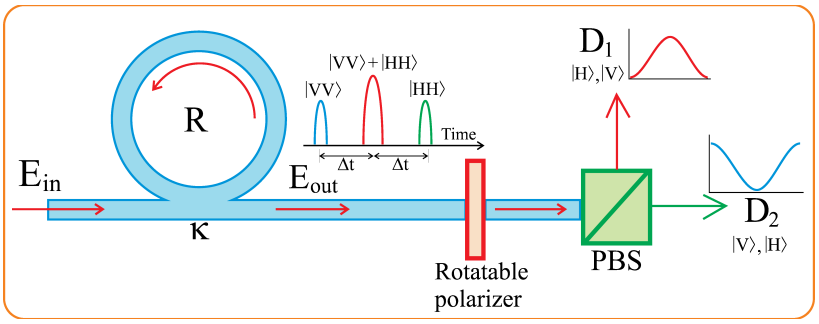

Figure 3: A schematic of an entangled photon pair manipulation within a ring resonator. The Bell's state is propagating to a rotatable polarizer and then is split by a beam splitter (PBS) flying to detector D_1 and D_2.

5. CONCLUSION

We successfully modified and developed the potential energy distribution of photon by setting the disturbance of multiperturbation potential energy in a fiber Bragg grating. It is found that the potential well under Bragg resonance condition is not symmetrical and conserved. The higher perturbation series representing the potential well is much indifferent of the equilibrium in both odd and even nonlinear parametric factor of n.

ACKNOWLEDGMENT

The authors would like to thanks the Institute of Advanced Photonics and Sciences, Enabling Science & Nanotechnology (ESciNano) Research Alliance University Teknologi Malaysia, Malaysia, University of Riau, Indonesia and National Science Fellowship, Malaysia for general support in this research.

REFERENCES

1. Kashyap, R., *Fiber Bragg Gratings*, Academic Press, San Diego, 1999.
2. Malomed, B. A., *Soliton Management in Periodic Systems*, Springer, New York, 2006.
3. Winful, H. G., J. H. Marburger, and E. Garmire, *Appl. Phys. Lett.*, Vol. 35, 379, 1979.
4. Kivshar, Y. S. and G. P. Agrawal, *Optical Soliton: From Fibers to Photonics Crystal*, Academic Press, USA, 2003.
5. Chow, K. W., I. M. Merhasin, B. A. Malomed, K. Nakkeeran, K. Senthilnathan, and P. K. A. Wai, "Periodic waves in fiber Bragg gratings," *Phys. Rev. E*, Vol. 77, 026602, 2008.
6. Senthilnathan, K. and K. Porsezian, "Symmetry-breaking instability in gap soliton," *Optics Commun.*, Vol. 227, 295–299, 2003.
7. Porsezian, K. and K. Senthilnathan, "Solitons in fiber Bragg grating," *Guided Wave Optical Components and Devices: Basics, Technology and Applications*, Bishnu P. Pal (Eds.), 251–279, Academic Press, USA, 2006.
8. Chen, W. and D. L. Mills, "Gap solitons and the nonlinear optical response of supperlattices," *Phys. Rev. Lett.*, Vol. 58, 160–163, 1987.
9. Mill, D. L. and S. E. Trullinger, "Gap solitons in nonlinear periodic structures," *Phys. Rev. B*, Vol. 36, 947, 1987.
10. Sipe, J. E. and H. G. Winful, "Nonlinear Schröedinger solitons in a periodic structure," *Opt. Lett.*, Vol. 13, 132, 1988.
11. Christodoulides, D. N. and R. I. Joseph, "Slow Bragg solitons in nonlinear periodic structures," *Phys. Rev. Lett.*, Vol. 62, 1746, 1989.
12. Aceves, A. B. and S. Wabnitz, "Self-induced transparency solitons in nonlinear refractive periodic media," *Phys. Lett. A*, Vol. 141, 37, 1989.
13. De Sterke, C. M., D. G. Salinas, and J. E. Sipe, "Coupled-mode theory for light propagation through deep nonlinear gratings," *Phys. Rev. E*, Vol. 54, No. 2, 1996.
14. Conti, C. and S. Trillo, "Bifurcation of gap solitons through catastrophe theory," *Phys. Rev. E*, Vol. 64, 036617, 2001.
15. Yupapin, P. P. and S. Suchat, "Entangle photon generation using fiber optic Mach-Zehnder interferometer incorporating nonlinear effect in a fiber ring resonator," *Nanophotonics (JNP)*, Vol. 1, 13504-1, 2007.
16. Pornsuwancharoen, N. and P. P. Yupapin, "Entangled photon states recovery and cloning via the micro ring resonators and an add/drop multiplexer," *Int. J. Light and Electron Opt.*, doi:10.1016/j.ijleo.2008.09.034.

Novel Multi Channels — Multi Layers Atom Transportation and Quantum Security Using Dynamic Tweezer for Communication Link

C. Vongchumyen[1], **S. Mitatha**[1], **and P. P. Yupapin**[2]

[1]Hybrid Computing Research Laboratory, Department of Computer Engineering, Faculty of Engineering
King Mongkut's Institute of Technology Ladkrabang, Bangkok 10520, Thailand
[2]Advanced Research Center for Photonics, Physics Division, Faculty of Science
King Mongkut's Institute of Technology Ladkrabang, Bangkok 10520, Thailand

Abstract— We propose a novel system that can be used to form the security using quantum technique in communication link. Further more, it can form multi channels — multi layers communication link by using the transportation of an atom via dynamic tweezer. The system consist on two parts. First, the system for generating the dynamic tweezer, which used to collect an atom and transport via wavelength router. Second, the modulator which use to modulate the trapped atom in tweezer with microwave signal. After we uplink the modulated signal via microwave communication link, the received signal still have a trapped atom which can be detected/demodulated to read back. Further more, quantum security can be obtained by using quantum processing unit to detect atom polarization. If the communication has been trapped, The modulated atom will be lost and cannot be detect by the receiver, So we knew that the security has been broken.

1. INTRODUCTION

Dynamic optical tweezers are a powerful tool for use in the three-dimensional rotation of and translation (location manipulation) of nano-structures such as micro- and nano-particles as well as living micro-organisms [1]. We have described a new concept of developing dynamic optical tweezers source using a Gaussian pulse. The developed tweezers has many potential applications in electron, ion, atom and molecule probing and manipulation as well as DNA probing and transportation. Furthermore, the soliton pulse generator is a simple and compact design, making it more commercially viable. We also present the very interesting work of the use of a dynamic optical tweezers as a probe and transport of atoms or molecules via communication links, which is important to ensure that the transported atom/molecule is not lost in the link media. The propose system also have a quantum-molecular state to ensure the security of the communication link. Finally we also show that our proposed system can be use in multi-channels which mean, More than one communication channel can exist in only one media link which no interfere to each other.

2. DYNAMIC OPTICAL TWEEZERS GENERATION

Light from a monochromatic light source is launched into a ring resonator with constant light field amplitude (E_0) and random phase modulation as shown in Fig. 1, which is the combination of terms in attenuation (α) and phase (ϕ_0) constants, which results in temporal coherence degradation. Hence, the time dependent input light field (E_{in}), without pumping term, can be expressed as

$$E_{in}(t) = E_0 \exp^{-\alpha L + j\phi_0(t)} . \tag{1}$$

where L is a propagation distance (waveguide length).

The input optical field as shown in Eq. (1), i.e., a Gaussian pulse, is input into a nonlinear microring resonator. By using the appropriate parameters, the chaotic signal is obtained. To retrieve the signals from the chaotic noise, we propose to use the add/drop device with the appropriate parameters. This is given in details as followings. The optical outputs of a ring resonator add/drop filter can be given by the Eqs. (2) and (3) [2].

$$\left|\frac{E_t}{E_{in}}\right|^2 = \frac{(1-\kappa_1) - 2\sqrt{1-\kappa_1}\cdot\sqrt{1-\kappa_2}\, e^{-\frac{\alpha}{2}L}\cos(k_n L) + (1-\kappa_2)e^{-\alpha L}}{1 + (1-\kappa_1)(1-\kappa_2)e^{-\alpha L} - 2\sqrt{1-\kappa_1}\cdot\sqrt{1-\kappa_2}\, e^{-\frac{\alpha}{2}L}\cos(k_n L)} \tag{2}$$

and

$$\left|\frac{E_d}{E_{in}}\right|^2 = \frac{\kappa_1\kappa_2 e^{-\frac{\alpha}{2}L}}{1 + (1-\kappa_1)(1-\kappa_2)e^{-\alpha L} - 2\sqrt{1-\kappa_1}\cdot\sqrt{1-\kappa_2}\, e^{-\frac{\alpha}{2}L}\cos(k_n L)} \tag{3}$$

where E_t and E_d represents the optical fields of the throughput and drop ports respectively. The transmitted output can be controlled and obtained by choosing the suitable coupling ratio of the ring resonator, which is well derived and described by reference [3]. Where $\beta = kn_{eff}$ represents the propagation constant, n_{eff} is the effective refractive index of the waveguide, and the circumference of the ring is $L = 2\pi R$, here R is the radius of the ring. In the following, new parameters will be used for simplification, where $\phi = \beta L$ is the phase constant. The chaotic noise cancellation can be managed by using the specific parameters of the add/drop device, which the required signals at the specific wavelength band can be filtered and retrieved. κ_1 and κ_2 are coupling coefficient of add/drop filters, $k_n = 2\pi/\lambda$ is the wave propagation number for in a vacuum, and the waveguide (ring resonator) loss is $\alpha = 0.5\,\mathrm{dBmm}^{-1}$. The fractional coupler intensity loss is $\gamma = 0.1$. In the case of add/drop device, the nonlinear refractive index is neglected.

3. QUANTUM-MOLECULAR COMMUNICATION SECURITY

Let us consider that the case when the optical tweezers output from the throughput port in Fig. 1 is partially input into the quantum processor unit as shown in Fig. 2. Generally, there are two pairs of possible polarization entangled photons forming within the ring device, which are represented by the four polarization orientation angles as [0°, 90°], [135° and 180°]. These can be formed by using the optical component called the polarization rotatable device and a polarizing beam splitter (PBS). In this concept, we assume that the polarized photon can be performed by using the proposed arrangement. Where each pair of the transmitted qubits can be randomly formed the entangled photon pairs. To begin this concept, we introduce the technique that can be used to create the entangled photon pair (qubits) as shown in Fig. 2, a polarization coupler that separates the basic vertical and horizontal polarization states corresponds to an optical switch between the short and the long pulses. We assume those horizontally polarized pulses with a temporal separation of Δt. The coherence time of the consecutive pulses is larger than Δt. Then the following state is created by Eq. (4) [4].

$$|\Phi\rangle_p = |1, H\rangle_s |1, H\rangle_i + |2, H\rangle_s |2, H\rangle_i \tag{4}$$

In the expression $|k, H\rangle$, k is the number of time slots (1 or 2), where denotes the state of polarization [horizontal $|H\rangle$ or vertical $|V\rangle$], and the subscript identifies whether the state is the signal (s) or the idler (i) state. In Eq. (4), for simplicity, we have omitted an amplitude term that is common to all product states. We employ the same simplification in subsequent equations in this paper. This two-photon state with $|H\rangle$ polarization shown by Eq. (4) is input into the orthogonal polarization-delay circuit shown schematically. The delay circuit consists of a coupler and the difference between the round-trip times of the microring resonator, which is equal to Δt. The microring is tilted by

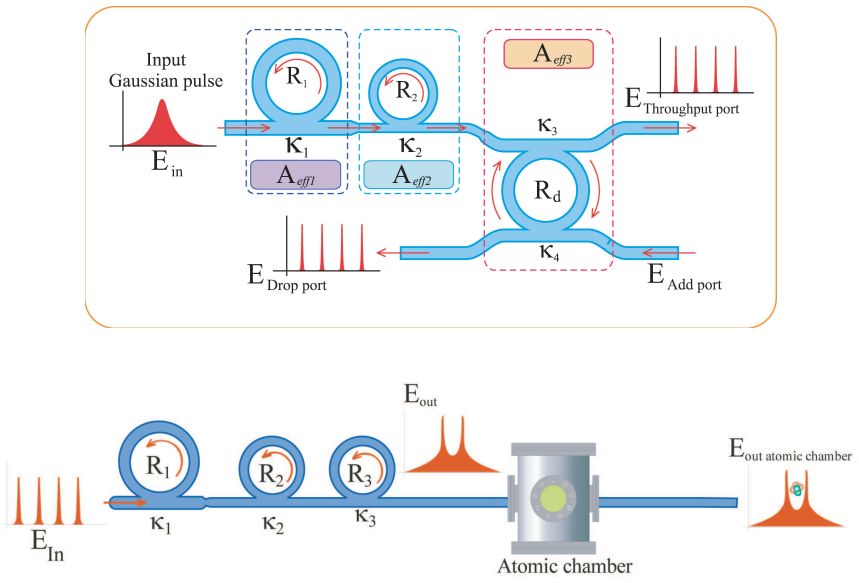

Figure 1: A schematic of a Gaussian soliton generation system with trapped atom from atomic chamber, where R_s: ring radii, κ_s: coupling coefficients, R_d: an add/drop ring radius, $A_{eff}s$: effective areas.

changing the round trip of the ring is converted into $|V\rangle$ at the delay circuit output. That is the delay circuits convert $|k,H\rangle$ to be

$$r\,|k,H\rangle + t_2\exp(i\phi)\,|k{+}1,V\rangle + rt_2\exp(i_2\phi)\,|k{+}2,H\rangle + r_2t_2\exp(i_3\phi)\,|k{+}3,V\rangle\,.$$

where t and r is the amplitude transmittances to cross and bar ports in a coupler. Then Eq. (4) is converted into the polarized state by the delay circuit as

$$\begin{aligned}|\Phi\rangle &= [|1,H\rangle_s + \exp(i\phi_s)\,|2,V\rangle_s] \times [|1,H\rangle_i + \exp(i\phi_i)\,|2,V\rangle_i] \\ &\quad +[|2,H\rangle_s + \exp(i\phi_s)\,|3,V\rangle_s] \times [|2,H\rangle_i + \exp(i\phi_i)\,|2,V\rangle_i] \\ &= [|1,H\rangle_s\,|1,H\rangle_i + \exp(i\phi_i)\,|1,H\rangle_s\,|2,V\rangle_i] + \exp(i\phi_s)\,|2,V\rangle_s\,|1,H\rangle_i \\ &\quad +\exp[i\,(\phi_s+\phi_i)]\,|2,V\rangle_s\,|2,V\rangle_i + |2,H\rangle_s\,|2,H\rangle_i \\ &\quad +\exp\,(i\phi_i)\,|2,H\rangle_s\,|3,V\rangle_i + \exp\,(i\phi_s)\,|3,V\rangle_s\,|2,H\rangle_i + \exp[i\,(\phi_s+\phi_i)]\,|3,V\rangle_s\,|3,V\rangle_i \end{aligned} \quad (5)$$

By the coincidence counts in the second time slot, we can extract the fourth and fifth terms. As a result, we can obtain the following polarization entangled state as

$$|\Phi\rangle = |2,H\rangle_s\,|2,H\rangle_i + \exp[i\,(\phi_s+\phi_i)]\,|2,V\rangle_s\,|2,V\rangle_i \quad (6)$$

We assume that the response time of the Kerr effect is much less than the cavity round-trip time. Because of the Kerr nonlinearity of the optical device, the strong pulses acquire an intensity dependent phase shift during propagation. The interference of light pulses at a coupler introduces the output beam, which is entangled. Due to the polarization states of light pulses are changed and converted while circulating in the delay circuit, where the polarization entangled photon pairs can be generated. The entangled photons of the nonlinear ring resonator are separated to be the signal and idler photon probability. The polarization angle adjustment device is applied to investigate the orientation and optical output intensity, this concept is well described by the published work [5]. The transporter states can be controlled and identified by using the quantum processing system after as shown in Fig. 2.

By using the reasonable dark-bright soliton input power, the tunable optical tweezer can be controlled, which can provide the entangled photon as the dynamic optical tweezer probe. The smallest tweezer width of 16 nm is generated and achieved. In application, such a behavior can be used to confine the suitable size of light pulse or molecule, which can be employed in the same way of the optical tweezer. But in this case the terms dynamic probing is come to be a realistic function, therefore, the transportation of the trapped atom/molecule/photon by a single photon is plausible. For simplicity, the entangled photons power is attenuated to be a single photon be fore the detection, therefore, the separation between photon and molecule is employed the same way of a single photon detection scheme. This means that the detection of the transported single atom/molecule can be configured by using the single photon detection method. Thus, the transported molecule/atom with long distance link via quantum-molecular transporter is realized. Furthermore, the secured hybrid quantum-molecular communication can be implemented within the existed transmission link.

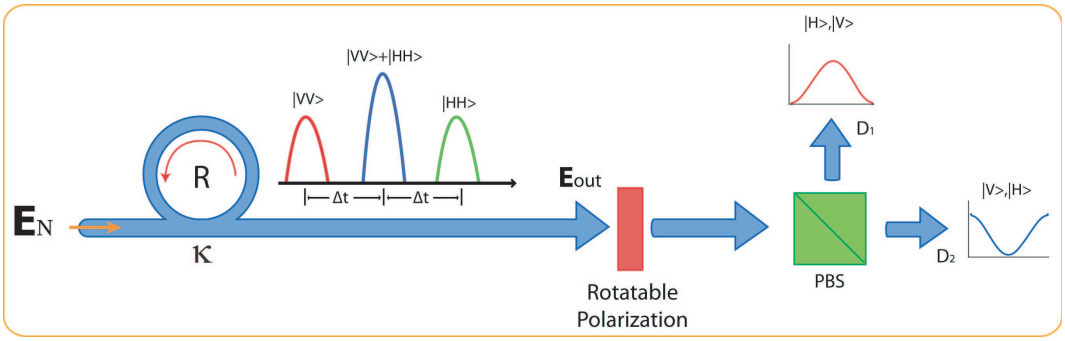

Figure 2: A schematic of an entangled photon pair manipulation within a ring resonator. The Bell's state is propagating to a rotatable polarizer and then is split by a beam splitter (PBS) flying to detector D_1 and D_2.

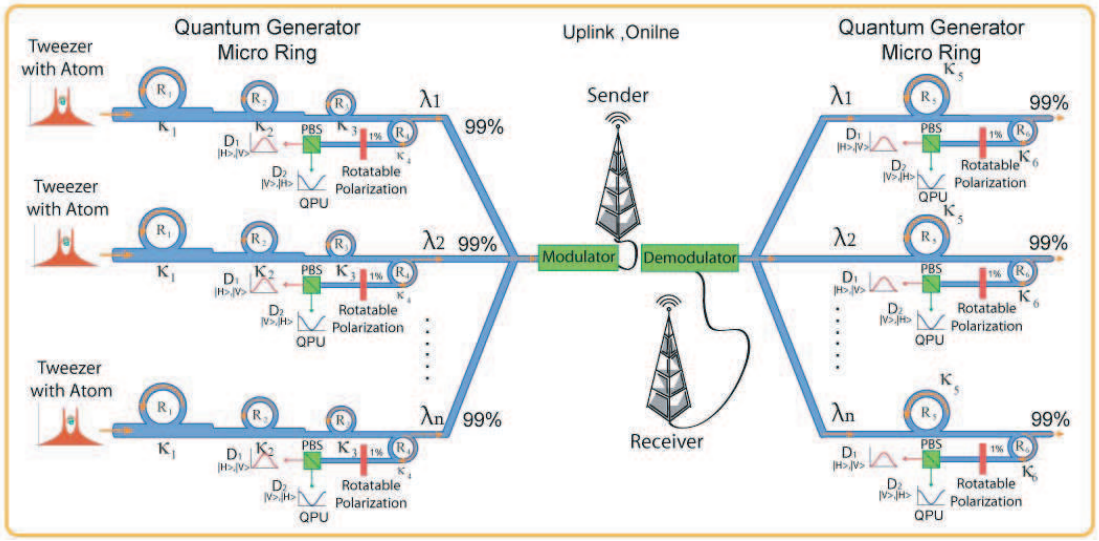

Figure 3: A schematic of the atomic and quantum molecular transmission using dynamic optical tweezers.

4. MULTI CHANNELS — MULTI LAYERS ATOM TRANSPORTATION AND QUANTUM SECURITY

From Fig. 1, by using the reasonable optical input power into the microring system, the tunable optical tweezers can be controlled, which can provide the entangled photon as the dynamic optical tweezers probe. The smallest tweezer width of 11 nm is generated and achieved. In application, such a behavior can be used to confine the suitable size of light pulse or atom, which can be employed in the same way of the optical tweezers. But in this case the terms dynamic probing becomes to be a realistic function, therefore, the transportation of the trapped atom/atom/photon by a single photon is plausible.

For simplicity, the entangled photons power is attenuated to be a single photon be fore the detection, therefore, the separation between photon and atom is employed the same way of a single photon detection scheme. This means that the detection of the transported single atom/atom can be configured by using the single photon detection method. Thus, the transported atom/atom with long distance link via quantum-molecular transporter is realized. Furthermore, the secured hybrid quantum-molecular communication can be implemented within the existed transmission link as shown in Fig. 3. The transmitter unit can be used to generate the quantum codes within the series of micro ring resonators and the cloning unit, which is operated by the add/drop filter (R_{dN1}). The receiver unit can be used to detect the quantum bits via the optical link, which can be obtained via the end quantum processor and the reference states can be recognized by using the cloning unit, which is operated by the add/drop filter (R_{dN2}). The remaining part of a system is the parallel processing system using the multi transporters multiplexing via an optical multiplexer as shown in the schematic diagram in Fig. 3. The multi transporters (arrays) are allowed to form and transmit via the optical link, where the transporters with different wavelengths (λ_N) can be generated and obtained which is available for multi atoms transportation. Moreover, the atom identification can be recognized and confirmed by using the transporter quantum state.

5. CONCLUSION

We have proposed a new system of security communication link using the trapped atom by dynamic optical tweezers and quantum-molecular state. Begin with the generation of optical tweezers using a Gaussian pulse as an input for the microring resonator. Then the optical tweezers have fed to atomic chamber to collect an atom. After that, Optical tweezers with trapped atom propagate to quantum generator microring to detect state and sent to modulator to modulate with conventional communication link. Finally, the receiver have received the optical tweezers using demodulator. The trapped atom and quantum state have been detect for ensure the security of the communication link. In case of security breach, The trapped atom must be lost or quantum state has been changed or both. Further more, The proposed system can be use in multi channels — multi

layers communication link, which mean more than user or communication pipe can use the same conventional communication link such as microwave link.

REFERENCES

1. Ashkin, A., J. M. Dziedzic, J. E. Bjorkholm, and S. Chu, "Observation of a single-beam gradient force optical trap for dielectric particles," *Opt. Lett.*, Vol. 11, 288–290, 1986.
2. Yupapin, P. P. and W. Suwancharoen, "Chaotic signal generation and cancellation using a micro ring resonator incorporating an optical add/drop multiplexer," *Opt. Commun.*, Vol. 280, No. 2, 343–350, 2007.
3. Yupapin, P. P., P. Saeung, and C. Li, "Characteristics of complementary ring-resonator add/drop filters modeling by using graphical approach," *Opt. Commun.*, Vol. 272, 81–86, 2007.
4. Suchat, S., W. Khannam, and P. P. Yupapin, "Quantum key distribution via an optical wireless communication link for telephone network," *Opt. Eng. Lett.*, Vol. 46, No. 10, 100502–100511, 2007.
5. Yupapin, P. P. and S. Suchat, "Entangle photon generation using fiber optic Mach-Zehnder interferometer incorporating nonlinear effect in a fiber ring resonator," *Nanophotonics (JNP)*, Vol. 1, 13504, 2007.

Generalized DNA Codes via Nonlinear Micro Ring Resonator for Signal Security Use

W. Chatsri[1], **W. Siririth**[1, 2], **S. Mitatha**[1], **O. Pingern**[3], **and P. P. Yupapin**[4]

[1]Department of Computer Engineering, Faculty of Engineering
King Mongkut's Institute of Technology Ladkrabang, Bangkok 10520, Thailand
[2]Faculty of Engineering, Chiangrai College, Chiangrai 57000, Thailand
[3]Faculty of Science, Ramkhamhaeng University, Bangkok 10400, Thailand
[4]Advanced Research Center for Photonics, Faculty of Science
King Mongkut's Institute of Technology Ladkrabang, Bangkok 10520, Thailand

Abstract— We propose a new design of a security scheme by using the nonlinear behaviors of light pulses in a micro ring resonator for signal security application. The DNA codes can be performed and modulated by the generated carrier within the ring system. The DNA codes can be generated and formed by the logical pulses "*A*" or "*T*" or "*C*" or "*G*" by using the signal quantizing method, which can be randomly coded by controlling the specific optical input coupling power, i.e., coupling coefficient and ring radii. Simulation results when the ring radius used is 10.0 μm, A_{eff} = 25 μm^2, and the other selected parameters are closed to the practical device values that are presented and discussed. The security concept provided by DNA codes can be generated using the random control of coupling powers. For instance, the controlled input power used is between 2.0 and 3.5 mW, whereas the quantizing threshold powers and the traveling roundtrips are 0.3–0.4 mW and 8, 000–10, 000, respectively. In application, the required information data can be secured in the transmission lines in the public networks.

1. INTRODUCTION

Recently, Mitatha et al. [1] have shown that the secured communication message in the present technology via the microring resonator device has shown the promising realistic application. One of the application of the practical device using a microring radius of 10 μm has been reported [2, 3]. The nonlinear behaviors of light in a microring resonator have been investigated and used for communication security [4, 5]. Morover, when such a device is fabricated within the range of a micrometer scale [2, 3], it can be used incorporating a system such as an access point, optical wireless LAN, computing system, and computer networks. The message coding and the nonlinear effect of the coding process and control signal encoding were studied. The system used consists of three methods, such as (1) control input power (mW); (2) control threshold power (mW); and (3) timing control.

In recent years, semiconductor microring resonators have received great interest as potential building blocks for optoelectronic integrated circuits due to their ultra compactness and small size, which can lead to high device integration densities. Moreover, the field buildup inside the ring cavity can be used for all optical signal processing functions based on enhanced nonlinear effects [6]. In principle, The DNA coding methods are processed by sampling, quantizing, and synchronization. In this paper, we have proposed the extended details of our previous work [7], where the other point of view from its applications is the optical output which can be formed by the DNA codes. The selected input signals can be used to control the required DNA encoding, which can be distributed into the wavelength router or optical wireless link. These can be applied into the optical networks to encrypt and the required communication data can be retrieved. The ring parameters used are based on the practical device parameters as shown in references [2, 3]. Simulation results obtained have shown the potential of application for secure wireless link in the optical networks. The basic theory of a microring resonator is reviewed, the DNA quantizing and coding and control are presented in detail.

2. CHAOTIC SIGNAL GENERATION

A simple device schematic diagram is as shown in Fig. 1, when the light from a monochromatic light source is launched into a ring resonator with constant light field amplitude (E_0) and random phase modulation ($\varnothing_0$), which is the combination of terms in attenuation (α) and phase (f_0) constants,

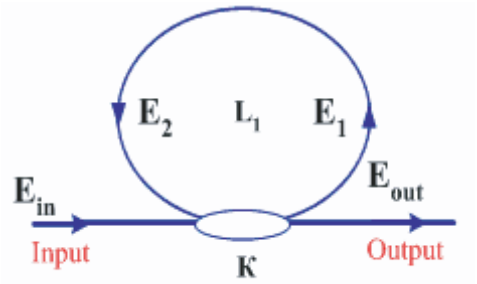

Figure 1: A schematic diagram of micro ring resonator.

which results in temporal coherence degradation. Hence, the time dependent input light field (E_{in}), without pumping term, can be expressed as [8]

$$E_{in}(t) = E_0 \exp^{-\alpha L + j\phi_0(t)}. \tag{1}$$

The optical fields E_1 and E_2 represent the right and left hand circulations in a ring resonator, respectivelty. Where L is a propagation distance (waveguide length). We assume that the nonlinearity of the optical ring resonator is of the Kerr-type, i.e., the refractive index is given by

$$n = n_0 + n_2 I = n_0 + \left(\frac{n_2}{A_{eff}}\right) P, \tag{2}$$

where n_0 and n_2 are the linear and nonlinear refractive indexes, respectively. I and P are the optical intensity and optical power, respectively. The effective mode core area of the device is given by A_{eff}. For the microring and nanoring resonators, the effective mode core areas range from 0.10 to $0.50\,\mu m^2$ [9, 10].

When a Gaussian pulse is input and propagated within a ring resonator, the resonant output is formed, thus, the normalized output of the light field is the ratio between the output and input fields ($E_{out}(t)$ and $E_{in}(t)$) in each roundtrip, which can be expressed as [11]

$$\left|\frac{E_{out}(t)}{E_{in}(t)}\right|^2 = (1-\gamma)\left[1 - \frac{\left(1-(1-\gamma)\,x^2\right)\kappa}{\left(1-x\sqrt{1-\gamma}\sqrt{1-\kappa}\right)^2 + 4\,x\sqrt{1-\gamma}\sqrt{1-\kappa}\sin^2\left(\frac{\phi}{2}\right)}\right] \tag{3}$$

Equation (3) indicates that a ring resonator in the particular case is very similar to a Fabry-Perot cavity, which has an input and output mirror with a field reflectivity, $(1-\kappa)$, and a fully reflecting mirror. k is the coupling coefficient, and $x = \exp(-\alpha L/2)$ represents a roundtrip loss coefficient, $\phi_0 = kLn_0$ and $\phi_{NL} = kL(\frac{n_2}{A_{eff}})P$ are the linear and nonlinear phase shifts, $k = 2\pi/\lambda$ is the wave propagation number in a vacuum. Where L and are a waveguide length and linear absorption coefficient, respectively. In this work, the iterative method is introduced to obtain the results as shown in Eq. (3), similarly, when the output field is connected and input into the other ring resonators.

This nonlinear behavior of light traveling in a single ring resonator (SRR) was investigated, where the parameters of the system were fixed to $\lambda_0 = 1.55\,\mu m$, $n_0 = 3.34$, $A_{eff} = 25\,\mu m^2$, $\alpha = 0.5\,dB$, where the practical bending loss of the waveguide fabricated by InGaAsP/InP is confirmed by reference [6], where the propagation loss as low as $1.3 \pm 0.2\,dB/mm$ at $1.55\,\mu m$ [12], $\gamma = 0.1$, and $R_1 = 10\,\mu m$. The coupling coefficient of the micro ring resonator coupler was fixed in this investigation to $\kappa = 0.0225$. The nonlinear refractive index was $n_2 = 2.2 \times 10^{-15}\,m^2/W$ [13], and the 20, 000 iterations of round-trips inside the optical fiber ring plotted. We assume that $\phi_L = 0$ for simplicity.

To design the nonlinear micro ring resonator, firstly, the nonlinear behaviour of light in the ring is required to characterize. The nonlinear behavior of the micro ring resonator with the roundtrips of 10, 000 is as shown in Fig. 2. When the ring radius is $10\,\mu m$, the nonlinear effect is not occurred as shown in Fig. 2(a). It is occurred when the ring radius is $20\,\mu m$ as shown in Fig. 2(b), where the filter characteristics have also shown.

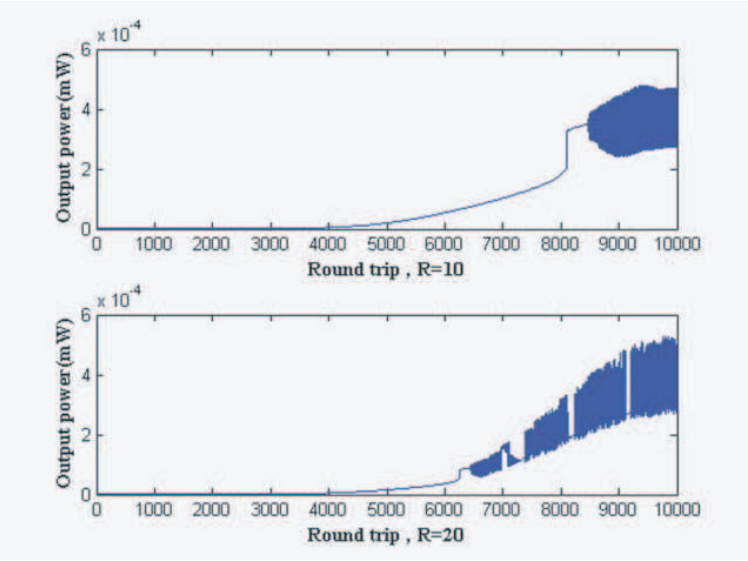

Figure 2: Shows the nonlinear behaviors of light in a micro ring resonator with (a) $R = 10\,\mu\text{m}$ and (b) $R = 20\,\mu\text{m}$.

3. DNA ENCODING

The signals are generated by using Eq. (3), which can be electronically formed by the digital codes as the following details. The quantitatively present logic coding can be expressed by Eq. (4).

$$u(v) = \begin{cases} A, & v < 3.0\,\text{mW} \\ T, & 3.0\,\text{mW} \le v < 3.5\,\text{mW} \\ C, & 3.5\,\text{mW} \le v < 4.0\,\text{mW} \\ G, & v \ge 4.0\,\text{mW} \end{cases} \tag{4}$$

Furthermore, when $u(v)$ represents the logic states, v is the signal power. The quantization and re-quantization can be processed the similar transfer characteristics. We assume that the quantizing involved is infinite, which means that the system input signal is never clipped by saturation of the quantizing. In this case, the corresponding transfer functions of the quantizing output to its input can be expressed analytically in terms of the quantizing step size as detail in reference [14].

The logical code with the logic state "A" or "T" or "C" or "G" is generated from the previous description, after the chaotic behaviors of the device are characterized, the next step is that random coding can be generated by controlling the input optical power, which then enters into the microring device. The required DNA codes can be electronically generated.

The DNA coding creation can be processed as the followings: (i) The signals can be generated within a ring resonator by controlling the optical input power which can be specified by the roundtrip number, i.e., time, (ii) to start the DNA coding with the threshold power, where it is marked before averaging using least-square method, (iii) the clipping signals is introduced, (iv) the DNA code generation is completed by using the approximation and sampling methods.

The first DNA codes generation is as shown in Fig. 3. The relationship between the output signals and roundtrips is as shown in Fig. 3(a), the nonlinear behavior occurs when the roundtrips number is 10, 000. Fig. 3(b) the encoding roundtrips are from 8,900–8,950. Fig. 3(c) shows the clipping signals, 3(d) the clipping signals is performed by using the least- squares method, and 3(e) the DNA codes is obtained using the approximation method, which the logic code obtained is [GACCCCCCTGACCTGAGTGACCTGAGACC CCTGACCTGACCCTGACCTGAC], which there are 50 logic codes, a roundtrip time is 10^{-12} sec.

Similarly, Fig. 4 are the results which are described as the following figure captions. Fig. 4(a), the optical output power is 0.5 mW, with 10, 000 roundtrips, where the threshold power is between 0.30 and 0.40 mW with the encoding roundtrips that range between 9050 and 9100 as shown in Fig. 4(b); where 4(c) shows the clipping signals, and the least-squares method is applied as shown in Fig. 4(d). There are 50 logic codes obtained with a bit time of 32×10^{-12} sec as shown in Fig. 4(e).

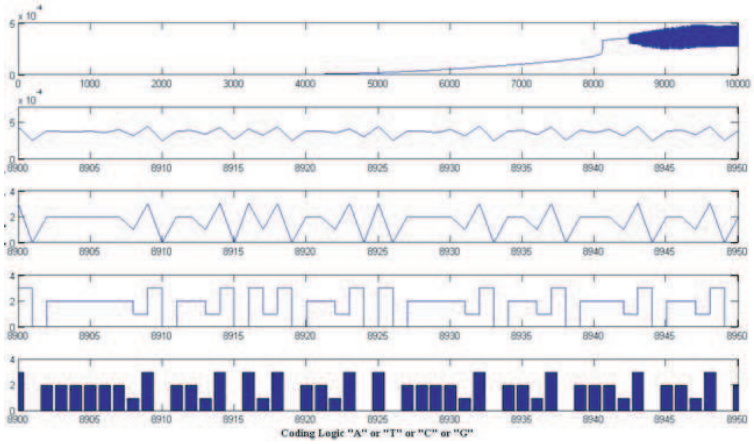

Figure 3: Show the DNA codes: [GACCCCCCTGACCTGAGTGACCTGAGACCCCTGACCTGACCCT-GACCTGAC].

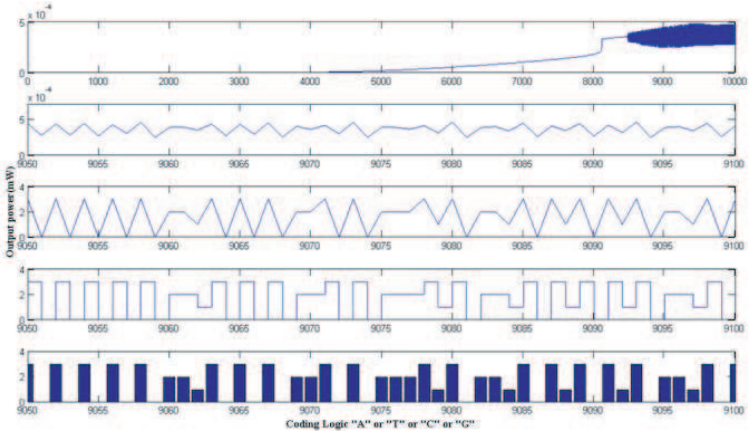

Figure 4: Show the DNA codes: [GAGAGAGAGACCTGAGAGACCGAGACCCGTGACCTGAGTGAGT-GACCTGAG].

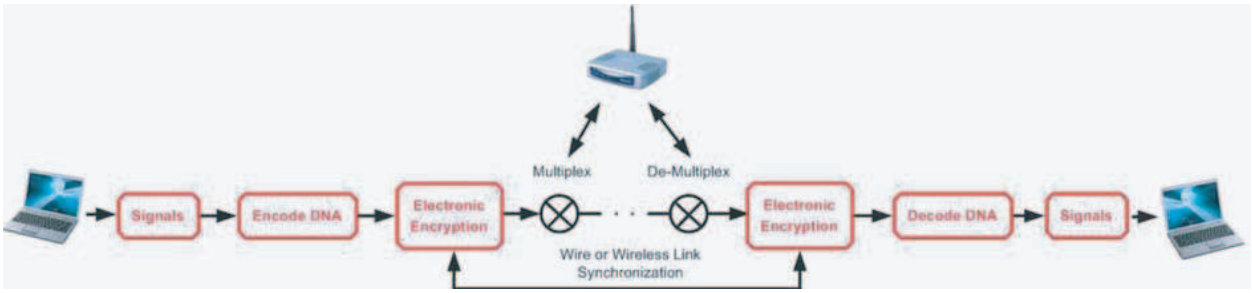

Figure 5: The schematic diagram of the synchronous encryption and the encryption system.

4. CONCLUSION

From Fig. 5, the signals are generated by using the micro ring part, while the DNA codes are electronically performed by the encryption data. The signals are multiplexed and transmitted via either wire or wireless links to the required receivers. The transmitted signals are received and de-multiplexed, where the synchronously decryption to the encryption data is processed before the DNA codes being intercepted by the specific users for signal security.

We have proposed the use of a microring resonator to generate the DNA codes, where the advantages of such a device are (1) the signal are randomly encoded, (2) easy to design an implement, and finally (3) the control optical power could be selected. In an application, such a proposed device can be fabricated and implemented in the communication. For examples, an access point,

optical wireless LAN, computing system, and computer networks. The signal can be encoded by using the electronically synchronized technique, where the required message can be successfully decoded by subtracting the oscillation. This is operated by the receiver on the transmitted signal by using the least-squares method. We have demonstrated that the signal is logically encoded by using the waveforms of the transmitter and signal of the receiver output. Thus, we can use the proposed system for the alternative security technique that can provide the secure transmission of a message by logical coding using the electronic quantizing, and coding by using the microring incorporating in the communication transmission.

REFERENCES

1. Mitatha, S., K. Dejhan, P. P. Yupapin, and N. Pornsuwancharoen, "High-capacity and security packet switching using the nonlinear effects in micro ring resonators," *International Journal of Light and Electron. Optics*, DOI: 10.1016/j.ijleo.2008.05.032.
2. Morand, A., Y. Zhang, B. Martin, K. P. Huy, D. Amans, and P. Benech, "Ultra-compact microdisk resonator filters on SOI substrate," *Opt. Exp.*, Vol. 14, No. 26, 12814–12821, 2000.
3. Van, V., T. A. Ibrahim, P. P. Absil, F. G. Jhonson, R. Grover, and P. T. Ho, "Optical signal processing using nonlinear semiconductor microring resonators," *IEEE J. Quantum Electron.*, Vol. 8, 705–713, 2002.
4. Yupapin, P. P., P. Saeung, and W. Suwancharoen, "Coupler-loss and coupling-coefficient dependence of bistability and instability in a fiber ring resonator: nonlinear behaviors," *J. of Nonlinear Optical Physics & Materials (JNOPM)*, Vol. 16, 111–118, 2007.
5. Yupapin, P. P., W. Suwanchareon, and S. Suchat, "Nonlinearity penalties and benefits of light traveling in a fiber optic ring resonator," *International Journal of Light and Electron. Optics*, DOI: 10.1016/j.ijleo.2007.07.009.
6. Aizawa, T., K. G. Ravikumar, Y. Nagasawa, T. Sekiguchi, and T. Watanabe, "InGaAsP/InP NQW direction couple switch with small and low-loss bends for fiber array coupling," *IEEE Photonics Technol. Lett.*, Vol. 6, 709–711, 1994.
7. Yupapin, P. P. and W. Suwancharoen, "Chaotic signal generation and cancellation using a microring resonator incorporating an optical add/drop multiplexer," *Opt. Commun.*, Vol. 280, No. 2, 343–350, 2007.
8. Deng, D. and Q. Guo, "Ince-Gaussian solitons in strongly nonlocal nonlinear media," *Opt. Lett.*, Vol. 32, 3206–3208, 2007.
9. Kokubun, Y., Y. Hatakeyama, M. Ogata, S. Suzuki, and N. Zaizen, "Fabrication technologies for vertically coupled micro ring resonator with multilevel crossing busline and ultracompact-ring radius," *IEEE J. Sel. Top. Quantum Electron.*, Vol. 11, 4–10, 2005.
10. Su, Y., F. Liu, and Q. Li, "System performance of slow-light buffering, and storage in silicon nano-waveguide," *Proc. SPIE*, Vol. 6783, 67832, 2007.
11. Yupapin, P. P., P. Saeung, and C. Li, "Characteristics of complementary ring-resonator add/drop filters modeling by using graphical approach," *Opt. Commun.*, Vol. 272, 81–86, 2007.
12. Xiao, S., M. H. Khan, H. Shen, and M. Qi, "Compact silicon micro ring resonators with ultra-low propagation loss in the C band," *Opt. Exp.*, Vol. 15, No. 22, 14467–14475, 2007.
13. Little, B. E., S. T. Chu, J. V. Hryniewicz, and P. P. Absil, "Filter synthesis for periodically coupled micro ring resonators," *Opt. Lett.*, Vol. 25, No. 5, 344–346, 2000.
14. Valley, G. C., "Photonic analog-to-digital converters," *Opt. Exp.*, Vol. 15, No. 5, 1955–1982, 2007.

Perfume Distribution Using Molecular Networking via an Optical Wireless Link

X. Louangvilay[1], **M. Tassakorn**[2], **S. Mitatha**[1], **and P. P. Yupapin**[2]

[1]Hybrid Computing Research Laboratory, Faculty of Engineering
King Mongkut's Institute of Technology Ladkrabang, Bangkok 10520, Thailand
[2]Advanced Research Center for Photonics, Faculty of Science
King Mongkut's Institute of Technology Ladkrabang, Bangkok 10520, Thailand

Abstract— We propose a new system of a molecular-quantum networking using the optical tweezers, whereas the transportation of molecules via wavelength router and network can be performed. In addition, the molecule transportation states can be identified by using the quantum states of the transporters, which can be formed in the network. The proposed fabricated material used is **InGaAsP/InP**, which can provide the required output signals. The design system consists of a nonlinear microring/nanoring resonator system incorporating an add/drop filter and a wavelength router. The transporter can be formed by the dark soliton, the optical transporter is tuned and amplified by the bright soliton and transmitted into the network. In applications, the use of the proposed system incorporating a nanoscale communication and networking via wavelength router is available for long distance link.

1. INTRODUCTION

Optical tweezers technique has become a powerful tool for manipulation of micrometer-sized particles in three spatial dimensions [1]. Initially, the useful static tweezer is recognized, and the dynamic tweezer is now realized in practical work. Typically by using the continuous-wave (cw) lasers, the spatial control of atoms, beyond their trapping in stationary potentials, has been continuously gaining importance in investigations of ultra cold gases and in the application of atomic ensembles and single atoms for cavity quantum electrodynamics (QED) and quantum information studies. Recent progress includes the trapping and control of single atoms in dynamic potentials [2, 3], the sub-micron positioning of individual atoms with standing-wave potentials [4, 5], micro-structured and dynamic traps for Bose-Einstein condensates [6–8] and, as another example, the realization of chaotic dynamics in atom-optics "billiards" [9–11]. Recently, Matthias et al. [12] have shown that the transfer of trapped atoms between two optical potentials could be performed. In this paper, we present a novel system of the optical tweezers storage using a dark-bright soliton pulses propagating within an add/drop optical filter. The multiplexing signals with different wavelengths of the dark solitions are controlled and amplified within the system. The dynamic behaviors of dark bright soliton interaction is analyzed and described. The storage signals are controlled and tuned to be an optical probe which is known as the optical tweezers. The optical tweezers storage is obtained by using the embedded nanoring resonator within the add/drop optical filter system. In application, the optical tweezers can be stored and trapped light/atom, which can be formed the tweezer memory.

2. PERFUME TRAPPING TOOL

We are looking for a stationary dark soliton pulse, which is introduced into the multistage microring resonators as shown in Fig. 1 [13]. The input optical field (E_{in}) of the dark soliton pulse input and the add optical fied (E_{add}) of the bright soliton pulse at add port are given by [14]

$$\begin{aligned} E_{in}(t) &= A \tanh\left[\frac{T}{T_0}\right] \exp\left[\left(\frac{z}{2L_D}\right) - i\omega_0 t\right], \\ E_{add}(t) &= A \operatorname{sech}\left[\frac{T}{T_0}\right] \exp\left[\left(\frac{z}{2L_D}\right) - i\omega_0 t\right], \end{aligned} \tag{1}$$

where A and z are the optical field amplitude and propagation distance, respectively. T is a soliton pulse propagation time in a frame moving at the group velocity, $T = t - \beta_1 * z$, where β_1 and β_2 are the coefficients of the linear and second-order terms of Taylor expansion of the propagation constant. $\mathrm{LD} = T_0^2/|\beta_2|$ is the dispersion length of the soliton pulse. T_0 in equation is a soliton pulse

propagation time at initial input (or soliton pulse width), where t is the soliton phase shift time, and the frequency shift of the soliton is ω_0. This solution describes a pulse that keeps its temporal width invariance as it propagates, and thus is called a temporal soliton. When a soliton peak intensity ($|\beta_2/\Gamma T_0^2|$) is given, then T_0 is known. For the soliton pulse in the microring device, a balance should be achieved between the dispersion length (LD) and the nonlinear length (LNL $= 1/\Gamma\phi_{\rm NL}$), where $\Gamma = n_2 * k_0$, is the length scale over which dispersive or nonlinear effects makes the beam become wider or narrower. For a soliton pulse, there is a balance between dispersion and nonlinear lengths, hence LD = LNL.

When light propagates within the nonlinear material (medium), the refractive index (n) of light within the medium is given by

$$n = n_0 + n_2 I = n_0 + \frac{n_2}{A_{eff}} P, \tag{2}$$

where n_0 and n_2 are the linear and nonlinear refractive indexes, respectively. I and P are the optical intensity and optical power, respectively. The effective mode core area of the device is given by A_{eff}. For the microring resonator (MRR) and nanoring resonator (NRR), the effective mode core areas range from 0.50 to 0.10 μm^2. When a soliton pulse is input and propagated within a MRR, as shown in Fig. 1, which consists of a series MRRs. The resonant output is formed, thus, the ormalized output of the light field is the ratio between the output and input fields [$E_{out}(t)$ and

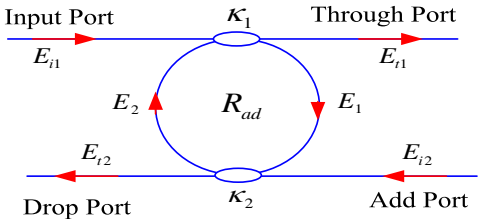

Figure 1. A schematic diagram of an add/drop filter.

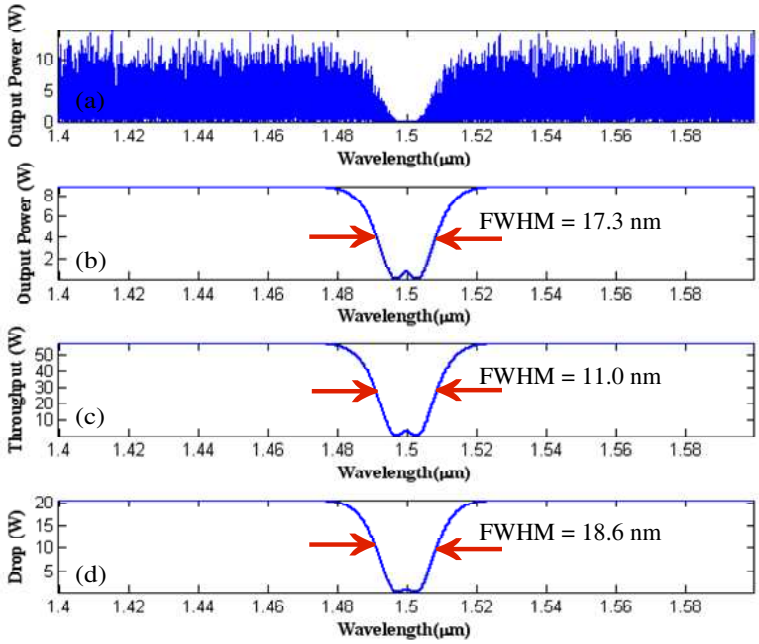

Figure 2. Result of the optical tweezers in the add/drop filter system, where $R_{ad} = 15\,\mu m$, $\kappa_1 = 0.35$ and $\kappa_2 = 0.7$. (a) Dark soliton input power, (b) dynamic tweezer, (c) throughput port signal, and (d) drop port signal.

$E_{in}(t)]$ in each roundtrip, which is given by

$$\left|\frac{E_{out}(t)}{E_{in}(t)}\right| = (1-\gamma)\left[1 - \frac{\left(1-(1-\gamma)x^2\right)\kappa}{\left(1-x\sqrt{1-\gamma}\sqrt{1-\kappa}\right)^2 + 4x\sqrt{1-\gamma}\sqrt{1-\kappa}\sin^2\left(\frac{\phi}{2}\right)}\right] \tag{3}$$

The close form of Eq. (3) indicates that a ring resonator in this particular case is very similar to a Fabry-Perot cavity, which has an input and output mirror with a field reflectivity, $(1-\kappa)$, and a fully reflecting mirror. κ is the coupling coefficient, and $x = \exp(-\alpha L/2)$ represents a roundtrip loss coefficient, $\phi_0 = kLn_0$ and $\phi_{\rm NL} = kLn_2|E_{in}|_2$ are the linear and nonlinear phase shifts, $k = 2\pi/\lambda$ is the wave propagation number in a vacuum, where L and α are waveguide length and linear absorption coefficient, respectively. In this work, the iterative method is introduced to obtain the results as shown in Eq. (3), and similarly, when the output field is connected and input into the other ring resonators.

To retrieve the signals from the chaotic noise, we propose to use the add/drop device with the appropriate parameters. This is given in the following details. The optical circuits of ring-resonator add/drop filters for the throughput and drop port can be given by Eqs. (4) and (5), respectively [13, 14]

$$\left|\frac{E_t}{E_{in}}\right|^2 = \frac{(1-\kappa_1) - 2\sqrt{1-\kappa_1}\cdot\sqrt{1-\kappa_2}\,e^{-\frac{\alpha}{2}L}\cos(k_nL) + (1-\kappa_2)e^{-\alpha L}}{1+(1-\kappa_1)(1-\kappa_2)e^{-\alpha L} - 2\sqrt{1-\kappa_1}\cdot\sqrt{1-\kappa_2}\,e^{-\frac{\alpha}{2}L}\cos(k_nL)} \tag{4}$$

$$\left|\frac{E_d}{E_{in}}\right|^2 = \frac{\kappa_1\kappa_2 e^{-\frac{\alpha}{2}L}}{1+(1-\kappa_1)(1-\kappa_2)e^{-\alpha L} - 2\sqrt{1-\kappa_1}\cdot\sqrt{1-\kappa_2}\,e^{-\frac{\alpha}{2}L}\cos(k_nL)} \tag{5}$$

where E_t and E_d represent the optical fields of the throughput and drop ports, respectively. $\beta = kn_{eff}$ is the propagation constant, n_{eff} is the effective refractive index of the waveguide, and the circumference of the ring is $L = 2\pi R$, with R as the radius of the ring. In the following, new parameters will be used for simplification with $\phi = \beta L$ as the phase constant. The chaotic noise cancellation can be managed by using the specific parameters of the add/drop device, and the required signals can be retrieved by the specific users. κ_1 and κ_2 are the coupling coefficient of the add/drop filters, $kn = 2\pi/\lambda$ is the wave propagation number for in a vacuum, and where the waveguide (ring resonator) loss is $\alpha = 0.5\,\mathrm{dBmm}^{-1}$. The fractional coupler intensity loss is $\gamma = 0.1$. In the case of the add/drop device, the nonlinear refractive index is neglected.

By controlling the bright soliton which is input into the add port as shown in Fig. 1, the dynamic behaviour of optical tweezers is occurred and seen. The used parameters are the add/drop optical filter radius $R_{ad} = 15\,\mu\mathrm{m}$, the coupling coefficients $\kappa_1 = 0.35$ and $\kappa_2 = 0.7$, and the dark and bright solitons are generated at the central wavelength $\lambda_0 = 1.5\,\mu\mathrm{m}$. When the bright soliton propagating into the add/drop system, the dark-bright soliton collision within the add/drop system is occurred as shown in Figs. 2(a)–(b). The smallest tweezer width (full width at half maximum, FWHM) of 11 nm is obtained. The maximum power is 50 W, which means that the optical tweezers probe in the form of intense field, i.e., potential well is formed, which can be used to trap/confine atom/light. The dark soliton valley dept, i.e., potential well, is changed when it is modulated by the trapping energy (dark-bright solitons interaction) as shown in Fig. 2(b). The trapping of photon within the dark well is occurred and seen. The recovery of trapped atom/photon can be obtained by using the dark-bright soliton conversion behavior, which is well analyzed by Sarapat et al. [13], where the trapped photon or molecule can be released an seen separately from the dark soliton pulse, in practice, in this case the bright soliton is become alive and seen.

3. TUNABLE AND STORAGE TRAPPING TOOL

The schematic diagram of the optical tweezers storage is designed and shown in Fig. 3. In operation, to form the memory unit, a nanoring resonator is embedded within the add/drop optical filter system. The nanoring resonator radius (R_{ring}) and the coupling coefficient (κ) are 100 nm and 0.15, respectively. The parameters of the add/drop optical filter system are set the same as the previous section. In the system design, the dark soliton pulse is input into the input port through the coupler with the coupling coefficient is $\kappa_1 = 0.35$. It is partially input into the nanoring resonator with 20,000 roundtrips, where the storage signal is observed, the memory time is noted.

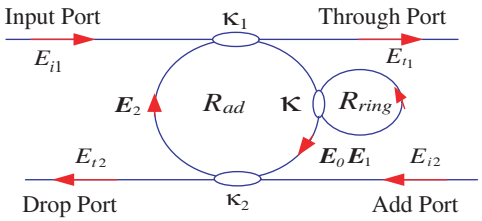

Figure 3. A schematic diagram of storage optical tweezers.

The output field (E_{t1}) at throughput port is expressed by

$$E_{t1} = -x_1x_2y_2\sqrt{\kappa_1}E_{i2}e^{-\frac{\alpha L}{2}-jk_n\frac{L}{2}} + \left[\frac{x_2x_3\kappa_1\sqrt{\kappa_2}E_0E_{i1}\left(e^{-\frac{\alpha L}{2}-jk_n\frac{L}{2}}\right)^2 + x_3x_4y_1y_2\sqrt{\kappa_1}\sqrt{\kappa_2}E_0E_{i2}\left(e^{-\frac{\alpha L}{2}-jk_n\frac{L}{2}}\right)^3}{1-x_1x_2y_1y_2E_0\left(e^{-\frac{\alpha L}{2}-jk_n\frac{L}{2}}\right)^2}\right], \quad (6)$$

where the $x_1 = \sqrt{1-\gamma_1}$, $x_2 = \sqrt{1-\gamma_2}$, $x_3 = 1-\gamma_1$, $x_4 = 1-\gamma_2$, $y_1 = \sqrt{1-\kappa_1}$ and $y_2 = \sqrt{1-\kappa_2}$.

The power output (P_{t1}) at throughput port is given by

$$P_{t1} = |E_{t1}|^2. \quad (7)$$

The output field (E_{t2}) at drop port is

$$E_{t2} = x_2y_2E_{i2} + \left[\frac{x_1x_2\sqrt{\kappa_1}\sqrt{\kappa_2}E_0E_{i1}e^{-\frac{\alpha L}{2}-jk_n\frac{L}{2}} + x_1x_3y_1y_2\sqrt{\kappa_2}E_0E_{i2}\left(e^{-\frac{\alpha L}{2}-jk_n\frac{L}{2}}\right)^2}{1-x_1x_2y_1y_2E_0\left(e^{-\frac{\alpha L}{2}-jk_n\frac{L}{2}}\right)^2}\right], \quad (8)$$

The power output (P_{t2}) at drop port is

$$P_{t2} = |E_{t2}|^2. \quad (9)$$

The optical tweezers storage signals within the add/drop system is as shown in Fig. 4. We found that the storage time is 1.2 ns, the tweezer widths of the storage tweezers in add/drop at the throughput and drop ports are 19.2, 17.6 and 18.6 ns, respectively. In Figs. 4(a)–(c), the tweezers in the form of potential wells are seen, which can be used for atom/molecule trapping. The potential well dept (peak valley) can be controlled by adjusting the system parameters, for instance, the bright soliton input power at the add port and the coupling coefficients. The potential well of the tweezers is tuned to be the single well and seen at the add port, as shown in Fig. 4(c). In application, the optical tweezers in the design system can be tuned and amplified as shown in Figs. 2 and 4. Therefore, the tunable optical tweezers can be controlled by the dark-bright soliton collision within the add/drop optical system by adjusting the parameters of the input power at the input and add ports, respectively. The output power at the throughput port is shown in Fig. 2(c), where the single potential well with the optical power of 15 W is seen.

4. PERFUME TRAPPING AND TRANSPORTATION VIA WIRELESS LINK

From Fig. 4, by using the reasonable optical input power into the microring system, the tunable optical tweezers can be controlled, which can provide the entangled photon as the dynamic optical tweezers probe. The smallest tweezers width of 17.6 nm is generated and achieved. In application, such a behavior can be used to confine the suitable size of light pulse or molecule, which can be employed in the same way of the optical tweezers. But in this case the terms dynamic probing is come to be a realistic function, therefore, the transportation of the trapped atom/molecule/photon by a single photon is plausible. For simplicity, the entangled photons power is attenuated to be a single photon be fore the detection, therefore, the separation between photon and molecule is employed the same way of a single photon detection scheme. This means that the detection of the transported single atom/molecule can be configured by using the single photon detection method. Thus, the transported molecule/atom with long distance link via molecular transporter is realized.

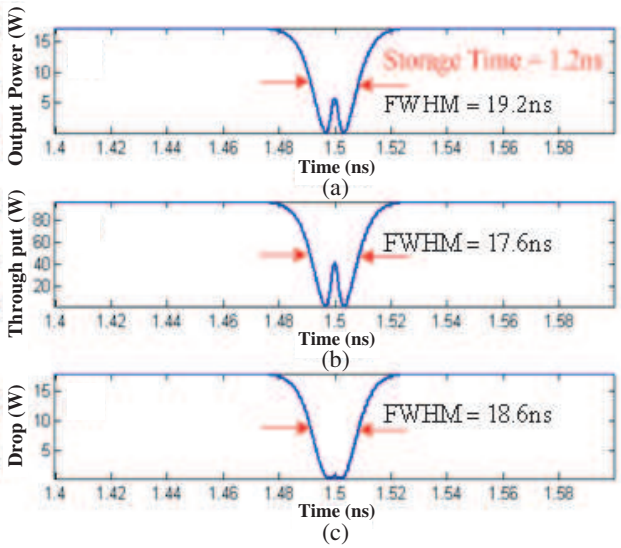

Figure 4. Result of the optical tweezers storage signals in the add/drop system, where $R_{ad} = 15\,\mu\text{m}$ and $R_{ring} = 100\,\text{nm}$, $\kappa = 0.15$, $\kappa_1 = 0.35$ and $\kappa_2 = 0.1$. (a) storage tweezer, (b) throughput port signal, and (c) drop port signal.

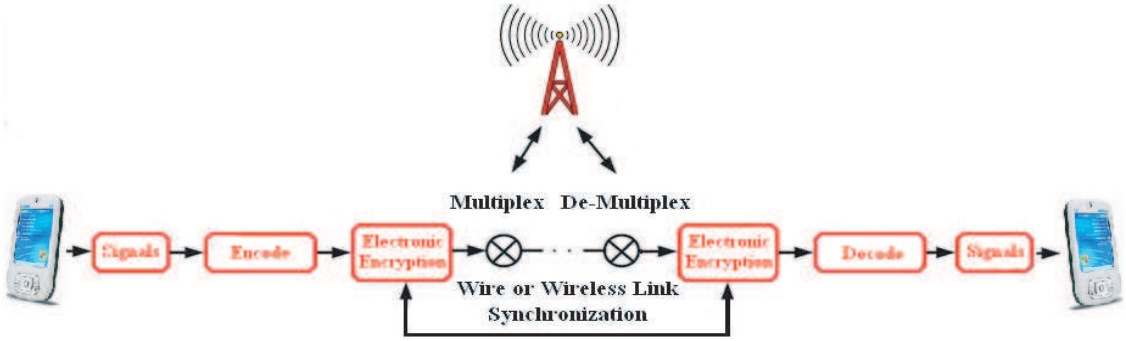

Figure 5. The schematic diagram of the molecular transporter via wireless.

Furthermore, the secured hybrid molecular communication can be implemented within the existed transmission link.

From Fig. 5, the signals are generated by using the micro ring part, while the codes are electronically performed by the encryption data. The signals are multiplexed and transmitted via either wire or wireless links to the required receivers. The transmitted signals are received and de-multiplexed, where the synchronously decryption to the encryption data is processed before the codes being intercepted by the specific operation case.

5. CONCLUSION

We have proposed the interesting idea where perfume molecule distribution via an optical wireless link can be formed. The generated optical tweezers can be performed the rapping tools, tuned and storage. The smallest tweezers width of 17.6 nm is generated and achieved. In application, such a behavior can be used to confine the suitable size of light pulse or molecule and transported via the communication link.

ACKNOWLEDGMENT

We would like to give our acknowledge to the AUN/SEED-Net for the fully financial support to Mr. Xaythavy LOUANGVILAY in higher education at International College, King Mongkut's Institute of Technology Ladkrabang (KMITL), Bangkok 10520, Thailand.

REFERENCES

1. Ashkin, A., J. M. Dziedzic, J. E. Bjorkholm, and S. Chu, "Observation of a single-beam gradient force optical trap for dielectric particles," *Opt. Lett.*, Vol. 11, 288–290, 1986.
2. Bergamini, S., B. Darqui, M. Jones, L. Jacubowiez, A. Browaeys, and P. Grangier, "Holographic generation of microtrap arrays for single atoms by use of a programmable phase modulator," *J. Opt. Soc. Am. B*, Vol. 21, 1889–1894, 2004.
3. Yavuz, D. D., P. B. Kulatunga, E. Urban, T. A. Johnson, N. Proite, T. Henage, T. G. Walker, and M. Saffman, "Fast ground state manipulation of neutral atoms in microscopic optical traps," *Phys. Rev. Lett.*, Vol. 96, 063001, 2006.
4. Schrader, D., I. Dotsenko, M. Khudaverdyan, Y. Miroshnychenko, A. Rauschenbeutel, and D. Meschede, "Neutral atom quantum register," *Phys. Rev. Lett.*, Vol. 93, 150501, 2004.
5. Sauer, J. A., K. M. Fortier, M. S. Chang, C. D. Hamley, and M. S. Chapman, "Submicrometer position control of single trapped neutral atoms," *Phys. Rev. A*, Vol. 69, 051804(R), 2004.
6. Meyrath, T. P., F. Schreck, J. L. Hanssen, C.-S. Chuu, and M. G. Raizen, "Bose-Einstein condensate in a box," *Phys. Rev. A*, Vol. 71, 041604(R), 2005.
7. Boyer, V., R. M. Godun, G. Smirne, D. Cassettari, C. M. Chandrashekar, A. B. Deb, Z. J. Laczik, and C. J. Foot, "Dynamic manipulation of Bose-Einstein condensates with a spatial light modulator," *Phys. Rev. A*, Vol. 73, 031402(R), 2006.
8. Carpentier, A. V., J. Belmonte-Beitia, H. Michinel, and V. M. Perez-Garcia, "Laser tweezers for atomic solitons," *J. of Mod. Opt.*, Vol. 55, No. 17, 2819–2829, 2008.
9. Milner, V., J. L. Hanssen, W. C. Campbell, and M. G. Raizen, "Optical billiards for atoms," *Phys. Rev. Lett.*, Vol. 86, 1514–1516, 2001.
10. Friedman, N., A. Kaplan, D. Carasso, and N. Davidson, "Observation of chaotic and regular dynamics in atom-optics billiards," *Phys. Rev. Lett.*, Vol. 86, 1518–1520, 2001.
11. Li, M. and J. Arlt, "Trapping multiple particles in single optical tweezers," *Opt. Commun.*, Vol. 281, 135–140, 2008.
12. Schulz, M., H. Crepaz, F. Schmidt-Kaler, J. Eschner, and R. Blatt, "Transfer of trapped atoms between two optical tweezer potentials," *J. of Mod. Opt.*, Vol. 54, No. 11, 1619–1626, 2007.
13. Sarapat, K., N. Sangwara, K. Srinuanjan, P. P. Yupapin, and N. Pornsuwancharoen, "Novel dark-bright optical solitons conversion system and power amplification," *Opt. Eng.*, Vol. 48, 045004, 2009.

Multi Transporters Generation for High Density Molecule Transportation via Optical Communication

S. Thongmee[1], **S. Pipatsart**[2], **and P. P. Yupapin**[2]

[1]Department of Electronics Technology, Faculty of Science
Ramkhamhaeng University, Bangkok 10240, Thailand
[2]Advanced Research Center for Photonics, Faculty of Science
King Mongkut's Institute of Technology Ladkrabang, Bangkok 10520, Thailand

Abstract— We propose a novel system of a quantum-molecular cryptography using the optical tweezers, whereas the transportation of molecules in the communication system can be performed. The molecule transportation states can be identified by using a single photon state of the transporter, which can be formed in the transmission line. The proposed fabricated material used is InGaAsP/InP, which can provide the required output signals. The design system consists of a nonlinear microring/nanoring resonator system incorporating an add/drop filter and a quantum signal processor. The transporter can be formed by the dark soliton, where the optical transporter is tuned and attenuated to be a single photon by the bright soliton control and transmitted into the link. In applications, the use of the proposed system incorporating a quantum processor can be performed the secured molecular communication.

1. INTRODUCTION

Recently, several research works have shown that use of dark and bright soliton in various applications can be realized [1–6], where one of them has shown that the secured signals in the communication link can be retrieved by using a suitable an add/drop filter that is connected into the transmission line. The other promising application of a dark soliton signal [7] is for the large guard band of two different frequencies which can be achieved by using a dark soliton generation scheme and trapping a dark soliton pulse within a nanoring resonator [8]. Furthermore, the dark soliton pulse shows a more stable behavior than the bright solitons with respect to the perturbations such as amplifier noise, fiber losses, and intra-pulse stimulated Raman scattering [9]. It is found that the dark soliton pulses propagation in a lossy fiber, spreads in time at approximately half the rate of bright solitons. Recently, the localized dark solitons in the add/drop filter has been reported [10]. In this paper, the use of dark and bright solitons propagating within the proposed ring resonator systems is investigated and described, where the use of suitable parameters based on the realistic device is discussed. The potential of using the generated dark soliton signals for single photon tweezer and molecular transporter, especially, for the hybrid quantum-molecular communication and transportation in the communication network, which is described in details.

Bright and dark soliton pulses are introduced into the multi-stage nanoring resonators as shown in Fig. 1, the input time dependent optical field (E_{in}) of the bright and dark soliton pulses input are given by an Equations (1) and (2) [8], respectively.

$$E_{in}(t) = A \sec h\left[\frac{T}{T_0}\right] \exp\left[\left(\frac{z}{2L_D}\right) - i\omega_0 t\right] \tag{1}$$

and

$$E_{in}(t) = A \tanh\left[\frac{T}{T_0}\right] \exp\left[\left(\frac{z}{2L_D}\right) - i\omega_0 t\right] \tag{2}$$

where A and z are the optical field amplitude and propagation distance, respectively. T is a soliton pulse propagation time in a frame moving at the group velocity, $T = t - \beta_1 * z$, where β_1 and β_2 are the coefficients of the linear and second-order terms of Taylor expansion of the propagation constant. $L_D = T_0^2/|\beta_2|$ is the dispersion length of the soliton pulse. T_0 in equation is a soliton pulse propagation time at initial input (or soliton pulse width), where t is the soliton phase shift time, and the frequency shift of the soliton is ω_0. This solution describes a pulse that keeps its temporal width invariance as it propagates, and thus is called a temporal soliton. When a soliton peak intensity ($|\beta_2/\Gamma T_0^2|$) is given, then T_0 is known. For the soliton pulse in the microring device, a balance should be achieved between the dispersion length (L_D) and the nonlinear length ($L_{NL} = 1/\Gamma\phi_{NL}$),

where $\Gamma = n_2 * k_0$, is the length scale over which dispersive or nonlinear effects makes the beam become wider or narrower. For a soliton pulse, there is a balance between dispersion and nonlinear lengths, hence $L_D = L_{NL}$. Similarly, the output soliton of the system in Fig. 2 can be calculated by using Gaussian equations as given in the above case.

We assume that the nonlinearity of the optical ring resonator is of the Kerr-type, i.e., the refractive index is given by

$$n = n_0 + n_2 I = n_0 + (\frac{n_2}{A_{eff}})P, \tag{3}$$

where n_0 and n_2 are the linear and nonlinear refractive indexes, respectively. I and P are the optical intensity and optical power, respectively. The effective mode core area of the device is given by A_{eff}. For the microring and nanoring resonators, the effective mode core areas range from 0.10 to $0.50\,\mu m^2$ [11, 12].

When a Gaussian pulse is input and propagated within a fiber ring resonator, the resonant output is formed, thus, the normalized output of the light field is the ratio between the output and input fields ($E_{out}(t)$ and $E_{in}(t)$) in each roundtrip, which can be expressed as [13]

$$\left|\frac{E_{out}(t)}{E_{in}(t)}\right|^2 = (1-\gamma)\left[1 - \frac{(1-(1-\gamma)\,x^2)\kappa}{(1-x\sqrt{1-\gamma}\sqrt{1-\kappa})^2 + 4x\sqrt{1-\gamma}\sqrt{1-\kappa}\sin^2(\frac{\phi}{2})}\right] \tag{4}$$

Equation (4) indicates that a ring resonator in the particular case is very similar to a Fabry-Perot cavity, which has an input and output mirror with a field reflectivity, $(1-\kappa)$, and a fully reflecting mirror. k is the coupling coefficient, and $x = \exp(-\alpha L/2)$ represents a roundtrip loss coefficient, $\phi_0 = kLn_0$ and $\phi_{NL} = kL(\frac{n_2}{A_{eff}})P$ are the linear and nonlinear phase shifts, $k = 2\pi/\lambda$ is the wave propagation number in a vacuum. Where L and α are a waveguide length and linear absorption coefficient, respectively. In this work, the iterative method is introduced to obtain the results as shown in Equation (4), similarly, when the output field is connected and input into the other ring resonators.

The input optical field as shown in Equations (1) and (2), i.e., a soliton pulse, is input into a nonlinear microring resonator. By using the appropriate parameters, the chaotic signal is obtained by using Equation (4). To retrieve the signals from the chaotic noise, we propose to use the add/drop device with the appropriate parameters. This is given in details as followings. The optical outputs of a ring resonator add/drop filter can be given by the Equations (5) and (6) [14].

$$\left|\frac{E_t}{E_{in}}\right|^2 = \frac{(1-\kappa_1) - 2\sqrt{1-\kappa_1}\cdot\sqrt{1-\kappa_2}e^{-\frac{\alpha}{2}L}\cos(k_nL) + (1-\kappa_2)\,e^{-\alpha L}}{1+(1-\kappa_1)\,(1-\kappa_2)\,e^{-\alpha L} - 2\sqrt{1-\kappa_1}\cdot\sqrt{1-\kappa_2}e^{-\frac{\alpha}{2}L}\cos(k_nL)} \tag{5}$$

and

$$\left|\frac{E_d}{E_{in}}\right|^2 = \frac{\kappa_1\kappa_2 e^{-\frac{\alpha}{2}L}}{1+(1-\kappa_1)\,(1-\kappa_2)\,e^{-\alpha L} - 2\sqrt{1-\kappa_1}\cdot\sqrt{1-\kappa_2}e^{-\frac{\alpha}{2}L}\cos(k_nL)} \tag{6}$$

where E_t and E_d represents the optical fields of the throughput and drop ports respectively. The transmitted output can be controlled and obtained by choosing the suitable coupling ratio of the ring resonator, which is well derived and described by reference [14]. Where $\beta = kn_{eff}$ represents the propagation constant, n_{eff} is the effective refractive index of the waveguide, and the circumference of the ring is $L = 2\pi R$, here R is the radius of the ring. In the following, new parameters will be used for simplification, where $\phi = \beta L$ is the phase constant. The chaotic noise cancellation can be managed by using the specific parameters of the add/drop device, which the required signals at the specific wavelength band can be filtered and retrieved. κ_1 and κ_2 are coupling coefficient of add/drop filters, $k_n = 2\pi/\lambda$ is the wave propagation number for in a vacuum, and the waveguide (ring resonator) loss is $\alpha = 0.5\,\mathrm{dBmm^{-1}}$. The fractional coupler intensity loss is $\gamma = 0.1$. In the case of add/drop device, the nonlinear refractive index is neglected.

2. SINGLE MOLECULE TRANSPORTER GENERATION

In operation, a dark soliton pulse with 50-ns pulse width with the maximum power of 0.65 W is input into the dark-bright soliton conversion system as shown in Fig. 1. The suitable ring parameters are ring radii, where $R_1 = 10.0\,\mu m$, $R_2 = 7.0\,\mu m$, and $R_3 = 5.0\,\mu m$. In order to make the system associate with the practical device [11, 12] the selected parameters of the system are fixed to $\lambda_0 =$

1.50 µm, $n_0 = 3.34$ (InGaAsP/InP). The effective core areas are $A_{eff} = 0.50$, 0.25, and 0.10 µm^2 for a microring resonator (MRR) and nanoring resonator (NRR), respectively. The waveguide and coupling loses are $\alpha = 0.5\,\mathrm{dBmm}^{-1}$ and $\gamma = 0.1$, respectively, and the coupling coefficients κ_s of the MRR are ranged from 0.05 to 0.90. The nonlinear refractive index is $n_2 = 2.2 \times 10^{-13}\,\mathrm{m}^2/\mathrm{W}$. In this case, the waveguide loss used is $0.5\,\mathrm{dBmm}^{-1}$. The input dark soliton pulse is chopped (sliced) into the smaller output signals of the filtering signals within the rings R_2 and R_3. We find that the output signals from R_3 are smaller than from R_1, which is more difficult to detect when it is used in the link. In fact, the multistage ring system is proposed due to the different core effective areas of the rings in the system, where the effective areas can be transferred from 0.50 to 0.10 µm^2 with some losses. The soliton signals in R_3 is entered in the add/drop filter, where the dark-bright soliton conversion can be performed by using Equations (5) and (6). The dynamic dark soliton control can be configured to be an optical dynamic tool known as an optical tweezers, where more details of optical tweezers can be found in references [15, 16]. After the bright soliton input is added into the system via add port as shown in Fig. 2, the optical tweezers behavior is occurred. The parameters of system are used the same as the previous case. The bright soliton is generated with the central wavelength $\lambda_0 = 1.5$ µm, when the bright soliton propagating into the add/drop system, the dark-bright soliton collision in add/drop system is seen. The dark soliton valley dept, i.e., potential well is changed when it is modulated by the trapping energy (dark-bright solitons interaction) as shown in Fig. 2. The dynamic dark soliton (optical tweezers) occurs

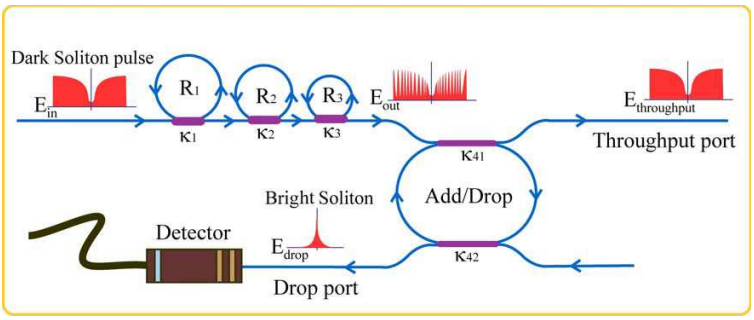

Figure 1: Schematic of a dark-bright soliton conversion system, where R_s is the ring radii, κ_s is the coupling coefficient, and κ_{41} and κ_{42} are the add/drop coupling coefficients.

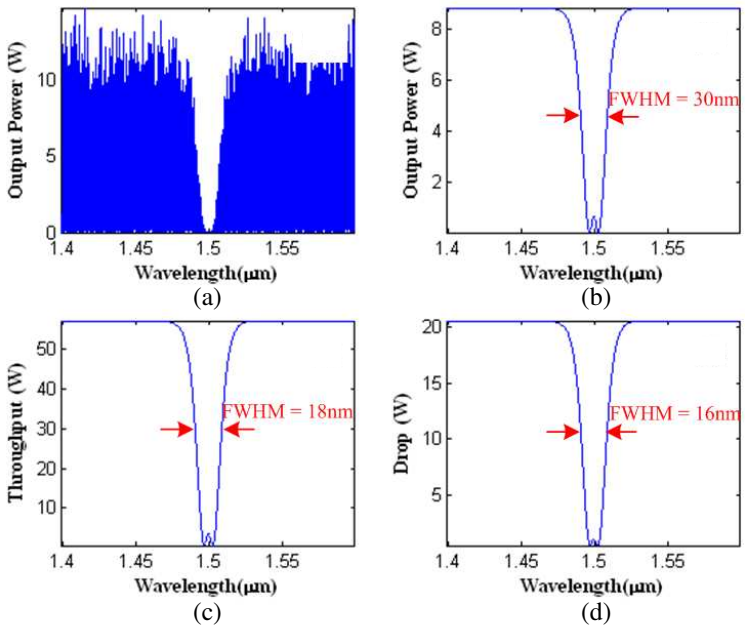

Figure 2: The dynamic dark soliton(optical tweezers) occurs within add/drop tunable filter, where (a) add/drop signals, (b) dark-bright soliton collision, (c) optical tweezers at throughput port, and (d) optical tweezers at drop port.

within add/drop tunable filter, when the bright soliton is input into the add port with the central wavelength $\lambda_0 = 1.5\,\mu$m. (a) add/drop signals, (b) dark-bright soliton collision, (c) optical tweezers at throughput port, and (d) optical tweezers at drop port. The recovery photon can be obtained by using the dark-bright soliton conversion, which is well analyzed by Sarapat et al. [6], where the trapped photon or molecule can be released or separated from the dark soliton pulse, in practice, in this case the bright soliton is become alive and seen.

3. MULTI-WAVELENGTH TRANSPORTERS

The received part can be used to detect the quantum bits via the optical link, which can be obtained via the end quantum processor and the reference states can be recognized by using the cloning unit, which is operated by the add/drop filter (R_{dN2}), used to be Bob as shown in the schematic diagram in Fig. 3. The transmitted part (extended from Fig. 1) can be used to generate the high capacity packet of quantum codes within the series of micro ring resonators and the cloning unit, which is operated by the add/drop filter (R_{dN1}), used to be Alice as shown in the schematic diagram in Fig. 4. The remaining part of a system of the quantum signal and parallel processing using Gaussian pulses via an optical multiplexer is as shown in the schematic diagram in Fig. 5.

By using the reasonable dark-bright soliton input power, the tunable optical tweezer can be controlled, which can provide the entangled photon as the dynamic optical tweezer probe. The smallest tweezer width of 16 nm is generated and achieved. In application, such a behavior can be used to confine the suitable size of light pulse or molecule, which can be employed in the same way of the optical tweezer. But in this case the terms dynamic probing is come to be a realistic function, therefore, the transportation of the trapped atom/molecule/photon by a single photon is plausible. For simplicity, the entangled photons power is attenuated to be a single photon be fore the detection, therefore, the separation between photon and molecule is employed the same way of a single photon

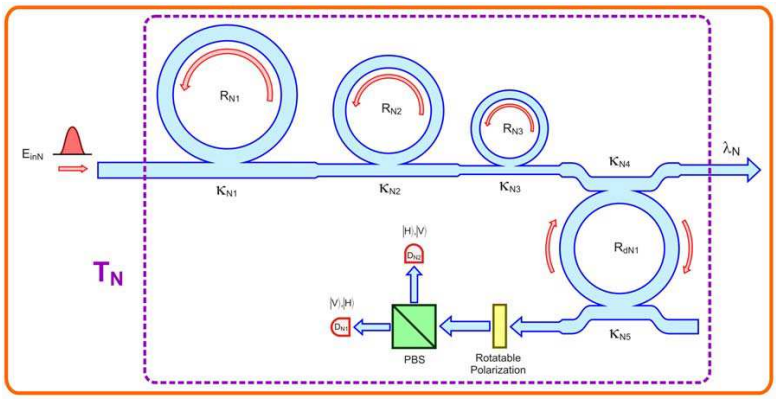

Figure 3: A schematic of a Gaussian soliton generation system, where R_{NS}: ring radii, κ_{NS}: coupling coefficients, R_{dNS}: an add/drop ring radius, can be used to be the received part.

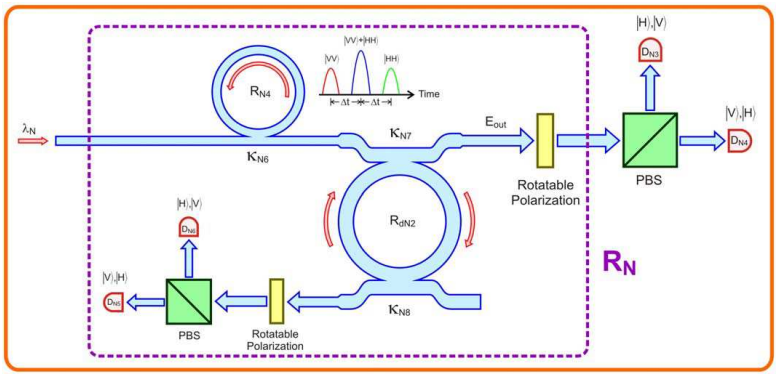

Figure 4: A schematic of an entangled photon pair manipulation within a ring resonator. The quantum state is propagating to a rotatable polarizer and then is split by a beam splitter (PBS) flying to detector D_{N3} and D_{N4}.

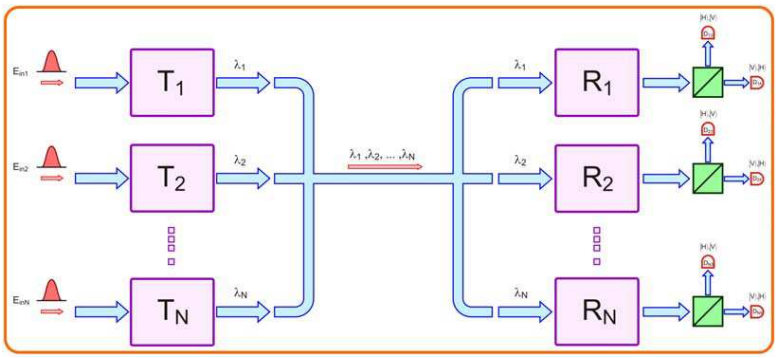

Figure 5: A schematic of a system of the quantum signal and parallel processing using Gaussian pulses via an optical multiplexer, where R_N: the received part, T_N: the transmitted part.

detection scheme. This means that the detection of the transported single atom/molecule can be configured by using the single photon detection method. Thus, the transported molecule/atom with long distance link via quantum-molecular transporter is realized. Furthermore, the secured hybrid quantum-molecular communication can be implemented within the existed transmission link.

4. CONCLUSION

We have demonstrated that some interesting results can be obtained when the laser pulse is propagated within the nonlinear optical ring resonator, especially, in microring and nanoring resonators, which can be used to perform many applications. For instance, the broad spectrum of a monochromatic source with the reasonable power can be generated and achieved by using a dark soliton can be converted to be a bright soliton by using the ring resonator system incorporating the add/drop multiplexer, which can be configured as a dynamic optical tweezers. The use of quantum tweezers for quantum-molecular communication/cryptography via a single photon based technology in the communication link is plausible.

REFERENCES

1. Pornsuwancharoen, N., U. Dunmeekaew, and P. P. Yupapin, "Multi-soliton generation using a microring resonator system for DWDM based soliton communication," *Microw. and Opt. Technol. Lett.*, Vol. 51, No. 5, 1374–1377, 2009.
2. Yupapin, P. P., N. Pornsuwanchroen, and S. Chaiyasoonthorn, "Attosecond pulse generation using nonlinear microring resonators," *Microw. and Opt. Technol. Lett.*, Vol. 50, No. 12, 3108–3011, 2008.
3. Pornsuwancharoen, N. and P. P. Yupapin, "Generalized fast, slow, stop, and store light optically within a nanoring resonator," *Microw. and Opt. Technol. Lett.*, Vol. 51, No. 4, 899–902, 2009.
4. Pornsuwancharoen, N., S. Chaiyasoonthorn, and P. P. Yupapin, "Fast and slow lights generation using chaotic signals in the nonlinear microring resonators for communication security," *Opt. Eng.*, Vol. 48, No. 1, 50005-1–5, 2009.
5. Yupapin, P. P. and N. Pornsuwancharoen, "Proposed nonlinear microring resonator arrangement for stopping and storing light," *IEEE Photon. Technol. Lett.*, Vol. 21, 404–406, 2009.
6. Sarapat, K., N. Sangwara, K. Srinuanjan, P. P. Yupapin, and N. Pornsuwancharoen, "Novel dark-bright optical solitons conversion system and power amplification," *Opt. Eng.*, Vol. 48, 045004-1–7, 2009.
7. Mitatha, S., N. Pornsuwancharoen, and P. P. Yupapin, "A simultaneous short-wave and millimeter-wave generation using a soliton pulse within a nano-waveguide," *IEEE Photon. Technol. Lett.*, Vol. 21, 932–934, 2009.
8. Agrawal, G. P., *Nonlinear Fiber Optics*, 4th Edition, Academic Press, New York, 2007.
9. Heidari, M. E., M. K. Moravvej-Farshi, and A. Zariffkar, "Multichannel wavelength conversion using fourth-order soliton decay," *J. Lightwave Technol.*, Vol. 25, 2571–2578, 2007.
10. Charoenmee, A., N. Pornsuwancharoen, and P. P. Yupapin, "Trapping a dark soliton pulse within a nanoring resonator," *International J. of Light and Electron Optics*, 2009. doi:10.1016/j.ijleo.2009.03.015.

11. Kokubun, Y., Y. Hatakeyama, M. Ogata, S. Suzuki, and N. Zaizen, "Fabrication technologies for vertically coupled microring resonator with multilevel crossing busline and ultracompact-ring radius," *IEEE J. Sel. Top. Quantum Electron.*, Vol. 11, 4–10, 2005.
12. Su, Y., F. Liu, and Q. Li, "System performance of slow-light buffering, and storage in silicon nano-waveguide," *Proc. SPIE*, Vol. 6783, 67832P, 2007.
13. Yupapin, P. P., P. Saeung, and C. Li, "Characteristics of complementary ring-resonator add/drop filters modeling by using graphical approach," *Opt. Commun.*, Vol. 272, 81–86, 2007.
14. Yupapin, P. P. and W. Suwancharoen, "Chaotic signal generation and cancellation using a microring resonator incorporating an optical add/drop multiplexer," *Opt. Commun.*, Vol. 280/2, 343–350, 2007.
15. Yuan, L., Z. Liu, J. Yang, and C. Guan, "Twin-core fiber optical tweezers," *Opt. Exp.*, Vol. 16, 4559–4566, 2008.
16. Malagninoa, N., G. Pescea, A. Sassoa, and E. Arimondo, "Measurements of trapping efficiency and stiffness in optical tweezers," *Opt. Commun.*, Vol. 214, 15–24, 2002.
17. Suchat, S., W. Khannam, and P. P. Yupapin, "Quantum key distribution via an optical wireless communication link for telephone network," *Opt. Eng. Lett.*, Vol. 46, No. 10, 100502-1–5, 2007.
18. Yupapin, P. P. and S. Suchat, "Entangle photon generation using fiber optic Mach-Zehnder interferometer incorporating nonlinear effect in a fiber ring resonator," *Nanophotonics (JNP)*, Vol. 1, 13504-1–7, 2007.

Multi Quantum-molecular Transportation via Multi Wavelength Layers in a Wavelength Router

S. Chaiyasoonthorn[1] and P. P. Yupapin[2]

[1]Department of Electronics Technology, Faculty of Science
Ramkhamhaeng University, Bangkok 10240, Thailand
[2]Advanced Research Center for Photonics, Faculty of Science
King Mongkut's Institute of Technology Ladkrabang, Bangkok 10520, Thailand

Abstract— We propose a new system of a multi molecular transporters generation for hybrid signal processing and networking applications. The transportation of molecules via multi tweezers in the wavelength layer and network can be performed. The design system consists of a nonlinear microring/nanoring resonator system incorporating an add/drop filter and a wavelength router. The multi transporters with different wavelengths can be generated and formed by the multi optical tweezers. The multiplexed transporters can be use for high capacity molecular signal processing and communication in the hybrid networks. In applications, the use of the proposed system incorporating a nanoscale communication and networking via the multi wavelength layer and routers is available for high density molecule transportation and long distance link.

1. INTRODUCTION

Bright and Dark Soliton behaviors have been widely investigated in different forms [1, 2]. The use of soliton, i.e., bright soliton in long distance communication link has been implemented for nearly two decades, however, the interesting works using bright solitton in communication remain, whereas the use a soliton pulse within a micro ring resonator for communication security. This means that we can use the dark soliton penalty due to the low level of the peak power to be the benefit, where the promising idea is that a dark soliton can be performed the communication transmission carrier where the recovery can be retrieved by the dark-bright soliton conversion. Recently, several research works have shown that use of dark and bright soliton in various applications can be realized [3–8], where one of them has shown that the secured signals in the communication link can be retrieved by using a suitable an add/drop filter that is connected into the transmission line. The other promising application of a dark soliton signal [9] is for the large guard band of two different frequencies which can be achieved by using a dark soliton generation scheme and trapping a dark soliton pulse within a nanoring resonator [10]. In this paper, the use of dark and bright solitons propagating within the proposed ring resonator systems is investigated and described, where the use of suitable parameters based on the realistic device is discussed. The potential of using the generated dark soliton signals for single photon tweezer and molecular transporter, especially, for the hybrid quantum-molecular communication and transportation in the communication network, which is described in details.

Bright and dark soliton pulses are introduced into the multi-stage nanoring resonators as shown in Fig. 1, the input time dependent optical field (E_{in}) of the bright and dark soliton pulses input are given by an Eq. (1) and (2) [8], respectively.

$$E_{in}(t) = A \operatorname{sec h}\left[\frac{T}{T_0}\right] \exp\left[\left(\frac{z}{2L_D}\right) - i\omega_0 t\right] \tag{1}$$

and

$$E_{in}(t) = A \tanh\left[\frac{T}{T_0}\right] \exp\left[\left(\frac{z}{2L_D}\right) - i\omega_0 t\right] \tag{2}$$

where A and z are the optical field amplitude and propagation distance, respectively. T is a soliton pulse propagation time in a frame moving at the group velocity, $T = t - \beta_1 * z$, where β_1 and β_2 are the coefficients of the linear and second-order terms of Taylor expansion of the propagation constant. $L_D = T_0^2/|\beta_2|$ is the dispersion length of the soliton pulse. T_0 in equation is a soliton pulse propagation time at initial input (or soliton pulse width), where t is the soliton phase shift time, and the frequency shift of the soliton is ω_0. This solution describes a pulse that keeps its temporal width invariance as it propagates, and thus is called a temporal soliton. When a soliton peak intensity

($|\beta_2/\Gamma T_0^2|$) is given, then T_0 is known. For the soliton pulse in the microring device, a balance should be achieved between the dispersion length (L_D) and the nonlinear length ($L_{NL} = 1/\Gamma\phi_{NL}$), where $\Gamma = n_2 * k_0$, is the length scale over which dispersive or nonlinear effects makes the beam become wider or narrower. For a soliton pulse, there is a balance between dispersion and nonlinear lengths, hence $L_D = L_{NL}$. Similarly, the output soliton of the system in Fig. 2 can be calculated by using Gaussian equations as given in the above case.

We assume that the nonlinearity of the optical ring resonator is of the Kerr-type, i.e., the refractive index is given by

$$n = n_0 + n_2 I = n_0 + \left(\frac{n_2}{A_{eff}}\right) P, \tag{3}$$

where n_0 and n_2 are the linear and nonlinear refractive indexes, respectively. I and P are the optical intensity and optical power, respectively. The effective mode core area of the device is given by A_{eff}. For the microring and nanoring resonators, the effective mode core areas range from 0.10 to 0.50 μm^2 [11, 12]

When a Gaussian pulse is input and propagated within a fiber ring resonator, the resonant output is formed, thus, the normalized output of the light field is the ratio between the output and input fields ($E_{out}(t)$ and $E_{in}(t)$) in each roundtrip, which can be expressed as [13]

$$\left|\frac{E_{out}(t)}{E_{in}(t)}\right|^2 = (1-\gamma)\left[1 - \frac{\left(1-(1-\gamma)\,x^2\right)\kappa}{(1-x\sqrt{1-\gamma}\sqrt{1-\kappa})^2 + 4x\sqrt{1-\gamma}\sqrt{1-\kappa}\sin^2\left(\frac{\phi}{2}\right)}\right] \tag{4}$$

Equation (4) indicates that a ring resonator in the particular case is very similar to a Fabry-Perot cavity, which has an input and output mirror with a field reflectivity, $(1-\kappa)$, and a fully reflecting mirror. k is the coupling coefficient, and $x = \exp(-\alpha L/2)$ represents a roundtrip loss coefficient, $\phi_0 = kLn_0$ and $\phi_{NL} = kL(\frac{n_2}{A_{eff}})P$ are the linear and nonlinear phase shifts, $k = 2\pi/\lambda$ is the wave propagation number in a vacuum. Where L and α are a waveguide length and linear absorption coefficient, respectively. In this work, the iterative method is introduced to obtain the results as shown in Eq. (4), similarly, when the output field is connected and input into the other ring resonators.

The input optical field as shown in Eqs. (1) and (2), i.e., a soliton pulse, is input into a nonlinear microring resonator. By using the appropriate parameters, the chaotic signal is obtained by using Eq. (4). To retrieve the signals from the chaotic noise, we propose to use the add/drop device with the appropriate parameters. This is given in details as followings. The optical outputs of a ring resonator add/drop filter can be given by the Eqs. (5) and (6) [14].

$$\left|\frac{E_t}{E_{in}}\right|^2 = \frac{(1-\kappa_1) - 2\sqrt{1-\kappa_1}\cdot\sqrt{1-\kappa_2}e^{-\frac{\alpha}{2}L}\cos(k_nL) + (1-\kappa_2)\,e^{-\alpha L}}{1+(1-\kappa_1)(1-\kappa_2)\,e^{-\alpha L} - 2\sqrt{1-\kappa_1}\cdot\sqrt{1-\kappa_2}e^{-\frac{\alpha}{2}L}\cos(k_nL)} \tag{5}$$

and

$$\left|\frac{E_d}{E_{in}}\right|^2 = \frac{\kappa_1\kappa_2 e^{-\frac{\alpha}{2}L}}{1+(1-\kappa_1)(1-\kappa_2)\,e^{-\alpha L} - 2\sqrt{1-\kappa_1}\cdot\sqrt{1-\kappa_2}e^{-\frac{\alpha}{2}L}\cos(k_nL)} \tag{6}$$

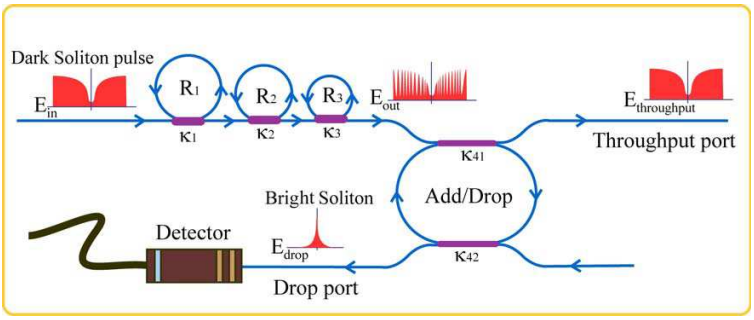

Figure 1: Schematic of a dark-bright soliton conversion system, where R_s is the ring radii, κ_s is the coupling coefficient, and κ_{41} and κ_{42} are the add/drop coupling coefficients.

where E_t and E_d represents the optical fields of the throughput and drop ports respectively. The transmitted output can be controlled and obtained by choosing the suitable coupling ratio of the ring resonator, which is well derived and described by reference [14]. Where $\beta = kn_{eff}$ represents the propagation constant, n_{eff} is the effective refractive index of the waveguide, and the circumference of the ring is $L = 2\pi R$, here R is the radius of the ring. In the following, new parameters will be used for simplification, where $\phi = \beta L$ is the phase constant. The chaotic noise cancellation can be managed by using the specific parameters of the add/drop device, which the required signals at the specific wavelength band can be filtered and retrieved. κ_1 and κ_2 are coupling coefficient of add/drop filters, $k_n = 2\pi/\lambda$ is the wave propagation number for in a vacuum, and the waveguide (ring resonator) loss is $\alpha = 0.5\,\mathrm{dBmm}^{-1}$. The fractional coupler intensity loss is $\gamma = 0.1$. In the case of add/drop device, the nonlinear refractive index is neglected.

2. MULTI QUANTUM-MOLECULAR TRANSPORTERS

In operation, a dark soliton pulse with 50-ns pulse width with the maximum power of 0.65 W is input into the dark-bright soliton conversion system as shown in Fig. 1. The suitable ring parameters are ring radii, where $R_1 = 10.0\,\mu\mathrm{m}$, $R_2 = 7.0\,\mu\mathrm{m}$, and $R_3 = 5.0\,\mu\mathrm{m}$. In order to make the system associate with the practical device [11, 12] the selected parameters of the system are fixed to $\lambda_0 = 1.50\,\mu\mathrm{m}$, $n_0 = 3.34$ (InGaAsP/InP). The effective core areas are $A_{eff} = 0.50$, 0.25, and $0.10\,\mu\mathrm{m}^2$ for a microring resonator (MRR) and nanoring resonator (NRR), respectively. The waveguide and coupling loses are $\alpha = 0.5\,\mathrm{dBmm}^{-1}$ and $\gamma = 0.1$, respectively, and the coupling coefficients κ_s of the MRR are ranged from 0.05 to 0.90. The nonlinear refractive index is $n_2 = 2.2 \times 10^{-13}\,\mathrm{m}^2/\mathrm{W}$. In this case, the waveguide loss used is $0.5\,\mathrm{dBmm}^{-1}$. The input dark soliton pulse is chopped (sliced) into the smaller output signals of the filtering signals within the rings R_2 and R_3. We find that the output signals from R_3 are smaller than from R_1, which is more difficult to detect when it is used in the link. In fact, the multistage ring system is proposed due to the different core effective areas of the rings in the system, where the effective areas can be transferred from 0.50 to $0.10\,\mu\mathrm{m}^2$ with some losses. The soliton signals in R_3 is entered in the add/drop filter, where the dark-bright soliton conversion can be performed by using Eqs. (5) and (6). The dynamic dark soliton control can be configured to be an optical dynamic tool known as an optical tweezers, where more details of optical tweezers can be found in references [15, 16]. After the bright soliton input is added into the system via add port as shown in Fig. 2, the optical tweezers behavior is occurred. The parameters of system are used the same as the previous case. The bright soliton is generated with the central wavelength $\lambda_0 = 1.5\,\mu\mathrm{m}$, when the bright soliton propagating into the add/drop system, the dark-

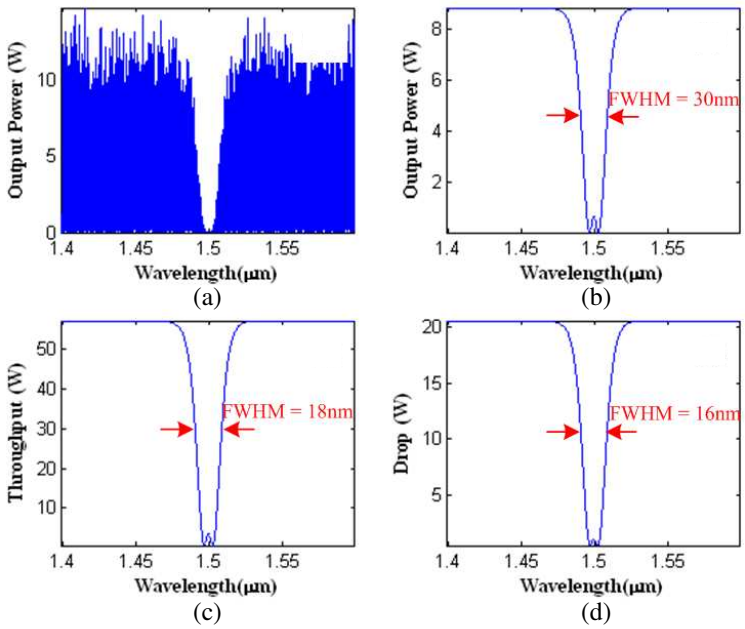

Figure 2: The dynamic dark soliton(optical tweezers) occurs within add/drop tunable filter, where (a) add/drop signals, (b) dark-bright soliton collision, (c) optical tweezers at throughput port, and (d) optical tweezers at drop port.

bright soliton collision in add/drop system is seen. The dark soliton valley dept, i.e., potential well is changed when it is modulated by the trapping energy (dark-bright solitons interaction) as shown in Fig. 2. The dynamic dark soliton (optical tweezers) occurs within add/drop tunable filter, when the bright soliton is input into the add port with the central wavelength $\lambda_0 = 1.5\,\mu$m. (a) add/drop signals, (b) dark-bright soliton collision, (c) optical tweezers at throughput port, and (d) optical tweezers at drop port. The recovery photon can be obtained by using the dark-bright soliton conversion, which is well analyzed by Sarapat et al. [6], where the trapped photon or molecule can be released or separated from the dark soliton pulse, in practice, in this case the bright soliton is become alive and seen.

Let us consider that the case when the optical tweezers output from the throughput port in Figs. 1 and 2 is partially input into the quantum processor unit as shown in Fig. 3. Generally, there are two pairs of possible polarization entangled photons forming within the ring device, which are represented by the four polarization orientation angles as [0°, 90°], [135° and 180°]. These can be formed by using the optical component called the polarization rotatable device and a polarizing beam splitter (PBS). In this concept, we assume that the polarized photon can be performed by using the proposed arrangement. Where each pair of the transmitted qubits can be randomly formed the entangled photon pairs. To begin this concept, we introduce the technique that can be used to create the entangled photon pair (qubits) as shown in Fig. 3, a polarization coupler that separates the basic vertical and horizontal polarization states corresponds to an optical switch between the short and the long pulses. We assume those horizontally polarized pulses with a temporal separation of Δt. The coherence time of the consecutive pulses is larger than Δt. Then the following state is created by Eq. (7) [17].

$$|\Phi\rangle_p = |1,H\rangle_s\,|1,H\rangle_i + |2,H\rangle_s\,|2,H\rangle_i \tag{7}$$

In the expression $|k,H\rangle$, k is the number of time slots (1 or 2), where denotes the state of polarization [horizontal $|H\rangle$ or vertical $|V\rangle$], and the subscript identifies whether the state is the signal (s) or the idler (i) state. In Eq. (7), for simplicity, we have omitted an amplitude term that is common to all product states. We employ the same simplification in subsequent equations in this paper. This two-photon state with $|H\rangle$ polarization shown by Eq. (7) is input into the orthogonal polarization-delay circuit shown schematically. The delay circuit consists of a coupler and the difference between the round-trip times of the microring resonator, which is equal to Δt. The microring is tilted by changing the round trip of the ring is converted into $|V\rangle$ at the delay circuit output. That is the delay circuits convert $|k,H\rangle$ to be $r|k,H\rangle + t_2\exp(i\phi)|k+1,V\rangle + rt_2\exp(i_2\phi)|k+2,H\rangle + r_2t_2\exp(i_3\phi)|k+3,V\rangle$, where t and r is the amplitude transmittances to cross and bar ports in a coupler. Then Eq. (7) is converted into the polarized state by the delay circuit as

$$\begin{aligned}
|\Phi\rangle &= [|1,H\rangle_s + \exp(i\phi_s)|2,V\rangle_s] \times [|1,H\rangle_i + \exp(i\phi_i)|2,V\rangle_i] \\
&\quad + [|2,H\rangle_s + \exp(i\phi_s)|3,V\rangle_s] \times [|2,H\rangle_i + \exp(i\phi_i)|2,V\rangle_i] \\
&= [|1,H\rangle_s|1,H\rangle_i + \exp(i\phi_i)|1,H\rangle_s|2,V\rangle_i] + \exp(i\phi_s)|2,V\rangle_s|1,H\rangle_i \\
&\quad + \exp[i(\phi_s+\phi_i)]|2,V\rangle_s|2,V\rangle_i + |2,H\rangle_s|2,H\rangle_i + \exp(i\phi_i)|2,H\rangle_s|3,V\rangle_i \\
&\quad + \exp(i\phi_s)|3,V\rangle_s|2,H\rangle_i + \exp[i(\phi_s+\phi_i)]|3,V\rangle_s|3,V\rangle_i
\end{aligned} \tag{8}$$

By the coincidence counts in the second time slot, we can extract the fourth and fifth terms. As a result, we can obtain the following polarization entangled state as

$$|\Phi\rangle = |2,H\rangle_s\,|2,H\rangle_i + \exp[i\,(\phi_s+\phi_i)]\,|2,V\rangle_s\,|2,V\rangle_i \tag{9}$$

We assume that the response time of the Kerr effect is much less than the cavity round-trip time. Because of the Kerr nonlinearity of the optical device, the strong pulses acquire an intensity dependent phase shift during propagation. The interference of light pulses at a coupler introduces the output beam, which is entangled. Due to the polarization states of light pulses are changed and converted while circulating in the delay circuit, where the polarization entangled photon pairs can be generated. The entangled photons of the nonlinear ring resonator are separated to be the signal and idler photon probability. The polarization angle adjustment device is applied to investigate the orientation and optical output intensity, this concept is well described by the published work [18]. The transporter states can be controlled and identified by using the quantum processing system after as shown in Fig. 3.

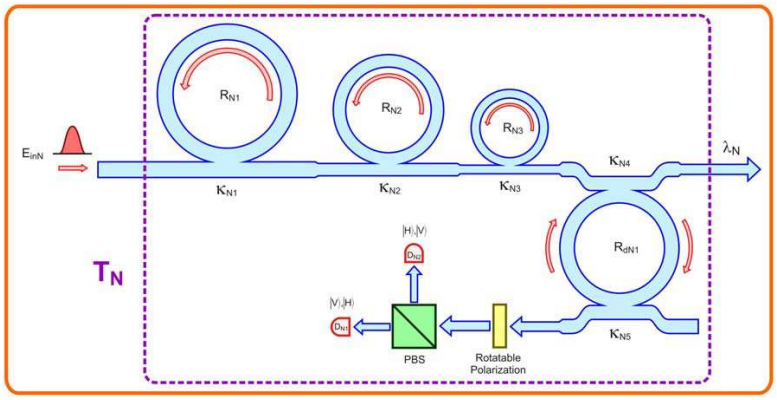

Figure 3: A schematic of a Gaussian soliton generation system, where R_{NS}: ring radii, κ_{NS}: coupling coefficients, R_{dNS}: an add/drop ring radius, can be used to be the received part.

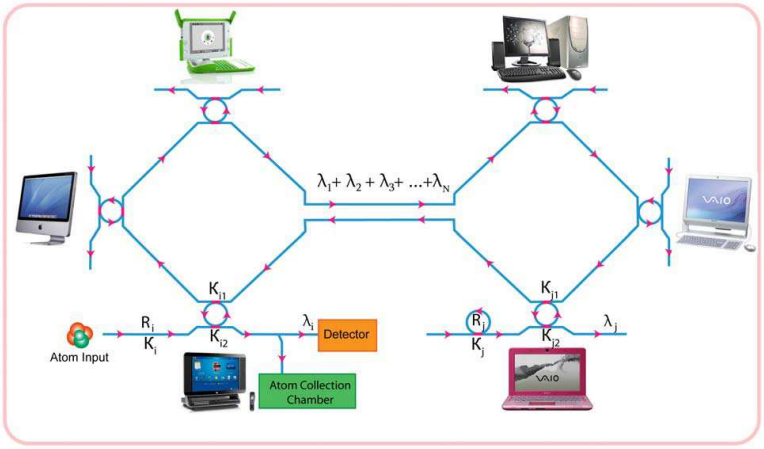

Figure 4: A schematic of atomic/molecular router and network system, where R_i, R_j: ring radii and κ_{is}, κ_{js} are the coupling coefficients.

3. QUANTUM-MOLECULAR TRANSPORTATION VIA MULTI WAVELENGTH LAYERS

By using the reasonable dark-bright soliton input power, the tunable optical tweezer can be controlled, which can be used as the dynamic optical tweezer probe. The smallest tweezer width of 16 nm is generated and achieved. In application, such a behavior can be used to confine the suitable size of light pulse or molecule, which can be employed in the same way of the optical tweezer. But in this case the terms dynamic probing is come to be a realistic function, therefore, the transportation of the trapped atom/molecule/photon is plausible. Moreover, the trapped states of the transported atom/molecule can be configured by using the quantum processor as shown in Fig. 3. Thus, the transported atom with long distance link via quantum tweezer is realized.

From the above reasons, the transmission of atoms/molecules from dark soliton pulses via a wavelength router is plausible, which can be described by the following reasons: (i) a dark soliton pulse can propagate into the optical device/media, (ii) atom/molecule being trapped by tweezers force during the movement, the atom/molecule recovery can be realized by using the optical detection scheme, where the dark-bright soliton conversion technique is also available [6]. However, the separation of atoms/molecules from light pulse is required to have the specific environment, which becomes the interesting research area, where light with the specific wavelength (λ_i) is detected by a detector, while the required molecule is absorbed by the specific environment. The atom/molecule states can be allocated by using the quantum processing unit as shown in Fig. 3, where the corresponding states of the transmitted atom/molecule between input and output states can be recognized and formed the secret information. Therefore, in practice, the quantum processing unit is required to connect into the system, where the input and output states can be linked and obtained the required information.

4. CONCLUSION

We have demonstrated that some interesting results can be obtained when the laser pulse is propagated within the nonlinear optical ring resonator, especially, in microring and nanoring resonators, which can be used to perform many applications. For instance, the broad spectrum of a monochromatic source with the reasonable power can be generated and achieved by using a dark soliton can be converted to be a bright soliton by using the ring resonator system incorporating the add/drop multiplexer, which can be configured as a dynamic optical tweezers. The use of quantum tweezers for quantum-molecular communication/cryptography via a single photon based technology in the communication link is plausible.

REFERENCES

1. Kivshar, Y. S. and B. Luther-Davies, "Dark optical solitons: Physics and applications," *Phys. Rep.*, Vol. 298, 81, 1998.
2. Zhao, W. and E. Bourkoff, "Propagation properties of dark solitons," *Opt. Lett.*, Vol. 14, 703–705, 1989.
3. Pornsuwancharoen, N., U. Dunmeekaew, and P. P. Yupapin, "Multi-soliton generation using a microring resonator system for DWDM based soliton communication," *Microw. and Opt. Technol. Lett.*, Vol. 51, No. 5, 1374–1377, 2009.
4. Yupapin, P. P., N. Pornsuwanchroen, and S. Chaiyasoonthorn, "Attosecond pulse generation using nonlinear microring resonators," *Microw. and Opt. Technol. Lett.*, Vol. 50, No. 12, 3108–3011, 2008.
5. Pornsuwancharoen, N. and P. P. Yupapin, "Generalized fast, slow, stop, and store light optically within a nanoring resonator," *Microw. and Opt. Technol. Lett.*, Vol. 51, No. 4, 899–902, 2009.
6. Pornsuwancharoen, N., S. Chaiyasoonthorn, and P. P. Yupapin, "Fast and slow lights generation using chaotic signals in the nonlinear microring resonators for communication security," *Opt. Eng.*, Vol. 48, No. 1, 50005-1–5, 2009.
7. Yupapin, P. P. and N. Pornsuwancharoen, "Proposed nonlinear microring resonator arrangement for stopping and storing light," *IEEE Photon. Technol. Lett.*, Vol. 21, 404–406, 2009.
8. Sarapat, K., N. Sangwara, K. Srinuanjan, P. P. Yupapin, and N. Pornsuwancharoen, "Novel dark-bright optical solitons conversion system and power amplification," *Opt. Eng.*, Vol. 48, 045004-1–7, 2009.
9. Mitatha, S., N. Pornsuwancharoen, and P. P. Yupapin, "A simultaneous short-wave and millimeter-wave generation using a soliton pulse within a nano-waveguide," *IEEE Photon. Technol. Lett.*, Vol. 21, 932–934, 2009.
10. Agrawal, G. P., *Nonlinear Fiber Optics*, 4th Edition, Academic Press, New York, 2007.
11. Kokubun, Y., Y. Hatakeyama, M. Ogata, S. Suzuki, and N. Zaizen, "Fabrication technologies for vertically coupled microring resonator with multilevel crossing busline and ultracompact-ring radius," *IEEE J. Sel. Top. Quantum Electron.*, Vol. 11, 4–10, 2005.
12. Su, Y., F. Liu, and Q. Li, "System performance of slow-light buffering, and storage in silicon nano-waveguide," *Proc. SPIE*, Vol. 6783, 67832P, 2007.
13. Yupapin, P. P., P. Saeung, and C. Li, "Characteristics of complementary ring-resonator add/drop filters modeling by using graphical approach," *Opt. Commun.*, Vol. 272, 81–86, 2007.
14. Yupapin, P. P. and W. Suwancharoen, "Chaotic signal generation and cancellation using a microring resonator incorporating an optical add/drop multiplexer," *Opt. Commun.*, Vol. 280/2, 343–350, 2007.
15. Yuan, L., Z. Liu, J. Yang, and C. Guan, "Twin-core fiber optical tweezers," *Opt. Exp.*, Vol. 16, 4559–4566, 2008.
16. Malagninoa, N., G. Pescea, A. Sassoa, and E. Arimondo, "Measurements of trapping efficiency and stiffness in optical tweezers," *Opt. Commun.*, Vol. 214, 15–24, 2002.
17. Suchat, S., W. Khannam, and P. P. Yupapin, "Quantum key distribution via an optical wireless communication link for telephone network," *Opt. Eng. Lett.*, Vol. 46, No. 10, 100502-1–5, 2007.
18. Yupapin, P. P. and S. Suchat, "Entangle photon generation using fiber optic Mach-Zehnder interferometer incorporating nonlinear effect in a fiber ring resonator," *Nanophotonics (JNP)*, Vol. 1, 13504-1–7, 2007.

Molecule Transportation via Hybrid MUX/DEMUX System

N. Sangwaranatee[1], **P. Chaiyachate**[2], **S. Mitatha**[3], **and P. P. Yupapin**[2]

[1]Faculty of Science and Technology, Rajamangala University of Technology Krungthep, Thailand
[2]Advanced Research Center for Photonics, Faculty of Science
King Mongkut's Institute of Technology, Ladkrabang, Bangkok 10520, Thailand
[3]Department of Computer Engineering, Faculty of Engineering
King Mongkut's Institute of Technology, Ladkrabang, Bangkok 10520, Thailand

Abstract— We propose a new system of quantum signal and parallel processing using Gaussian pulses propagating within a nonlinear ring resonator system. To increase the channel capacity and security, the optical embedded multiplexer is operated incorporating a quantum processing unit via an optical multiplexer. The transmitted part can be used to generate the high capacity packet of quantum codes within the series of microring resonators. The received part can be used to detect the quantum bits (qubits) via the optical link, which can be obtained via the far ended quantum processor. The reference states can be recognized by using the cloning unit, which is operated by the add/drop filter. Two add/drop filters that are in two parts can be used to be presented as Alice and Bob, respectively, in quantum communication. Results obtained have shown that the multiplexed wavelengths can be formed by using the multiple operating systems, which is allowed to obtain the filtering signals at the end users (Bob). In application, the embedded system within the computer processing unit is available for quantum computer. Furthermore, such a concept is also available for hybrid communications, for instance, wire/wireless, satellite, which will be focused in the future research works.

1. INTRODUCTION

Quantum key distribution has been recognized as the very good candidate for information security. Many research works have been reported in the last decade. Recently, Suchat et al. [1] have reported the interesting concept of continuous variable quantum key distribution via a simultaneous optical-wireless up-down-link system, where they have shown that the continuous variable quantum key distribution (KQD) could be performed via the chaotic signals that generated by a nonlinear micro-ring resonator system, with appropriate soliton input power and micro-ring resonator. They have also shown that the different time slot entangled photons can be formed randomly, which can be used to select two different frequency bands for up-down-link converters within a single system. Yupapin et al. [2] have proposed a new technique for QKD that can be used to make the communication transmission security and implemented with a small device for such as mobile telephone hand set. This technique used Kerr nonlinear type of light in the microring resonator to generate the superposition of the chaotic signal via a four-wave mixing type that introduced the second-harmonic pulse. An experimental technique of communication security via the quantum chaotic encoding has been investigated by Yupapin and Chunpang [3], where the use of quantum-chaotic encoding of light traveling in a fiber ring resonator to generate two different codes i.e., quantum bits and chaotic signal was investigated. Mitatha et al. [4] have proposed the system of secured packet switching using the nonlinear behaviors of light in microring resonator, which can be made high-capacity and security switching in transmission line. Such a system can be used for the security requirement by using the tunable band pass and band stop filters. Another technique [5] used the nonlinear behavior of light in microring resonator for packet switching start-stop bits generation, which has shown that the generated start-stop bits can used to be secured codes. Yupapin et al. [6] have shown that the entangled photon states can be recovered by using the entangled states with the lower input to higher amplitude using pumping EDF and tilting PC. Next system [7] of the quantum key generation via a microring resonator for mobile telephone network can be used for the conversation messages and secured by using a quantum code/decode (CODEC) technique incorporated in the public networks. Another system [8] has shown the dissipative effect of the entangled photons that the entangled strength measurement depends on three main factors; the nonlinear susceptibility of the third harmonic generation, the damping rate that represents loss of energy from the system to the reservoir, and the diffusion of fluctuations in the reservoir into the entangled photon modes. Up to date, there is no quantum parallel processing manipulation using a common laser (Gaussian pulse) via an optical multiplexer. In this paper, we have proposed the use of nonlinear microring resonator to form the high capacity quantum codes, where the packet

of quantum codes can be generated by using Gaussian light pulse propagating with the series of microring resonator. In application, the device can be embedded within the computer processing unit with using to increase the capacity and the speed for quantum computer. Furthermore, such a concept is also available for hybrid communications, for instance, wire/wireless or satellite. However, to give the reader familiarity, the theoretical background of multi-light source generation is reviewed.

2. MULTI-LIGHT SOURCE GENERATION

Light from a monochromatic light source is launched into a ring resonator with constant light field amplitude (E_0) and random phase modulation, which is the combination of terms in attenuation (α) and phase(ϕ_0) constants, which results in temporal coherence degradation. Hence, the time dependent input light field (E_{in}), without pumping term, can be expressed as

$$E_{in}(t) = E_0 \exp^{-\alpha L + j\phi_0(t)}. \tag{1}$$

where L is a propagation distance (waveguide length).

We assume that the nonlinearity of the optical ring resonator is of the Kerr-type, i.e., the refractive index is given by

$$n = n_0 + n_2 I = n_0 + \left(\frac{n_2}{A_{eff}}\right) P, \tag{2}$$

where n_0 and n_2 are the linear and nonlinear refractive indexes, respectively. I and P are the optical intensity and optical power, respectively. The effective mode core area of the device is given by A_{eff}. For the microring and nanoring resonators, the effective mode core areas range from 0.10 to $0.50\,\mu m^2$ [9].

When a Gaussian pulse is input and propagated within a fiber ring resonator, the resonant output is formed, thus, the normalized output of the light field is the ratio between the output and input fields ($E_{out}(t)$ and $E_{in}(t)$) in each roundtrip, which can be expressed as [10]

$$\left|\frac{E_{out}(t)}{E_{in}(t)}\right|^2 = (1-\gamma)\left[1 - \frac{\left(1-(1-\gamma)\,x^2\right)\kappa}{\left(1-x\sqrt{1-\gamma}\sqrt{1-\kappa}\right)^2 + 4x\sqrt{1-\gamma}\sqrt{1-\kappa}\sin^2\left(\frac{\phi}{2}\right)}\right] \tag{3}$$

Equation (3) indicates that a ring resonator in the particular case is very similar to a Fabry-Perot cavity, which has an input and output mirror with a field reflectivity, $(1-\kappa)$, and a fully reflecting mirror. κ is the coupling coefficient, and $x = \exp(-\alpha L/2)$ represents a roundtrip loss coefficient, $\phi_0 = kLn_0$ and $\phi_{NL} = kL(\frac{n_2}{A_{eff}})P$ are the linear and nonlinear phase shifts, $k = 2\pi/\lambda$ is the wave propagation number in a vacuum. Where L and α are a waveguide length and linear absorption coefficient, respectively. In this work, the iterative method is introduced to obtain the results as shown in Equation (3), similarly, when the output field is connected and input into the other ring resonators.

The input optical field as shown in Equation (1), i.e., a Gaussian pulse, is input into a nonlinear microring resonator. By using the appropriate parameters, the chaotic signal is obtained by using Equation (3). To retrieve the signals from the chaotic noise, we propose to use the add/drop device with the appropriate parameters. This is given in details as followings. The optical outputs of a ring resonator add/drop filter can be given by the Equations (4) and (5) [11].

$$\left|\frac{E_t}{E_{in}}\right|^2 = \frac{(1-\kappa_1) - 2\sqrt{1-\kappa_1}\cdot\sqrt{1-\kappa_2}e^{-\frac{\alpha}{2}L}\cos(k_n L) + (1-\kappa_2)\,e^{-\alpha L}}{1+(1-\kappa_1)(1-\kappa_2)\,e^{-\alpha L} - 2\sqrt{1-\kappa_1}\cdot\sqrt{1-\kappa_2}e^{-\frac{\alpha}{2}L}\cos(k_n L)} \tag{4}$$

and

$$\left|\frac{E_d}{E_{in}}\right|^2 = \frac{\kappa_1\kappa_2 e^{-\frac{\alpha}{2}L}}{1+(1-\kappa_1)(1-\kappa_2)\,e^{-\alpha L} - 2\sqrt{1-\kappa_1}\cdot\sqrt{1-\kappa_2}e^{-\frac{\alpha}{2}L}\cos(k_n L)} \tag{5}$$

where E_t and E_d represents the optical fields of the throughput and drop ports respectively. The transmitted output can be controlled and obtained by choosing the suitable coupling ratio of the ring resonator, which is well derived and described by reference [11]. Where $\beta = kn_{eff}$ represents the propagation constant, n_{eff} is the effective refractive index of the waveguide, and the circumference

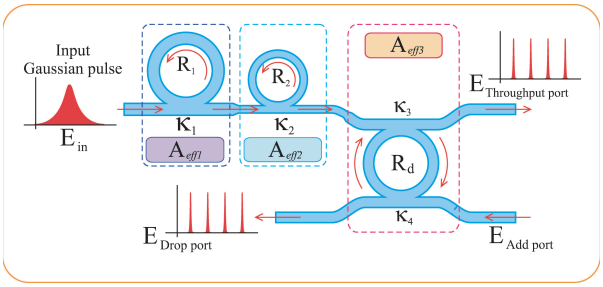

Figure 1: A schematic of a Gaussian soliton generation system, where R_s: Ring radii, κ_s: Coupling coefficients, R_d: An add/drop ring radius, $A_{eff}s$: Effective areas.

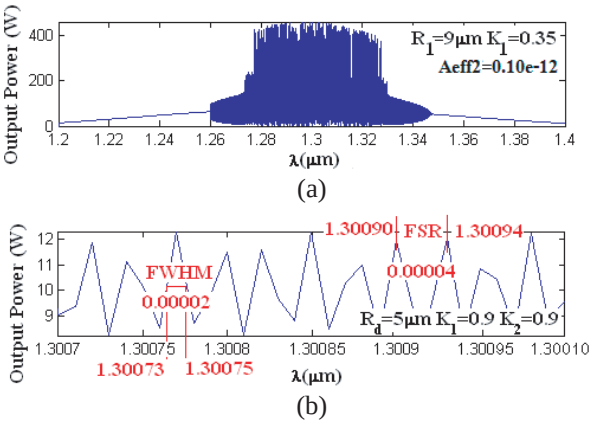

Figure 2: Result of the spatial pulses with center wavelength at 1.30 μm, where (a) large bandwidth signals, (b) filtering and amplifying signals from the drop port.

of the ring is $L = 2\pi R$, here R is the radius of the ring. In the following, new parameters will be used for simplification, where $\phi = \beta L$ is the phase constant. The chaotic noise cancellation can be managed by using the specific parameters of the add/drop device, which the required signals at the specific wavelength band can be filtered and retrieved. κ_1 and κ_2 are coupling coefficient of add/drop filters, $k_n = 2\pi/\lambda$ is the wave propagation number for in a vacuum, and the waveguide (ring resonator) loss is $\alpha = 0.5\,\mathrm{dBmm}^{-1}$. The fractional coupler intensity loss is $\gamma = 0.1$. In the case of add/drop device, the nonlinear refractive index is neglected.

From Fig. 1, in principle, light pulse is sliced to be the discrete signal and amplified within the first ring, where more signal amplification can be obtained by using the smaller ring device (second ring). Finally, the required signals can be obtained via a drop port of the add/drop filter. In operation, an optical field in the form of Gaussian pulse from a laser source at the specified center wavelength is input into the system. From Fig. 2, the Gaussian pulse with center wavelength (λ_0) at 0.40 μm, pulse width (Full Width at Half Maximum, **FWHM**) of 20 ns, peak power at 2 W is input into the system as shown in Fig. 2(a). The large bandwidth signals can be seen within the first microring device, and shown in Fig. 2(b). The suitable ring parameters are used, for instance, ring radii $R_1 = 9.0\,\mu\mathrm{m}$, $R_2 = 9.0\,\mu\mathrm{m}$, and $R_d = 5.0\,\mu\mathrm{m}$. In order to make the system associate with the practical device [12], the selected parameters of the system are fixed to $n_0 = 3.34$ (**InGaAsP/InP**), $A_{eff} = 0.50\,\mu\mathrm{m}^2$ and $0.25\,\mu\mathrm{m}^2$ for a microring and add/drop ring resonator, respectively, $\alpha = 0.5\,\mathrm{dBmm}^{-1}$, $\gamma = 0.1$. In this investigation, the coupling coefficient (kappa, κ) of the microring resonator is ranged from 0.55 to 0.90. The nonlinear refractive index of the microring used is $n_2 = 2.2 \times 10^{-17}\,\mathrm{m}^2/\mathrm{W}$. In this case, the attenuation of light propagates within the system (i.e., wave guided) used is $0.5\,\mathrm{dBmm}^{-1}$. After light is input into the system, the Gaussian pulse is chopped (sliced) into a smaller signal spreading over the spectrum due to the nonlinear effects [11], which is shown in Fig. 2(a). The large bandwidth signal is generated within the first ring device. In applications, the specific input or out wavelengths can be used and generated. For instance, the different center wavelengths of the input pulse can be ranged from 1.3, 1.5 μm as shown in Figs. 2–4, where the suitable parameters are used and shown in the figures.

We have shown that the multi-wavelength bands can be generated by using a Gaussian pulse propagating within the microring resonator system, which is available for the extended DWDM with the wavelength center at 1.30, 1.50 μm, which can be used with the existed public networks, where the non-dispersive wavelength (1.30 μm) can be extended and used to increase the communication capacity, furthermore, for long distance link, the pumping is not required in such a system. One of the results with the center wavelength at 1.50 μm has shown that the spatial pulse width of 1.0 nm and the spectrum range of 3.0 nm can be generated and achieved, which is as shown in Fig. 3(b). Moreover, the problem of signal collision can be solved by using the suitable FSR design [10]. In general, by using the wider range of ring parameters, the spectral range of the output can be covered wider range instead of fraction of nm. The large increasing in peak power is seen when light propagates from the large to small effective core area, where the other parameter is the coupling

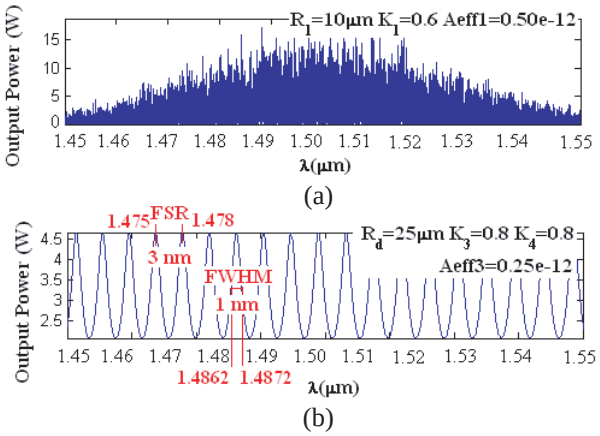

Figure 3: Results of the spatial pulses with center wavelength at 1.50 μm, where (a) large bandwidth signals, (b) filtering and amplifying signals from the drop port.

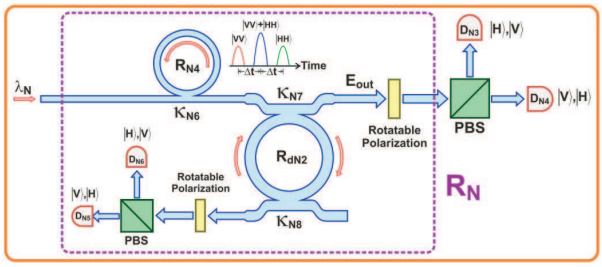

Figure 4: A schematic of a quantum tweezers generation system at the transmission unit (T_N), where $R_N S$: Ring radii, $\kappa_N S$: Coupling coefficients, $R_{dN} S$: An add/drop ring radius, can be used to be the received part, PBS: Polarizing Beamsplitter, D_N: Detectors.

coefficient. However, the amplified power is required to control to keep the device being realistic.

3. QUANTUM PARALLEL PROCESSING VIA AN OPTICAL MULTIPLEXER

Let us consider that the case when the photon output is input into the quantum processor unit. Generally, there are two pairs of possible polarization entangled photons forming within the ring device, which are represented by the four polarization orientation angles as [0°, 90°], [135° and 180°]. These can be formed by using the optical component called the polarization rotatable device and a polarizing beam splitter (PBS). In this concept, we assume that the polarized photon can be performed by using the proposed arrangement. Where each pair of the transmitted qubits can be randomly formed the entangled photon pairs. To begin this concept, we introduce the technique that can be used to create the entangled photon pair (qubits) as shown in Fig. 4, a polarization coupler that separates the basic vertical and horizontal polarization states corresponds to an optical switch between the short and the long pulses. We assume those horizontally polarized pulses with a temporal separation of Δt. The coherence time of the consecutive pulses is larger than Δt. Then the following state is created by Equation (6) [13].

$$|\Phi\rangle_p = |1, H\rangle_s |1, H\rangle_i + |2, H\rangle_s |2, H\rangle_i \tag{6}$$

In the expression $|k, H\rangle$, k is the number of time slots (1 or 2), where denotes the state of polarization [horizontal $|H\rangle$ or vertical $|V\rangle$], and the subscript identifies whether the state is the signal (s) or the idler (i) state. In Equation (6), for simplicity, we have omitted an amplitude term that is common to all product states. We employ the same simplification in subsequent equations in this paper. This two-photon state with $|H\rangle$ polarization shown by Equation (6) is input into the orthogonal polarization-delay circuit shown schematically. The delay circuit consists of a coupler and the difference between the round-trip times of the microring resonator, which is equal to Δt. The microring is tilted by changing the round trip of the ring is converted into $|V\rangle$ at the delay circuit output. That is the delay circuits convert $|k, H\rangle$ to be

$$r\,|k, H\rangle + t_2 \exp(i\phi)\,|k+1, V\rangle + rt_2 \exp(i_2\phi)\,|k+2, H\rangle + r_2 t_2 \exp(i_3\phi)\,|k+3, V\rangle$$

where t and r is the amplitude transmittances to cross and bar ports in a coupler. Then Equation (6)

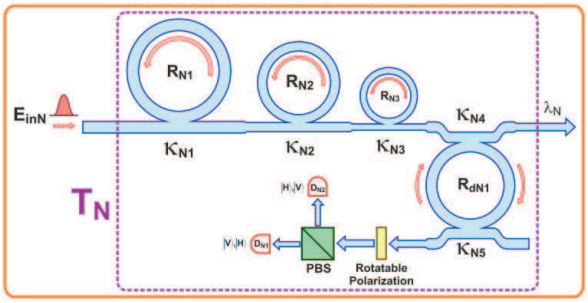

Figure 5: A schematic of the quantum tweezers manipulation within a ring resonator at the receiver unit (R_N). The quantum state is propagating to a rotatable polarizer and then is split by a beam splitter (PBS) flying to detector D_{N3} and D_{N4}.

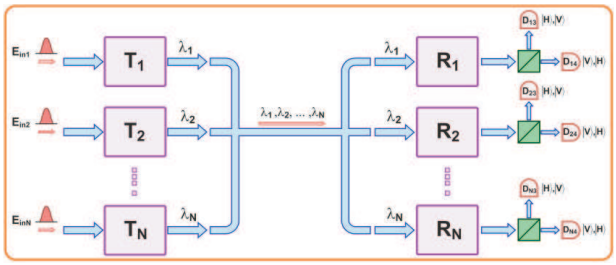

Figure 6: A schematic of a system of the transporters transmission system via an optical link, where R_N: The receiver part, T_N: The transmitter part.

is converted into the polarized state by the delay circuit as

$$\begin{aligned}|\Phi\rangle &= [|1,H\rangle_s + \exp(i\phi_s)\,|2,V\rangle_s] \times [|1,H\rangle_i + \exp(i\phi_i)\,|2,V\rangle_i] \\ &\quad + [|2,H\rangle_s + \exp(i\phi_s)\,|3,V\rangle_s] \times [|2,H\rangle_i + \exp(i\phi_i)\,|2,V\rangle_i] \\ &= [|1,H\rangle_s\,|1,H\rangle_i + \exp(i\phi_i)\,|1,H\rangle_s\,|2,V\rangle_i] + \exp(i\phi_s)\,|2,V\rangle_s\,|1,H\rangle_i \\ &\quad + \exp[i\,(\phi_s+\phi_i)]\,|2,V\rangle_s\,|2,V\rangle_i + |2,H\rangle_s\,|2,H\rangle_i + \exp\,(i\phi_i)\,|2,H\rangle_s\,|3,V\rangle_i \\ &\quad + \exp\,(i\phi_s)\,|3,V\rangle_s\,|2,H\rangle_i + \exp[i\,(\phi_s+\phi_i)]\,|3,V\rangle_s\,|3,V\rangle_i \end{aligned} \tag{7}$$

By the coincidence counts in the second time slot, we can extract the fourth and fifth terms. As a result, we can obtain the following polarization entangled state as

$$|\Phi\rangle = |2,H\rangle_s\,|2,H\rangle_i + \exp[i\,(\phi_s+\phi_i)]\,|2,V\rangle_s\,|2,V\rangle_i \tag{8}$$

We assume that the response time of the Kerr effect is much less than the cavity round-trip time. Because of the Kerr nonlinearity of the optical device, the strong pulses acquire an intensity dependent phase shift during propagation. The interference of light pulses at a coupler introduces the output beam, which is entangled. Due to the polarization states of light pulses are changed and converted while circulating in the delay circuit, where the polarization entangled photon pairs can be generated. The entangled photons of the nonlinear ring resonator are separated to be the signal and idler photon probability. The polarization angle adjustment device is applied to investigate the orientation and optical output intensity, this concept is well described by the published work [13, 14]. The transporter states can be controlled and identified by using the quantum processing system as shown in Figs. 4 and 5.

The transmitter unit can be used to generate the quantum codes within the series of microring resonators and the cloning unit [6], which is operated by the add/drop filter (R_{dN1}). The receiver unit can be used to detect the quantum bits via the optical link, which can be obtained via the end quantum processor and the reference states can be recognized by using the cloning unit, which is operated by the add/drop filter (R_{dN2}) as shown in the schematic diagram in Figs. 4 and 5. The remaining part of a system is the parallel processing system which can be combined the high capacity secret information via an optical multiplexer as shown in the schematic diagram in Fig. 6. The multiplexed quantum codes are allowed to form and transmit the secret information via the available link, where the quantum keys with different wavelengths (λ_N) can be generated and obtained, which is available for high capacity transmission of the secured information. In application, the packet switching of data can be secured by using the quantum codes which is known as quantum packet switching technique.

4. CONCLUSION

We have demonstrated that some interesting results can be obtained when the common laser pulse is propagated within the nonlinear optical ring resonator, especially, in microring and nanoring resonators, which can be used to perform many applications. For instance, the broad spectrum of a monochromatic source with the reasonable power can be generated and achieved. By using a

Gaussian pulse, it can be converted to be a broad light source by using the ring resonator system incorporating the add/drop multiplexer, which can be configured as multi light sources. Results obtained have shown that the multiplexed sources with different wavelengths can be formed by using the multiple operating systems. In application, the embedded system within the computer processing unit is available for quantum computer to increase the channel capacity and security. Furthermore, such a concept is also available for hybrid communications, for instance, wire/wireless or satellite communication, where the use of quantum encoding for high capacity quantum communication/cryptography via a single photon based technology in the communication link in the network is plausible.

REFERENCES

1. Suchat, S., N. Pornsuwancharoen, and P. P. Yupapin, "Continuous variable quantum key distribution via a simultaneous optical wireless up-down-link system," *Int. J. Light Electron. Opt.*, 2009.
2. Yupapin, P. P., S. Thongme, and K. Sarapat, "Second-harmonic generation via microring resonators for optimum entangled photon visibility," *Int. J. Light Electron. Opt.*, 2009.
3. Yupapin, P. P. and P. Chunpang, "A quantum-chaotic encoding system using an erbium-doped fiber amplifier in a fiber ringresonator," *Int. J. Light Electron. Opt.*, 2008.
4. Mitatha, S., K. Dejhan, P. P. Yupapin, and N. Pornsuwancharoen, "High-capacity and security packet switching using the nonlinear effects in microring resonators," *Int. J. Light Electron. Opt.*, 2008.
5. Mitatha, S., K. Dejhan, P. P. Yupapin, and N. Pornsuwancharoen, "Packet switching start-stop bits generation based on bifurcation behavior of light in a microring resonator," *Int. J. Light Electron. Opt.*, 2008.
6. Yupapin, P. P. and W. Suwancharoen, "Entangled photon states generation and regeneration using a nonlinear fiber ring resonator," *Int. J. Light Electron. Opt.*, 2008.
7. Yupapin, P. P., "Generalized quantum key distribution via microring resonator for mobile telephone networks," *Int. J. Light Electron. Opt.*, 2008.
8. Sripakdee, C. and P. P. Yupapin, "Quantum noise generated by four-wave mixing process with in a fiber ring resonator," *Int. J. Light Electron. Opt.*, 2009.
9. Su, Y., F. Liu, and Q. Li, "System performance of slow-light buffering, and storage in silicon nano-waveguide," *Proc. SPIE*, Vol. 6783, 67832, 2007.
10. Yupapin, P. P., P. Saeung, and C. Li, "Characteristics of complementary ring-resonator add/drop filters modeling by using graphical approach," *Opt. Commun.*, Vol. 272, 81–86, 2007.
11. Yupapin, P. P. and W. Suwancharoen, "Chaotic signal generation and cancellation using a microring resonator incorporating an optical add/drop multiplexer," *Opt. Commun.*, Vol. 280, No. 2, 343–350, 2007.
12. Kokubun, Y., Y. Hatakeyama, M. Ogata, S. Suzuki, and N. Zaizen, "Fabrication technologies for vertically coupled microring resonator with multilevel crossing busline and ultracompact-ring radius," *IEEE J. Sel. Top. Quantum Electron.*, Vol. 11, 4–10, 2005.
13. Suchat, S., W. Khannam, and P. P. Yupapin, "Quantum key distribution via an optical wireless communication link for telephone network," *Opt. Eng. Lett.*, Vol. 46, No. 10, 100502-1-5, 2007.
14. Yupapin, P. P. and S. Suchat, "Entangle photon generation using fiber optic Mach-Zehnder interferometer incorporating nonlinear effect in a fiber ring resonator," *Journal of Nanophotonics*, Vol. 1, 13504-1-7, 2007.

Plasmonic Nanoparticles as Terahertz Oscillators

Xiaobing Cai and Gengkai Hu
School of Aerospace Engineering, Beijing Institute of Technology
Beijing 100081, China

Abstract— In a highly nonuniform radiation field of hertz dipole induced by polarized laser lights, the gradient force exerted on a plasmonic nanoparticle is extremely large when the laser is excited near Fröhlich frequency. The force always tends to pull the nanoparticle back to the central position of the radiation field where the electric field is maximal. According to this mechanism, a nanoparticle oscillator and a rotational oscillator of a spheroidal nanoparticle are proposed with operating frequency up to terahertz.

1. INTRODUCTION

Micromechanical oscillators or resonators are very useful in variety fields such as ultra-sensitive mass detection [1, 2], radio-frequency signal processing [3, 4]. With help of multiwalled carbon nanotubes (MWNT), Zheng and Jiang proposed a nanoscale oscillator which extends the operating frequency of mechanical resonance up to several gigahertz [5]. In their report, they show that there is a very large van der Waals potential energy when the inner tube of the MWNT is pulled out of its equilibrium position, this van der Waals force tends to attract the inner tube back to its initial equilibrium position in order to minimize the total energy. Due to the large ratio between the van der Waals force and the mass of the core shell of the MWNT, the proposed nanoscale resonator can operate at a frequency of gigahertz. In this letter, we will show that even larger ratio of force to mass can be found in other mechanical system than that experienced by the multi-wall nanotube, thus the operating frequency of mechanical oscillators can be probably enhanced to terahertz (THz).

A typical case of large ratio of force to mass is associated with the optical tweezers [6–10] (initially proposed by Ashkin [11]), the gradient force of a laser beam is used to manipulate nano-objects. Chaumet et al. [6]. theoretically show that a force of several pN can be induced by the radiation field of a 5 W laser beam near a tungsten probe. Miao and Lin also experimentally show that a pN force can be achieved by exciting a polarized laser on an Au nanoparticle array [7, 12]. The works used to compute the optical forces on small particles in a gradient field are well documented [13–15]. Since the gradient force is quadratic with the intensity of electric field, the gradient force exerted on a nanoparticle by the radiation field can be easily enhanced to the amplitude comparable to the van der Waals force exerted on the core shell of the MWNT, this make it possible to create another type of gigahertz oscillator by the gradient force of a laser beam. In addition, the gradient force imposed on a plasmonic nanoparticle can be hundred times larger than that on a traditional nanoparticle, this may lead to a plasmonic nanoparticle oscillator with operating frequency up to terahertz. In the following, we will demonstrate the principle of a plasmonic nanoparticle oscillator.

2. DIELECTROPHORESIS FORCE OF PLASMONIC PARTICLES

A simple oscillator contains at least two factors: a mass and a restoring force [16]. Let's start with characterization of the restoring force of the proposed oscillator. For a hertz dipole, its radiation field in the far field is reduced to the following simple expression [17, 18]:

$$\mathbf{E} = -\widehat{\theta}\,\frac{k^2 p}{4\pi\varepsilon_0 r}\sin\theta\cos(kr-\omega t). \tag{1}$$

where p is the dipole moment, $\mathbf{E}$ is the radiated electric field, k is wavenumber, ε_0 is the permittivity of the surrounding medium, r is the radial distance between the observing point and the center of the dipole. Noting that the variables k^2, p and $1/r$ are small quantities at low frequency and far distance, the radiation field of the dipole is usually not considerable. However, for a laser beam and on a nanoscale, these variables are of very large magnitude, so it is possible to produce a huge gradient force. The dipole moment p can be generated in many ways: such as by exciting localized surface plasmon on Au nanoparticles with a polarized laser [7], or evanescent illumination at a tungsten probe apex [6], or illumination under total internal reflection on gold pads [9]. Our proposed model is close to the first one, with the magnitude of the dipole moment p linearly related to the incident electric field of the polarized laser beam [7].

The gradient force (known also as dielectroporesis force) exerted on a particle in a nonuniform field E_0 depends on the gradient of the field and the dielectric constant of the particle ε_p: $\mathbf{F} = (\alpha/2)\,\nabla E_0^2$ [19], where $\alpha = 4\pi\varepsilon_0 a^3 K(\varepsilon_0, \varepsilon_p)$, and a is the radius of the particle, $K(\varepsilon_0, \varepsilon_p)$ is the Clausius-Mossotti (CM) factor characterizing the strength of the polarization of the particle. Combined with Eq. (1), the gradient force induced by the radiation field can be written as:

$$\mathbf{F} = (\alpha/2)\left(\frac{k^2 p}{4\pi\varepsilon_0}\right)^2 \left(-\widehat{r}\,\frac{2}{r^3}\sin^2\theta + \widehat{\theta}\,\frac{2}{r^3}\sin\theta\cos\theta\right). \tag{2}$$

As shown in Fig. 1, two gold pads with a distance $2h$ are under illumination of a polarized laser to generate hertz dipoles, a nanoparticle is placed at the central point between the pads. Supposing the nanoparticle has a tiny displacement x ($x \ll h$) from the center point along the horizontal direction, the restoring force can be obtained from Eq. (2) as:

$$\mathbf{F}_x = \mathbf{F}_r\cos\theta + \mathbf{F}_\theta\sin\theta \approx -(\alpha/2)\left(\frac{k^2 p}{4\pi\varepsilon_0}\right)^2 \frac{8}{h^4}x. \tag{3}$$

The relations $h \approx r$, $\sin\theta \approx 1$ and $\cos\theta \approx x/h$ are used to derive Eq. (3). The symmetry of the system leads to zeros force along y-axis, i.e., $\mathbf{F}_y = 0$. As shown by Miao and Lin [7], the restoring force calculated from Eq. (3) is of the scale of several pN for a 10 nm particle placed in the radiation field of a 0.1 mW laser beam focused into a 100 μm^2 spot at the distance of 1 μm. Noting that $\mathbf{F}_x \propto p^2 \propto E_0^2 \propto P$ (P is the power of the laser), the restoring force can be easily enhanced to 10 nN by using a 1 W laser beam while other parameters are kept unchanged. Therefore, one can find that the restoring force shown here is on the same scale as that stated in Zheng's model [5], so an oscillator with gigahertz operating frequency can also be proposed.

Since K usually takes the form $(\varepsilon_p - \varepsilon_0)/(\varepsilon_p + 2\varepsilon_0)$, for most traditional materials $\varepsilon_p > \varepsilon_0$, one could find $0 < K < 1$, so the gradient force $\mathbf{F}$ is only governed by the term ∇E_0^2. However, by using plasmonics particles with negative permittivty [20–22], the Clausius-Mossotti factor can take any value. For example, nearing so called Fröhlich frequency, the permittivity of the particle $\varepsilon_p = -2\varepsilon_0$ [23], K can be infinitely large. To avoid singularity, more précised analysis on CM factor can be conducted by using the exact expression of the electric dipole polarizability $\alpha = (6\pi i\varepsilon_0/k^3)a_1$, where a_1 is the electric dipole coefficient derived from Mie theory [23, 24]:

$$a_1 = \frac{n\psi_1(nx)\psi_1'(x) - \psi_1(x)\psi_1'(nx)}{n\psi_1(nx)\xi_1'(x) - \xi_1(x)\psi_1'(nx)}, \tag{4}$$

with ψ_1 and ξ_1 being Riccati-Bessel functions and $x = ka$, $n = \sqrt{\varepsilon_p}/\sqrt{\varepsilon_0}$. Keeping the power of the laser beam unchanged, the restoring force can be conveniently enhanced to 10 μN by using a nanoparticle with a dielectric constant of $\varepsilon_p = -2.03\varepsilon_0$ (see in Fig. 2). This value is chosen to make the CM factor positive and maximal.

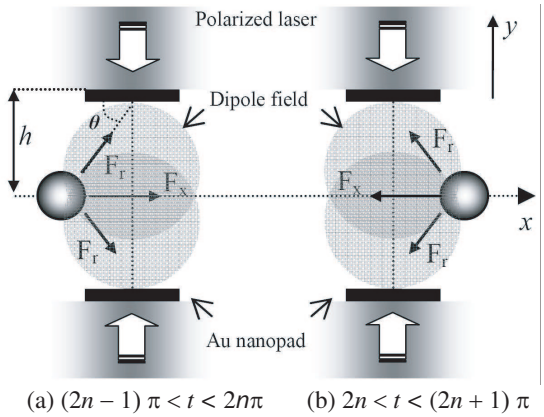

Figure 1: Scheme of model configuration. Two gold pads (typical radius 1 μm) are under illumination of a laser beam to served as hertz dipoles. A nanoparticle is placed in the radiation field of the pads and thus exerted on a restoring force F_x.

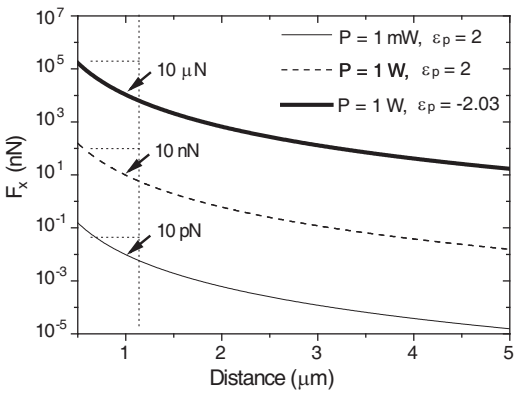

Figure 2: Restoring force of nanoparticles with different values of permittivity. The force experienced by plasmonic particle is estimated to be 1000 times higher than that of ordinary particles.

3. OSCILLATING FREQUENCY

Compared Eq. (3) of the restoring force with a mass-spring system, the effective stiffness of the nanoparticle system can be found $\kappa_{\text{eff}} = (\alpha/2)\,(k^2 p/4\pi\varepsilon_0)^2(8/h^4)$. Thus the operating frequency of the nanoparticle oscillator can be written as [16]:

$$\omega_0 = \sqrt{\frac{\kappa_{\text{eff}}}{m}} = \frac{k^2 p}{2\pi\varepsilon_0 h^2}\sqrt{\frac{\alpha}{m}}, \tag{5}$$

with m being the mass of the nanoparticle. It is found that the operating frequency can be easily tuned by the power of the incident laser beam.

Figure 3 shows the calculated operating frequency from Eq. (5) for the nanoparticles with $\varepsilon_p = 2.0\varepsilon_0$ and $\varepsilon_p = -2.03\varepsilon_0$ respectively. The radii of the particles are assumed to be 10 nm, and the densities are taken from that of gold. For epsilon positive nanoparticle, the resonance frequency is found to be 0.25 GHz under a 1 W laser power illumination. For the plasmonic particle, the resonance frequency is increased to 13.5 GHz under the same illumination. As for epsilon positive nanoparticles, the CM factor is independent of the particle radius, while the dipole polarizability and the mass both rely on a^3, thus the resonance frequency will not be affected by the size of the particle as long as $a \ll \lambda$. From Eq. (4), suitable permittivity and radius should be chosen to obtain maximal dipole polarizability. The insert in Fig. 3 shows the resonance frequency of an aluminum particle with a radius of 2.5 nm and a distance of $h = 0.5\,\mu$m. The wavelength of the laser beam is of 147 nm, at this wavelength the permittivity of the aluminum equals to $\varepsilon_p = (-2.2 + 0.2i)\varepsilon_0$ [25]. One would find that the operation frequency is enhanced to 0.57 THz while a laser beam with power of 10 W is used. Supposing the nanoparitlce is place at $x_0 = 50$ nm from its equilibrium position, its potential energy can be estimated by $U = (1/2)\kappa_{\text{eff}} x_0^2$. Thus the velocity of the Al nanoparticle is estimated to be $v_0 = (\omega_0/2\pi)x_0 = 4546$ m/s when it passes the central position where the restoring force is zero.

For a spherical particle, the gradient force imposes only a net force on the particle. However, for an ellipsoidal particle it will experience a torque as well as the net force. Assuming the particle is a spheroid, with α being the angle between its long axis and the direction of the electric field. In a radiation field with $\theta = \pi/2$, the electric filed is horizontal. According to Landau et al. [26], the torque can be calculated by:

$$T = \frac{\varepsilon_p(\varepsilon_p - \varepsilon_0)^2\,|1 - 3\zeta|\,|E|^2\,V \sin 2\alpha}{8\pi[\zeta\varepsilon_p + \varepsilon_0 - \varepsilon_p][(1-\zeta)\varepsilon_p + \varepsilon_0 + \zeta\varepsilon_0]}, \tag{6}$$

where ζ is the depolarizing factor of the spheroid along the long axis. The torque is directed so that it tends to turn the long axis parallel to the electric field, so it's a 'restoring torque'. The effect of the restoring torque on the redirection of the ellipsoidal particle is similar as that of the restoring force. When an ellipsoidal particle is placed in a dipole field with $\alpha = \alpha_0$, the torque

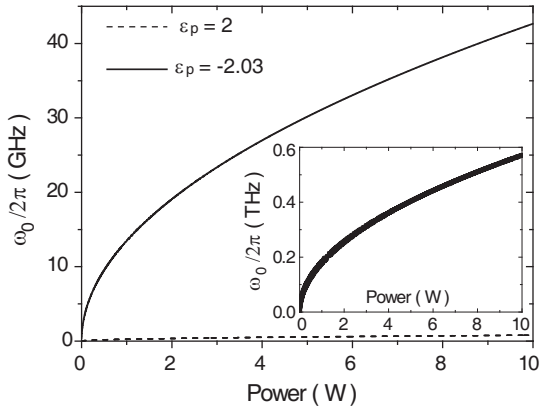

Figure 3: Tunable nature of the oscillators by incident laser power. Resonance frequency of plasmonic nanoparticle is estimated much higher than that of ordinary nanoparticle.

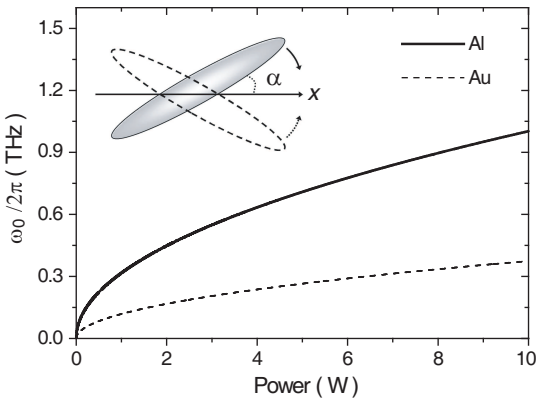

Figure 4: Vibrating frequency of spheroidal nanoparticles versus incident laser power.

turns the particle to the direction $\alpha = 0$. Due to the inertia, the particle keeps oscillating round its equilibrium position. The related vibrating frequency can be obtained by $\omega_0 = \sqrt{\eta_{\text{eff}}/I_{xx}}$, with $\eta_{\text{eff}} = T/\alpha$ being the torsional stiffness, $I_{xx} = 2mb^2/5$ is the moment of the inertia, b is short semiaxe. For the same Al and Au ellipsoidal particles, with long semiaxe $a = 20\,\text{nm}$, and $b = 5\,\text{nm}$, under the same dipole field as discussed in Fig. 3, the vibration frequencies are calculated and shown in Fig. 4, the Al ellipsoidal particle is estimated to vibrate at a frequency up to 1.0 terahertz under a laser power of 10 W. The high frequency vibration is expected to be used as the propeller of molecular motors.

The distance between the nanoparticle and the gold pads is assumed to be large enough so that the van der Waals force can be neglected in our model. Since the resonance frequency of the oscillator is much lower than that of the incident laser beam, the restoring force will be perturbed by the laser fluctuation although Eq. (3) is a time-averaged expression. However, the direction of the restoring force will be not affected by the laser fluctuation as the gradient force (Eq. (2)) always points to the center position of the gold pads. Recognizing that the balance position along y-axis is unstable, the high frequency oscillator may be severely damaged, some extra restriction should be applied to the nanoparticle along vertical direction for implementation.

The realization of the oscillators would be extremely challenging, as the nanopaticle oscillators is not self-detecting as nanotube oscillators [4, 27]. Experimental implementation is proposed to start with measuring the restoring force or gradient force of nanoparticles experienced in the radiation field of hertz dipoles. Techniques used in the optical tweezers would be helpful [6–11].

4. CONCLUSION

The gradient force and torque of plasmonic particles under dipole field are calculated, dramatically enhancement of the force and torque are found for particles near Fröhlich frequency. Mie scattering theories are used to accurately predict such gradient force. Based on the huge gradient force and torque of plasmonic particles, terahertz frequency oscillator and rotational oscillator are shown in an optical tweezer system. Transformation of kinetic energy and potential energy is discussed.

ACKNOWLEDGMENT

This work was supported by the National Natural Science Foundation of China (10325210, 10832002, 90605001), and the National Basic Research Program of China (2006CB601204), and Beijing Municipal Commission of Education project under grant 20080739027.

REFERENCES

1. Sidles, J. A., J. L. Garbini, K. J. Bruland, D. Rugar, O. Züger, S. Hoen, and C. S. Yannoni, "Magnetic-resonance force microscopy," *Rev. Mod. Phys.*, Vol. 67, 249, 1995.
2. Roukes, M., "Plenty of room indeed," *Sci. Am.*, Vol. 285, 48, 2001.
3. Nguyen, C. T. C., "Frequency-selective MEMS for miniaturized low-power communication devices," *IEEE Trans. Microwave Theory Tech.*, Vol. 47, 1486, 1999.
4. Sazonova, V., Y. Yaish, H. Üstünel, D. Roundy, T. A. Arias, and P. L. McEuen, "A tunable carbon nanotube electromechanical oscillator," *Science*, Vol. 431, 284, 2004.
5. Zheng, Q. and Q. Jiang, "Multiwalled carbon nanotubes as gigahertz oscillators," *Phys. Rev. Lett.*, Vol. 88, 045503, 2002.
6. Chaumet, P. C., A. Rahmani, and M. Nieto-Vesperinas, "Optical trapping and manipulation of nano-objects with an apertureless probe," *Phys. Rev. Lett.*, Vol. 88, 123601, 2002.
7. Miao, X. and L. Y. Lin, "Large dielectrophoresis force and torque induced by localized surface plasmon resonance of Au nanoparticle array," *Opt. Lett.*, Vol. 32, 295, 2007.
8. Novotny, L., R. X. Bian, and X. S. Xie, "Theory of nanometric optical tweezers," *Phys. Rev. Lett.*, Vol. 79, 645, 1997.
9. Righini, M., G. Volpe, C. Girard, D. Petrov, and R. Quidant, "Surface plasmon optical tweezers: Tunable optical manipulation in the femtonweton range," *Phys. Rev. Lett.*, Vol. 100, 186804, 2008.
10. Grigorenko, A. N., N. W. Roberts, M. R. Dickinson, and Y. Zhang, "Nanometric optical tweezers based on nanostructured substrates," *Nat. Photo.*, Vol. 2, 365, 2008.
11. Ashkin, A., "Optical trapping and manipulation of neutral particles using lasers," *Proc. Natl. Acad. Sci.*, Vol. 94, 4853, USA, 1997.

12. Miao, X., B. K. Wilson, S. H. Pun, and L. Y. Lin, "Optical manipulation of micro/submicron sized particles and biomolecules through plasmonics," *Opt. Express*, Vol. 16, 13517, 2008.
13. Ashkin, A., J. M. Dziedzic, J. E. Bjorkholm, and S. Chu, "Observation of a single-beam gradient force optical trap for dielectric particles," *Opt. Lett.*, Vol. 11, 288, 1986.
14. Chaumet, P. C. and M. N. Vesperinas, "Time-averaged total force on a dipolar sphere in an electromagnetic field," *Opt. Lett.*, Vol. 25, 1065, 2000.
15. Chaumet, P. C. and A. Rahmani, "Electromagnetic force and torque on magnetic and negative-index scatters," *Opt. Express*, Vol. 17, 2224, 2008.
16. Kinsler, L. E., A. R. Frey, A. B. Coppens, and J. V. Sanders, *Fundamentals of Acoustics*, 4th Edition, John Wiley and Sons, New York, 2000.
17. Kong, J. A., *Electromagnetic Wave Theory*, John Wiley and Sons, New York, 1987.
18. Jackson, J. D., *Classical Electrodynamics*, 3rd Edition, John Wiley and Sons, New York, 1999.
19. Jones, T. B., *Electromechanics of Particles*, Cambridge U. Press, 1995.
20. Veselago, V. G., "The electrodynamics of substances with simultaneously negative values of ε and μ," *Sov. Phys. Usp.*, Vol. 10, 509, 1968.
21. Pendry, J. B., A. J. Holden, W. J. Stewart, and I. Youngs, "Extremely low frequency plasmons in metallic mesostructures," *Phys. Rev. Lett.*, Vol. 76, 4773, 1996.
22. Shelby, R. A., D. R. Smith, and S. Schultz, "Experimental verification of a negative index of refraction," *Science*, Vol. 292, 77, 2001.
23. Dungey, C. E. and C. F. Bohren, "Light scattering by nonspherical particles: A refinement to the coupled-dipole method," *J. Opt. Soc. Am. A*, Vol. 8, 81, 1991.
24. Bohren, C. F. and D. R. Huffman, *Absorption and Scattering of Light by Small Particles*, John Wiley and Sons, New York, 1983.
25. Ehrenreich, H., H. R. Philipp, and B. Segall, "Optical properties of aluminum," *Phys. Rev.*, Vol. 132, 1918, 1963.
26. Landau, L. D., E. M. Lifshitz, and L. P. Pitaevskii, *Electrodynamics of Continuous Media*, Butterworth-Heinemann, 1984.
27. Shim, S., M. Imboden, and P. Mohanty, "Synchronized oscillation in coupled nanomechanical oscillators," *Science*, Vol. 316, 95, 2007.

Microwave Absorption Properties of Cobalt Nanowires Fabricated by Pulse Electrodeposition

Wenbing Chen, **Mangui Han**, **and Longjiang Deng**
State Key Laboratory of Electronic Thin Films and Integrated Devices
University of Science and Technology of China, Chengdu 610054, China

Abstract— In this work, cobalt nanowires with a preferred growth orientation have been fabricated by a pulse electrodeposition method. The imaginary part of the permeability spectra for the nanowire/paraffin composite samples exhibit a strong absorption peak at 6.1 GHz and two minor peaks at above 10 GHz. It is determined that the peak at 6.1 GHz is attributed to the natural resonance mechanism and the other two peaks are caused by eddy current effect. We have fitted the permeability spectra attributed to natural resonance using the LLG equation. Calculation based on the Kittel equation substantiates our explanation. The electromagnetic wave reflection loss values of the nanowire/paraffin composite indicate that cobalt nanowires composites can be used for microwave absorption.

1. INTRODUCTION

One of the urgent problems plaguing the modern world is the widespread electromagnetic pollution (EMP), brought about by the growing development of wireless telecommunication. To combat this problem, considerable efforts have been devoted to explore novel microwave absorption materials that can meet requirements like strong absorption in a wide frequency range and light weight [1–4]. Low-dimensional ferromagnetic nanowires provide one solution to the EMP problem [5, 6]. One facile way to manufacture metal nanowires is to utilize electrodeposition and porous template such as anodic aluminum oxide (AAO) and polycarbonate membrane. Nanowires deposited in these templates have several advantages. First of all, their diameters usually are smaller than the skin depth, ensuring the propagation of microwaves and the repression of eddy current effect. In addition, the dielectric nature of the templates helps reduce the electric conductivity, which is also desirable for microwave absorption. Moreover, as pointed out by Encinas and co-workers [5], the resonance frequency of nanowire array can be tuned over a large range by varying the porosity of the template, the geometry of nanowires, the type of the magnetic material, and the magnetization states of nanowires.

In this work, cobalt nanowires have been fabricated within the AAO templates through a pulse electrodeposition method. The nanowires were released from the template and mixed with paraffin wax in order to investigate their microwave absorption properties in the range of 0.5∼18 GHz. Their behaviours have been discussed by combining the nanowires' morphology, crystal structure, static magnetic property, and classic theories such as the LLG and Kittel equations.

2. EXPERIMENTAL DETAILS

The AAO templates with nominal pore size of 200 nm and thickness of 60 µm were purchased from Whatman Corp.®. A typical three-electrode cell was used for electrodeposition. Pulsed electrodeposition was carried out by employing two voltage steps alternatively throughout the experiment: −1.5 V versus a saturated calomel electrode (SCE) for 5 seconds followed by −0.4 V versus SCE for 1.5 seconds. When the voltage was −1.5 V, cobalt was deposited in the AAO template; when the voltage was −0.4 V, the deposition was halted and Co ions were restored in the depleted region near the Au electrode. The deposition-relaxation cycle may help improve the crystal quality and homogeneity of the deposited nanowires [7, 8]. The electrolyte consisted of 100 g/L $CoSO_4{\cdot}7H_2O$ and 30 g/L H_3BO_3. The pH of the electrolyte was adjusted to 3.0 with HCl. The crystal structure of the as-prepared cobalt nanowires within the AAO template was investigated using X-ray powder diffraction (XRD, Cu K_α radiation). The static magnetic properties of the as-prepared nanowire array were characterized by a vibrating sample magnetometer (VSM). To investigate the morphology and microwave properties of the cobalt nanowires, the as-prepared sample was dissolved with a 4 wt% NaOH solution for 24 hours and then rinsed with de-ionized water repeatedly until the solution was neutralized. The morphology of the liberated nanowires was observed by a scanning electron microscopy (SEM) equipped with energy dispersive x-ray spectrometer (EDS). Then the cobalt nanowires were randomly dispersed in paraffin wax with the

nanowires' weight ratio of 50% in the composites. The nanowire/paraffin composite samples were pressed into a toroidal shape with outer diameter of 7 mm and inner diameter of 3 mm for microwave measurement. The complex relative permittivity and permeability of the composite samples were measured by an Agilent Vector Network Analyzer 8720 in the range of 0.5–18 GHz. All experiments were conducted at room temperature.

3. RESULTS AND DISCUSSIONS

Figures 1(a) and (b) shows the morphology of the cobalt nanowires after dissolving the AAO template. The diameter of the nanowires is around 200 nm and the length of the nanowire is around 6 µm. It is clear that after dissolving the AAO template completely, cobalt nanowires are released from the template, see Fig. 1(b). The XRD data shows that Co nanowires in the AAO template have a preferential growth direction along the [110] direction, implying that the magnetocrystalline easy axis of the cobalt nanowires — the [002] direction — is perpendicular to the wire length [9, 10].

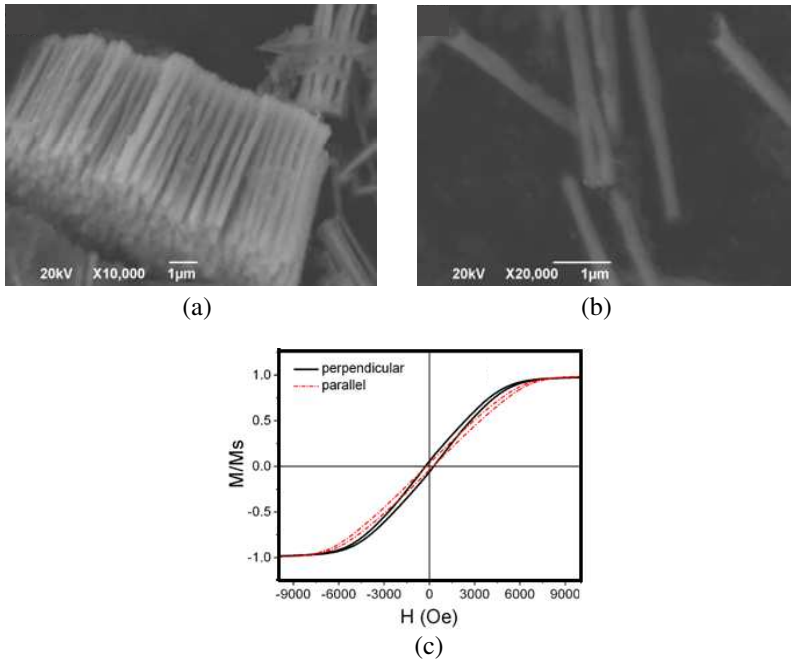

Figure 1: SEM image of cobalt nanowires in (a) and (b): (a) shows the side view of the Co nanowire array after partial dissolution of the AAO template; (b) is the well dispersed nanowires after dissolving the AAO template completely; (c) shows the magnetic hysteresis loops of Co nanowires array.

Illustrated in Fig. 1(c) are the normalized magnetic hysterersis loops of the cobalt nanowire array in the AAO template. The measurements were made with the external magnetic field applied perpendicular and parallel to the wire length. It is evident that the easy axis of the nanowires is normal to the wire length, corroborating the XRD results. However, the normalized remanence (M_r/M_s) for both loops is smaller than 0.1 and the coercivities are low (276 Oe when magnetic field is perpendicular to the wire length and 220 Oe when magnetic field is parallel to the wire length), which suggests that the large shape anisotropy associated with nanowires is greatly undermined. For cobalt nanowires, the shape anisotropy Kshape is estimated to the as large as 6×10^5 J/m^3 by using the equation [11].

$$K_{shape} = \mu_0(N_x - N_z)M_s^2/2, \tag{1}$$

where μ_0 is permeability of vacuum, M_s (14×10^5 A/m) is the saturation magnetization of cobalt; N_x, N_z are the demagnetizing factors in the directions normal and parallel to the wire length, respectively. The shape anisotropy would usually align the magnetic moments along the wire length and lead to a square shape of hysteresis loop when the magnetic field is applied parallel to the wire length. The reason we have not observed an obvious anisotropy behaviors is that there are other factors affecting the alignment of magnetic moments, such as magnetocrystalline anisotropy and magnetostatic interaction [12, 13].

The frequency (f) dependence of relative complex permittivity and permeability for the nanowire/paraffin composite sample is shown in Figs. 2 (a) and (b). It can be observed that the imaginary part of permittivity (ε'') exhibits one major peak at around $f = 5\,\mathrm{GHz}$ and one minor peak at around $f = 10\,\mathrm{GHz}$. The inset in Fig. 2(a) demonstrates that the $\varepsilon' - \varepsilon''$ relation is mainly composed of a typical Cole-Cole semicircle, indicating that the permittivity spectra conform to the Debye relaxation model [14]. The permeability spectra of the nanowire/paraffin composite samples are shown in Fig. 2(b). The real part (μ') firstly increases in the $0.5 \sim 5.5\,\mathrm{GHz}$ region and then decreases in the $5.5 \sim 6.9\,\mathrm{GHz}$ regime, after which the value of μ' shows minor fluctuations at around $f = 12.3 \sim 13.5$ and $14.8 \sim 16.5\,\mathrm{GHz}$. In the meantime, the imaginary part (μ'') shows a major peak at around $f = 6.1\,\mathrm{GHz}$ and two minor peaks at around $f = 12$ and $16\,\mathrm{GHz}$. Generally, magnetic loss is attributed to hysterersis, domain-wall displacement, natural resonance, and eddy current effect [15]. Hysterersis could be neglected when a weak field is applied and domain-wall displacement can be ruled out since it only happens in the MHz region, not in the GHz arena. Now consider the eddy current effect and natural resonance mechanism. If the magnetic loss only results from eddy current loss, the value of C should

$$C = \mu''\mu'^{-2} f^{-1} = 2\pi\mu_0\sigma d^2/3 \tag{2}$$

be a constant when the frequency is varied [16]. In the Equation (2), σ refers to the electric conductivity, d is the diameter of nanowires. Fig. 3(a) shows the value of C as a function of frequency. As can be seen, when $f < 10\,\mathrm{GHz}$, C changes drastically, but when $f > 10\,\mathrm{GHz}$, C remains approximately a constant. Thus the peak of μ'' at $f = 6.1\,\mathrm{GHz}$ is not caused by eddy-current loss. In other words, this peak originates only from natural resonance mechanism. Meanwhile, the other two minor peaks at around $f = 12$ and $16\,\mathrm{GHz}$ are ascribed to eddy current effect, which may be brought about by the large diameter of single cobalt nanowire approaching the skin depth. This indicates the importance of reducing the diameter of nanowires in order to suppress eddy current loss in the GHz region.

The dynamic permeability spectrum stemming from natural resonance could be fitted by the Landau-Lifshitz-Gilbert (LLG) equation. After including the shape anisotropy, we can solve the LLG equation and obtain μ' and μ'' as a function of frequency:

$$\mu' = 1 + \mu_i \frac{f_m f_y [f_x f_y - (1+\alpha^2)(2\pi f)^2] + \alpha^2 (2\pi f)^2 f_m (f_x + f_y)}{[f_x f_y - (1+\alpha^2)(2\pi f)^2]^2 + \alpha^2 (2\pi f)^2 (f_x + f_y)^2}, \tag{3}$$

$$\mu'' = \mu_i \frac{2\pi f \alpha f_m f_y (f_x + f_y) - 2\pi f \alpha f_m [f_x f_y - (1+\alpha^2)(2\pi f)^2]}{[f_x f_y - (1+\alpha^2)(2\pi f)^2]^2 + \alpha^2 (2\pi f)^2 (f_x + f_y)^2}, \tag{4}$$

$$f_m = \gamma M_s, \quad f_x = (N_x - N_z) f_m, \quad f_y = (N_y + N_k - N_z) f_m, \tag{5}$$

where γ ($2.21 \times 10^5\,\mathrm{mA^{-1}S^{-1}}$) is the Gilbert gyromagnetic ratio, α is the damping constant, μ_i is the initial permeability, f is the frequency. N_x, N_y, N_z are the demagnetizing factors in the X, Y, Z direction. The value of M_s is chosen as $14 \times 10^5\,\mathrm{A/m}$, which is close to the saturation magnetization of bulk cobalt and cobalt nanowires reported in previous works [17]. Exploiting the above formula, $\mu'' \sim f$ spectrum is fitted firstly and the fitted parameters are then used to calculate the $\mu' \sim f$ spectrum. The fitted results are displayed in Fig. 2(b). The best agreement between experiment results and calculation could be obtained when the resonance frequency $f_{res} = 6.1\,\mathrm{GHz}$ and $K_1 = 5.794 \times 10^5\,\mathrm{J/m^3}$, $\alpha = 0.098$, $\mu_i = 0.158$. Deserving special mention is the value of K_1, which is very close to the value of shape anisotropy and large enough to compete with it. The Kittel equation is employed to evaluate the fitted resonance frequency and related parameters [18]. When the easy axis is perpendicular to the wire length, the Kittel equation gives:

$$f_{res} = \frac{\gamma}{2\pi} \sqrt{((N_x - N_z)M_s - H_k)(N_x - N_z)M_s} \tag{6}$$

where $H_k = 2K_1/\mu_0 M_s$ is the effective magnetocrystalline field. The calculated resonance frequency is $f_{res} = 6.03\,\mathrm{GHz}$, which matches well with the experimental value and the LLG solution. This justifies our proposal that the peak of μ'' at $f = 6.1\,\mathrm{GHz}$ is due to natural resonance and this value is a result of the competition between shape anisotropy and other factors such as magnetocrystalline anisotropy and magnetostatic interaction. Using the experimental data and the transmission line theory, the reflection loss R (dB) of the nanowire/paraffin composite samples is calculated [2], as shown in Fig. 3(b). As shown, the minimum reflection loss value is $R = -23.5\,\mathrm{dB}$ around $6.5\,\mathrm{GHz}$

for nanowire/paraffin sample with a thickness of 5 mm and weight ratio of 50%. It is worth noting that the eddy current effect is also suppressed in this frequency regime. It is clear that cobalt nanowires are one of promising candidates as a microwave absorber.

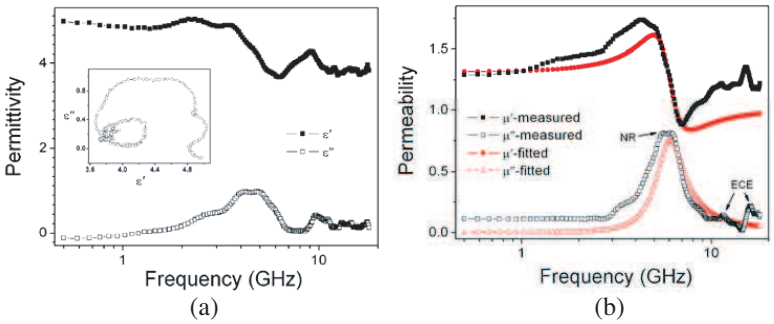

Figure 2: (a) The measured relative complex permittivity spectra, the inset in (a) shows the relation between ε' and ε'' (Cole-Cole semicircle). (b) The measured and fitted relative complex permeability spectra. NR denotes "natural resonance", ECE denotes "eddy current effect".

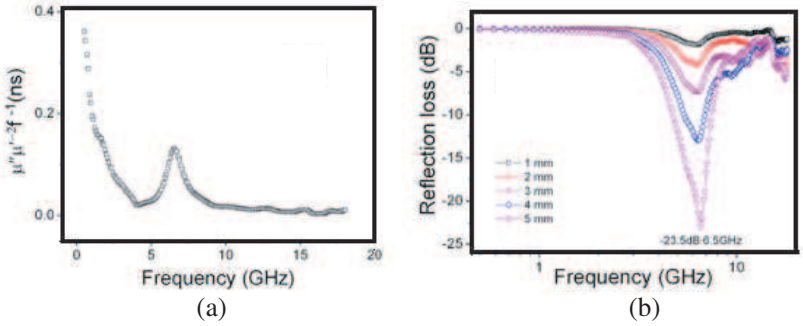

Figure 3: The value of $\mu''\mu'^{-2}f^{-1}$ as a function of frequency in (a), and the reflection loss of Co nanowires composites with different thickness in (b).

4. CONCLUSIONS

Cobalt nanowires with preferred growth orientation were prepared by pulsed electrodeposition. It is found that there is a strong absorption peak at 6.1 GHz in the imaginary part of their permeability spectra, which is believed arising from natural resonance. The reflection loss value for the nanowire/paraffin composite sample with thickness of 5 mm and weight ratio of 50% can reach −23.5 dB at around 6.5 GHz while the eddy current effect is also suppressed, indicating its potential application as microwave absorbers.

ACKNOWLEDGMENT

This work is financially supported by NSFC (No. 60701016) and NSFC-RS (Royal Society, UK) international jointed program (No. 60911130130).

REFERENCES

1. Han, M. and L. Deng, *Appl. Phys. Lett.*, Vol. 90, 011108, 2007.
2. Han, M., Y. Ou, D. Liang, and L. Deng, *Chin. Phy. B*, Vol. 18, 1601, 2009.
3. Liu, Q. and D. Zhang, *Appl. Phys. Lett.*, Vol. 93, 013110, 2008.
4. Dong, X. L., X. F. Zhang, and H. Huang, *Appl. Phys. Lett.*, Vol. 92, 013127, 2008.
5. Encinas, A., L. Vila, M. Darques, J. M. George, and L. Piraux, *Nanotechnology*, Vol. 18, 065705, 2007.
6. Gao, B., Q. F. Liu, F. S. Li, J. Feng, and D. S. Xue, *J. Phys. D: Appl. Phys.*, Vol. 41, 235005, 2008.
7. Zhang, J., G. A. Jones, S. E. Donnelly, and G. H. Li, *J. Appl. Phys.*, Vol. 101, 054310, 2007.

8. Ursache, A., J. T. Goldbach, T. P. Russell, and M. T. Tuominen, *J. Appl. Phys.*, Vol. 97, 10J322, 2005.
9. Han, X. H., Q. F. Liu, Y. Ren, R. L. Liu, and F. S. Li, *J. Phys. D: Appl. Phys.*, Vol. 42, 095005, 2009.
10. Li, D. D., R. S. Thompson, G. Bergmann, and J. G. Lu, *Adv. Mater.*, Vol. 20, 4575, 2008.
11. Qunadjela, K., R. Ferré, J. L. Maurice, L. Piraux, and S. Dubois, *J. Appl. Phys.*, Vol. 81, 5455, 1997.
12. Li, F. S., T. Wang, L. Y. Ren, and J. R. Sun, *J. Phys.: Condens. Matter*, Vol. 16, 8053, 2004.
13. Encinas-Oropesa, A., M. Demand, and L. Piraux, *Phys. Rev. B*, Vol. 63, 104415, 2001.
14. Fang, J. X. and Z. W. Yin, *Physics of Dielectric Materials*, 45, Science, Beijing, 2000.
15. Liao, S. B., *Ferromagnetism*, 6, 127, 139, Science, Beijing, 1998.
16. Wu, M. Z., Y. D. Zhang, S. Hui, and T. D. Xiao, *Appl. Phys. Lett.*, Vol. 80, 4404, 2002.
17. Goglio, G., S. Pignard, A. Radulescu, and L. Piraux, *Appl. Phys. Lett.*, Vol. 75, 1769, 1999.
18. Kittel, C., *Phys. Rev.*, Vol. 73, 155, 1948.

Microwave Susceptibility Dispersion Spectra of Nanodot Arrays with Perpendicular Anisotropy

Wenbing Chen and Mangui Han
State Key Laboratory of Electronic Thin Films and Integrated Devices
University of Electronic Science and Technology of China, Chengdu 610054, China

Abstract— The zero-field microwave susceptibility dispersion spectra of 3×3 cylindrical nanodot arrays with perpendicular anisotropy have been studied by means of OOMMF. It is revealed that the remnant domain states of these nanodot arrays evolve as a function of the interdot distance. Increasing the interdot distance from 10 nm to 60 nm, the domain state for the central dot transforms from stripe-domain structure to bi-domain bubble state, to multi-domain bubble state, and finally to single domain flowering state. The corresponding dynamic susceptibility spectra of these nanodot arrays show different resonance peaks, each related to a unique domain state. It is distinguished that magnetostatic interaction between nanodots is the cause for the evolution of the domain states and the susceptibility spectra with the interdot distance, which suggests a potential way to utilize the dynamic properties of nanodot arrays.

1. INTRODUCTION

Magnetic nanodots with perpendicular anisotropy have received a lot of attention in recent years due to their potential applications in data storage industry [1]. The dynamic susceptibility of these nanodots is of critical importance for magnetic recording applications because it controls the magnetization switching process [2]. To exploit the dynamic susceptibility of magnetic nanodots, it is necessary to understand their domain states. N. Vukadinovic et al. have revealed that single nanodot with uniaxial perpendicular anisotropy can exhibit a variety of remnant magnetization states such as the bubble state, the vortex sate, and the stripe-domain state by adjusting the geometry of the nanodot and the strength of the anisotropy [1, 3]. However, to our knowledge, few works have addressed the effect of magnetostatic interaction on the dynamic susceptibility spectra of nanodot arrays. In this work, we find that the remnant magnetization states of nanodots can be controlled by putting them in an array and tuning the interdot distance. The dynamic susceptibility spectra associated with different domain states are also obtained through micromagnetic simulation. The behavior of a single isolated nanodot is also simulated for comparison.

2. MICROMAGNETIC SIMULATIONS

The micromagnetic simulations are performed using the public domain 3D OOMMF by solving the Landau-Lifshitz-Gilbert (LLG) equation as a function of time [4]. The material parameters in OOMMF for cobalt are taken: saturation magnetization $M_s = 14 \times 10^5$ A/m, exchange stiffness constant $A = 30 \times 10^{-12}$ J/m, anisotropy constant $K_1 = 5.2 \times 10^5$ J/m^3. The direction of the anisotropy constant is set to be along the length direction (Z-direction) of the nanodots to ensure perpendicular anisotropy. The gyromagnetic ratio γ is set to be 2.21×10^5 mA^{-1}S^{-1} and the damping constant α is set to be 0.015. A cubic cell size of $5 \times 5 \times 5$ nm^3 is taken. The field-dependent behavior of a single isolated cylindrical nanodot with height of 50 nm and its corresponding 3×3 periodic arrays is simulated. For the purpose of comparison, the diameter of these nanodots is fixed to be 100 nm and the adjacent interdot distance (edge-to-edge spacing d) is varied from 10 nm to 60 nm.

The dynamic susceptibility spectra are obtained following the routes described in Refs. [2] and [5]. Firstly, the equilibrium configuration of magnetization is obtained in the absence of external magnetic applied field. Then a weak pulse field assuming the form of $H(t) = 1000 \exp(-10^9 t)$ (t in s, H in A/m) is applied perpendicular to the long axis of the dots. The dynamic response of magnetization is tracked under the pulse field. Both the pulse field and excited magnetization are then processed by a Fast Fourier Transform approach, after which the susceptibility spectrum $\chi(\omega)$ are calculated by:

$$\chi(\omega) = M(\omega)/H(\omega) = \chi' - i\chi'', \tag{1}$$

where ω is the frequency, $M(\omega)$ and $H(\omega)$ are the expressions in frequency domain for magnetization and pulse field after FFT treatment, respectively; χ' refers to the real part of $\chi(\omega)$ and χ'' denotes the imaginary part.

3. RESULTS AND DISCUSSIONS

Figure 1 demonstrates the remnant magnetization states for a 3×3 nanodot array with different interdot distance d. Fig. 2 shows their corresponding susceptibility spectra. As can be seen, the stable magnetization state for a single isolated nanodot with diameter of 100 nm and height of 50 nm is flowering state (Fig. 2). In contrast, the nanodots in the 3×3 arrays exhibit a variety of domain states as the interdot distance varies. When $d = 10$ nm (Fig. 1(a)), the dot at the center of the array exhibits a stripe-domain pattern, with most of its magnetization pointing down and the rest pointing up. The dots situated at its right and bottom show two stripe-domain walls, which are separated by 180° domains. It is worth noting that the shape of the domain walls is asymmetric, arising from the strong dipolar interaction between the dots in the array. Other dots in the array display uniform flowering domain, the geometry of which is also slightly distorted.

As d increases to 20 nm, the magnetization state for the dot at the center evolves into concentric bi-domain bubble states (Fig. 1(b)). The inner domain of the bubble state is upward magnetized and the outer domain is downward magnetized; between them is a circular domain wall, twisted with a Bloch character at the dot center and a Néel character at the dot surfaces. Detailed descriptions of the magnetization configuration of the bubble state can be found in Refs. [1] and [3]. In the meantime, the dots surrounding the central dot show similar two stripe-domain structure: at the center of the dot the magnetization points upward and at the two edges of the dot the magnetization points downward. Other dots at the corner of the array manifest stable flowering state, since they are less affected by adjacent dots.

When d further increases to 30 and 40 nm, all the dots in the array display single-domain flowering state except the one situated at the center of the array. The central dot for the array with $d = 30$ nm is confined in a bubble state with four tips stretched out by the influence from surrounding elements. As d becomes 40 nm, the influence from surrounding elements is decreased and the domain state for the central dot is stabilized in the bubble state. Eventually, all dots in the array are able to support the single-domain flowering state when d increases to 60 nm (not shown here), resulting from the diminished magnetostatic interaction between the dots.

The susceptibility spectrum for single nanodot is shown in Fig. 2. Three resonance peaks A1, A2, and A3 can be identified in the frequency range of $0 \sim 50$ GHz, located at 9.3, 16.5, and 20 GHz, respectively. Previous investigations on nanowires and nanodots reveal that peaks A2 and A3 are related to the magnetization distribution at the bulk part of the dot, whereas peak A1 is due to the splay pattern of the surface magnetization configuration. The intensity of the A1 peak is stronger than that of A2 and A3, which is ascribed to the fact that the volume of the surface magnetization is larger than that of the bulk magnetization. Due to the existence of the flowering state for all the dot arrays, the three resonance peaks also sustain for all arrays, with their intensity and position being modified. In the case of nanodot array with $d = 60$ nm and all dots in the array showing flowering state, the position of the three resonance peaks is shifted to the lower frequency region and peak A1 and A2 are split due to the minor inhomogeneity of the magnetization configuration in each dot.

For nanodot array with $d = 40$ nm, new resonance peaks B4 and B5 arise as a result of the bubble state, situated at 12.7 and 16 GHz, respectively. As a matter of fact, the bubble state should give rise to three resonance peaks: one associated with the inner domain, one resulted from the outer domain and one ascribed to the circular domain wall [1, 3]. Note that the magnetization of the inner domain is in the same direction as that of the flowering state surrounding the central dot, so it is highly possible that the resonance peak corresponding to the inner domain is obscured by the resonance peaks arising from the flowering state. For nanodot array with $d = 30$ nm, the magnetization configuration for the central dot show four additional tips. Accordingly, a new resonance peak C6 emerges on its susceptibility spectrum. When the nanodot array with $d = 20$ nm display stripe-domain structure, its susceptibility spectrum exhibit corresponding resonance peak D7, along with the characteristic peak B4 of the bubble state. When the bubble state disappears in the domains state of the nanodot array with $d = 10$ nm, its corresponding resonance peaks also vanish. In the meantime, the irregular stripe domain pattern in Fig. 1(a) is responsible for the rough shape of peak D7, D8, and D9.

While many factors account for the domain patterns and susceptibility spectra of nanodot arrays, magnetostatic interaction between nanodots is the prime variable as interdot distance d varies. It is revealed that magnetostatic interaction energy between nanodots would decrease as d adds up [6, 7]. Thus it is understandable that when d increases to an extent ($d > 60$ nm in our simulation), the domain states for nanodot arrays would behave like that of a single dot and their

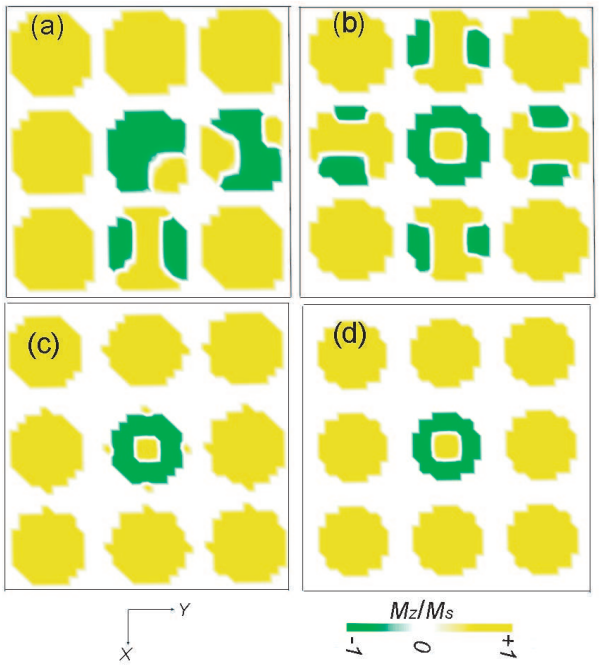

Figure 1: Zero-field domain state for a 3×3 nanodot array with different interdot distance d (top view). (a) $d = 10$ nm; (b) $d = 20$ nm; (c) $d = 30$ nm; (d) $d = 40$ nm.

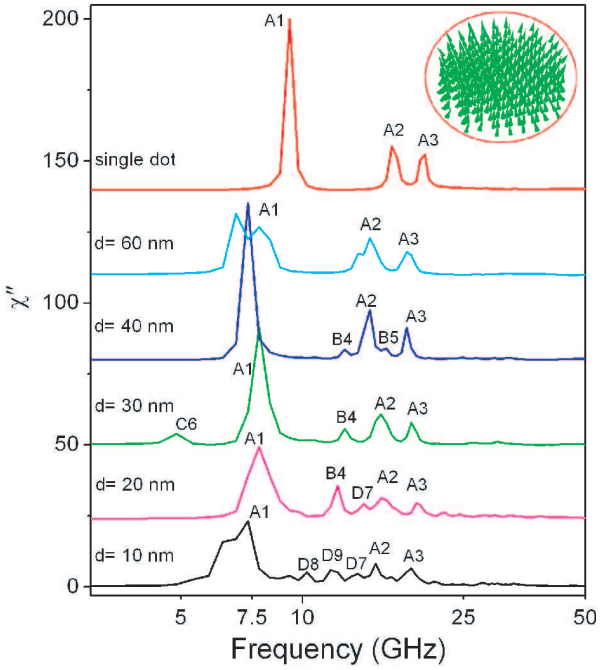

Figure 2: The microwave susceptibility dispersion spectra for a single nanodot and nanodot arrays with different interdot distance d. The inset shows the remnant state for a single isolated nanodot (flowering state).

corresponding susceptibility spectra also show resonance peaks much like that of the single dot. The rich domain states demonstrated by the nanodot arrays, along with their diversified susceptibility spectra, provide an opportunity to tailor, design and exploit their dynamic properties.

4. CONCLUSIONS

The zero-field microwave susceptibility spectra for 3×3 nanodot arrays with different interdot distance d have been simulated through OOMMF. It is found that their remnant magnetization states evolve as a function of d. For instance, the domain state for the central dot transforms from stripe-domain structure to bi-domain bubble state, to multi-domain bubble state, and finally to single domain flowering state. Accordingly, their corresponding dynamic susceptibility spectra show different resonance peaks, each related to a unique domain state. Since magnetostatic interaction between nanodots is the prime variable as interdot distance d varies, it is responsible for the variation of the domain states and their corresponding dynamic susceptibility spectra, which offers another way to exploit the dynamic properties of nanodot arrays.

ACKNOWLEDGMENT

This work is supported by NSFC (No. 60701016) and NSFC — the Royal Society of United Kingdom international jointed project (No. 60911130130).

REFERENCES

1. Vukadinovic, N. and F. Boust, "Three-dimensional micromagnetic simulations of magnetic excitations in cylindrical nanodots with perpendicular anisotropy," *Phys. Rev. B*, Vol. 75, No. 1, 014420.1–014420.8, 2007.
2. Gérardin, O., J. B. Youssef, H. Le Gall, N. Vukadinovic, P. M. Jacquart, and M. J. Donahue, "Micromagnetics of the dynamic susceptibility for coupled Permalloy stripes, " *J. Appl. Phys.*, Vol. 88, No. 10, 5899–5903, 2000.
3. Vukadinovic, N. and F. Boust, "Three-dimensional micromagnetic simulations of multidomain bubble-state excitation spectrum in ferromagnetic cylindrical nanodots," *Phys. Rev. B*, Vol. 78, No. 18, 184411.1–184411.10, 2008.

4. Donahue, M. J. and D. G. Porter, *OOMMF User's Guide*, Version 1.2a3, 2002. (http://math.nist.gov/oommf).
5. Dao, N., M. J. Donahue, I. Dumitru, L. Spinu, S. L. Whittenburg, and J. C. Lodder, "Dynamic susceptibility of nanopillars," *Nanotechnology*, Vol. 15, S634–S638, 2004.
6. Escrig, J., S. Allende, D. Altbir, and M. Bahiana, "Magnetostatic interactions between magnetic nanotubes," *Appl. Phys. Lett.*, Vol. 93, No. 2, 023101.1–023101.3, 2008.
7. Beleggia, M., S. Tandon, Y. Zhu, and M. De Graef, "On the magnetostatic interactions between nanoparticles of arbitrary shape," *J. Magn. Magn. Mater.*, Vol. 278, 270–284, 2004.

Thickness Effects on Microwave Magnetic Properties of FeCoBSi Films Deposited on Flexible Substrate

Haipeng Lu, Jing Yang, and Longjiang Deng
State Key Laboratory of Electronic Thin Films and Integrated Devices
University of Electronic Science and Technology of China
Chengdu 610054, China

Abstract— The FeCoBSi thin films were deposited on the flexible mylar substrates by DC magnetron sputtering. The as-deposited films showed as an amorphous structure. Permeability characteristics in the range of 0.5–18 GHz were investigated. The values of permeability increased with an increasing thickness of the films when the thickness was less than 1 μm. This unusual result may be due to the various microstructures, stress or defects of the films. When the thickness was more than 1 μm, the values of both permeability and resonance frequency decreased significantly. The results may be attributed to the increase of eddy current loss. The electric properties, including sheet resistance and resistivity for the films with various thicknesses, have also been investigated.

1. INTRODUCTION

Materials with high microwave permeability are of practical importance for a number of applications. As ferromagnetic films with in-plane anisotropy are able to overcome the Snoek's limits, they might obtain larger values of microwave permeability than bulk magnets [1]. So a lot of research has been carried out to develop ferromagnetic thin films for the use in high frequency devices such as high-frequency micro inductors or micro transformers. However, more and more new applications such as flexible EMI suppressors require flectional samples which under a suitable form [2]. This was the motivation for the experimental study of thin films deposited on thin flexible substrates.

Observed MW permeability of ferromagnetic alloys is typically lower than the intrinsic permeability because of skin effect. Even if the film thickness d is less than skin depth δ; eddy currents widen the absorption line and therefore lower the operating frequencies of a magnet. Hence, to reveal the high intrinsic MW permeability of a ferromagnetic alloy film, the condition $d \ll \delta$ should be satisfied [3].

Iron-based films are known with high saturation magnetization. Alloying iron with cobalt, boron and silicon may result in the materials with high saturation magnetization and appropriate anisotropy or resistivity. Such films may have high permeability at frequencies of several GHz [4, 5].

The paper deals with FeCoBSi films based on flexible mylar substrates, aiming at the structure and microwave properties of the films. The thickness effects on microwave magnetic properties of the laminates and the FeCoBSi films were specialized studied. The effect of film thickness on the electric properties was also investigated.

2. EXPERIMENTAL

$Fe_{66}Co_{17}B_{16}Si_1$ thin films were produced on flexible 11.5 μm thick mylar substrates by DC magnetron sputtering. The microstructure of the thin films was examined using X-ray diffractometry (XRD) with Cu $K\alpha$ radiation, and the electrical resistivity of the samples is determined by a standard four-point method. The microwave permeability is measured in the frequency range of 0.5–18 GHz by the technique that implies winding a film into a roll for a coaxial line [6]. Since an alternating electric field is normal to the film plane and magnetic field is in-plane, the technique simulates the magnetic performance of laminates. As the relationships between the intrinsic properties of inclusion and the effective properties of the composite are well known, measuring the composite properties leads to the intrinsic electromagnetic properties of the ferromagnetic inclusions.

3. RESULT AND DISCUSSION

The X-ray diffraction spectra for FeCoBSi thin film deposited on a flexible mylar substrate is shown in Fig. 1. There is only one peak at the position about 25.5° in the figure, which is the peak of the mylar substrate. The XRD spectra dos not exhibit any clear (110) peak of α-Fe or α-FeCo phase. It means the FeCoBSi films prepared on thin flexible mylar substrates have an amorphous structure. Actually, it is difficult to obtain crystallized metal films on such flexible thin substrate

by our sputtering process. The temperature of the centre area for magnetron sputtering is much higher than the temperature the flexible mylar substrates could endure. To make the thin films and substrate no curling, deformation and even burned down during the sputtering process, it need to be flexible substrate close to water-cooling system. It also can not be imposed any heat treatment after sputtering. So the films usually present an amorphous structure. Amorphous structure is beneficial to obtaining lower coercivity and larger permeability.

The MW performance of an arbitrary magnetic film can be estimated by a useful integral analogue of Acher's law [7]:

$$\frac{2}{\pi}\int_0^\infty \mu''(f) f df = k_A (\gamma 4\pi M_s)^2 \tag{1}$$

where $\mu''(f)$ is the imaginary part of permeability component related to microwave magnetic field applied in the film plane along the hard axis, f is the frequency, k_A is a randomization factor. Value of k_A helps to understand film quality. The closer is k_A to unity, the better is the film from the viewpoint of microwave application. A perfect film with uniform magnetization and in-plane anisotropy has k_A =1, and the best value for the isotropic in-plane sample, $k_A = 0.5$. As we did not induce anisotropy during the sputtering process, the FeCoBSi film shows isotropic in-plane. So the internal in-plane magnetic moment is random orientation. In this case, k_A in Eq. (1) is ≤ 0.5.

The permeability spectra for the laminates filled with FeCoBSi films with various thicknesses are shown in Figs. 2(a) and 2(b). From the figures, increasing the film thickness leads to an increase in the level for the real part and imaginary part of the permeability of the laminates. It is attributed to the increasing ferromagnetic inclusions' volume fraction. With the increasing of the ferromagnetic inclusions, the saturation magnetization values of the laminates increased, which was proportional

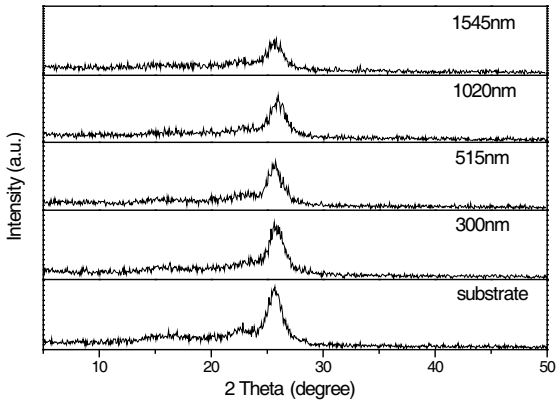

Figure 1: Thickness effects on X-ray diffraction spectra of FeCoBSi thin film deposited on a flexible mylar substrate.

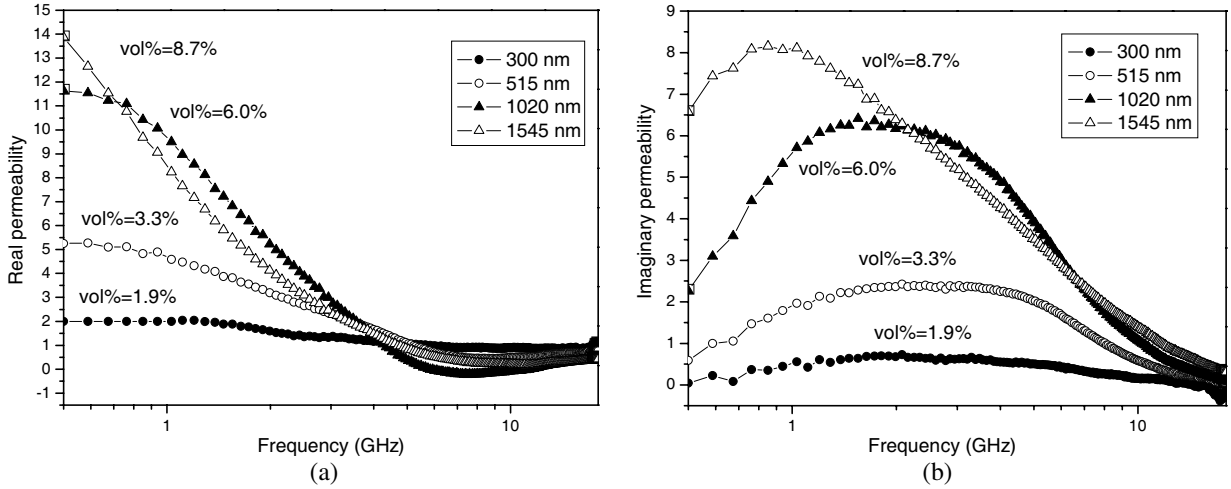

Figure 2: The real part (a) and imaginary part (b) of the complex permeability spectra for the laminates filled with FeCoBSi films with various thicknesses.

to the Acher's constant. Therefore, increasing the ferromagnetic inclusions by increasing the film thicknesses in the laminates lead to an increase in the level of permeability.

The intrinsic magnetic spectra for the FeCoBSi films with a range of thicknesses are shown in Fig. 3. From the magnetic spectra, the general trend is that the ferromagnetic resonances shift toward the low frequencies with the increasing thickness. When the thickness was more than 1 μm, the values of both permeability and resonance frequency decreased significantly. The results may be attributed to the increase of eddy current loss. In thick films, the skin effect is pronounced. The magnetic absorption spectrum may be formed mainly by the skin effect, with the contribution from the ferromagnetic resonance being negligible. In this case the absorption peak is located at the frequency where the penetration depth is equal to the film thickness. Therefore, the effective permeability of the thick FeCoBSi films is much smaller than the permeability of the thin FeCoBSi films.

But we also noticed that the values of permeability increased with an increasing thickness of the films when the thickness was less than 1 μm. It is worthy of attention because the phenomenon is neither consistent with the theory of demagnetizing fields [8] nor consistent with most reports [9]. This unusual result may be due to the various microstructures, stress, defects, etc.

The effect of film thickness on the electric properties was also investigated. Table 1 shows the room-temperature sheet resistance R_s and resitivity for the films with various thicknesses. The general trend is that resistance decreases with increasing thicknesses. Relatively high resistance for a thinner film demonstrates the effects of worse microstructure, defects and the mylar-film interface. The values of the resistivity for the films are of the order $10^{-3}\,\Omega$cm, which is larger than the value for crystalline FeCoBSi films or for FeCoBSi films on rigid substrates [10]. The high resistivities, on the one hand, result from the amorphous structure. It has been reported that amorphous Fe-based films have higher resistivity than nanocrystalline films and bulk large-size crystalline materials have the lowest resistivity [11]. On the other hand, the higher resistivities should also result from the effect of the mylar substrate.

The high resistivity is obviously an advantage for the high frequency application of the soft magnetic film since the eddy loss can be reduced by an increasing electrical resistance due to an increasing skin depth. But if the high values of resistivity were attributed to the imperfect magnetic structure or the defects of the film, the permeability would typically be worse.

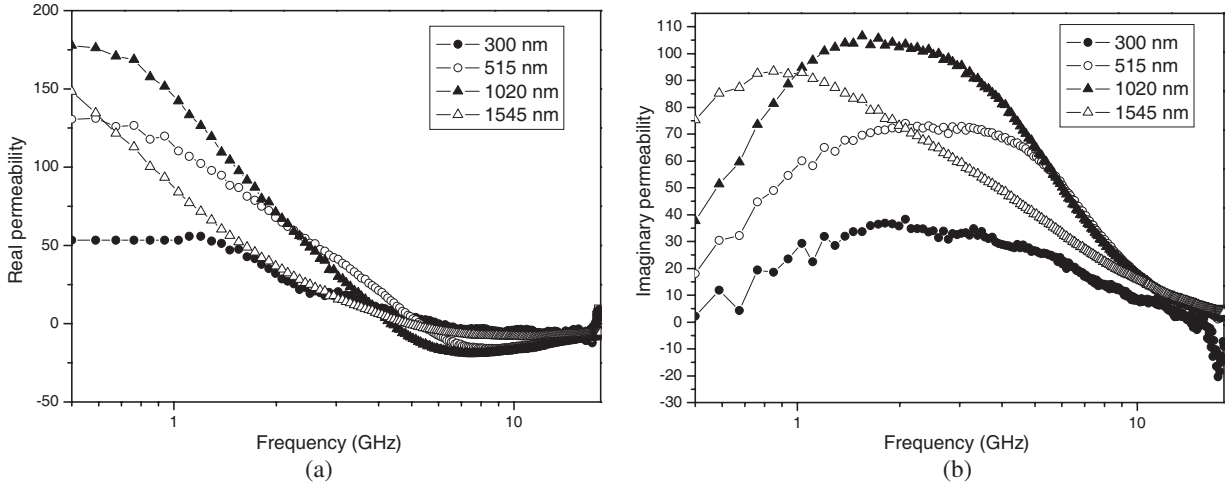

Figure 3: The real part (a) and imaginary part (b) of the intrinsic magnetic spectra for the FeCoBSi films with various thicknesses.

Table 1: Thickness effects on the electrical resistivity of FeCoBSi films deposited on flexible substrate.

Thickness (nm)	300	515	1020	1545
Rs ($\Omega/\square$)	116.9	60.2	29.2	7.7
ρ ($\times 10^{-3}\,\Omega$cm)	3.51	3.10	2.98	1.07

4. CONCLUSIONS

The FeCoBSi thin films on the flexible mylar substrates were produced by DC magnetron sputtering. The as-deposited films showed as an amorphous structure. The coaxial technique has been used for characterizing the microwave properties. The ferromagnetic resonances shift toward the low frequencies with the increasing film thickness. When the thickness was more than 1 μm, the values of both permeability and resonance frequency decreased significantly. When the thickness was less than 1 μm, the values of permeability increased with an increasing thickness of the films. This unusual result may be due to the various microstructures, stress, defects, etc. The electric properties of the thin film on mylar with various thicknesses were also studied. The high resistivity is usually an advantage for the high frequency application of the soft magnetic film. But if the high values of resistivity were attributed to the imperfect magnetic structure or the defects of the film, the permeability would typically be worse.

ACKNOWLEDGMENT

The authors would like to thank Prof. Jianliang Xie for fruitful discussion and valuable remarks.

REFERENCES

1. Iakubov, I. T., A. N. Lagarkov, S. A. Maklakov, A. V. Osipov, K. N. Rozanov, I. A. Ryzhikov, and S. N. Starostenko, "Microwave permeability of composites filled with thin Fe films," *Journal of Magnetism and Magnetic Materials*, Vol. 300, No. 1, 74–77, 2006.
2. Valls, O., D. Damiani, and O. Acher, "High frequency permeability of CoFeV thin films deposited on thin flexible substrates," *Digests of the Intermag Conference*, FD07, Amsterdam, Netherlands, April 2002.
3. Iakubov, I. T., A. N. Lagarkov, S. A. Maklakov, A. V. Osipov, K. N. Rozanov, I. A. Ryzhikov, and S. N. Starostenko, "Microwave permeability of laminates with thin Fe-based films," *Journal of Magnetism and Magnetic Materials*, Vol. 272–276, No. 3, 2208–2210, 2004.
4. Chen, L. H., S. L. Cheng, C. T. Hsieh, Y. H. Shih, S. Jin, and R. B. Van Dover, "Ultrahigh frequency properties of amorphous Co-Fe-Zr-B thin films," *IEEE Transactions on Magnetics*, Vol. 37, No. 4, 2242–2244, 2001.
5. Frommberger, M., J. McCord, and E. Quandt, "High-frequency properties of FeCoSiB thin films with crossed anisotropy," *IEEE Transactions on Magnetics*, Vol. 40, No. 4, 2703–2705, 2004.
6. Acher, O., J. L. Vermeulen, and P. M. Jacquart, "Permeability measurement on ferromagnetic thin films from 50 MHz up to 18 GHz," *Journal of Magnetism and Magnetic Materials*, Vol. 136, No. 3, 269–278, 1994.
7. Iakubov, I. T., A. N. Lagarkov, S. A. Maklakov, A. V. Osipov, K. N. Rozanov, I. A. Ryzhikov, N. A. Simonov, and S. N. Starostenko, "Experimental study of microwave permeability of thin Fe films," *Journal of Magnetism and Magnetic Materials*, Vol. 258–259, 195–197, 2003.
8. Acher, O. and A. L. Adenot, "Bounds on the dynamic properties of magnetic materials," *Physical Review B*, Vol. 62, No. 17, 11324–11327, 2000.
9. Liu, Z. W., Y. Liu, L. Yan, C. Y. Tan, and C. K. Ong, "Thickness-dependent properties of FeTaN thin films deposited on flexible substrate," *Journal of Applied Physics*, Vol. 99, No. 4, 043903, 2006.
10. Bekker, V., K. Seemann, and H. Leiste, "Development and optimisation of thin soft ferromagnetic Fe-Co-Ta-N and Fe-Co-Al-N films with in-plane uniaxial anisotropy for HF applications," *Journal of Magnetism and Magnetic Materials*, Vol. 296, No. 1, 37–45, 2006.
11. Viala, B., M. K. Minor, and J. A. Barnard, "Microstructure and magnetism in FeTaN films deposited in the nanocrystalline state," *Journal of Applied Physics*, Vol. 80, No. 7, 3941, 1996.

Effect of the Very Thin Dielectric Film on the Transmission Properties of the FSS

Xinyu Hou, **Wenming Tian**, **and Yongxing Che**
State Key Laboratory of Electronic Thin Films and Integrated Devices
School of Microelectronics and Solid-State Electronics
University of Electronic Science and Technology of China
Chengdu 610054, China

Abstract— This paper investigated the influential rule of the thickness and dielectric constant of thin film material to the resonant frequency of single-layer FSS in practical fabrication. Firstly, ring loop and four-legged loaded elements of single-layer FSS without considering the effect of thin film is designed and simulated. The results show that the resonant frequency (f_0) bounds when the dielectric thickness is $1/4\lambda$ and $3/4\lambda$ for both structures, and this is very agree with FSS theory. Then thin film material is added between the FSS and dielectric layer. The simulated results show that the f_0 changes when the thin film's thickness and dielectric constant varies, and f_0 bounds at some frequency value. This illuminates that the thickness and dielectric constant of thin film material is paramount factor for the f_0 of single-layer FSS in practical fabrication.

1. INTRODUCTION

Frequency selective surface (FSS) has been extensively studied over these years due to its extensive application in microwaves, infrared, even in optical spectrum. In order to obtain special resonant frequency and bandwidth performance, the element of the FSS is often designed with different configurations to ensure electromagnetic wave fully pass or reflected at its resonant frequency. Whereas the bandwidths of the FSS is determined not only by the single element, but also the array arrangement, the resonance characteristics of different element shape can supply us a good start in FSS design by choosing proper element [1, 2]. The frequency characteristics of the FSS are influenced greatly by the style of unit, and the dielectric layer acting the support role of the structure. When the dielectric thickness reaches some value, the resonance frequency of the FSS which embedded in the dielectric layers will be stable [3]. The transmission coefficient of a two-layer periodic array structure using symmetrical and asymmetrical method has been detailed analyzed in [4].

Various methods have been proposed for the analysis of FSS under the infinite-array approximation, namely, the periodic method of moments (MoM) [1], equivalent-circuit modes [5], the finite difference time-domain (FDTD) method [6], and the finite-element method (FEM) [7].

This paper investigates the effect of thin film material in a single-layer FSS to its resonant frequency using FDTD method. This study is meaningful for the practical application of the FSS, and well explained the disagreement of some testing results with pre-design.

2. FORMULATION AND MODELING

The FSS is under study modeled as a one dielectric layer structure, see Figure 1, where A^+ and B^- are column matrices containing the mode coefficients of the total incident field. The column matrices A^- and B^+ contain the mode coefficients of the total scattered field. The characteristics of the FSS are given by a scattering matrix S,

$$\begin{pmatrix} A^- \\ \overline{B^+} \end{pmatrix} = S \begin{pmatrix} A^+ \\ \overline{B^-} \end{pmatrix} = \begin{pmatrix} S_{11} & S_{12} \\ S_{21} & S_{22} \end{pmatrix} \begin{pmatrix} A^+ \\ \overline{B^-} \end{pmatrix}$$

Given a known inter-element periodicity (P), the frequency for onset of grating lobes for angle of incidence η can be predicted using [1]:

$$f = \frac{C}{P(\sin\eta + 1)} \text{ (Hz)}$$

where c is the velocity of light.

The geometry of the FSS element is depicted in Figure 2. We show two different FSS units in this paper, i.e., four-legged loaded element and ring loop element to find the relation between

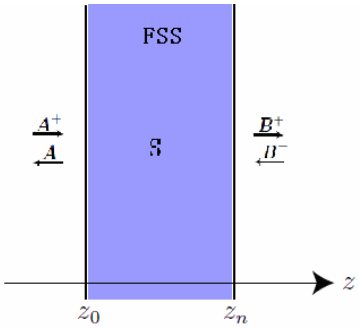

Figure 1: Frequency selective structure represented as a scattering matrix.

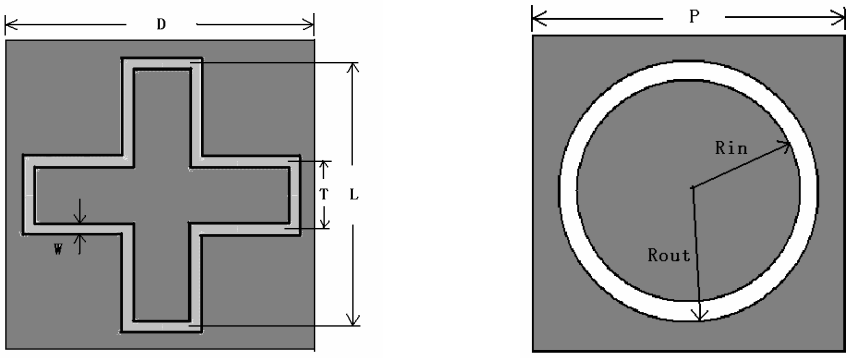

Figure 2: Geometry of two different elements of the FSS: four legged loaded element and ring slot element.

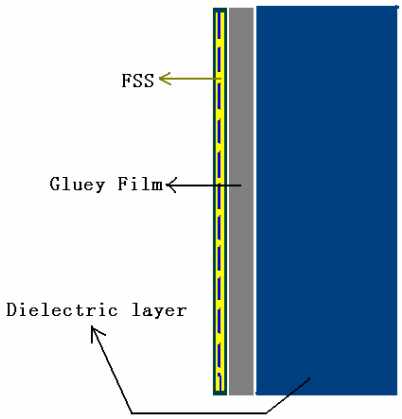

Figure 3: Sandwich structure of single-layer FSS loaded with thin film.

resonant frequency f_0 and thickness of the dielectric layer. The FSS is assumed to be infinitely extended in the xy-plane. The z-axis is assumed to be orthogonal to the surface of the perfectly conducting FSS. These apertures are spaced periodically along the x-axis and y-axis with the same period $D = P = 7\,\text{mm}$. For ring loop FSS, the inner radius loop Rin $= 3\,\text{mm}$ and the loop width $w = 0.18\,\text{mm}$. For four-legged loaded element, the parameter of unit are $L = 5.5\,\text{mm}$, $T = 1.4\,\text{mm}$ and slot width $w = 0.18\,\text{mm}$. In these two case, the same FR-4 electronic board is used as dielectric substrates, with thickness of $h = 7.15\,\text{mm}$, exactly the half dielectric wavelength corresponding to the resonant frequency of the FSS. The difference is that we consider a very thin film between the FSS and the dielectric substrate in one case, whereas we didn't consider it in other case.

3. SIMULATED RESULTS

From Figure 4, we can see that when the thickness of dielectric substrate h_sub varies, the relation between f_0 and thickness of dielectric layer changes regularly for both FSS elements and f_0 bounds at the same dielectric thickness. However, although the two curves have similar changing regularity, the changing rate of four-legged loaded element is much smaller than the ring loop one. This means

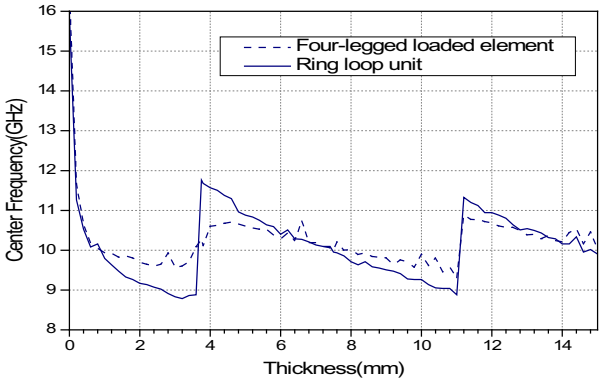

Figure 4: f_0 vs. thickness of dielectric substrate.

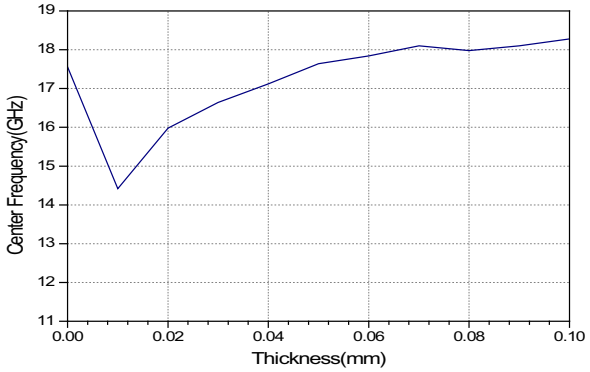

Figure 5: f_0 vs. thickness of thin film ($\varepsilon = 2.3$) material.

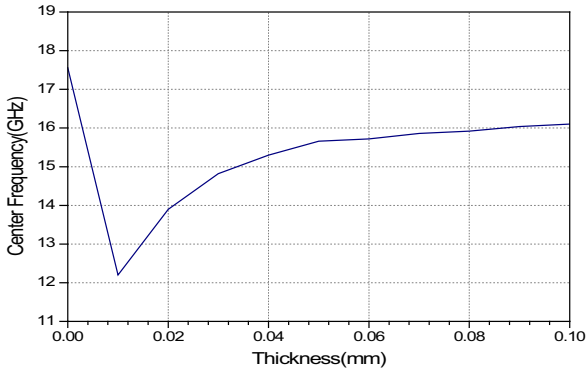

Figure 6: f_0 vs. thickness of thin film ($\varepsilon = 4.4$) material.

that the rule between f_0 and dielectric thickness is decided by the thickness of substrate, not FSS unit. But the four-legged loaded element is more stable than the ring loop unit. So in practical fabrication, four-legged loaded element is usually chosen as periodic unit.

Figure 5 and Figure 6 shows that when thin film material is added between FSS and dielectric layer, f_0 changes along with the thickness of thin film material varying. And, the changing rate increases with the dielectric constant increases. From the results curve we find that, when the thickness of thin film material is only 20 μm, the resonant frequency of designed FSS shifts about 1.6 GHz and 2.6 GHz when the dielectric constant of thin film material is 2.32 and 4.4 respectively. The simulated results accurately illustrate that, in practical fabrication, such as pasting single-layer FSS inside of a radome, why the experimental results and designed results are different. In other words, because of the dielectric constant and thickness of thin film is not assured accurately, the resonant frequency of experiment shifts about 1.3 GHz compared with pre-designed f_0.

In practical fabrication, the gluey film material is used as thin film material. For gluey film material having the similar characteristics as dielectric, we consider it as a thin film dielectric layer in simulation. If the glue is assorted manually, the dielectric constant of the glue is hardly assured accurately. And in fabrication, the thickness of thin film is also hardly assured. The above reasons lead to the experimental results not agrees with pre-designed results.

4. CONCLUSION

From the above results we can find that, for the same single-layer FSS, same period, different FSS units, the relation between f_0 and the thickness of dielectric layer have the similar regularity. And the simulated results illustrates that four-legged loaded element is more stable than the ring loop one. But when thin film material is added between FSS and dielectric layer, f_0 varies with the thickness of thin film material changing. And the changing rate increases with the dielectric constant increases. This illustrates that the thickness and dielectric constant of thin film material greatly affects the resonant frequency of single-layer FSS. Therefore, thin film material's dielectric constant and thickness must be pre-considered before practical fabrication. This can avoid resonant

frequency shift between designed and testing results.

REFERENCES

1. Munk, B. A., *Frequency Selective Surfaces: Theory and Design*, John Wiley & Sons Inc., New York, 2000.
2. Mittra, R., "A look at some challenging problems in computational electromagnetic," *IEEE Antennas and Propagation Magazine*, Vol. 45, No. 5, 18–32, 2004.
3. Luebbers, R. J. and B. A. Munk, "Some effects of dielectric loading on periodic slot arrays," *IEEE Trans. on Antennas Propagation*, Vol. 26, No. 4, 536–542, 1990.
4. Hou, X., W. Wan, and M. Tong, "Characteristic analysis of symmetrical two-layer FSSs," *Electronic Science Journal*, Vol. 21, No. 4, 569–572, 1999.
5. Lee, C. K. and R. J. Langley, "Equivalent circuit models for frequency selective surfaces at oblique angles of incidence," *Proc. IEE Microwaves Opt. Antennas*, Vol. 132, 395–399, 1985.
6. Harms, P., R. Mittra, and K. Wai, "Implementation of the periodic boundary condition in the finite-difference time-domain algorithm for FSS structures," *IEEE Trans. Antennas Propagation*, Vol. 42, 1317–1324, 1994.
7. Lucas, E. W. and T. P. Fontatna, "A 3D hybrid finite element/boundary element method for the unified radiation and scattering analysis of general infinite periodic arrays," *IEEE Trans. Antennas Propagation*, Vol. 43, 190–120, 1995.

High Frequency Characteristics and Electrical Properties of Multilayer FeCoHfO/AlO_x Films

Yu-Ming Kuo[1], **Shandong Li**[2], **Jenq-Gong Duh**[1], **and Su-Yueh Tsai**[3]

[1]Department of Material Science and Engineering, National Tsing Hua University
Hsinchu 30013, Taiwan, R.O.C.
[2]Department of Physics, Fujian Normal University, Fuzhou 35007, China
[3]Precision Instrument Center, National Tsing Hua University, Hsinchu 30013, Taiwan, R.O.C.

Abstract— For the high frequency application in mobile communication technology, the operating frequency is over 3 GHz, hence the ferromagnetic resonance frequency (f_{res}) of magnetic films must be over 3 GHz. In this study, FeCoHfO alloy is chosen as a promising material system for this application. Inserting an insulator (e.g., AlO_x) layer into ferromagnetic layers is a good way to enhance the resistivity and therefore to reduce the eddy current loss. A significant reduction of hard axis anisotropic field was observed when the number of multilayer reached five. With this optimum condition of [FeCoHfO (400 nm)/AlO_x (10 nm)]$_3$, favorable magnetic properties (effective anisotropy field of 110 Oe), high frequency characteristics (permeability $\sim$ 100 at 100 MHz and ferromagnetic resonance frequency over 3 GHz) and high electrical resistivity $\rho \sim 1074\,\mu\Omega$cm were obtained.

1. INTRODUCTION

Soft magnetic thin films with high magnetic moments have been studied intensively because they are of significance both in micromagnetic devices and high-frequency applications, such as planar inductors and transformers used in integrated circuits, which also require the high ferromagnetic resonance frequency (f_{FMR}) [1]. Magnetic thin films can not only be utilized to fabricate microinductors but also to enhance the inductance of magnetic inductors. The magnetic thin films provide favorable alternatives in reduction of the device dimensions and in the development of electromagnetic high frequency devices [2]. According to the Kittel's equation, the magnetic resonance frequency is defined as

$$f_{\mathrm{FMR}} = \frac{\lambda}{2\pi}\sqrt{\frac{M_S H_k}{\mu_0}} \tag{1}$$

where f_{FMR} is ferromagnetic resonance frequency, M_S is saturation magnetization, μ_0 is the initial permeability, γ is the gyromagnetic factor, and the anisotropy field is defined as $H_K = 2K_u/M_S$. The appropriate H_K, and M_S should be as high as possible [3–5] to increase the ferromagnetic resonance frequency.

The magnetic thin films applied in high-frequency inductors are supposed to have high M_S, low coercive field (H_C), and appropriate in-plane uniaxial anisotropy (H_K) to increase ferromagnetic resonance frequency (f_{FMR}) and permeability (μ'). Meanwhile, high resistivity (ρ) is necessary to decrease eddy current loss in high frequency range. Nanocomposite oxygen-based soft magnetic films, FeCo-X-O (X = Hf, Zr, Al, etc.) show excellent soft magnetic properties [6, 7]. However, uniaxial anisotropy of these films should be improved further for high-frequency applications.

In this work, the multilayered film technique laminating the magnetic layers with non-magnetic oxide spacers is exploited to achieve appropriate uniaxial anisotropy field in FeCoHfO, aiming to obtain good soft magnetic properties for application in high-frequency inductors. The effects of the stacking levels on the microstructure, tensile stress, electrical resistivity and domain structures have been investigated, and their relationships between the magnetic and high frequency characteristics were discussed.

2. EXPERIMENTAL

The FeCoHfO/AlO_x multilayer films were deposited on Si (100) substrates by dc reactive magnetron co-sputtering with Ar + O_2 gases in a working pressure 1×10^{-3} Torr. The power of the Fe_7Co_3, Hf and Al targets was 200, 50 and 50 W, respectively. The multilayered structure was the FeCoHfO ferromagnetic layer with total thickness of 1.2 µm separated by AlO_x interlayers with 10 nm in thickness. The t/d ratio refers to the thickness ratio of the AlO_x (t = 10 nm) spacer to single-layered FeCoHfO (d). The samples were named as Mx, where the x refers to the number of the

ferromagnetic layers in one film. For example, $M3$ refers to the multilayer film composed of three ferromagnetic layers. The as-deposited FeCoHfO/AlO_x multilayer films were annealed at 300°C for 3 hours along hard axis in presence of a magnetic field of 2 kOe. Magnetic properties were measured with a vibrating sample magnetometer (VSM), and the permeability was evaluated using PMF-3000 permeameter with a maximum frequency of 3 GHz. A high-resolution transmission electron microscope (HRTEM, JEOL-3000F, Japan) was employed to investigate the detailed microstructure of the multilayer films. The magnetic domain structure was observed by magnetic force microscope (MFM). The residual stress was measured using the scanning laser curvature method.

3. RESULTS AND DISCUSSION

Figure 1(a) shows the change of H_K and MFM images with stacking levels in FeCoHfO/AlO_x multilayer films. The anisotropic field is reduced with the number of stacking layers. When the stacking level increases from one to three layers, the H_K obviously decreased. When magnetic thin films exhibit a perpendicular anisotropic field, the stripe domains are observed. Fig. 1(a) shows a stripe domain for the sample $M1$ where bright-to-dark contrast came from the magnetization canted up or down out of the film plane, demonstrating the presence of perpendicular anisotropy. Therefore, the sample $M1$ has a large value of the anisotropic field. However, typical characteristics of in-plane anisotropy were observed in samples $M3$–$M5$. The stripe domain was eliminated, and the non-contrasted MFM image was observed. Hence, samples $M3$–$M5$ had the smaller values of the anisotropic field. The effective anisotropy field of sample $M3$ was 110 Oe. If the stripe domain exists in thin film, it will affect the limiting value of in-plane microwave permeability due to the influence of the dynamic demagnetizing fields at the domain walls [8], and therefore the permeability is relatively lower than the film without stripe domain.

The bright-field HRTEM images and corresponding electronic diffraction pattern indicating samples of $M1$ and $M3$ are shown in Figs. 1(b)–1(c). There are several sharper rings, assigned as (110), (200), (211) and (220) planes of bcc FeCo. The average grain size of FeCo grains is 2–5 nm. In addition, one hazy and broad ring comes from amorphous HfO_2.

As discussed before, the anisotropic filed is reduced with the increase of the number of stacking layers (see Fig. 1(a)). The anisotropic field is influenced by magnetocrystalline anisotropy and magneto-elastic anisotropy. According to random anisotropy theory [9], the effective magnetic anisotropy ($\langle K \rangle$) is expressed as:

$$\langle K \rangle = K_1 \left(\frac{D}{L_{ex}} \right)^{\frac{3}{2}} \tag{2}$$

where K_1 is the magnetic crystalline anisotropy constant, D is grain size, and L_{ex} is the exchange length. For very small grains, the ferromagnetic exchange interaction forces the magnetic moments to align parallel to each other. Thus, the effective anisotropy will be an average over several grains and will be reduced in magnitude [10]. When the grain size D is smaller than the exchange length L_{ex}, the effective anisotropy provided from magnetocrystalline anisotropy is very small value ($\langle K \rangle$) (by Eq. (2)). From TEM analysis, the average grain size of the FeCoHfO film (D_{FeCo}) is 2–5 nm (see Figs. 1(b)–1(c)). The exchange length of FeCo phase ($L_{ex\text{-}\mathrm{FeCo}}$) is about 32 nm [11]. The magnetocrystalline anisotropy of the investigated multilayer films was calculated to be a very small value around 0.61 kJ/m^3.

In this case, magneto-elastic anisotropy plays an important role in magnetic anisotropy. The magneto-elastic anisotropy can be described as follows [12],

$$K_\sigma = -\frac{3}{2}\lambda_S \cdot \sigma \tag{3}$$

where λ_S is the saturation magentostriction, and σ is the stress. It is revealed that the stress is reduced with the increase of the number of stacking layers (see Fig. 2). With the variation of the stacking levels, the anisotropic field and stress exhibit a similar trend, which strongly indicates that the inner stress is associated with the magnetic anisotropy in the FeCoHfO/AlO_x multilayer films.

The eddy current loss is one of the main dissipation factors. The resistivity of the FeCoHfO/AlO_x multilayer films increases with the stacking levels (see Fig. 2). The resistivity is significantly dependent on the microstructure [13]. When the amorphous insulator (AlO_x) layer is inserted into the crystalline FeCoHfO films, the transport electrons are scattered by the amorphous region, giving rise to an enhancement of resistivity.

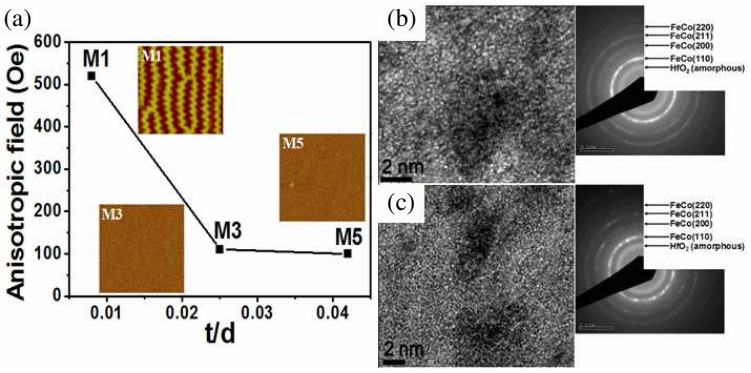

Figure 1: (a) Dependence of MFM images ($5 \times 5\,\mu m^2$) and anisotropic field of FeCoHfO/AlO_x multilayer films on the stacking levels, and high-resolution TEM images and selected area diffraction patterns of the FeCoHfO/AlO_x multilayer films with various stacking levels, (b) one layer, and (c) three layers.

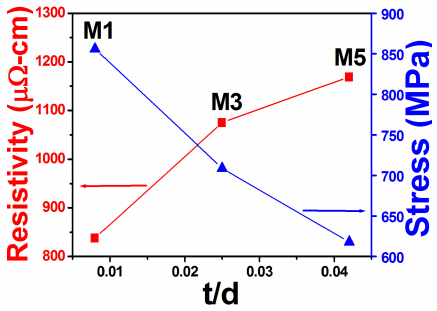

Figure 2: Dependence of the resistivity and stress of the FeCoHfO/AlO_x multilayer films as the function of t/d ratio.

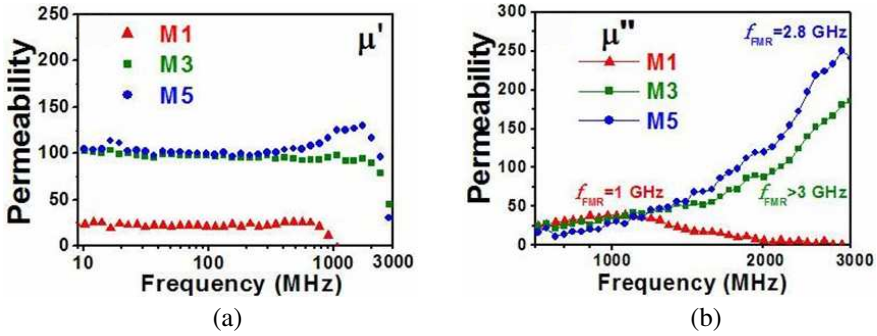

Figure 3: (a) real parts of complex permeability (μ') and (b) imaginary parts of complex permeability (μ'') of FeCoHfO/AlO_x multilayer films with various stacking levels measured along the hard axis. The stacking levels are one layer, three layers and five layers.

With respect to μ' of samples $M1$–$M5$ (see Fig. 3(a)), the stripe domain was observed in samples $M1$, and therefore the permeability of $M1$ is expected to be relatively lower than those of $M3$ and $M5$.

The increasing permeability (μ') with the stacking layers can be attributed to the enhancement of resisitivity and reduction of anisotropy field. Fig. 3(b) shows the imaginary part of complex permeability (μ'') for FeCoHfO/AlO_x multilayer films with various stacking levels. When the stacking level increases from three to five layers, the H_K is slightly decreased (see Fig. 1(a)). Hence the sample $M3$ exhibited ferromagnetic resonance frequency larger than 3 GHz. The ferromagnetic resonance frequency of sample $M5$ with only 2.8 GHz was lower than that of sample $M3$.

In summary, the sample $M3$ exhibited excellent high frequency and electrical resistivity properties. The resistivity of sample $M3$ was over 1000 μΩcm. The permeability (μ') of sample $M3$ was around 100 at 100 MHz, and the ferromagnetic resonance frequency exceeded 3 GHz.

4. CONCLUSIONS

Soft magnetic FeCoHfO/AlO_x multilayered films with favorable high frequency magnetic properties were successfully deposited by dc sputtering. A significant reduction of effective uniaxial anisotropic field was observed when the number of layers reached five. The influence of stacking levels on the microstructure, stress, magnetic and electrical properties and high-frequency characteristics was investigated. The multilayer structures reduce the stress in the FeCoHfO/AlO_x samples, and the decreasing stress leads to the lower anisotropic field. The suitable anisotropic field obviously enhances the ferromagnetic resonance frequency in FeCoHfO thin films. The ferromagnetic resonance frequency of sample $M3$ is enhanced in excess of 3 GHz, with permeability around 100 at 100 MHz and high electrical resistivity $\rho \sim 1074\,\mu\Omega$cm. It is demonstrated that the FeCoHfO/AlO_x multilayered structure possesses potential application in high-frequency electromagnetic devices.

REFERENCES

1. Korenivski, V., "GHz magnetic film inductors," *Journal of Magnetism and Magnetic Materials*, Vol. 215, 800–806, 2000.
2. Yamaguchi, M., K. Suezawa, K. I. Arai, Y. Takahashi, S. Kikuchi, Y. Shimada, W. D. Li, S. Tanabe, and K. Ito, "Microfabrication and characteristics of magnetic thin-film inductors in the ultrahigh frequency region," *Journal of Applied Physics*, Vol. 85, No. 11, 7919–7922, 1999.
3. Li, W. D., Y. Q. Sun, and C. R. Sullivan, "High-frequency resistivity of soft magnetic granular films," *IEEE Transactions on Magnetics*, Vol. 41, No. 10, 3283–3285, 2005.
4. Li, S., Z. G. Huang, and J. G. Duh, "Ultrahigh-frequency ferromagnetic properties of FeCoHf films deposited by gradient sputtering," *Applied Physics Letters*, Vol. 92, No. 9, 2008.
5. Li, S., Z. R. Yuan, and J. G. Duh, "High-frequency ferromagnetic properties of as-deposited FeCoZr films with uniaxial magnetic anisotropy," *Journal of Physics D: Applied Physics*, Vol. 41, No. 5, 2008.
6. Ohnuma, S., H. Fujimori, S. Mitani, and T. Matsumoto, "High-frequency magnetic properties in metal-nonmetal granular films," *Journal of Applied Physics*, Vol. 79, No. 8, 5130–5135, 1996.
7. Li, S., J. G. Duh, and C. N. Liao, "High-frequency ferromagnetic inductors covered by as-deposited FeCoAlO films with stress-induced uniaxial anisotropy," *Thin Solid Films*, Vol. 516, No. 21, 7748–7752, 2008.
8. Acher, O., C. Boscher, B. Brulé, G. Perrin, N. Vukadinovic, G. Suran, and H. Joisten, "Microwave permeability of ferromagnetic thin films with stripe domain structure," *Journal of Applied Physics*, Vol. 81, No. 8, 4057–4059, 1997.
9. Herzer, G., "Grain-size dependence of coercivity and permeability in nanocrystalline ferromagnets," *IEEE Transactions on Magnetics*, Vol. 26, No. 5, 1397–1402, 1990.
10. Thomas, S., S. H. Al-Harthi, D. Sakthikumar, I. A. Al-Omari, R. V. Ramanujan, Y. Yoshida, and M. R. Anantharaman, "Microstructure and random magnetic anisotropy in Fe-Ni based nanocrystalline thin films," *Journal of Physics D: Applied Physics*, Vol. 41, No. 15, 155009, 2008.
11. Sun, N. X., Q. F. Xiao, and B. York, "Stress, microstructure, and magnetic softness of high saturation magnetization (B-s) FeCoN films," *Journal of Applied Physics*, Vol. 97, No. 10, 10F906, 2005.
12. Cullity, B. D., *Introduction to Magnetic Materials*, 2nd Edition, Wiley-IEEE Press, 2008.
13. Ikeda, K., K. Kobayashi, and M. Fujimoto, "Multilayer nanogranular magnetic thin films for GHz applications," *Journal of Applied Physics*, Vol. 92, No. 9, 5395–5400, 2002.

A Novel Method to Solve the Complex Transcendental Equation for the Permittivity Determination in Short-circuited Line

Changying Wu, **Jianzhou Li**, **Gao Wei**, **and Jiadong Xu**
School of Electronic Information, Northwestern Polytechnical University
Xi'an 710129, China

Abstract— The precise permittivity determination of dielectric materials has been a very important task for ever-increasing microwave and millimeter-wave applications. For these reasons, various microwave techniques, each with its unique advantage and constraints, are introduced to characterize the electrical properties of materials. Owing to its relative simplicity, broad frequency coverage and higher accuracy, short-circuited line method, a type of non-resonant method, is widely utilized for characterization of materials. However, obtaining the electrical permittivity from the experimental measurements requires solving a transcendental equation of the form $(\tanh z)/z = c$ on the complex plane, where c is obtained experimentally. In solving these transcendental equations, iterative numerical methods are employed, of which the more commonly used is the Nowton-Raphson method. However, the main problem is that the transcendental equation has many roots, and it is difficult for its solution to converge to the correct value unless a very good initial guess is provided using some extra approach. In this presentation, a mathematical procedure is proposed which combines contour integral method, full-label triangles method, and simplex method for solving the transcendental equation on the complex plane which arises in the short-circuited line method. Although this equation possesses infinite solutions, only one of them is physical. Before deciding which of the solutions is the physical one it is better to find all possible permittivity in the given range. In our procedure, a formula of contour integral is used to determine the root number of the transcendental equation in the given range after the singularities are eliminated. And the equation is solved by simplex method from the initial values found by full-label triangles method. The main advantage of this procedure is that all roots can be solved only one time. The inherent ambiguity in the transcendental equation is avoided with the aid of measurement results at adjacent frequency. By using this procedure, a precise characterization of the complex permittivity is possible, thus overcoming some limitations of previous methods. Simulation and measurement of reference material have been carried out to validate the method.

1. INTRODUCTION

Two kinds of microwave techniques, resonant method and non-resonant method, have been widely utilized to characterize the permittivity of dielectric at microwave and millimeter wave band [1]. In the non-resonant method, the permittivity is calculated from the scattering parameters of a transmission line in which the specimen is placed. Short-circuited line method, a type of non-resonant method, is widely used owing to its relative simplicity, broad frequency coverage and higher accuracy. However, obtaining the electrical permittivity from the experimental measurements requires solving a transcendental equation on the complex plane [2].

Various methods have been used to solve the complex transcendental equation, such as: one-dimensional techniques for low-loss materials [3], chart method [4], linear equation approximation [5], Newton-Raphson method [6], Kuhn's algorithm [7], and simplex method [8]. Among these methods, Newton-Raphson method, Kuhn's algorithm, and simplex method can achieve more precision than others. However, Newton-Raphson method and simplex method need initial value first, and only converge to local optimal point. Although Kuhn's algorithm can find all zeros, it is complex to program.

In this paper, simplex method is introduced to solve complex transcendental equation. And a method which is easy to program is used to find all initial points one time. One disadvantage of this method is it consumes a tiny long time compared with other precision method. But the difference of time consumption is hard to be discovered.

2. FUNDAMENTAL THEORY

2.1. Derivation of the Equation

The specimen with the thickness of l_1 is placed at the end of a shorted waveguide as shown in Fig. 1. And the distance between the shorted plane and the reference plane is l_0. If the measurement

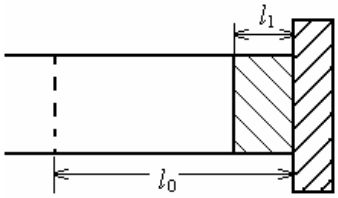

Figure 1: Schematic of shorted waveguide method.

reflection coefficient is Γ_1, the reflection coefficient at the interface of air and the specimen is

$$\Gamma_L = \Gamma_1 \exp\left[\mathrm{j}2\beta_0\left(l_0 - l_1\right)\right] \tag{1}$$

where β_0 is the phase factor of mode TE10. l_0 can be deduced from φ_0, the phase of reflection coefficient of empty shorted waveguide.

$$l_0 = \frac{\pi - \varphi_0}{2\beta_0} \tag{2}$$

Therefore, the input impedance at the interface of air and the specimen is

$$Z_L = Z_0 \frac{1+\Gamma_L}{1-\Gamma_L} \tag{3}$$

Alternately, the specimen filled in the waveguide is considered as a lossy transmission line. So the input impedance is also expressed as

$$Z_L = Z_1 \mathrm{th}(\gamma_1 l_1) \tag{4}$$

where $\gamma_1 = \alpha_1 + \mathrm{j}\beta_1$ and $Z_1 = \mathrm{j}\omega\mu_0/\gamma_1$ is the propagation constant and characteristic impedance respectively. Eq. (3) equals Eq. (4), so

$$\frac{\mathrm{th}(\gamma_1 l_1)}{\gamma_1 l_1} = \frac{1}{\mathrm{j}\beta_0 l_1}\frac{1+\Gamma_L}{1-\Gamma_L} \tag{5}$$

The right part of the equation is measurable. Therefore the permittivity can be solved if the γ_1 is get from the above equation. Let right part of Eq. (5) be A and $z = \gamma_1 l_1$, the equation is simplified to

$$\frac{\mathrm{th}(z)}{z} = A \tag{6}$$

In order to eliminate the singular points of Eq. (6), the two parts of the equation is multiplied by $z(\mathrm{e}^{2z}+1)$. Thus, the equation changes into

$$f(z) = (Az-1)\mathrm{e}^{2z} + Az + 1 = 0 \tag{7}$$

2.2. Number of Roots

Equation (7) has infinite roots in the complex plane. Only one of them is physical. And several of them are the possible ones. Therefore, the possible range of z or γ_1 is derived from the range of possible permittivity. Let the possible range of z in complex be D. Obviously, $f(z)$ is an analytic function in D. Let L be the simple closed curve around D. And L does not have zero of $f(z)$. Process contour integral along L [9], and let

$$s^k = \frac{1}{2\pi\mathrm{j}} \oint_L z^k \frac{f'(z)}{f(z)} \mathrm{d}z \tag{8}$$

so,

$$s^k = \sum_{p=1}^{n} \xi_p^k \tag{9}$$

where ξ_p, $p = 1, 2, \ldots, n$ are zeros of $f(z)$ in D. The number of roots n of $f(z)$ in D can be deduced from Eqs. (9) and (10) if k equals 0.

$$n = \frac{1}{2\pi\mathrm{j}} \oint_L \frac{f'(z)}{f(z)} \mathrm{d}z \tag{10}$$

2.3. Initial Values

Full-label triangle method is used to find the initial values. To begin with it, triangulation is applied in the possible domain D first. Then, $f(z)$ is calculated at the vertexes of the triangles, and the phase of $f(z)$ is confined in $(-\pi, \pi]$. Label the vertexes by

$$L(z) = \begin{cases} 1, & -\pi/3 \le \arg f(z) \le \pi/3 \\ 2, & \pi/3 < \arg f(z) \le \pi \\ 3, & -\pi < \arg f(z) \le -\pi/3 \end{cases} \tag{11}$$

A triangle is full labeled if the labels of three vertexes are 1, 2, and 3 respectively. $f(z)$ is the mapping from complex plane Z of z into W. Complex plane W is divided into three equal sectors by $L(z)$. The label $L(z)$ of z in Z is determined by which sector that $W = f(z)$ is located in W. The mappings in W of the three vertexes of full label triangles are surround the origin and distributed in the three vectors. Because the preimage of the origin in W is the zero of $f(z) = 0$, there must have zeros of $f(z) = 0$ near the full-label triangles. If the number of full-label triangle in D is less than the number of zero n, that means there are at least two zeros near one full-label triangle. For this reason, triangulation should be refined until the number of full label triangle equals n.

2.4. Determining the Permittivity

The complex transcendental equation is solved by simplex method from the initial values, n full-label triangles [8]. Simplex method is a searching method using reflection, contraction, and expansion to optimizing the objective function. Until the standard deviation of objective function of three vertexes of the full-label triangles is less than a small value to obtain a certain precision, the mean of the three vertexes of the full label triangles is used as the root of $f(z) = 0$. Then, the permittivity is got from z or γ_1.

$$\varepsilon_r = \varepsilon_r' - \mathrm{j}\varepsilon_r'' = \left(\frac{\lambda_0}{\lambda_c}\right)^2 - \left(\frac{\lambda_0}{2\pi}\right)^2 \gamma_1^2 \tag{12}$$

The simplex method can found n roots in the possible domain. However, only one root is the real value. Others are caused by the phase ambiguity. The roots which are not physical change more rapid versus frequency than the physical one [5]. Therefore, the physical one can be distinguished by the measurement result at near frequency.

3. SIMULATION AND EXPERIMENT RESULT

A simulation and experiment result are used to verify the validity and practicability of the method presented above. In the simulation, a specimen is deposited in the end of a BJ100 waveguide. The thickness of the specimen is 4 mm, the relative permittivity is $4.4(1 - \mathrm{j}0.02)$, and the simulation frequency band is $9 \sim 11$ GHz. The reflection coefficients of empty short waveguide and dielectric-filled short waveguide are calculated theoretically. Assuming the possible permittivity range is $1 \sim 50$, the permittivity and loss tangent is calculated using the two reflection coefficient and shown in Fig. 2. It is seen that there are two sets of values. One set of values remain stable versus frequency, and other set of values bend obviously. So, the stable set of values is affirmed physical. At 10 GHz, the value of the stable curve is $4.3999999969(1 - \mathrm{j}0.0200000002)$ which is consistent with theoretical value.

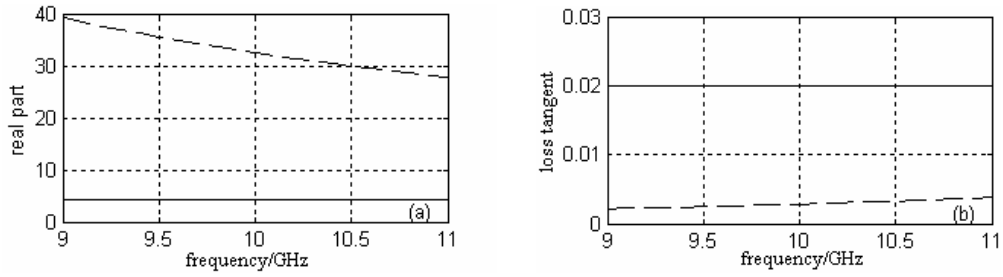

Figure 2: The calculated permittivity.

A piece of PTFE with thickness of 4.83 mm is measurement at X band by six-port equipment. And its permittivity is calculated by the measurement coefficient with the method mentioned above. The result is 2.04, which is consistent with the value in literature.

4. CONCLUSION

A numerical method for complex transcendental equation which has to be solved in the permittivity determination in short-circuited line has been presented. The method can solve all the roots in one time without the need of initial values and is easy to program. The validity and practicability is verified by simulation and measurement results.

ACKNOWLEDGMENT

This work was supported by Aoxiang Plan of Northwestern Polytechnical University.

REFERENCES

1. Tang, Z. X. and B. Zhang, "The measurement method for permittivity and permeability of medium at microwave frequencies," *Acta Metrologica Sinica*, Vol. 28, No. 4, 383–387, 2007.
2. Long, Y. L., H. Y. Jiang, and X. L. Long "Study on the numerical method for complex transcendental equations in electromagnetic theory," *Journal of Microwaves*, Vol. 15, No. 2, 179–184, 1999.
3. Muqaibel, A. H. and A. Safaai-Jazi, "A new formulation for characterization of materials based on measured insertion transfer function," *IEEE Transactions on Microwave Theory and Techniques*, Vol. 51, No. 8, 1946–1951, 2003.
4. Iglesias, T. P., A. Seoane, and J. Rivas, "An algorithm for solving roberts-von hippel equation: Separation of close solutions," *IEEE Transactions on Instrumentation and Measurement*, Vol. 42, No. 3, 760–763, 1993.
5. Iglesias, T. P., A. Seoane, and J. Rivas, "Improved method for suppression of ambiguity in measurements of permittivity in low and high loss materials with short-circuited line technique," *Electronics Letters*, Vol. 29, No. 4, 360–362, 1993.
6. Iglesias, T. P. and S. M. Pereira, "Distributed parameters for low-frequency dielectric characterization of liquids with open-ended coaxial cell," *IEEE Transactions on Instrumentation and Measurement*, Vol. 55, No. 1, 176–179, 2006.
7. Gao, L. and B. Yang, "An efficient implementation of Kuhn's algorithm," *Journal of Harbin Shipbuilding Engineering Institute*, Vol. 14, No. 1, 66–73, 1993.
8. Jia, J. L., "Study on application of simplex method in measurement of soil's complex permittivity," *Journal of Sichuan University (Natural Science Edition)*, Vol. 42, No. 6, 1185–1188, 2005
9. Long, Y. L., X. L. Wen, and C. F. Xie, "An implementation of a root finding algorithm for transcendental functions in a complex plane," *Journal on Numerical Methods and Computer Applications*, No. 2, 88–92, 1994.

Adaptor Calibration Using a Matched Load and an Adjustable Shorter without Specified Phases

Changying Wu, **Kuisong Zheng**, **Gao Wei**, **and Jiadong Xu**
School of Electronic Information, Northwestern Polytechnical University, Xi'an 710129, China

Abstract— The vector network analyzer (VNA) has been widely applied in the measurement of microwave devices with wide frequency bandwidths. Particularly, the measurement of the complex reflection coefficients of waveguide devices is its important applications. Due to connecting the devices to be measured to the VNA with a coaxial-to-waveguide adaptor, the systemic error caused by the defect of the coaxial-to-waveguide adaptor will be introduced. For solving the problem, the calibration of the coaxial-to-waveguide adaptor is needed by connecting a series of known standard components to the measurement system. Subsequently, the systemic error can be obtained by analyzing the measurement results of the known standard components. The traditional calibration method uses three standard components, i.e., a load, a short circuit, and an offset short with known phase. However, with the traditional calibration method, the exact location of the short plane is difficult to be determined at the range of millimeter wave frequencies. In this paper, a novel calibration procedure using a matched load and an adjustable shorter with several unspecified phases is proposed to reduce the systemic error caused by the adaptor. The advantage of this method is only to define one shorter plane as reference plane. During the calibration process, the position of the piston is unnecessary to be recorded. More offset shorts are used; more accurate de-embedding effect can be get. The proposed calibration method is especially fitted to the system calibration at the range of millimeter wave frequencies, where the accuracy of the system calibration is very sensitive to the position of standard short plane. The measured results show that the module of corrected S_{11} of a shorter is less than 0.1 dB with linear phase delay and the corrected S_{11} of a matched load is below -40 dB. The results are much more accurate than the raw readings, 1.3 dB and -15 dB respectively, before the adaptor calibration. It is also shown that the technique is resistant to the error of the adjustable shorter position and is easy to implement.

1. INTRODUCTION

Calibration is an important part in the procedure of microwave measurement. A coaxial-to-waveguide adaptor has to be used when measuring a waveguide load with a VNA, because the VNA has only coaxial ports. The phase shift and reflection of coaxial-to-waveguide adaptor vary with operating frequency. So the error caused by adaptor has to be removed by calibration before measurement. The purpose of calibration is to resolve the S-parameter of two-port network, and then the reflection of waveguide load is deduced form the measurement result of VNA.

Theoretically, the solution of S-parameter of two-port network is based on three standard components, i.e., a shorter, an open circuit, and a matched load. In practice, the open circuit is replaced by an offset shorter because waveguide open circuit doesn't exist. However, the position of an adjustable shorter is difficult to be determined accurately at high frequency. In this paper, a calibration method which doesn't need the phase information of an adjustable shorter is presented. The method uses a matched load and an adjustable shorter with at least three unspecified phases, and one of position of adjustable shorter is used as a reference plane. That means the scale on the piston need not to be read. In the calibration, based on the reflection coefficients of adjustable shorter are in the same circumference, the S-parameter of adaptor is calculated. This calibration method is easy to implement, and the validity was verified by experiment.

2. THEORITICAL ANALYSIS

The configuration of reflection coefficient measurement of waveguide load by VNA is shown in Fig. 1. In this measurement, the reflection coefficient at waveguide load is Γ_L, the reflection coefficient measured by VNA is Γ_{in}, and the S-parameter of coaxial-to-waveguide is symboled by S, as described in Fig. 1.

The relation between reflection coefficients of two ports of a two-port network is:

$$\Gamma_{\text{in}} = S_{11} + \frac{S_{12}S_{21}\Gamma_L}{1 - S_{22}\Gamma_L} \tag{1}$$

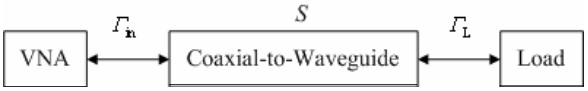

Figure 1: Configuration of calibration measurement.

By connecting a matched load, S_{11} can be obtained by

$$S_{11} = \Gamma_{\text{in,match}} \tag{2}$$

Connecting an adjustable shorter to the adaptor, the reflection coefficient at the load is expressed as

$$\Gamma_{L,\text{short},i} = \frac{(\Gamma_{\text{in,short},i} - \Gamma_{\text{in,match}})}{(\Gamma_{\text{in,short},i} - \Gamma_{\text{in,match}})\, S_{22} + S_{12}^2} \tag{3}$$

or

$$\Gamma_{L,\text{short},i} = \frac{A_i + jB_i}{(A_i + jB_i)\,(x_1 + jy_1) + x_2 + jy_2}$$

where i is the index of the position of the adjustable shorter, and $\Gamma_{L,\text{short},i}$ is the ith reflection coefficient at the adjustable shorter. A_i and B_i are real and imaginary parts of $\Gamma_{\text{in,short},i} - \Gamma_{\text{in,match}}$ which are measurable. x_1, y_1, x_2, and y_2 are real and imaginary parts of S_{22} and S_{12}^2 which need to be solved. As the module of reflection coefficient of adjustable shorter is equal to unity, Eq. (3) can be replaced as

$$\left(A_i^2 + B_i^2\right)\left(x_1^2 + y_1^2\right) + \left(x_2^2 + y_2^2\right) + 2A_i\,(x_1x_2 + y_1y_2) + 2B_i\,(x_1y_2 - y_1x_2) = A_i^2 + B_i^2 \tag{4}$$

Let the first position of adjustable shorter be a reference plane. Eq. (3) becomes

$$\frac{A_1 + jB_1}{(A_1 + jB_1)\,(x_1 + jy_1) + x_2 + jy_2} = -1 \tag{5}$$

Substituting Eq. (5) into Eq. (4) and eliminating x_2 and y_2, one get

$$\mathbf{a}_1\left(x_1^2 + y_1^2\right) + \mathbf{a}_2x_1 + \mathbf{a}_3y_1 = \mathbf{b} \tag{6}$$

where $\mathbf{a}_1$, $\mathbf{a}_2$, $\mathbf{a}_3$, and $\mathbf{b}$ can be expressed by A_i and B_i which are measurable. Eq. (6) has two unknowns, therefore $\mathbf{a}_1$, $\mathbf{a}_2$, and $\mathbf{a}_3$ must be correlated. Provided that

$$c_1\mathbf{a}_1 + c_2\mathbf{a}_2 = \mathbf{a}_3 \tag{7}$$

Eq. (6) is replaced as

$$\mathbf{a}_1\left(x_1^2 + y_1^2 + c_1y_1\right) + \mathbf{a}_2\,(x_1 + c_2y_1) = \mathbf{b} \tag{8}$$

From the expression of $\mathbf{a}_1$, $\mathbf{a}_2$, and $\mathbf{b}$, it can be deduced that

$$\left[\ \mathbf{a}_1 \quad \mathbf{a}_2\ \right] \cdot \begin{bmatrix} 1 \\ -1 \end{bmatrix} \equiv \mathbf{b} \tag{9}$$

One get

$$x_1^2 + y_1^2 + c_1y_1 \equiv 1, \quad x_1 + c_2y_1 \equiv -1 \tag{10}$$

Then, S_{22} and $S_{12}S_{21}$ can be deduced from Eq. (10) and Eq. (5). Finally, Γ_L is calculated by S-parameter and Γ_{in}

$$\Gamma_L = \frac{\Gamma_{\text{in}} - S_{11}}{S_{12}S_{21} + \Gamma_{\text{in}}S_{22} - S_{11}S_{22}} \tag{11}$$

3. CALIBRATION PROCEDURE

Based on the theoretical analysis in Section 2, the calibration procedure is:

1). Connect a matched load, and measure the $\Gamma_{\text{in,match}}$ which is equal to S_{11};
2). Connect adjustable shorter, rotate it, and measure the $\Gamma_{\text{in,short},i}$ at different position, $i = 1, 2, \ldots, n$, $n \geq 3$;
3). Calculate $\mathbf{a}_1$, $\mathbf{a}_2$, $\mathbf{a}_3$, c_1, and c_2 from Eqs. (7)–(9);
4). Calculate S_{22} and $S_{12}S_{21}$ from Eq. (5) and Eq. (10);
5). Calculate Γ_L from Eq. (11).

4. EXPERIMENT

The validity is verified by experimental result measured by VNA (Agilent E8363E) from 8 GHz to 12 GHz. The coaxial-to-waveguide adaptor is connected to port 1 or VNA, and the dimension of the waveguide is 22.86 mm × 10.16 mm. Using the proposed method, the reflection coefficients of a matched load and an adjustable shorter are measured and calculated. More than 10 different positions of adjustable are used. And the first of the positions is set as the reference plane. The S_{11} after calibration and raw measuration S_{11} before calibration of a shorter and a matched load are shown in Fig. 2. It can be seen that the module of corrected S_{11} of a shorter is less than 0.1 dB compared with the raw readings of 1.3 dB and the calibrated S_{11} of a matched load is below −40 dB compared with the raw readings of 40 dB. The results are much more accurate than the raw readings before the adaptor calibration.

Theoretically, reflection data of only three positions of adjustable shorter are enough to calibrate the adaptor. Calibration error caused by measurement will be reduced and calibration will perform better if data of more positions are used. Therefore, least-squares method is used to solve Eq. (7). The maximum S_{11} of a shorter after calibration decreases if the number of position used is increasing shown in Fig. 3. If the number exceeds 8, the S_{11} becomes very low. In practical, the number of position can be easily obtained by just pulling and pushing the piston.

The performance of this calibration is also revealed by the tangent method used in characterizing the discontinuous of transmission line. The discontinuous part can be represented as an ideal transformer with ratio N and the transformer is θ_1 and θ_2 away from the reference planes of the two port. When an adjustable shorter is connected to port 2, the electric length ϕ_2 from the reference plane of port 2 to short plane and the electric length ϕ_1 from the reference plane of port 1 to node position have a relation from which the ratio N can be obtained. The curves of ϕ_1 versus ϕ_2 of the adaptor before and after calibration are shown in Fig. 4. Calculated from the $\phi_1 - \phi_2$ curve, the ratio N of the adaptor before and after calibration are 1.79 and 1.09, respectively.

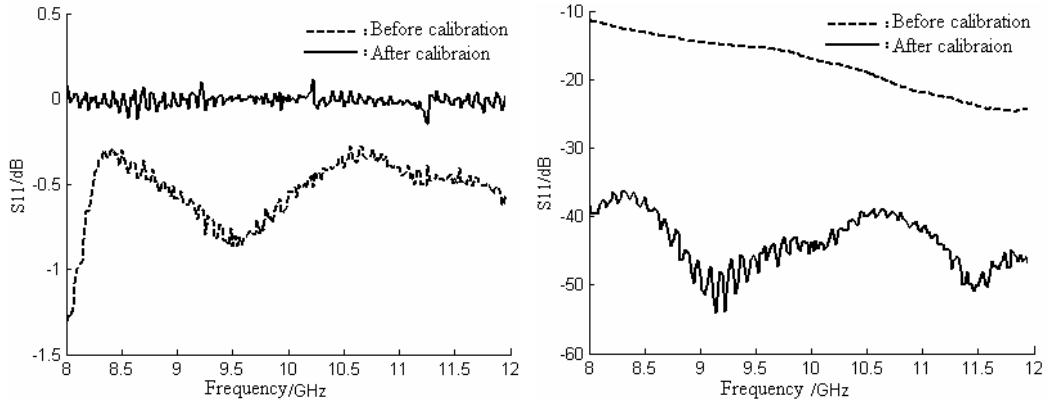

(a) S_{11} of a shorter (b) S_{11} or a matched load

Figure 2: Module of S_{11} after and before calibration.

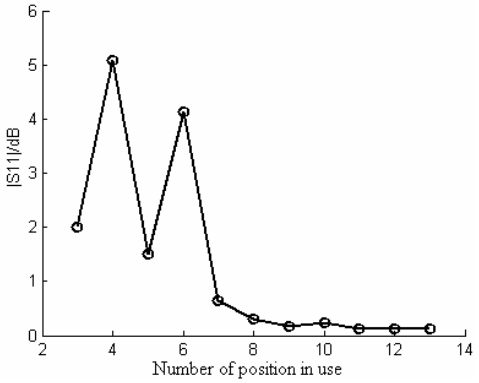

Figure 3: The maximum S_{11} of a shorter after calibration versus number of position in use.

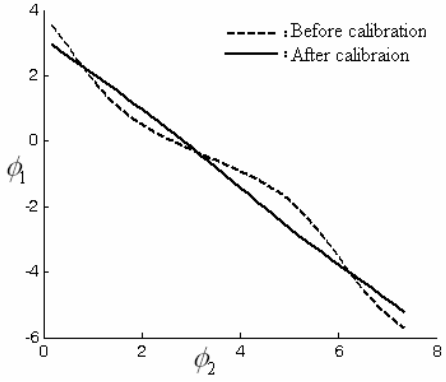

Figure 4: ϕ_1-ϕ_2 curve.

5. CONCLUSION

An adaptor calibration method with only a matched load and an adjustable shorter has been presented. During the calibration procedure, it is very flexible to pull and push the piston because its position need not to be recorded, thus the error is eliminated. And the performance of the calibration can be improved by using the data of more of the positions which is easy to implement. Another advantage of this method is that the computation formulas are concise. The validity is verified by measurement results.

ACKNOWLEDGMENT

This work was supported by Aoxiang Plan of Northwestern Polytechnical University.

REFERENCES

1. Huang, C. C. and H. C. Lin, "A novel calibration algorithm with unknown line-series-shunt standards for broadband S-parameter measurement," *IEEE Transactions on Instrumentation and Measurement*, Vol. 57, No. 5, 891–895, 2008.
2. Monzo-Cabrera, J., J. L. Pedreno-Molina, A. Lozano-Guerrero, and A. Toledo-Moreo, "A novel design of a robust ten-port microwave reflectometer with autonomous calibration by using neural networks," *IEEE Transactions on Microwave Theory and Techniques*, Vol. 56, No. 4, 946–961, 2008.
3. Liu, Z. Y. and R. M. Weikle, "A reflectometer calibration method resistant to waveguide flange misalignment," *IEEE Transactions on Microwave Theory and Techniques*, Vol. 54, No. 6, 2447–2452, 2006.
4. Qiao, L. and S. P. Yeo, "Correction of adaptor errors in reflection-coefficient measurements of waveguide devices," *Singapore ICCS'94 Conference Proceedings*, No. 3, 949–951, 1994.
5. Stevens, N. and L. Matens, "Sensitivity study on the measurement of the reflection coefficient in a short-circuited rectangular waveguide filled with a liquid," *Proceedings of the 18th IEEE Instrumentation and Measurement Technology Conference*, No. 3, 1747–1749, 2001.

A Highly Miniaturized Broadband on-chip Impedance Transformer Employing Periodically Arrayed Ground Structure on Silicon RFIC

Jeong-Gab Ju, **Young-Bae Park**, **Bo-Ra Jung**,
Jang-Hyeon Jung, **Suk-Youb Kang**, **and Young Yun**
Department of Radio Sciences and Engineering, Korea Maritime University, Korea

Abstract— In this work, using a coplanar waveguide employing Periodically Arrayed Ground Structure(PAGS) on silicon RFIC, a highly miniaturized and broadband on-chip impedance transformer was developed for application to low impedance matching in broadband. Its size was $0.01\,\mathrm{mm}^2$ on silicon substrate, which was 6.99% of the one fabricated by conventional coplanar waveguide. The transformer showed a good RF performance from 1 to 40 GHz.

1. INTRODUCTION

With the evolution of silicon CMOS device process technology, demands for fully-integrated CMOS RFIC, including all matching components, have increased in the wireless communication systems market [1]. However, bulky passive components such as conventional impedance transformers and dividers have been fabricated outside of RFIC owing to their large sizes [2] and most microwave circuits and antennas use some form of impedance transformers, and in many applications wide band transformers are required [9]. To solve this problem, transmission line employing periodic structure on GaAs and silicon substrate were reported [6, 7].

In this paper, a coplanar waveguide employing Periodically Arrayed Ground Structure (PAGS) [8] was fabricated on silicon substrate, and its basic characteristic was investigated. The coplanar waveguide employing PAGS exhibited a wavelength much shorter than the conventional one. In addition, using the coplanar waveguide employing PAGS, a highly miniaturised on-chip impedance transformer was developed for silicon RFIC applications.

2. STRUCTURE OF COPLANAR WAVEGUIDE EMPLOYING PAGS

We proposed CPW (Coplanar waveguide) employing PAGS [8], which is shown in Fig. 1. It shows a top view and corresponds to a cross-sectional view of the CPW employing PAGS. As shown in Fig. 1, PAGS exists at the interface between the SiO_2 film and the silicon substrate, and it was electrically connected to top-side ground planes (GND planes) through the contacts. Therefore, PAGS was grounded through GND planes. As is well known, a conventional CPW without PAGS has only a periodical capacitance C_a per unit length, while the CPW employing PAGS has an additional capacitance, C_b as well as C_a, owing to PAGS. As shown in this figure, C_b is capacitance between the line and PAGS. Therefore, we can see that the CPW with PAGS exhibits much lower characteristic impedance (Z_0) and shorter guided-wavelength (λ_g) than conventional one, because Z_0 and λ_g are inversely proportional to the periodical capacitance, in other words, $Z_0 = (L/C)^{0.5}$ and $\lambda_g = 1/[f \cdot (LC)^{0.5}]$ [3, 4].

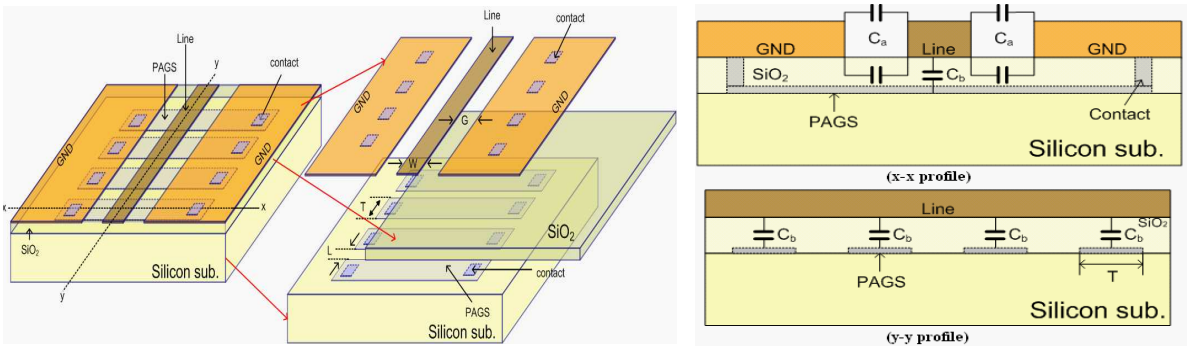

Figure 1: Structure of coplanar waveguide employing PAGS.

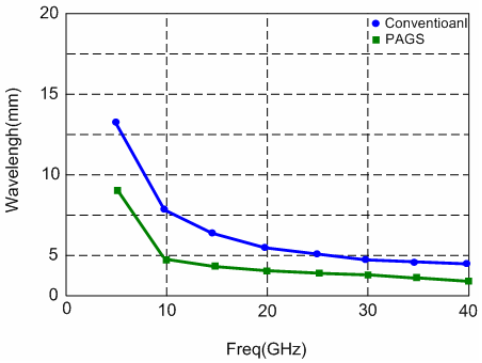

Figure 2: Wavelength of CPW employing PAGS and conventional one.

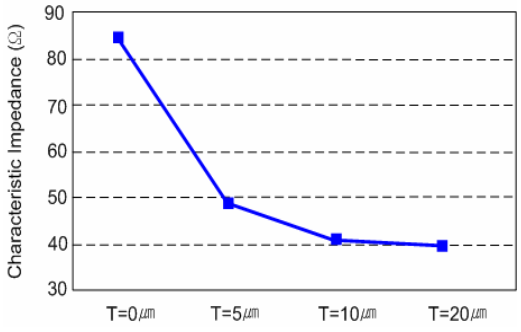

Figure 3: Characteristic impedance of the CPW with PAGS.

As shown in Fig. 2, the novel transmission line with PAGS exhibits a much shorter λ_g than the conventional one. The CPW was fabricated on a silicon substrate with a height of 600 mm. Fig. 3 shows the characteristic impedance the CPW employing PAGS. From Fig. 1, we can see that an increase of strip width 'T' results in an enhancement of periodical capacitance C_b owing to an increase in capacitive area. Therefore, as shown in Fig. 3, the characteristic impedance Z_0 of the CPW employing PAGS could be easily controlled by changing the strip width 'T', because Z_0 depends on the periodic capacitance of the transmission line. These results indicate that highly miniaturised passive components with various impedances can be realised using the CPW employing PAGS.

3. IMPEDANCE TRANSFORMER EMPLOYING CPW WITH PAGS

In this paper, using PAGS structure on silicon substrate, an impedance transformer was fabricated on silicon substrate. Fig. 4 shows a photograph of the single section $l/4$ impedance transformer employing a PAGS structure on a silicon substrate. The characteristic impedance Z_0 of the transformer is given by $Z_0 = (Z_{C_1} Z_{C_2})^{0.5}$ [3, 4], where Z_{C_1} and Z_{C_2} are the source and load impedance, respectively, as shown in Fig. 4. In this work, Z_{C_1} and Z_{C_2} are 50 and 28 Ω, respectively, and Z_0 is 37.5 Ω. For a centre frequency of 21 GHz, the length of the $l/4$ transformer, which was determined from Fig. 2, is 0.5 mm, and the line width W is 20 mm. Therefore, the size of the transformer is 0.01 mm^2, which is 6.99% the size of the transformer fabricated by a conventional CPW. The size comparison of the transformers is summarized in Table 1.

Figure 5 shows measured return loss S_{11} and insertion loss S_{21} of transformers, respectively. As shown Fig. 5 the return and insertion loss are −45 and −1.3 dB, respectively, at a centre frequency of 21 GHz. We can observe return loss values better than −11.5 dB from 1 to 40 GHz, and insertion

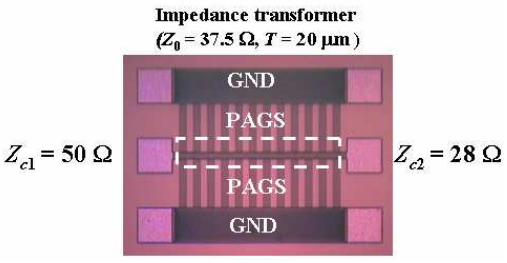

Figure 4: A photography of the impedance transformer of the CPW with PAGS.

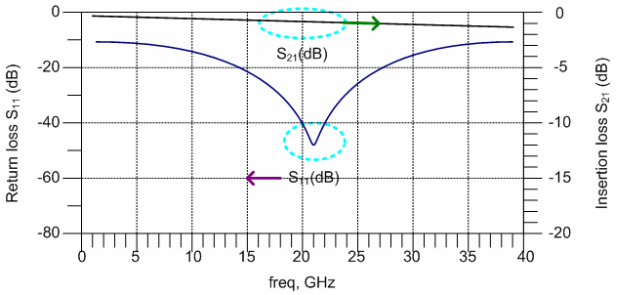

Figure 5: Measured return and insertion loss of the CPW with PAGS.

Table 1: Size of conventional CPW and PAGS on silicon substrate.

Distribution	W (μm)	$\lambda_g/4$ (mm)	Size (mm^2)
Conventional coplanar waveguide	130	1.1	0.143
PAGS	20	0.5	0.01

loss values better than −1.93 dB in the above frequency range, which mainly originate from a high conductivity of silicon substrate [1, 5].

4. CONCLUSIONS

The CPW employing PAGS showed a wavelength much shorter than the conventional one. The impedance transformer CPW employing PAGS showed good RF performance from 1 to 40 GHz, and its size was 0.01 mm^2, which is 6.99% of the conventional one. The characteristic impedance of the CPW employing PAGS was easily controlled by changing the strip width of PAGS. According to the results, it was found that the PAGS structure is a promising candidate for application to a development of highly miniaturized broaband on-chip passive components on Si RFIC.

ACKNOWLEDGMENT

This research was supported by the MKE (The Ministry of Knowledge Economy), Korea, under the ITRC (Information Technology Research Center) support program supervised by the NIPA (National IT Industry Promotion Agency) (NIPA-2009-C1090-0903-0007). This work was financially supported by the Ministry of Knowledge Economy (MKE) and the Korea Industrial Technology Foundation (KOTEF) through the Human Resource Training Project for Strategic Technology. This work was partly sponsored by KETI (Korea Electronics Technology Institute). This work was also partly supported by ETRI SoC Industry Promotion Center, Human Resource Development Project for IT SoC Architect.

REFERENCES

1. Zargari, M. and D. Su, "Challenges in designing CMOS wireless systems-on-a-chip," *IEICE Trnas. Electron.*, Vol. E90-C, 1142–1148, 2007.
2. Chongcheawchamnam, M., N. Siripon, and I. D. Robertson, "Design and performance of improved lumped distributed Wilkinson divider topology," *Electron. Lett.*, Vol. 37, No. 8, 501–503, 2001.
3. Pozar, D. M., *Microwave Engineering*, 2nd Edition, Chap. 8, Addison-Wesley, 1990.
4. Pozar, D. M., *Electronics Letters*, Vol. 45, No. 5, February 26, 2009.
5. Long, J. R., "Passive components for silicon RF and MMIC design," *IEICE Trans. Electron.*, Vol. E86-C, 1022–1031, 2003.
6. Yun, Y., "A novel microstrip line structure employing a periodically perforated ground metal and its application to highly miniaturized and low impedance passive components fabricated on GaAs MMIC," *IEEE Transactions on Microwave Theory and Technique*, Vol. 53, No. 6, 1951–1959, June 2005.
7. Cheung, T. S. D. and J. R. Long, "Shielded passive devices for silicon-based monolithic microwave and millimeter-wave integrated circuits," *IEEE Journal of Solid-State Cicuits*, Vol. 41, 1183–1200, May 2006.
8. Yun, Y., et al., "Miniaturized on-chip branch-line coupler employing periodically arrayed grounded-strip structure for application to silicon RFIC," *Microwave Journal*, to be published.
9. Bahl, I. J., "Broadband and compact impedance transformers for microwave circuits," *Microwave Magazine, IEEE*, Vol. 7, No. 4, 56–62, August 2006.

Highly Miniaturized On-chip 90° Hybrid Coupler Employing Transmission Line with Periodic Structure

Bo-Ra Jung, Young-Bae Park, Suk-Youb Kang, Jang-Hyeon Jung, Jeong-Gab Ju, and Young Yun
Department Radio Communication Engineering, Korea Maritime University, Republic of Korea

Abstract— In this study, we propose a highly miniaturize on-chip 90° Hybrid Coupler on radio frequency integrated circuit (RFIC), which was fabricated by a coplanar line employing periodically arrayed grounded-strip structure (PAGS). Using the coplanar waveguide employing PAGS, we can realized a miniaturized 90° Hybrid Coupler on Silicon RFIC. The 90° Hybrid Coupler exhibited good performances from 41.75 to 50 GHz, and its size was $0.46 \times 0.55\,\mathrm{mm}^2$, which is 37% of conventional one. The coplanar waveguide employing PAGS exhibited much shorter wavelength than conventional one. Using the coplanar waveguide employing PAGS, we fabricated a highly miniaturized 90° Hybrid Coupler on silicon substrate for U band RFIC applications.

1. INTRODUCTION

Nowadays, demands for fully integrated and miniaturized RFIC (Radio Frequency Integrated Circuits) have increased in wireless communication system. Especially, according to an evolution of silicon CMOS device process technology, fully integrated silicon ICs (Integrated Circuits) including RF and based-band block have been developed [1]. However, passive components such as coupler, divider and filters are fabricated in outside of ICs due to their bulky sizes, which have been a great obstacle to a realization of a fully-integrated silicon front-end design [10]. To solve this problem, short wavelength transmission line applicable to a development of miniaturized passive components on silicon substrate should be developed.

Using PBG (Photonic Band Gap) structure, a number of miniaturized passive components have been fabricated on GaAs and Teflon substrate to date [2, 3]. However, a short wavelength transmission line and miniaturized passive components on silicon substrate have not been studied yet, because a study on silicon passive components has been focused on a development of low loss structure such as PGS (Patterned Ground Shield) due to the high conductivity of silicon substrate [4].

In this study, in order to realize highly miniaturized passive components on silicon RFICs, we proposed a novel coplanar waveguide employing periodically arrayed grounded-strip structure (PAGS) that has much shorter wavelength than conventional structure. Using the coplanar waveguide employing PAGS, we can realized a highly miniaturized 90° Hybrid Coupler for U band silicon RFIC application.

2. A SHORT WAVELENGTH COPLANAR WAVEGUIDE EMPLOYING PAGS

Figure 1 shows a structure of the coplanar waveguide employing PAGS. As shown in Fig. 1, PAGS was inserted at the interface between SiO_2 film and silicon substrate, and it was electrically connected to top-side ground planes (GND planes) through the contacts. Therefore, PAGS was grounded through GND planes. As is well known, conventional coplanar waveguide without PAGS has only a periodical capacitance C_a (C_a is shown in Fig. 1) per a unit length, while the coplanar waveguide employing PAGS has additional capacitance C_b as well as C_b due to PAGS. As shown in Fig. 1, C_b is a additional capacitance between line and PAGS. In other words, a total capacitance (per unit length) of the coplanar waveguide employing PAGS corresponds to $C_a + C_b$, but, it corresponds to C_a for a conventional coplanar waveguide without PAGS. Therefore, the coplanar waveguide employing PAGS exhibits wavelength (λ_g) much shorter than conventional one, because λ_g is inversely proportional to the periodical capacitance, in other words, $\lambda_g = 1/[f \cdot (LC)^{0.5}]$ [11].

3. MEASURED RESULTS

Using the periodically arrayed grounded-strip structure (PAGS) on silicon substrate [9], we fabricateda highly miniaturized 90° hybrid coupler for U band silicon RFIC application. Fig. 2 shows power division, isolation and return loss characteristics of the 90° hybrid coupler employing PAGS. We can observe good power division characteristic from 41.75 to 50 GHz. Concretely, S_{21} and S_{31}

exhibit a value of −5.7 dB at 46 GHz. In a frequency range of 41.75–50 GHz, S_{21} and S_{31} show a value of -5.9 ± 0.5 and -5.5 ± 0.5 dB, respectively. Actually, a value of power division of the 90° hybrid coupler fabricated on Teflon substrate [6] is about -5 ± 0.5 dB, and the 90° hybrid coupler employing PAGS shows a loss higher 0.7 dB than conventional one, which originated from high conductivity of silicon substrate. Isolation characteristic (S_{41}) shows a value of −18.1 dB at 46 GHz, and a value of $-13 \sim -18.1$ dB in a frequency range of 41.75–50 GHz. All ports show the same return loss due to symmetry of the structure, and only S_{11} was plotted in Fig. 1. The S_{11} shows a value of −11.1 dB at 46 GHz, and lower than −10 dB in a frequency range of 41.75–50 GHz. Also, Fig. 2 also shows the phase division characteristic of the 90° hybrid coupler employing PAGS. The phase division shows a value of 90.1° at 46 GHz, and a value of $90 \pm 4.8°$ in a frequency range of 41.75–50 GHz.

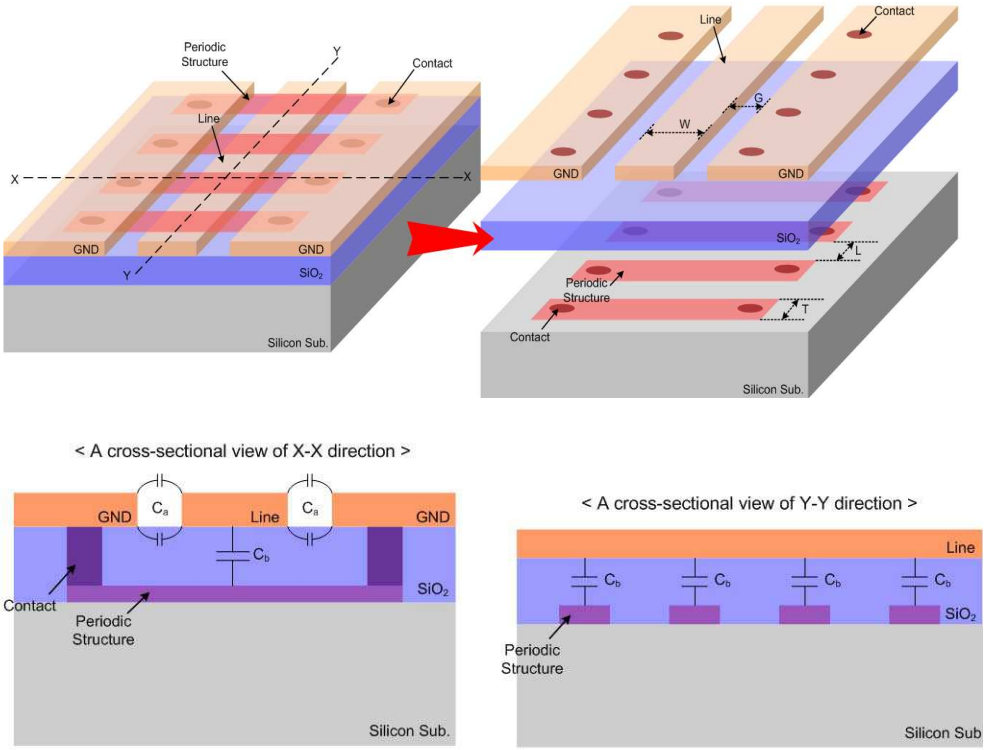

Figure 1: A structure of the coplanar waveguide employing PAGS.

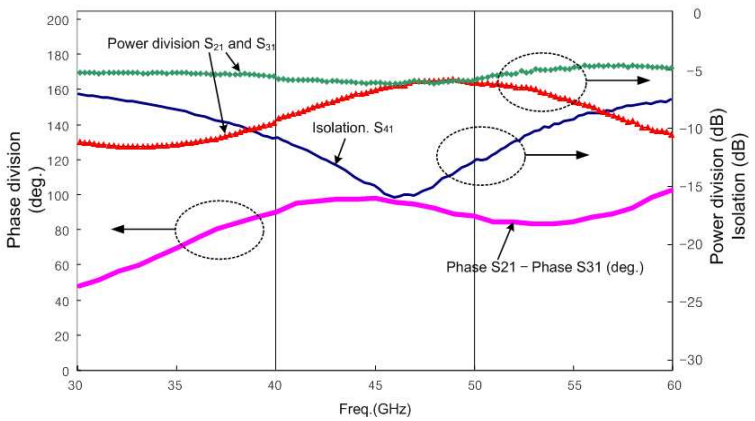

Figure 2: A measured RF characteristics of the hybrid coupler employing PAGS.

4. CONCLUSIONS

The coplanar waveguide employing PAGS exhibited much shorter wavelength than conventional one. Above all result, using coplanar waveguide employing PAGS, we can realize a highly miniaturized 90° hybrid coupler on silicon substrate for U band RFIC application. The novel 90° hybrid coupler shows good RF performance from 41.75 to 50 GHz and its size of the was $0.46 \times 0.55\,\mathrm{mm}^2$, which is 37% of conventional one. The coplanar waveguide employing PAGS exhibited much shorter wavelength than conventional one. Using the coplanar waveguide employing PAGS, we fabricated a highly miniaturized 90° Hybrid Coupler on silicon substrate for U band RFIC applications.

ACKNOWLEDGMENT

This research was supported by the MKE (The Ministry of Knowledge Economy), Korea, under the ITRC (Information Technology Research Center) support program supervised by the NIPA (National IT Industry Promotion Agency) (NIPA-2009-C1090-0903-0007). This work was financially supported by the Ministry of Knowledge Economy (MKE) and the Korea Industrial Technology Foundation (KOTEF) through the Human Resource Training Project for Strategic Technology. This work was partly sponsored by KETI (Korea Electronics Technology Institute). This work was also partly supported by ETRI SoC Industry Promotion Center, Human Resource Development Project for IT SoC Architect.

REFERENCES

1. Zargari, M. and D. Su, "Challenges in designing CMOS wireless systems-on-a-chip," *IEICE Trans. Electron.*, Vol. E90-C, No. 6, 1142–1148, Jun. 2007.
2. Yang, F. R., K. P. Ma, Y. Qian, and T. Itoh, "A UC-PBG structure and its applications for microwave circuits," *IEEE Trans. Microwave Theory Tech.*, Vol. 47, No. 8, 1509–1514, Aug. 1999.
3. Kim, C. S., J. S. Park, D. Ahn, and J. B. Lim, "A novel 1-D periodic defected ground structure for planar circuits," *IEEE Microwave Guided Wave Lett.*, Vol. 10, No. 4, 131–133, Apr. 2001.
4. Lin, Y. S., C. C. Chen, H. B. Liang, T. Wang, and S. S. Lu, "Characterization and modeling of pattern ground shield and silicon-substrate effects on radio-frequency monolithic bifilar transformers for ultra-wide band radio-frequency integrated circuit applications," *Jpn. J. Appl. Phys.*, Vol. 46, No. 1, 65–70, 2007.
5. Yun, Y., M. Nishijima, M. Katsuno, H. Ishida, K. Minagawa, T. Nobusada, and T. Tanaka, "A fully-integrated broadband amplifier MMIC employing a novel chip size package," *IEEE Trans. Microwave Theory Tech.*, Vol. 50, 2930–2937, Dec. 2002.
6. Bahl, I. and P. Bhartia, *Microwave Solid State Circuit Design*, Vol. 4, John Wiley & Sons, New York, 1988.
7. Cheung, T. S. D. and J. R. Long, "Shielded passive devices for silicon-based monolithic microwave and millimeter-wave integrated circuits," *IEEE Journal of Solid-State Cicuits*, Vol. 41, 1183–1200, May 2006.
8. Yun, Y., "A novel microstrip line structure employing a periodically perforated ground metal and its application to highly miniaturized and low impedance passive components fabricated on GaAs MMIC," *IEEE Transactions on Microwave Theory and Tech.*, Vol. 53, No. 6, 1951–1959, Jun. 2005.
9. Yun, Y., et al., "Miniaturized on-chip branch-line coupler employing periodically arrayed grounded-strip structure for application to silicon RFIC," *Microwave Journal*, to be published.
10. Chongcheawchamnam, M., N. Siripon, and I. D. Robertson, "Design and performance of improved lumped distributed Wilkinson divider topology," *Electron. Letters*, Vol. 37, No. 8, 501–503, 2001.
11. Pozar, D. M., "Microwave engineering," Addison-Wesley, 2nd Edition, Vol. 8, 1990, *Electron. Letters*, Vol. 45, No. 5, Feb. 26, 2009.

An Artificial-transmission-line-based Miniaturized Doubly Balanced Ring Mixer

C. H. Lai, Y. T. Cheng, and T. G. Ma
Department of Electrical Engineering, National Taiwan University of Science and Technology
Taipei, Taiwan, R.O.C.

Abstract— In this paper, a miniaturized doubly balanced ring mixer is presented and investigated. The proposed miniaturized mixer is composed of two novel Marchand baluns, four diodes in a ring configuration and a pair of LPF filters. By utilizing the newly proposed coupled artificial transmission lines, the new Marchand balun features a compact size and comparable operating bandwidth as its conventional counterpart. The doubly balanced ring mixer is fabricated on a six-layered printed circuit board and occupies an area of 16.7 by 16 mm^2. The conversion loss of the ring mixer is less than 11 dB as the RF frequency varies from 1.1 to 3 GHz. The isolations between all three ports remain pretty good for frequencies up to 4.5 GHz, and the 1-dB compression power is 5 dBm.

1. INTRODUCTION

Microwave mixer is one of the core components in the RF front end. Due to the nonlinearly characteristics, the mixer is commonly used for frequency up-conversion or down-conversion. Several different architectures of the mixers have been introduced in [1]. It is observed that the doubly balanced mixer can be applied for achieving even better performances. The ring configurations are capable of providing a wider dynamic range, good port-to-port isolations, and good rejection of even-order spurious responses. The doubly balanced ring mixer consists of two Marchand baluns and four diodes. However, the Marchand balun, comprising two sections of quarter-wavelength coupled lines, still occupies a large area and hence requires a more compact design. Various advanced miniaturized designs have been proposed in the literatures [2, 3]. By replacing the conventional coupled lines with coupled artificial transmission lines (ATLs) [4, 5], the Marchand balun, the most critical part in a doubly balanced mixer, could demonstrate a very compact size. The coupled artificial transmission lines used is a modification of the design in [6, 7]. The goal of this paper is to develop a new miniaturized doubly balanced ring mixer using the novel coupled artificial transmission lines.

2. NOVEL MINIATURIZED MARCHAND BALUN

Figure 1 illustrates the circuit layout of the miniaturized Marchand balun. The balun was fabricated on a six-layered printed circuit board with Rogers RO4003C substrates. To enhance the coupling between the coupled lines, the spacing between metal layer $M3$ and $M4$ is 8 mils. The substrate thicknesses between all other layers, on the other hand, are 20 mils. The developed Marchand balun consists of two cascaded sections of coupled artificial transmission lines, i.e., the miniaturized broadside coupler in [4], along with an additional artificial line for compensation. The operating principle of the miniaturized Marchand balun has been investigated in detail in [5], and was redesigned to 2.4 GHz for the application of the ring mixer in this paper. In addition, three stripline-to-conductor-backed coplanar waveguide transitions are connected to the input/output ports for measuring purpose. In a back-to-back configuration, the insertion loss of the transition is less than 1 dB over the band of concern. The vias around the ports are used to suppress higher order modes. Although not shown in Fig. 1, the Marchand balun is surrounded by a row of vias to prevent potential exterior interference during measurement.

The dimensions of the proposed miniaturized Marchand balun were determined by Ansoft HFSS. The balun features a very compact size of 15.925 by 4.2 mm^2, or equivalently, 0.234 by $0.062\lambda_g^2$. Here λ_g is referred to as the guided wavelength of a 50 Ω stripline in the same substrate at 2.4 GHz. The simulation was completed by HFSS while the measurement was performed using an Agilent performance network analyzer (PNA) E8363B along with a probe station. In the simulation the conductors were modeled by infinitely thin perfect conductors due to insufficient computing resource. The 40A-GSG-400-DP-W probe heads from Picoprobe® were used for measurement. Fig. 2(a) shows the simulated and measured S-parameters of the Marchand balun at all ports. The measured 10-dB return loss (RL) bandwidth is 1.87–3.50 GHz, i.e., a fractional bandwidth of 68%. The

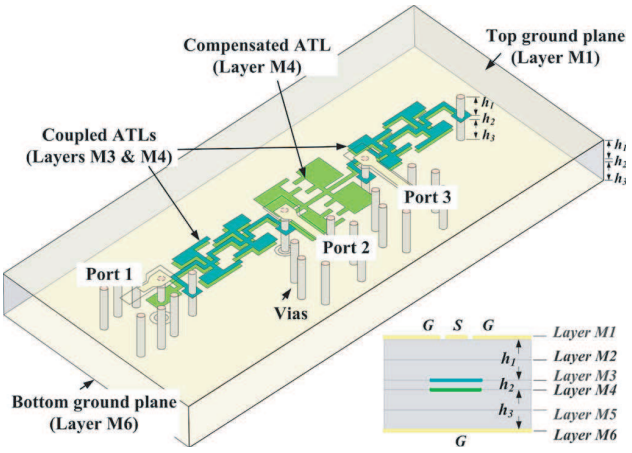

Figure 1: Circuit layout of the miniaturized Marchand balun. Three-dimensional view and the cross-sectional view. $h_1 = h_3 = 40$ mil, and $h_2 = 8$ mil.

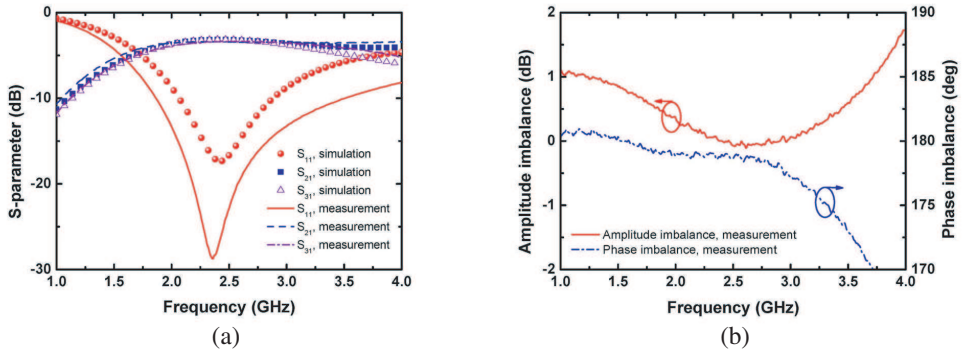

Figure 2: Comparisons of the simulated and measured results of the miniaturized Marchand balun: (a) S-parameters. (b) Amplitude and phase imbalance.

maximum return loss is 28.8 dB, and the minimum insertion loss is 3.31 dB. At the center frequency, the measured insertion losses at ports 2 and 3 are 3.41 dB and 3.40 dB, respectively. The measured phase difference is 179 degrees. The measured amplitude and phase imbalance between the two balanced ports is illustrated in Fig. 2(b). From 1.87 to 3.07 GHz, the proposed balun simultaneously meet the following specifications: return loss $\geq$ 10 dB, amplitude imbalance $\leq$ 0.5 dB, and phase imbalance $\leq$ 3 degrees. This corresponds to a fractional bandwidth of 50%. The discrepancy between the simulated and measured results can be mostly attributed to the nonideal effects of the ignored finite conductor thicknesses. The fabrication tolerance and the uncertainty of the termination resistors may contribute to the discrepancy as well.

3. MINIATURIZED DOUBLY BALANCED RING MIXER

The standard topology of a doubly balanced ring mixer is shown in Fig. 3(a). The unbalanced ports of the baluns are separately connected to the RF and LO ports, respectively. The four diodes are arranged in a ring configuration, and are serially connected to the balanced ports of the two baluns for signal mixing. The LO signal can drive the ring quad diodes into nonlinear operation, which are in turn mixed by the RF signal. The IF signal, in our design, is retrieved at the output ports of the RF balun with an air bridge, as shown in Fig. 3(b). Two second-order lowpass filters with a cutoff frequency of 150 MHz, are used at the IF port to avoid the potential interference from the LO signal. In addition, to avoid the incorrectly short circuits at the ends of the coupled-line sections at the IF frequency, two AC-coupled capacitors are added to the output ports of the RF balun to separate the RF and IF signals. A complete circuit layout of the proposed ring mixer is shown in Fig. 3(c). The slight difference between the two baluns are owing to the different operating frequency, i.e., 2.3 and 2.4 GHz, respectively, at the RF and LO ports. The mixer was fabricated on the same six-layered printed circuit board as the Marchand balun design. The overall dimension of the proposed doubly balanced ring mixer is merely 16.7 by 16 mm^2.

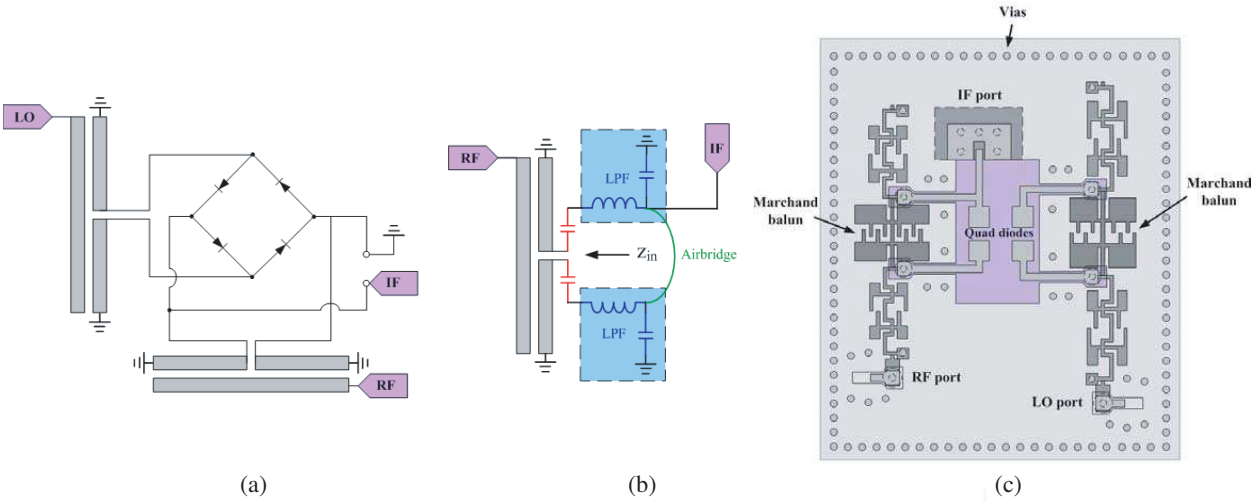

Figure 3: (a) Configuration of a doubly balanced ring mixer. (b) Lowpass filter along with AC-coupled capacitors for acquiring IF signal. (c) Circuit layout of the proposed miniaturized doubly balanced ring mixer.

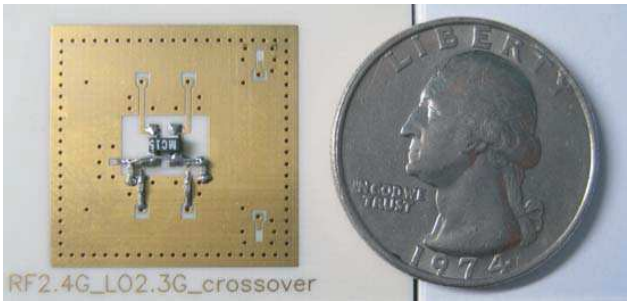

Figure 4: Photograph of the miniaturized doubly balanced ring mixer.

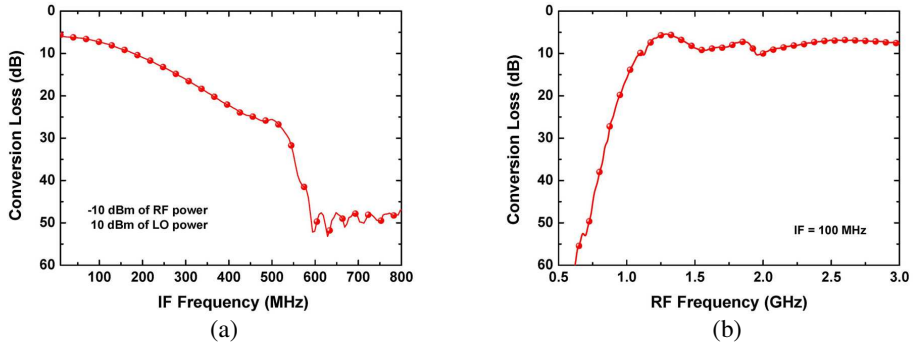

Figure 5: Measured conversion loss of the proposed mixer: (a) As a function of IF frequency with fixed LO frequency. (b) As a function of RF frequency with fixed IF frequency.

A fabricated sample of the proposed doubly balanced ring mixer is shown in Fig. 4. The surface mount Schottky crossover quads from MA-COM (MA4E2072M-1068) was used as the mixing diodes. The lowpass filters were realized by chip inductors and capacitors. The measurement was carried out by three coplanar on-wafer GSG probes along with an Agilent PNA E8363B in frequency-offset mode. An Agilent signal generator E4438C is served as the LO source. The power levels of the RF and LO signals are -10 and 10 dBm, respectively, throughout the measurement. Fig. 5(a) illustrates the measured conversion loss of the proposed ring mixer with respect to variation of the IF frequency. The LO frequency is 2.3 GHz. The conversion loss (CL) is better than 7.3 dB from 10 to 150 MHz, and has a minimum value of 5.4 dB. As illustrated in Fig. 5(b), with a fixed IF frequency of 100 MHz, the measured conversion loss is smaller than 11 dB between 1.1 and 3 GHz. In addition, the conversion loss is 7.8 dB when the RF frequency is 2.4 GHz. The mea-

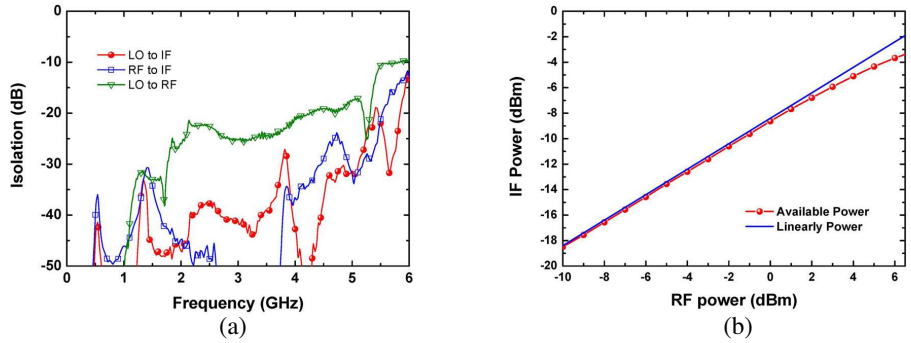

(a) (b)

Figure 6: (a) Measured isolations of the proposed mixer between the RF, LO and IF ports. The LO and RF power levels are −10 and 10 dBm. (b) Linearity of the proposed miniaturized doubly balanced ring mixer.

sured isolations between all three ports, i.e., the RF, LO and IF ports, are described in Fig. 6(a). The LO-to-IF and RF-to-IF isolations are better than 30 dB from 0.1 to 4.5 GHz and from 0.1 to 3.77 GHz, respectively. Meanwhile, the LO-to-RF isolation is better than 20 dB up to 4 GHz. Fig. 6(b) illustrates the IF output power versus the swept RF input power. According to the figure, the 1-dB compression point is 5 dBm at a LO power level of 10 dBm.

4. CONCLUSIONS

In this paper, a novel miniaturized doubly balanced ring mixer has been investigated and experimentally verified. The baluns are realized by coupled artificial transmission lines with extraordinarily compact sizes. The proposed mixer merely occupies an area of 16.7 by 16 mm^2. It provides good performances in terms of the conversion loss, port-to-port isolations and linearity. The proposed design can be applied to MMIC fabrication process as well. With better line resolution, which is 0.1 mm in the current design, it is believed that the size reduction capability can be further improved.

REFERENCES

1. Pozar, D. M., *Microwave Engineering*, Wiley, New York, 2005.
2. Chiang, M.-J., H.-S. Wu, and C. K. C. Tzuang, "A compact CMOS Marchand balun incorporating meandered multilayer edge-coupled transmission lines," *IEEE MTT-S Int. Microw. Symp. Dig.*, 125–128, 2009.
3. Guo, Y. X., Z. Y. Zhang, L. C. Ong, and M.Y. W. Chia, "A novel LTCC miniaturized dualband balun," *IEEE Microwave Wireless Comp. Lett.*, Vol. 16, No. 3, 143–145, 2006.
4. Ma, T.-G. and Y.-T. Cheng, "Miniaturized broadside coupler using coupled slow-wave artificial lines," *Electron. Lett.*, Vol. 45, No. 10, 511–512, 2009.
5. Ma, T.-G. and Y.-T. Cheng, "A miniaturized multilayered Marchand balun using coupled artificial transmission lines," *IEEE Microwave Wireless Comp. Lett.*, Vol. 19, No. 7, 446–448, 2009.
6. Wang, C.-W., T.-G. Ma, and C.-F. Yang, "A new planar artificial transmission line and its applications to a miniaturized Butler matrix," *IEEE Trans. Microw. Theory Tech.*, Vol. 55, No. 12, 2792–2801, 2007.
7. Ma, T.-G., C.-W. Wang, R.-C. Hua, and J.-W. Tsai, "A modified quasi-Yagi antenna with a new compact microstrip-to-coplanar strip transition using artificial transmission lines," *IEEE Trans. Antennas Propag.*, Vol. 57, No. 8, 2469–2474, 2009.

Experimental Study of a Longitudinal Magnetic Filter

C. Polyon, S. Photharin, and K. Wiangnon
Department of Physics, Faculty of Science, Ubon Ratchathani University
Ubon Ratchathani, Thailand

Abstract— The purpose of this work was to set up a magnetic filtration in laboratory scale. Theoretical discussions for a longitudinal magnetic filtration are described. A magnetic filter was designed and built to capture magnetic-particle samples (paramagnetic, diamagnetic or ferromagnetic materials) in fluid flowing in the direction of a uniform external magnetic field from 0 to 105.4 mT. The samples, Fe powder with diameter less than 75 µm suspending in a PVC pipe flowing at a constant velocity of 1.7 mm/s, were captured by a bed of spherical collectors (85 pieces with diameter 3.455 mm for each), ferromagnetic materials. In order to obtain the filter performance, efficiencies of both the filter and the collectors were discussed relative to the previous magnetic field range. The experimental results show good agreement with the theoretical calculation from related reports.

1. INTRODUCTION

A magnetic filter is a tool to remove magnetic particles from fluid systems. The process to removal of these particles is called a "magnetic filtration". Many researches about a magnetic filtration were both by theoretical models and by experiments [1–17]. In principle, a magnetic filter consists of a nonmagnetic (stainless steel) canister, filled with paramagnetic or ferromagnetic matrix elements, called collectors, and a magnetic field sufficient to saturate the elements. The magnetic filter is separated in two types: a longitudinal magnetic filter and a transverse magnetic filter [4, 7, 9]. For the first type, direction of flowing fluid is parallel to the direction of an applied magnetic field. In the second, the direction of the flowing fluid is perpendicular to the direction of the applied field. Most magnetic filtration experiments are performed with collectors using a single wire or spheres made from ferromagnetic materials [3, 5, 6, 11]. These methods were used for many applications [6, 10–12, 14, 15, 17].

The purpose of this research was to study efficiencies of a longitudinal magnetic filter and spherical collectors by experiments in applied magnetic fields from 0 to 105.4 mT In this work, the filter was built and used to capture magnetic particles. The efficiency for either filter or collectors was discussed and compared to theoretical calculation from the previous reports [4, 7].

2. LONGITUDINAL MAGNETIC FILTRATION

Many theoretical models about a magnetic filtration have been reported [1, 2, 4, 7–9, 13, 16]. The model for the longitudinal magnetic filtration is also purposed [4, 7]. In the model, by using an effective medium treatment, spherical collectors and fluid system replacing by a sphere with radius a and a fluid shell with radius b, called a composite sphere, immerging in an effective medium, as shown in Fig. 1. The fluid flows passing through collectors in the z direction, the same direction of a uniform applied magnetic field ($\vec{H}_0$). The composite sphere is represented by a packing fraction γ^3, actual volume fraction of the collectors to the fluid in the filter ($\gamma^3 = a^3/b^3$). When magnetic particles moves to the collectors, some of these particles are attracted and captured by the collectors on account of magnetic forces ($\vec{f}_m$) induced from the applied magnetic field. However, effects from drag forces ($\vec{f}_d$) are also considered With neglect of inertial, gravitational and (short-ranged) electrical forces the equation of motion for the magnetic particles becomes

$$\vec{f}_d + \vec{f}_m = \vec{0} \tag{1}$$

From Equation (1), theoretical efficiency (ε_T) of the collectors used in the model could be calculated by a following equation

$$\varepsilon_T = 1 - \exp\left(-\frac{3A_c\gamma^3 L}{4\pi a^3}\right) \tag{2}$$

where L is the length of the filter bed. A_c is the capture area, a cross section area that moving magnetic particles are captured. For the longitudinal design, $A_c = \pi r_c^2$, and r_c is the capture radius.

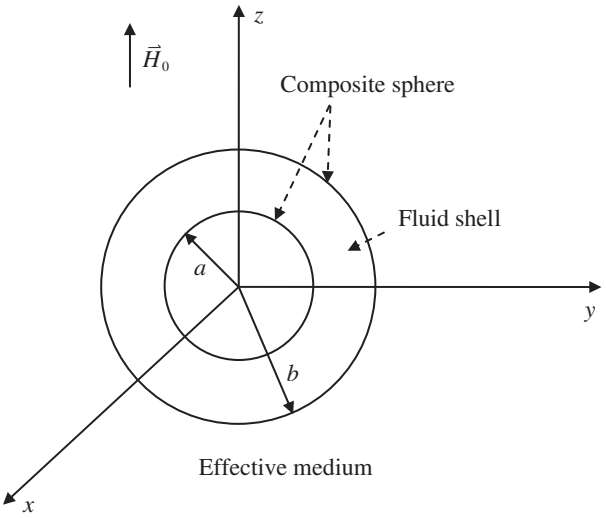

Figure 1: A composite sphere immerging in an effective medium.

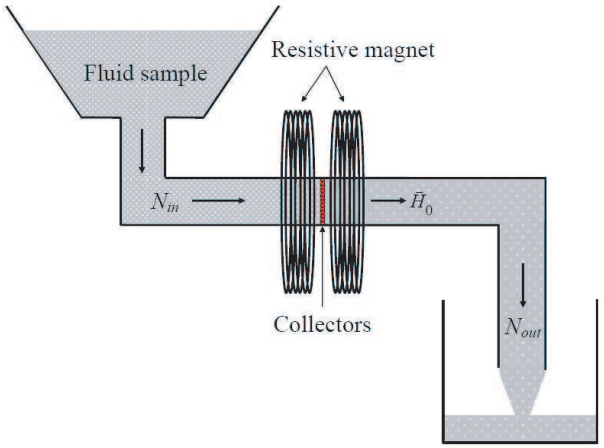

Figure 2: Diagram of an experimental longitudinal magnetic filter.

In general, experimental efficiency (ε_E) for a filter or collectors can be written by

$$\varepsilon_E = \frac{N_{cap}}{N_{in}} \tag{3}$$

where N_{in} is the number of magnetic particles entering the collectors and $N_{cap} = N_{in} - N_{out}$ is the number of magnetic particles captured by the collectors, and N_{out} is a number of magnetic particles passing through the collectors.

3. MATERIALS AND METHODS

A longitudinal magnetic filter was designed and built in our laboratory (Applied Magnetic Fields Research, Ubon Ratchathani University). The filter was composed of a bed of spherical collectors, 85 pieces with diameter 3.455 mm for each, placed in a PVC pipe with internal diameter 40.85 mm The collectors were placed in the direction parallel to an applied magnetic field producing from a 235 mT resistive magnet system with two solenoid coils (Walker Scientific, Model HV-4H, USA) and a current supply (Walker Scientific, Model HS7354A, USA) Diagram of an experimental longitudinal magnetic filter is shown in Fig. 2.

In order to study the capture of magnetic field particles, the longitudinal magnetic filtration experiments were performed at room temperature with a fluid sample flowing with a constant velocity of 1.7 mm/s in the applied magnetic field varied from 0 to 105.4 mT The sample could be prepared by mixing Fe power (dimension $\leq$ 75 µm) with water by ratio of 14,000 ml water per 50 ml Fe powder. Efficiencies of the collectors and the filter could be calculated by using Equation (3). In the equation, the number of magnetic particles suspended in the fluid were measured in concentration of Fe powder in water (unit of mg/ml) by weighting the mass of Fe powder for each sample before and after filtrated in the same water volume. In this process, the water in the sample was removed by filtration with a very good piece of filter paper. Finally, efficiencies in percents (%) for both filter and collectors were plotted as a function of the applied magnetic filed in the 0–105.4 mT range.

4. RESULTS AND DISCUSSIONS

Figure 3 shows the efficiency of the longitudinal magnetic filter (dashed line and black-triangle points) and that of the collectors (solid line and black-square points) versus the applied magnetic field varied from 0 to 105.4 mT. Experimental results show that the efficiencies for both filter and collectors rapidly increase during the magnetic field range between 0 and 18 mT. The efficiencies still increase to saturated values (99% for the filter and 96% for the collectors) during the magnetic field range between 18 and 105.4 mT. In the figure, the efficiency for the filter is greater than that of its collectors, which has a value at 68%, although the applied magnetic field is switched off. That is because of, in the experiments, Fe powder suspended in water dropped under a gravitational field

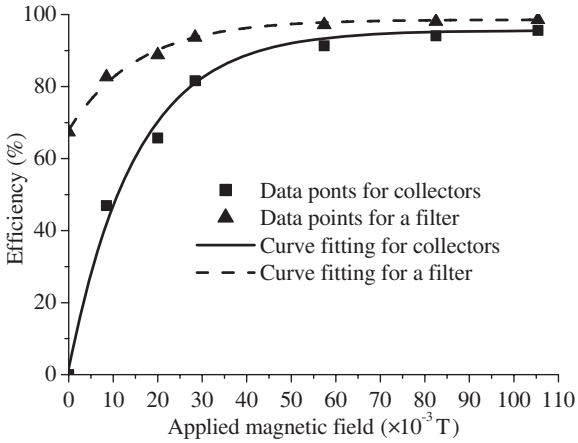

Figure 3: Efficiency of the longitudinal magnetic filter (dashed line and black-triangle points) and that of the collectors (solid line and black-square points) versus the applied magnetic field between 0 and 105.4 mT. The fluid sample is Fe powder suspended in water.

before entering into the collectors resulting in a higher efficiency for the filter than the collectors. Compared to the previous reports [4, 7], the experimental data trend to be correspond to the theoretical calculation.

5. CONCLUSION

In this work, efficiencies of both longitudinal filter and collectors increase to a saturated value and these approaches one hundreds percents when increasing the applied magnetic field from 0 to 105.4 mT. These data quite agree with the theoretical calculation in the previous reports [4, 7]. Further work should study experiments on a transverse magnetic filter and try to use the filter with a wastewater sample.

ACKNOWLEDGMENT

This work was supported by Physics Department, Science Faculty, Ubon Ratchathani University, Thailand.

REFERENCES

1. Briss, R. R., R. Gerber, and M. B. Howard, "Magnetic interaction between a strongly magnetized sphere and weakly magnetized particles carried by fluid flow," *J. Magn. Mat.*, Vol. 15–18, 1565–1566, 1980.
2. Friedlaender, F. J., R. Gerber, W. Kurz, and R. R. Briss, "Particle motion near and capture on sphere in HGMS," *IEEE Trans. Magn.*, Vol. 17, No. 6, 2801–2803, 1981.
3. Parker, M. R., "Magnetic filtration by a current-carrying wire matrix," *IEEE Trans. Magn.*, Vol. 17, No. 6, 2816–2818, 1981.
4. Moyer, C. A., M. Natenapit, and S. Arajs, "Magnetic filtration particles in laminar flow through a bed of spheres," *J. Magn. Mat.*, Vol. 44, 99–104, 1984.
5. Arajs, S., C. A. Moyer, R. Aidun, and E. Matijevic, "Magnetic filtration of submicroscropic particles through a packed bed of spheres," *J. Appl. Phys.*, Vol. 57, No. 1, 4286–4288, 1985.
6. Haque, M. F., R. Aidun, C. Moyer, and S. Arajs, "Magnetic filtration of submicron hematite particles," *J. Appl. Phys.*, Vol. 63, No. 8, 3239–3240, 1988.
7. Natenapit, M. "Effective medium treatment of laminar flow in magnetic filtration," *J. Appl. Phys.*, Vol. 78, No. 7, 4353–4359, 1995.
8. Badescu, V., V. Muariu, O. Rotariu, and N. Rezlescu, "A new modeling of the initial buildup evolution on a wire in an axial HGMF filter," *J. Magn. Mat.*, Vol. 163, 225–231, 1996.
9. Natenapit, M. and W. Sanglek, "Capture radius of magnetic particles in random cylindrical matrices in high gradient magnetic separation," *J. Appl. Phys.*, Vol. 85, No. 2, 660–664, 1999.
10. Franzreb, M. and W. H. Höll, "Phosphate removal by high-gradient magnetic filtration using permanent magnet," *IEEE Trans. Appl. Supercond.*, Vol. 10, No. 1, 923–926, 2000.
11. Takayasu, M., D. R. Kelland, and J. V. Minervini, "Continuous magnetic separation of blood components from whole blood," *IEEE Trans. Appl. Supercond.*, Vol. 10, No. 2, 398–401, 2000.

12. Zarutskaya, T. and M. Shapiro, "Capture of nanoparticles by magnetic filters," *J. Aerosol Sci.*, Vol. 31, No. 8, 907-921, 2000.
13. Künkül, A., A. Ekmekyapar, C. Akmil, and T. Abbasov, "Effect of operating parameters on magnetic filtration processes," *Ind. Eng. Chem. Res.*, Vol. 43, 161–165, 2004
14. Kim, Y. and D. E. Luzzi, "Purification of pulsed laser synthesized single wall carbon nanotubes by magnetic filtration," *J. Chem. B.*, Vol. 109, 16636–16643, 2005.
15. Sandulyak, A. A. and A. V. Sandulyak, "Prospects for use of magnetic separator filter performance," *Glass and Ceramics*, Vol. 63, No. 11–12, 391–394, 2006.
16. Abbasov, T. " Magnetic filtration with magnetized granular beds: Basics principles and filter performance," *China Particuology*, Vol. 5, 71–83, 2007.
17. Alvaro, A., J. M. Rodriguez, P. A. Augusto, and A. M. Esté, "Magnetic filtration of an iron oxide aerosol by means of magnetizable grates," *China Particuology*, Vol. 5, 140–144, 2007.

A Novel Type Phase Shifter Using Rat Race Hybrid

Jan-Dong Tseng, Chien-Wen Ting, and Chien-Hua Su
Department of Electronic Engineering, National Chin-Yi University of Technology
35, Lane 215, Sec. 1, Chung-Shan Road, Taiping, Taichung 411, Taiwan, R.O.C.

Abstract— In this paper, we proposed a novel type phase shifter using rat-race hybrid with one additional quarter-wavelength transmission line for phase compensation and two varactors as phase controlling elements. The circuit has been simulated by IE3D and fabricated on FR-4 substrate. The simulated and measured results are in good agreement with in the frequency of interest.

1. INTRODUCTION

Phase shifters are widely used in phase array radar systems [1, 2] for radiation beam steering on searching and tracking, and modern wireless communication system's base station antennas for adjusting the radiation coverage to improve the service quality. Phase shifter circuit can be simply made by different transmission lines and switches. In 1965, J. F. White used high power PIN diodes and transmission lines created L/S bands phase shifter circuit [3]. Cheah, Y. C., Paoloni, F. J. proposed a variable attenuators and phase shifters also using PIN diodes in 1984 [4]. Neidert, R. E., Krowne, C. M. in 1985 proposed a voltage-controlled phase shifter [5]. Lian, C., Rosenau, S. A., Zhang, W. K., Chang, C. C., Domier, C. W. and Luhmann, N. C. used lumped element in phase shifter design in 2000 [6].

The deployment of Radio Frequency Identification (RFID) is increasingly popular in many fields, ranging from access control, livestock management to logistics, and the available frequency band are 125 kHz, 13.56 MHz, 869 MHz, 902–928 MHz, 2.45 GHz, and 5.8 GHz. As the antenna is an integral part of whole RFID system design, the antenna is crucial to the overall system performance.

The proposed phase shift circuit is shown Fig. 1, port 3 is input, port 2 is output, and port 4 is shunted to ground through a capacitor, port 1 is also shunted to ground through a quarter-wave transmission line and a capacitor with the same value as that at port 4. The circuit forming a phase shift structure in which the phase will change with the capacitor values. The proposed structure has been simulated by using the software, IE3D, to have a comparison on phase shift between the simulation and measurement results.

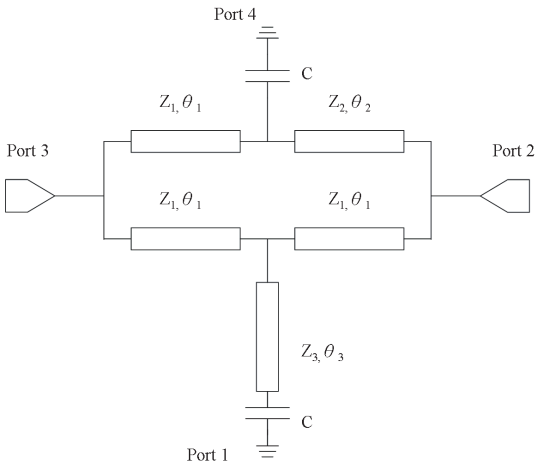

Figure 1: Schematic diagram of the proposed phase shift circuit.

2. CIRCUIT ANALYSIS

The proposed phase shifter circuit shown in Fig. 1can be divided into upper and lower half circuits, as depicted in Figs. 2 (a) and (b) respectively, where θ_1, θ_2 and θ_3 denote the electrical lengths, Z_1

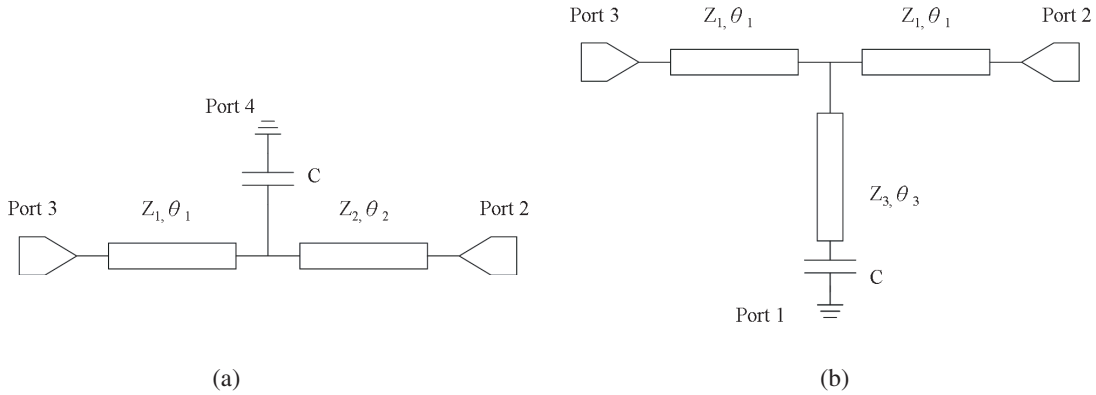

Figure 2: (a) The upper half part of the proposed circuit. (b) The lower half part of the proposed circuit.

and Z_2 are the characteristic impedances. The upper half circuit, cascaded by two transmission line sections and lump circuit, can be expressed in matrix form of Eq. (1), and the lower half circuit is in Eq. (2), where Z_C is the impedance of capacitor and Z_{in} is the input impedance of the transmission line, Z_3 and θ_3 connected with shunted capacitor C.

$$\begin{bmatrix} \cos\theta_1 & jZ_o\sin\theta_1 \\ j\dfrac{1}{Z_o}\sin\theta_1 & \cos\theta_1 \end{bmatrix} \cdot \begin{bmatrix} 1 & 0 \\ \dfrac{1}{Z_c} & 1 \end{bmatrix} \cdot \begin{bmatrix} \cos\theta_2 & jZ_o\sin\theta_2 \\ j\dfrac{1}{Z_o}\sin\theta_2 & \cos\theta_2 \end{bmatrix} \tag{1}$$

$$\begin{bmatrix} \cos\theta_1 & jZ_o\sin\theta_1 \\ j\dfrac{1}{Z_o}\sin\theta_1 & \cos\theta_1 \end{bmatrix} \cdot \begin{bmatrix} 1 & 0 \\ \dfrac{1}{Z_{in}} & 1 \end{bmatrix} \cdot \begin{bmatrix} \cos\theta_1 & jZ_o\sin\theta_1 \\ j\dfrac{1}{Z_o}\sin\theta_1 & \cos\theta_1 \end{bmatrix} \tag{2}$$

$$Z_c = \frac{1}{j\omega C} \tag{3}$$

$$Z_{in} = Z_{TL} \cdot \frac{Z_c + j \cdot Z_{TL} \cdot \tan\theta_3}{Z_{TL} + j \cdot Z_c \cdot \tan\theta_3} \tag{4}$$

The total transmission matrix, $ABCD$ matrix, shown in Eq. (1) has the elements A_1, B_1, C_1 and D_1, shown in Eqs. (5)–(8) respectively, and vise versus Eq. (2) is expressed in Eqs. (9)–(12).

$$A_1 = \cos\theta_2\left(\cos\theta_1 + \frac{jZ_o\sin\theta_1}{Z_c}\right) - \sin\theta_1 \cdot \sin\theta_2) \tag{5}$$

$$B_1 = jZ_o\sin\theta_2\left(\cos\theta_1 + \frac{jZ_o\sin\theta_1}{Z_c}\right) + jZ_o\sin\theta_1\cos\theta) \tag{6}$$

$$C_1 = \cos\theta_2\left(\frac{j\sin\theta_1}{Z_o} + \frac{\cos\theta_1}{Z_c}\right) + \frac{j\cos\theta_1\sin\theta_2}{Z_o} \tag{7}$$

$$D_1 = jZ_o\sin\theta_2\left(\frac{j\sin\theta_1}{Z_o} + \frac{\cos\theta_1}{Z_c}\right) + \cos\theta_1 \cdot \cos\theta_2) \tag{8}$$

$$A_2 = -\sin^2\theta_1 + \cos\theta_1\left[\cos\theta_1 + \frac{jZ_o\sin\theta_1(Z_{TL} + \frac{\tan\theta_3}{\omega C})}{Z_{TL}\,(Z_c + jZ_{TL}\tan\theta_3)}\right] \tag{9}$$

$$B_2 = jZ_o\cos\theta_1\sin\theta_1 + jZ_o\sin\theta_1\left[\cos\theta_1 + \frac{jZ_o\sin\theta_1(Z_{TL} + \frac{\tan\theta_3}{\omega C})}{Z_{TL}\,(Z_c + jZ_{TL}\tan\theta_3)}\right] \tag{10}$$

$$C_2 = \frac{j\cos\theta_1\sin\theta_1}{Z_o} + \cos\theta_1\left[\frac{j\sin\theta_1}{Z_o} + \frac{\cos\theta_1(Z_{TL} + \frac{\tan\theta_3}{\omega C})}{Z_{TL}\,(Z_c + jZ_{TL}\tan\theta_3)}\right] \tag{11}$$

$$D_2 = \cos^2\theta_1 + jZ_o\sin\theta_1\left[\frac{j\sin\theta_1}{Z_o} + \frac{\cos\theta_1(Z_{TL} + \frac{\tan\theta_3}{\omega C})}{Z_{TL}\,(Z_c + jZ_{TL}\tan\theta_3)}\right] \tag{12}$$

The whole circuits $ABCD$ matrix with elements A, B, C and D are in Eqs. (13)–(16) respectively. The matrix can then transfers into scattering parameters as Eqs. (17) and (18). The phase of S_{21} has the expression of Eq. (19). Where Eq. (19) a and jb denote the real part and image part of S_{21} parameters respectively.

$$A = \frac{A_1B_2 + A_2B_1}{B_1 + B_2} \tag{13}$$

$$B = \frac{B_1B_2}{B_1 + B_2} \tag{14}$$

$$C = \frac{(A_2 - A_1)(D_1 - D_2) + (B_1 + B_2)(C_1 + C_2)}{B_1 + B_2} \tag{15}$$

$$D = \frac{D_1B_2 + B_1D_2}{B_1 + B_2} \tag{16}$$

$$\mathrm{S}_{11} = \frac{A + \frac{B}{Z_o} - C \times Z_o - D}{A + \frac{B}{Z_o} + C \times Z_o + D} \tag{17}$$

$$\mathrm{S}_{21} = \frac{2}{A + \frac{B}{Z_o} + C \times Z_o + D} \tag{18}$$

$$\angle S_{21} = \tan^{-1}\frac{jb}{a} \tag{19}$$

When $Z_1 = Z_2 = Z_3 = 70.7\,\Omega$, $\theta_1 = 90°$, $\theta_2 = 270°$, $\theta_3 = 90°$ are carried in the Eqs. (18) and (19) with center frequency 925 MHz and capacitance 2.81 pF, we can get $S_{21} = -0.1259 - j0.9359$ with phase $-97.65°$; and the $S_{21} = -0.7728 - j0.6009$ with phase $-142.13°$ while center frequency is 2.45 GHz and capacitance 2.81 pF. By knowing the scattering parameter S_{21} at the center frequency, we can determine phase changing at different capacitance values.

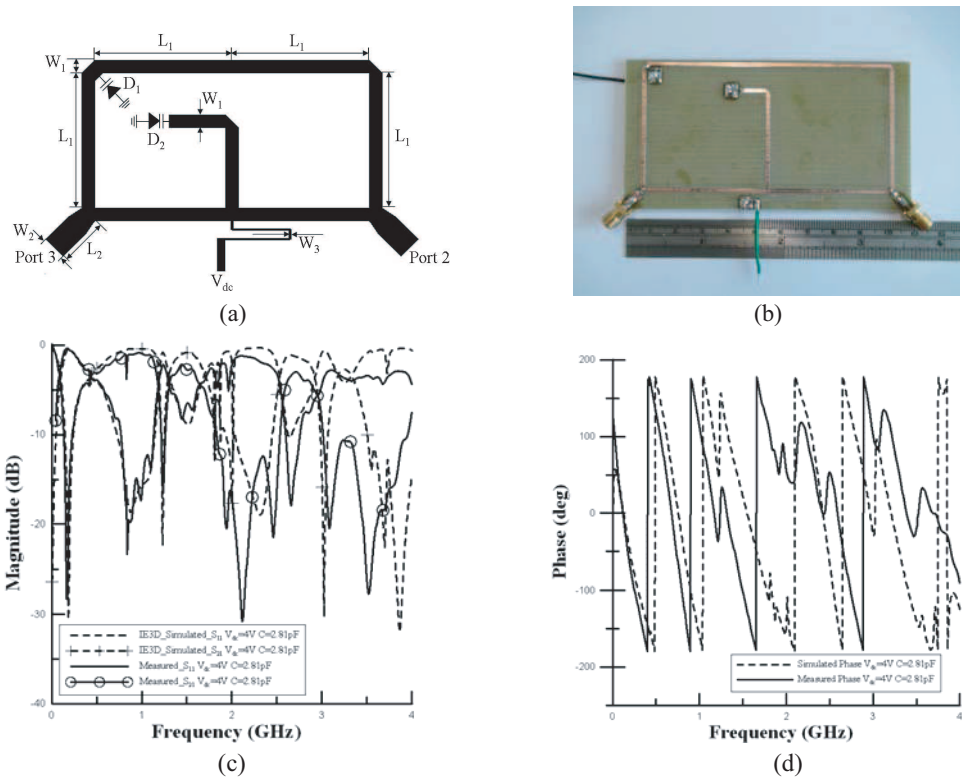

Figure 3: (a) The layout of the 925 MHz phase shifting circuit. (b) The 925 MHz phase shifting circuit fabricated on FR-4 substrate. (c) The simulated and measured magnitude results of the phase shifting circuit at 925 MHz. (d) The simulated and measured phases of the 925 MHz phase shift circuit.

3. CIRCUIT DESIGN

A phase shift circuit was implemented based on the derived equations and simulated by using EM simulation tool, IE3D. FR-4 substrate was used, with thickness 1.6 mm and dielectric constant 4.3. The two varactors (D_1 and D_2) model no. SMV1234, SKYWORK, are applied on the two circuits of center frequency 925 MHz and 2.45 GHz with a range from 1.32 pF to 9.63 pF. The characteristic impedances of input and output port are both 50 Ohm.

The layout of the circuit is shown in Fig. 3(a). The lengths of L_1, L_2, W_1 and W_2 can be calculated by Line Gauge of IE3D are 46.02, 4.5, 47.55, 1.64, 3.1 and 0.41 mm respectively, at 925 MHz. This physical circuit is shown in Fig. 3(b) with 95.32 mm × 52.12 mm. The frequency response of both simulation and measurement results is shown in Fig. 3(c), where the dash line

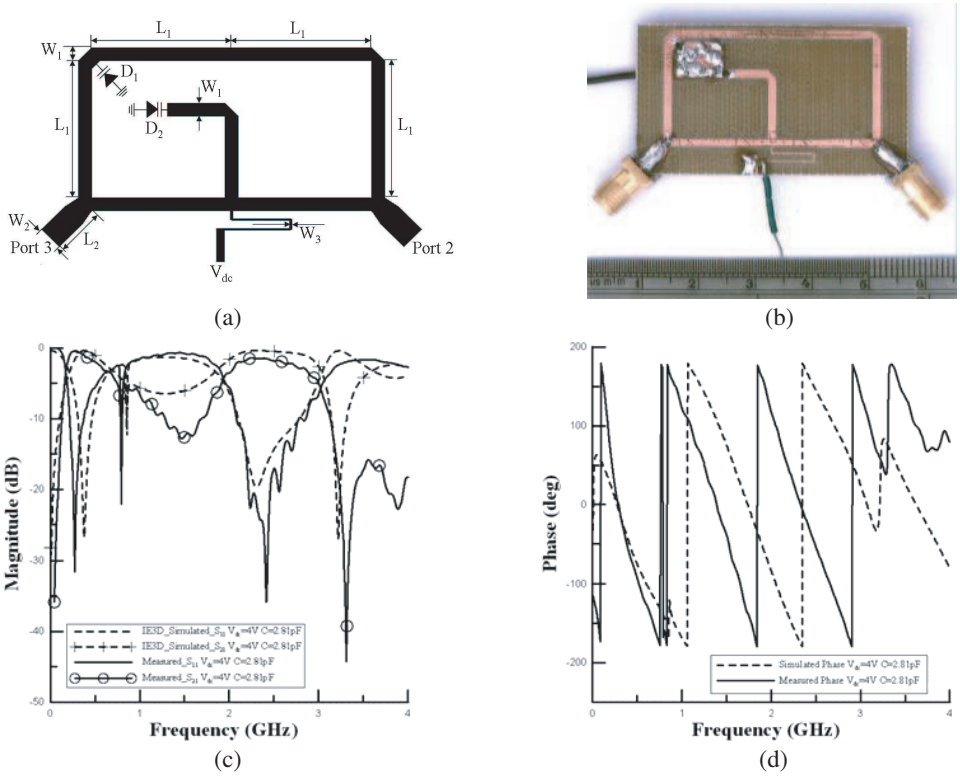

Figure 4: (a) The layout of the 2.45 GHz phase shifting circuit. (b) The 2.45 GHz phase shifting circuit fabricated on FR-4 substrate. (c) The simulated and measured magnitude results of the phase shifting circuit at 2.45 GHz. (d) The simulated and measured phases of the 2.45 GHz phase shift circuit.

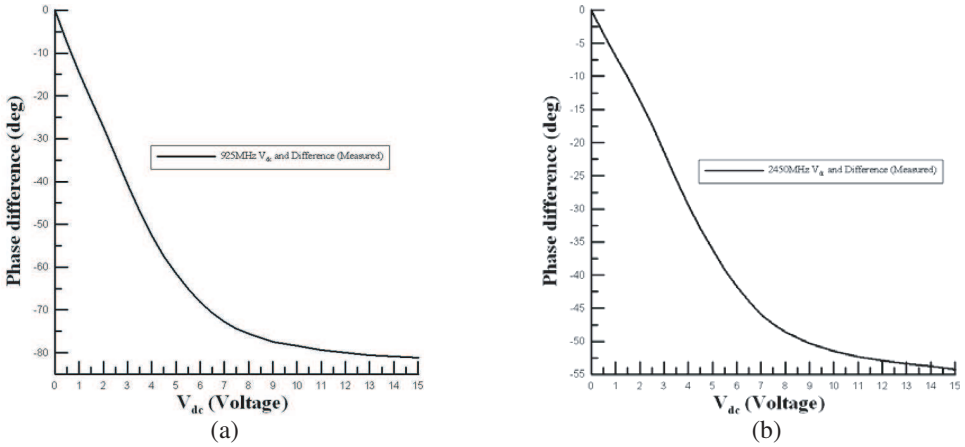

Figure 5: (a) The measured results of the 925 MHz phase shifting circuit. (b) The measured results of the 2.45 GHz phase shifting circuit.

denotes the simulation results by IE3D, solid line is measured results when the varactors biased at 4 V. The corresponding phase of S_{21} is shown in Fig. 3(d). It has a good agreement of frequency response between measurement and simulation at 925 MHz.

The Figs. 4(a)–4(d) demonstrate the simulated and measured results of another phase shifter circuit designed at 2.45 GHz, where the circuit dimension are 38.02 mm × 23.13 mm, L_1: 17.37 mm, L_2: 4.52 mm and L_3: 17.95 mm, W_1: 1.64 mm, W_2: 3.1 mm and W_3: 0.41 mm.

The relationship between phase changing and the bias voltage of varactors are shown in Fig. 5(a) and Fig. 5(b) at 925 MHz and 2.45 GHz respectively. The varactors bias voltage from 0 V–5 V at 925 MHz and 0 V–7 V at 2.45 GHz has a good linearity result shown in Fig. 5(a) and Fig. 5(b).

4. CONCLUSIONS

In this paper, we proposed a novel type phase shifter using rat-race hybrid with one additional quarter-wavelength transmission line for phase compensation and two varactors as phase controlling elements. The equivalent circuit of this phase shifting structure was obtained by calculating the $ABCD$ matrices. The phase will be changed by the different capacitor values or different bias voltages applying to varactors. The circuit has been simulated by IE3D and fabricated in FR-4 substrate. The simulated and measured results are in a good agreement with in the frequency of interest.

REFERENCES

1. Mailloux, R. J., "Antenna array architecture," *Proc. IEEE*, Vol. 80, No. 1, 163–172, Jan. 1992.
2. Hansen, R. C., "Array pattern control and synthesis," *Proc. IEEE*, Vol. 80, No. 1, 141–151, Jan. 1992.
3. White, J. F., "High power, p-i-n diode controlled microwave transmission phase shifters," *IEEE Transactions on Microwave Theory and Techniques*, Vol. 13, 233–242, Mar. 1965.
4. Cheah, Y. C. and F. J. Paoloni, "Design of a microwave PIN diode complex weight circuit," *Electronic Letters*, Vol. 20, 822–824, Sep. 1984.
5. Neidert, R. E. and C. M. Krowne, "Voltage variable microwave phase shifter," *Electronic Letters*, Vol. 21, 636–638, Jul. 1985.
6. Lian, C., S. A. Rosenau, W. K. Zhang, C. C. Chang, C. W. Domierm, and N. C. Luhman, "Advances in solid-state array technology for microwave and millimeter-wave applications," *The 2nd International Conference on ICMMT 2000 Microwave and Millimeter Wave Technology*, No. 9, 10–15, Sep. 2000.

Design of a Class F Power Amplifier

Tian He[1] **and Uma Balaji**[2]

[1]California State University Chico, Chico, CA 95926, USA
[2]Farmingdale State College, Farmingdale, NY 11735, USA

Abstract— A Class F power amplifier (PA) at 2.5 GHz has been designed and fabricated. Test results show 15.7 dB gain with 75.75% power added efficiency (PAE), at an input level of 25 dBm. The design procedure is presented, with various issues illustrated and addressed. A new method is proposed to obtain the optimum load and source impedances without iterations, which would usually be necessary.

1. INTRODUCTION

The Class F amplifier is a reduced angle amplifier with load harmonic modulation control to shape the drain voltage in a way that it does not or rarely does coincide with drain current, thus greatly reducing the power dissipated by the device, and hence further increasing the efficiency without having to drive the amplifier into compression. The theory has been well explained by Cripps [1] and Raab [2].

Design of a Class F amplifier involves matching network design at the fundamental frequency, and load harmonic tuning network design up to certain order harmonics. The common practice is to present a short circuit at the even order harmonics, and an open circuit at the odd order harmonic. Note that shorting the even order harmonics has its sound theoretical foundation, while the principle regarding odd order harmonics is just a folklore notion, the insight on which has been discussed by Cripps [1]. In most cases only the second and third order harmonics are considered, since higher order harmonic control would lead to more complexity and possibly further loss [3]. Some published papers have reported Class F power amplifiers with efficiency around 80% at 2 GHz or lower frequencies [4, 5]. This paper presents the design of a Class F power amplifier at 2.5 GHz, which is required to deliver at least 5 W output power P_{out} with no more than 25 dBm input power.

2. DESIGN

The transistor chosen is Cree CGH40010 GaN HEMT. It is biased at $V_{DD} = 28$ V, $I_{DQ} = 200$ mA. A corresponding large signal model is provided by Cree, Inc. The software used is AWR Microwave Office. Taconic *ORCER RF-35* is chosen to be the board material with a thickness of 60 mils, while the metal is 1 oz copper. RF-35 has a stable ϵ_r of 3.5 over a wide frequency band from 2 GHz to 10 GHz, and a dissipation factor of 0.0018 at 2.5 GHz. The design procedure is illustrated in the following subsections.

2.1. Prototyping Using Ideal Components

Usually the first step would be to get the optimum load impedance that induces maximum saturation power, and the source impedance that presents maximum transistor gate voltage. In the case of this design however, these parameters are already provided in the data sheet — at the fundamental frequency $f_0 = 2.5$ GHz, optimum load impedance Z_L is $6.37-j0.1$, and optimum source impedance Z_S is $4.0-j4.0$.

If it were a Class A amplifier, one would be able to start designing the matching network right away given Z_L and Z_S. However, since the Class F amplifier design involves load harmonic control, which undoubtedly would change the load impedance at the fundamental frequency f_0, it is reasonable to design the harmonic control circuitry, and then complete additional load circuitry that presents Z_L at f_0 to the transistor output.

It is beneficial to first build up a prototype with lossless transmission lines (TLs), and ideal lumped components, just to verify that Z_L and Z_S indeed produce the required performance. Figure 1 shows the load network, where TL3 and TL4 together presents an open circuit to the drain at the $3f_0$, TL5 works as the RF choke and also presents a short circuit to the drain at $2f_0$. The rest of the circuit makes sure that Z_L is presented to the transistor drain at f_0.

The source matching is a basic process thus is not shown here. The P_{out}/PAE vs. input power (P_{in}) plot is shown in Figure 2. It is observed that maximum efficiency of this configuration is 84.34%, with P_{out} more than 39 dBm. However it should be noted that at that point the amplifier has already reached well into saturation.

2.2. Design with Lossy Components

As the design evolves to lossy components, several problems need to be addressed. One is that lumped components of certain values at such high frequencies might not be available. For example, in the matching network prototype the DC blocking capacitors have a value of 1000 pF. This is already close to the upper bound of chip capacitors at 2.5 GHz. Thus they should be replaced with smaller, more practical ones. However the reason why such large capacitance was chosen in the first place is to make sure its impedance is small enough at f_0 to be ignored. Once the capacitance is changed to a much smaller value, the matching network needs to be redesigned. Therefore it is suggested this should be considered at the stage of ideal circuit prototyping to save some repetitive work. In this design, 0.7 pF is chosen as the DC blocking capacitance, and it is considered when designing the matching networks.

Another problem is the effect of the microstrip line junction on the lengths of the lines connected to it. Figure 3 shows four microstrip lines connected by a junction component named "MCROSS" in Microwave Office. When designing the impedance network four such TLs are connected to an artificial "point", which has no physical dimensions whatsoever. But in practice it is necessary to

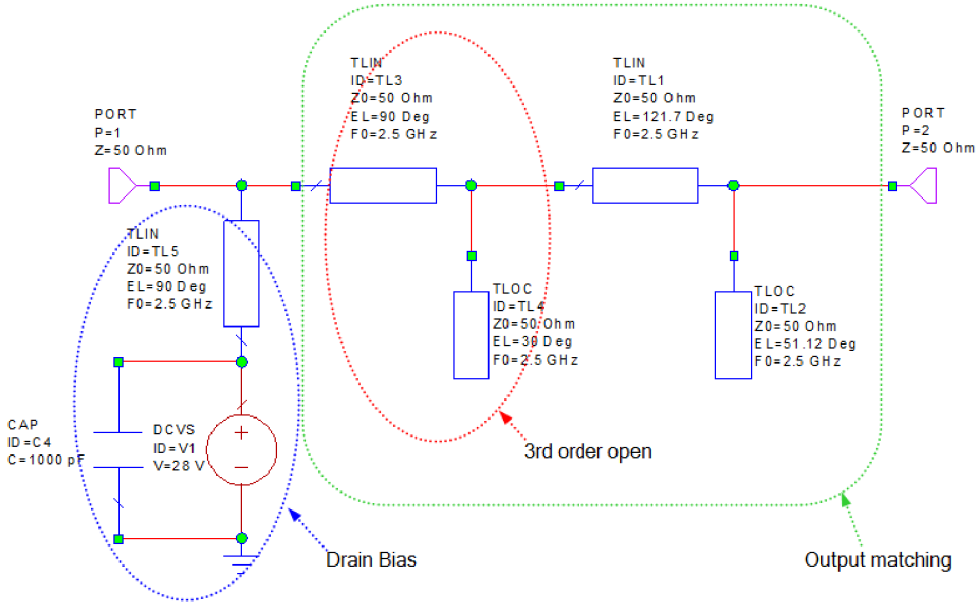

Figure 1: Ideal load network.

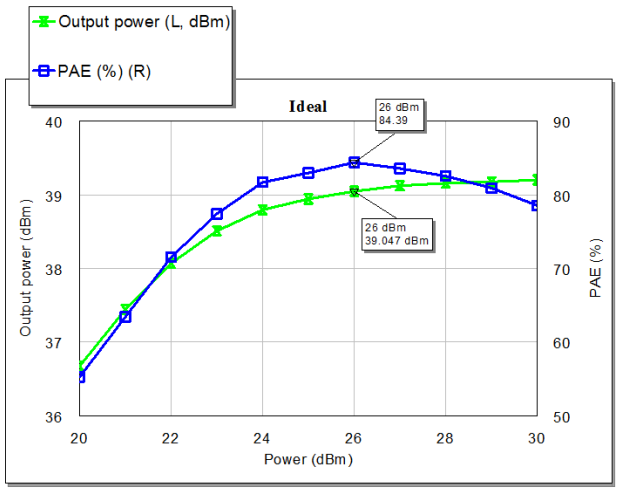

Figure 2: P_{out} and PAE vs. P_{in} of the amplifier prototype using ideal components.

investigate the junction.

Figure 4 is to explain how to connect several lines together. W1 to W4 are widths of the connected lines, whose reference planes are the black dashed lines, meaning the "MCROSS" component is bounded by the black dashed lines. However, in practice the artificial "point" mentioned above is usually transformed into two reference planes represented by the red dashed line. For this reason, if the line connected to port 1 of the junction has a length of L in the design, once it is connected in Microwave Office with "MCROSS", 0.5·W4 has to be subtracted from L. The same principle applied for all other ports.

With the problems above solved, the design becomes a simple task. However, tuning or optimization is inevitable after the initial design, for small variations of TL length can affect the performance severely at GHz frequencies. Using the optimizer in Microwave Office, it is fairly easy to make the matching network present the desired impedance at a certain frequency.

For the load network, first the harmonic control circuit is tuned, followed by optimization at f_0. Note that short at 2nd order harmonic can be quite accurate, while open circuit at 3rd order harmonic may not necessarily yield infinite impedance. The best value in this example is 2200 Ω, which is good enough to get a high efficiency. The simulation result is shown in Figure 5, where it is observed that both power and efficiency are lower than their counterparts in the ideal case. Microwave Office is used for the PCB design. And the final board is shown in Figure 6. Note that different capacitors are connected in parallel in the bias circuits so that their resonances can be cancelled out, and sudden changes of the bias voltages can be prevented.

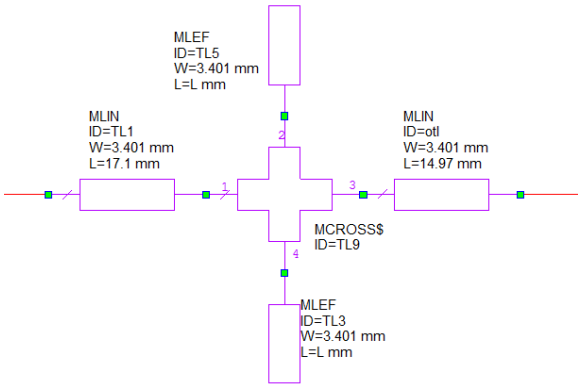

Figure 3: Four microstrip lines with a junction.

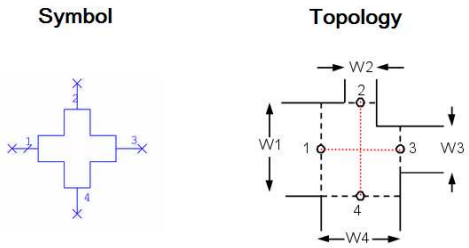

Figure 4: Illustration of the microstrip line junction.

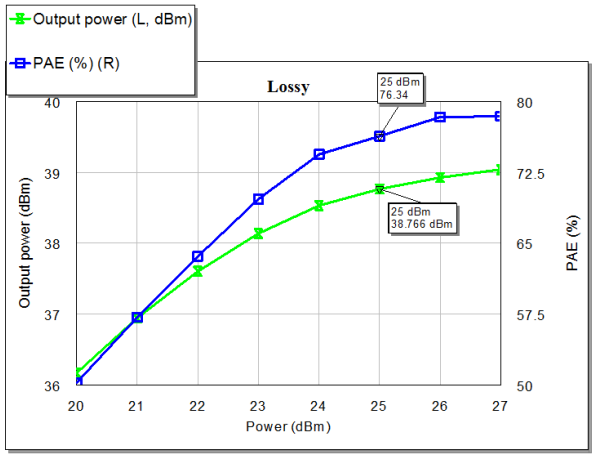

Figure 5: P_{out} and PAE vs. P_{in} of the amplifier using lossy components.

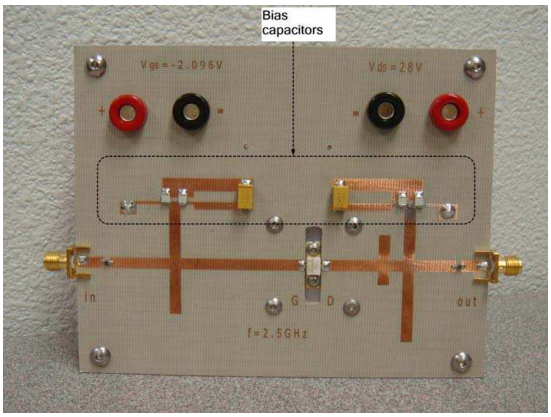

Figure 6: Final board.

3. MEASUREMENTS

Measurements are performed at f_0, and the results are shown in Table 1. With these measurement results, the DC power dissipated by the transistor is 15.4 W, and the PAE is 75.75%.

Table 1: Measurement results.

P_{in} (dBm)	Gain (dB)	P_{out} (dBm)	$I_{drain_{dc}}$ (A)	$V_{drain_{dc}}$ (V)
25	15.785	40.785	0.55	28

4. NEW METHOD TO OBTAIN OPTIMUM IMPEDANCES

Although in this design the optimum impedances are readily available from the datasheet, one can always obtain them by performing load pulling and source pulling. This is usually a back-and-forth process, since one might not be able to pull both sides simultaneously.

To avoid this process, one could reason that it is the duty of the load network to sustain maximum drain voltage swing just when the drain current swing reaches its maximum value, and the load impedance that makes this happen is the optimum load impedance. With this principle, pulling can be performed without repetition whether in a simulator or with actual pulling devices. In the simulator, first, a voltage source is connected directly to the transistor gate to make sure the drain current reaches its maximum swing. And then, load pull can be performed to get the Z_L. Finally, the load impedance is set to Z_L and source pull is performed to get Z_S.

Regarding the final step, if one wishes to measure the input large signal impedance of the transistor and use the conjugate of that value as Z_S, it also works. There is however an interesting point here. At the input side of the amplifier, what matters is how much gate voltage swing is available given a certain input power. While what conjugate matching guarantees is maximum power transfer. These are actually two different problems. Suppose the large signal admittance of the transistor is $Y_{in} = G_{in} + jB_{in}$, it is not difficult to deduce the relation between gate power P_g and gate voltage V_g, as shown in Equation (1), from which one can tell that maximum gate power indeed corresponds to maximum gate voltage swing.

$$P_g = 0.5 \cdot |V_g|^2 \cdot G_{in} \tag{1}$$

5. CONCLUSION

The design procedure of a Class F amplifier has been presented, with various practical design issues addressed. A novel means of obtaining optimum impedances is discussed, with the relation between transistor gate voltage and power elucidated.

ACKNOWLEDGMENT

The authors wish to thank Cree, Inc. for providing sample transistors. Many thanks to AWR Corporation for providing free educational licenses of Microwave Office. Many thanks to Taconic for donating board materials. Many thanks to Mr. Ken Beals for providing measurement equipments.

REFERENCES

1. Cripps, S., *RF Power Amplifier for Wireless Communications*, 2nd Edition, Artech House, Inc, Norwood, 2006.
2. Raab, F., "Class-F power amplifier with maximally flat waveforms," *IEEE Tran. MTT*, Vol. 45, No. 11, 2007–2012, 1997.
3. Gao, S., "High-efficiency class F RF/microwave power amplifiers," *IEEE Microwave Mag.*, Vol. 7, No. 1, 40–48, 2006.
4. Schmelzer, D. and S. Long, "A GaN HEMT class F amplifier at 2 GHz with 80% PAE," *IEEE Compound Semiconductor IC Symposium*, 96–99, San Antonio, USA, November 2006.
5. Woo, Y. Y., Y. Yang, I. Kim and B. Kim, "Efficiency comparison between highly efficient Class-F and inverse Class-F power amplifiers," *IEEE Microwave Mag.*, Vol. 8, No. 3, 100–110, 2007.

A Study on Equivalent Circuit of Short Wavelength Microstrip Line Employing PPGM on GaAs MMIC

Jang-Hyeon Jung, **Bo-Ra Jung**, **Young-Bae Park**, **Se-Ho Kim**, **Jeong-Gab Ju**, **Suk-Youb Kang**, **Dong-Woo Kang**, **Mi-Jung Kim**, **Byeong-Su Lim**, **Cheol-Hee Do**, **and Young Yun**
Department of Radio Sciences and Engineering, Korea Maritime University, Korea

Abstract— In this work, equivalent circuit of short wavelength microstrip line employing periodically perforated ground metal (PPGM) were investigated using theoretical analysis. Equivalent circuits for the PPGM cell were extracted, and all lumped circuit parameters were expressed by closed-form equation. For application to miniaturized on-chip passive components, Wilkinson power divider and imped-ance transformer employing microstrip line with PPGM were fabricated on GaAs MMIC. The size of power divider and impedance transformer were 6 and 0.64% of the conventional ones. Above results reveal that the transmission line employing PPGM is a promising candidate for a development of matching and passive elements on MMIC.

1. INTRODUCTION

Recently, demands for highly integrated and miniaturized monolithic microwave integrated circuit (MMICs) have increased in wireless communication systems market. However, the signal coupling between adjacent lines have been an obstacle for chip size reduction, because a large spacing between adjacent lines is required to suppress the signal coupling in higj frequency.

In this work, we propose the short wavelength microstrip line employing PPGM (Periodically Perforated Ground Metal), and its equivalent circuit was thoroughly studied for application to circuit design. Using a microstrip line employing PPGM on GaAs MMIC, a highly miniaturized and broadband on-chip impedance transformer was developed for application to low impedance matching in broadband.

2. STRUCTURE OF MICROSTRIP LINE EMPLOYING PPGM AND ITS WAVELENGTH CHARACTERISTIC

Figure 1 shows the structure of the microstrip line employing PPGM, and its cross-sectional view according to Y-Y direction. As shown in Fig. 1, PPGM was inserted at the interface between SiN film and GaAs substrate, and it was electrically connected to backside GND metal through the via-holes. As is well known, conventional microstrip line without PPGM has only a periodical capacitance C_a (C_a is shown in Fig. 1) per a unit length, while the microstrip line employing PPGM has additional capacitance C_b as well as C_a due to PPGM. Therefore, as shown in Table 1, the microstrip line with PPGM exhibits much shorter guided-wavelength (λ_g) than conventional one, because λ_g is inversely proportional to the periodical capacitance, in other words, $\lambda_g = 1/[f \cdot (LC)^{0.5}]$. The characteristic impedance Z_0 and guided-wavelength λ_g for the conventional microstrip line. Above results indicate that highly miniaturized passive circuits can be realized by using the microstrip line employing PPGM. We can deduce that the above structure shows high isolation characteristics from equivalent circuit.

$$Z_0 = \sqrt{\frac{L}{C}} \qquad \lambda_g = \frac{1}{f\sqrt{LC}} \tag{1}$$

$$Z_0 = \sqrt{\frac{L}{C_a + C_b}} \quad \lambda_g = \frac{1}{f\sqrt{L(C_a + C_b)}} \tag{2}$$

Equation (1) is characteristic impedance and wavelength of conventional microstrip line. L and C correspond to the periodical inductance and capacitance of the LC equivalent circuit of the conventional microstrip line. Equation (2) is characteristic impedance and wavelength of PPGM structure. From (1) and (2), we can see that the microstrip line employing PPGM will exhibit lower Z_0 and λ_g than the conventional one. We can control the value of the additional capacitance C_b by changing the spacing T of Fig. 1, which enables an adjustment of values for Z_0 and λ_g.

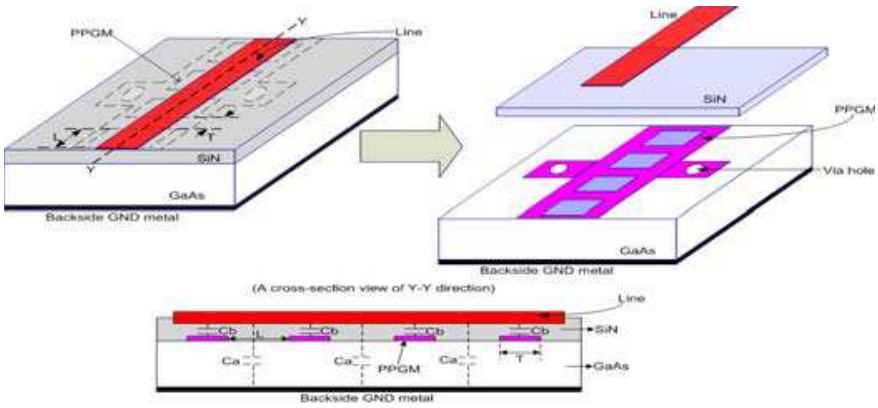

Figure 1: Structure of microstrip line employing PPGM.

Table 1: Measured wavelength (λ_g) for the microstrip line employing PPGM and conventional one at 20 GHz.

Microstrip line employing PPGM	2.2 mm
Conventional microstrip line	5.6 mm

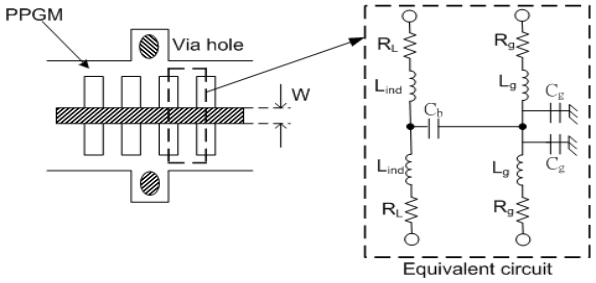

Figure 2: An equivalent circuit for a unit cell of the microstrip line employing PPGM.

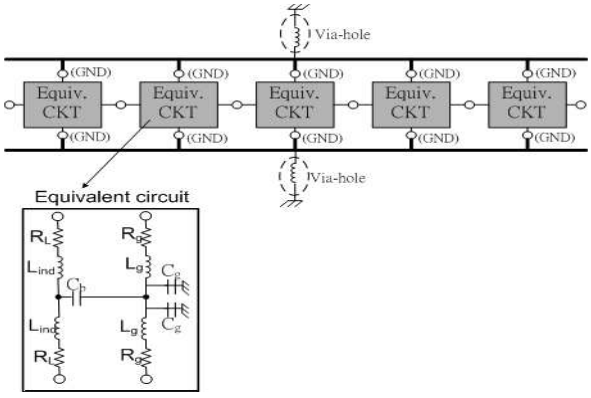

Figure 3: The equivalent circuit for microstrip line employing PPGM.

3. EQUIVALENT CIRCUIT OF MICROSTRIP LINE EMPLOYING PPGM

Figure 2 shows the equivalent circuit of adjacent two lines, which corresponds to the equivalent circuit of the Nth unit section of the periodic structure surrounded by rectangular box in Fig. 1. C_b corresponds to the capacitance between top line and PPGM, which is shown in Fig. 1, and it is proportional to the cross area $W \cdot T$ of line of line and PPGM (As shown in Fig. 1, W and T are the width of top lines and the periodic strips of PPGM, respectively). R_g and L_g are resistance and inductance originating from the loss and current flow of the periodic strip of PPGM with width T, respectively. C_g corresponds to the capacitance between PPGM and backside metal of GaAs substrate. L_{ind} is parasitic inductance originating from via-holes.

Figure 3 shows an equivalent circuit of the microstrip line employing PPGM. As shown in this figure, a number of the equivalent circuits of unit section are connected to each other, and via-hole was expressed as lumped inductor. The capacitance and inductance of the equivalent circuit are given by,

$$L_{ind} = \left[0.0267 - \left(\frac{T}{W}\right) \times 0.776 + \left(\frac{T}{W}\right)^2 \times 0.0533\right] \text{ nH} \tag{3}$$

$$C_b = \left[0.0933 + \left(\frac{T}{d_i}\right) \times 6 \times 10^{-4} - \left(\frac{T}{d_i}\right)^2 \times 1.33 \times 10^{-6}\right] \text{ pF} \tag{4}$$

where, W, T and d_i are top line width, width of periodic metal strip and the thickness of SiN (See

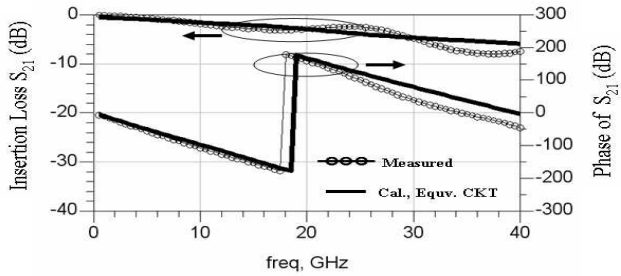

Figure 4: Measured and calculated insertion loss S_{21} for microstrip line employing PPGM.

Fig. 1). The whole equivalent circuit is shown in Fig. 3. As shown in this figure, a number of the equivalent circuits of unit section are connected to each other, and via-hole was expressed as lumped inductor.

Figure 4 shows measured and calculated insertion loss S_{21} for microstrip line employing PPGM. For the calculation result, equivalent circuit of Fig. 3 and above closed form equations were used. As shown in this figure, we can observe a fairly good agreement between calculated and measured results.

4. CONCLUSIONS

In this work, equivalent circuit of microstrip line employing PPGM were investigated using theoretical analysis. Above result indicates that the transmission lines employing PPGM is very useful for application to compact signal lines of highly integrated MMIC requiring a high isolation characteristics between lines. According to results, a much better isolation characteristic was observed from the adjacent microstrip lines employing PPGM compared with conventional microstrip lines, and the frequency range for high isolation was easily controlled by changing the PPGM structure.

For simplification of design process, equivalent circuits for the PPGM cell were extracted, and all lumped circuit parameters were expressed by closed-form equation. The calculated results showed a comparatively good agreement with measured ones.

For application to miniaturized on-chip passive components, Wilkinson power divider and impedance transformer employing microstrip line with PPGM were fabricated on GaAs MMIC. The size of power divider and impedance transformer were 6 and 0.64% of the conventional ones. Above results reveal that the transmission line employing PPGM is a promising candidate for a development of matching and passive elements on MMIC.

ACKNOWLEDGMENT

This research was supported by the MKE(The Ministry of Knowledge Economy), Korea, under the ITRC (Information Technology Research Center) support program supervised by the NIPA (National IT Industry Promotion Agency) (NIPA-2009-C1090-0903-0007). This work was financially supported by the Ministry of Knowledge Economy (MKE) and the Korea Industrial Technology Foundation (KOTEF) through the Human Resource Training Project for Strategic Technology. This work was partly sponsored by KETI (Korea Electronics Technology Institute). This work was also partly supported by ETRI SoC Industry Promotion Center, Human Resource Development Project for IT SoC Architect.

REFERENCES

1. Yun, Y., et al., "Basic RF characteristics of the microstrip line employing periodically perforataed ground metal and its application to highly miniaturized on-chip passive components on GaAs MMIC," *IEEE Trans. Microwave Theory Tech.*, Vol. 54, No. 10, 3805–3817, Oct. 2006.
2. Pozar, D. M., *Microwave Engineering*, Addison Wesley, Reading, MA, 1990.
3. Yang, F. R., K. P. Ma, Y. Qian, and T. Itoh, "A UC-PBG structure and its applications for microwave circuits," *IEEE Trans. Microwave Theory Tech.*, Vol. 47, No. 8, 1509–1514, Aug. 1999.
4. Wadell, B. C., *Transmission Line Design Handbook*, Ch. 3, Artech House, Boston, MA, 1991.
5. Yun, Y., J. W. Jung, K. M. Kim, H. C. Kim, W. J. Jang, H. G. Ji, and H. K. Ahn, "Experimental study on isolation characteristics between adjacent microstrip lines employing periodically perforated ground metal for application to highly integrated GaAs MMICs," *Microwave and Wireless Components Letters*, Vol. 17, No. 10, 703–705, Oct. 2007.

A Design of the LTCC Balanced-to-Unbalanced Bandpass Filters

Yujie Zhao, **Yali Qin**, **and Shuwei Yang**
Zhejiang Key Research Lab of Fiber-optic Communication Technology, China

Abstract— This paper presents a design method of a balanced-to-unbalanced bandpass filter by using multilayer configuration provided by LTCC (Low Temperature Co-fired Ceramic) technology. The design method for the balun is based on three quarter-wave-length transmission lines. By using the high-frequency simulation software, a balun bandpass filter with two transmission zeros is designed, whose center frequency is 2.45 GHz. Its insertion loss is less than 3.5 dB and size is 2.0 mm × 1.25 mm × 0.9 mm, which is widely used for wireless communication systems. It has smaller size than the balun filter manufactured on PCB (Printed Circuit Board).

1. INTRODUCTION

With the development of the wireless communication technology, the demand of compact and low loss components is increased. To meet the requirements, many efforts have been focused on the integration of passive components, which usually work in a cascade fashion [1–3]. LTCC technology becomes more and more useful for the productions of the device. Over the pass few years, several balanced filters have been developed which focus on the integration of the bandpass filter and balun to form a three-port balanced bandpass filter [4-7]. Among them, microstrip balanced filters are proposed with bulky size. In [8, 9], the proposed balanced filters using LTCC technology have smaller size. Concerning the balun, the planar version of Marchand balun has been adopted for a long time due to its good amplitude and phase characteristics. Then, the three line baluns which have smaller size have been presented [9, 10].

In this paper, we utilize a second order filter using SIR (Stepped Impedance Resonators) to reduce the size of filter. In order to improve the suppression performance at the stopband, two transmission zeros are introduced into the proposed filter, one below the passband and the other above the passband. The balun is based on three quarter-wave-length transmission lines, and each line is implemented as a spiral line for size reduction. At last, by using the high-frequency simulation software, a balanced bandpass fiter realized in 9 layers has been designed, whose center frequency is 2.45 GHz. Its insertion loss is less than 4 dB and size is 2.1 mm × 1.25 mm × 0.9 mm, which is widely used for wireless communication systems such as bluetooth and WLAN system.

2. FILTER DESIGN

There is magnetic and electric coupling between adjacent resonators. In this paper, a second order filter is chosen as shown in Fig. 1(a) [10–12]. To enhance the suppression, the transmission zeros are introduced. A lumped capacitive C_3 between input and output port is added to produce two transmission zeros. If the capacitive mutual coupling is too small to be neglected as Fig. 1(b), one transmission zero is blow the passband while the other is up the passband. With the C_3 increased, the frequencies of the transmission zeros are more and more close to the center frequency as shown in Fig. 2.

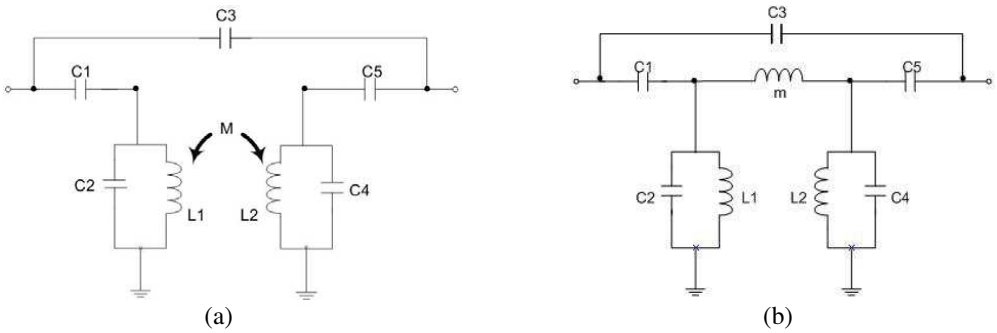

Figure 1: (a) Schematic of two second bandpass filter. (b) Equivalent circuit of the filter structure.

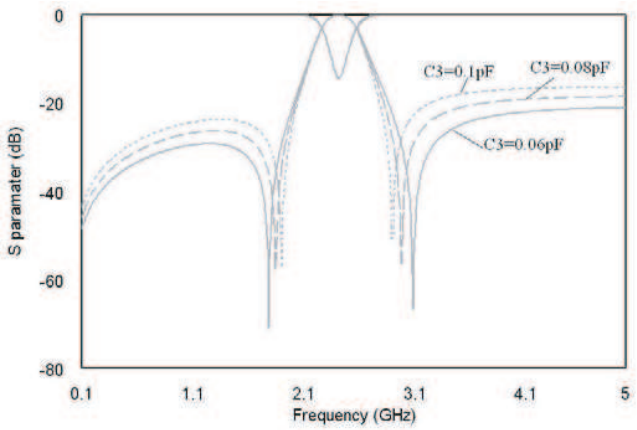

Figure 2: Frequency response of two second bandpass filter with different value of C_3.

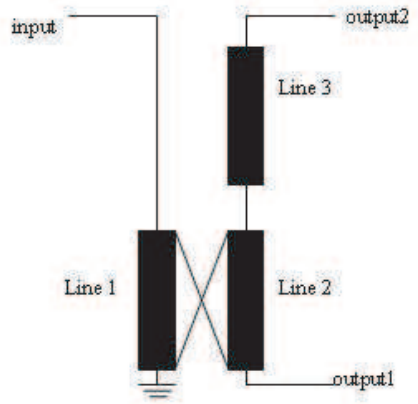

Figure 3: Schematic of the three line balun.

When $C_3 = 0.06\,\text{pF}$, the frequencies of transmission zeros are near 1.6 GHz and 3.1 GHz with 68.07 dB and 73.92 dB insertion loss. With C_3 increased to 0.08 pF, the transmission zeros locate at 1.84 GHz and 2.98 GHz.

3. BULAN DESIGN

The balun is a necessary passive component for converting an unbalanced signal into two balanced signals with the same magnitude and reverse phase. In this paper, a three-line balun is designed. Fig. 3 shows the equivalent circuit for the proposed balun based on three quarter-wave-length transmission lines.

From [9], we can know the impedance matrix $[Z]$ of the circuit in Fig. 3 is

$$[Z] = \begin{bmatrix} 0 & \frac{-jC_{33}}{\nu C_{12} C_{33}} & \frac{jC_{22}}{\nu C_{12} C_{33}} \\ \frac{-jC_{33}}{\nu C_{12} C_{33}} & 0 & 0 \\ \frac{jC_{22}}{\nu C_{12} C_{33}} & 0 & 0 \end{bmatrix} \tag{1}$$

where ν denotes the velocity of TEM-mode wave propagation in the medium, and the capacitance matrix $[C]$ is

$$[C] = \begin{bmatrix} C_{11} & C_{12} & C_{13} \\ C_{21} & C_{22} & C_{23} \\ C_{31} & C_{32} & C_{33} \end{bmatrix} = \begin{bmatrix} c'_{11} + c'_{12} & -c'_{12} & 0 \\ -c'_{12} & c'_{21} + c'_{22} & 0 \\ 0 & 0 & c'_{33} \end{bmatrix} \tag{2}$$

where c'_{ii} $(i = 1, 2, 3)$ denotes capacitance per unit length between transmission line i and ground, and c'_{12} and c'_{21} denotes capacitance per unit length between transmission line 1 and 2.

4. DESIGN OF THE BALANCED FILTER AND SIMULATION RESULTS

The balanced filter is realized as a combination of the filter and the balun. The 3-D structure is presented in Fig. 4. It has 9 mental layers with 3 ground planes. The filter using SIR structure is located in upper part and balun with spiral structure is located in lower part. They are connected

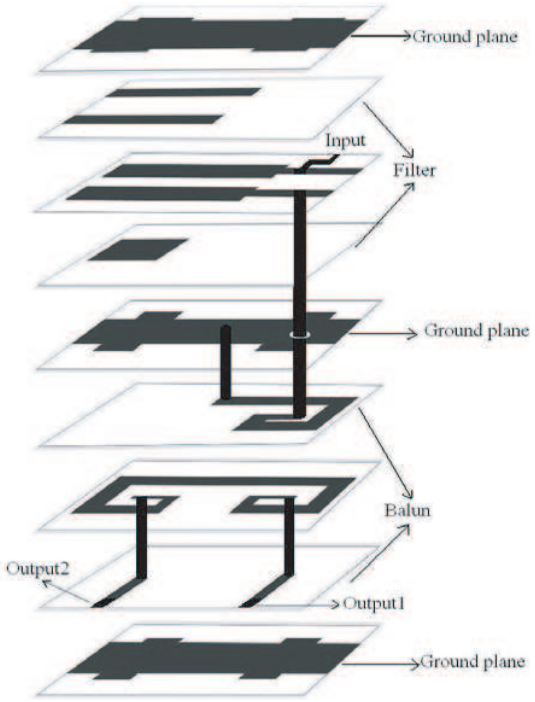

Figure 4: 3-D LTCC structure of the balanced filter.

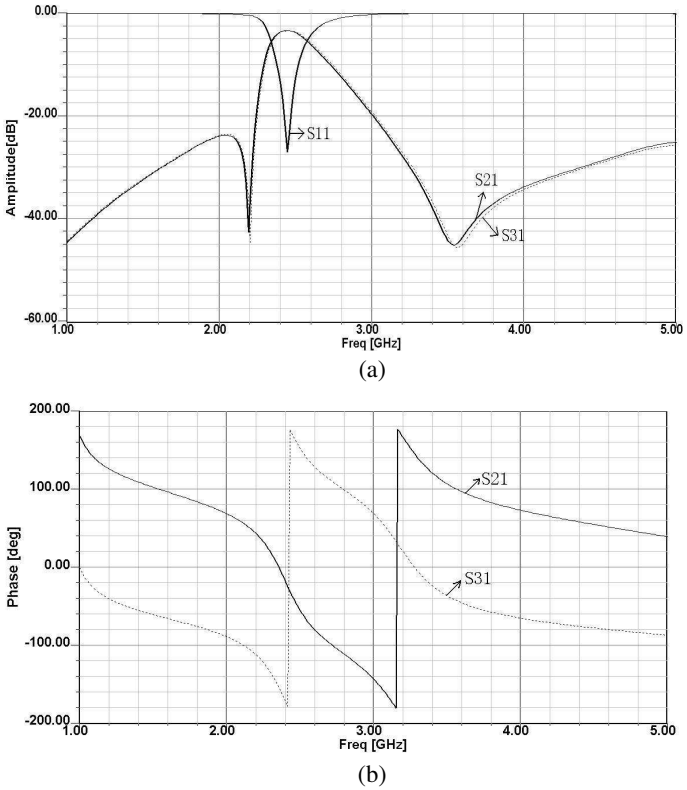

Figure 5: Simulated results of the designed balanced filter. (a) Amplitude response of the balanced filter. (b) Phase response of the balanced filter.

with via holes. Consequently, the middle ground plane is used for isolating the filter and balun. Unbalanced input and balanced outputs impedances are also 50 Ω and the size of the designed balanced filter is 2.0 mm × 1.25 mm × 0.9 mm.

Figure 5 shows the simulation results of the balanced filter by HFSS. As shown in Fig. 5(a), the balanced filter is designed to operate in the 2.4 GHz–2.5 GHz frequency. The maximum insertion loss in the passband is 3.48 dB. And the two transmission zeros are located at 2.19 GHz and 3.54 GHz with 42.52 dB and 44.99 dB insertion loss of S_{21}, while 2.2 GHz and 3.57 GHz with 44.67 dB and 45.46 dB of S_{31}. Fig. 5(b) shows that the phase difference between the two balanced outputs is about 180 degree.

5. CONCLUSION

In this paper, by using multilayer configuration which provided by LTCC technology, a balanced bandpass filter composed of a 2-port filter and a 3-port balun with an unbalanced input and two balanced outputs has been designed. It has well amplitude and phase response. The size of the balanced filter with 2.45 GHz center frequency is 2.0 mm × 1.25 mm × 0.9 mm, which is widely used for wireless communication systems such as bluetooth and WLAN system.

ACKNOWLEDGMENT

The author would like to thank Professor Qin for giving some useful advice. Many thanks are also given to the Shen Zhen Shun Luo Electronic Limited Company for the financial support.

REFERENCES

1. Lim, K., S. Pinel, M. Davis, A. Sutono, and C.-H. Lee, "RF-system-on-package (SOP) for wireless communications," *IEEE Microwave Magazine*, Vol. 3, 88–89, 2002.
2. Rambabu, K. and J. Bornemann, "Simplified analysis technique for the initial design of LTCC filters with all-capacitive," *IEEE Transactions on Microwave Theory and Techniques*, Vol. 53, No. 5, 1787–1791, 2005.
3. Sung, H.-M., C.-J. Chen, L.-J. Wang, and W.-S. Ko, "The characteristics of low temperature Co-fired multilayer chip LC filters," *IEEE Transactions on Magnetics*, Vol. 34, No. 4, 1363–1365, 1998.
4. Ziroff, A., M. Nalezinski, and W. Menzel, "A 40 GHz LTCC receiver module using a novel submerged balancing filter structure," *Proceedings of Radio and Wireless Conference*, 151–154, Boston, USA, August 2003.
5. Lin, S.-C., P.-H. Deng, and Y.-S. Lin, "Wide-stopband microstrip bandpass filters using dissimilar quarter-wavelength stepped-impedance resonators," *IEEE Transactions on Microwave Theory and Techniques*, Vol. 54, No. 3, 1011–1018, 2006.
6. Wu, C.-H., C.-H. Wang, and C. H. Chen, "Stopband-extended balanced bandpass filters using coupled stepped-impedance resonators," *IEEE Microwave and Wireless Components Letters*, Vol. 55, No. 2, 287–295, 2007.
7. Wu, C. H., C.-H. Wang, and C. H. Chen, "Novel balanced coupled-line bandpass filters with common-mode noise resonators," *IEEE Transactions on Microwave Theory and Techniques*, Vol. 17, No. 7, 1787–1791, 2007.
8. Park, M. C., B. H. Lee, and D. S. Park, "A laminated balance filter using LTCC technology," *Proceedings of Asia-Pacific Conference*, 2974–2977, Suzhou, China, December 2005.
9. Lee, B. H., D. S. Park, and S. S. Park, "Design of new three-line balun and its implementation using multilayer configuration," *IEEE Transactions on Microwave Theory and Techniques*, Vol. 54, No. 4, 1405–1414, 2006.
10. Sakhnenko, S., D. Orlenko, and K. Markov, "Low profile LTCC balanced filter based on a lumped elements balun for WiMAX applications," *IEEE MTT-S International Microwave Symposium Digest*, 1111–1114, AtlantaHome, USA, June 2008.
11. Razalli, M. S., A. Ismail, M. A. Mahdi, and M. N. Bin Hamidon, "Novel compact "via-less" ultra-wide band filter utilizing capacitive microstrip patch," *Progress In Electromagnetics Research*, PIER 91, 213–227, 2009.
12. Wang, X.-H., B.-Z. Wang, and K. J. Chen, "Compact broadband dual-band bandpass filters using slotted ground structures," *Progress In Electromagnetics Research*, PIER 82, 151–166, 2008.

A Comparative Study of the Field Dependence of the Properties of Colloidal Suspensions of Nanoparticles and of Magnetic Microspheres

P. C. Fannin[1], **C. N. Marin**[2], **C. Couper**[1], **I. Malaescu**[2], **and N. Stefu**[2]

[1]Department of Electronic and Electrical Engineering, Trinity College, Dublin 2, Ireland
[2]Faculty of Physics, West University of Timisoara, B-dul V. Parvan, No. 4, Timisoara 300223, Romania

Abstract— Measurements of the frequency and field dependence of the complex magnetic susceptibility, $\chi(\omega, H) = \chi'(\omega, H) - i\chi''(\omega, H)$ of a magnetic fluid and a suspension of magnetic beads over the frequency range 100 Hz to 1 MHz are presented. A magnetic polarizing field, H, is applied to both samples, first in a forward direction and then in a reverse direction. The resulting data is then used to investigate the dominant relaxation mechanisms and also the hysteresis properties of the samples.

1. INTRODUCTION

Colloidal suspensions of nano-particles and of magnetic beads, or microspheres as they are often referred to, are of current interest particularly in the medical area [1]. A common factor in both types of fluids is that they both comprise of nano-particles, with the ferrofluid comprising of nano-particles, of diameter 10 nm, with, say, a volume fraction of 5%, whilst the microspheres, of diameter say 200 nm, may contain a 50% volume fraction of nanoparticles [2, 3]. After manufacture the latter colloid consists of microspheres which have an emulsifier on their surface; the emulsifier forming a layer at the interface between the magnetic fluid droplets and the water.

Thus it is of interest to examine how the dynamic properties of both types of suspensions act in response to both ac and dc magnetic fields. This comparison may be realized through measurement of the frequency dependent complex susceptibility, $\chi(\omega) = \chi'(\omega) - i\chi''(\omega)$, of the suspensions. In particular one can determine which relaxation mechanism, Brownian [4] or Neel [5] dominates [6].

Both colloids consist of single domain particles which have a magnetic moment, m_p, given by, $m_p = Msv$ where Ms denotes the saturation magnetisation and v is the magnetic volume of the particle.

The Brownian relaxation time τ_B is given by [4]

$$\tau_B = 4\pi r^3 \eta / kT \tag{1}$$

where r is the hydrodynamic radius of the particle, η is the dynamic viscosity of the carrier liquid, k is Boltzmann's constant and T is the temperature.

In the case of the Néel relaxation mechanism, the relaxation time, τ_N was estimated by Néel [5] to be:

$$\tau_N = \tau_0 \exp(\sigma) \tag{2}$$

τ_0 is a damping time and $\sigma = Kv/kT$, where K is the anisotropy constant of the particle.

2. COMPLEX SUSCEPTIBILITY

The frequency dependent susceptibility, $\chi(\omega)$, may be written in terms of its real and imaginary components, where, $\chi(\omega) = \chi'(\omega) - i\chi''(\omega)$.

The theory developed by Debye [7, 8] to account for the anomalous dielectric dispersion in dipolar fluids may be used for the analogous case of magnetic colloids in the frequency range used here. According to Debye's theory, $\chi(\omega)$ has a frequency dependence as given by the equation,

$$\chi(\omega) - \chi_\infty = (\chi_0 - \chi_\infty)/(1 + i\omega\tau) \tag{3}$$

where

$$\chi_0 = nm^2/3kT\mu_0 \tag{4}$$

and

$$\tau = 1/\omega_{\max} = 1/2\pi f_{\max} \tag{5}$$

where $f_{\max}$ is the frequency at which $\chi''(\omega)$ is a maximum, n is the particle number density and χ_0 and χ_∞ indicate susceptibility values at $\omega = 0$ and at very high frequencies.

Thus by determining $f_{\max}$, Equations (1) and (5) enable one to obtain the mean particle size and also identify the existence of aggregation in the sample.

2.1. Polarising Field (H)

To examine the polarising field response of the samples an external polarising field, H, is applied to the samples and assuming the Langevin function for the magnetization of the samples, an expression for the field dependence of the a.c. susceptibility, $\chi(\omega, H)$, can be written as follows [9],

$$\chi(\omega, H) = \frac{\chi_0 (1 + f(H)) - \chi_\infty}{1 + i\omega\tau(H)} + \chi_\infty \tag{6}$$

with

$$(1 + f(H)) = 3\left[1 + \left(\frac{kT}{mH}\right)^2 - \coth^2\left(\frac{mH}{kT}\right)\right] \tag{7}$$

For increasing values of polarising field, Equations (6) and (7) predict, respectively,

i) a reduction in both $\chi'(\omega)$ and $\chi''(\omega)$ with increasing biasing field and,
ii) a corresponding shift in $f_{\max}$ due to the polarizing field dependence of the relaxation time, $\tau(H)$. For instance, in the case of the Brownian relaxation time [10],

$$\tau_B(H) = \tau_B \frac{\xi}{L(\xi)}\left[1 - \coth^2(\xi) + \xi^{-2}\right] \tag{8}$$

with $\xi = \frac{mH}{kT}$ and τ_B given by Equation (1).

3. EXPERIMENTAL AND RESULTS

Complex magnetic susceptibility measurements, over the frequency range 100 Hz to 1 MHz, were made by means of the toroidal technique [11] in conjunction with a Hewlett Packard RF Bridge 4291A. A high permeability toroid wound with twenty excitation turns was used. A second coil comprising of 3 turns was also wound on the toroid and connected to a stabilized D. C. supply to provide biasing magnetic fields, H. The biasing field was varied from 0 to 13.6 kA/m; the approximate values of H used being, 0, 2.7 kA/m, 5.5 kA/m, 8.2 kA/m, 10.9 kA/m and 13.6 kA/m.

Here we present the results of measurements performed on two colloidal samples, sample 1 was a 110 G colloidal suspension of magnetite in water, of mean radius 5 nm and a surfactant of oleic acid, whilst sample 2 was a dilute (0.06% vol fraction) magnetic emulsion of 200 nm spheres; the spheres contained maghemite (γFe_2O_3) particles of mean particle radius 10 nm.

3.1. Sample 1

Figure 1 shows a plots of $\chi'(\omega, H)$ and $\chi''(\omega, H)$ obtained for sample 1 over the polarising field, H, range, 0 up to 13.6 kA/m and back down to 0. All are shown to have Debye type profiles with $f_{\max}$ varying from 5.4 kHz to 20 kHz; these frequencies being indicative of Brownian relaxation [12]. The shift of $f_{\max}$ towards higher frequencies with the increase of H is in agreement with Equation (8). $f_{\max} = 5.4$ kHz, corresponding to zero polarizing field, is indicative of the presence of aggregation and the increase in $f_{\max}$ corresponds to an apparent decrease in average hydrodynamic aggregate size.

It is also noted that both $\chi'(\omega)$ and $\chi''(\omega)$ decrease with increasing polasirising field, H, as predicted by Equations (6) and (7).

Figure 1 also shows the similarity between the profiles for a cyclic variation of H thereby indicating that no hysteresis [13] has resulted from the polarizing process. This is further confirmed by Fig. 2 which is a plot of χ_0 against H in a forward and reverse direction of polarization; χ_0 being taken as the value of $\chi'(\omega)$ at a frequency of 100 Hz.

3.2. Sample 2

Complex susceptibility measurements were then performed on sample 2. Since the sample was a dilute one, no useful signal was obtained below 200 Hz and for convenience, the static susceptibility, χ_0 was taken to be equivalent to the values of $\chi'(\omega)$ obtained at 400 Hz. Fig. 3 shows the $\chi''(\omega)$ component of the susceptibility spectra. One can observe that $\chi''(\omega)$ exhibits a relaxation peak in

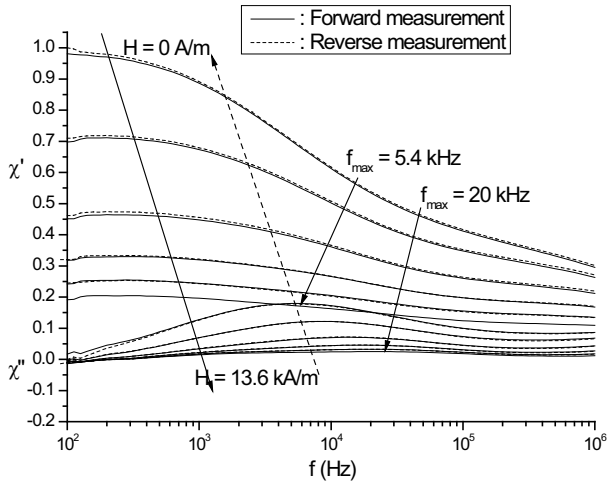

Figure 1: Plot of $\chi'(\omega, H)$ and $\chi''(\omega, H)$ (forward and reverse) against f (Hz).

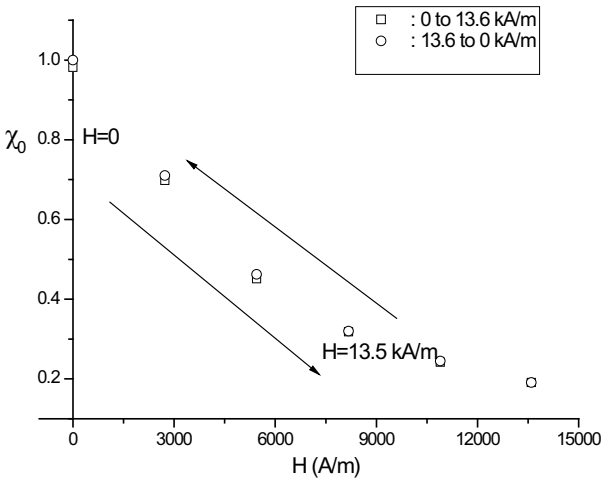

Figure 2: Plots of χ_0 against H over polarising field range, 0 up to 13.6 kA/m and back down to 0.

the low frequency region and another peak in the high frequency region. In stark contrast with sample 1, the amplitude of the low frequency relaxation peak is found to increase with increasing H and $f_{\max}$ varies from approx between 200–300 Hz to 1.8 kHz, over the range of H.

Figure 4 shows a plot of χ_0 against H for sample 2, and an interesting feature emerges in that after an initial decrease, χ_0 starts to increase until $H = 13.6\,\mathrm{kA/m}$. Again this is in contrast to what happens in the case of sample 1 where the equivalent components decrease with increasing H. However, on decreasing H, the increase in χ_0 continues up to a value of $H = 8\,\mathrm{kA/m}$, after which it falls to a value of approximately, $H = 4.5\,\mathrm{kA/m}$. Following a further decrease in H, χ_0 decreases rapidly to a value approximately equal to the unpolarised case. This hysteresis effect [14] is not observed in the case of sample 1.

4. RELAXATION MECHANISMS

The dominant relaxation mechanism in sample 1 was Brownian, but what of the microspheres, where consideration must be given to the sphere itself and the particles within the sphere?

Considering the possibility of Néel relaxation of the microspheres, from Equation (2) we have $\tau_N = \tau_0 \exp(\sigma)$, $\sigma = Kv/k_BT$. Thus for spheres of radius 100 nm, with $K = 9.5 \cdot 10^3\,\mathrm{J/m^3}$, one gets a value of $\sigma = 9.6 \cdot 10^3$, which gives an exponentially large relaxation time, corresponding to an almost zero frequency. This thus rules out this possibility.

Assuming the possible rotation of microspheres within the carrier liquid (water), from Equa-

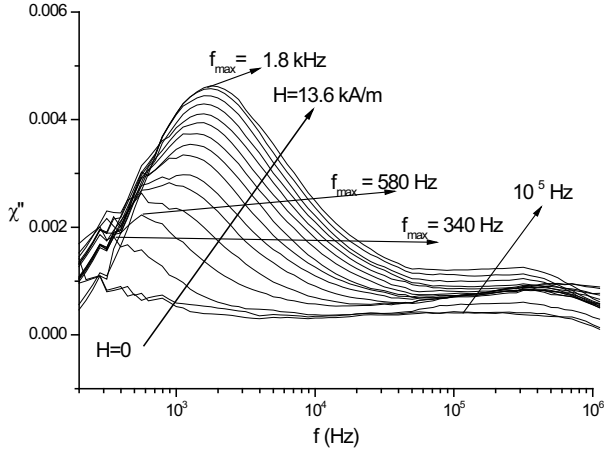

Figure 3: Plot of $\chi''(\omega)$ against f (Hz) for sample 2, for 16 values of polarizing field, H.

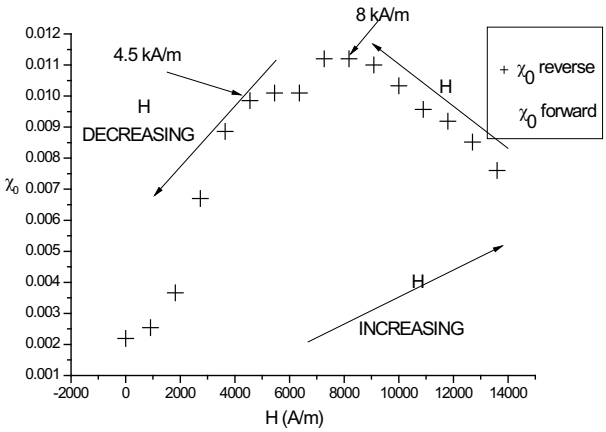

Figure 4: Plot of χ_0 against H for sample 2, for 16 values of polarizing field range, 0 up to 13.6 kA/m and back down to 0.

tion (1) with the spheres of radius 100 nm, the dynamic viscosity of water, $\eta = 1$ cP and the temperature of 300 K, one obtains a Brownian relaxation time in order of $3 \cdot 10^{-3}$ s. With this value in Equation (5) one gets an $f_{\max}$ of the relaxation peak of 50 Hz. This is slightly smaller than the observed $f_{\max}$ in zero polarizing field (see Fig. 3). In Ref. [15], it is clearly demonstrated that the nanoparticles of a magnetic fluid still experience Brownian rotation below the freezing temperature of the carrier liquid, if the surfactant remains liquid. In other words, if the dynamic viscosity of the surfactant is smaller than the dynamic viscosity of the carrier liquid, then the particles can relax through Brownian rotation within the surfactant layer. In the case of sample 2, assuming the rotation of the microspheres within the emulsifier layer with, say, a dynamic viscosity $\eta = 0.5$ cP, one gets a frequency, $f_{\max}$, corresponding to the maximum of χ'', of 106 Hz. This is within the frequency range where the loss-peaks were detected in zero polarizing field.

Now considering the maghemite particles which are extremely confined (closely packed) inside the microspheres, due to the elimination of their mechanical degree of freedom, they cannot experience Brownian rotation.

However, if the Neel time is evaluated for a smaller particle of radius 10 nm, the value of σ equals 9.6 and using a value of $\tau_0 = 10^{-10}$ s, as suggested in [16] for maghemite, one gets $f_{\max} = 10^5$ Hz. This value corresponds closely with the high frequency peak of Fig. 3, obtained for $H = 0$. Previously [14] the generally accepted value of $\tau_0 = 10^{-9}$ s was used resulting in inaccurate deductions being made.

Thus, using a value of $\tau_0 = 10^{-10}$ s, it appears that the low frequency loss peaks detected are mainly due to the Brownian relaxation arising out of the rotation of the microspheres within the emulsifier layer and the high frequency relaxation peaks are due to the Néel relaxation process in the nanoparticles within the microspheres.

5. CONCLUSIONS

In this paper, measurements of the frequency dependent, complex susceptibility, $\chi(\omega) = \chi'(\omega) - i\chi''(\omega)$, over the frequency range 100 Hz to 1 MHz, of a magnetic fluid comprised of magnetite particles and a magnetic suspension consisting of 200 nm spherical beads, containing maghemite (γFe_2O_3) nanoparticles, have been presented. It has been shown that, unlike in the case of ferrofluids where the amplitude of the static susceptibility, χ_0, decreases with increasing polarizing field, H, the general trend in the case of the emulsion is for the amplitude of the static susceptibility to increase with increasing H.

Within the measured frequency range, the magnetic fluid experience a Brownian relaxation process and the magnetic suspension of microspheres exhibits Brownian relaxation due to the rotation of the microspheres within the emulsifier layer and Néel relaxation process due to the nanoparticles within the microspheres.

Finally, by means of the application of a reverse polarizing field the existence of a hysterises effect was confirmed in the case of the microspheres but not in case of the ferrofluid.

ACKNOWLEDGMENT

Acknowledgement is due to A. McCarthy, C. Mac Oireachtaigh, E. Bertrand, L. Cohen-Tannoudji, and also to ESA for the part funding of this work.

REFERENCES

1. Montagne, F., O. Mondain-Monval, C. Pichot, H. Mozzanega, and A. Elaissari, *J. Magn. Magn. Mater.*, Vol. 250, 302, 2002.
2. www.ademtech.com.
3. Fannin, P. C., L. Cohen-Tannoudji, E. Bertrand, A. T. Giannitsis, C. M. Oireachtaigh, and J. Bibette, *J. Magn. Magn. Mater.*, Vol. 303, 147, 2006.
4. Brown, W. F., *J. Appl. Phys.*, Vol. 34, 1319, 1963.
5. Néel, L., *Ann. Géophys.*, Vol. 5, 99, 1949.
6. Fannin, P. C. and S. W. Charles, "The study of a ferrofluid exhibiting both Brownian and Néel relaxation," *J. Phys. D: Appl. Phys.*, Vol. 22, 187–191, 1989.
7. Debye, P., *Polar Molecules*, The Chemical Catalog Company, New York, 1929.
8. Fannin, P. C., "Wideband measurement and analysis techniques for the determination of the frequency dependent, complex susceptibility of magnetic fluids," *Advances in Chemical Physics*, Vol. 104, 181–292, 1998.
9. Fannin, P. C., B. K. P. Scaife, and S. W. Charles, *J. Magn. Magn. Mater.*, Vol. 72, 95, 1988.

10. Raikher, Y. L. and M. I. Shliomis, *Adv. Chem. Phys., Relaxation Phenomena in Condensed Matter*, Ch. 8, Vol. 87, 595–751, 1994.
11. Fannin, P. C., B. K. P. Scaife, and S. W. Charles, *J. Phys. E. Sci. Instrum.*, Vol. 19, 238, 1986.
12. Fannin, P. C. and A. T. Giannitsis, *J. Mol. Liq.*, Vol. 114, 89, 2004.
13. Fannin, P. C., S. W. Charles, C. M. Oireachtaigh, and S. Odenbach, *J. Magn. Magn. Mater.*, Vol. 302, 1, 2006.
14. Fannin, P. C., C. M. Oireachtaigh, E. Bertrand, and L. Cohen-Tannoudji, *J. Magn. Magn. Mater.*, Vol. 300, No. 1, 210, 2006.
15. Philipse, A. P., *Langmuir*, Vol. 21, No. 4, 1187–1191, 2005.
16. Dormann, J. L., D. Fiorani, and E. Tronc, *J. Magn. Magn. Mater.*, Vol. 202, 251–267, 1999.

PIFA Antenna with Coupling Effect for Bandwidth Enhanced Design and Measurement

Kekun Chang[1], **Guan-Yu Chen**[1], **Jwo-Shiun Sun**[1], **and Y. D. Chen**[2]

[1]Department of Electronic Engineering, National Taipei University of Technology, Taiwan
[2]Antenna and EMC Laboratory, HTC Corporation, Taiwan

Abstract— A traditional multi-band planar inverted-F (PIFA) antenna by a preferred embodiment makes use of an open slot loop or multi slot. The slots are formed to cause multiple frequency dependent nulls in the EM current field modal distribution. A built-in, low-profile antenna having a PIFA antenna and a parasitic element by top loading having a wide bandwidth to facilitate wireless mobile within a plurality of frequency bands is designed, disclosed and measured.

1. INTRODUCTION

Along with the monopole, patch and slot antennas, the inverted-F antenna (IFA) has become of primary importance for portable and handheld wireless communication units. Planar inverted-F antennas have been widely applied in the mobile phone as internal antennas. Designing an internal antenna is challenging because of its close proximity to other metallic objects (shielding cans, screws, and battery). The planar inverted-F antenna (PIFA) has become the main candidate for such applications since it performs reasonably well compared to other alternatives when operated close to a ground plane. It is known as a high efficiency quasi-omnidirectional antenna. The inverted-F antenna, wire or planar (PIFA), is a low-profile modification of the quarter-wave monopole, and thus belongs to the group of unbalanced antennas.

There is a huge amount of research and development work on classical and novel single IFA configurations The PIFA antenna is popular for mobile handset (Figure 1) because of its low profile and compact size. The conventional PIFA usually cannot provide a wide operating band to cover GSM850/900/1800/1900/UMTS operation. If we consider merging of technologies where both TDMA and GSM are integrated in one phone, triple-band or even quad-band antennas may be needed. For instance, consider a device that operates in the TDMA 800, GSM 900, and TDMA/GSM 1900 MHz and UMTS bands. This means that the device operates in the 824–894 MHz, 880–960 MHz, 1850–1990 MHz and 2110–2170 MHz bands. Thus in the lower band the bandwidth required is 136 MHz which is almost twice as much of that required for GSM or TDMA alone. This is no doubt very difficult to obtain with a PIFA. For the achievement of additional operating bandwidths, parasitic or additional resonant elements are added. The PIFA is designed to reference a ground plane [1–3].

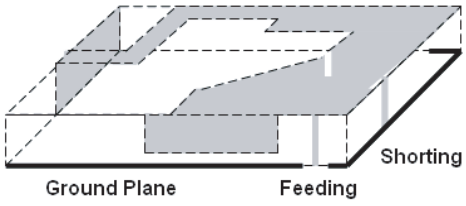

Figure 1: Traditional PIFA.

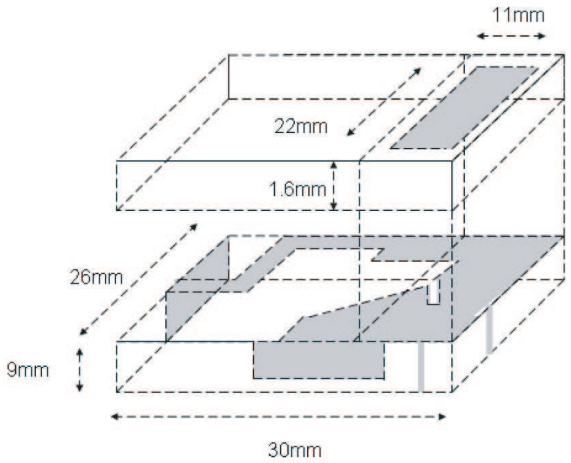

Figure 2: The proposed PIFA.

In this paper we propose a new type of the ultra-wideband PIFA with a parasitic element by top loading for the desired wideband operation in the mobile phone. Experimental and simulation results are presented and discussed.

2. ANTENNA DESIGN

The proposed PIFA (Figure 2) presents results from a comprehensive investigation on the performance of a conventional PIFA with a parasitical patch radiator to enhance antenna bandwidth. The geometry of the antenna is shown in Figure 2. It is apparent that there are two layers. The bottom layer consists of a printed circuit board (30 mm by 26 mm) and two metallic strips. The detail description of this layer can be found from Figure 2. The antenna is on the top layer at a height, 9 mm from the PCB. The air is as the dielectric in between the antenna and the PCB. From Figure 1, one of the vertical elements connecting the antenna and the PCB is the RF feed. In practice this will be a signal pin connecting the antenna and the RF signal pad on the PCB. In Figure 2 more detailed description of the antenna is shown. One parasitical patch radiator is on the above of the PIFA. The height between the parasitical patch and PIFA is 9 mm. The entire volume of the proposed antenna is 30 mm by 26 mm by 19.6 mm. The height of 9 mm is a small separation between the parasitical patch and the PIFA. The parasitical patch is floating on the PIFA.

The proposed PIFA with coupling effect antenna is analyzed and the influence of structure on bandwidth, gain, and radiation efficiency are presented. These results (Figure 3) are very useful in the design of a PIFA for applications requiring a parasitical radiator. Enhanced gain of PIFA antenna loaded with a parasitical patch has been demonstrated.

3. MEASUREMENT RESULTS

An important parameter associated with antenna characterization is the radiation efficiency. It is defined as

$$\eta = \frac{P_r}{P_r + P_L} \tag{1}$$

where P_t is the radiated power, P_L is the power loss in the antenna.

Measurements show that the bandwidth of the antenna can be improved without sacrificing the antenna radiation efficiency (Figure 4 and Figure 5). The gain enhancement mechanism, bandwidth, and antenna radiation gain and patterns are presented and discussed. The new radiators are

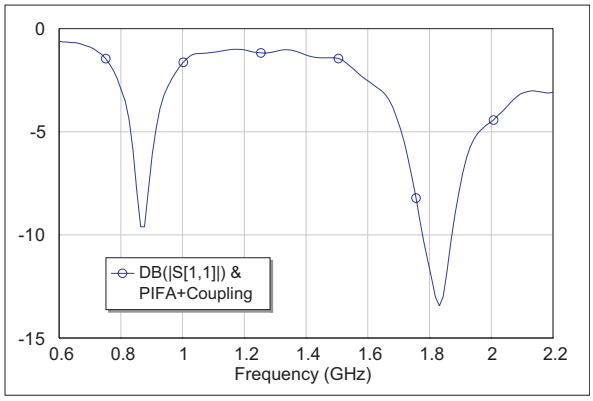

Figure 3: The measured data of proposed PIFA.

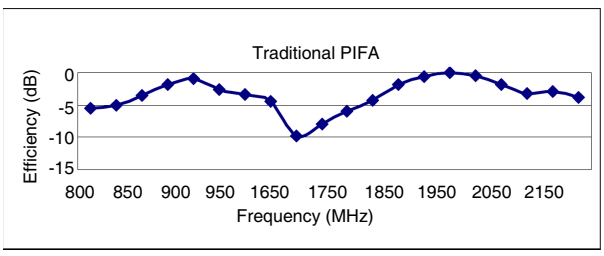

Figure 4: The measured data of traditional PIFA.

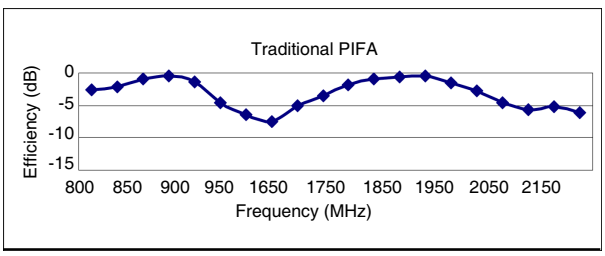

Figure 5: The measured data of proposed PI.

developed by adding parasitic elements or tuning devices to a familiar PIFA. Simulation based upon the method of moments (Microwave Office) is used to model the performance of the antennas. Comparisons with measured results on fabricated antenna structures are provided for simulations validation. Slot loaded has applied on PIFA antenna and investigated in this paper. Multi slots are inserted to reach multi band operations, respectively.

The antennas resonance frequencies are selected in the GSM, DCS, and PCS band to be compatible with commercial mobile phone applications. The antennas are designed, analyzed and fabricated using substrates as foam with $\varepsilon_r = 3.0$ and FR4 with $\varepsilon_r = 4.5$. Compact size operation is achieved by using trapezoidal shorted capacitive plate between the antenna radiator and the ground plane and top loading by a EM coupling. Computed return loss data for the proposed antenna is shown in Figure 3. As can be seen the antenna has two distinct resonances around 850/900 MHz and 1800/1900/2100 MHz. This enhances the antenna efficiency from conventional PIFA antenna. The antenna efficiency characteristics are acceptable in all cases with gain about -1 to -6.5 dB. The simulated 900 MHz current distribution by HFSS is shown in Figure 6, 1900 MHz is shown in Figure 7. The Measured 3D radiation pattern with 900 MHz of Proposed PIFA is shown in Figure 7. The -6 dB antenna impedance bandwidth is better and for all operating frequency bands and radiation pattern is acceptable in 3D OTA antenna measurement system [4, 5].

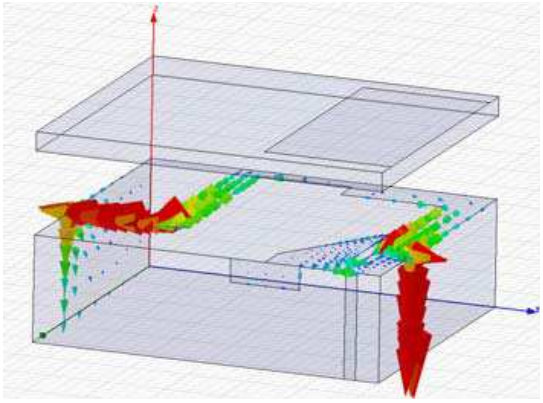

Figure 6: Current distribution of 900 MHz.

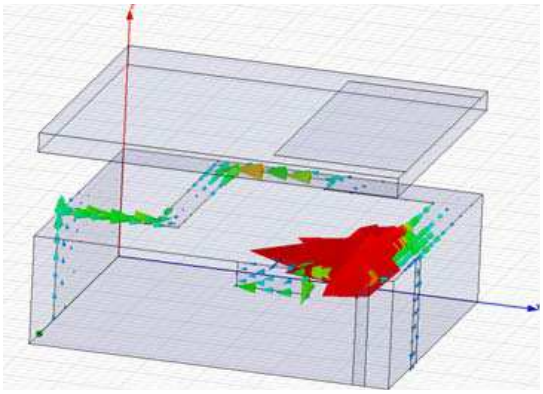

Figure 7: Current distribution of 1900 MHz.

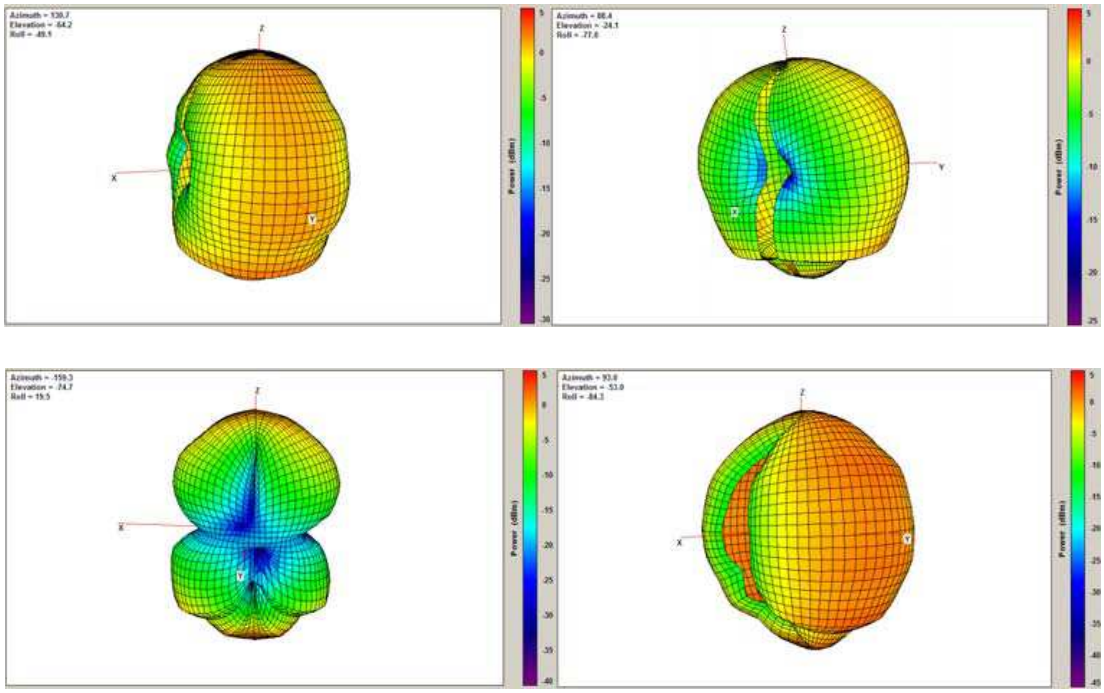

Figure 8: The measured 3D radiation pattern of proposed PIFA.

4. CONCLUSIONS

A dual-wideband band planar inverted-F antenna (PIFA), designed here, covers both 850–960 MHz and 1710–1990 MHz used in all GSM and CDMA2000 standards. Simulated and measured return loss and radiation patterns of the antenna are presented and are in reasonable agreement. Experimental results indicate a very wide operational bandwidth for PDA phone application.

ACKNOWLEDGMENT

The authors would like to thank the Antenna and EMC research laboratory, HTC Corporation, for their assistance in wireless and system integration measurements.

REFERENCES

1. Balanis, C. A., *Antenna Theory*, John Wiley & Sons, Inc, 1997.
2. Kraus, J. D. and R. J. Marhefka, *Antennas for All Applications*, McGraw-Hill, 2002.
3. Wong, K. L., *Planar Antennas for Wireless Communication*, John Wiley & Sons, Inc, 2003.
4. Chen, G. Y., J. S. Sun, and Y. D. Chen, "The 3D far-field antenna measurement technology for radiation efficiency, mean effective gain and diversity antenna operation," *2006 The 7th International Symposium on Antennas, Propagation, and EM Theory* (*2006 ISAPE*), 42–45. Guilin, China, Oct. 2006.
5. Chen, G. Y., J. S. Sun, C. H. Lin, K. K. Tiong, and Y. D. Chen, "Small Antenna Measurement Facilities," *PIERS Proceedings*, 157–158, Hangzhou, China, March 24–28, 2008.

Corrugated Tapered Slot Antenna Design and Measurement

Kekun Chang[1], **Guan-Yu Chen**[1], **Jwo-Shiun Sun**[1], **and Y. D. Chen**[2]

[1]Department of Electronic Engineering, National Taipei University of Technology, Taiwan
[2]Antenna and EMC Laboratory, HTC Corporation, Taiwan

Abstract— The Marchand balun for microwave band as a feeding network structure that effectively excited corrugated tapered slot antenna geometry is proposed. The designed antenna has the merits such as wideband, simple feeding network, low profile compact size with fairly good antenna performances.

1. INTRODUCTION

The radiation mechanism of a tapered slot antenna is based on traveling wave propagation along the tapered aperture slot, which results in an end-fire antenna. Tapered slot antenna exhibits some advantages such as wideband, wide scanning, high gain, low cross polarization and symmetrical E and H plane radiation patterns [1–6] for an array or embedded circuits as antenna radiating elements. The designed antenna can be used not only for EMC measurements, but also for broadband communication systems.

In this paper, the Marchand balun with a balanced to unbalanced transition is shown good impedance matching and easy to integration and fabrication and the frame of the planar structure on corrugated tapered slot antenna was experimentally investigated. Measured system [7] and results indicate that effects have significant impacts on the return loss, input impedance, radiation patterns and antenna gain of the corrugated tapered slot antenna.

2. ANTENNA DESIGN

The Marchand balun for microwave band as a feeding network structure that effectively excited corrugated tapered slot antenna geometry is proposed (Figure 1). The designed antenna has the merits such as wideband, simple feeding network, and low profile compact size with fairly good antenna performances. The radiation mechanism of a tapered slot antenna is based on traveling wave propagation along the tapered aperture slot, which results in an end-fire antenna. The distance between inner slot line at the feed location is small and the waves are tightly bound. As the slot line widens, the bound becomes weaker gradually. The narrow slot line decides high frequency band, otherwise the wide slot line decides low frequency band. Tapered slot antenna exhibits some advantages such as wideband, wide scanning, high gain, low cross polarization and symmetrical E and H plane radiation patterns. In this paper, the Marchand balun with a balanced to unbalanced transition is shown good impedance matching and easy to integration and fabrication and the frame of the planar structure on corrugated tapered slot antenna was experimentally investigated. The designed antenna fed by microstrip-slot transition is presented. It exhibits the merits of geometric simplicity, wide bandwidth, lightweight, low cross polarization, and high peak gain.

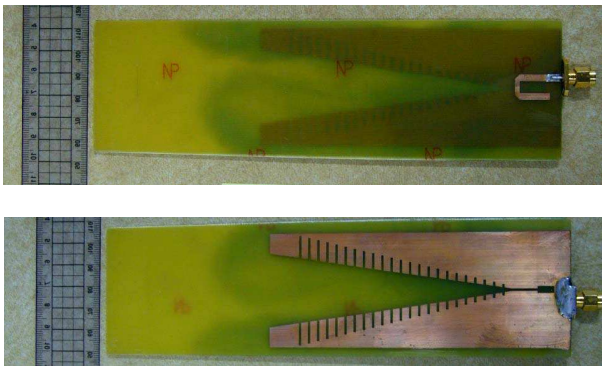

Figure 1: Corrugated tapered slot antenna.

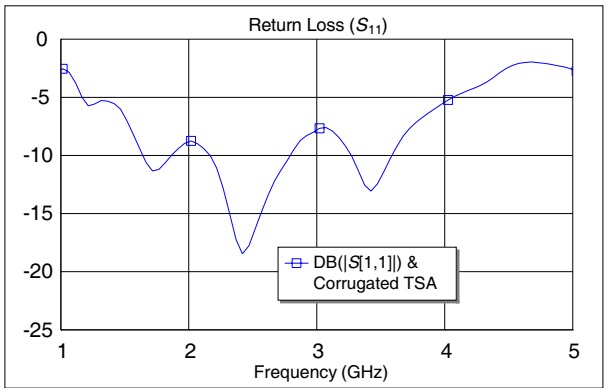

Figure 2: The measured data of corrugated tapered slot antenna.

On small antennas undesired surface currents on the outlines lead to near field radiation and thereby to a reduced gain as well as high side lobe levels. Especially in short-range radar applications there is a need of very linear phase behavior and compact antennas with a narrow 3 dB beam width. To suppress the currents on small antennas corrugations had been studied. Corrugations are well known for horn antennas suppressing higher modes and therefore guaranteeing polarization pureness. This type of corrugation has been found unfavourable in a two dimensional slot antenna since they tend to be a constraint to an undisturbed radiation. Corrugated flares at the edges of the antenna for the use in antenna arrays. However, the influence of these corrugations on antennas for radar application had been found too small.

The design parameters are dielectric constant and thickness of the substrate, conductor width and the gap width of the slot. The feed port is located across the narrow slot, where a 50 Ω coaxial line is connected, the location of the feed point is also important for impedance matching. The antenna is designed to be fabricated on a low-cost FR4 substrate, the thickness of which is 1 mm. We chose a value of 4.5 as the relative permittivity of the dielectric. If we select higher relative permittivity dielectric, the size of the antenna will be smaller while possessing similar requirements. To obtain a good bandwidth, the translation from the microstrip line to the radiation part should be carefully designed. For the antipodal structure of the antenna, the wideband translation is possible. The main part of the antenna is two pieces of quarter triangle. The major goal of the work is to find a planar antenna with low return loss, high gain and good radiation patterns in the frequency range between 2 and 4 GHz. We get a set of geometric parameters as shown in the Figure 1.

3. MEASUREMENT RESULTS

For return loss measurements, an Agilent E8357A network analyzer is used. The measured return loss is shown in Figure 2. The return loss is good over the entire 2 to 4 GHz range, so it satisfies the proposed requirement. As one can see, very wide-band impedance matching is achieved. It can be found that at low frequency band, the patterns are much similar to that of a dipole. Because the effective region is located at the top of the antenna, the bottom part has little effects on the radiation. At medium and high frequency bands, the patterns behave more directivity. Because of the effective region is moved to the middle part, the bottom part acts as a reflector.

Experimental investigation of antennas with Marchand balun and aperture configuration has been carried using network analyzer Agilent E8537A in the frequency range of 2 to 4 GHz. The radiation patterns in Figure 3 and Figure 4 and peak gain in Table 1. Figure 3 and Figure 4 show the measured radiation pattern. It shows the proposed antenna has a comparatively stable and symmetrical pattern and low side lobes through the operating band. Measured results indicate that effects have significant impacts on the return loss, input impedance, radiation patterns and antenna gain of this antenna. One of the important parameters for the UWB antennas, especially when used to send/receive pulsed signals, is the time domain response. This tapered slot antenna is suitable for UWB impulse radio operation and application.

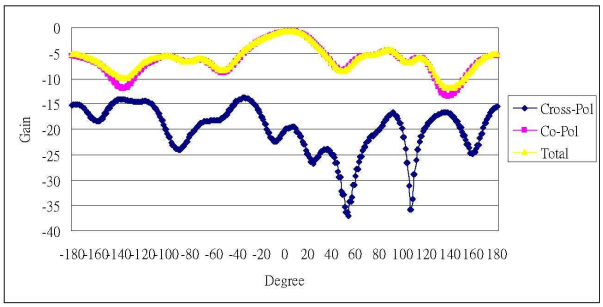

Figure 3: The 2.5 GHz measured data of H-plane.

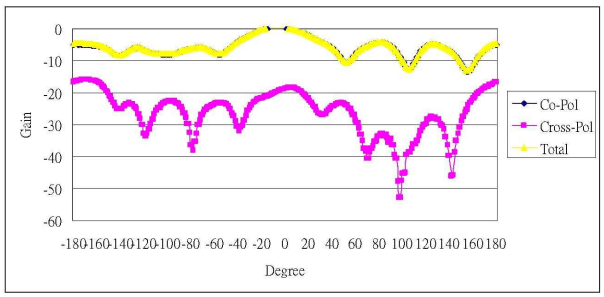

Figure 4: The 2.5 GHz measured data of E-plane.

Table 1: The measured data of antenna gain.

Frequency (GHz)	1.5	2	2.5	3
Gain (dBi)	4.3	5.3	5.8	4.6

4. CONCLUSIONS

The designed corrugated tapered slot antenna fed by a Marchand balun and the transition is presented. The Marchand balun allowed somewhat widening the frequency band of antenna as well as improved antenna characteristics. It exhibits the merits of geometric simplicity, wide bandwidth, lightweight, low cross polarization, and high peak gain. This corrugated tapered slot antenna is suitable for UWB impulse radio operation and application.

ACKNOWLEDGMENT

The authors would like to thank the Antenna and EMC research laboratory, HTC Corporation, for their assistance in wireless and system integration measurements.

REFERENCES

1. Lee, K. F. and W. Chen, *Advances in Microstrip and Printed Antennas*, John Wiley & Sons, Inc., 1997.
2. Schaubert, D. H., J. A. Aas, M. E. Cooley, and N. E. Buris, "Moment method analysis of infinite stripline fed tapered slot antenna arrays with a ground plane," *IEEE Trans. Antennas Propagation*, Vol. 42, 1161–1166, Aug. 1994.
3. Chio, T. H. and D. H. Schaubert, "Parameter study and design of wide band widescan dual polarized tapered slot antenna arrays," *IEEE Transactions on Antennas and Propagation*, Vol. 48, 879–886, Jun. 2000
4. Simons, R. N. and R. Q. Lee, "New techniques for exciting linearly tapered slot antennas with coplanar waveguide," *IEE Electronics Lett.*, Vol. 28, 620–621, Mar. 1992
5. Knott, P. and A. Bell, "Coaxially fed tapered tapered slot antenna," *IEE Electronics Lett.*, Vol. 37, 1103–1104, Aug. 2001
6. Lee, R. T. and G. S. Smith, "On the characteristic impedance of the TEM horn antenna," *IEEE Transactions on Antennas and Propagation*, Vol. 52, 315–318, Jan. 2004
7. Chen, G. Y., J. S. Sun, and Y. D. Chen, "The 3D far-field antenna measurement technology for radiation efficiency, mean effective gain and diversity antenna operation," *2006 The 7th International Symposium on Antennas, Propagation, and EM Theory (2006 ISAPE)*, 42–45, Guilin, China, Oct. 2006.

Ultra-wideband (UWB) Dipole Antenna Design and Measurement

Guan-Yu Chen[1], **Kekun Chang**[1], **Jwo-Shiun Sun**[1], **and Y. D. Chen**[2]

[1]Department of Electronic Engineering, National Taipei University of Technology, Taiwan
[2]Antenna and EMC Laboratory, HTC Corporation, Taiwan

Abstract— An ultra small low-profile, low-Q circular arms dipole antenna for ultra-wideband (UWB) operations is proposed. A circular arms dipole radiator with tapered effect is used to enhance the impedance matching and frequency range. The designed UWB antenna for 2 to 15 GHz is attainable.

1. INTRODUCTION

The design [1, 2] of a UWB dipole antenna with circular arms has simulated and measured. This UWB dipole has omni-directional radiation pattern and wide bandwidth is obtained by using circular arms. The balun feeding with ferrite core removes unwanted radiation pattern disturbances and canceled unbalanced current distribution.

2. ANTENNA DESIGN

This paper proposes an omni-directional UWB dipole antenna (Figure 1), low voltage standing wave ratio (VSWR), and easy to construct antenna for ultra wideband (UWB) systems. The designed antenna uses the balanced coaxial feed line to excite dipole antenna. The UWB dipole antenna suitable for IEEE 802.15.3a and IEEE 802.16 UWB communication applications at 3.1–10.6 GHz and 2–11 GHz bands is presented [3]. This paper discusses the phenomenon of dispersal in UWB antennas and presents a simple design to evaluate the radiated fields from antennas structures.

Table 1: The measured data of antenna gain.

Frequency (GHz)	2	3	4	5
Gain (dBi)	2.6	2.9	3.2	3.9
Frequency (GHz)	6	7	8	9
Gain (dBi)	4.2	4.5	5.2	5.6

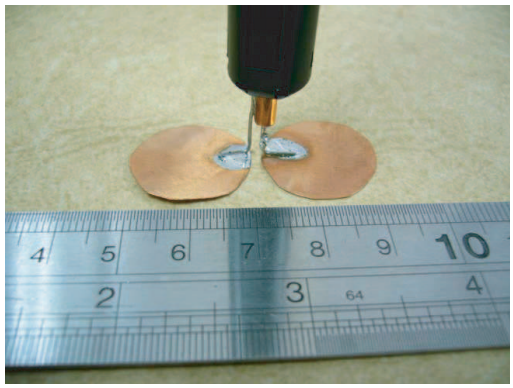

Figure 1: The proposed UWB dipole antenna.

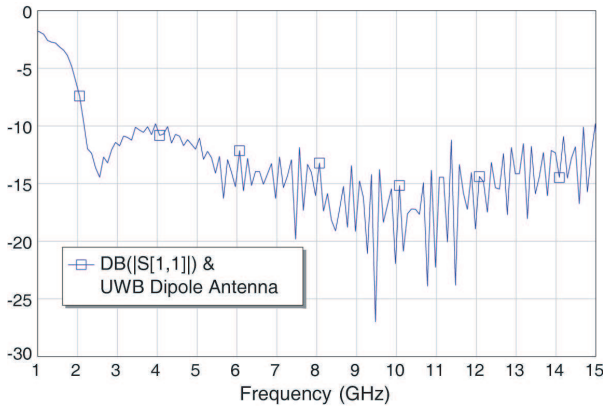

Figure 2: The measured data of S_{11}.

3. MEASUREMENT RESULTS

Measured results exhibits extend return loss bandwidth (Figure 2), gain (Table 1), and lower omni-directional pattern in Figures 3, 4, 5 and 6. The proposed UWB dipole antenna structure is capable of achieving broadband and omni-direction characteristics within 2–11 GHz for UWB wireless communication applications.

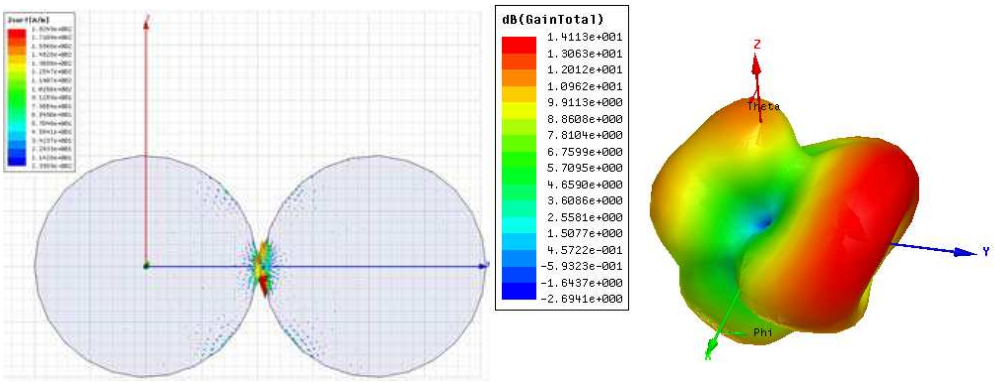

Figure 3: Current distribution and radiation pattern at 2.4 GHz.

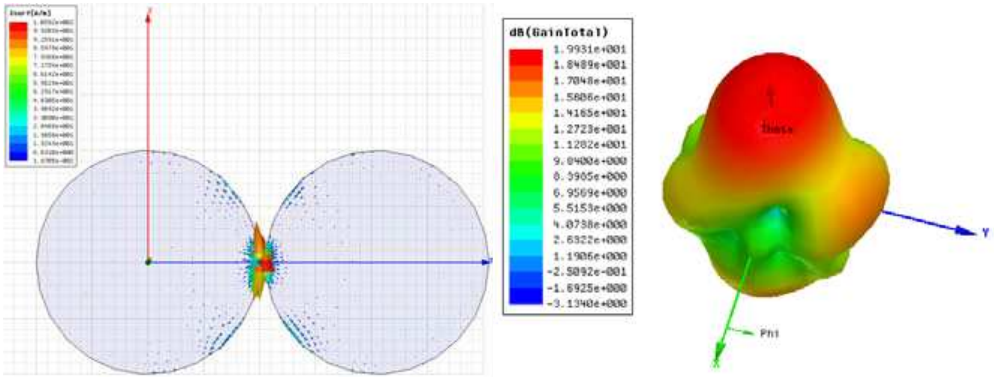

Figure 4: Current distribution and radiation pattern at 3.8 GHz.

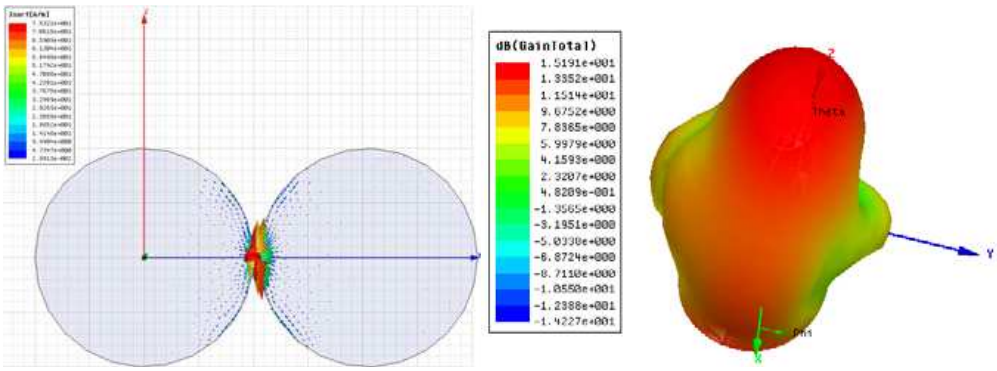

Figure 5: Current distribution and radiation pattern at 4.5 GHz.

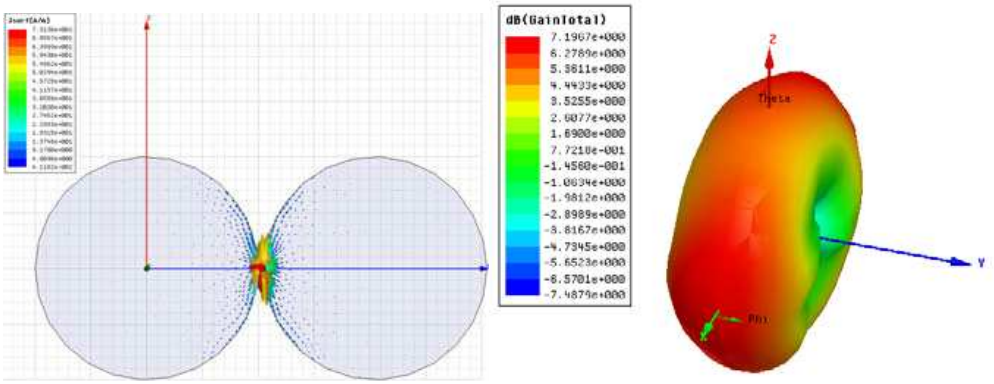

Figure 6: Current distribution and radiation pattern at 5.2 GHz.

4. CONCLUSION

The very small UWB dipole antenna of a circular arms dipole radiator is successfully developed. This designed antenna covers quite wide band from 2 GHz to 15 GHz. Evidently, it is very useful for many kinds of wireless communications.

ACKNOWLEDGMENT

The authors would like to thank the Antenna and EMC research laboratory, HTC Corporation, for their assistance in wireless and system integration measurements.

REFERENCES

1. Balanis, C. A., *Antenna Theory*, John Wiley & Sons, Inc, 1997.
2. Kraus, J. D. and R. J. Marhefka, *Antennas for All Applications*, McGraw-Hill, 2002.
3. Chen, G. Y. and J. S. Sun, "A novel cylindrical UWB antenna," *Microwave & Optical Technology Letters*, Vol. 51, 217–218, Jan. 2009.

Wire Inverted-F Antenna Design for WLAN and Bluetooth Operation

Kuo-Liang Wu[1], **Guan-Yu Chen**[1], **Jwo-Shiun Sun**[1], **and Y. D. Chen**[2]

[1]Department of Electronic Engineering, National Taipei University of Technology, Taiwan
[2]Antenna and EMC Laboratory, HTC Corporation, Taiwan

Abstract— An inverted-F antenna has a folded line section so as to shorten the length from the corresponding monopole antenna in this design. In high performance folded inverted-F antenna for WLAN and Bluetooth operations, where size, profile, and performance are of major considerations, compacter length of antenna are desirable.

1. INTRODUCTION

A high performance wire inverted-F antenna fabricated using a metal wire line as radiator is presented. A prototype of the proposed inverted-F antenna with a compact area size is implemented, and the multi-function WLAN/Bluetooth antenna shows a wide operating bandwidth (2400 MHz ∼ 2500 MHz) for WLAN and Bluetooth bandwidth, making it easy to cover the IEEE 802.11b and IEEE 802.11g bands for wireless communication and high speed wireless communication operations.

A high performance monopole antenna fabricated using a folded wire line and a metal patch as radiator is presented. A prototype of the proposed monopole antenna with a compact area size of 20 mm × 10 mm is implemented, and the multi-band WLAN antenna shows a wide operating bandwidth of about 200 MHz and 1000 MHz for low band and high band, bandwidth, making it easy to cover the IEEE 802.11a, IEEE 802.11b, IEEE 802.11g and IEEE 802.11n (MIMO) bands for wireless communication and future 4G wireless operation of a mobile VoIP/VoWLAN handset phone.

The Institute of Electrical and Electronics Engineers (IEEE) has defined the most important characteristics of wireless LAN in the 802.11a, 802.11b, 802.11g and 802.11n group of standards of wireless network communication. Data is transmit ted predominantly in the radio frequency range 2.4 GHz and 5 GHz. In this implement, the study mainly focuses on the current trends in development of compact and low profile multi-media PDA and smart mobile phone and provides a wideband monopole antenna design suitable for application in wireless LAN communicating system in the near future. By utilizing the monopole antenna structure, the proposed antenna design is easy to be embedded into the mobile phone co-integration operation. Some antenna structures [15] to satisfy specific bandwidth specifications for modern wireless LAN communication systems such as IEEE 802.11a (5.15–5.35 GHz and 5.47–5.825 GHz), IEEE 802.11b (2.4–2.485 GHz), IEEE 802.11g (2.4–2.485 GHz) and IEEE 802.11n (2.4–2.485 GHz, 5.15–5.35 GHz and 5.47–5.825 GHz) have been implemented and developed. Antennas that can be easily integrated on the RF circuit board and module of a wireless device for wireless consumer electronics operations has been reported recently. In this implement, the study mainly focuses on the current trends in development of compact and low profile Wi-Fi PDA and smart mobile phone and provides a wideband monopole antenna design sui table for application in wireless LAN communicating system in the near future.

In this design, the innovative monopole antenna for single fed to excite dual radiator path is presented. These proposed antennas can find applications in wireless LAN IEEE 802.11a/b/g/n and VoIP/WiFi wireless systems application. The design of a dual wideband monopole antenna with dual path of folded wire and metal patch radiator with applications for wireless VoIP and VoWLAN uses is investigated. With the broadside radiations, the proposed dual wideband monopole antenna carries a stable gain variation in the 2.4–2.5 GHz and 5–6 GHz bands, respectively.

2. ANTENNA DESIGN AND RESULTS

In this paper, the shorting monopole antenna has several advantages over conventional monopole-like antenna and planar antenna for mobile handsets [1]. The co-design of folded metal wire antenna can overcome the problem of narrow band of the conventional antenna. By adding a low-Q resonator as a radiator, the coupling between the folded wire radiators can be improved and measured [2–4]. The design of monopole antenna with folded path of wire line radiator for WLAN

applications and results are shown in Figure 1 and Table 1, respectively. The proposed folded inverted-F wire antenna is designed of compact size of 8.5 mm × 7 mm × 6 mm. This long folded wire radiator has a total length of about 21.5 mm, which excited band operation. The total length of the effective radiator wire path of the designed antenna is close to one quarter wavelength at free space of the center frequency about 2450 MHz of operation band. By fine-tuning the length of the length of the folded radiator, the antenna resonant frequencies can be effectively control led. Further, characteristics simulations and measurements are conducted about a folded line structure applicable to WLAN/BT 2.4 GHz antenna operation, and the like, wherein the total length of the meander line antenna is set between 0.25 wave-lengths at 2450 MHz center frequency.

An internal small antenna usually suffers from degradation in performance of narrow bandwidth and radiation efficiency. In this experiment, we design and fabricate a dual broadband interior type wire and metal patch monopole with a high performance radiation pattern over a design operation band using dual path, as shown in Figure 1. It has a measured return loss bandwidth (referenced −10 dB) about 200 MHz with center frequency at 2.35 GHz (2.25–2.45 GHz) and 1000 MHz with center frequency at 5.375 GHz (5–6 GHz), as shown in (Figure 2). With the rapid growth of mobile Wi-Fi technique, wireless communication devices are more mini-size and had multi-band wireless functions.

In this thesis, the dual wideband monopole antenna has several advantages over convent ional monopole-like antenna and planar antenna for mobile handsets. The small compact and low profile antenna radiator structure such as the wire and metal patch monopole antenna that can be mounted on the portable equipment are becoming very attractive for the VoIP and VoWLAN communications application. In this design, we designed a novel compact internal wire monopole antenna for multi-band operation covering the IEEE 802.11a/b/g/n and Bluetooth co-existed bands and applications. In this design, multi-band monopole antenna for Wireless LAN antenna device applications is proposed. This kind of folded wire and metal patch monopole antenna co-design can overcome the narrow bandwidth problem that happens to the convent ional patch antenna; in practical application, when electronic components are placed very close to the conventional antenna, large degradation of the antenna performance will occur.

In the proposed wire antennas, by adding a low-Q resonator factor as a wideband radiator design, antenna coupling between the low band and high band radiator can be improved and enhanced antenna bandwidth. We present an innovative wire monopole antenna suitable for application as

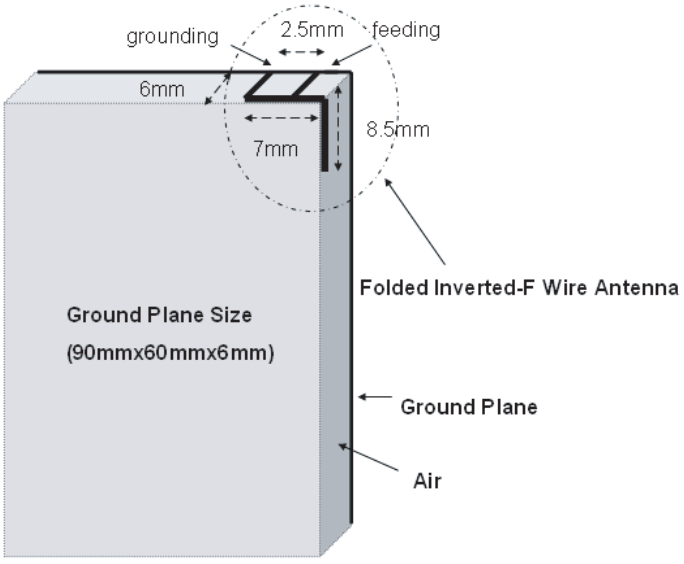

Figure 1: The proposed antenna.

Table 1: Measured gain data.

Frequency (MHz)	2400	2420	2440	2460	2480	2500
Gain (dBi)	3.1	3.1	3.3	3.6	3.5	3.2

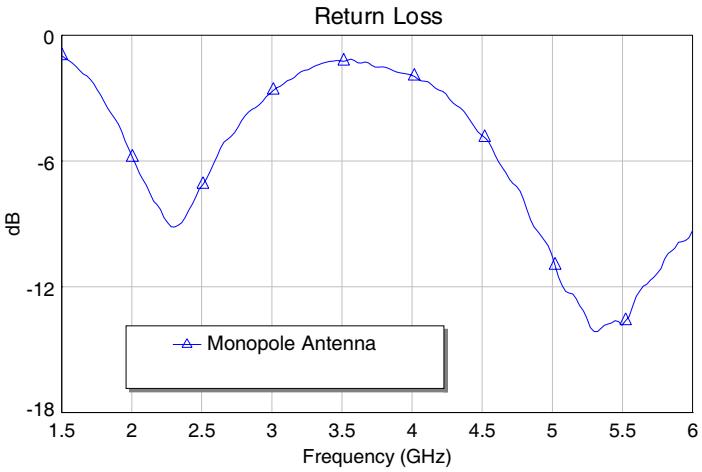

Figure 2: Measured data of return loss.

an internal antenna co-integration on mobile PDA handheld. The proposed dual path monopole antenna is designed on a practical PCB size (100 mm × 60 mm), which serves as a support for the monopole, and has a radiator compact size of (20 mm × 10 mm). which excited high band antenna bandwidth of the metal patch monopole antenna.

With the finite dimensions of the folded wire monopole antenna in this design, the total length of the effective radiator wire path of the antenna is close to one quarter wavelength at free space of the center frequency of low band and high band, the low band resonant frequency of the long wire radiator occurs at about 2350 MHz center frequency and high band resonant frequency of the short wire radiator occurs at about 5375 MHz center frequency. In addition, by fine-tuning the length of the wire length of the long and short metal patch radiators, the antenna resonant frequency of the bandwidth can be effectively controlled, but antenna multi-coupling effect for multi-interference by long folded wire and short metal patch so the antenna resonant frequency has affected with each other.

3. CONCLUSION

This design focuses on the structure of the wireless headset antenna application of 2.4 GHz ISM band system. The low material cost as well as the high product stability and apply the antenna design of WLAN/BT for PDA headset. Base on the EM simulation and measurement results, the folded line monopole antenna is applied for the ISM frequency band 2400 MHz–2500 MHz operation.

ACKNOWLEDGMENT

The authors would like to thank the Antenna and EMC research laboratory, HTC Corporation, for their assistance in wireless and system integration measurements.

REFERENCES

1. Kraus, J. D. and R. J. Marhefka, *Antennas for All Applications*, McGraw-Hill, 2002.
2. Chen, G. Y., J. S. Sun, K. Chang, and Y. D. Chen, "Antenna pattern measurement," *PIERS Proceedings*, 331–333, Beijing, China, March 23–27, 2009.
3. Chen, G. Y., J. S. Sun, C. H. Lin, K. K. Tiong, and Y. D. Chen, "Small antenna measurement facilities," *PIERS Proceedings*, 157–158, Hangzhou, China, March 24–28, 2008.
4. Chen, G. Y., C. H. Lin, J. S. Sun, K. K. Tiong, and Y. D. Chen, "3D far-field antenna scanning technique apply to radiation efficiency and mean effective gain measurement," *IEEE TENCON 2007*, 113, Taipei, Taiwan, October 2007.

Meander Line Antenna for GPS Phone Operation

Kuo-Liang Wu[1], **Guan-Yu Chen**[1], **Jwo-Shiun Sun**[1], **and Y. D. Chen**[2]

[1]Department of Electronic Engineering, National Taipei University of Technology, Taiwan
[2]Antenna and EMC Laboratory, HTC Corporation, Taiwan

Abstract— A meander line antenna has several meander line sections so as to shorten the length from the corresponding monopole antenna in this design. In high performance meander line antenna for GPS and A-GPA applications, where size, profile, and performance are of major considerations, shorter length of antenna are desirable.

1. INTRODUCTION

The general GPS functions of PDA support the assisted functionali ty in 2.5/3G wireless networks. Traditional antennas [1] such as monopoles, dipoles and patches are not suitable to meet the requirements of modern wireless communication and highly demanding mobile GPS systems. As a result, there is the need for alternative approaches to small antenna and high performance design. This paper describes a miniaturized meander shorting monopole for integration in modern GPS wireless systems. GPS is a satellite-based positioning system operated by the United States Department of Defense was officially put into operation in 1995. Using the difference in the radio signal propagation times of at least three of the 24 GPS satellites, a GPS receiver can accurately determine its position worldwide to within a few meters. Signals for civil use are transmitted at a frequency of 1575.42 MHz and bands. The general GPS functions of PDA support the assisted functionality in 2.5/3G wireless networks. Traditional antennas such as monopoles, dipoles and patches are not suitable to meet the requirements of modern wireless communication and highly demanding mobile GPS systems. As a result, there is the need for alternative approaches to small antenna and high performance design. This design describes a miniaturized meander shorting monopole for integration in modern GPS wireless systems.

This thesis accomplished a GPS band for meander inverted-F monopole antenna structure and easy applied mobile cellular phone application. The measured and simulated data including return loss, antenna gain and radiation patterns are presented.

2. ANTENNA DESIGN AND RESULTS

The resonance mode of a shorting meander wire antenna covers the GPS communication bandwidth of 1571.42–1579.42 MHz. The simple wire tuning expansion are introduced to confine the resonance mode region and to facilitate the frequency modes and impedance match expansion easily for antenna and wireless system integration design. The design requirements for GPS antenna is combined into multiple objective goals, such as simplicity of the antenna geometry, radiation pattern, return loss, antenna impedance and polarizations. This design in general to a mobile communication apparatus and global positioning system antenna, and more particularly to a mobile communication system, which utilizes a small-scale metal for the GPS antenna design. Further,

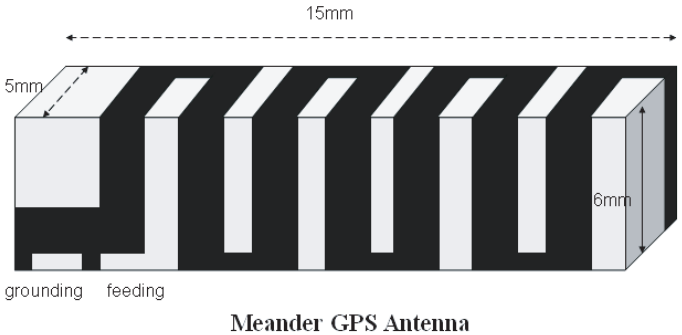

Figure 1: The proposed antenna.

characteristics simulations and measurements are conducted about a meander line structure applicable to GPS antenna operation, and the like, wherein the total length of the meander line antenna is set between 0.25 wave-lengths at 1575 MHz center frequency. The resonance mode of a shorting meander wire antenna. covers the GPS communication bandwidth of 1571.42–1579.42 MHz. The simple wire tuning expansion are introduced to confine the resonance mode region and to facilitate the frequency modes and impedance match expansion easily for antenna and wireless system integration design. This design proposes meander shorting monopole antenna design for single-band GPS wireless communications, especially for PDA and Smart mobile phones. The single-frequency design for mobile handset mainly utilizes meander line to excite radiation mode. By tuning the dimensions of meander line, the VSWR ratio of the antenna's resonance frequency can be achieved, which makes it very promising for GPS and A-GPS operations.

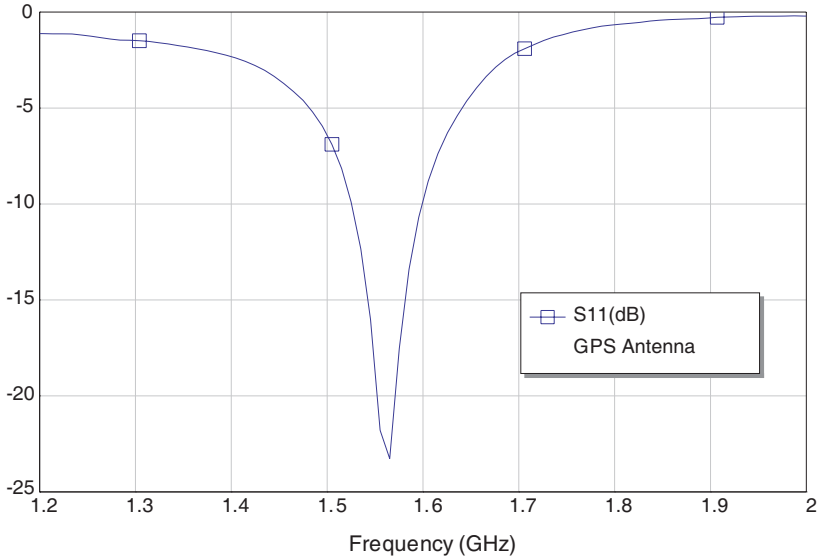

Figure 2: The measured data of S_{11}.

Table 1: The measured data of antenna gain.

Frequency (GHz)	1.48	1.5	1.52	1.54
Gain (dBi)	3.1	3.6	3.4	3.5
Frequency (GHz)	1.56	1.58	1.6	1.62
Gain (dBi)	3.4	3.8	3.7	3.3

3. CONCLUSIONS

This structure focuses on design of the wireless PDA headset application of 1575 MHz GPS band system. The low material cost as well as the high product stability and apply the antenna design of GPS system for PDA headset. Base on the EM simulation and measurement results, the meander line monopole antenna is applied for the GPS band operation.

This article describes a low profile, compact, meander loaded monopole antenna with single feed. A shorting type monopole is used to enhance the impedance matching. This provides a low radiation resistance within the GPS band. Shorting meander inverted-F monopole antenna leads to a middle gain. In addition, the meander loading also permits the antenna's height and to be reduced antenna size. This antenna also offers a characteristic of high radiation efficiency. Antenna bandwidth of 3.8% (1.53 to 1.59 GHz) was experimentally obtained for a return loss −10 dB. In well known antenna design techniques a matching structure is typically employed to provide matching between the antenna and the GPS circuitry for efficient transfer of energy.

ACKNOWLEDGMENT

The authors would like to thank the Antenna and EMC research laboratory, HTC Corporation, for their assistance in wireless and system integration measurements.

REFERENCES

1. Kraus, J. D. and R. J. Marhefka, *Antennas for All Applications*, McGraw-Hill, 2002.
2. Chen, G.-Y., J.-S. Sun, K. Chang, and Y. D. Chen, "Antenna pattern measurement," *PIERS Proceedings*, 331–333, Beijing, China, March 23–27, 2009.
3. Chen, G.-Y., J.-S. Sun, C.-H. Lin, K.-K. Tiong, and Y. D. Chen, "Small antenna measurement facilities," *PIERS Proceedings*, 157–158, Hangzhou, China, March 24–28, 2008.
4. Chen, G.-Y., C.-H. Lin, J.-S. Sun, K.-K. Tiong, and Y. D. Chen, "3D far-field antenna scanning technique apply to radiation efficiency and mean effective gain measurement," *IEEE Region 10 Conference TENCON 2007*, 113, Taipei, Taiwan, October 2007.

Antenna Measurement System for CTIA OTA Operation

Guan-Yu Chen[1], **Kuo-Liang Wu**[1], **Jwo-Shiun Sun**[1], **and Y. D. Chen**[2]

[1]Department of Electronic Engineering, National Taipei University of Technology, Taiwan
[2]Antenna and EMC Laboratory, HTC Corporation, Taiwan

Abstract— The mobile phone under test of far-field range testing has been the plan at the Cellular Telecommunications & Internet Association (CTIA) certification program [1, 2] test requirements for performing radiated power and receiver performance measurement.

1. INTRODUCTION

In this study, facilities of mobile phone measurement have recently commissioned a spherical far-field measurement system (Figure 1). The low profile far-field spherical scan system provides significant advantages over the older far-field testing including elimination of problem of simple theta (θ) and phi (ϕ) rotary axis with indoor far-field range testing, complete measurement characterization of the antenna, and improved accuracy. This thesis discusses the antenna and wireless system integration tested with the antenna efficiency, mean effective gain, total radiated power (TRP), total isotropic sensitivity (TIS), and spherical antenna measurement for far-field wireless network system, and the measured results being achieved. Three-dimensional field pat tern of a directional antenna with maximum radiation in z-direction at $\theta = 0°$. Most of the radiation is contained in a main beam (or lobe) accompanied by radiation also in minor lobes (side and back). Between the lobes are nulls where the field goes to zero. The radiation in any direction is specified by the angles θ and ϕ. The direction of the point P is at angles $\theta = 30°$ and $\phi = 85°$. this pattern is symmetrical in ϕ and a function only of θ.

2. 3D FAR-FIELD ANTENNA MEASUREMENT SYSTEM AND EXPERIMENTS

In this study, the author has established a 3D far-field antenna measurement system. Based on this 3D spherical far-field measurement system, the low-profile mobile antennas measurements and mobile phone for wireless network are applied. The 3D antenna measurement system and study can be applied to wireless OTA measurement. The fields around an antenna may be divided into two principal regions, one near the antenna called the near field or Fresnel zone and one at a large distance called the far field or Fraunhofer zone. Referring to, the boundary between the two may be arbitrarily taken to be at a radius.

In the far or Fraunhofer region, the measurable field components are transverse to the radial direct ion from the antenna and all power flow is directed radially outward. In the far field the shape of the field pattern is independent of the distance [4]. In the near or Fresnel region, the longitudinal component of the electric field may be significant and power flow is not entirely radial. In the near field, the shape of the field pattern depends, in general, on the distance.

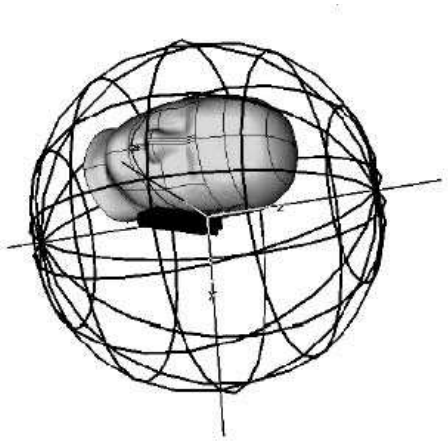

Figure 1: 3D antenna measurement system.

Two-dimensional field, power and decibel plots of the 3-D antenna pattern of. Taking a slice through the middle of the 3-dimensional pattern of results in the 2-dimensional pattern at (a). It is a field pattern (proportional to the electric field E in V/m) with normalized relative field $E_n(\theta) = 1$ at $\theta = 0°$. The half-power beam width (HPBW) $= 40°$ is me as before and assured at the $E = 0.707$ level.

3. 3D ANTENNA MEASUREMENT PRINCIPLE

3D antenna system is a measurement of the RF device's transmitter performance. This measurement procedure records 3D antenna pattern every 15 and 30 degrees for the total of 528 and 120 points (2 orthogonal linear polarizations × 12 theta's data × 24 phi's data and 2 orthogonal linear polarizations × 5 theta's data × 12 phi's data). As a result, a 3D pat tern is obtained showing maximum and minimum points of transmitter performance. This section discusses the methodology [3, 4] of 3D polarization measurement and environment. Directivity (D), equation is defined as the ratio of the wave radiation intensity in certain direction to the average radiation intensity, and show the spherical coordinates used for measurement.

4. 3D ANTENNA MEASUREMENT SYSTEM FOR WIRELESS NETWORK

In this measurement system [5–10], each transmit-test spherical-scan file shall contain measurements for 11 theta cuts × 24 phi cuts × 2 polarizations. Based on samples measured every 15 degrees of rotation for each cut, 528 measurements are thus recorded in each transmit test file. Assuming that theta is a complete sphere measured with N theta intervals and M phi intervals, then the total radiated power (TRP) may be calculated. Receiver performance is equally important to the overall system performance, as is transmitter performance. The downlink or subscriber unit receiver path is integral to the quality of the devices operation. Poor receiver radiated performance can cause the user of the subscriber unit to hear a low quality voice signal. This can also cause the subscriber unit to lose the base station signal resulting in abrupt termination of the cell. This test plan requires spherical effective radiated receiver sensitivity (termed total isotropic sensitivity, TIS) to be measured. Assuming that theta is a complete sphere measured with N theta intervals and M phi intervals, then the total isotropic sensitivity (TIS) may be calculated. The spherical far field antenna measurement systems are rotated and measured for a full spherical scan of the radiated AUT or mobile test. High-accuracy far-field antenna measurement for spherical scan system is suitable for low gain characteristic of the mobile under test for spherical far-field scan and full 3 dimension field energy by numerical formula computation for measurement error can be seriously reduced, resulting in evaluation of measurement environment of antenna under test and detailed full spherical scan operation. The spherical far-field instrument and software co-design systems are created not only for high accuracy but also for high stability in the testing environment. This system is designed to measure the directivity, gain, efficiency for passive antenna condition and total radiated power (TRP), total isotropic sensitivity (TIS) for mobile phone radiated RF power and receiver sensitivity performance with 3D integral. Measurement systems are used in the $EIRP_\theta(\theta_i, \theta_j)$ and $EIRP_\phi(\theta_i, \theta_j)$ for TRP radiated power and $EIS_\theta(\theta_i, \theta_j)$ and $EIS_\phi(\theta_i, \theta_j)$ for TIS receiver sensitivity calculation. In this study, the measurement system is set for the specific communication channel for uplink and downlink with based station and mobile terminal link.

5. CONCLUSIONS

The 3D antenna system for spherical far-field techniques and system are applied in a spherical far-field antenna system. The system can be applied on antenna parameters measurement of gain, directivity and radiation efficiency. And this 3D antenna system can be applied on mean effective gain (MEG), diversity antenna measurement, MIMO terminal antennas measurement for 3D spherical far-field measurement.

ACKNOWLEDGMENT

The authors would like to thank the Antenna and EMC research laboratory, HTC Corporation, for their assistance in wireless and system integration measurements.

REFERENCES

1. *CTIA*, http://www.ctia.org/.
2. *Test Plane for Mobile Station over the Air Performance*, Revision 2.1, Cellular Telecommunications & Internet Association (CTIA), Washington, D.C., Apr. 2005.

3. Stutzman, L. W., *Antenna Theory and Design*, John Wiley, 1998.
4. Balanis, A. C., *Antenna Theory*, John Wiley, 2005.
5. Chen, G. Y., S. Y. Huang, W. F. Yen, J. S. Sun, Y. D. Chen, C. H. Lin, J. Y. Yang, and C. Y. Lin, "The spherical antenna measurement and spherical absorption rate (SAR) for near field radiation evaluation," *2005 Asia Pacific Symposium on EMC (2005 APEMC)*, 128–135, Taipei, Taiwan, Dec. 2005.
6. Chen, G. Y., J. S. Sun, S. Y. Huang, Y. D. Chen, C. H. Lin, and J. Y. Yang, "Flexible monopole antenna for mobile phone co-design and 3D far-field antenna scanning technique apply to total radiation efficiency and mean effective gain measurement," *2006 China-Japan Joint Microwave Conference (2006 CJMW)*, 89–92, Chengdu, China, Aug. 2006.
7. Chen, G. Y., J. S. Sun, S. Y. Huang, Y. D. Chen, C. H. Lin, and J. Y. Yang, "Mobile handset measurement for wireless system networking," *2006 China-Japan Joint Microwave Conference (2006 CJMW)*, 698–701, Chengdu, China, Aug. 2006.
8. Chen, G. Y., J. S. Sun, K. Chang, and Y. D. Chen, "Antenna pattern measurement," *PIERS Proceedings*, 331–333, Beijing, China, Mar. 2009.
9. Chen, G. Y., J. S. Sun, C. H. Lin, K. K. Tiong, and Y. D. Chen, "Small antenna measurement facilities," *PIERS Proceedings*, 157–158, Hangzhou, China, Mar. 2008.
10. Chen, G. Y., C. H. Lin, J. S. Sun, K. K. Tiong, and Y. D. Chen, "3D far-field antenna scanning technique apply to radiation efficiency and mean effective gain measurement," *IEEE TENCON 2007*, 113, Taipei, Taiwan, Oct. 2007.

New Antenna System Measurement Technology for GPS OTA Operation

Jui-Yi Yang[1], **Guan-Yu Chen**[2], **Yung-Sheng Chen**[1], **Jwo-Shiun Sun**[2], **and Y. D. Chen**[3]

[1]Department of Electrical Engineering, Yuan Ze University, Taiwan
[2]Department of Electronic Engineering, National Taipei University of Technology, Taiwan
[3]Antenna and EMC Laboratory, HTC Corporation, Taiwan

Abstract— Built in Bluetooth wireless transmission allows easy GPS sensitivity record on the go without the hassle of external USB connections and wire cable anytime, anywhere.

1. INTRODUCTION

With the rise in location based services (LBS) applications and the need to meet E911 positioning requirements, the number of mobile cellular devices supporting Assisted GPS (A-GPS) is steadily growing. More recently, industry organizations, including Cellular Telecommunications & Internet Association CTIA, have recognized the need to create standardized test procedures for A-GPS Over The Air (OTA) testing to objectively specify and validate acceptable performance.

2. A-GPS OTA MEASUREMENT AND ENVIRONMENT

A CTIA subgroup has completed a section on A-GPS OTA testing, incorporated in version 3.0 of the CTIA Test Plan for Mobile Station Over-the-Air Performance. In this study, a new 3D antenna measurement system associated with GPS test systems ensures 3D GPS antenna radiated pattern measurement, sensitivity measurement, and GPS intermediate channel measurement. It will be fully compliant with the CTIA's test plan for mobile station over-the-air performance. Bluetooth (BT) transmission (Figure 1 and Figure 2) is adopted to replace traditional USB data link by cable (Figure 2), and thus to reduce cable effect and EMI crosstalk by USB cable for 3D antenna OTA

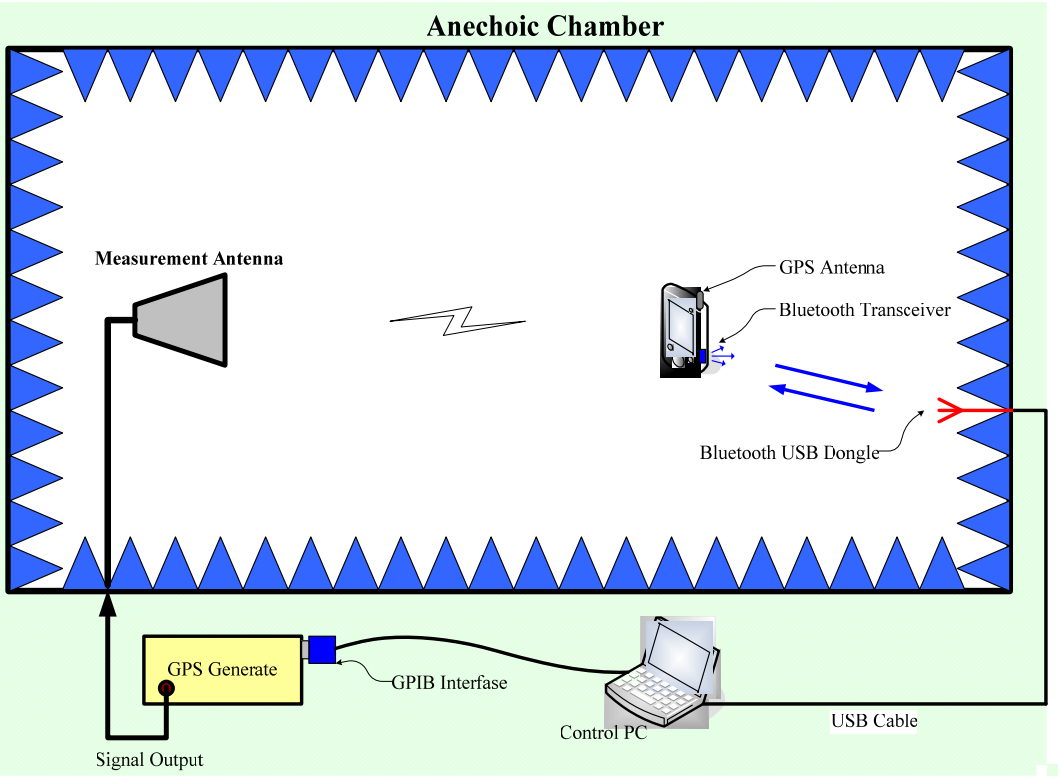

Figure 1: The proposed GPS OTA measurement.

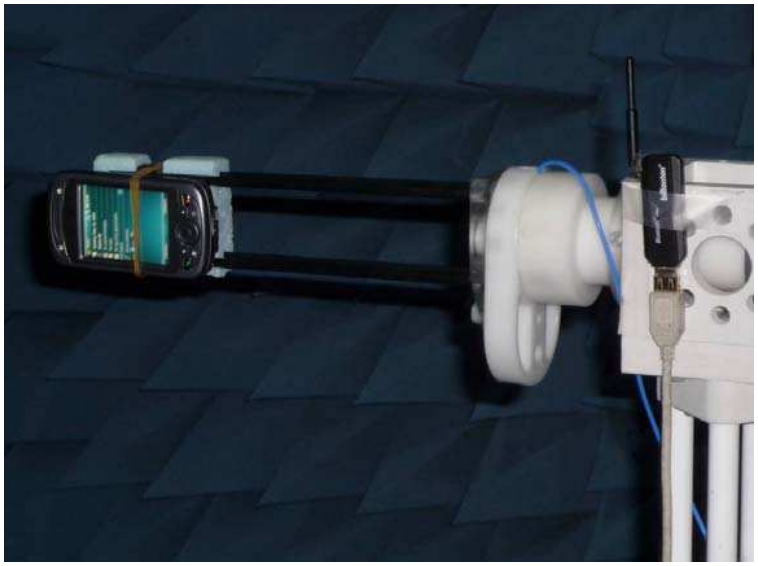

Figure 2: The proposed GPS OTA measurement without cable effect.

measurement. BT is an open wireless protocol for exchanging data over short distances from fixed and mobile devices, creating personal area networks originally conceived as a wireless alternative to RS232 data cables. It can connect to Personal Digital Assistant (PDA) and Notebook (NB) devices, overcoming problems of synchronization. Based on this new measurement technology can improve GPS and A-GPS receiver sensitivity measurement by 3D antenna OTA system. The mobile phone under test of far-field range testing has been the plan at the Cellular Telecommunications & Internet Association (CTIA) certification program test [1] requirements for performing radiated power and receiver performance measurement. In literatures [2, 3], facilities of antenna pattern measurement have recently commissioned a spherical far-field measurement system [4]. The low profile far-field spherical scan system provides significant advantages over the older far-field testing including elimination problem of simple theta and phi rotary axis with indoor far-field range testing, complete measurement characterization of the antenna, and improved accuracy. This study discusses the antenna and wireless system integration tested, spherical antenna measurement for A-GPS far-field

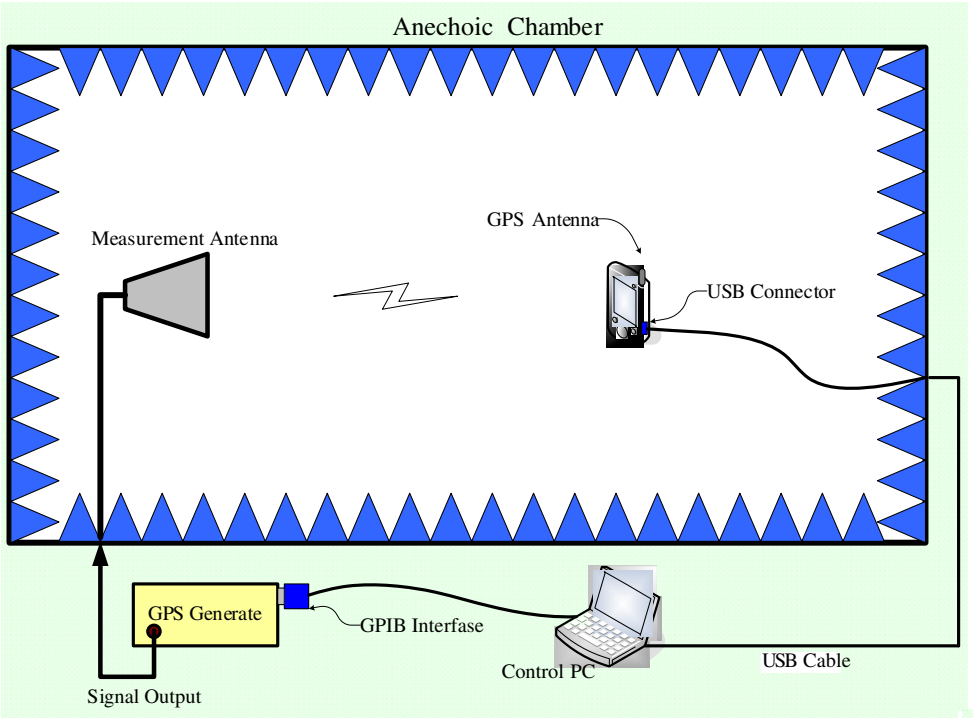

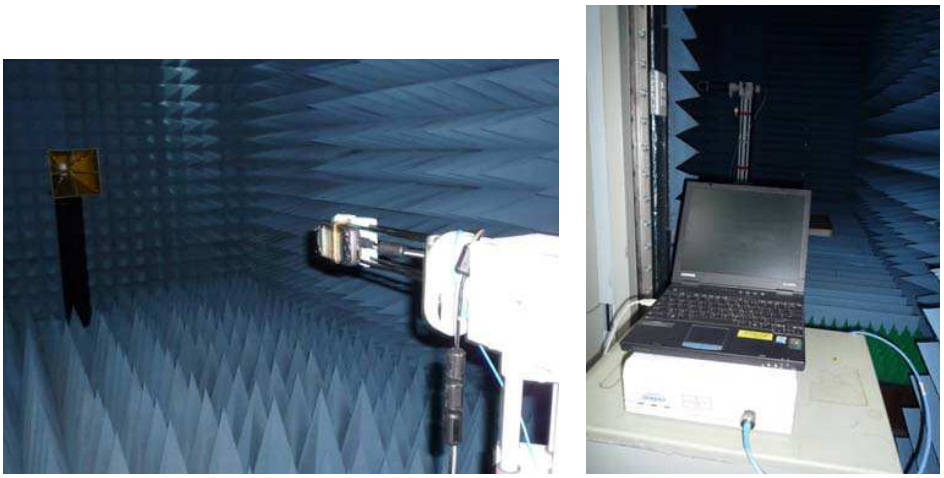

(a) (b)

Figure 3: The traditional GPS OTA measurement with (a) cable effect (cable add ferrite core or Balun choke), and (b) USB interference.

system, and the results being achieved.

3. MEASUREMENT

The GPS measurement will be assumed to be a carrier-to-noise ratio (CNR) but it is not limited to that measurement type. Upper Hemisphere Isotropic Sensitivity is seen to be Equation (1).

$$UHIS \cong EIS_{xf}(\theta_f, \phi_f) = \frac{CNR_{xf}(\theta_f, \phi_f)}{\frac{\pi}{2NM}\left[\sum_{i=1}^{\frac{N}{2}-1}\sum_{j=0}^{M-1}\left[CNR_\theta(\theta_i, \phi_j) + CNR_\phi(\theta_i, \phi_j)\right]\sin(\theta_i) + \frac{1}{2}\sum_{j=0}^{M-1}\left[CNR_\theta\left(\theta_{\frac{N}{2}, \phi_j}\right) + CNR_\phi\left(\theta_{\frac{N}{2}}, \phi_j\right)\right]\right]} \quad (1)$$

4. CONCLUSION

We have built and set the test room of phone under tests of far-field range and based on the Cellular Telecommunications & Internet Association (CTIA) certification program test requirements for performing GPS or A-GPS OTA antenna performance measurement. The performance of mobile handset antennas in free space and beside a new test method is evaluated with radiation pattern measurements in the 3D antenna chamber and radio receiver channel measurements.

ACKNOWLEDGMENT

The authors would like to thank the Antenna and EMC research laboratory, HTC Corporation, for their assistance in wireless and system integration measurements.

REFERENCES

1. "Test plane for mobile station over the air performance," Revision 3.0, Cellular Telecommunications & Internet Association (CTIA), Washington, D.C., 2009.
2. Chen, G.-Y., J.-S. Sun, K. Chang, and Y. D. Chen, "Antenna pattern measurement," *PIERS Proceedings*, 331–333, Beijing, China, March 23–27, 2009.
3. Chen, G.-Y., J.-S. Sun, C.-H. Lin, K.-K. Tiong, and Y. D. Chen, "Small antenna measurement facilities," *PIERS Proceedings*, 157–158, Hangzhou, China, March 24–28, 2008.
4. Chen, G.-Y., C.-H. Lin, J.-S. Sun, K.-K. Tiong, and Y. D. Chen, "3D far-field antenna scanning technique apply to radiation efficiency and mean effective gain measurement," *IEEE TENCON 2007*, 113, Taipei, Taiwan, October 2007.

Double-ridged Horn for 3D Antenna Measurement

Jui-Yi Yang[1], **Guan-Yu Chen**[2], **Yung-Sheng Chen**[1], **Jwo-Shiun Sun**[2], **and Y. D. Chen**[3]

[1]Department of Electrical Engineering, Yuan Ze University, Taiwan
[2]Department of Electronic Engineering, National Taipei University of Technology, Taiwan
[3]Antenna and EMC Laboratory, HTC Corporation, Taiwan

Abstract— The horn antenna by 3D antenna measurement and verification are used to frequency range of Cellular Telecommunications & Internet Association (CTIA) Over The Air (OTA) chamber. The double ridge horn antenna generates high electric fields required for radiated immunity and emissions measurements and antenna calibration.

1. 3D ANTENNA MEASUREMENT FOR DOUBLE RIDGE HORN

A 1–18 GHz broadband double ridged horn antenna (Figure 1) by 3D far field pattern measurement is studied [1–4]. The measurements are in good agreement with the theories over the 1–18 GHz operational bandwidth (Figure 3) and indicate that the use of double ridged horn in antenna chamber application (Figure 2) and The VSWR data (Figure 4). This paper will discuss the high gain antenna measured by spherical far-field system. Antenna measurement technique refers to the testing of antenna to ensure that the antenna meets specifications or simply to characterize it. Typical parameters of antennas are radiation pattern (Figure 5 to Figure 10), gain (Table 1), beamwidth, polarization, and impedance. Based on 3D antenna measurement is the ratio of power actually radiated to the power put into the antenna terminals. This paper presents a 3D antenna measurement system which allows, in addition to standard far field measurements, a full 3D measurement of the radiation pattern of a double ridged horn antenna. To prove measurement results, a simple antenna system has been created, which allows comparison with simulation and theory results.

Table 1: Measured gain data.

Frequency (GHz)	1	2	3	4	5	6
Gain (dBi)	6.5	9.9	9.9	13.3	13.6	14.5

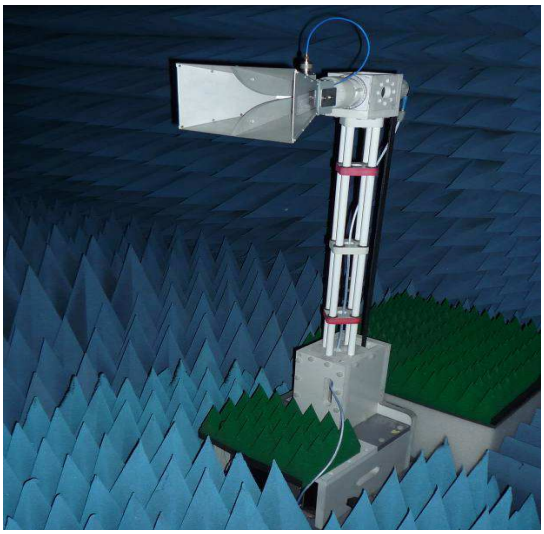

Figure 1: Double ridged horn antenna.

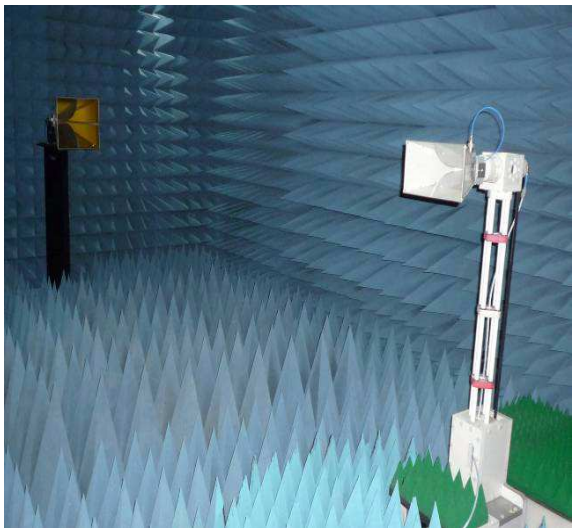

Figure 2: Double ridged horn antenna by 3D antenna measurement.

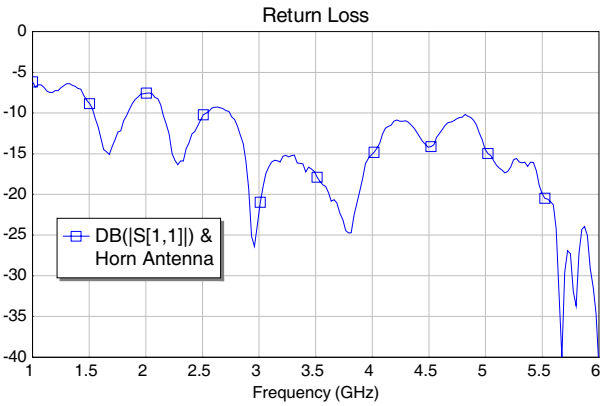

Figure 3: The Measured data of double ridged horn antenna.

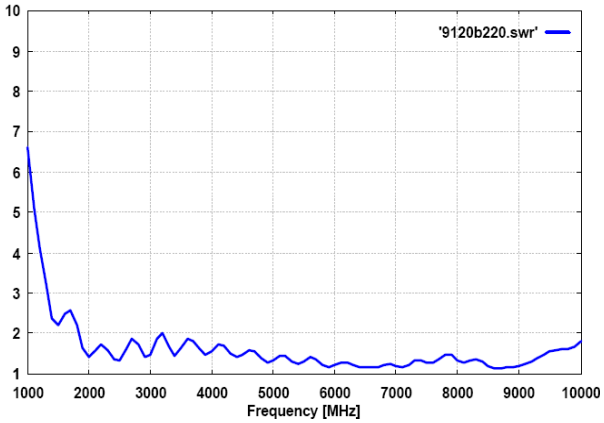

Figure 4: The VSWR data of double ridged horn antenna.

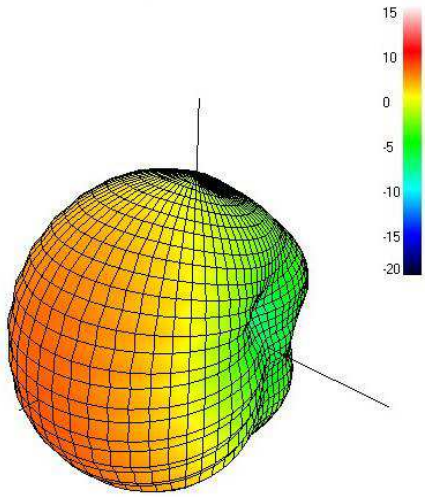

Figure 5: The measured data of 1 GHz radiation pattern.

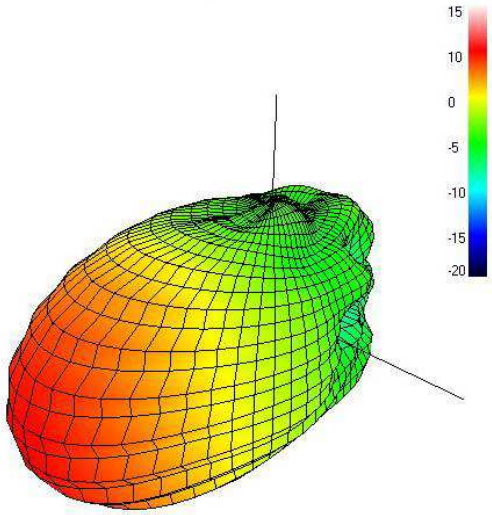

Figure 6: The measured data of 2 GHz radiation pattern.

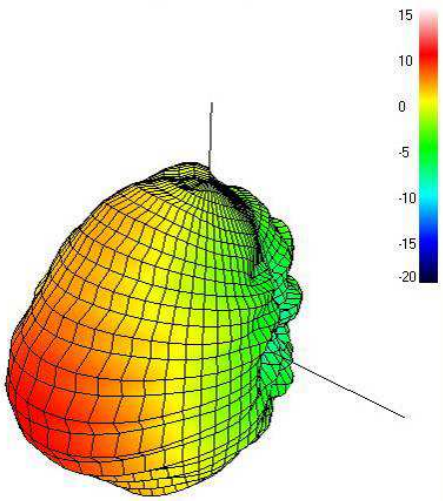

Figure 7: The measured data of 3 GHz radiation pattern.

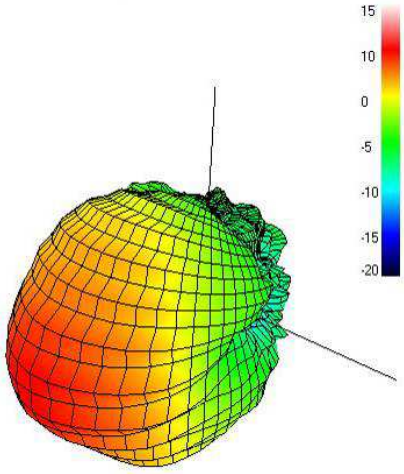

Figure 8: The measured data of 4 GHz radiation pattern.

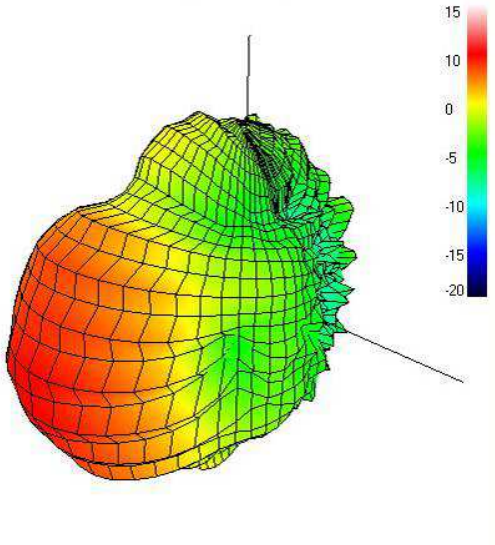

Figure 9: The measured data of 5 GHz radiation pattern.

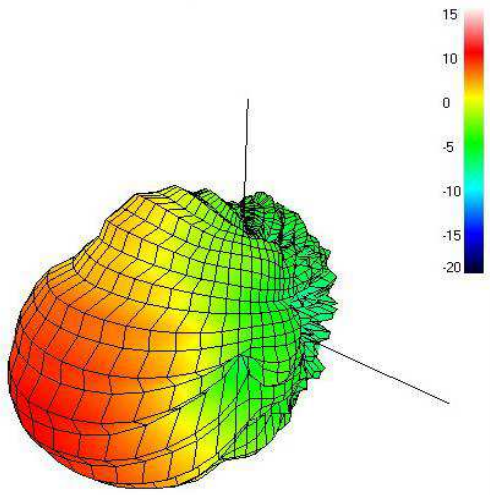

Figure 10: The measured data of 6 GHz radiation pattern.

2. CONCLUSION

The double ridge horn antenna is a broadband antenna that offers excellent performance over the frequency range of 1 GHz to 18 GHz. High radiated efficiency, high gain and low Voltage Standing Wave Ratio (VSWR). Field strength generated under free-space conditions at a separation from the antenna aperture. If environmental reflections are present, this may lead to frequency and height dependent field strengths. The power figures refer to a 50 W source and an unmodulated (cw) signal. An 80% Amplitude Modulation requires a 1.8 times higher voltage, resulting in 3.24 times higher power compared to cw. A field strength increase of factor 10 requires 100 times amplifier-power.

ACKNOWLEDGMENT

The authors would like to thank the Antenna and EMC research laboratory, HTC Corporation, for their assistance in wireless and system integration measurements.

REFERENCES

1. Chen, G.-Y., J.-S. Sun, K. Chang, and Y. D. Chen, "Antenna pattern measurement," *PIERS Proceedings*, Beijing, China, 331–333, March 23–27, 2009.
2. Chen, G.-Y., J.-S. Sun, and Y. D. Chen, "The tapered TEM horn antenna design for EMC and radiation measurement," *2006 The 7th International Symposium on Antennas, Propagation, and EM Theory*, 50–53, Guilin, China, October 2006.
3. Chen, G.-Y., J.-S. Sun, and Y. D. Chen, "The 3D far-field antenna measurement technology for radiation efficiency, mean effective gain and diversity antenna operation," *2006 The 7th International Symposium on Antennas, Propagation, and EM Theory*, 42–45, Guilin, China, October 2006.
4. Sun, J.-S., G.-Y. Chen, K. L. Wu, J. Y. Guo, C. H. Lin, K. K. Tiong, J. H. Wu, Y. D. Chen, and J. C. Huang, "TEM horn antenna design and measurement," *URSI/SRS 2007 Radio Science Conference and Taiwan-Japan Joint Meeting on Antennas and Propagation*, 23, Chung-Li, Taiwan, March 2007.

Novel Dynamic Optical Tweezers Array Generation Using Dark Soliton Control within an Add/Drop Multiplexer

N. Pornsuwancharoen[1], C. Tanaponjarus[2], U. Dunmeekaew[1, 2], and P. P. Yupapin[2]

[1]Nano Photonics Research Group, Department of Electrical Engineering
Faculty of Industry and Technology, Rajamangala University of Technology Isan
Sakhon Nakon Campus, Sakhon Nakon 47160, Thailand
[2]Advance Research Center for Photonics, Faculty of Science
King Mongkut's Institute of Technology Ladkrabang, Bangkok 10520, Thailand

Abstract— We proposes a novel system of the optical tweezers array generation using dark soliton control within and add/drop filter. The dynamic tweezers are generated within an add/drop filter, where the number of tweezers within the add/drop filter can be tuned and amplified. The smallest tuned tweezers width is 0.02 nm is achieved, where the number of tweezers is 10 in an array. We have also theoretically shown that the dynamic tweezers can be controlled and tuned by varies the couple coefficient (κ) between 0.1–0.9 and the radius of ring resonator between 10–20 μm, which is available for trapping and transportation in the communication up-link system via a add/drop filter. In application, the transmission of tweezers with different molecules and wavelengths can be performed within the transmission link, which is available for high density molecular transportation.

1. INTRODUCTION

Optical tweezers are a powerful tool for use in the three-dimensional rotation of and translation (location manipulation) of nano-structures such as micro- and nano-particles as well as living micro-organisms [1]. Many research works have been concentrated on the static tweezers [2–6], which it can not move. The benefit offered by optical tweezers is the ability to interact with nano-scaled objects in a non-invasive manner, i.e., there is no physical contact with the sample, thus preserving many important characteristics of the sample, such as the manipulation of a cell with no harm to the cell. Optical tweezers are now widely used and they are particularly powerful in the field of microbiology [7–9] to study cell–cell interactions, manipulate organelles without breaking the cell membrane and to measure adhesion forces between cells. In this paper, we describe a new concept of developing an optical tweezers source using a dark soliton pulse. The developed tweezers has many potential applications in electron, ion, atom and molecule probing and manipulation as well as DNA probing and transportation. Furthermore, the soliton pulse generator is a simple and compact design, making it more commercially viable. In this paper, we present the theoretical background in the physical model concept, where potential well can be formed by the barrier of optical filed. The change in potential value, i.e., gradient of potential can produce force that can be used to confine/trap atoms/molecule. Furthermore, the change in potential well is still stable in some conditions, which mean that the dynamic optical tweezers is plausible, therefore, the transportation of atoms/molecules in the optical network via a dark soliton being realized in the near future. In application, the high capacity tweezers can be formed by using the tweezers array [10], which is available for high capacity transportation via optical wireless link [11]. In this work, the optical wireless carrier generation is also reviewed.

2. THEORETICAL BACKGROUND

To perform the proposed concept, a bright soliton pulse is introduced into the multi-stage nano ring resonators as shown in Fig. 1, the input optical field (E_{in}) of the bright and dark soliton pulses input are given by an Eqs. (1) and (2) as [11]

$$E_{in}(t) = A \sec h\left[\frac{T}{T_0}\right] \exp\left[\left(\frac{z}{2L_D}\right) - i\omega_0 t\right] \tag{1}$$

$$E_{in}(t) = A \tan h\left[\frac{T}{T_0}\right] \exp\left[\left(\frac{z}{2L_D}\right) - i\omega_0 t\right] \tag{2}$$

where A and z are the optical field amplitude and propagation distance, respectively. T is a soliton pulse propagation time in a frame moving at the group velocity, $T = t - \beta_1 * z$, where β_1 and β_2

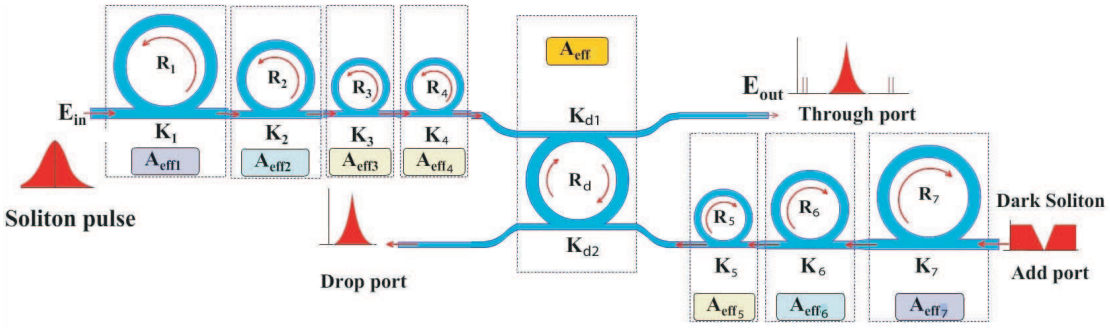

Figure 1: Shows a schematic diagram of the dynamic optical tweezers array.

are the coefficients of the linear and second order terms of Taylor expansion of the propagation constant. $L_D = T_0^2/|\beta_2|$ is the dispersion length of the soliton pulse. T_0 in equation is the initial soliton pulse width. Where t is the soliton phase shift time, and he frequency shift of the soliton is ω_0. This solution describes a pulse that keeps its temporal width invariance as it propagates, and thus is called a temporal soliton. When a soliton peak intensity ($|\beta_2/\Gamma T_0^2|$) is given, then is known. For the soliton pulse in the micro ring device, a balance should be achieved between the dispersion length (L_D) and the nonlinear length ($L_{NL} = (1/\Gamma\phi_{NL})$, where $\Gamma = n_2 * k_0$, is the length scale over which dispersive or nonlinear effects makes the beam becomes wider or narrower. For a soliton pulse, there is a balance between dispersion and nonlinear lengths, hence $L_D = L_{NL}$.

We assume that the nonlinearity of the optical ring resonator is of the Kerr-type, i.e., the refractive index is given by

$$n = n_0 + n_2 I = n_0 + \left(\frac{n_2}{A_{eff}}\right) P, \tag{3}$$

where n_0 and n_2 are the linear and nonlinear refractive indexes, respectively. I and P are the optical intensity and optical power, respectively. The effective mode core area of the device is given by A_{eff}. For the microring and nanoring resonators, the effective mode core areas range from 0.10 to 0.50 μm^2 [12].

When a Gaussian pulse is input and propagated within a fiber ring resonator, the resonant output is formed, thus, the normalized output of the light field is the ratio between the output and input fields ($E_{out}(t)$ and $E_{in}(t)$) in each roundtrip, which can be expressed as [13]

$$\left|\frac{E_{out}(t)}{E_{in}(t)}\right|^2 = (1-\gamma)\left[1 - \frac{\left(1-(1-\gamma)x^2\right)\kappa}{\left(1-x\sqrt{1-\gamma}\sqrt{1-\kappa}\right)^2 + 4x\sqrt{1-\gamma}\sqrt{1-\kappa}\sin^2\left(\frac{\phi}{2}\right)}\right] \tag{4}$$

Equation (3) indicates that a ring resonator in the particular case is very similar to a Fabry-Perot cavity, which has an input and output mirror with a field reflectivity, $(1-\kappa)$, and a fully reflecting mirror. k is the coupling coefficient, and $x = \exp(-\alpha L/2)$ represents a roundtrip loss coefficient, $\phi_0 = kLn_0$ and $\phi_{NL} = kL(\frac{n_2}{A_{eff}})P$ are the linear and nonlinear phase shifts, $k = 2\pi/\lambda$ is the wave propagation number in a vacuum. Where L and α are a waveguide length and linear absorption coefficient, respectively. In this work, the iterative method is introduced to obtain the results as shown in Equation (4), similarly, when the output field is connected and input into the other ring resonators.

The input optical field as shown in Equation (1), i.e., a Gaussian pulse, is input into a nonlinear microring resonator. By using the appropriate parameters, the chaotic signal is obtained by using Equation (3). To retrieve the signals from the chaotic noise, we propose to use the add/drop device with the appropriate parameters. This is given in details as followings. The optical outputs of a ring resonator add/drop filter can be given by the Equations (5) and (6).

$$\left|\frac{E_t}{E_{in}}\right|^2 = \frac{(1-\kappa_1) - 2\sqrt{1-\kappa_1}\cdot\sqrt{1-\kappa_2}e^{-\frac{\alpha}{2}L}\cos(k_n L) + (1-\kappa_2)e^{-\alpha L}}{1 + (1-\kappa_1)(1-\kappa_2)e^{-\alpha L} - 2\sqrt{1-\kappa_1}\cdot\sqrt{1-\kappa_2}e^{-\frac{\alpha}{2}L}\cos(k_n L)} \tag{5}$$

and

$$\left|\frac{E_d}{E_{in}}\right|^2 = \frac{\kappa_1\kappa_2 e^{-\frac{\alpha}{2}L}}{1+(1-\kappa_1)(1-\kappa_2)e^{-\alpha L} - 2\sqrt{1-\kappa_1}\cdot\sqrt{1-\kappa_2}e^{-\frac{\alpha}{2}L}\cos(k_n L)} \tag{6}$$

where E_t and E_d represents the optical fields of the throughput and drop ports respectively. The transmitted output can be controlled and obtained by choosing the suitable coupling ratio of the ring resonator, which is well derived and described by reference [14]. Where $\beta = kn_{eff}$ represents the propagation constant, n_{eff} is the effective refractive index of the waveguide, and the circumference of the ring is $L = 2\pi R$, here R is the radius of the ring. In the following, new parameters will be used for simplification, where $\phi = \beta L$ is the phase constant. The chaotic noise cancellation can be managed by using the specific parameters of the add/drop device, which the required signals at the specific wavelength band can be filtered and retrieved. κ_1 and κ_2 are coupling coefficient of add/drop filters, $k_n = 2\pi/\lambda$ is the wave propagation number for in a vacuum, and the waveguide (ring resonator) loss is $\alpha = 0.5\,\mathrm{dBmm}^{-1}$. The fractional coupler intensity loss is $\gamma = 0.1$. In the case of add/drop device, the nonlinear refractive index is neglected.

3. DYNAMIC TWEEZERS ARRAY

From Fig. 2 shows the uplink carrier signal at 2 GHz generated by the micro ring resonators, where (a) chaotic signal of ring resonator, the radius of the first ring (R_1) is 10 µm, and the coupling coefficient (κ_1) is 0.9713, (b) the radius of the second ring (R_2) is 10 µm, the coupling coefficient (κ_2) is 0.9723, (c) the radius of the third ring (R_3) is 10 µm, the couple coefficient (κ_3) is 0.9768, and (d) the radius of the fourth ring (R_4) is 10 µm, the coupling coefficient (κ_4) is 0.9768. Fig. 3 shows the optical tweezers array before mixing using Add/drop multiplexer, where (a) input power is 1 W, (b) the radius of the first ring (R_5) is 11.5 µm, the coupling coefficient (κ_5) is 0.90, (c) the radius of the second ring (R_6) is 12 µm, the coupling coefficient (κ_6) is 0.50, and (d) the radius of the third ring (R_7) is 16 µm, the coupling coefficient (κ_7) is 0.45. Fig. 4 shows the expansion of the output of $R_3(d)$ with the tweezers width is 4.025 to 4.075 nm, and free spectrum range is 0.050 nm within the period of 100 ns. Fig. 5 shows the expansion of the output of $R_3(d)$ with the tweezers width is 5.925 to 5.945 nm, and free spectrum range is 0.020 nm within the period of 100 ns.

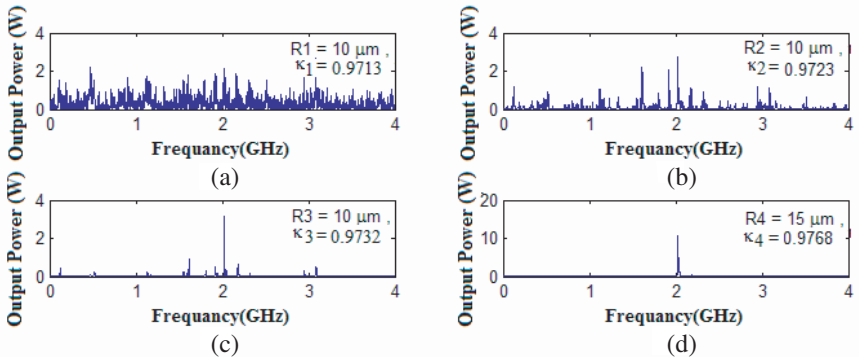

Figure 2: Shows the uplink carrier signal at 2 GHz generated by the micro ring resonators.

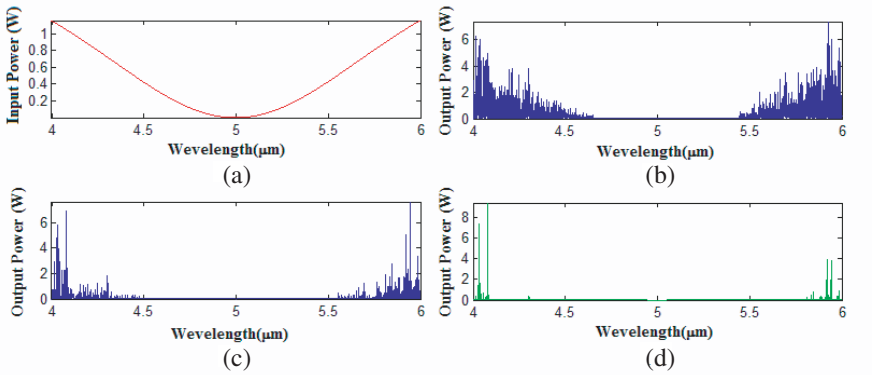

Figure 3: Shows the tweezers array before mixing using add/drop multiplexer.

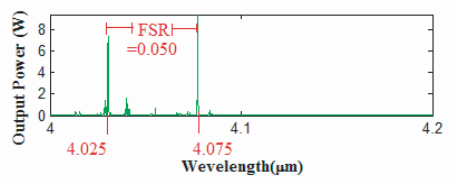

Figure 4: Shows the expansion of the output of $R_3(d)$ with the tweezers.

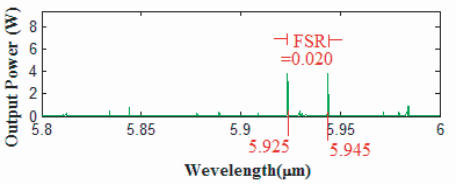

Figure 5: Shows the expansion of the output of $R_3(d)$ with the tweezers.

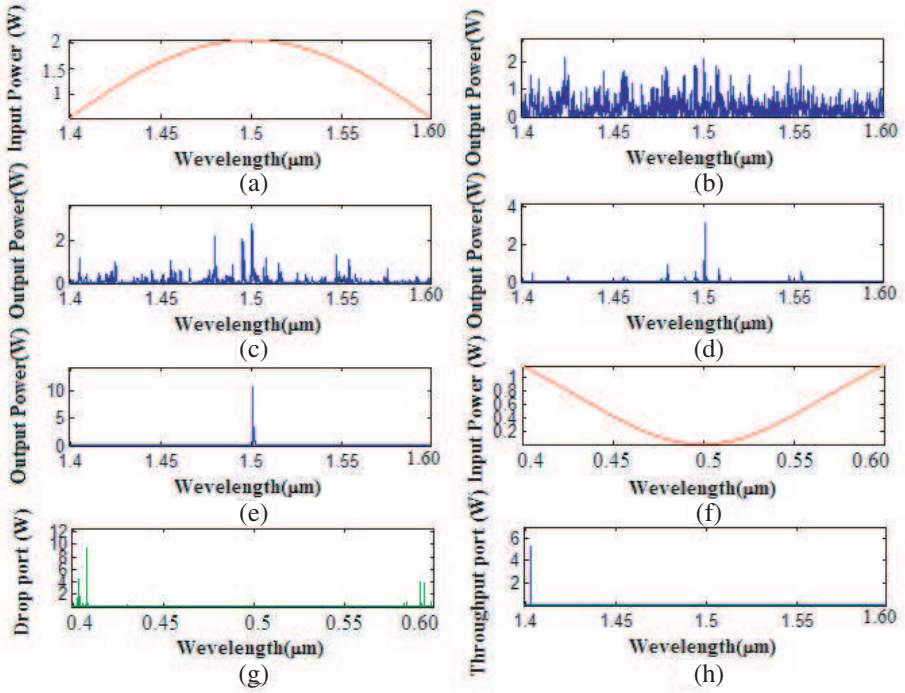

Figure 6: Shows the result of add/drop multiplexing with the carrier frequency is 2 GHz, the center wavelength is 1.5 μm, and the array tweezers between is 551 to 554 nm.

Figure 6 shows the results of (a) soliton input power which is 2 W, (b) The chaotic signal of ring resonator and the radius with the first ring (R_1) is 10 μm, and the coupling coefficient (κ_1) is 0.9713, (c) the radius of the second ring (R_2) is 10 μm, and the coupling coefficient (κ_2) is 0.9723, (d) the radius of the third ring (R_3) is 10 μm, and the coupling coefficient (κ_3) is 0.9768, (e) the radius of the fourth ring (R_4) is 10 μm, and the coupling coefficient (κ_4) is 0.9768, (f) input signal of dark soliton with the center wavelength is at 500 nm, (g) the dynamic optical tweezers array ranges between 0.410–0.412 μm, and 0.591–0.592 μm, (h) the output signal at throughput port with the center wavelength is at 1.5 μm, and the radius of add/drop filter (R_d) is 50 μm, the coupling coefficient of add/drop filter is $\kappa_{d1} = \kappa_{d2} = 0.5$.

4. CONCLUSION

We have presented the achievement of the dynamic optical tweezers array generation by using microring resonator system, whereas the free spectrum range obtained is between 0.02–0.05 nm, which is shown the of dynamic optical tweezers array function. In applications, the small optical tweezes system can be employed, where the multi-tweezers can be generated and controlled. This is allowed to use for multi molecules or atoms transportation via the optical wireless link [11]. Finally, we claimed this system is the novel design for dynamic optical tweezers array by using dark soliton control within an add/drop multiplexer, which is a simple technique.

ACKNOWLEDGMENT

This project is supported and granted by the Thailand Research Fund (TRF). The authors are within the Nano Photonic Research Group (NPRG), Rajamangala University of Technology Isan,

Sakhon-Nakon Campus and Advance Research Center for Photonics (ARCP), Faculty of Science King Mongkut's Institute of Technology Ladkrabang, Bangkok, Thailand.

REFERENCES

1. Ashkin, A., J. M. Dziedzic, J. E. Bjorkholm, and S. Chu, "Observation of a single-beam gradient force optical trap for dielectric particles," *Opt. Lett.*, Vol. 11, 288–290, 1986.
2. Eriksen, R. L., V. R. Daria, and J. Glückstad, "Fully dynamic multiple-beam optical tweezers," *Opt. Express*, Vol. 10, 597–602, 2002.
3. Rodrigo, P. J., V. R. Daria, and J. Glückstad, "Real-time interactive optical micromanipulation of a mixture of high- and low-index particles," *Opt. Express*, Vol. 12, 1417–1425, 2004.
4. Liesener, J., M. Reicherter, T. Haist, and H. J. Tiziani, "Multi-functional optical tweezers using computer generated holograms," *Opt. Commun.*, Vol. 185, 77–82, 2000.
5. Curtis, J. E., B. A. Koss, and D. G. Grier, "Dynamic holographic optical tweezers," *Opt. Commun.*, Vol. 207, 169–175, 2002.
6. Hossack, W. J., E. Theofanidou, J. Crain, K. Heggarty, and M. Birch, "High-speed holographic optical tweezers using a ferroelectric liquid crystal microdisplay," *Opt. Express*, Vol. 11, 2053–2059, 2003.
7. Boyer, V., R. M. Godun, G. Smirne, D. Cassettari, C. M. Chandrashekar, A. B. Deb, Z. J. Laczik, and C. J. Foot, "Dynamic manipulation of Bose-Einstein condensates with a spatial light modulator," *Phys. Rev. A*, Vol. 73, 031402(R), 2006.
8. Carpentier, A. V., J. Belmonte-Beitia, H. Michinel, and V. M. Perez-Garcia, "Laser tweezers for atomic solitons," *J. of Mod. Opt.*, Vol. 55, No. 17, 2819–2829, 2008.
9. Milner, V., J. L. Hanssen, W. C. Campbell, and M. G. Raizen, "Optical billiards for atoms," *Phys. Rev. Lett.*, Vol. 86, 1514–1516, 2001.
10. Korda, P. T., M. B. Taylor, and D. G. Grier, "Kinetically locked-in colloidal transport in an array of optical tweezers," *Phys. Rev. Lett.*, Vol. 89, 128301, 2002.
11. Mithata, S., N. Pornsuwancharoen, and P. P. Yupapin, "A simultaneous short wave and millimeter wave generation using a soliton pulse within a nano-waveguide," *IEEE Photon. Technol. Lett.*, Vol. 21, No. 13, 932–934, 2009.
12. Kokubun, Y., Y. Hatakeyama, M. Ogata, S. Suzuki, and N. Zaizen, "Fabrication technologies for vertically coupled micro ring resonator with multilevel crossing busline and ultracompact-ring radius," *IEEE J. Sel. Top. Quantum Electron.*, Vol. 11, 4–10, 2005.
13. Yupapin, P. P. and W. Suwancharoen, "Chaotic signal generation and cancellation using a microring resonator incorporating an optical add/drop multiplexer," *Opt. Commun.*, Vol. 280, No. 2, 343–350, 2007.
14. Yupapin, P. P., P. Saeung, and C. Li, "Characteristics of complementary ring-resonator add/drop filters modeling by using graphical approach," *Opt. Commun.*, Vol. 272, 81–86, 2007.